Transactions of the ASME, Journal of Heat Transfer (ISSN 0022-1481) is published monthly by The American Society of Mechanical Engineers, Three Park Avenue, New York, NY 10016. Periodicals postage paid at New York, NY and additional mailing offices. POSTMASTER: Send address changes to Transactions of the ASME, Journal of Heat Transfer, c/o THE AMERICAN SOCIETY OF MECHANICAL ENGINEERS, 22 Law Drive, Box 2300, Fairfield, NJ 07007-2300. **CHANGES OF ADDRESS** must be received at Society headquarters seven weeks before they are to be effective. Please send old label and new address. **STATEMENT from By-Laws.** The Society shall not be responsible for statements or opinions advanced in papers or ... printed in its publications (B7.1, Para. 3).

Journal of Heat Transfer

Published Monthly by ASME

VOLUME 132 • NUMBER 3 • MARCH 2010

RESEARCH PAPERS

(Contents continued on inside back cover)

This journal is printed on acid-free paper, which exceeds the ANSI Z39.48-1992 specification for permanence of paper and library materials. ♾™
♻ 85% recycled content, including 10% post-consumer fibers.

Journal of Heat Transfer **Volume 132, Number 3** **MARCH 2010**

The ASME Journal of Heat Transfer is abstracted and indexed in the following:

Applied Science and Technology Index, Chemical Abstracts, Chemical Engineering and Biotechnology Abstracts (Electronic equivalent of Process and Chemical Engineering), Civil Engineering Abstracts, Compendex (The electronic equivalent of Engineering Index), Corrosion Abstracts, Current Contents, E & P Health, Safety, and Environment, Ei EncompassLit, Engineered Materials Abstracts, Engineering Index, Enviroline (The electronic equivalent of Environment Abstracts), Environment Abstracts, Environmental Engineering Abstracts, Environmental Science and Pollution Management, Fluidex, Fuel and Energy Abstracts, Index to Scientific Reviews, INSPEC, International Building Services Abstracts, Mechanical & Transportation Engineering Abstracts, Mechanical Engineering Abstracts, METADEX (The electronic equivalent of Metals Abstracts and Alloys Index), Petroleum Abstracts, Process and Chemical Engineering, Referativnyi Zhurnal, Science Citation Index, SciSearch (The electronic equivalent of Science Citation Index), Theoretical Chemical Engineering

Analysis of Bioheat Transport Through a Dual Layer Biological Media

Shadi Mahjoob

Kambiz Vafai[1]
Fellow ASME
e-mail: vafai@engr.ucr.edu

Department of Mechanical Engineering,
University of California,
Riverside, CA 92521

A comprehensive analysis of bioheat transport through a double layer and multilayer biological media is presented in this work. Analytical solutions have been developed for blood and tissue phase temperatures and overall heat exchange correlations, incorporating thermal conduction in tissue and vascular system, blood-tissue convective heat exchange, metabolic heat generation, and imposed heat flux, utilizing both local thermal nonequilibrium and equilibrium models in porous media theory. Detailed solutions as well as Nusselt number distributions are given, for the first time, for two primary conditions, namely, isolated core region and uniform core temperature. The solutions incorporate the pertinent effective parameters for each layer, such as volume fraction of the vascular space, ratio of the blood, and the tissue matrix thermal conductivities, interfacial blood-tissue heat exchange, tissue/organ depth, arterial flow rate and temperature, body core temperature, imposed hyperthermia heat flux, metabolic heat generation, and blood physical properties. Interface temperature profiles are also obtained based on the continuity of temperature and heat flux through the interface and the physics of the problem. Comparisons between these analytical solutions and limiting cases from previous works display an excellent agreement. These analytical solutions establish a comprehensive presentation of bioheat transport, which can be used to clarify various physical phenomena as well as establishing a detailed benchmark for future works in this area.
[DOI: 10.1115/1.4000060]

Keywords: bioheat transfer, biological tissue/organ, hyperthermia, porous media, multilayer media

1 Introduction

Hyperthermia treatment is recognized as one of the main cancer therapies following surgery, chemotherapy, and radiation techniques. Understanding thermal transport and temperature distribution within biological tissues and body organs are important therapeutic aspects related to this treatment [1,2]. This technique is also utilized for eradication or reduction in benign tumors, repair of sports injuries, modification and remodeling of a targeted tissue [3], gene therapy, and immunotherapy (vaccination) [4]. In hyperthermia, the tumor cells will be heated to a therapeutic value, typically 40°C–45°C, to damage or kill the cancer cells [5,6]. Although it has been known for many years that fever can damage the cancer cells, hyperthermia technique is more recently being developed as a cancer treatment by controlling and focusing the heat on the cancer cells. This technique is being utilized for several types of cancer [7].

In contrast to healthy cells, a tumor is a tightly packed body of cells in which blood circulation is restricted. Heat can cut off the oxygen and vital nutrients from the abnormal cells, resulting in a breakdown in the tumor's vascular system and destruction of the cell's metabolism and subsequent devastation of the tumor cells. In addition, heat causes the formation of certain proteins in the diseased cancer cells, the so-called heat shock proteins, which appear on the surface of the degenerated cells. The body's immune system detects these proteins as extraneous cells, making the abnormal cells visible to the immune system.

Hyperthermia technique also improves the efficiency of other cancer therapies such as chemotherapy and radiotherapy [4,8,9]. Insolated cells, which would not respond to chemotherapy or radiation alone, would be subjected to heat treatment. Hyperthermia, in conjunction with chemotherapy, causes the drug to penetrate deeper into the tumor while augmenting the efficacy of the drug delivered to the tumor. Hyperthermia treatment can be utilized either on the whole body or locally targeting the cancer cells, utilizing warm water bath balloons and blankets, hot wax, inductive coils (similar to those in electric blankets), thermal chambers, ultra-high frequency sound waves, microwave, and laser [7].

Heat transport through biological tissues, represented by bioheat models, involves thermal conduction in tissue and vascular system, blood-tissue convection, and perfusion (through capillary tubes within the tissues) and also metabolic heat generation. Assuming local thermal equilibrium between the blood and the tissue, Pennes [10] represented one of the early and simplified bioheat equations. This model has been further developed by others such as Charny [11], Wulff [12], Klinger [13], Chen and Holmes [14], Weinbaum et al. [15–17], Mitchell and Myers [18], Keller and Seilder [19], Chen and Xu [20], Baish et al. [21,22], and Abraham and Sparrow [23]. Description of the established bioheat transport models can be found in the literature [11,24–26].

Advantages of utilizing porous media theory in modeling bioheat transfer, due to fewer assumptions as compared with different established bioheat transfer models, are stressed by Khanafer and Vafai [26], Nakayama and Kuwahara [27], Khaled and Vafai [28], and Mahjoob and Vafai [7]. The biological structure can be treated as a blood saturated porous matrix including cells and interstices, the so-called tissue. Utilizing the porous media theory, nonthermal equilibrium between the blood and the tissue is addressed and the blood-tissue convective heat exchange is taken into account. Volume averaging over each of the blood and tissue phases results in an energy equation for each individual phase [29–37,7], known as the local thermal nonequilibrium model. The volume averaging

[1]Corresponding author.
Contributed by the Heat Transfer Division of ASME for publication in the JOURNAL OF HEAT TRANSFER. Manuscript received June 10, 2009; final manuscript received August 12, 2009; published online December 30, 2009. Editor: Yogesh Jaluria.

over a representative elementary volume containing both the blood and tissue phases results in a local thermal equilibrium model referred to as the one equation model.

One of the shortcomings in most bioheat studies is modeling the target tissue/organ as a single tissue/organ with the same tissue properties. This type of modeling may not predict precisely heat transport through tissue layers in which there is a considerable variation in properties of the adjacent layers. As such, there would be a need to develop and utilize bioheat model for a dual layer. Dual layer bioheat modeling is also important relative to skin bioheat transport and burn injuries [38,39]. In addition, in hyperthermia treatment, utilizing a two layer model (consisting of cancerous and normal tissue layers) gives a more accurate prediction of temperature profile and heat transport through these layers [40].

Due to the importance of accurate prediction of temperature profile in tissues/organs in thermal therapies such as hyperthermia, heat transport through multilayer biological tissues has been investigated in this work. Mahjoob and Vafai [7] previously developed, for the first time, comprehensive analytical solutions for tissue and blood temperature profiles and heat transfer correlations for a single layer tissue subject to an imposed heat flux. In this work, bioheat transport through dual layer tissues subject to an imposed heat flux is investigated comprehensively. Precise correlations are obtained for the first time for a two layer media, which can be extended to a multilayer media.

Utilizing the local thermal nonequilibrium model of porous media theory, exact solutions for the tissue and blood temperature distributions in each layer are established, for the first time, for two primary tissue/organ models representing isolated and uniform temperature conditions. Each layer can have its own properties independent of the other layer. These exact solutions can be utilized for different types of tissues and organs considering each layer's effective parameters such as the vascular volume fraction, tissue matrix permeability and size, blood pressure and velocity, metabolic heat generation, and also imposed heat flux and body core temperature. As a result, the current models for temperature prediction during thermal therapies can be modified to present a more accurate temperature distribution within healthy and diseased cells.

2 Modeling and Formulation

2.1 Problem Description. Biological media usually consist of blood vessels, cells, and interstitial space, which can be categorized as vascular and extravascular regions (Fig. 1(*a*)). As such, a biological structure can be modeled as a porous matrix, including cells and interstitial space, called tissue, in which the blood infiltrates through. In this work, a dual layer, which can be expanded to a multilayer, biological media subject to an imposed heat flux, as in hyperthermia, while incorporating blood and tissue local heat exchange, is investigated. The blood and tissue temperature profiles in each layer are established analytically, incorporating the effects of the imposed heat flux, blood and tissue physical properties, arterial blood velocity, volume fraction of the vascular space and geometrical properties of the biological structure, internal heat generation within the tissue (e.g., metabolic heat generation) at each layer, and the heat penetration depth. The analysis is performed for two primary conditions, namely, isolated core region and uniform core temperature conditions. For the first model, a thermally isolated boundary condition exists at a depth of (D_1+D_2) from the surface of the tissue, where D_1 is the thickness of the layer exposed to the heat flux and D_2 is the thickness of the adjacent layer. This model is also applicable as a symmetry thermal boundary condition, in which the heat flux is imposed from both sides of the organ (Fig. 1(*b*)). The second primary model is based on the physical representation of the core tissue/organ at a prescribed temperature value at depth (D_1+D_2) through imposition of a uniform temperature at that depth. Flow is considered to be hydraulically and thermally developed. Natural convection and radiation are assumed to be negligible and thermodynamic properties of the tissue and blood are considered to be temperature independent over the range of temperature variations considered in bioheat transport applications.

2.2 Physical Description of Governing Equations and Boundary Conditions. The anatomic structure is modeled as a porous medium consisting of the blood and the tissue (solid matrix) phases. The governing energy equations for the blood and tissue phases incorporating internal heat sources (e.g., metabolic reactions) and local thermal nonequilibrium conditions, developed based on the theory of porous media [26–37], are represented in Ref. [7]. The imposed heat flux at the organ's surface can be represented under the local thermal nonequilibrium conditions, in which the flux is divided between the two tissue and blood phases based on their effective thermal conductivity and temperature gradient. The temperature at the tissue/organ surface subject to imposed heat flux is likely to be uniform and the same as those of the tissue solid matrix and the blood adjacent the organ surface [7,33,36,37].

The external heat flux influences the tissue within a depth of D_1+D_2. As discussed earlier, two primary models are investigated for the boundary condition at the depth of D_1+D_2 from the surface, which is subject to a given heat flux. These are the (i) isolated core region and (ii) uniform core temperature (T_c) at a depth (D_1+D_2), as shown in Fig. 1. The value of the uniform temperature (T_c) can be assigned as the body core temperature or a safe temperature so as not to damage the healthy tissues. At the interface of the layers, the continuity of temperature and flux is valid. The tissue and blood temperatures at the interface of the layers $(T_{t,i}$ and $T_{b,i})$ should be evaluated by solving the governing equations in each layer and applying the boundary conditions.

2.3 Normalization. The governing equations are normalized by utilizing the following nondimensional variables (j is a layer indicator, which is either 1 or 2 for the first or second tissue layer, respectively):

$$\eta = \frac{y}{D_1}, \quad \theta_{b,j} = \frac{k_{t,\mathrm{eff},1}(\langle T_{b,j}\rangle^b - T_s)}{q_s D_1}, \quad \theta_{t,j} = \frac{k_{t,\mathrm{eff},1}(\langle T_{t,j}\rangle^t - T_s)}{q_s D_1}$$

$$\Phi_j = \frac{(1-\varepsilon_j)D_1\dot{q}_{\mathrm{gen},j}}{q_s}, \quad \mathrm{Bi}_j = \frac{h_{tb,j}a_{tb,j}D_1^2}{k_{t,\mathrm{eff},1}}, \quad \kappa = \frac{k_{b,\mathrm{eff},1}}{k_{t,\mathrm{eff},1}} \tag{1}$$

$$\xi_t = \frac{k_{t,\mathrm{eff},2}}{k_{t,\mathrm{eff},1}}, \quad \xi_b = \frac{k_{b,\mathrm{eff},2}}{k_{t,\mathrm{eff},1}}, \quad D = \frac{D_1}{D_2}$$

where parameters $\langle T_b\rangle^b$, $\langle T_t\rangle^t$, $k_{b,\mathrm{eff}}$, $k_{t,\mathrm{eff}}$, and ε represent the intrinsic phase average blood and tissue temperatures, blood and tissue effective thermal conductivities, and porosity (the volume fraction of the vascular space), respectively. The blood-tissue interfacial heat transfer coefficient is represented by h_{tb} and the specific surface area by a_{tb}, and $\dot{q}_{\mathrm{gen}}$ is the heat generation within the biological tissue (e.g., metabolic heat generation) [7]. The Biot number Bi in this case represents the ratio of the conduction resistance within the tissue matrix to the thermal resistance associated with the internal convective heat exchange between the tissue matrix and the blood phase.

2.4 Governing Equations and Boundary Conditions. Biological tissues differ from each other in both their porous features and compositions. Therapeutic approaches can be optimized through understanding a range of phenomena including the response of tissues under different physiological conditions. Tissue usually consists of blood vessels, cells, and interstitial space, which can be, categorized as vascular and extravascular regions. The properties of tissues can be approximated based on the assumption that it is a homogeneous porous medium. Direct measurement of the properties of tissues is difficult. Efforts have been devoted to the characterization of the pertinent parameters. The

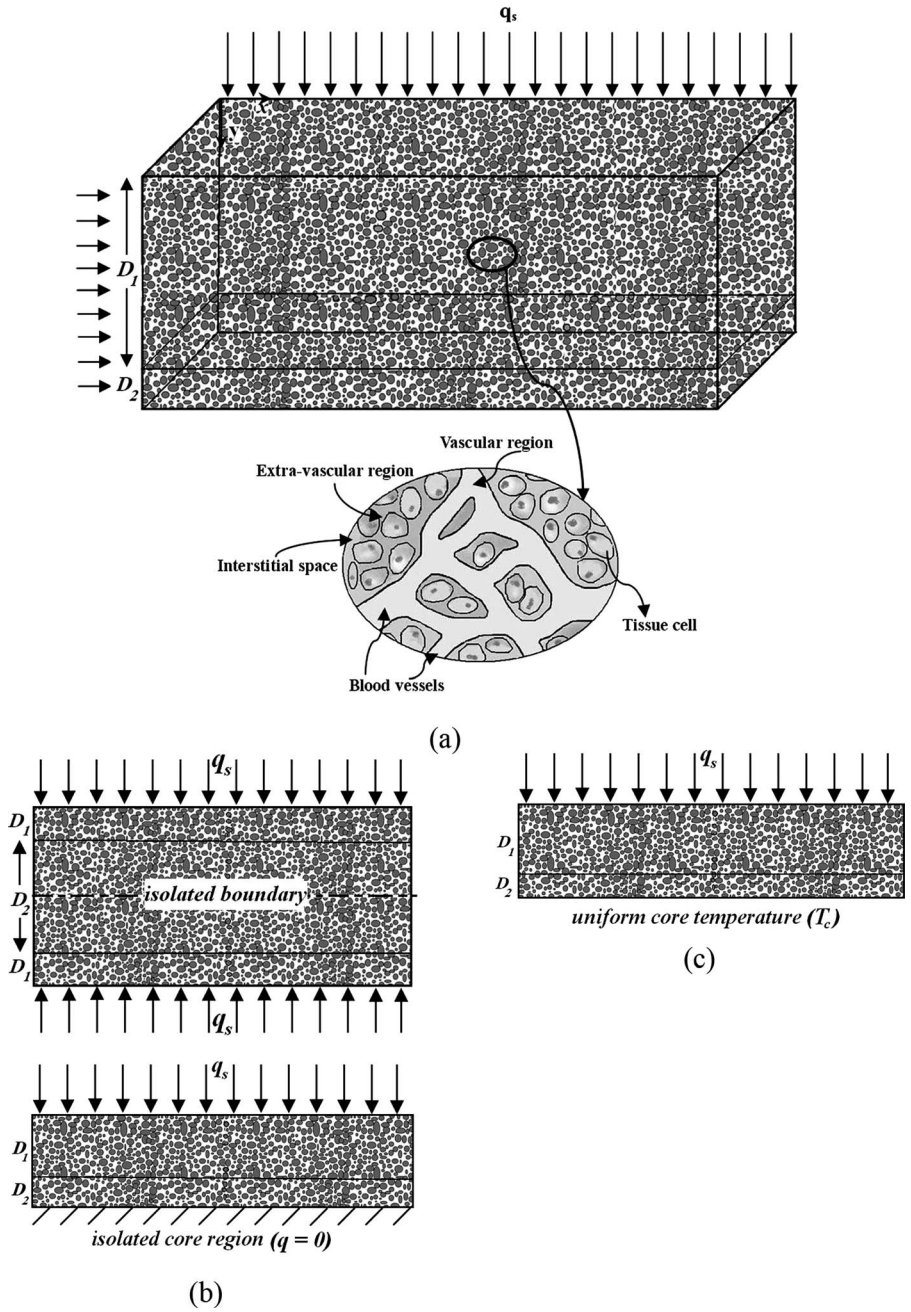

Fig. 1 Schematic diagram of (*a*) the multilayer tissue-vascular system, (*b*) model I (peripheral heat flux or isolated core region), and (*c*) model II (uniform core temperature)

obtained analytical expressions offer a versatile approach by allowing incorporation of variations in the representative volume fraction as well as various physical attributes. Some prior investigations have been performed based on the assumption that the arterial wall layers/tissues are porous structures with physical properties, which can be identified using the pore theory described by Khakpour and Vafai [41]. The properties for various layers can be based upon appropriate pore theory [41,42], fiber matrix models [42–47], and in vivo and in vitro experiments. The governing equations given by Mahjoob and Vafai [7] can be casted as follows:

First layer (with an imposed heat flux at the top):

$$\kappa \frac{\partial^4 \theta_{b,1}}{\partial \eta^4} - \mathrm{Bi}_1(1+k)\left(\frac{\partial^2 \theta_{b,1}}{\partial \eta^2}\right) = \Lambda \tag{2}$$

$$\kappa \frac{\partial^4 \theta_{t,1}}{\partial \eta^4} - \mathrm{Bi}_1(1+k)\left(\frac{\partial^2 \theta_{t,1}}{\partial \eta^2}\right) = \Lambda \tag{3}$$

Second layer (with an isolated or uniform temperature region at the bottom):

$$\xi_b \frac{\partial^4 \theta_{b,2}}{\partial \eta^4} - \mathrm{Bi}_2\left(1+\frac{\xi_b}{\xi_t}\right)\frac{\partial^2 \theta_{b,2}}{\partial \eta^2} = \Lambda' \tag{4}$$

$$\xi_b \frac{\partial^4 \theta_{t,2}}{\partial \eta^4} - \mathrm{Bi}_2\left(1+\frac{\xi_b}{\xi_t}\right)\frac{\partial^2 \theta_{t,2}}{\partial \eta^2} = \Lambda' \tag{5}$$

where in model I (isolated core region)

$$\Lambda = -\mathrm{Bi}_1(1+\kappa f_1 + g_1) \tag{6}$$

$$\Lambda' = \frac{D\mathrm{Bi}_2}{\xi_t}(\kappa f_1 + g_1) \tag{7}$$

and in model II (uniform core temperature)

$$\Lambda = -\mathrm{Bi}_1(1 + \kappa\theta_{b,i} + \theta_{t,i}) \tag{8}$$

$$\Lambda' = \mathrm{Bi}_2\left\{-D^2\left(1 + \frac{\xi_b}{\xi_t}\right)\theta_c + \frac{D(D\xi_b + \kappa)}{\xi_t}\theta_{b,i} + \frac{D(D\xi_t + 1)}{\xi_t}\theta_{t,i}\right\} \tag{9}$$

and

$$f_1 = \left.\frac{\partial\theta_{b,1}}{\partial\eta}\right|_{\eta=1} \tag{10}$$

$$g_1 = \left.\frac{\partial\theta_{t,1}}{\partial\eta}\right|_{\eta=1} \tag{11}$$

$$\theta_c = \frac{k_{t,\mathrm{eff},1}(T_c - T_s)}{q_s D_1} \tag{12}$$

$$\theta_{b,i} = \frac{k_{t,\mathrm{eff},1}(T_{b,i} - T_s)}{q_s D_1} \tag{13}$$

$$\theta_{t,i} = \frac{k_{t,\mathrm{eff},1}(T_{t,i} - T_s)}{q_s D_1} \tag{14}$$

Furthermore, the normalized boundary conditions are presented for each model as follows. Additional boundary conditions to solve the obtained fourth order blood/tissue energy equations (Eqs. (2)–(9)) can be obtained by evaluating the second or third order derivatives of θ_b and θ_t at the boundaries. This results in the following set of boundary conditions for each model:

Boundary conditions:

$$\theta_{b,1}|_{\eta=0} = \theta_{t,1}|_{\eta=0} = 0 \tag{15}$$

$$\theta_{b,1}|_{\eta=1} = \theta_{b,2}|_{\eta=1} = \theta_{b,i} \tag{16}$$

$$\theta_{t,1}|_{\eta=1} = \theta_{t,2}|_{\eta=1} = \theta_{t,i} \tag{17}$$

$$\left.\frac{\partial^2\theta_{t,1}}{\partial\eta^2}\right|_{\eta=0} = -\Phi_1 \tag{18}$$

$$\left.\frac{\partial^2\theta_{t,1}}{\partial\eta^2}\right|_{\eta=1} = -\Phi_1 + \mathrm{Bi}_1(\theta_{t,i} - \theta_{b,i}) \tag{19}$$

$$\left.\frac{\partial^2\theta_{t,2}}{\partial\eta^2}\right|_{\eta=1} = \frac{-1}{\xi_t}(\Phi_2 + \mathrm{Bi}_2(\theta_{b,i} - \theta_{t,i})) \tag{20}$$

$$\kappa\left.\frac{\partial\theta_{b,1}}{\partial\eta}\right|_{\eta=1} + \left.\frac{\partial\theta_{t,1}}{\partial\eta}\right|_{\eta=1} = \xi_b\left.\frac{\partial\theta_{b,2}}{\partial\eta}\right|_{\eta=1} + \xi_t\left.\frac{\partial\theta_{t,2}}{\partial\eta}\right|_{\eta=1} \tag{21}$$

The other normalized boundary conditions for the two primary models are as follows:

For model I (isolated core region):

$$\left.\frac{\partial^2\theta_{b,1}}{\partial\eta^2}\right|_{\eta=0} = \frac{1}{\kappa}(1 + \Phi_1 + \kappa f_1 + g_1) \tag{22}$$

$$\left.\frac{\partial^2\theta_{b,1}}{\partial\eta^2}\right|_{\eta=1} = \frac{1}{\kappa}(1 + \Phi_1 + \kappa f_1 + g_1 + \mathrm{Bi}_1(\theta_{b,i} - \theta_{t,i})) \tag{23}$$

$$\left.\frac{\partial^2\theta_{b,2}}{\partial\eta^2}\right|_{\eta=1} = \frac{1}{\xi_b}(-D(\kappa f_1 + g_1) + \Phi_2 + \mathrm{Bi}_2(\theta_{b,i} - \theta_{t,i})) \tag{24}$$

$$\left.\frac{\partial\theta_{b,2}}{\partial\eta}\right|_{\eta=1+1/D} = \left.\frac{\partial\theta_{t,2}}{\partial\eta}\right|_{\eta=1+1/D} = 0 \tag{25}$$

$$\left.\frac{\partial^3\theta_{b,2}}{\partial\eta^3}\right|_{\eta=1+1/D} = \left.\frac{\partial^3\theta_{t,2}}{\partial\eta^3}\right|_{\eta=1+1/D} = 0 \tag{26}$$

and for model II (uniform core temperature):

$$\left.\frac{\partial^2\theta_{b,1}}{\partial\eta^2}\right|_{\eta=0} = \frac{1}{\kappa}(1 + \Phi_1 + \kappa\theta_{b,i} + \theta_{t,i}) \tag{27}$$

$$\left.\frac{\partial^2\theta_{b,1}}{\partial\eta^2}\right|_{\eta=1} = \frac{1}{\kappa}(1 + \Phi_1 + (\kappa + \mathrm{Bi}_1)\theta_{b,i} + (1 - \mathrm{Bi}_1)\theta_{t,i}) \tag{28}$$

$$\left.\frac{\partial^2\theta_{b,2}}{\partial\eta^2}\right|_{\eta=1} = \frac{1}{\xi_b}[\{\mathrm{Bi}_2 - D(D\xi_b + \kappa)\}\theta_{b,i} - \{\mathrm{Bi}_2 + D(D\xi_t + 1)\}\theta_{t,i} + \Phi_2] + D^2\left(1 + \frac{\xi_t}{\xi_b}\right)\theta_c \tag{29}$$

$$\theta_{b,2}|_{\eta=1+1/D} = \theta_{t,2}|_{\eta=1+1/D} = \theta_c \tag{30}$$

$$\left.\frac{\partial^2\theta_{b,2}}{\partial\eta^2}\right|_{\eta=1+1/D} = -D\left(D + \frac{\kappa}{\xi_b}\right)\theta_{b,i} - \frac{D}{\xi_b}(D\xi_t + 1)\theta_{t,i} + D^2\left(1 + \frac{\xi_t}{\xi_b}\right)\theta_c + \frac{\Phi_2}{\xi_b} \tag{31}$$

$$\left.\frac{\partial^2\theta_{t,2}}{\partial\eta^2}\right|_{\eta=1+1/D} = -\frac{\Phi_2}{\xi_t} \tag{32}$$

2.5 Blood, Tissue, and Surface Temperature Fields. Blood and tissue phase temperature distributions can be obtained by solving the governing equations and utilizing the Neumann and Dirichlet boundary conditions. After a lengthy analysis, the blood and tissue temperature profiles are obtained as follows (for brevity, the volume averaging sign ($\langle\ \rangle$) is dropped).

2.5.1 Model I: Isolated Core Region

2.5.1.1 First layer.

$$\theta_{b,1} = \frac{1}{1+\kappa}\left(\frac{\eta}{2}\{(1 + \kappa f_1 + g_1)\eta - [1 - 2\kappa\theta_{b,i} - 2\theta_{t,i} + \kappa f_1 + g_1]\} - \frac{1 + (1+\kappa)\Phi_1 + \kappa f_1 + g_1}{(1+\kappa)\mathrm{Bi}_1}\left\{1 - \frac{e^{\lambda\eta} + e^{\lambda(1-\eta)}}{1 + e^{\lambda}}\right\} + (\theta_{b,i} - \theta_{t,i})\frac{e^{\lambda(1+\eta)} - e^{\lambda(1-\eta)}}{e^{2\lambda} - 1}\right) \tag{33}$$

$$\theta_{t,1} = \frac{1}{1+\kappa}\left(\frac{\eta}{2}\{(1 + \kappa f_1 + g_1)\eta - [1 - 2\kappa\theta_{b,i} - 2\theta_{t,i} + \kappa f_1 + g_1]\} + \frac{\kappa[1 + (1+\kappa)\Phi_1 + \kappa f_1 + g_1]}{(1+\kappa)\mathrm{Bi}_1}\left\{1 - \frac{e^{\lambda\eta} + e^{\lambda(1-\eta)}}{1 + e^{\lambda}}\right\} - \kappa(\theta_{b,i} - \theta_{t,i})\frac{e^{\lambda(1+\eta)} - e^{\lambda(1-\eta)}}{e^{2\lambda} - 1}\right) \tag{34}$$

where

$$\lambda = \sqrt{\mathrm{Bi}_1(1+\kappa)/\kappa} \tag{35}$$

The blood $\theta_{b,i}$ and tissue $\theta_{t,i}$ temperatures at the interface would be evaluated after obtaining their corresponding temperature profiles in the second layer. Terms f_1 and g_1 can be evaluated based on their definition (Eqs. (10) and (11)) and the obtained blood and tissue temperature profiles in the first layer. This results in

$$f_1 = \frac{1}{1+\kappa}\left(\frac{\{2+(1+\kappa)\Phi_1+2\kappa\theta_{b,i}+2\theta_{t,i}\}(e^{\lambda}-1)}{\lambda\kappa(1+e^{\lambda})} + \lambda(\theta_{b,i}-\theta_{t,i})\frac{e^{2\lambda}+1}{e^{2\lambda}-1}+1+2\kappa\theta_{b,i}+2\theta_{t,i}\right) \quad (36)$$

$$g_1 = \frac{-1}{1+\kappa}\left(\frac{\{2+(1+\kappa)\Phi_1+2\kappa\theta_{b,i}+2\theta_{t,i}\}(e^{\lambda}-1)}{\lambda(1+e^{\lambda})} + \lambda\kappa(\theta_{b,i}-\theta_{t,i})\frac{e^{2\lambda}+1}{e^{2\lambda}-1}-1-2\kappa\theta_{b,i}-2\theta_{t,i}\right) \quad (37)$$

Substituting f_1 and g_1 in Eqs. (33) and (34) gives

$$\theta_{b,1} = \frac{1}{1+\kappa}\left(\eta\{(1+\kappa\theta_{b,i}+\theta_{t,i})\eta-1\}+(\theta_{b,i}-\theta_{t,i})\frac{e^{\lambda(1+\eta)}-e^{\lambda(1-\eta)}}{e^{2\lambda}-1} - \frac{2(1+\kappa\theta_{b,i}+\theta_{t,i})+(1+\kappa)\Phi_1}{(1+\kappa)\mathrm{Bi}_1}\left\{1-\frac{e^{\lambda\eta}+e^{\lambda(1-\eta)}}{1+e^{\lambda}}\right\}\right) \quad (38)$$

$$\theta_{t,1} = \frac{1}{1+\kappa}\left(\eta\{(1+\kappa\theta_{b,i}+\theta_{t,i})\eta-1\}-\kappa(\theta_{b,i}-\theta_{t,i})\frac{e^{\lambda(1+\eta)}-e^{\lambda(1-\eta)}}{e^{2\lambda}-1}+\frac{\kappa[2(1+\kappa\theta_{b,i}+\theta_{t,i})+(1+\kappa)\Phi_1]}{(1+\kappa)\mathrm{Bi}_1} \times\left\{1-\frac{e^{\lambda\eta}+e^{\lambda(1-\eta)}}{1+e^{\lambda}}\right\}\right) \quad (39)$$

As such, the temperature difference between the tissue and blood phases and the blood mean temperature can be written as

$$\Delta\theta_1 = \theta_{t,1}-\theta_{b,1} = (\theta_{b,i}-\theta_{t,i})\frac{e^{\lambda(1-\eta)}-e^{\lambda(1+\eta)}}{e^{2\lambda}-1} + \frac{2(1+\kappa\theta_{b,i}+\theta_{t,i})+(1+\kappa)\Phi_1}{(1+\kappa)\mathrm{Bi}_1}\left\{1-\frac{e^{\lambda\eta}+e^{\lambda(1-\eta)}}{1+e^{\lambda}}\right\} \quad (40)$$

$$\theta_{b,1,m} = \left(\frac{2[2+2\kappa\theta_{b,i}+2\theta_{t,i}+(1+\kappa)\Phi_1]}{\lambda^3\kappa(1+\kappa)}+\frac{\theta_{b,i}-\theta_{t,i}}{\lambda(1+\kappa)}\right)\left(\frac{e^{\lambda}-1}{e^{\lambda}+1}\right) + \frac{-1+2\kappa\theta_{b,i}+2\theta_{t,i}}{6(1+\kappa)}-\frac{1}{\lambda^2\kappa(1+\kappa)} \times\{2+2\kappa\theta_{b,i}+2\theta_{t,i}+(1+\kappa)\Phi_1\} \quad (41)$$

2.5.1.2 Second layer.

$$\theta_{b,2} = \frac{1}{(\xi_b+\xi_t)}\left((1+2\kappa\theta_{b,i}+2\theta_{t,i})\left\{\left(\frac{-D}{2}\eta+D+1\right)\eta-1-\frac{D}{2}+\frac{D\xi_t^2}{\mathrm{Bi}_2(\xi_b+\xi_t)}\right\}+\xi_t\left(\theta_{b,i}-\theta_{t,i}+\frac{\Phi_2}{\mathrm{Bi}_2} - \frac{D\xi_t(1+2\kappa\theta_{b,i}+2\theta_{t,i})}{\mathrm{Bi}_2(\xi_b+\xi_t)}\right)\left(\frac{e^{\lambda'(\eta-1)}+e^{\lambda'(1+(2/D)-\eta)}}{e^{2\lambda'/D}+1}\right) + \xi_b\theta_{b,i}+\xi_t\theta_{t,i}-\frac{\xi_t\Phi_2}{\mathrm{Bi}_2}\right) \quad (42)$$

$$\theta_{t,2} = \frac{1}{(\xi_b+\xi_t)}\left((1+2\kappa\theta_{b,i}+2\theta_{t,i})\left\{\left(\frac{-D}{2}\eta+D+1\right)\eta-1-D/2-\frac{D\xi_b\xi_t}{\mathrm{Bi}_2(\xi_b+\xi_t)}\right\}-\xi_b\left(\theta_{b,i}-\theta_{t,i}+\frac{\Phi_2}{\mathrm{Bi}_2} - \frac{D\xi_t(1+2\kappa\theta_{b,i}+2\theta_{t,i})}{\mathrm{Bi}_2(\xi_b+\xi_t)}\right)\left(\frac{e^{\lambda'(\eta-1)}+e^{\lambda'(1+(2/D)-\eta)}}{e^{2\lambda'/D}+1}\right) + \xi_b\theta_{b,i}+\xi_t\theta_{t,i}+\frac{\xi_b\Phi_2}{\mathrm{Bi}_2}\right) \quad (43)$$

where

$$\lambda' = \sqrt{\frac{\xi_b+\xi_t}{\xi_b\xi_t}\mathrm{Bi}_2} \quad (44)$$

Based on the above results, the temperature difference between the tissue and blood phases for the second layer is obtained as

$$\Delta\theta_2 = \theta_{t,2}-\theta_{b,2} = -\left(\theta_{b,i}-\theta_{t,i}+\frac{\Phi_2}{\mathrm{Bi}_2}-\frac{D\xi_t(1+2\kappa\theta_{b,i}+2\theta_{t,i})}{\mathrm{Bi}_2(\xi_b+\xi_t)}\right) \times\left(\frac{e^{\lambda'(\eta-1)}+e^{\lambda'(1+(2/D)-\eta)}}{e^{2\lambda'/D}+1}\right)-\frac{D\xi_t(1+2\kappa\theta_{b,i}+2\theta_{t,i})}{\mathrm{Bi}_2(\xi_b+\xi_t)}+\frac{\Phi_2}{\mathrm{Bi}_2} \quad (45)$$

Finally, the mean blood temperature for the second layer can be written as

$$\theta_{b,2,m} = D\xi_t\left(\frac{\mathrm{Bi}_2(\xi_b+\xi_t)(\theta_{b,i}-\theta_{t,i})-D\xi_t(1+2\kappa\theta_{b,i}+2\theta_{t,i})+(\xi_b+\xi_t)\Phi_2}{\lambda'\mathrm{Bi}_2(\xi_b+\xi_t)^2}\right)\frac{e^{2\lambda'/D}-1}{e^{2\lambda'/D}+1}+(1+2\kappa\theta_{b,i}+2\theta_{t,i})\left\{\frac{1}{3D(\xi_b+\xi_t)}+\frac{D\xi_t^2}{\mathrm{Bi}_2(\xi_b+\xi_t)^2}\right\} + \frac{\xi_b\theta_{b,i}+\xi_t\theta_{t,i}}{\xi_b+\xi_t}-\frac{\xi_t\Phi_2}{\mathrm{Bi}_2(\xi_b+\xi_t)} \quad (46)$$

2.5.1.3 Interface blood and tissue temperatures. To evaluate the blood and tissue temperatures at the interface of the layers ($\theta_{b,i}$ and $\theta_{t,i}$), two equations are required. One of these equations is obtained based on the fully developed temperature profile subject to a uniform heat flux on one side and an insulated condition on the other side. This results in

$$1+2\kappa\theta_{b,i}+2\theta_{t,i} = \frac{(\rho c_p u_a)_1 D_1 D_2(1-\varepsilon_2)\dot{q}_{\mathrm{gen},2}-(\rho c_p u_a)_2 D_2(q_s+D_1(1-\varepsilon_1)\dot{q}_{\mathrm{gen},1})}{q_s[(\rho c_p u_a)_2 D_2+(\rho c_p u_a)_1 D_1]} \quad (47)$$

The other equation is obtained by utilizing the derived analytical solution for a single layer [7]. The temperature profiles for the blood and tissue phases in a double layer (present work) are taken to be the same as those in a single layer [7], within the distance of D_1 from the surface subject to an imposed heat flux. Rewriting the developed equations for a single layer [7] in the present coordinate system $(0 \le \eta \le 1+(1/D))$ gives

$$\theta_{t,i} - \theta_{b,i} = \frac{\dfrac{D_1}{(D_1+D_2)} + (1+\kappa)\Phi_1}{(1+\kappa)\mathrm{Bi}_1}\left(1 - \frac{e^{\lambda} + e^{\lambda(1+(2D_2/D_1))}}{1+e^{2\lambda(1+(D_2/D_1))}}\right) \tag{48}$$

The above two equations (Eqs. (59) and (60)) result in

$$\theta_{t,i} = \frac{1}{2(1+\kappa)}\left(\frac{(\rho c_p u_a)_1 D_1 D_2(1-\varepsilon_2)\dot{q}_{\mathrm{gen},2} - (\rho c_p u_a)_2 D_2(q_s + D_1(1-\varepsilon_1)\dot{q}_{\mathrm{gen},1})}{q_s[(\rho c_p u_a)_2 D_2 + (\rho c_p u_a)_1 D_1]} + 2\kappa\frac{D_1 + (1+\kappa)(D_1+D_2)\Phi_1}{(1+\kappa)(D_1+D_2)\mathrm{Bi}_1}\left(1 - \frac{e^{\lambda} + e^{\lambda(1+(2D_2/D_1))}}{1+e^{2\lambda(1+(D_2/D_1))}}\right) - 1\right) \tag{49}$$

$$\theta_{b,i} = \frac{1}{2(1+\kappa)}\left\{\frac{(\rho c_p u_a)_1 D_1 D_2(1-\varepsilon_2)\dot{q}_{\mathrm{gen},2} - (\rho c_p u_a)_2 D_2(q_s + D_1(1-\varepsilon_1)\dot{q}_{\mathrm{gen},1})}{q_s[(\rho c_p u_a)_2 D_2 + (\rho c_p u_a)_1 D_1]} - 1\right\} - \frac{D_1 + (1+\kappa)(D_1+D_2)\Phi_1}{(1+\kappa)^2(D_1+D_2)\mathrm{Bi}_1}\left(1 - \frac{e^{\lambda} + e^{\lambda(1+(2D_2/D_1))}}{1+e^{2\lambda(1+(D_2/D_1))}}\right) \tag{50}$$

The dimensional blood mean temperature and the body organ surface temperature, which is subject to an imposed heat flux, are derived to be

$$T_{b,1,m} = \frac{q_s + (1-\varepsilon_1)D_1\dot{q}_{\mathrm{gen},1} + D_2(1-\varepsilon_2)\dot{q}_{\mathrm{gen},2}}{(\rho c_p u_a)_2 D_2 + (\rho c_p u_a)_1 D_1}x + T_{a,1} \tag{51}$$

$$T_{b,2,m} = \frac{q_s + D_1(1-\varepsilon_1)\dot{q}_{\mathrm{gen},1} + (1-\varepsilon_2)D_2\dot{q}_{\mathrm{gen},2}}{(\rho c_p u_a)_2 D_2 + (\rho c_p u_a)_1 D_1}x + T_{a,2} \tag{52}$$

$$\begin{aligned} T_s = &-\frac{q_s D_1}{k_{t,\mathrm{eff},1}}\left(\left(\frac{4(e^{\lambda}-1)}{\lambda^3\kappa(e^{\lambda}+1)} + \frac{1}{3} - \frac{2}{\lambda^2\kappa}\right)\frac{(\rho c_p u_a)_1 D_1(-q_s + D_2(1-\varepsilon_2)\dot{q}_{\mathrm{gen},2}) - (\rho c_p u_a)_2 D_2(2q_s + D_1(1-\varepsilon_1)\dot{q}_{\mathrm{gen},1})}{2q_s(1+\kappa)[(\rho c_p u_a)_2 D_2 + (\rho c_p u_a)_1 D_1]}\right. \\ &\left. + \left(\frac{2[2+(1+\kappa)\Phi_1]}{\lambda^3\kappa(1+\kappa)} - \frac{D_1 + (1+\kappa)(D_1+D_2)\Phi_1}{\lambda(1+\kappa)^2(D_1+D_2)\mathrm{Bi}_1}\left(1 - \frac{e^{\lambda} + e^{\lambda(1+(2D_2/D_1))}}{1+e^{2\lambda(1+(D_2/D_1))}}\right)\right)\left(\frac{e^{\lambda}-1}{e^{\lambda}+1}\right) - \frac{1}{6(1+\kappa)} - \frac{2+(1+\kappa)\Phi_1}{\lambda^2\kappa(1+\kappa)}\right) \\ &+ \frac{q_s + (1-\varepsilon_1)D_1\dot{q}_{\mathrm{gen},1} + D_2(1-\varepsilon_2)q_{\mathrm{gen},2}}{(\rho c_p u_a)_2 D_2 + (\rho c_p u_a)_1 D_1}x + T_{a,1} \end{aligned} \tag{53}$$

The Nusselt number can be represented as

$$\mathrm{Nu}_s = \frac{h_s D_h}{k_{b,\mathrm{eff},1}} = \frac{-2}{\kappa\theta_{b,1,m}}\left(1 + \frac{1}{D}\right) = \frac{\dfrac{-2}{\kappa}\left(1+\dfrac{1}{D}\right)}{\left(\left(\dfrac{2[2+2\kappa\theta_{b,i}+2\theta_{t,i}+(1+\kappa)\Phi_1]}{\lambda^3\kappa(1+\kappa)} + \dfrac{\theta_{b,i}-\theta_{t,i}}{\lambda(1+\kappa)}\right)\left(\dfrac{e^{\lambda}-1}{e^{\lambda}+1}\right) + \dfrac{-1+2\kappa\theta_{b,i}+2\theta_{t,i}}{6(1+\kappa)} - \dfrac{1}{\lambda^2\kappa(1+\kappa)}(2+2\kappa\theta_{b,i}+2\theta_{t,i}+(1+\kappa)\Phi_1)\right)} \tag{54}$$

2.5.2 Model II: Uniform Core Temperature

2.5.2.1 First layer.

$$\theta_{b,1} = \frac{1}{(1+\kappa)}\left(\frac{\kappa\theta_{b,i}+\theta_{t,i}+1}{2}\eta^2 + \frac{\kappa\theta_{b,i}+\theta_{t,i}-1}{2}\eta - \frac{1}{\mathrm{Bi}_1}\left(\frac{\kappa\theta_{b,i}+\theta_{t,i}+1}{1+\kappa} + \Phi_1\right)\left\{1 - \frac{(e^{\lambda\eta}+e^{\lambda(1-\eta)})}{(1+e^{\lambda})}\right\} + (\theta_{b,i}-\theta_{t,i})\frac{e^{\lambda(1+\eta)} - e^{\lambda(1-\eta)}}{e^{2\lambda}-1}\right) \tag{55}$$

$$\theta_{t,1} = \frac{1}{(1+\kappa)}\left(\frac{\kappa\theta_{b,i}+\theta_{t,i}+1}{2}\eta^2 + \frac{\kappa\theta_{b,i}+\theta_{t,i}-1}{2}\eta + \frac{\kappa}{\mathrm{Bi}_1}\left(\frac{\kappa\theta_{b,i}+\theta_{t,i}+1}{1+\kappa} + \Phi_1\right)\left\{1 - \frac{(e^{\lambda\eta}+e^{\lambda(1-\eta)})}{(1+e^{\lambda})}\right\} - \kappa(\theta_{b,i}-\theta_{t,i})\frac{e^{\lambda(1+\eta)} - e^{\lambda(1-\eta)}}{e^{2\lambda}-1}\right) \tag{56}$$

where

$$\lambda = \sqrt{\mathrm{Bi}_1(1+\kappa)/\kappa} \tag{57}$$

and

$$\Delta\theta_1 = \theta_{t,1} - \theta_{b,1} = \frac{1}{\mathrm{Bi}_1}\left(\frac{\kappa\theta_{b,i} + \theta_{t,i} + 1}{1+\kappa} + \Phi_1\right)\left\{1 - \frac{(e^{\lambda\eta} + e^{\lambda(1-\eta)})}{(1+e^{\lambda})}\right\} - (\theta_{b,i} - \theta_{t,i})\frac{e^{\lambda(1+\eta)} - e^{\lambda(1-\eta)}}{e^{2\lambda} - 1} \tag{58}$$

$$\theta_{b,1,m} = \frac{1}{(1+\kappa)}\left((\kappa\theta_{b,i} + \theta_{t,i} + 1)\left(\frac{5}{12} - \frac{1}{\mathrm{Bi}_1(1+\kappa)}\left\{1 - \frac{2(e^{\lambda}-1)}{\lambda(1+e^{\lambda})}\right\}\right) - \frac{\Phi_1}{\mathrm{Bi}_1}\left\{1 - \frac{2(e^{\lambda}-1)}{\lambda(1+e^{\lambda})}\right\} + \frac{(\theta_{b,i} - \theta_{t,i})(e^{\lambda}-1)}{\lambda(1+e^{\lambda})} - \frac{1}{2}\right) \tag{59}$$

2.5.2.2 Second layer.

$$\theta_{b,2} = \frac{A(e^{\lambda'(1+(2/D)-\eta)} - e^{\lambda'(\eta-1)}) + B(e^{\lambda'(1+(1/D)-\eta)} - e^{\lambda'((1/D)-1+\eta)})}{(e^{(2\lambda'/D)} - 1)} + \left(\frac{D^2}{2}\theta_c - \frac{D(D\xi_b+\kappa)}{2(\xi_b+\xi_t)}\theta_{b,i} - \frac{D(D\xi_t+1)}{2(\xi_b+\xi_t)}\theta_{t,i}\right)\eta^2$$
$$+ \left\{D(0.5-D)\theta_c + \frac{\theta_{b,i}}{\xi_b+\xi_t}[-\xi_b D + (D+0.5)(D\xi_b+\kappa_1)] + \frac{\theta_{t,i}}{\xi_b+\xi_t}[-D\xi_t + (D+0.5)(D\xi_t+1)]\right\}\eta$$
$$- \theta_c\left(\frac{D^2\xi_t^2}{\mathrm{Bi}_2(\xi_b+\xi_t)} + \frac{D}{2}(1-D)\right) + \frac{\theta_{b,i}}{\xi_b+\xi_t}\left(\begin{array}{l} -\dfrac{D\xi_b\xi_t(D\xi_b+\kappa)}{\mathrm{Bi}_2(\xi_b+\xi_t)} + \dfrac{D\xi_t(D\xi_b+\kappa)}{\mathrm{Bi}_2} + \\ \xi_b(1+D) - \dfrac{(1+D)}{2}(D\xi_b+\kappa) \end{array}\right)$$
$$+ \frac{\theta_{t,i}}{\xi_b+\xi_t}\left(-\frac{D\xi_b\xi_t(D\xi_t+1)}{\mathrm{Bi}_2(\xi_b+\xi_t)} + \frac{D\xi_t(D\xi_t+1)}{\mathrm{Bi}_2} - \frac{(1+D)}{2}(D\xi_t+1) + \xi_t(1+D)\right) - \frac{\xi_t\Phi_2}{\mathrm{Bi}_2(\xi_b+\xi_t)} \tag{60}$$

$$\theta_{t,2} = \frac{A'(e^{\lambda'(1+(2/D)-\eta)} - e^{\lambda'(\eta-1)}) + B'(e^{\lambda'(1+(1/D)-\eta)} - e^{\lambda'((1/D)-1+\eta)})}{(e^{(2\lambda'/D)} - 1)} + \left(\frac{D^2}{2}\theta_c - \frac{D(D\xi_b+\kappa)}{2(\xi_b+\xi_t)}\theta_{b,i} - \frac{D(D\xi_t+1)}{2(\xi_b+\xi_t)}\theta_{t,i}\right)\eta^2$$
$$+ \left\{D(0.5-D)\theta_c + \frac{\theta_{b,i}}{\xi_b+\xi_t}[-\xi_b D + (D+0.5)(D\xi_b+\kappa_1)] + \frac{\theta_{t,i}}{\xi_b+\xi_t}[-D\xi_t + (D+0.5)(D\xi_t+1)]\right\}\eta + \theta_c\left(\frac{D^2\xi_b\xi_t}{\mathrm{Bi}_2(\xi_b+\xi_t)} + \frac{D}{2}(D-1)\right)$$
$$- \frac{\theta_{b,i}}{\xi_b+\xi_t}\left(\begin{array}{l} \dfrac{D\xi_b\xi_t(D\xi_b+\kappa)}{\mathrm{Bi}_2(\xi_b+\xi_t)} + \dfrac{D(D\xi_b+\kappa)}{2} - \\ \xi_b(1+D) + \dfrac{D\xi_b+\kappa}{2} \end{array}\right) - \frac{\theta_{t,i}}{\xi_b+\xi_t}\left(\frac{D\xi_b\xi_t(D\xi_t+1)}{\mathrm{Bi}_2(\xi_b+\xi_t)} + \frac{D(D\xi_t+1)}{2} + \frac{D\xi_t+1}{2} - \xi_t(1+D)\right) + \frac{\xi_b\Phi_2}{\mathrm{Bi}_2(\xi_b+\xi_t)} \tag{61}$$

$$\Delta\theta_2 = \theta_{t,2} - \theta_{b,2} = \frac{A''(e^{\lambda'(1+(2/D)-\eta)} - e^{\lambda'(\eta-1)}) + B''(e^{\lambda'(1+(1/D)-\eta)} - e^{\lambda'((1/D)-1+\eta)})}{(e^{(2\lambda'/D)} - 1)} + \frac{\xi_t D^2}{\mathrm{Bi}_2}\theta_c - \frac{D\xi_t(D\xi_b+\kappa)}{\mathrm{Bi}_2(\xi_b+\xi_t)}\theta_{b,i} - \frac{D\xi_t(D\xi_t+1)}{\mathrm{Bi}_2(\xi_b+\xi_t)}\theta_{t,i} + \frac{\Phi_2}{\mathrm{Bi}_2} \tag{62}$$

where

$$A = \frac{\xi_t}{\xi_b+\xi_t}\left\{\frac{\xi_t D^2}{\mathrm{Bi}_2}\theta_c + \left(1 - \frac{D\xi_t(D\xi_b+\kappa)}{\mathrm{Bi}_2(\xi_b+\xi_t)}\right)\theta_{b,i} - \left(1 + \frac{D\xi_t(D\xi_t+1)}{\mathrm{Bi}_2(\xi_b+\xi_t)}\right)\theta_{t,i} + \frac{\Phi_2}{\mathrm{Bi}_2}\right\} \tag{63}$$

$$B = \frac{\xi_t}{(\xi_b+\xi_t)\mathrm{Bi}_2}\left\{-\xi_t D^2\theta_c + \frac{D\xi_t(D\xi_b+\kappa)}{(\xi_b+\xi_t)}\theta_{b,i} + \frac{D\xi_t(D\xi_t+1)}{(\xi_b+\xi_t)}\theta_{t,i} - \Phi_2\right\} \tag{64}$$

$$A' = \frac{\xi_t}{\xi_b+\xi_t}\left\{-\frac{\xi_b D^2}{\mathrm{Bi}_2}\theta_c + \left(-\frac{\xi_b}{\xi_t} + \frac{D\xi_b(D\xi_b+\kappa)}{\mathrm{Bi}_2(\xi_b+\xi_t)}\right)\theta_{b,i} + \left(\frac{\xi_b}{\xi_t} + \frac{D\xi_b(D\xi_t+1)}{\mathrm{Bi}_2(\xi_b+\xi_t)}\right)\theta_{t,i} - \frac{\xi_b\Phi_2}{\mathrm{Bi}_2\xi_t}\right\} \tag{65}$$

$$B' = \frac{\xi_t}{\xi_b+\xi_t}\left\{\frac{\xi_b D^2}{\mathrm{Bi}_2}\theta_c - \frac{D\xi_b(D\xi_b+\kappa)}{\mathrm{Bi}_2(\xi_b+\xi_t)}\theta_{b,i} - \frac{D\xi_b(D\xi_t+1)}{\mathrm{Bi}_2(\xi_b+\xi_t)}\theta_{t,i} + \frac{\xi_b\Phi_2}{\mathrm{Bi}_2\xi_t}\right\} \tag{66}$$

$$A'' = -\frac{\xi_t D^2}{\mathrm{Bi}_2}\theta_c + \left(\frac{D\xi_t(D\xi_b+\kappa)}{\mathrm{Bi}_2(\xi_b+\xi_t)} - 1\right)\theta_{b,i} + \left(\frac{D\xi_t(D\xi_t+1)}{\mathrm{Bi}_2(\xi_b+\xi_t)} + 1\right)\theta_{t,i} - \frac{\Phi_2}{\mathrm{Bi}_2} \tag{67}$$

$$B'' = \frac{\xi_t D^2}{\mathrm{Bi}_2}\theta_c - \frac{D\xi_t(D\xi_b+\kappa)}{\mathrm{Bi}_2(\xi_b+\xi_t)}\theta_{b,i} - \frac{D\xi_t(D\xi_t+1)}{\mathrm{Bi}_2(\xi_b+\xi_t)}\theta_{t,i} + \frac{\Phi_2}{\mathrm{Bi}_2} \tag{68}$$

$$\lambda' = \sqrt{\frac{\xi_b+\xi_t}{\xi_b\xi_t}\mathrm{Bi}_2} \tag{69}$$

2.5.2.3 Interface blood and tissue temperatures. Blood and tissue temperatures at the interface of the layers ($\theta_{b,i}$ and $\theta_{t,i}$) can be evaluated by utilizing the boundary condition given by Eq. (21), the derived analytical solution for one layer hyperthermia for the equivalent case [7], and the derived profiles for blood and tissue in each layer. This results in

$$\theta_{t,i} = \frac{1}{2(1+\kappa)+D(\xi_b+\xi_t)}\left(\frac{(2\kappa+D\xi_b)\left\{(1+\kappa)\left[\theta_c+\Phi_1\left(1+\frac{1}{D}\right)^2\right]+\frac{1}{D}+1\right\}}{(1+\kappa)\mathrm{Bi}_1\left(1+\frac{1}{D}\right)^2}\left[1-\frac{e^{\lambda}+e^{\lambda/D}}{1+e^{\lambda(1+(1/D))}}\right]+D(\xi_b+\xi_t)\theta_c-1\right) \tag{70}$$

$$\theta_{b,i} = \frac{1}{2(1+\kappa)+D(\xi_b+\xi_t)}\left(-\frac{(2+D\xi_t)\left\{(1+\kappa)\left[\theta_c+\Phi_1\left(1+\frac{1}{D}\right)^2\right]+\frac{1}{D}+1\right\}}{(1+\kappa)\mathrm{Bi}_1\left(1+\frac{1}{D}\right)^2}\left[1-\frac{e^{\lambda}+e^{\lambda/D}}{1+e^{\lambda(1+(1/D))}}\right]+D(\xi_b+\xi_t)\theta_c-1\right) \tag{71}$$

The dimensional blood mean temperature, body organ surface temperature, and heat exchange rate represented by a Nusselt number at the body organ surface, which is subjected to an imposed heat flux, are derived to be

$$T_{b,1,m} = \frac{q_s x}{(\rho c_p u_a)_1 D_1\left[\begin{matrix}2(1+\kappa)+\\ D(\xi_b+\xi_t)\end{matrix}\right]}\left(D(\xi_b+\xi_t)[1+(1+\kappa)\theta_c]+\kappa+1+D(\xi_b-\kappa\xi_t)\left[\frac{(1+\kappa)\left[\theta_c+\Phi_1\left(1+\frac{1}{D}\right)^2\right]+\frac{1}{D}+1}{(1+\kappa)\mathrm{Bi}_1\left(1+\frac{1}{D}\right)^2}\right]\times\left[1-\frac{e^{\lambda}+e^{\lambda/D}}{1+e^{\lambda(1+(1/D))}}\right]\right)+\frac{(1-\varepsilon_1)\dot{q}_{\mathrm{gen},1}}{(\rho c_p u_a)_1}x+T_{a,1} \tag{72}$$

$$T_{b,2,m} = \frac{q_s x}{(\rho c_p u_a)_2 D_2\left[\begin{matrix}2(1+\kappa)+\\ D(\xi_b+\xi_t)\end{matrix}\right]}\left(D(\xi_b+\xi_t)[1+(1+\kappa)\theta_c]+\kappa+1+D(\xi_b-\kappa\xi_t)\left[\frac{(1+\kappa)\left[\theta_c+\Phi_1\left(1+\frac{1}{D}\right)^2\right]+\frac{1}{D}+1}{(1+\kappa)\mathrm{Bi}_1\left(1+\frac{1}{D}\right)^2}\right]\times\left[1-\frac{e^{\lambda}+e^{\lambda/D}}{1+e^{\lambda(1+(1/D))}}\right]\right)+\frac{(1-\varepsilon_2)\dot{q}_{\mathrm{gen},2}}{(\rho c_p u_a)_2}x+T_{a,2} \tag{73}$$

$$T_s = \frac{q_s x}{(\rho c_p u_a)_1 D_1(2(1+\kappa)+D(\xi_b+\xi_t))}\left(D(\xi_b+\xi_t)[1+(1+\kappa)\theta_c]+\kappa+1+D(\xi_b-\kappa\xi_t)\left[\frac{(1+\kappa)\left[\theta_c+\Phi_1\left(1+\frac{1}{D}\right)^2\right]+\frac{1}{D}+1}{(1+\kappa)\mathrm{Bi}_1\left(1+\frac{1}{D}\right)^2}\right]\times\left[1-\frac{e^{\lambda}+e^{\lambda/D}}{1+e^{\lambda(1+(1/D))}}\right]\right)-\frac{q_s D_1}{k_{t,\mathrm{eff},1}(1+\kappa)}\left(\Delta\left(\frac{5}{12}-\frac{1}{\mathrm{Bi}_1(1+\kappa)}\left\{1-\frac{2(e^{\lambda}-1)}{\lambda(1+e^{\lambda})}\right\}\right)-\frac{\Phi_1}{\mathrm{Bi}_1}\left\{1-\frac{2(e^{\lambda}-1)}{\lambda(1+e^{\lambda})}\right\}-\frac{\left\{(1+\kappa)\left[\theta_c+\Phi_1\left(1+\frac{1}{D}\right)^2\right]+\frac{1}{D}+1\right\}\left[1-\frac{e^{\lambda}+e^{\lambda/D}}{1+e^{\lambda(1+(1/D))}}\right](e^{\lambda}-1)}{(1+\kappa)\lambda\mathrm{Bi}_1(1+e^{\lambda})\left(1+\frac{1}{D}\right)^2}-\frac{1}{2}\right)+\frac{(1-\varepsilon_1)\dot{q}_{\mathrm{gen},1}}{(\rho c_p u_a)_1}x+T_{a,1} \tag{74}$$

$$\mathrm{Nu}_s = \frac{h_s D_h}{k_{b,\mathrm{eff},1}} = \frac{-2}{\kappa\theta_{b,1,m}}\left(1+\frac{1}{D}\right)$$

$$= \frac{\frac{-2}{\kappa}\left(1+\frac{1}{D}\right)}{\frac{1}{(1+\kappa)}\left(\Delta\left(\frac{5}{12}-\frac{1}{\mathrm{Bi}_1(1+\kappa)}\left\{1-\frac{2(e^{\lambda}-1)}{\lambda(1+e^{\lambda})}\right\}\right)-\frac{\Phi_1}{\mathrm{Bi}_1}\left\{1-\frac{2(e^{\lambda}-1)}{\lambda(1+e^{\lambda})}\right\}-\frac{\left\{(1+\kappa)\left[\theta_c+\Phi_1\left(1+\frac{1}{D}\right)^2\right]+\frac{1}{D}+1\right\}\left[1-\frac{e^{\lambda}+e^{\lambda/D}}{1+e^{\lambda(1+(1/D))}}\right](e^{\lambda}-1)}{(1+\kappa)\lambda\mathrm{Bi}_1(1+e^{\lambda})\left(1+\frac{1}{D}\right)^2}-\frac{1}{2}\right)} \tag{75}$$

where

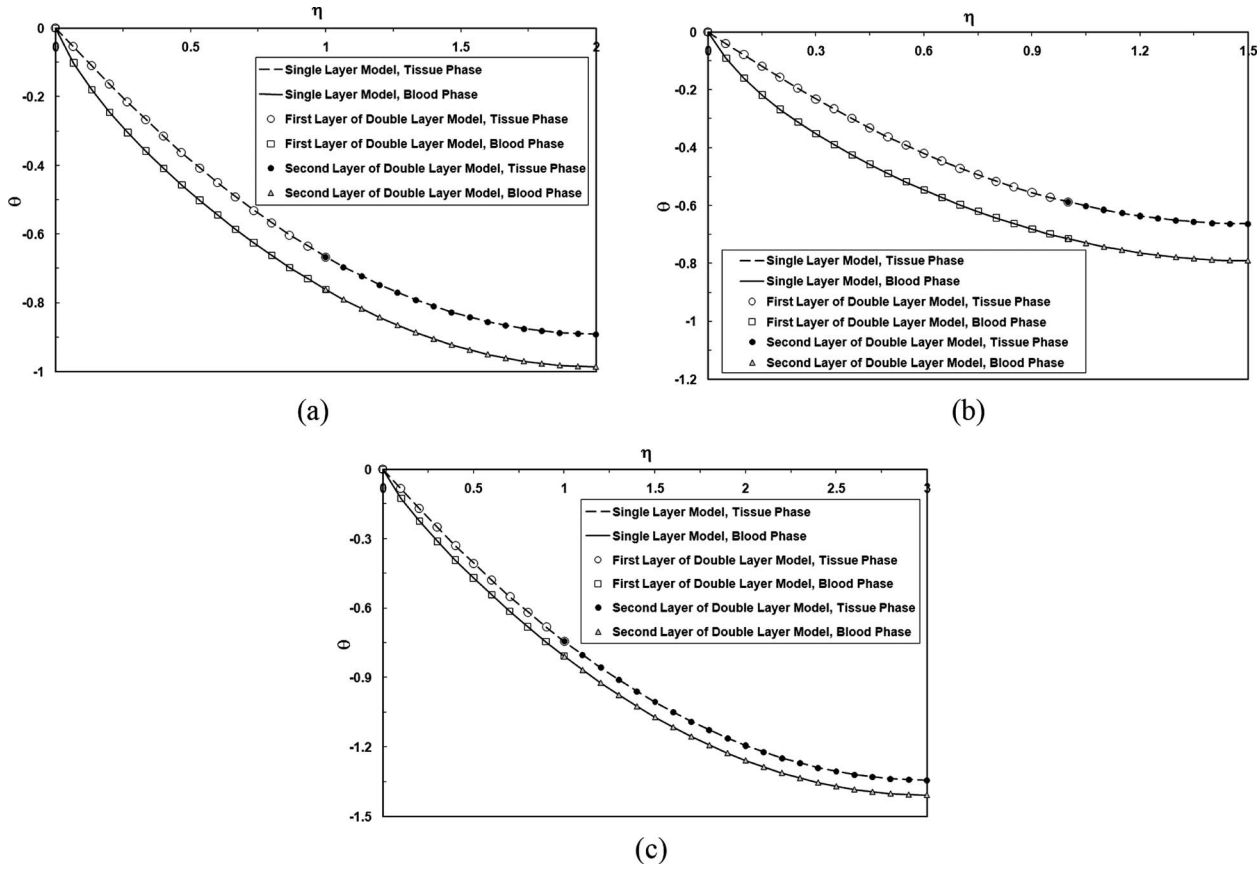

Fig. 2 Comparison of the temperature profiles obtained from double layer analytical solution with similar properties (utilizing two equation modeling) with those obtained from a single layer model [7] for blood and tissue phases with model I (isolated core region) for κ=0.111, ξ_b=0.111, ξ_t=1, $\varepsilon_1=\varepsilon_2$=0.1 and $Bi_1=Bi_2$=10, (*a*) D=1, (*b*) D=2, and (*c*) D=1/2

$$\Delta = \frac{1}{2(1+\kappa)+D(\xi_b+\xi_t)}\left(D(\xi_b+\xi_t)[1+(1+\kappa)\theta_c]+\kappa+1+D(\xi_b-\kappa\xi_t)\left[\frac{(1+\kappa)\left[\theta_c+\Phi_1\left(1+\frac{1}{D}\right)^2\right]+\frac{1}{D}+1}{(1+\kappa)\mathrm{Bi}_1\left(1+\frac{1}{D}\right)^2}\right] \times\left[1-\frac{e^{\lambda}+e^{\lambda/D}}{1+e^{\lambda(1+(1/D))}}\right]\right) \tag{76}$$

2.6 Simplified Solution. A simplified solution can be obtained by assuming thermal equilibrium between the blood and tissue phases, i.e., $\theta_1=\theta_{b,1}=\theta_{t,1}$ and $\theta_2=\theta_{b,2}=\theta_{t,2}$. Adding the energy equations and utilizing the boundary conditions (Eqs. (15)–(32)), and following the same procedure described for the nonequilibrium model, the blood and tissue temperature distributions and the Nusselt number are obtained as follows:

For model I (isolated core region):

$$\theta_{b,1}=\theta_{t,1}=\frac{\eta}{1+\kappa}([1+(1+\kappa)\theta_i]\eta-1) \tag{77}$$

$$\theta_{b,2}=\theta_{t,2}=\frac{1+2(1+\kappa)\theta_i}{2(\xi_b+\xi_t)}\left\{D\left(-\eta+2\left(1+\frac{1}{D}\right)\right)\eta-D-2\right\}+\theta_i \tag{78}$$

where

$$\theta_i=\frac{(\rho c_p u_a)_1 D_1[-q_s+\dot{q}_{\mathrm{gen},2}(1-\varepsilon_2)D_2]-(\rho c_p u_a)_2 D_2[2q_s+\dot{q}_{\mathrm{gen},1}(1-\varepsilon_1)D_1]}{2q_s(1+\kappa)[(\rho c_p u_a)_1 D_1+(\rho c_p u_a)_2 D_2]} \tag{79}$$

and

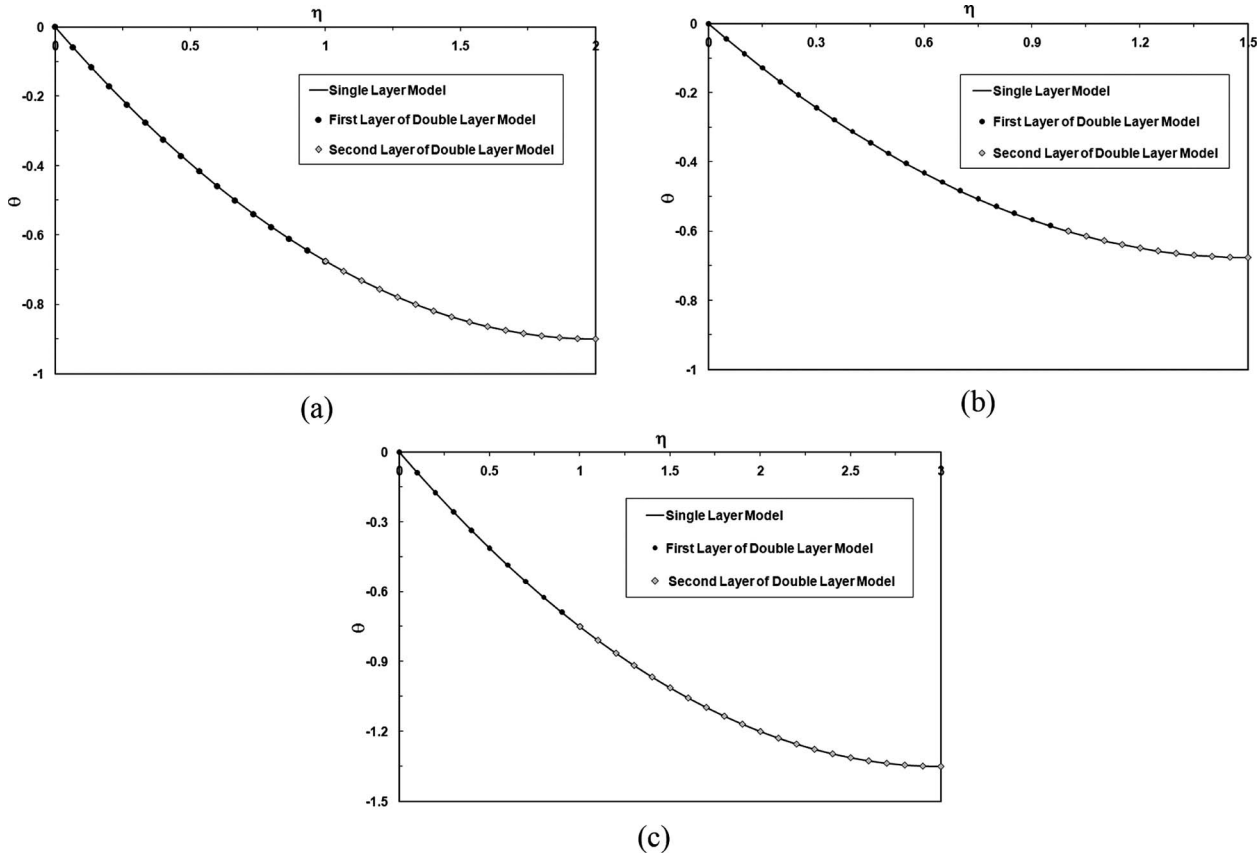

Fig. 3 Comparison of the temperature profiles obtained from double layer analytical solution with similar properties (utilizing one equation modeling) with those obtained from a single layer model [7], for model I (isolated core region) with κ=0.111, ξ_b=0.111, ξ_t=1, $\varepsilon_1=\varepsilon_2$=0.1 and $Bi_1=Bi_2$=10, (*a*) *D*=1, (*b*) *D*=2, and (*c*) *D*=1/2

$$\theta_{b,1,m} = \frac{1}{3}\theta_i - \frac{1}{6(1+\kappa)} \tag{80}$$

$$\theta_{b,2,m} = \left(1 + \frac{2(1+\kappa)}{3(\xi_b + \xi_t)D}\right)\theta_i + \frac{1}{3(\xi_b + \xi_t)D} \tag{81}$$

$$T_{1,m} = \frac{q_s + \dot{q}_{\text{gen},1}(1-\varepsilon_1)D_1 + \dot{q}_{\text{gen},2}(1-\varepsilon_2)D_2}{(\rho c_p u_a)_1 D_1 + (\rho c_p u_a)_2 D_2}x + T_{a,1} \tag{82}$$

$$T_{2,m} = \frac{q_s + \dot{q}_{\text{gen},1}(1-\varepsilon_1)D_1 + \dot{q}_{\text{gen},2}(1-\varepsilon_2)D_2}{(\rho c_p u_a)_1 D_1 + (\rho c_p u_a)_2 D_2}x + T_{a,2} \tag{83}$$

$$T_s = \frac{q_s + D_1(1-\varepsilon_1)\dot{q}_{\text{gen},1} + \dot{q}_{\text{gen},2}(1-\varepsilon_2)D_2}{(\rho c_p u_a)_1 D_1 + (\rho c_p u_a)_2 D_2}x + \frac{q_s D_1}{6(1+\kappa)k_{t,\text{eff},1}} + T_{a,1} - \frac{D_1}{3k_{t,\text{eff},1}}\left(\frac{(\rho c_p u_a)_1 D_1[-q_s + \dot{q}_{\text{gen},2}(1-\varepsilon_2)D_2] - (\rho c_p u_a)_2 D_2[2q_s + \dot{q}_{\text{gen},1}(1-\varepsilon_1)D_1]}{2(1+\kappa)[(\rho c_p u_a)_1 D_1 + (\rho c_p u_a)_2 D_2]}\right) \tag{84}$$

$$\text{Nu}_s = \frac{h_s D_h}{k_{b,\text{eff},1}} = \frac{-2}{\kappa\theta_{b,1,m}}\left(1 + \frac{1}{D}\right) = \frac{12q_s\dfrac{(1+\kappa)}{\kappa}[(\rho c_p u_a)_1 D_1 + (\rho c_p u_a)_2 D_2]\left(1 + \dfrac{1}{D}\right)}{(\rho c_p u_a)_1 D_1[2q_s - \dot{q}_{\text{gen},2}(1-\varepsilon_2)D_2] + (\rho c_p u_a)_2 D_2[3q_s + \dot{q}_{\text{gen},1}(1-\varepsilon_1)D_1]} \tag{85}$$

and for model II (uniform core temperature):

$$\theta_{b,1} = \theta_{t,1} = \frac{\eta}{1+\kappa}\left([1 + (1+\kappa)\theta_i]\left(\frac{\eta+1}{2}\right) - 1\right) \tag{86}$$

$$\theta_{b,2} = \theta_{t,2} = \frac{D\eta(\eta-2)}{2}\left(D(\theta_c-\theta_i) - \frac{1+\kappa}{\xi_b+\xi_t}\theta_i\right) + \frac{\eta}{2}\left(D(\theta_c-\theta_i) + \frac{1+\kappa}{\xi_b+\xi_t}\theta_i\right) + \frac{D(D-1)}{2}(\theta_c-\theta_i) + \left(1 - \frac{1+D}{2}\frac{1+\kappa}{\xi_b+\xi_t}\right)\theta_i \quad (87)$$

where

$$\theta_i = \frac{D(\xi_b+\xi_t)\theta_c - 1}{D(\xi_b+\xi_t) + 2(1+\kappa)} \quad (88)$$

and

$$\theta_{b,1,m} = \frac{5}{12}\theta_i - \frac{1}{12(1+\kappa)} \quad (89)$$

$$\theta_{b,2,m} = \frac{5}{12}\theta_c + \left(\frac{7}{12} + \frac{1+\kappa}{12D(\xi_b+\xi_t)}\right)\theta_i \quad (90)$$

$$T_{1,m} = \frac{1}{(\rho c_p u_a)_1 D_1}\left(\frac{D(\xi_b+\xi_t)\theta_c - 1}{D(\xi_b+\xi_t) + 2(1+\kappa)} q_s(1+\kappa) + q_s + \dot{q}_{\text{gen},1}(1-\varepsilon_1)D_1\right)x + T_{a,1} \quad (91)$$

$$T_{2,m} = \frac{1}{(\rho c_p u_a)_2 D_2} \times \left(\frac{1 - D(\xi_b+\xi_t)\theta_c}{D(\xi_b+\xi_t) + 2(1+\kappa)} q_s[D(\xi_b+\xi_t) + \kappa + 1] + q_s D(\xi_b+\xi_t)\theta_c + \dot{q}_{\text{gen},2}(1-\varepsilon_2)D_2\right)x + T_{a,2} \quad (92)$$

$$T_s = \frac{x}{(\rho c_p u_a)_1 D_1}\left(\frac{q_s(1+\kappa)(D(\xi_b+\xi_t)\theta_c - 1)}{D(\xi_b+\xi_t) + 2(1+\kappa)} + q_s + \dot{q}_{\text{gen},1}(1-\varepsilon_1)D_1\right) + \frac{q_s D_1}{12k_{t,\text{eff},1}}\left(\frac{5\{1 - D(\xi_b+\xi_t)\theta_c\}}{D(\xi_b+\xi_t) + 2(1+\kappa)} + \frac{1}{1+\kappa}\right) + T_{a,1} \quad (93)$$

$$\text{Nu}_s = \frac{h_s D_h}{k_{b,\text{eff},1}} = \frac{-2}{\kappa\theta_{b,1,m}}\left(1 + \frac{1}{D}\right) = \frac{\frac{-24}{\kappa}\left(1 + \frac{1}{D}\right)}{\frac{5(D(\xi_b+\xi_t)\theta_c - 1)}{D(\xi_b+\xi_t) + 2(1+\kappa)} - \frac{1}{1+\kappa}} \quad (94)$$

3 Results and Discussions

The presented analytical expressions allow for incorporating variations in the representative volume fraction as well as various physical attributes. Comparing temperature profiles for any of the single layers with the available data in the literature provided detailed validations. Exact solutions for forced convective flow through a channel filled with a porous medium and subject to an imposed heat flux (which is equivalent to the isolated core region model without a metabolic heat generation) were presented in the works of Lee and Vafai [33] and Marafie and Vafai [37]. As such, the tissue and blood temperature profiles were compared with analytical correlations obtained by Lee and Vafai [33]. The temperature distributions were found to be in excellent agreement for both phases with the results presented by Lee and Vafai [33] for a variety of blood-tissue interstitial heat exchange parameters. The blood and tissue temperature profiles were also found to be in excellent agreement with the analytical and numerical results of Marafie and Vafai [37]. Numerical results based on an implicit, pressure-based, cell-centered finite volume method, second order upwinding and under relaxation, was also compared with the obtained analytical temperature distribution for single layer model for both isolated and uniform core temperature condition models. These comparisons were found to be in excellent agreement and were presented in some detail in the works of Mahjoob and Vafai [7]. The temperature profiles obtained from the present analytical correlations can effectively predict the tissue and blood temperatures. The temperature distribution is very crucial for an effective thermal therapy such as hyperthermia cancer treatment. Based on the cited values in the literature [26], a typical volume fraction of 0.1 for the vascular system is utilized. However, the present established analytical expressions allow for incorporating variations in the representative volume fraction as well as various physical attributes. Figures 2(*a*)–2(*c*) represent the blood and tissue temperature profiles for a dual layer region, incorporating isolated core region for different layer thickness ratio (D). Since the physical properties of both layers is the same, the profiles have been compared with the profiles obtained from the exact solutions for a single layer with equivalent properties [7]. The comparison indi-

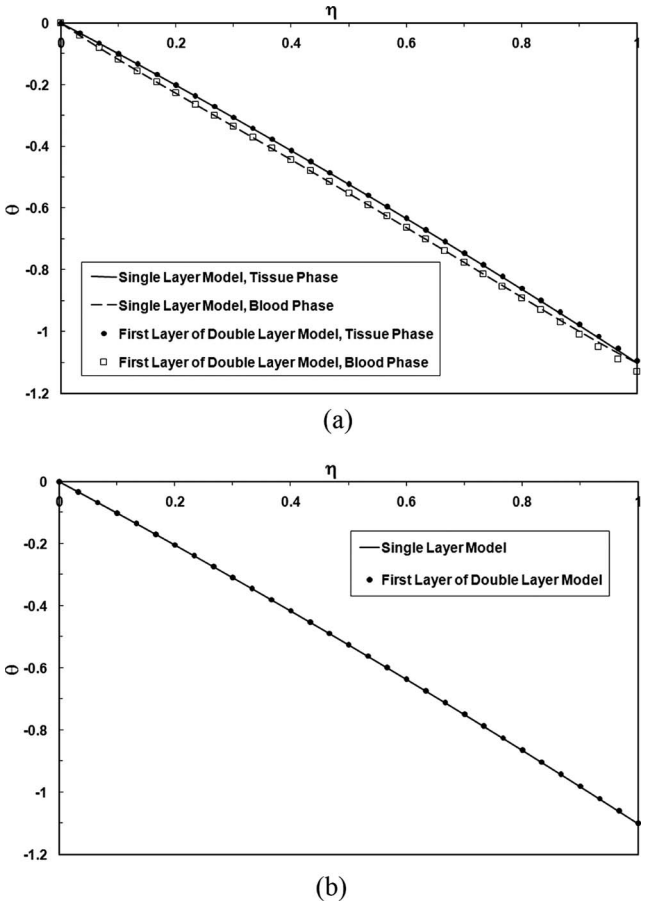

Fig. 4 Comparison of the temperature profiles obtained from the first layer of the double layer analytical solution with those obtained from a single layer model [7] for model II (uniform core temperature) with κ=0.111, ξ_b=0.111, ξ_t=1, $\varepsilon_1=\varepsilon_2$=0.1, and $\text{Bi}_1=\text{Bi}_2$=10, utilizing (*a*) two equation and (*b*) one equation models

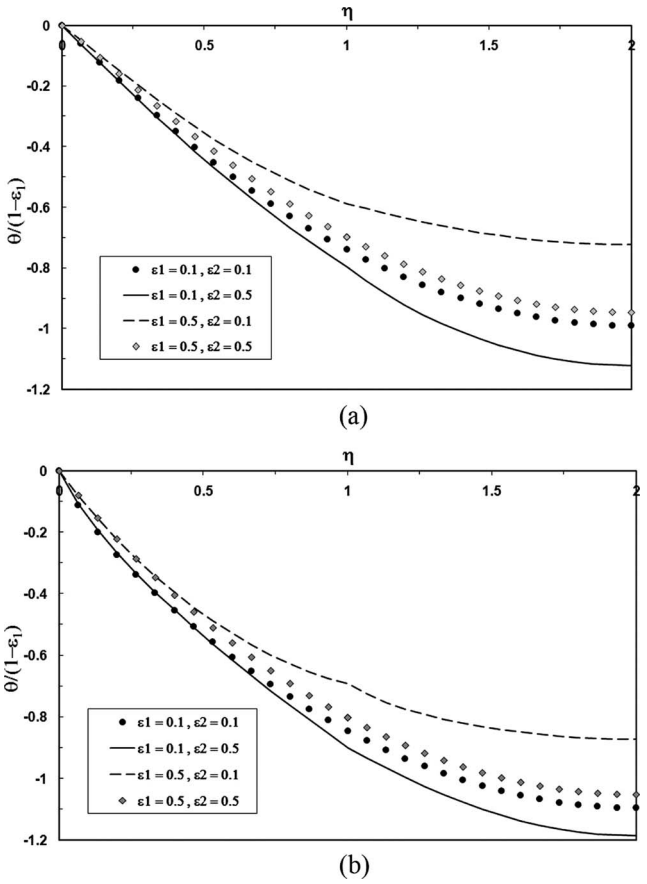

Fig. 5 The effect of vascular volume fraction variation in biological layers, for model I (isolated core region), for similar blood and tissue properties in the layers, $D=1$, $Bi_1=Bi_2=10$, $\Phi_1/(1-\varepsilon_1)=\Phi_2/(1-\varepsilon_2)=0.55$, (*a*) tissue phase, (*b*) blood phase

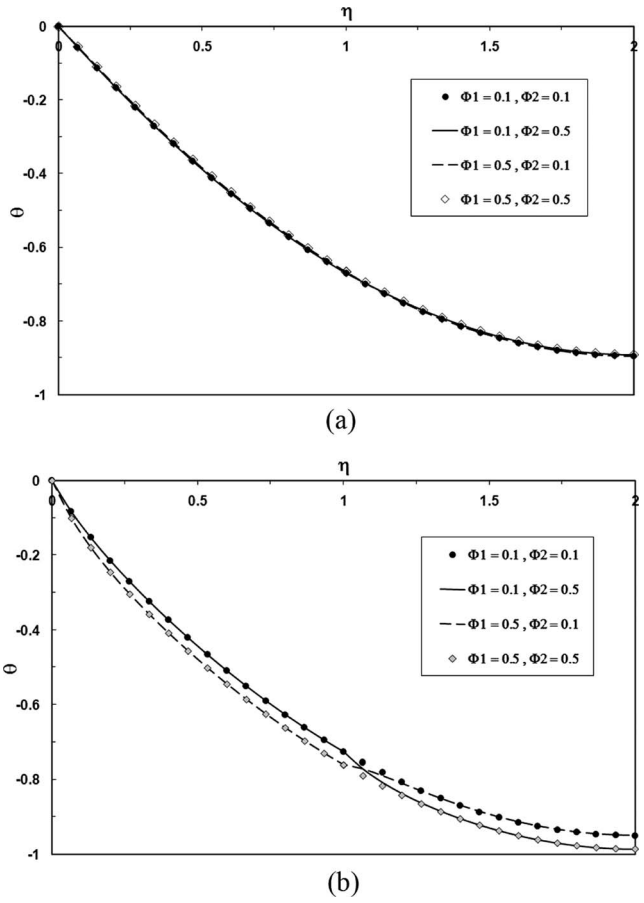

Fig. 6 The effect of metabolic heat generation in biological layers, for model I (isolated core region), for similar blood and tissue properties in the layers, $D=1$, $\kappa=0.111$, $\xi_b=0.111$, $\xi_t=1$, $\varepsilon_1=\varepsilon_2=0.1$, $Bi_1=Bi_2=10$, (*a*) tissue phase, (*b*) blood phase

cates an excellent agreement in all cases. In Figs. 3(*a*)–3(*c*), the temperature profiles for each layer of the double layer analytical solution (utilizing one equation model) are compared with those obtained for the single layer model [7], for model I (isolated core region), under equivalent conditions. The comparisons also indicate a very good agreement.

The temperature profiles obtained from model II (uniform core temperature) are presented in Fig. 4. Tissue and blood temperature profiles obtained for the first of the double layer analytical solution (utilizing the two equation model) are compared with those obtained for the single layer model [7] under the equivalent conditions. The comparison displays a very good agreement. Comparison is also done for the case of one equation model, further validating the present analytical solution (Fig. 4(*b*)).

Figure 5 displays the effect of vascular volume fraction on the blood and tissue temperature profiles in a dual layer biological media. An increase in the volume fraction, in the cases with uniform vascular volume fraction in both layers, results in a more uniform temperature profile through the layers, possibly leading to a more effective hyperthermia treatment. It should be noted that a change in the vascular volume fraction also translates in a change in the blood and tissue effective thermal conductivities. The body regulates the temperature during hyperthermia treatment by utilizing the arterial blood, while modifying the vascular volume fraction of the biological structure. The natural body thermal regulation system increases or decreases the vascular volume fraction of the biological structure when exposed to a higher or lower temperature, respectively. The physical attributes obtained from this analytical solution can be used to improve the efficiency of thermal therapy techniques. An increase in the vascular volume fraction of the second layer increases the nonuniformity in temperature profiles. However, the tissue and blood temperature uniformity is more prominently affected by the vascular volume fraction of the first layer, which is subject to the imposed heat flux.

Figure 6 represents the effect of metabolic heat generation on the blood and tissue temperature profiles. As can be seen the metabolic heat generation has more pronounced effect on the nondimensional blood phase since temperature rise in the tissue phase and organ's surface is higher than that of the blood phase. As such, a larger heat generation ratio results in higher temperatures in the organ as well as the blood within it and more distinct temperature nonuniformity. The effect of variable heat generation on the biological layers is also presented in Fig. 6. In the previous works by authors, the effects of thermal conductivities of the tissue and blood phases and the nondimensional Biot number (Bi) have been discussed extensively [7,33,48–50].

4 Conclusions

A detailed analysis of bioheat transport through dual layer biological media is presented in this work for the first time. These analytical solutions enable an understanding of heat transfer processes and temperature distributions within biological media, which are key issues in thermal therapy techniques. The comprehensive analytical solutions represent the blood and tissue temperature distributions as well as the Nusselt number correlations for two primary conditions, namely, isolated core region and uniform core temperature. The analytical solutions encompass various pertinent parameters such as the volume fraction of the vas-

cular system, the blood and tissue thermal conductivities, interfacial blood-tissue heat exchange, metabolic heat generation, tissue/organ depth, arterial velocity and temperature, body core temperature, imposed hyperthermia heat flux, and the blood's physical properties. Analytical solutions are also presented for a simplified case corresponding to local thermal equilibrium between the blood and tissue phases. The comparisons, utilizing both local thermal nonequilibrium and equilibrium assumptions, indicate an excellent agreement. The effect of the variable vascular volume fraction and metabolic heat generation within the biological media is also discussed.

Nomenclature

a_{tb} = specific surface area (m^{-1})
Bi = Biot number, $h_{tb}a_{tb}D_1^2/k_{t,\mathrm{eff},1}$
c_p = blood specific heat ($J\,kg^{-1}\,K^{-1}$)
D_1 = depth of the first layer of tissue/organ (m)
D_2 = depth of the second layer of tissue/organ (m)
D = nondimensional parameter for depth, D_1/D_2
D_h = hydraulic diameter of the channel, $2(D_1+D_2)$ (m)
h_{tb} = blood-tissue interstitial heat transfer coefficient ($W\,m^{-2}\,K^{-1}$)
h_s = surface heat transfer coefficient for the thermal nonequilibrium model, $q_s/(T_s\text{-}T_{b,m,1})$ ($W\,m^{-2}\,K^{-1}$)
$k_{b,\mathrm{eff}}$ = effective thermal conductivity of the blood phase ($W\,m^{-1}\,K^{-1}$)
$k_{t,\mathrm{eff}}$ = effective thermal conductivity of the tissue phase ($W\,m^{-1}\,K^{-1}$)
Nu_s = Nusselt number at the organ's surface
q = heat flux ($W\,m^{-2}$)
q_s = heat flux at the body organ surface ($W\,m^{-2}$)
$\dot{q}_{\mathrm{gen}}$ = heat generation within the biological tissue ($W\,m^{-3}$)
T = temperature (K)
T_a = arterial blood temperature entering the organ (K)
$T_{b,m}$ = blood mean temperature (K)
T_c = body core temperature (K)
T_s = temperature of the body organ surface subject to an imposed heat flux (K)
u_a = arterial blood velocity entering the tissue layer ($m\,s^{-1}$)
x = longitudinal coordinate (m)
y = transverse coordinate (m)

Greek Symbols

η = nondimensional transverse coordinate, y/D_1
Φ = nondimensional heat generation within the biological tissue, $(1-\varepsilon)D_1\dot{q}_{\mathrm{gen}}/q_s$
κ = ratio of the effective blood thermal conductivity to that of the tissue in the first layer, $k_{b,\mathrm{eff},1}/k_{t,\mathrm{eff},1}$
ρ = blood density ($kg\,m^{-3}$)
ξ_b = nondimensional effective blood thermal conductivity of the second layer, $k_{b,\mathrm{eff},2}/k_{t,\mathrm{eff},1}$
ξ_t = nondimensional effective tissue thermal conductivity of the second layer, $k_{t,\mathrm{eff},2}/k_{t,\mathrm{eff},1}$
λ = parameter, $\sqrt{\mathrm{Bi}_1(1+\kappa)/\kappa}$
λ' = parameter, $\sqrt{(\xi_b+\xi_t)\mathrm{Bi}_2/\xi_b\xi_t}$
θ = nondimensional temperature, $k_{t,\mathrm{eff},1}(T-T_s)/q_sD_1$
$\theta_{b,m}$ = nondimensional blood mean temperature
θ_c = nondimensional body core temperature, $k_{t,\mathrm{eff},1}(T_c-T_s)/q_sD_1$
$\Delta\theta$ = nondimensional temperature difference between tissue and blood phases
ω = blood perfusion rate (s^{-1})

Subscripts/Superscripts

1 = first layer
2 = second layer
B = blood phase
b,m = blood mean
c = body core
eff = effective property
j = indicator
s = body organ surface subject to an imposed heat flux
t = tissue phase

Symbol

$\langle\,\rangle$ = intrinsic volume average of a quantity

References

[1] Oleson, J. R., Dewhirst, M. W., Harrelson, J. M., Leopold, K. A., Samulski, T. V., and Tso, C. Y., 1989, "Tumor Temperature Distributions Predict Hyperthermia Effect," Int. J. Radiat. Oncol. Biol. Phys., **16**(3), pp. 559–70.
[2] Field, S. B., and Hand, J. W., 1990, *An Introduction to the Practical Aspects of Clinical Hyperthermia*, Taylor & Francis, New York.
[3] Diederich, C. J., 2005, "Thermal Ablation and High-Temperature Thermal Therapy: Overview of Technology and Clinical Implementation," Int. J. Hyperthermia, **21**(8), pp. 745–753.
[4] Wust, P., Hildebrandt, B., Sreenivasa, G., Rau, B., Gellermann, J., Riess, H., Felix, R., and Schlag, P. M., 2002, "Hyperthermia in Combined Treatment of Cancer," Lancet Oncol., **3**(8), pp. 487–497.
[5] Hall, E. J., and Roizin-Towle, L., 1984, "Biological Effects of Heat," Cancer Res., **44**, pp. 4708s–4713s.
[6] Field, S. B., 1987, "Hyperthermia in the Treatment of Cancer," Phys. Med. Biol., **32**(7), pp. 789–811.
[7] Mahjoob, S., and Vafai, K., 2009, "Analytical Characterization of Heat Transfer Through Biological Media Incorporating Hyperthermia Treatment," Int. J. Heat Mass Transfer, **52**(5–6), pp. 1608–1618.
[8] Urano, M., 1999, "For the Clinical Application of Thermochemotherapy Given at Mild Temperatures," Int. J. Hyperthermia, **15**(2), pp. 79–107.
[9] van der Zee, J., González González, D., van Rhoon, G. C., van Dijk, J. D. P., van Putten, W. L. J., and Hart, A. A. M., 2000, "Comparison of Radiotherapy Alone With Radiotherapy Plus Hyperthermia in Locally Advanced Pelvic Tumours: A Prospective, Randomised, Multicentre Trial," Lancet, **355**(9210), pp. 1119–1125.
[10] Pennes, H. H., 1948, "Analysis of Tissue and Arterial Blood Temperature in the Resting Human Forearm," J. Appl. Physiol., **1**, pp. 93–122.
[11] Charny, C. K., 1992, "Mathematical Models of Bioheat Transfer," Adv. Heat Transfer, **22**, pp. 19–155.
[12] Wulff, W., 1974, "The Energy Conservation Equation for Living Tissue," IEEE Trans. Biomed. Eng., **BME-21**(6), pp. 494–495.
[13] Klinger, H. G., 1974, "Heat Transfer in Perfused Biological Tissue—I: General Theory," Bull. Math. Biol., **36**(4), pp. 403–415.
[14] Chen, M. M., and Holmes, K. R., 1980, "Microvascular Contributions in Tissue Heat Transfer," Ann. N.Y. Acad. Sci., **335**, pp. 137–150.
[15] Weinbaum, S., Jiji, L. M., and Lemons, D. E., 1984, "Theory and Experiment for the Effect of Vascular Microstructure on Surface Tissue Heat Transfer. Part I. Anatomical Foundation and Model Conceptualization," ASME J. Biomech. Eng., **106**(4), pp. 321–330.
[16] Jiji, L. M., Weinbaum, S., and Lemons, D. E., 1984, "Theory and Experiment for the Effect of Vascular Microstructure on Surface Tissue Heat Transfer—Part II: Model Formulation and Solution," ASME J. Biomech. Eng., **106**(4), pp. 331–341.
[17] Weinbaum, S., and Jiji, L. M., 1985, "A New Simplified Bioheat Equation for the Effect of Blood Flow on Local Average Tissue Temperature," ASME J. Biomech. Eng., **107**(2), pp. 131–139.
[18] Mitchell, J. W., and Myers, G. E., 1968, "An Analytical Model of the Countercurrent Heat Exchange Phenomena," Biophys. J., **8**, pp. 897–911.
[19] Keller, K. H., and Seilder, L., 1971, "An Analysis of Peripheral Heat Transfer in Man," J. Appl. Physiol., **30**(5), pp. 779–789.
[20] Chen, C., and Xu, L. X., 2003, "A Vascular Model for Heat Transfer in an Isolated Pig Kidney During Water Bath Heating," ASME J. Heat Transfer, **125**(5), pp. 936–943.
[21] Baish, J. W., Ayyaswamy, P. S., and Foster, K. U., 1986, "Small Scale Temperature Fluctuations in Perfused Tissue During Local Hyperthermia," ASME J. Biomech. Eng., **108**(3), pp. 246–250.
[22] Baish, J. W., Ayyaswamy, P. S., and Foster, K. R., 1986, "Heat Transport Mechanisms in Vascular Tissues: A Model Comparison," ASME J. Biomech. Eng., **108**(4), pp. 324–331.
[23] Abraham, J. P., and Sparrow, E. M., 2007, "A Thermal-Ablation Bioheat Model Including Liquid-to-Vapor Phase Change, Pressure- and Necrosis-

Dependent Perfusion, and Moisture-Dependent Properties," Int. J. Heat Mass Transfer, **50**(13–14), pp. 2537–2544.
[24] Arkin, H., Xu, L. X., and Holmes, K. R., 1994, "Recent Developments in Modeling Heat Transfer in Blood Perfused Tissues," IEEE Trans. Biomed. Eng., **41**, pp. 97–107.
[25] Chato, J. C., 1980, "Heat Transfer to Blood Vessels," ASME J. Biomech. Eng., **102**(2), pp. 110–118.
[26] Khanafer, K., and Vafai, K., 2009, "Synthesis of Mathematical Models Representing Bioheat Transport," *Advance in Numerical Heat Transfer*, Vol. 3, W. J. Minkowycz and E. M. Sparrow, eds., Taylor & Francis, London, pp. 1–28.
[27] Nakayama, A., and Kuwahara, F., 2008, "A General Bioheat Transfer Model Based on the Theory of Porous Media," Int. J. Heat Mass Transfer, **51**(11–12), pp. 3190–3199.
[28] Khaled, A. R., and Vafai, K., 2003, "The Role of Porous Media in Modeling Flow and Heat Transfer in Biological Tissues," Int. J. Heat Mass Transfer, **46**, pp. 4989–5003.
[29] Vafai, K., and Tien, C. L., 1981, "Boundary and Inertia Effects on Flow and Heat Transfer in Porous Media," Int. J. Heat Mass Transfer, **24**, pp. 195–203.
[30] Sozen, M., and Vafai, K., 1990, "Analysis of the Non-Thermal Equilibrium Condensing Flow of a Gas Through a Packed Bed," Int. J. Heat Mass Transfer, **33**, pp. 1247–1261.
[31] Vafai, K., and Sozen, M., 1990, "Analysis of Energy and Momentum Transport for Fluid Flow Through a Porous Bed," ASME J. Heat Transfer, **112**, pp. 690–699.
[32] Quintard, M., and Whitaker, S., 2000, "Theoretical Analysis of Transport in Porous Media," *Handbook of Porous Media*, K. Vafai, ed., Marcel Dekker Inc., New York, pp. 1–52.
[33] Lee, D. Y., and Vafai, K., 1999, "Analytical Characterization and Conceptual Assessment of Solid and Fluid Temperature Differentials in Porous Media," Int. J. Heat Mass Transfer, **42**, pp. 423–435.
[34] Amiri, A., and Vafai, K., 1994, "Analysis of Dispersion Effects and Nonthermal Equilibrium, Non-Darcian, Variable Porosity Incompressible Flow Through Porous Medium," Int. J. Heat Mass Transfer, **37**, pp. 939–954.
[35] Alazmi, B., and Vafai, K., 2002, "Constant Wall Heat Flux Boundary Conditions in Porous Media Under Local Thermal Non-Equilibrium Conditions," Int. J. Heat Mass Transfer, **45**, pp. 3071–3087.
[36] Amiri, A., Vafai, K., and Kuzay, T. M., 1995, "Effect of Boundary Conditions on Non-Darcian Heat Transfer Through Porous Media and Experimental Comparisons," Numer. Heat Transfer, Part A, **27**, pp. 651–664.
[37] Marafie, A., and Vafai, K., 2001, "Analysis of Non-Darcian Effects on Temperature Differentials in Porous Media," Int. J. Heat Mass Transfer, **44**, pp. 4401–4411.
[38] Jiang, S. C., Ma, N., Li, H. J., and Zhang, X. X., 2002, "Effects of Thermal Properties and Geometrical Dimensions on Skin Burn Injuries," Burns, **28**(8), pp. 713–717.
[39] Wang, H., Dai, W., and Bejan, A., 2007, "Optimal Temperature Distribution in a 3D Triple-Layered Skin Structure Embedded With Artery and Vein Vasculature and Induced by Electromagnetic Radiation," Int. J. Heat Mass Transfer, **50**(9–10), pp. 1843–1854.
[40] Ma, N., Gao, X., and Zhang, X. X., 2004, "Two-Layer Simulation Model of Laser-Induced Interstitial Thermo-Therapy," Lasers Med. Sci., **18**, pp. 184–189.
[41] Khakpour, M., and Vafai, K., 2008, "A Critical Assessment of Arterial Transport Models," Int. J. Heat Mass Transfer, **51**, pp. 807–822.
[42] Curry, F. E., 1984, "Mechanics and Thermodynamics of Transcapillary Exchange," *Handbook of Physiology*, E. M. Renkin, ed., American Physiological Society, Bethesda, MD, Vol. IV, Chap. 8.
[43] Ogston, A. G., 1958, "The Spaces in a Uniform Random Suspension of Fibers," Trans. Faraday Soc., **54**, pp. 1754–1757.
[44] Ogston, A. G., Preston, B. N., and Wells, J. D., 1973, "On the Transport of Compact Particles Through Solutions of Chain-Polymer," Proc. R. Soc. London, Ser. A, **333**, pp. 297–316.
[45] Schnitzer, J. E., 1988, "Analysis of Steric Partition Behavior of Molecules in Membranes Using Statistical Physics. Application to Gel Chromatography and Electrophoresis," Biophys. J., **54**, pp. 1065–1076.
[46] Yuan, F., Chien, S., and Weinbaum, S., 1991, "A New View of Convective-Diffusive Transport Processes in the Arterial Intima," ASME J. Biomech. Eng., **113**(3), pp. 314–329.
[47] Huang, Y., Rumschitzki, D., Chien, S., and Weinbaum, S., 1994, "A Fiber Matrix Model for the Growth of Macromolecular Leakage Spots in the Arterial Intima," ASME J. Biomech. Eng., **116**, pp. 430–445.
[48] Mahjoob, S., and Vafai, K., 2009, "Analytical Characterization and Production of an Isothermal Surface for Biological and Electronics Applications," ASME J. Heat Transfer, **131**(5), p. 052604.
[49] Mahjoob, S., and Vafai, K., 2008, "A Synthesis of Fluid and Thermal Transport Models for Metal Foam Heat Exchangers," Int. J. Heat Mass Transfer, **51**(15–16), pp. 3701–3711.
[50] Mahjoob, S., Vafai, K., and Beer, N. R., 2008, "Rapid Microfluidic Thermal Cycler for Polymerase Chain Reaction Nucleic Acid Amplification," Int. J. Heat Mass Transfer, **51**(9–10), pp. 2109–2122.

Thermal Analysis and Optimization of Orthotropic Pin Fins: A Closed-Form Analytical Solution

Syed M. Zubair

A. F. M. Arif

Department of Mechanical Engineering,
King Fahd University of Petroleum and Minerals,
Dhahran 31261, Saudi Arabia

Mostafa H. Sharqawy
Department of Mechanical Engineering,
Massachusetts Institute of Technology,
77 Massachusetts Avenue,
Cambridge, MA 02139

Analytical solutions for temperature distribution, heat transfer rate, and fin efficiency and fin effectiveness are derived and presented for orthotropic two-dimensional pin fins subject to convective-tip boundary condition. The generalized results are presented and discussed in terms of dimensionless variables such as radial and axial Biot numbers (Bi_r, Bi_z), fin aspect ratio, L/R, and radial-to-axial conductivity ratio k^*. Several special cases are derived from the general solution, which includes the insulated-tip boundary condition. It is also demonstrated that the classical temperature distribution and heat transfer rate from the two-dimensional isotropic pin fin introduced earlier in literature can easily be recovered from the general solutions presented in this paper. Furthermore, dimensionless optimization results are presented for orthotropic pin fins that can help to solve many natural and forced convection pin fin problems. [DOI: 10.1115/1.4000059]

Keywords: orthotropic, pin fin, dimensionless heat transfer, optimization

1 Introduction

Recent advancements in polymer matrix composites have made such materials, which are viable options to conventional metals in the fabrication of heat sinks for air-cooled electronic components and assemblies. Other than the manufacturing advantages offered by such moldable composites, their relatively low density and lower coefficient of thermal expansion can provide a significant weight reduction and improve reliability in the package-heat sink and package-printed-circuit-board interfaces [1–5]. In addition, they consume significantly less fabrication energy than conventional aluminum heat sinks, thus, yielding an important contribution to sustainability. However, successful use of these nonmetallic composite materials in heat sinks requires careful thermofluid design and optimization and an insightful appreciation of the performance limits of polymer composite heat sinks.

It is important to emphasize that conventional polymers are expected to display thermal conductivities in the range of 0.1–0.5 W/m K. However, with the addition of high thermal conductivity, continuous carbon fibers these composites can reach thermal conductivities of about 400 W/m K in the fiber axis direction. Table 1 summarizes the thermal-mechanical properties of some of the typical polymeric composites. It can be seen that these composites display far lower thermal conductivities in the orthogonal (perpendicular to fiber axis) direction. Zweben [1,2] discussed that the use of pitch based discontinuous fibers results in axial conductivity of up to 100 W/m K and radial conductivity as low as the polymer conductivity of 0.4 W/m K.

There are several pin fin analyses that exist in literature [6–11], derivation of temperature, and heat flow equations for two-dimensional isotropic pin fins [9,12,13]. However, the impact of orthotropic thermal conductivity on the thermal performance of polymer composite fins has yet to be clearly established. Failure to properly account for the role of orthotropic material could limit the thermal designer's ability to predict and optimize the thermal performance of such polymer composite fins and heat sinks. Bahadur and co-worker [14,15] presented closed-form solutions for temperature distribution and heat transfer from orthotropic pin fins; although, their results cannot be reduced to the classical results of isotropic insulated-tip and convective-tip two-dimensional solutions. There is no such tangible proof given in their work [14,15]. Therefore, the solutions presented by them could not be considered as benchmark solutions.

The objective of this paper is to present general closed-form analytical results for polymeric composite fins, which can easily be reduced to several special cases. In addition, introduce a generalized design curve and correlations that can be used to obtain the optimum geometry of pin fins.

2 Analysis

Traditional fin thermal analysis is based on the Murray–Gardener [6,14] assumptions, which, along with other assumptions, neglect the presence of radial temperature gradients in the fin and anisotropy in the fin material. It is expected that for low Biot number fins, signifying fins that are nearly isothermal in the radial direction, the classical one-dimensional relations would apply. However, for large Bi fins with significant radial gradients, fin thermal performance can be expected to depart from the conventional fin relations. This behavior may be observed by considering heat conduction in both radial and axial orthotropic fins. In this regard, we consider a radially symmetric, pin fin with no internal heat generation, as shown in Fig. 1. The steady-state energy equation in a cylindrical coordinate system can be expressed as

$$\frac{1}{r}\frac{\partial}{\partial r}\left(k_r r\frac{\partial T}{\partial r}\right)+k_z\frac{\partial^2 T}{\partial z^2}=0 \tag{1}$$

We are seeking the solution of the above partial differential equation under the following boundary conditions:

$$\left.\frac{\partial T}{\partial r}\right|_{r=0}=0; \quad -k_r\left.\frac{\partial T}{\partial r}\right|_{r=R}=h_r(T(R,z)-T_\infty) \tag{2a}$$

and

Contributed by the Heat Transfer Division of ASME for publication in the JOURNAL OF HEAT TRANSFER. Manuscript received June 2, 2009; final manuscript received August 16, 2009; published online December 30, 2009. Editor: Yogesh Jaluria.

Table 1 Properties of selected composite materials for pin fin applications [1,2]

Reinforcement	Matrix	Thermal conductivity (W/m K) Longitudinal	Thermal conductivity (W/m K) Transverse	Density (g/cc)	CTE (ppm/K) Longitudinal	Modulus (GPa) Longitudinal
Continuous carbon fibers	Polymer	330	3–10	1.8	−1	186
Discontinuous carbon fibers	Polymer	10–100	3–10	1.7	4–7	30–140
Continuous carbon fibers	Aluminum	200–290	120–150	2.5	0–16	131
Discontinuous carbon fibers	Aluminum	190–230	120–150	2.5	3.0–9.5	14
Continuous carbon fibers	Copper	400–420	200	5.3–8.2	0.5–16	158
Discontinuous carbon fibers	Copper	300	200	6.8	6.5–9.5	NA
Continuous carbon fibers	Carbon	400	40	1.9	−1.0	255
Natural graphite	Epoxy	370	6.5	1.94	−2.4	NA

$$k_z \left.\frac{\partial T}{\partial z}\right|_{z=0} = h_z(T(r,0) - T_\infty); \quad T(r,L) = T_b \tag{2b}$$

Introducing the dimensionless variables as

$$r^* = \frac{r}{R}; \quad z^* = \frac{z}{L}; \quad k^* = \frac{k_r}{k_z}; \quad \beta^2 = k^*\frac{L^2}{R^2}$$
$$\mathrm{Bi}_r = \frac{h_r R}{k_r}; \quad \mathrm{Bi}_z = \frac{h_z L}{k_z}; \quad \text{and} \quad \theta = \frac{T - T_\infty}{T_b - T_\infty} \tag{3}$$

the differential equation and boundary conditions can be reduced to

$$\frac{1}{r^*}\frac{\partial}{\partial r^*}\left(r^*\frac{\partial\theta}{\partial r^*}\right) + \frac{1}{\beta^2}\frac{\partial^2\theta}{\partial z^{*2}} = 0 \tag{4}$$

$$\left.\frac{\partial\theta}{\partial r^*}\right|_{r^*=0} = 0; \qquad \left.\frac{\partial\theta}{\partial r^*}\right|_{r^*=1} + \mathrm{Bi}_r\theta(1,z^*) = 0 \tag{5a}$$

and

$$\left.\frac{\partial\theta}{\partial z^*}\right|_{z^*=0} - \mathrm{Bi}_z\theta(r^*,0) = 0; \quad \theta(r^*,1) = 1 \tag{5b}$$

It should be noted that the governing differential equation as well as the two boundary conditions in the r^* direction are homogeneous. In this regard, we use the separation of variable procedure to obtain the characteristic value problem in the homogeneous direction. This gives after some simplification

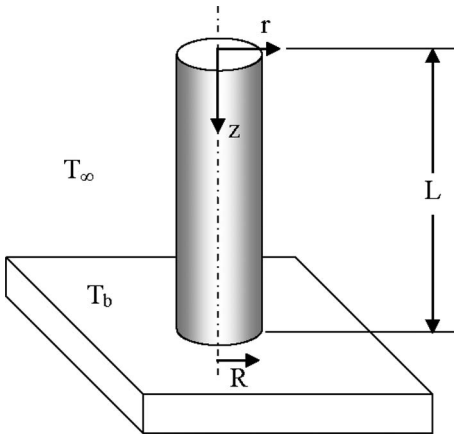

Fig. 1 Pin fin schematic

$$\theta(r^*,z^*) = \sum_{m=1}^{\infty}\frac{C_m J_0(\lambda_m r^*)}{\lambda_m\beta}[\lambda_m\beta\cosh(\lambda_m\beta z^*) + \mathrm{Bi}_z\sinh(\lambda_m\beta z^*)] \tag{6}$$

The eigenvalues (λ_m) are given by the convection boundary condition (refer to Eq. (5*a*)) as

$$J_1(\lambda_m) = \frac{\mathrm{Bi}_r}{\lambda_m}J_0(\lambda_m) \tag{7}$$

The constant C_m is calculated by making use of the nonhomogeneous boundary condition and recognizing the orthogonal properties of Bessel functions. This simplifies Eq. (6) to give

$$\theta(r^*,z^*) = \frac{T - T_\infty}{T_b - T_\infty} = 2\sum_{m=1}^{\infty}\frac{\lambda_m J_1(\lambda_m)J_0(\lambda_m r^*)}{J_0^2(\lambda_m)[\lambda_m^2 + \mathrm{Bi}_r^2]} \times\left[\frac{\lambda_m\beta\cosh(\lambda_m\beta z^*) + \mathrm{Bi}_z\sinh(\lambda_m\beta z^*)}{\lambda_m\beta\cosh(\lambda_m\beta) + \mathrm{Bi}_z\sinh(\lambda_m\beta)}\right] \tag{8}$$

The heat transfer rate from the fin base can be calculated from the equation

$$q_f = \int_0^R k_z\left.\frac{\partial T}{\partial z}\right|_{z=L} 2\pi r dr = \frac{2\pi R^2(T_b - T_\infty)k_z}{L}\int_0^1\left.\frac{\partial\theta}{\partial z^*}\right|_{z^*=1} r^* dr^* \tag{9}$$

Substituting $\theta(r^*,z^*)$ from Eq. (8), results in the dimensionless heat transfer rate from the fin base as

$$Q = \frac{q_f L}{4\pi k_z\beta(T_b - T_\infty)R^2} = \sum_{m=1}^{\infty}\frac{\lambda_m J_1^2(\lambda_m)}{J_0^2(\lambda_m)[\lambda_m^2 + \mathrm{Bi}_r^2]}\left[\frac{\lambda_m\beta\sinh(\lambda_m\beta) + \mathrm{Bi}_z\cosh(\lambda_m\beta)}{\lambda_m\beta\cosh(\lambda_m\beta) + \mathrm{Bi}_z\sinh(\lambda_m\beta)}\right] \tag{10}$$

The fin efficiency that is defined as heat transfer from the fin to the maximum possible heat transfer rate. That is, the entire fin surface is at the base temperature and can be expressed as

$$\eta_f = \frac{q_f}{q_{f,\max}} = \frac{4\beta(R/L)}{\mathrm{Bi}_z(2 + R/L)}\sum_{m=1}^{\infty}\frac{\lambda_m J_1^2(\lambda_m)}{J_0^2(\lambda_m)[\lambda_m^2 + \mathrm{Bi}_r^2]} \times\left[\frac{\lambda_m\beta\sinh(\lambda_m\beta) + \mathrm{Bi}_z\cosh(\lambda_m\beta)}{\lambda_m\beta\cosh(\lambda_m\beta) + \mathrm{Bi}_z\sinh(\lambda_m\beta)}\right] \tag{11}$$

The fin effectiveness that is a measure of examining thermal effectiveness of adding fins to a heat transfer surface, since the fin provide an additional resistance to heat transfer, is given by

$$\varepsilon_f = \frac{q_f}{q_{\text{no,fin}}} = \frac{4\beta}{\text{Bi}_z}\sum_{m=1}^{\infty}\frac{\lambda_m J_1^2(\lambda_m)}{J_0^2(\lambda_m)[\lambda_m^2+\text{Bi}_r^2]}\left[\frac{\lambda_m\beta\sinh(\lambda_m\beta)+\text{Bi}_z\cosh(\lambda_m\beta)}{\lambda_m\beta\cosh(\lambda_m\beta)+\text{Bi}_z\sinh(\lambda_m\beta)}\right] \quad (12)$$

3 Insulated-Tip Boundary Condition

It is interesting to examine the case of a typical insulated-tip boundary condition in which there is no heat transfer from the fin tip, i.e., substitute $\text{Bi}_z=0$ in the general solution (Eqs. (8) and (10)). This result in

$$\theta_{\text{ins}}(r^*,z^*) = 2\sum_{m=1}^{\infty}\frac{\lambda_m J_1(\lambda_m)J_0(\lambda_m r^*)}{J_0^2(\lambda_m)[\lambda_m^2+\text{Bi}_r^2]}\left[\frac{\cosh(\lambda_m\beta z^*)}{\cosh(\lambda_m\beta)}\right] \quad (13)$$

$$Q_{\text{ins}} = \sum_{m=1}^{\infty}\frac{\lambda_m J_1^2(\lambda_m)}{J_0^2(\lambda_m)[\lambda_m^2+\text{Bi}_r^2]}\tanh(\lambda_m\beta) \quad (14)$$

and

$$\eta_{f,\text{ins}} = \frac{q_{f,\text{ins}}}{q_{f,\text{ins,max}}} = \frac{2}{\beta\text{Bi}_r}\sum_{m=1}^{\infty}\frac{\lambda_m J_1^2(\lambda_m)}{J_0^2(\lambda_m)[\lambda_m^2+\text{Bi}_r^2]}\tanh(\lambda_m\beta) \quad (15)$$

$$\varepsilon_{f,\text{ins}} = \frac{q_{f,\text{ins}}}{q_{\text{no,fin,ins}}} = \frac{4}{\beta\text{Bi}_r(R/L)}\sum_{m=1}^{\infty}\frac{\lambda_m J_1^2(\lambda_m)}{J_0^2(\lambda_m)[\lambda_m^2+\text{Bi}_r^2]}\tanh(\lambda_m\beta) \quad (16)$$

4 Isotropic Two-Dimensional Fin

It can easily be shown from the general solution that the classical two-dimensional fin solution for constant thermal conductivity case can easily be recovered. In this regard $k_r=k_z=k$ and

$$\text{Bi}_z = \frac{hL}{k} = \frac{hR}{k}\frac{L}{R} = \text{Bi}\beta, \quad \text{where } \beta = \left(\frac{L}{R}\right) \quad (17)$$

This gives

$$\theta_{\text{iso}} = 2\sum_{m=1}^{\infty}\frac{\lambda_m J_1(\lambda_m)J_0(\lambda_m r^*)}{J_0^2(\lambda_m)[\lambda_m^2+\text{Bi}^2]}\left[\frac{\lambda_m\cosh(\lambda_m\beta z^*)+\text{Bi}\sinh(\lambda_m\beta z^*)}{\lambda_m\cosh(\lambda_m\beta)+\text{Bi}\sinh(\lambda_m\beta)}\right] \quad (18)$$

$$Q_{\text{iso}} = \sum_{m=1}^{\infty}\frac{\lambda_m J_1^2(\lambda_m)}{J_0^2(\lambda_m)[\lambda_m^2+\text{Bi}^2]}\left[\frac{\lambda_m\sinh(\lambda_m\beta)+\text{Bi}\cosh(\lambda_m\beta)}{\lambda_m\cosh(\lambda_m\beta)+\text{Bi}\sinh(\lambda_m\beta)}\right] \quad (19)$$

$$\eta_{f,\text{iso}} = \frac{q_{f,\text{iso}}}{q_{f,\text{iso,max}}} = \frac{4(R/L)}{\text{Bi}(2+R/L)}\sum_{m=1}^{\infty}\frac{\lambda_m J_1^2(\lambda_m)}{J_0^2(\lambda_m)[\lambda_m^2+\text{Bi}^2]}\times\left[\frac{\lambda_m\sinh(\lambda_m\beta)+\text{Bi}\cosh(\lambda_m\beta)}{\lambda_m\cosh(\lambda_m\beta)+\text{Bi}\sinh(\lambda_m\beta)}\right] \quad (20)$$

and

$$\varepsilon_{f,iso} = \frac{q_{f,\text{iso}}}{q_{\text{no,fin,iso}}} = \frac{4}{\text{Bi}}\sum_{m=1}^{\infty}\frac{\lambda_m J_1^2(\lambda_m)}{J_0^2(\lambda_m)[\lambda_m^2+\text{Bi}^2]}\left[\frac{\lambda_m\sinh(\lambda_m\beta)+\text{Bi}\cosh(\lambda_m\beta)}{\lambda_m\cosh(\lambda_m\beta)+\text{Bi}\sinh(\lambda_m\beta)}\right] \quad (21)$$

This is exactly the same temperature distribution and heat transfer results that are described in Ref. [9].

For the case of isotropic fin subjected to insulated-tip condition, we have

$$\theta_{\text{iso,ins}} = 2\sum_{m=1}^{\infty}\frac{\lambda_m J_1(\lambda_m)J_0(\lambda_m r^*)}{J_0^2(\lambda_m)[\lambda_m^2+\text{Bi}^2]}\left[\frac{\cosh(\lambda_m\beta z^*)}{\cosh(\lambda_m\beta)}\right] \quad (22)$$

$$Q_{\text{iso,ins}} = \sum_{m=1}^{\infty}\frac{\lambda_m J_1^2(\lambda_m)}{J_0^2(\lambda_m)[\lambda_m^2+\text{Bi}^2]}\tanh(\lambda_m\beta) \quad (23)$$

$$\eta_{f,\text{iso,ins}} = \frac{q_{f,\text{iso,ins}}}{q_{f,\text{iso,ins,max}}} = \frac{2(R/L)}{\text{Bi}}\sum_{m=1}^{\infty}\frac{\lambda_m J_1^2(\lambda_m)}{J_0^2(\lambda_m)[\lambda_m^2+\text{Bi}^2]}\tanh(\lambda_m\beta) \quad (24)$$

and

$$\varepsilon_{f,\text{iso,ins}} = \frac{q_{f,\text{iso,ins}}}{q_{\text{no,fin,iso}}} = \frac{4}{\text{Bi}}\sum_{m=1}^{\infty}\frac{\lambda_m J_1^2(\lambda_m)}{J_0^2(\lambda_m)[\lambda_m^2+\text{Bi}^2]}\tanh(\lambda_m\beta) \quad (25)$$

5 Approximate One-Term Solutions

It is interesting to examine only the one-term series solutions to see how far we are from the exact values. In this regard, the eigenvalues given by Eq. (7) can be solved for λ_1 as a function of Bi_r. Subsequently, the temperature distribution, heat transfer, fin efficiency, and effectiveness given by Eqs. (8) and (10)–(12) can be reduced to the following one-term solutions:

$$\theta_1(r^*,z^*) = AJ_0(\lambda_1 r^*)\left[\frac{\lambda_1\beta\cosh(\lambda_1\beta z^*)+\text{Bi}_z\sinh(\lambda_1\beta z^*)}{\lambda_1\beta\cosh(\lambda_1\beta)+\text{Bi}_z\sinh(\lambda_1\beta)}\right] \quad (26)$$

$$Q_1 = B\left[\frac{\lambda_1\beta\sinh(\lambda_1\beta)+\text{Bi}_z\cosh(\lambda_1\beta)}{\lambda_1\beta\cosh(\lambda_1\beta)+\text{Bi}_z\sinh(\lambda_1\beta)}\right] \quad (27)$$

$$\eta_{f,1} = \frac{4B\beta(R/L)}{\text{Bi}_z(2+R/L)}\left[\frac{\lambda_1\beta\sinh(\lambda_1\beta)+\text{Bi}_z\cosh(\lambda_1\beta)}{\lambda_1\beta\cosh(\lambda_1\beta)+\text{Bi}_z\sinh(\lambda_1\beta)}\right] \quad (28)$$

$$\varepsilon_{f,1} = \frac{4B\beta}{\text{Bi}_z}\left[\frac{\lambda_1\beta\sinh(\lambda_1\beta)+\text{Bi}_z\cosh(\lambda_1\beta)}{\lambda_1\beta\cosh(\lambda_1\beta)+\text{Bi}_z\sinh(\lambda_1\beta)}\right] \quad (29)$$

where the constants A and B are given by

$$A = \frac{2\lambda_1 J_1(\lambda_1)}{J_0^2(\lambda_1)[\lambda_1^2+\text{Bi}_r^2]} \quad (30)$$

$$B = \frac{\lambda_1 J_1^2(\lambda_1)}{J_0^2(\lambda_1)[\lambda_1^2+\text{Bi}_r^2]} \quad (31)$$

The values of λ_1 and the above constants A and B are given in Table 2 for several values of radial Biot number Bi_r.

6 One-Dimensional Fin Solution

For completeness purposes, we present the classical one-dimensional fin solution for a convective-tip boundary condition that is presented in a basic heat transfer text book [16]. These results, after some straight forward manipulations, are presented

Table 2 Eigenvalues and constants *A* and *B* as a function of radial Biot number

Bi_r	λ_1	A	B
0.1	0.4417	1.0246	0.1104
0.2	0.6170	1.0483	0.1541
0.3	0.7465	1.0712	0.1863
0.4	0.8516	1.0931	0.2123
0.5	0.9408	1.1143	0.2341
0.6	1.0184	1.1345	0.2530
0.7	1.0873	1.1539	0.2695
0.8	1.1490	1.1724	0.2842
0.9	1.2048	1.1902	0.2973
1.0	1.2558	1.2071	0.3090
1.1	1.3025	1.2232	0.3196
1.2	1.3456	1.2387	0.3292
1.3	1.3854	1.2533	0.3380
1.4	1.4225	1.2673	0.3459
1.5	1.4569	1.2807	0.3532
1.6	1.4892	1.2934	0.3598
1.7	1.5194	1.3055	0.3659
1.8	1.5477	1.3170	0.3715
1.9	1.5743	1.3279	0.3766
2.0	1.5994	1.3384	0.3813

in terms of the dimensionless variables that are introduced in the above two-dimensional orthotropic fin solutions. This results in

$$Q_{1D} = \frac{1}{2}\sqrt{\frac{\mathrm{Bi}_z}{2}(R/L)} \times \frac{\sinh(\sqrt{2\mathrm{Bi}_z(L/R)}) + \sqrt{\frac{\mathrm{Bi}_z}{2}(R/L)}\cosh(\sqrt{2\mathrm{Bi}_z(L/R)})}{\cosh(\sqrt{2\mathrm{Bi}_z(L/R)}) + \sqrt{\frac{\mathrm{Bi}_z}{2}(R/L)}\sinh(\sqrt{2\mathrm{Bi}_z(L/R)})} \tag{32}$$

$$\eta_{1D} = \frac{\sqrt{2\mathrm{Bi}_z(R/L)}}{\mathrm{Bi}_z(2+R/L)} \times \frac{\sinh(\sqrt{2\mathrm{Bi}_z(L/R)}) + \sqrt{\frac{\mathrm{Bi}_z}{2}(R/L)}\cosh(\sqrt{2\mathrm{Bi}_z(L/R)})}{\cosh(\sqrt{2\mathrm{Bi}_z(L/R)}) + \sqrt{\frac{\mathrm{Bi}_z}{2}(R/L)}\sinh(\sqrt{2\mathrm{Bi}_z(L/R)})} \tag{33}$$

and

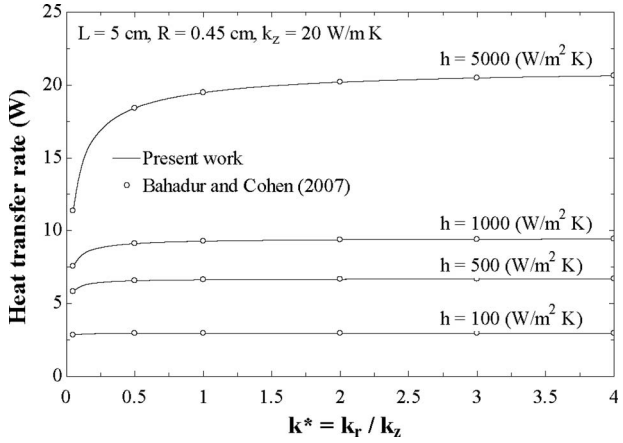

Fig. 2 Orthotropic pin fin heat transfer rate versus thermal conductivity ratio; comparison of results with Bahadur and Bar-Cohen [14]

$$\varepsilon_{1D} = \sqrt{\frac{2}{\mathrm{Bi}_z(R/L)}} \times \frac{\sinh(\sqrt{2\mathrm{Bi}_z(L/R)}) + \sqrt{\frac{\mathrm{Bi}_z}{2}(R/L)}\cosh(\sqrt{2\mathrm{Bi}_z(L/R)})}{\cosh(\sqrt{2\mathrm{Bi}_z(L/R)}) + \sqrt{\frac{\mathrm{Bi}_z}{2}(R/L)}\sinh(\sqrt{2\mathrm{Bi}_z(L/R)})} \tag{34}$$

7 Results and Discussion

In order to calculate temperature distribution, heat transfer rate, efficiency, and effectiveness, we first calculate the eigenvalues, which are given by Eq. (7). It is found that within the range of parameters studied (refer to Table 3), the number of eigenvalues required for first decimal convergence of the analytical solution is about 30 values.

For validating the analytical solutions presented in the previous section, we compare our result with those available in literature for a pin fin having $R=0.45$ cm, $L=5$ cm, and axial conductivity of $k_z=20$ W/m K. In this regard, Fig. 2 shows comparison of the fin heat transfer rate with that of Bahadur and Bar-Cohen [14], wherein the effect of radial to axial conductivity ratio is presented. As expected from the plot, it is a perfect match. We find that the fin heat transfer rate increases with k^* and asymptotically approaches the limiting value. For the low heat transfer coefficient investigated (100 W/m^2 K), the improvement is insignificant, while for the highest heat transfer coefficient (5000 W/m^2 K), a significant improvement is noticed. The asymptotic limit for low

Table 3 Range of control parameters studied

Parameter	Minimum (W/m K)	Maximum (W/m K)
k_r	3	200
k_z	10	420
h	10	5000
	natural convection, air cooling	forced convection, water cooling
Dimensionless		
k^*	0.001	1
Bi_r	0	20
Bi_z	0	50

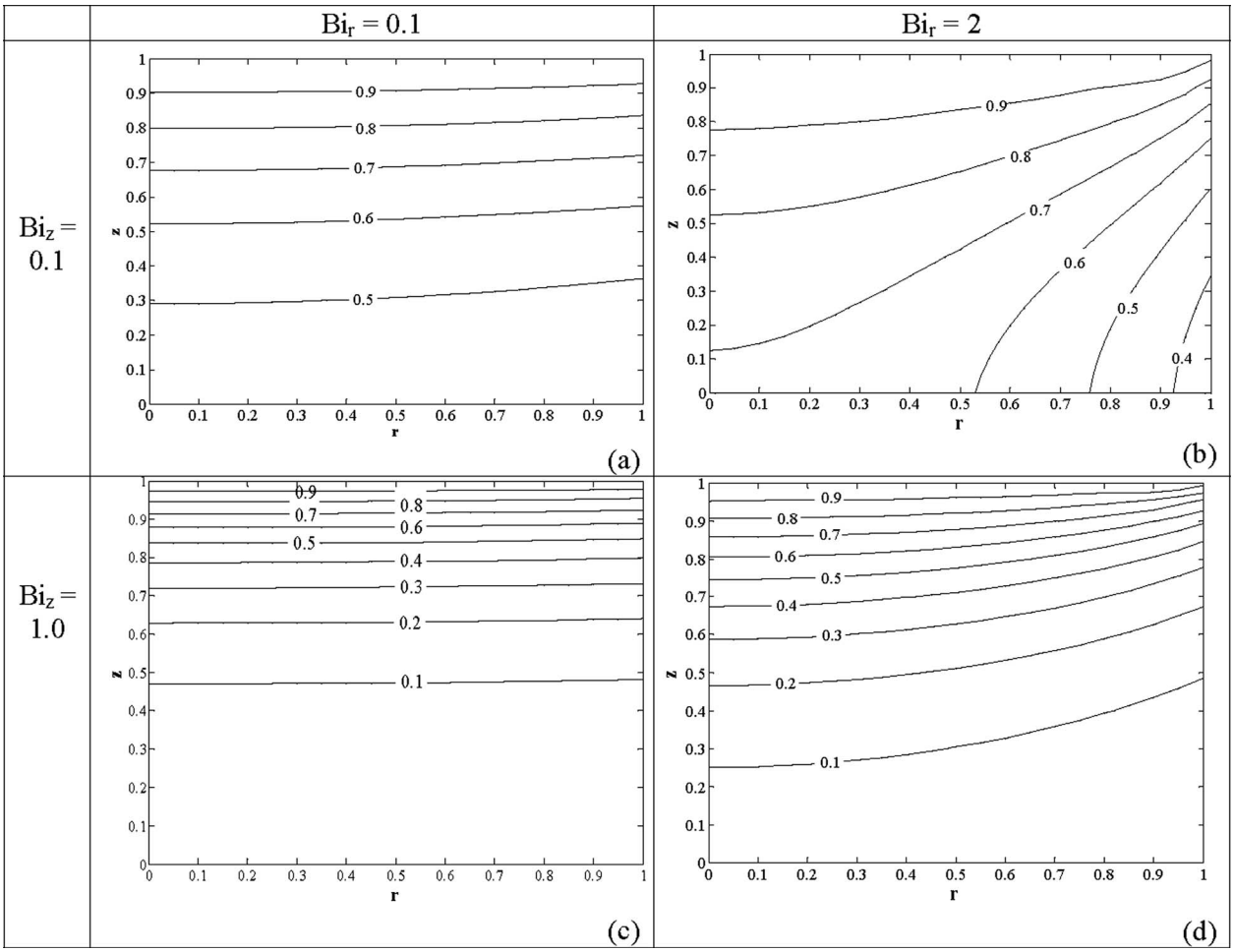

Fig. 3 Dimensionless temperature contour plots for a two-dimensional orthotropic pin fin having aspect ratio $L/R=10$: (*a*) radial Biot number $Bi_r=0.1$ and longitudinal Biot number $Bi_z=0.1$, (*b*) $Bi_r=2.0$ and $Bi_z=0.1$, (*c*) $Bi_r=0.1$ and $Bi_z=1.0$, and (*d*) $Bi_r=2.0$ and $Bi_z=1.0$

heat transfer coefficients is reached at k^* values of about unity, while for the high heat transfer coefficient applications that the fin could experience in forced convection heat exchangers, the heat transfer rate keeps on improving up to k^* values of 4.

The temperature distributions for a two-dimensional orthotropic pin fin given by Eq. (8) are plotted in Fig. 3 for a fin length-to-radius (or aspect) ratio $L/R=10$ and for different values of radial and axial Biot numbers. We notice that for an isotropic fin $k^*=1$ and $Bi_z=Bi_r(L/R)$. This represents case (c) in Fig. 3 for $Bi_r=0.1$ indicating that there are no temperature gradients in the radial direction. Therefore, one-dimensional fin solutions can be considered in such conditions. However for case (a), where $Bi_r=Bi_z=0.1$, some temperature gradients in radial direction are noticed when we compare with case (c). In addition, for large radial Biot number $Bi_r=2.0$ (refer to cases (b) and (d)), which corresponds to low thermal conductivity in the radial direction; it results in significant temperature gradients in the radial direction, particularly for case (b) when axial Biot number $Bi_z=0.1$. A tenfold increase in Bi_z for the same value of Bi_r (refer to case (d)) indicate a noteworthy change in temperature contours compared with case (c).

Figure 4 presents a plot of Eq. (10); that is, the dimensional heat transfer rate (Q) from the fin as a function of radial Biot number Bi_r for various values of thermal conductivity ratio k^* and $L/R=10$. It can be seen from the figure that Q increases with the increase in Bi_r. However, the dependency of conductivity ratio diminishes when the value of k^* approaches 1; that is, for the case of isotropic pin fin.

The fin efficiency and effectiveness results, given by Eqs. (11) and (12), are plotted as a function of radial Biot number Bi_r for various values of thermal conductivity ratio k^* and $L/R=10$ in Fig. 5. On comparing the effectiveness and efficiency relationship, we find that $\varepsilon_f=(1+2L/R)\eta_f$; therefore these are represented on the same figure. The figure shows that both the efficiency and effectiveness decreases asymptotically with the increase in values

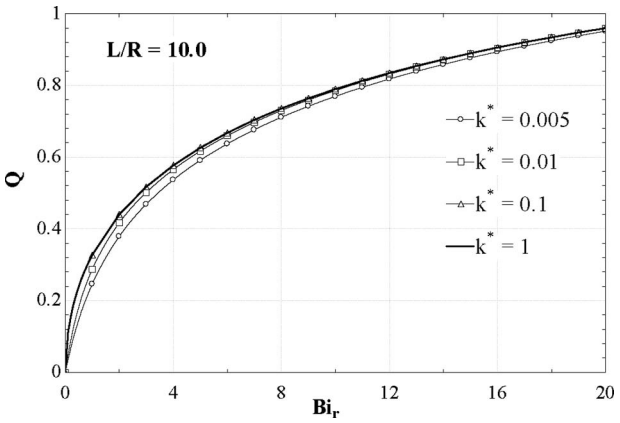

Fig. 4 Dimensionless heat transfer rate from the pin fin as a function of radial Biot number Bi_r and thermal conductivity ratio k^* for fin aspect ratio $L/R=10$

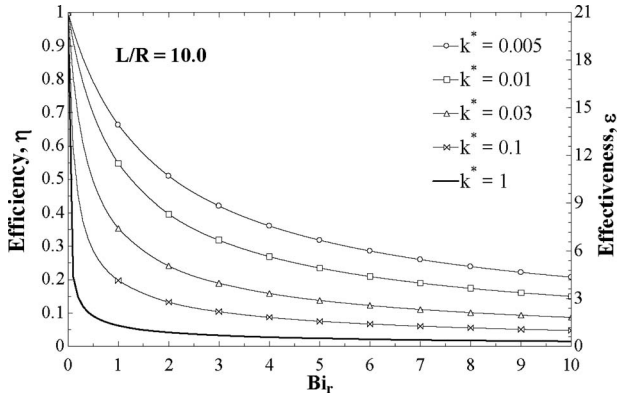

Fig. 5 Orthotropic pin fin efficiency and effectiveness as a function of radial Biot number Bi_r and thermal conductivity ratio k^* for fin aspect ratio $L/R=10$

of Bi_r and k^*. In addition, it can be seen that the use of fins that represents fin effectiveness greater than 1, is justified only for $Bi_r < 5.0$ and $k^* < 0.1$. However, for $k^* > 0.1$ and $Bi_r > 5.0$, the use of pin fins for heat transfer enhancement cannot be justified from thermal-economic considerations.

The plots of dimensionless heat transfer rate (Q) as a function of axial Biot number Bi_z for various values of thermal conductivity ratio k^* and $L/R=10$ are shown in Fig. 6. In contrast to Fig. 4, we find that Q decreases with the increase in k^*. It can be seen that for large values of conductivity ratio, the solution approaches one-dimensional (dimensionless or reduced) heat transfer rate given by Eq. (32). On the other hand, the plots of fin efficiency and effectives as a function of Bi_z (refer to Figs. 7(*a*) and 7(*b*)), clearly indicate that conventional one-dimensional fin performance results over predicts the orthotropic fin results principally for $k^* < 1.0$.

The errors in approximate one-term solution for both heat transfer and fin efficiency (refer to Eqs. (27) and (28)) are examined in Fig. 8 with respect to the complete solution. These curves demonstrate that error increases for the prediction of heat transfer rate and fin efficiency from one-term solution ($\geq 1\%$) when the radial Biot number $Bi_r > 0.3$ and axial Biot number $Bi_z < 0.5$. Therefore, one-term approximate solution will give reliable results if the above constraint is observed.

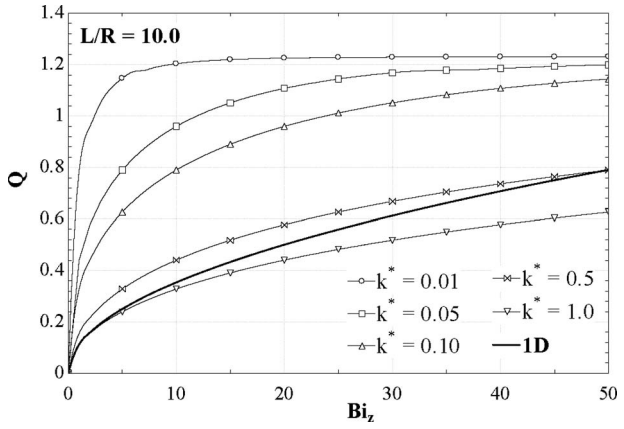

Fig. 6 Dimensionless heat transfer rate from the pin fin as a function of axial Biot number Bi_z and thermal conductivity ratio k^* for fin aspect ratio $L/R=10$; comparison with one-dimensional solution

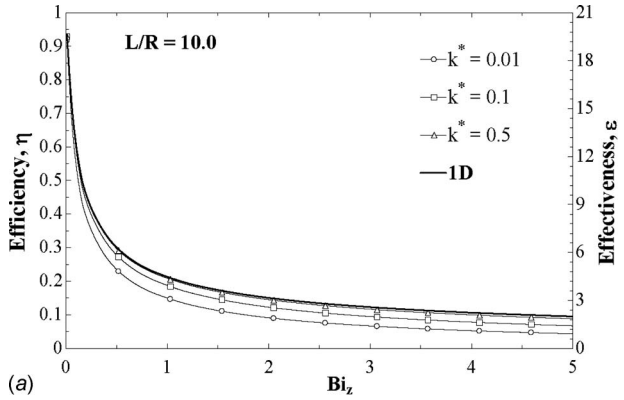

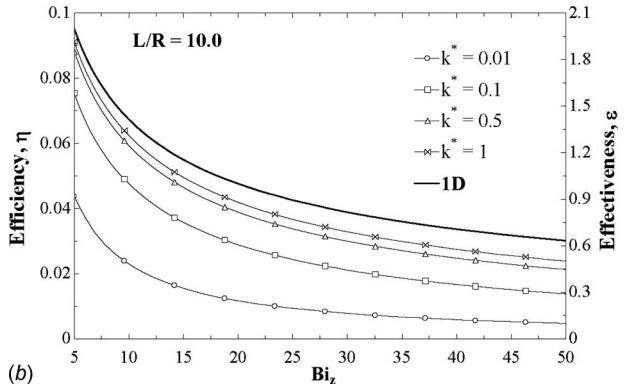

Fig. 7 Orthotropic pin fin efficiency and effectiveness as a function of axial Biot number Bi_z and thermal conductivity ratio k^* for fin aspect ratio $L/R=10$; comparison with one-dimensional solution: (*a*) low values of Bi_z and (*b*) high values of Bi_z

8 Fin Optimization

The fin optimal dimensions (R and L) can easily be calculated from the dimensionless heat transfer rate given by Eq. (10). In this regard, we introduce the dimensionless fin volume by the following relation:

$$V^* = \frac{V}{(k_z/h)^3} = \frac{\pi R^2 L}{(k_z/h)^3} = \frac{\pi \mathrm{Bi}_z^3}{(L/R)^2} \tag{35}$$

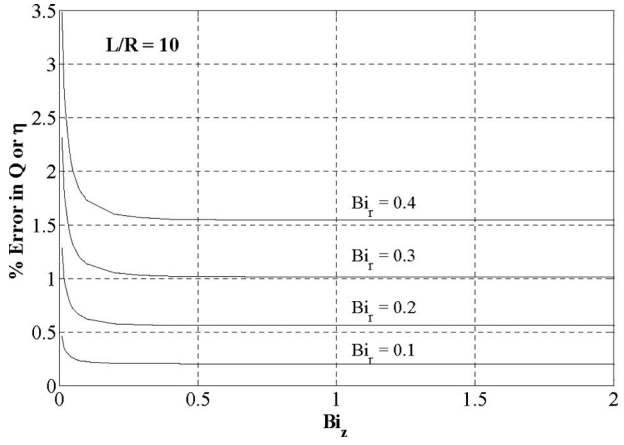

Fig. 8 Percentage error in approximate (one-term) solution for dimensionless heat transfer and efficiency as a function of radial and axial Biot numbers (Bi_r,Bi_z) for a fin aspect ratio $L/R=10$

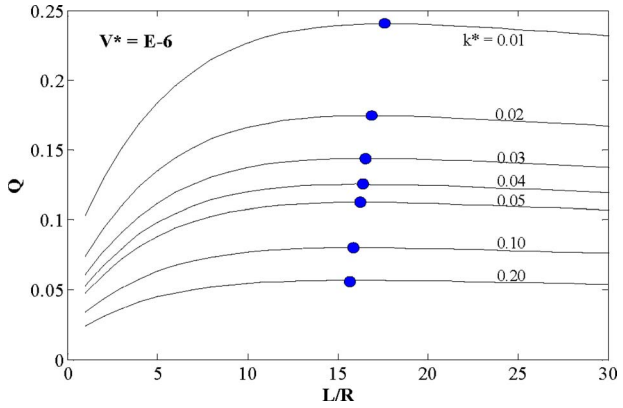

Fig. 9 Dimensionless heat transfer rate from the pin fin as a function of aspect ratio L/R and radial-to-axial thermal conductivity ratio k^* for a dimensionless fin volume $V^*=1\times10^{-6}$.

For a typical dimensionless fin volume $V^*=1\times10^{-6}$, we present dimensionless heat transfer rate as a function of fin aspect ratio L/R in Fig. 9 for different values of radial-to-axial thermal conductivity ratio k^*. The maximum Q points on the figure are marked for different values of k^*. It can be seen that the optimum value of aspect ratio L/R decreases slightly with k^*; however, it lies between $L/R=15$ and 17.5 for the range reported in the figure. While the effect of dimensionless volume V^* for a fixed value of conductivity ratio $k^*=0.05$ is shown in Fig. 10. This figure shows that the optimum value of the fin aspect ratio decreases considerably with the increase in dimensionless fin volume.

In Fig. 11, the optimum fin aspect ratio $(L/R)_{opt}$ is presented as a function of the dimensionless fin volume for different values of radial-to-axial thermal conductivity ratio k^*. In this regard, optimization algorithm based on golden section search and parabolic interpolation technique is used [17]. It should be noted that the objective function of the present optimization problem is the dimensionless heat rate (refer to Eq. (10)), which is considered as a continuous function. The optimization algorithm searches for an aspect ratio that maximizes the heat transfer rate within a specified interval of the aspect ratio. The optimal results, thus obtained for different values of V^* and k^* are plotted in Fig. 11. It is important to emphasize that these results are general and can be used for many orthotropic pin fin applications (natural to forced convection).

It is also important to compare the optimum aspect ratio of orthotropic two-dimensional pin fin numerical results with the case of isotropic one-dimensional pin fin analytical solution. The optimum radius of one-dimensional pin fin [18,19] is given by

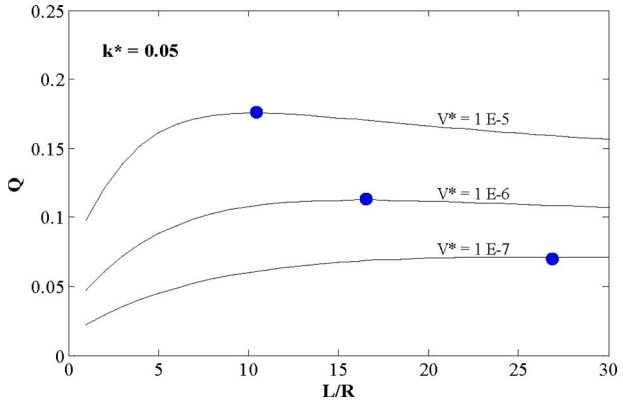

Fig. 10 Dimensionless heat transfer rate from the pin fin as a function of aspect ratio L/R and dimensionless fin volume V^* for a radial-to-axial thermal conductivity ratio $k^*=0.05$

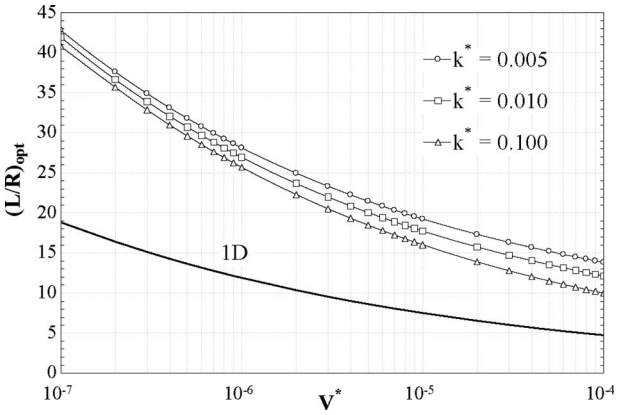

Fig. 11 Optimal fin aspect ratio, $(L/R)_{opt}$ as a function of dimensionless fin volume V^* for different values of radial-to-axial thermal conductivity ratio k^*; comparison with one-dimensional optimal solution

$$R_{opt}=0.75\left(\frac{hV^2}{k_z}\right)^{1/5} \tag{36}$$

Equation (36) can be rewritten in the following dimensionless form:

$$\left(\frac{L}{R}\right)_{opt}=0.75(V^*)^{-1/5} \tag{37}$$

The optimum pin fin aspect ratio thus obtained from Fig. 11 may be used for designing an orthotropic two-dimensional pin fin. However, these results can also be fitted in terms of correlations that can easily be used by thermal designers. In this regard, the best fit correlations that are obtained with a maximum deviation of 4% from the numerical results are

$$\left(\frac{L}{R}\right)_{opt}=a(V^*)^b \tag{38}$$

where for $0.005<k^*\leq0.04$ we get

$$a=0.621(k^*)^{-0.293} \tag{39a}$$

$$b=-0.018\ln(k^*)-0.26 \tag{39b}$$

and for $0.04<k^*<0.1$

$$a=1.198(k^*)^{-0.099} \tag{39c}$$

$$b=-0.007\ln(k^*)-0.221 \tag{39d}$$

It should be emphasized that all the optimization examples studied by Bahadur and Bar-Cohen [20] can easily be extracted from the results that are presented in Fig. 11.

As an illustration, we consider one of the problems of the optimum geometry of an orthotropic two-dimensional pin fin that is studied by Bahadur and Bar-Cohen [20] for natural convection application. The volume of the fin is taken as $V=3.2\times10^{-6}$ (m^3) and it has the following thermophysical properties: $k_r=0.3$ $(W/m\ K)$, $k_z=20$ $(W/m\ K)$, and $h=10$ $(W/m\ K)$.

Solution. First, we calculate the dimensionless volume and thermal conductivity ratio

$$V^*=\frac{V}{(k_z/h)^3}=\frac{3.2\times10^{-6}}{(20/10)^3}=4\times10^{-7}$$

$$k^*=\frac{k_r}{k_z}=\frac{0.3}{20}=0.015$$

Using Fig. 11, we find the optimum aspect ratio $(L/R)_{opt}=31.56$. This gives together with the pin fin volume definition

$$V = 3.18 \times 10^{-6} = 31.56\pi R^3$$

Therefore, we have $R_{opt} = 3.2$ (mm), and $L_{opt} = 10.1$ (cm). This is the same result as that obtained by Bahadur and Bar-Cohen [20].

9 Concluding Remarks

The limitations of solutions presented in Bahadur and coworker [14,15] are handled by reducing the problem in dimensionless coordinate system so that general solutions can be presented. The solutions are obtained for temperature distribution, heat transfer rate, and fin efficiency and fin effectiveness as benchmark solutions for a most important orthotropic pin fin problem. To establish the credibility of such solutions, all special cases given in other references are clearly demonstrated. The results are studied with respect to dimensionless variables such as radial and axial Biot numbers (Bi_r, Bi_z), fin aspect ratio L/R, and radial-to-axial conductivity ratio k^*. It is shown that the conventional one-dimensional fin performance results over predicts the orthotropic fin results principally for $k^* < 1.0$.

In addition one-term series solution (similar to the classical work of Heisler first presented in 1947 and still referenced in many heat transfer text books) is also provided. The limitations as well as the applicability of one-term solutions for two-dimensional orthotropic pin fin are also documented. The approximate solution shows that error increases for the prediction of heat transfer rate as well as fin efficiency ($\geq 1\%$) when the radial Biot number $Bi_r > 0.3$ and axial Biot number $Bi_z < 0.5$. Therefore, approximate solutions can only be utilized with the above restrictions of radial and axial Biot numbers.

The dimensionless representation also helped to demonstrate the fin optimization for a class of orthotropic pin fin problems, which is unique and never presented before in literature. In this regard, all fin optimization results presented by Bahadur and coworker [20,15] are shown to be special cases of the generalized optimization results presented in the paper. The optimization results are numerically obtained for various ranges of dimensionless fin volume and radial-to-axial thermal conductivity ratios. These results are shown to represent many applications of pin fin problems that cover both natural as well as forced convection applications; that is, very low to very high heat transfer coefficients. It is expected that the optimization results presented in the paper will be useful for the design and optimization of extended surfaces, particularly with the emerging composite (orthotropic) materials, which is anticipated to be the leading technology for finned heat transfer surfaces.

Acknowledgment

The authors acknowledge the support provided by the King Fahd University of Petroleum and Minerals through Project No. SB090009.

Nomenclature

Symbol

A = constant
B = constant
Bi = Biot number
C = constant
h = heat transfer coefficient ($W\ m^{-2}\ K^{-1}$)
k = thermal conductivity ($W\ m^{-1}\ K^{-1}$)
L = fin length (m)
Q = dimensionless heat transfer rate
q = heat transfer rate (W)
R = fin radius (m)
r = radial direction
T = temperature (°C)
V = pin fin volume (m^3)
z = distance from the fin tip (m)

Greek Symbols

β = dimensionless parameter defined in Eq. (3)
ε = fin effectiveness
η = fin efficiency
θ = dimensionless temperature
λ = eigenvalue

Subscripts

1 = one-term
1D = one-dimension
b = base
f = fin
ins = insulated
iso = isotropic
max = maximum
opt = optimum
r = radial
z = axial
∞ = ambient condition

Superscript

* = dimensionless

References

[1] Zweben, C., 2001, "Advanced Composites and Other Advanced Materials for Electronic Packaging Thermal Management," Materials 2001, International Symposium on Advanced Packaging Materials, Braselton, GA, March 11–14.
[2] Zweben, C., 2003, "Emerging High-Volume Commercial Applications for Thermally Conductive Carbon Fibers," *Proceedings of the 6th International Business Conference on the Global Outlook for Carbon Fiber*, San Diego, CA, Nov. 5–7.
[3] Shives, G., Norley, J., Smale, M., Chen, G., and Capp, J., 2004, "Comparative Thermal Performance Evaluation of Graphite/Epoxy Fin Heat Sinks," *Proceedings of Intersociety Conference on Thermal Phenomena (ITHERM)*, pp. 410–417.
[4] Bahadur, R., and Bar-Cohen, A., 2005, "Thermal Design and Optimization of Natural Convection Polymer Pin Fin Heat Sinks," IEEE Trans. Compon. Packag. Technol., **28**(2), pp. 238–246.
[5] Weber, E., 1999, "Development and Modeling of Thermally Conductive Polymer/Carbon Composites," Ph.D. thesis, Chemical Engineering Department, Michigan Technological University, Michigan.
[6] Gardner, K. A., 1945, "Efficiency of Extended Surfaces," Trans. ASME, **67**, pp. 621–631.
[7] Kern, D. A., and Kraus, A. D., 1972, *Extended Surface Heat Transfer*, McGraw-Hill, New York, pp. 114–115.
[8] Harper, D. R., and Brown, W. B., 1922, "Mathematical Equations for Heat Conduction in the Fins in Air Cooled Engines," NACA Technical Report No. 158.
[9] Kraus, A. D., Aziz, A., and Welty, J., 2001, *Extended Surface Heat Transfer*, Wiley, New York.
[10] Ozisik, M. N., 1993, *Heat Conduction*, 2nd ed., Wiley, New York.
[11] Gebhart, B., 1993, *Heat Conduction and Mass Diffusion*, McGraw-Hill, New York.
[12] Poulikakos, D., 1994, *Conduction Heat Transfer*, Prentice-Hall, Englewood Cliffs, NJ.
[13] Mikhailov, M. D., and Ozisik, M. N., 1984, *Unified Analysis and Solutions of Heat and Mass Diffusion*, Wiley, New York.
[14] Bahadur, R., and Bar-Cohen, A., 2007, "Orthotropic Thermal Conductivity Effect on Cylindrical Pin Fin Heat Transfer," Int. J. Heat Mass Transfer, **50**, pp. 1155–1162.
[15] Bahadur, R., 2005, "Characterization, Modeling and Optimization of Polymer Composite Pin Fins," Ph.D. thesis, University of Maryland, College Park, MD.
[16] Incropera, F. P., and DeWitt, D. P., 2002, *Introduction to Heat Transfer*, 4th ed., Wiley, New York.
[17] Press, W. H., Flannery, B. P., Teukolsky, S. A., and Vetterling, W. T., 2007, *Numerical Recipes: The Art of Scientific Computing*, 3rd ed., Cambridge University Press, London.
[18] Sonn, A., and Bar-Cohen, A., 1981, "Optimum Cylindrical Pin Fin," ASME J. Heat Transfer, **103**, pp. 814–815.
[19] Sharqawy, M. H., and Zubair, S. M., 2009, "Performance and Optimum Geometry of Spines With Simultaneous Heat and Mass Transfer," Int. J. Therm. Sci., **48**, pp. 2130–2138.
[20] Bahadur, R., and Bar-Cohen, A., 2006, "Analysis and Design of a Least Material Orthotropic Pin Fin Heat Sinks," Thermal and Thermomechanical Phenomena in Electronics Systems, ITHERM '06 Conference.

Pool Boiling Heat Transfer of Water on Finned Surfaces at Near Vacuum Pressures

Mark Aaron Chan

Christopher R. Yap

Kim Choon Ng[1]
e-mail: mpengkc@nus.edu.sg

Department of Mechanical Engineering,
National University of Singapore,
10 Kent Ridge Crescent,
Singapore 119260

This research paper presents a study of boiling heat transfer from longitudinal rectangular-finned surfaces immersed in saturated water at low vapor pressures. Finned surfaces with assorted fin spacing, fin thicknesses, and fin heights on a copper based surface have been investigated. All the finned surfaces were found to increase both boiling heat transfer coefficients and critical heat fluxes. An optimal fin thickness was found for a configuration, and heat transfer coefficients have been obtained at the pressures. Factors affecting the boiling characteristics have been identified and the optimal enhancement requires a balance of the active nucleation sites, bubble flow resistance, natural convection, thin film evaporation, liquid superheating, heat transfer area, bubble coalescence, and liquid reflux resistance. High speed visualization of vapor plug and vapor film generation on the boiling surfaces has revealed significant insights into the boiling mechanisms at low saturation pressures. [DOI: 10.1115/1.4000054]

Keywords: boiling, extended surfaces, subatmospheric pressure, boiling enhancement, thermosyphon, electronic cooling, bubble visualization

1 Introduction

Phase change phenomena enhance heat transfer as its heat fluxes could perform up to two orders higher than the single-phase heat transfer. The exponential rise in heat fluxes in electronic components has sparked a wave of interest in enhanced boiling from evaporator surfaces, mitigating the heat transfer "bottlenecks" of components and CPUs. Webb [1] showed some concepts of the boiling surface enhancement, namely, the integral-fin, sintered porous coating, re-entrant cavities, and other special structured surface geometries. In 1973, Westwater [2] and his colleagues studied the low-finned surfaces with bubbles larger than the interfin spacing create a vapor film at the root of the fins, causing significant heat transfer "resistance," leading to the liquid dry-out phenomenon. For bubbles smaller than the fin gap, the finned tube surfaces retain the ability to supply liquid to the base of fins for heat removal. Experimental data of Joudi and James [3] on the incipient boiling of water, R113, and methanol showed a pronounced temperature overshoot at incipience for the refrigerants except for water. Fath and Judd [4] and Gorenflo [5] visually observed the effects of pressure at vapor pressures up to 40 bars on pool boiling of R-22 on low-finned tubes. The heat transfer enhancement produced by finned tubes tends to decline with increasing heat flux and pressure, and approach asymptotically to the boiling performance of a plain tube, while the rate of heat transfer increases with heat fluxes and pressures.

McGillis et al. [6] studied the boiling of water on pin-finned surfaces and found that smaller fin gaps heat up the liquid more quickly than large fin gaps, making it effective at initiating the boiling and increasing the bubble departure frequency. Furthermore, they observed that fin thickness has insignificant influence on the boiling data. Other studies on boiling heat transfer with finned surfaces have focused on dielectric working fluids such as FC-72 and FC-87. Owing to the higher wettability, they are suitable for porous coating enhancements and immersion cooling. Rainey and You [7] studied microporous coated and plain pin-finned surfaces in a saturated FC-72 medium: Such porous coated finned surfaces provide significantly higher heat transfer coefficients over the plain finned surfaces, such that the influence of fin length is negligible. The pressure effect for both plain and microporous coated finned surfaces is similar to that for a flat surface, with nucleate pool boiling performance increasing with increased pressure [8,9]. Wei and Honda [10] evaluated the effects of fin geometry on silicon micropin fins in FC-72. With fixed thickness, the critical heat flux (CHF) increased monotonically with increasing fin height and a high CHF of 84.5 W/cm^2 has been reported with the combination of 50 μm thickness, 270 μm height, with gas-dissolved FC-72 at 45 K subcooling. Yu and Lu [11] visually observed that boiling on FC-72 on pin-finned surfaces began at the tip of the fin from where it spreads to the fin root and concluded that reducing the fin spacing and increasing the fin length increases the heat transfer rate. A pin-fin array having 4 mm fin height and 0.5 mm fin spacing showed five times more improvement compared with a plain surface. Pal and Joshi [12] have investigated the effect of liquid-filled volume on various stacked heights of their enhancement structure within a two-phase loop thermosyphon at subatmospheric pressures. They have concluded that an increase in the liquid-filled height is needed to produce the best performance in stack structures.

There is a dearth of boiling literature of water at near vacuum pressures and the present work aims to supplement the data and visualization of the open literature that deals with boiling heat transfer of water on plain and structured surfaces at subatmospheric pressures. Most published works, hitherto, tend to be confined in a small boiling footprint (defined here as smaller than the capillary or bubble length scale) and chamber: Such limitations induce significant "pressure excursion" or fluctuations as vapor release (vapor specific volume >20 m^3/kg near vacuum conditions) is significant, causing a distortion of the q-ΔT plot or boiling curve by as much as a few degrees above the saturation temperatures. The present work reports on the salient changes in the boiling curve, which are influenced by the rate of bubble formation, bubble inundation characteristics, and bubble motion through the fin spaces with assorted departure diameters. The boiling re-

[1]Corresponding author.

Contributed by the Heat Transfer Division of ASME for publication in the JOURNAL OF HEAT TRANSFER. Manuscript received March 23, 2009; final manuscript received August 17, 2009; published online December 29, 2009. Review conducted by Yogesh Jaluria.

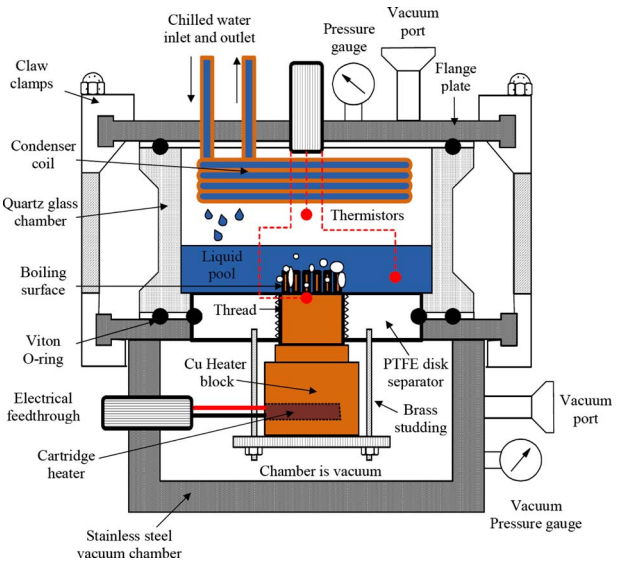

Fig. 1 Detailed schematic of the boiling/heater chamber

gimes of water on enhanced surfaces at working conditions found in two-phase thermosyphon coolers have been confirmed with high speed visualization.

2 Experimental Apparatus

The purpose-built pool boiling test facility used in the present work consists of six main components—pool boiling chamber, heater chamber, pressure monitoring system, vacuum and degassing system, measurement and data acquisition systems, and high speed video (HSV) camera with lighting. A schematic of the pool boiling chamber and the heater chamber is shown on Fig. 1. The boiling chamber is designed with a sufficiently large volume to avoid deviation from the saturation condition. The quartz boiling chamber holds the liquid pool of water with an internal diameter and height of 100 mm. This large chamber volume reduces the instantaneous pressure excursions when large vapor bubbles emanate in low pressure boiling, a difficulty observed by McGillis et al. [6]. A stainless steel blanking plate clamped on top of the boiling chamber holds multiple short flanges for vacuum connections. The copper condenser coils inlet and outlet, pressure transducer, electrical feed-through, and vacuum discharge valve are all connected to this plate. A temperature-controlled water bath supplies chilled water to the condenser coils to maintain the saturation pressure inside the chamber constant within ± 0.04 kPa. The transparent boiling chamber allowed the installation of an HSV camera (10,000 frames per second (fps)) with high magnification lens and lucent lighting to capture the fin root, fin spacing, and fin tip, as well as the bubble growth, ebullition, and interaction with adjacent bubbles and fins.

A polytetrafluoroethylene (PTFE) plate separator was used in between the boiling and the heater chamber. It has a radial static gland for O-ring seal to prevent water leakage and a threaded hole at the center for easy mounting and testing of many surfaces. All the test pieces (boiling surfaces) that have a base diameter of 30 mm and a height of 27 mm are made from a copper rod, an array of longitudinal rectangular fins are integrally formed on its surface: Assorted fin dimensions are used, i.e., fin spacing g (0.50 mm, 0.75 mm, and 1.0 mm), fin height h (0.75–15.0 mm), and fin thickness t (0.5 mm, 1.0 mm, and 2.0 mm).

The heater chamber is made of a stainless steel connector with three lateral angled flanges for vacuum connections. A copper heating block with three 150 W cartridge heater inserts is suspended onto the space using brass studding and it has no physical contact to avoid conduction heat loss to the ambient. A thermally conductive compound was used between the test piece and the heater block. Air is evacuated from this chamber to create a chamber pressure below 0.1 kPa, eliminating convection heat loss and leaving only the minor radiation heat loss in the chamber. A pressure transducer is attached to one of the chamber flanges and it constantly monitors the pressure level. An ac variable transformer and a high current electrical feed-through deliver electrical power to the cartridge heaters.

Two-wire thermistors having an accuracy of ± 0.1 K are used to measure the temperature levels on the boiling surface, the vapor space, the liquid bulk, and the ambient air. All the thermistor and pressure transducer (1–1000 mbar and $\pm 0.2\%$ accuracy) readings are gathered by a data acquisition system and data are stored into a personal computer. Multimeters are used to measure the voltage drop and the current in the heater circuit. The net heat input is computed after subtracting the heat loss component where the latter is determined from heat leak tests under no boiling condition. The boiling facility is assembled with standard high vacuum grade components and is capable of maintaining a pressure of as low as 10^{-7} mbar. A rotary vane pump with a displacement capacity of 7.0 m^3/h and an ultimate vacuum of 2×10^{-3} mbar was used for de-aeration.

The thermistors and the data acquisition system were calibrated with a master thermometer at five temperature intervals from 20–60°C to a maximum uncertainty of 0.1°C. The maximum relative uncertainty in the measurement of heat flux was 1.4%, while the current and voltage drop have an accuracy of 1%. The lowest superheat measured in the experiment was 1.98 K, hence the maximum relative uncertainty (with respect to the smallest temperature difference) in the heat transfer coefficient values is 7.3%.

3 Experimental Procedure

Before the experiment commences, the boiling chamber is filled with water to 60 mm above the base of the finned surface. The heater chamber is evacuated for 20 min to below 1 mbar and simultaneously the water is heated and boiled for 30 min. The system is cooled down to a steady state where the water is at a saturated state: The bulk liquid to the vapor space temperature differences are less than ± 0.1 K. The saturation pressure at the liquid/vapor temperature is checked using the pressure reading. Before all else, the data acquisition system starts recording the temperature and pressure readings at initial steady state conditions continuously until the very end of the test run. During a test run, the heat flux is raised in steps of 5 W/cm^2 from 5 W/cm^2 to a maximum of 75 W/cm^2 or when the CHF is just reached. The temperature bath supplies a constant chilled water temperature to the condenser coils, maintaining the chamber pressure at desired values of 2 kPa, 4 kPa, and 9 kPa absolute (in short, 2–4–9 kPa) and matching the heat input from the heater. When the temperature fluctuations of boiling surface are less than 0.3 K over a period of 300 s, steady state is assumed to be reached and the input power is recorded. Bubble formation and flow characteristics are recorded for visualization purposes using the HSV camera at a rate of 500 fps within a span of 2 s. First, pool boiling of water was performed on a plain copper surface at three 2–4–9 kPa pressures, after which finned surfaces of various geometries were tested at similar pressures.

4 Results and Discussion

Data gathered from the plain surface tests serve as a benchmark for boiling performance and they are compared with widely used empirical correlations. Figure 2 illustrates the good agreement of pool boiling test results with predictions from Cooper's correlation [13]. The minimum heat flux was 10 W/cm^2, below which intermittent ebullition occurred. Both the actual and predicted boiling curves shift to a higher superheat region at lower saturation pressures, implying a deterioration of boiling heat transfer at

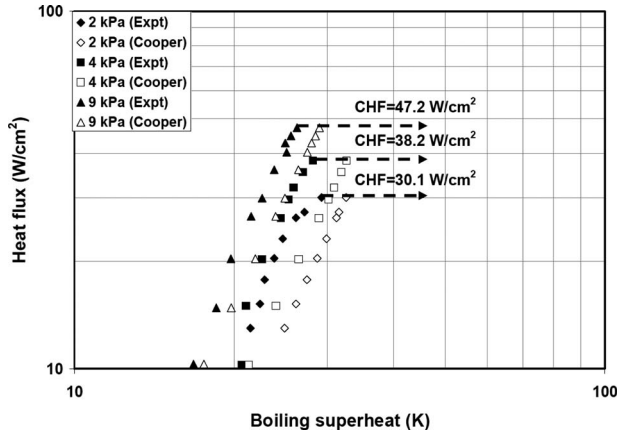

Fig. 2 Boiling curves of pool boiling on a plain copper surface at subatmospheric pressures of 2 kPa, 4 kPa, and 9 kPa. Experimental results with predictions from Cooper's correlation [13].

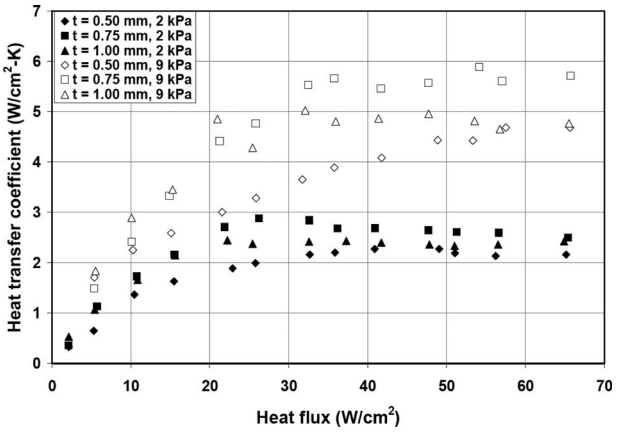

Fig. 4 Heat transfer coefficient versus heat flux (of footprint) for finned surfaces having different fin thicknesses with constant fin spacing (g)=0.5 mm and fin height (h)=15 mm at pressures of 2 kPa and 9 kPa

lower pressures. This is expected since the critical radius is decreased, thus providing less active nucleation sites. The steep slope of their boiling curves means that the boiling heat transfer coefficient rapidly increases with heat flux until the CHF is reached, which is indicated by Cooper's correlation [13]. The results show good agreement with those predicted. At 2–4–9 kPa, the slope of their boiling curves is similar and they differ by a maximum difference of 17%, 16%, and 11%, respectively. In the graph, the CHF of each curve is designated by a dashed arrow and is shown to be increasing in value at higher pressures. Using the critical heat flux of Zuber [14], Kutateladze [15], and Leinhard and co-workers [16–18], we employ the corrected CHF correlation (small heater dimensions) to predict the CHF for 2–4–9 kPa, which are 29.0 W/cm^2, 38.7 W/cm^2, and 53.8 W/cm^2, and the differences with the experimental values are only 3.8%, 1.3%, and 12.3%, respectively. This justifies the performance of the boiling test facility.

4.1 Effect of Fin Thickness. Figure 3 shows the boiling curves for assorted fin thickness (0.5–1 mm) at pressures of 2–9 kPa. As the fin thickness is increased from 0.5 mm to 0.75 mm, the boiling curve moves toward the left, an improvement in boiling performance but at 1.0 mm thickness the curve shifts back to the right. It is evident that 0.75 mm is the optimal fin thickness for this particular fin spacing and height. At a pressure of 2 kPa, the boiling curve of 1 mm thickness coincides with that of 0.75 mm thickness until a heat flux of 20 W/cm^2, where its slope starts to bend toward higher superheats. At a pressure of 9 kPa, 1 mm thick fin had the best performance for heat fluxes below 20 W/cm^2 and again its curve started to bend, intersecting the curves of 0.75 mm and 0.5 mm at heat fluxes around 25 W/cm^2 and 65 W/cm^2, respectively. This early deterioration of boiling performance is caused by thicker fins, which reduce the interfin space, hence adversely affecting the processes of continuous liquid refill and vapor escape. With thinner fins, there is a limited cross-sectional area for heat conduction to the fin tips, causing the fin-tip temperatures to approach the saturation temperature.

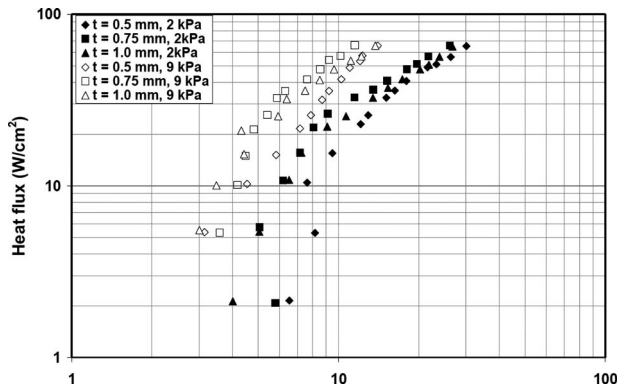

Fig. 3 Boiling curves for finned surfaces having different fin thicknesses with constant fin space (g)=0.5 mm and fin height (h)=15 mm at pressures of 2 kPa and 9 kPa

Figure 4 shows a boiling heat transfer coefficient (BHTC) based on the heater base area versus the heat flux chart. Generally the BHTC rises rapidly at low heat fluxes and reaches its peak before declining to an asymptotic value. Analyzing the 2 kPa pressure, there are peaks in the BHTC for each of the different fin thicknesses. The maximum BHTC for fin thicknesses of 0.5 mm, 0.75 mm, and 1 mm are located at heat fluxes of 41 W/cm^2, 26 W/cm^2, and 22 W/cm^2, respectively. For 9 kPa pressure, the maximum BHTC for 0.5 mm is not reached as it is beyond 75 W/cm^2, and the maximum BHTC for 0.75 mm and 1 mm are around 54.2 W/cm^2 and 32 W/cm^2, respectively. For thicker fins, its maximum BHTC is reached at lower heat flux. This heat flux is observed to be the point where the boiling curve starts to bend, caused by the lack of interfin spaces. Thicker fins can perform better in the lower heat flux region. For example, at 9 kPa, the 1 mm thick fins have a better boiling performance compared with the thinner 0.5 mm and 0.75 mm thick fins in the low heat flux region (below 24 W/cm^2). In the low heat flux region, boiling is yet to occur over the entire range of the interfin spacing, thicker fins can quickly superheat the liquid to activate nucleation sites in nonactive interfin spaces. Higher saturation pressure increases the maximum BHTC and shifts its location to higher heat flux values. As higher pressure entails higher vapor density, the formation of large vapor blobs enveloping the interfin spacing is delayed to higher heat fluxes. The optimal fin thickness of 0.75 mm had the best boiling performance at both 2 kPa and 9 kPa pressures with maximum BHTCs of 2.88 $W/cm^2\,K$ and 5.88 $W/cm^2\,K$, respectively. Furthermore this is despite having only an 80% heat transfer surface area relative to the 0.5 mm thick fins.

4.2 Effect of Fin Spacing. Figures 5 and 6 demonstrate the effect of fin spacing on the boiling curve of a finned surface. For the 2 kPa case, heat fluxes below 30 W/cm^2 the boiling curve of the smallest fin spacing of 0.5 mm is situated at the leftmost portion of the chart. To the right it is followed by 1.0 mm and 2.0 mm, which are both experiencing boiling hysteresis. This proves

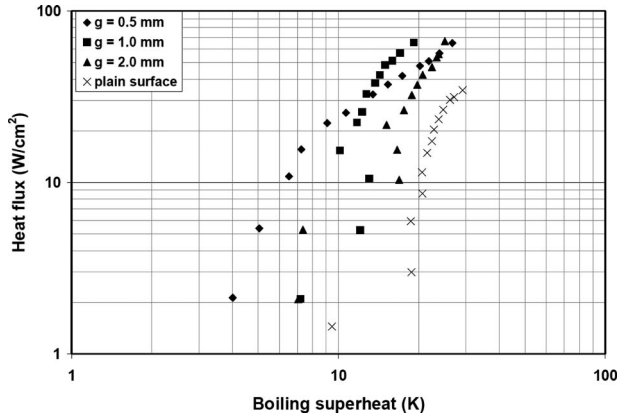

Fig. 5 Boiling curves for finned surfaces having different fin spacings with constant fin thickness (t)=1.0 mm and fin height (h)=15 mm at 2 kPa pressure. The plain surface data is measured with the same apparatus.

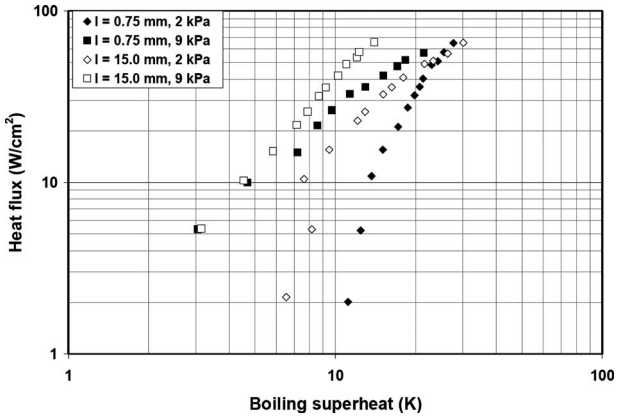

Fig. 7 Boiling curves for finned surfaces having different heights with constant fin spacing (g)=0.5 mm and fin thickness (t)=0.5 mm at pressures of 2 kPa and 9 kPa. The CHF is reached for the low-finned surface.

that even finned surfaces in water (which is a nonwetting liquid) are still susceptible to boiling hysteresis when fin spacings are large, despite the fact that results on plain surfaces showed no sign of hysteresis. Large fin spacing allows for cold liquid recirculation and this removes the superheated liquid near the base surface (thermal boundary layer), which could have been stagnantly heated to higher temperatures that will activate boiling nucleation sites. Hence boiling on finned surfaces with large fin spacing at low pressure would somehow enhance not the latent heat transfer mechanism but rather the single-phase natural convection, which are in a heat transfer "tug-of-war" at low heat fluxes. For heat fluxes above 30 W/cm^2, the boiling curve of 0.5 mm fin spacing starts to bend and it intersects the boiling curves of 1.0 mm and 2.0 mm at 32 W/cm^2 and 57 W/cm^2, respectively. This declining slope is an early sign of localized dry-out wherein all of the interfin spacing is occupied by vapor bubbles starting to constrict liquid replenishment. For the 9 kPa case, the boiling curve of 0.5 mm fin spacing again tilted toward higher superheats starting at 30 W/cm^2 and intersects the curve of 1.0 mm at 57 W/cm^2. The deterioration of the boiling performance at 9 kPa pressure occurred in the higher heat flux region compared with that at 2 kPa pressure, as bubbles are significantly smaller at higher pressures they are able to flow out of the narrow fin space thus deferring the formation of stagnant vapor film. The fin spacing 1.0 mm and 2.0 mm both have their boiling curve slope similar to that of a plain surface, which means that the fin space are large enough not to disrupt or confine bubble escape.

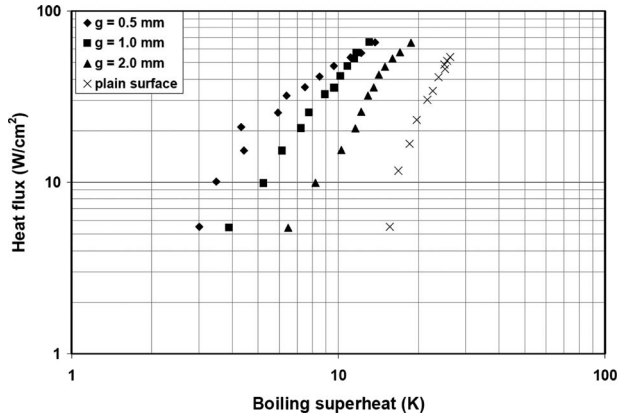

Fig. 6 Boiling curves for finned surfaces having different fin spacings with constant fin thickness (t)=1.0 mm and fin height (h)=15 mm at 9 kPa pressure

4.3 Effect of Fin Height. Figure 7 shows the boiling curves of two finned surfaces with different heights at pressures of 2–9 kPa. For 2 kPa pressure, at heat fluxes lower than 50 W/cm^2 the boiling curve of the high-finned surface is situated at lower superheats compared with that of the low-finned surface. Given the lack of nucleation sites, the contribution of natural convection to the heat transfer mechanism is increased at a lower pressure, thus some of the fins still operate at single-phase heat transfer mode. This benefited the high-finned surface, which has the most heat transfer area for natural convection. In the high heat flux region, the initial advantage that the high-finned surface had over that of the low-finned surface is diminished. Finally, the boiling curve of the high-finned surface intersects that of the low-finned surface at around 55 W/cm^2. This demonstrates that high fins creates significant friction flow resistance that impedes the escape of large bubbles from the fin root, rendering its huge heat transfer surface area useless. At 9 kPa, boiling curves of the high- and low-finned surfaces were coincident to one another and started to diverge at around 15 W/cm^2. This coincident portion indicates that additional heat transfer area employed by the high-finned surface is not utilized at low heat flux. Since latent heat transfer is seen to be the dominant heat transfer mechanism at 9 kPa, the high heat transfer coefficient would create a large temperature gradient across the height of the fin. With the fin-tip temperature near the saturation temperature, this can cause the high fins to act like the low fins at low heat flux. A CHF of 56 W/cm^2 was reached for the low-finned case at a pressure of 9 kPa. This elucidates that the high-finned surface cannot only provide an additional surface area for boiling heat transfer and nucleation, but they can physically prevent large bubbles from coalescing into a vapor blanket that could cover the whole heater surface and ultimately dry out.

4.4 Effect of the Pin-Fin Design. Figure 8 compares the boiling performances of rectangular fins and pin fins. The pin-fin design increases the heat transfer area and interfin volume to twice that of rectangular fins having similar dimensions. In the high heat flux region, pin fins augment the maximum BHTC to 3.2 W/cm^2 K (2 kPa case) and >6.0 W/cm^2 K (9 kPa case). This is a 30.6% and $>19.3\%$ improvement compared with that of rectangular fins for 2 kPa and 9 kPa pressures, respectively. This again showed that the adequate space for vapor escape and liquid refill provided by pin-finned surfaces can bring about an enhancement in the high heat flux region. In the low heat region, the pin fin performed slightly better at 2 kPa but worse at 9 kPa in com-

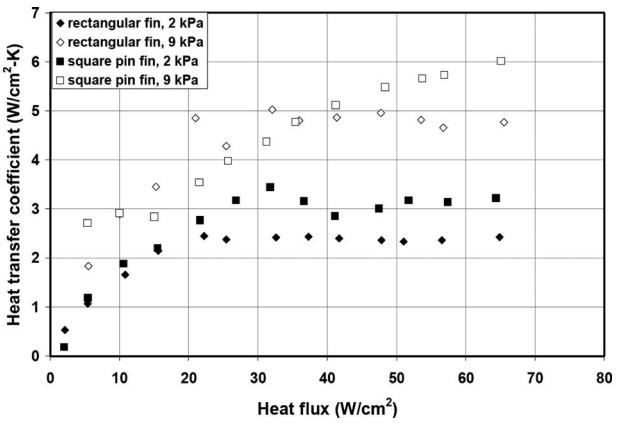

Fig. 8 Boiling curves for rectangular and square pin-finned surfaces with fin spacing (g)=0.5 mm, fin thickness (t) =1 mm, and fin height (h)=15 mm at 2 kPa and 9 kPa pressures

parison to the rectangular fin. This behavior supports the observation that the BHTC is significantly influenced by the heat transfer area at lower pressures.

5 Visualization

Figure 9(a) illustrates the boiling regime occurring on a finned surface. For a low heat flux of 5 W/cm^2 at 2 kPa pressure the ebullition process is continuous, but is occurring only on one

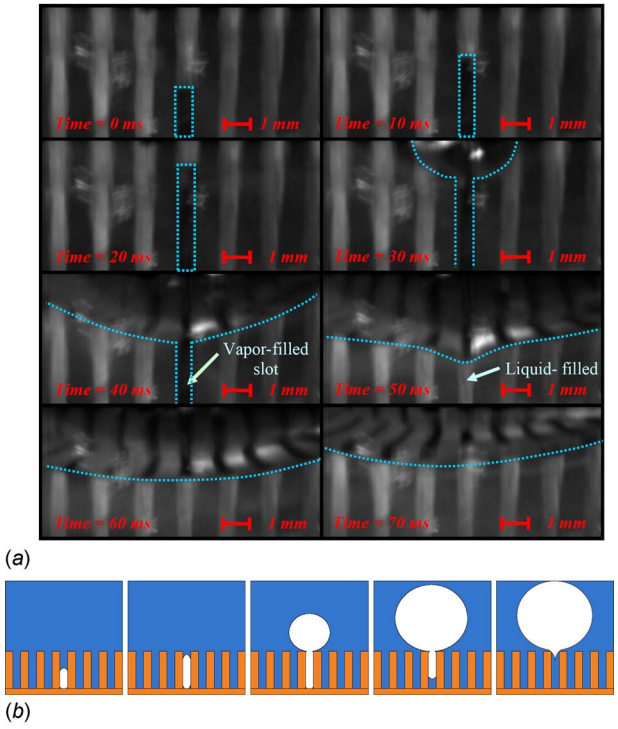

(a)

(b)

Fig. 9 (a) Water boiling on a finned surface (fin height =15 mm, fin spacing=0.5 mm, and fin thickness=1.0 mm) with heat flux of 5 W/cm^2 at 2 kPa pressure. The darkened slot at 40 ms shows the presence of a vapor plug within the fin space as no light is able to go through. At 50 ms, the same fin space is now filled with liquid as shown by the lighter contrast. (b) The graphical depiction of bubble growth and departure sequences in the narrow fin spacing.

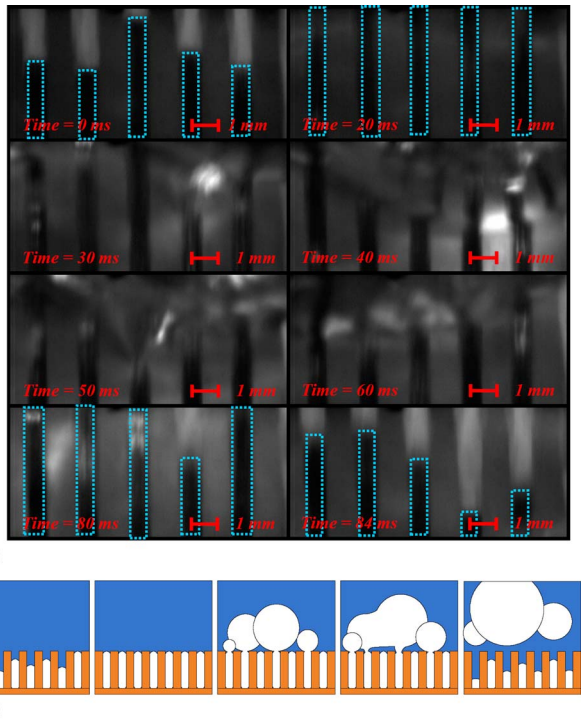

(a)

(b)

Fig. 10 (a) Water boiling on a finned surface (fin height =15 mm, fin spacing=0.5 mm, and fin thickness=1.0 mm) with a heat flux of 20 W/cm^2 at 2 kPa pressure and (b) the graphical depiction of growth, coalescence, and departure sequences of adjacent bubbles

nucleation site. Nucleation starts at the fin root between two adjacent fins. As the bubble grows, it is expected to have a large bubble departure diameter (60–80 times the size of the fin spacing), but given the narrow interfin spacing it is forced to take the shape of the fin space, thus forming a thin vertical vapor film/plug. This vapor film grows as it absorbs heat near the fin wall and base, shown in time frames 0 ms, 10 ms, and 20 ms. When it reaches the fin tip, the vapor retakes its supposed spherical shape and rapidly expands to a larger bubble, seen from 30 ms and 40 ms. As the bubble lifts off, it drags out the rest of the vapor film from the fin space, shown in 40 ms, 50 ms, 60 ms, and 70 ms intervals of Fig. 9(b). Finally, liquid fills up the fin space and the cycle repeats all over again. On occasion vapor film is seen to oscillate in size in the low heat flux region. This occurs while the vapor film is cooled by liquid convection and results in the film intermittently shrinking its size. As thin liquid film is created in between the vapor film and the solid fin, the heat transfer mechanism is similar to thin film evaporation, enhancing the contribution of latent heat transfer.

For a heat flux of 20 W/cm^2, nucleation occurred in all the interfin spaces, shown in Fig. 10(a). All the vapor films are growing simultaneously, and upon reaching the fin tip (from 0 ms to 20 ms), spherical bubbles are formed in close proximity to one another such that it allows bubble coalescence (from 30 ms to 60 ms). The newly merged bubble has greater buoyancy and increases its rate of ascension. This enables the spherical portion of the bubble to be detached or snapped from its film portion. As this boiling cycle cools down the fins, the vapor film left inside the fin spacing condenses and shrinks as the liquid starts to fill up the fin space all over again (shown in frames 80 ms and 84 ms in Fig. 10(a) and in Fig. 10(b)). Increasing the heat flux to 50 W/cm^2, bubbles continuously escape from the fin tip and the vapor film inside the fin spacing maintains its size without shrinking. This happens because the heat input is large enough such that the fins maintain a sizeable superheat and avoid condensation. This boil-

ing regime is similar to annular flow in pipes, in that there is a vapor core inside the fin space and the only path for liquid reflow is through the sides of the fin wall. The vapor film that constantly occupies the fin space impedes the liquid reflow, which causes the boiling performance to significantly deteriorate (previously shown in Fig. 5).

6 Conclusion

Increasing the pressure would increase the boiling heat transfer coefficient for both the finned and plain surfaces. Boiling at low pressures causes the formation of vapor films/plugs (compressed bubbles) inside a narrow fin spacing. A thin liquid film near the fin wall enhances evaporation. Visualization shows that in the low heat flux region, vapor plugs oscillate in size before escaping the fin space and eject out as spherical bubbles beyond the fins. At high heat fluxes, vapor films are present in all of the fin spaces, impeding the return of liquid and leading to a decline in the slope of the boiling curve.

At an optimal fin-thickness configuration, the maximum boiling heat transfer coefficients are 2.88 W/cm^2 K and 5.88 W/cm^2 K at pressures of 2 kPa and 9 kPa, respectively, and the heat transfer rates are well above the critical heat condition of the plain surfaces. At low pressures, boiling hysteresis is observed for finned surfaces with large fin spacings and this is due to the presence of natural convection phenomenon, i.e., delaying the onset of boiling and the boiling curve slope asymptotes to the one for plain surface. In the high heat flux region, a smaller interfin spacing constricts vapor escape as well as the liquid reflow into the fin spaces, resulting in a greater reduction in the slope of the boiling curve. High-finned surfaces provide more resistance for bubbles to depart from surfaces at high heat flux regions. The high rectangular fins prevent bubble coalescence, which delays the CHF occurrence to a higher heat flux value. A pin-fin design increases the maximum boiling heat transfer coefficient to 3.2 W/cm^2 K (2 kPa case) and >6.0 W/cm^2 K (9 kPa case), which is a 30.6% and $>19.3\%$ improvement compared with the coefficients for rectangular fins having similar fin spacing, height, and thickness for both cases of 2 kPa and 9 kPa pressures, respectively.

References

[1] Webb, R. L., 2004, "Odyssey of the Enhanced Surface," ASME J. Heat Transfer, **126**, pp. 1051–1059.
[2] Westwater, J. W., 1973, "Development of Extended Surfaces for Use in Boiling Liquids," AIChE Symp. Ser., **69**(131), pp. 1–9.
[3] Joudi, K. A., and James, D. D., 1977, "Incipient Boiling Characteristics at Atmospheric and Subatmospheric Pressures," ASME J. Heat Transfer, **99**, pp. 398–403.
[4] Fath, H. S., and Judd, R. L., 1978, "Influence of System Pressure on Micro-Layer Evaporation Heat Transfer," ASME J. Heat Transfer, **100**, pp. 49–55.
[5] Gorenflo, D., 1986, *Zum einsatz von rippnrohr in uberfluteten verdampfern bei hohen siededrucken*, Dtsch. Kälte. Klimatechn. Verien, pp. 315–332.
[6] McGillis, W. R., Fitch, J. S., Hamburgen, W. R., and Carey, V. P., 1990, "Pool Boiling Enhancement Techniques for Water at Low Pressure," WRL Research Report 90/9, Western Research Laboratory, Palo Alto.
[7] Rainey, K. N., and You, S. M., 2000, "Pool Boiling Heat Transfer From Plain and Microporous, Square Pin-Finned Surfaces in Saturated FC-72," ASME J. Heat Transfer, **122**, pp. 509–516.
[8] Rainey, K. N., You, S. M., and Lee, S., 2003, "Effect of Pressure, Subcooling, and Dissolved Gas on Pool Boiling Heat Transfer From Microporous, Square Pin-Finned Surfaces in FC-72," Int. J. Heat Mass Transfer, **46**, pp. 23–35.
[9] Rainey, K. N., You, S. M., and Lee, S., 2003, "Effect of Pressure, Subcooling, and Dissolved Gas on Pool Boiling Heat Transfer From Microporous Surfaces in FC-72," ASME J. Heat Transfer, **125**, pp. 75–83.
[10] Wei, J. J., and Honda, H., 2003, "Effects of Fin Geometry on Boiling Heat Transfer From Silicon Chips With Micro-Pin-Fins Immersed in FC-72," Int. J. Heat Mass Transfer, **46**, pp. 4059–4070.
[11] Yu, C. K., and Lu, D. C., 2007, "Pool Boiling Heat Transfer on Horizontal Rectangular Fin Array in Saturated FC-72," Int. J. Heat Mass Transfer, **50**, pp. 3624–3637.
[12] Pal, A., and Joshi, Y., 2008, "Boiling of Water at Subatmospheric Conditions With Enhanced Structures: Effect of Liquid Volume," ASME J. Electron. Packag., **130**(1), p. 011010.
[13] Cooper, M. G., 1984, "Saturation and Nucleate Pool Boiling—A Simple Correlation," Inst. Chem. Eng. Symp. Ser., **86**(2), pp. 785–793.
[14] Zuber, N., 1959, "Hydrodynamic Aspects of Boiling Heat Transfer," AEC Report No. AECU-4439.
[15] Kutateladze, S. S., 1948, "On the Transition to Film Boiling Under Natural Convection," Sovetskoe kotloturbostroenie (Soviet Boiler and Turbine Construction), **3**, pp. 10–12.
[16] Lienhard, J. H., and Dhir, V. K., 1973, "Extended Hydrodynamic Theory of the Peak and Minimum Pool Boiling Heat Fluxes," NASA Report No. NASA CR-2270.
[17] Lienhard, J. H., Dhir, V. K., and Riherd, D. M., 1973, "Peak Pool Boiling Heat-Flux Measurements on Finite Horizontal Flat Plates," ASME J. Heat Transfer, **95**, pp. 477–482.
[18] Lienhard, J. H., and Dhir, V. K., 1973, "Hydrodynamic Prediction of Peak Pool-Boiling Heat Fluxes From Finite Bodies," ASME J. Heat Transfer, **95**, pp. 152–158.

Confocal Microscopy for Capillary Film Measurements in a Flat Plate Heat Pipe

Frédéric Lefèvre[1]
e-mail: frederic.lefevre@insa-lyon.fr

Romuald Rullière

Stéphane Lips

Jocelyn Bonjour

Universite de Lyon, CNRS
INSA-Lyon, CETHIL, UMR5008,
F-69621,Villeurbanne, France
Universite Lyon 1, F-69622, France

This paper aims to show how confocal microscopy can be useful for characterizing menisci in a flat plate heat pipe made of silicon. The capillary structure is made of radial microgrooves whose width decreases from the periphery to the center of the system. A transparent plate is used to close the system and allow visualizations. The confocal method allows measuring both the liquid film shape inside the grooves and the condensate films on the fins. The film thickness is lower than 10 μm. The measurements show that the condensate film forms a drop connected to the meniscus in the grooves but their curvatures are reversed. As a result, a very thin region shall exist where the liquid formed by condensation is drained to the grooves. The drop curvature radius decreases from the condenser to the evaporator like the meniscus radius in the grooves. Therefore, a small part of the liquid is drained by the fins from the evaporator to the condenser. Furthermore, the condensate film covers a large part of the system and can also be in contact with the evaporator at high heat fluxes. [DOI: 10.1115/1.4000057]

Keywords: evaporation, condensation, flat plate heat pipes, thin film, capillarity

1 Introduction

Flat plate heat pipes (FPHPs) are microfluidic devices that are usually designed for thermal management of electronic components [1] but that can be used in others applications, such as the cooling of proton exchange membrane fuel cells [2]. They are used for their heat transfer capacity as well as their capacity of homogenizing the temperature.

A FPHP is a cavity of small thickness filled with a two-phase working fluid. Heat sources and heat sinks are located anywhere on the cavity with the other parts being insulated. Heat is transferred from heat sources to heat sinks by vaporization of the liquid and condensation of the vapor. The parts of the system where evaporation and condensation occur are the evaporator and the condenser, respectively. The liquid returns from the evaporator to the condenser through a capillary structure made of microgrooves, meshes, or sintered powder wicks. Since the 1990s, heat pipes have been miniaturized to respond to the demand in electronic cooling devices as small as the electronic components themselves. FPHPs are usually made of copper [2–4] to increase their heat transfer capability, but silicon systems are now preferred to create smaller devices [5,6]. Indeed, silicon is the material of microelectronic whose etching techniques can be used to realize very small capillary structures with various shapes. Furthermore, FPHPs in silicon can be integrated in the core of electronic components, avoiding the thermal contact resistance between the cooling device and the electronic components.

Although a lot of works have been published on flat plate heat pipes, the literature is poor in experimental papers, especially for silicon systems. Furthermore, the provided measurements are not sufficient to describe the behavior of these systems, but only to estimate their overall thermal performance. The physical phenomena that drive a heat pipe are complex and cannot be understood only with temperature sensors. The temperature field in these systems is mainly due to evaporation and condensation phenomena inside the capillary structure. The major part of the heat flux is transferred through thin films at both the evaporator and condenser locations [7,8]. The shape of the liquid films is the result of both heat transfer phenomena and capillary flows inside the capillary structure. Thus, heat transfer phenomena are highly linked to hydrodynamic parameters and to interfacial properties. Therefore, measurements of the location and the shape of liquid films inside a heat pipe are required in association with temperature measurements to understand the physical mechanisms that drive the system.

Capillary phenomena, evaporation, and condensation in microchannels have been the focus of a lot of single experimental papers these last years [9–11]. In a heat pipe, these phenomena are linked together and cannot be studied separately. Therefore, it is difficult to realize measurements in such a device. For example, micro particle image velocimetry (PIV) [12] is not helpful in heat pipes because the process of insemination is not appropriate. Indeed, any particles introduced in the liquid would be blocked at the evaporator because of their nonevaporative character. Measurements by means of a camera [9,11] or image-analyzing interferometry [10] is not feasible. Indeed, those measurement techniques require a FPHP totally transparent (including the capillary structure) to allow liquid thickness measurements inside the system. A transparent capillary structure would have a very bad thermal conductivity and, moreover, as heat sources and heat sinks have to be located on the system, it prevents any optical system to pass through the capillary structure. As a result, the liquid film can only be measured from above the capillary structure and not through it. A FPHP, made of two plates, one opaque including the capillary structure and one transparent, has to be realized. It has to be noticed that the experimental bench should sustain high pressure variations that occur in working conditions.

In this article, we present the capability of an experimental bench dedicated to measurements of liquid films inside a flat plate heat pipe in working conditions. The capillary structure is made of radial microgrooves etched in a silicon wafer. A transparent plate closes hermetically the heat pipe. A confocal microscope is used to measure the location of the liquid-vapor interface in the microgrooved capillary structure. The optical principles of the system are described in Fig. 1. A white light point source is imaged by a lens that has not been corrected for chromatic aberration on a

[1]Corresponding author.

Contributed by the Heat Transfer Division of ASME for publication in the JOURNAL OF HEAT TRANSFER. Manuscript received April 21, 2009; final manuscript received July 14, 2009; published online January 4, 2010. Assoc. Editor: Yogesh Juluria.

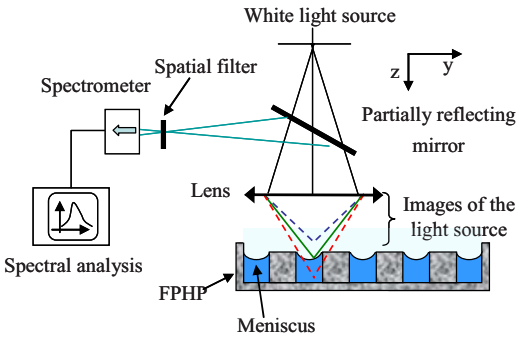

Fig. 1 Schematic confocal microscopy

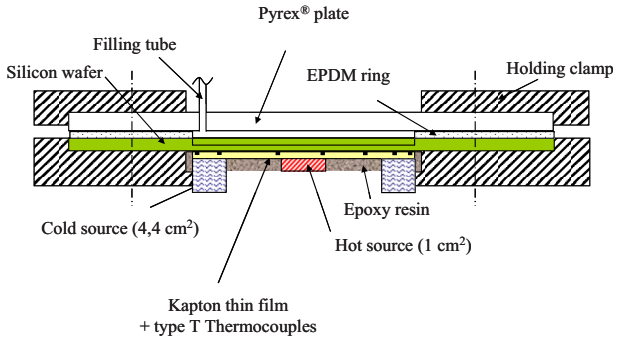

Fig. 3 Schematic of the FPHP test apparatus

series of monochromatic point images in the measurement space. The reflected light passes back through the lens and is directed toward a spectral detector by a partially reflecting mirror. The spectral analysis of the collected lights that are separated by a spatial filter allows the location of the surface to be measured. The monochromatic light having the highest intensity corresponds to the surface to be measured.

Finally, we present and analyze the results obtained using confocal microscopy coupled with temperature measurements on the wall. We especially focus on condensate films, whose thickness is lower than 10 μm and which have apparently never been measured in FPHPs.

2 Experimental Setup

The flat plate heat pipe under investigation is shown in Fig. 2. Its capillary structure, with a diameter of 50 mm, is etched on a silicon wafer of 100 mm in diameter and 525 μm in thickness. It is made of 72 radial microgrooves that are connected by crossed grooves at the center of the device. The etching depth is equal to 200 μm. The radial grooves have a rectangular cross section whose width varies from 670 μm at the periphery to 110 μm at the connection with the crossed grooves. These crossed grooves have a width equal to 100 μm and they are separated by fins of same width, which creates a network of 300 small posts of 100 $\times 100$ μm^2.

The FPHP is hermetically sealed on its upper face with a borosilicate plate, which allows the liquid/vapor meniscus observation in the grooves (Fig. 3). An EPDM ring is placed on all the nonetched surface of the silicon—between the silicon wafer and the transparent plate—to provide vacuum tightness. As a result, a 2 mm vapor space height is created above the etched area. A circular heat source is located in the middle of the silicon wafer. It is a thick resistor film with a surface of 1 cm^2. This resistor of 0.1 Ω is supplied by a 0–3 V dc power supply. Electric power is obtained by measuring the voltage drop across the heating resistor and the current intensity, owing to a calibrated resistance. As a result, the uncertainty due to the power measurement is negligible. The heat sink is a circular water heat exchanger (inlet diameter of 44 mm and outlet diameter of 50 mm; surface equals to 4.4 cm^2). The water flow rate is constant and the inlet temperature is controlled by means of a thermostatic bath in order to have a constant working temperature when the heat transfer rate increases. The working temperature of the FPHP is measured by a thermocouple located at the middle of the borosilicate plate. The entire FPHP is insulated as well as the borosilicate plate during the thermal tests. Nine thin calibrated thermocouples of type T—deposited on a Kapton film—are located along a diameter of the FPHP. The silicon wafer is submitted to high pressure variations in working conditions. Thus, as its thickness is very small, an epoxy resin is used to strengthen it and to avoid its breaking.

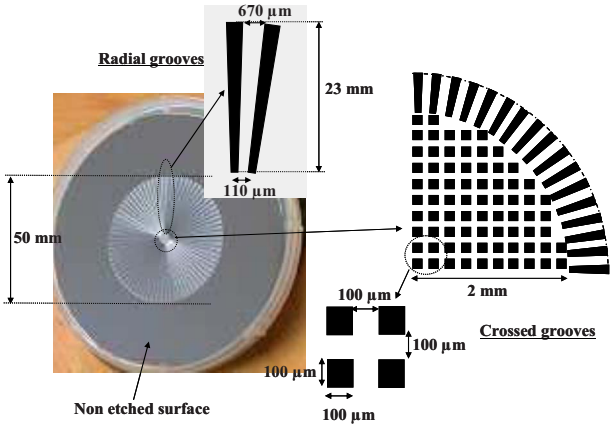

Fig. 2 Schematic of the silicon FPHP

A confocal microscope is used to measure the evolution of the meniscus curvature radius in the grooves, the FPHP being in horizontal orientation. The confocal microscope is a STIL Micromesure 2 system. The optical sensor has a nominal measuring range of 350.0 μm. The working distance is about 13 mm. The maximum measuring angle for specular reflection is equal to 27.4 deg. The optical sensor velocity is about 1 mm s^{-1}, which is fast enough for not thermally disturbing the measurement. Once the top of the groove is located by the sensor, the surface profile is recorded. The resulting data are used to estimate through a least square method the radius and the center coordinates of a circle that fits at best the experimental data. Several similar measurements are realized from the center to the periphery to obtain the meniscus curvature radius variation from the evaporator to the condenser.

Before the thermal tests, the FPHP has to be degassed and filled with a fluid and cleaned depending on a method already used in Ref. [2]. A filling tube provided with a tightness valve is connected to the FPHP through a hole made in the transparent plate. It has to be noticed that the amount of liquid to fill the grooves is about 0.13 ml, which is lower than the amount of fluid contained in the dead volumes among the filling tube and the valve. As a result, it is not possible to measure accurately the amount of fluid contained in the grooves in working conditions. Thus the filling ratio f_r will be defined as the amount of liquid measured through the transparent plate in vertical position divided by the volume of both the vapor space and the capillary structure.

3 Temperature Measurements

The FPHP has been tested in horizontal orientation with methanol as the working fluid. Indeed, this fluid has suitable thermal properties at this temperature level (high surface tension and latent heat of vaporization and small saturation pressure) and the wettability on silicon is very high compared with water for example. The working temperature was fixed to 30°C. Figure 4

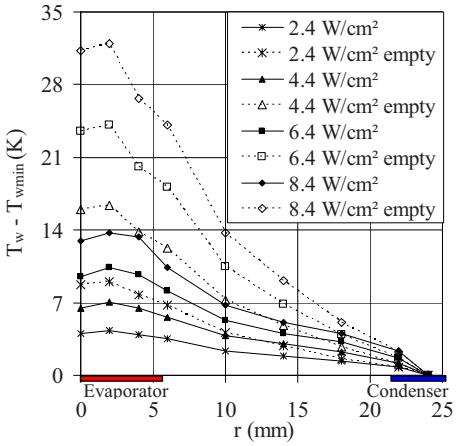

Fig. 4 Wall temperature profile along the empty FPHP and the FPHP filled with methanol (T_{work}=30°C, f_r=4.7%)

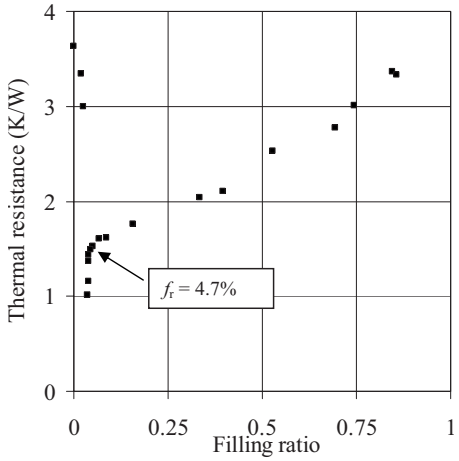

Fig. 6 Thermal resistance versus the filling ratio (T_{work}=30°C, q=8.4 W/cm²)

presents the temperature field measured for different heat fluxes (q=2.4–8.4 W/cm² by steps of 2 W/cm²). The solid lines correspond to the FPHP filled with methanol for a filling ratio of 4.7% and the dashed lines correspond to the empty heat pipe. The location and size of the evaporator and condenser are shown on the abscissa axis of this graph. For each heat flux, the maximum temperature difference is 2.5 times lower when the heat pipe is filled. This result is satisfactory but is not as good as it could be with a larger FPHP. As a comparison the maximum temperature difference was 20 times lower for the FPHP—made of copper and filled with the same fluid—tested by Rullière et al. [2], but the length of the heat pipe was 10 times higher than the radius of this heat pipe. In this application, a part of the heat flux is transferred directly by heat conduction in the wall. Indeed, the temperature gradients in the wall are never equal to zero in spite of the very small thickness of the wall. As a result, it is not easy to determine the saturation temperature; indeed, contrary to classical heat pipes, there is no zone of the adiabatic area where the temperature field is homogeneous. This is the reason why the working temperature is measured on the thermally isolated transparent wafer.

It has to be noticed that the heat pipe still works with heat fluxes higher than 8.4 W/cm², but beyond this value, nucleate boiling occurs. When bubbles appear, the transparent plate is wetted, which prevent observations that are the goal of this paper. Moreover, nucleate boiling in flat heat pipes has already been described in a previous paper [4].

Figure 5 presents the temperature field for a heat flux of 8.4 W/cm² and different filling ratios varying from 84.5%, when the system is nearly full of liquid, to 0%, when it is empty. The dashed lines correspond to filling ratios higher than 50% and the solid lines to filling ratios lower than 5%. The bold line is the temperature field when the heat pipe is empty.

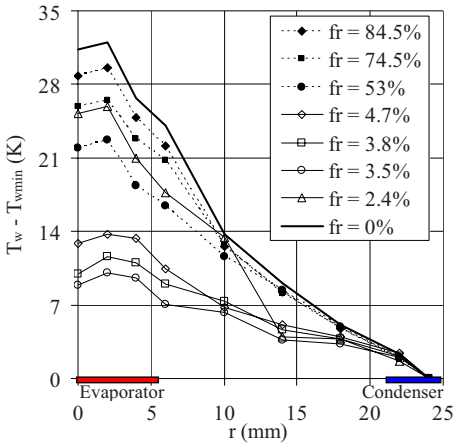

Fig. 5 Wall temperature profile along the empty FPHP and the FPHP filled with methanol (T_{work}=30°C)

The temperature gradients decrease when decreasing the filling ratio until a value of 3.5%, for which the minimum temperature difference is obtained. For high filling ratios, the temperature field in the area of the condenser is very close to that of the empty system, because the condenser is overfilled. Nevertheless, at the center of the system, the temperature gradients are smaller due to capillary two phase flow. For filling ratios lower than 5%, the decrease in the filling ratio affects both the evaporator and the condenser until a filling ratio of 2.4%, for which the dry out is reached between the heat source and the cold source. As a result, the temperature gradients remain small in the condenser but are close to that of the empty system in the evaporator.

The temperature measurements can be used to calculate the thermal resistance of the system, which is defined as the ratio of the difference between the mean evaporator temperature T_{evap} and the mean condenser temperature T_{cond} to the heat rate Q:

$$R_{th} = \frac{T_{evap} - T_{cond}}{Q}$$

The thermal resistance decreases nearly linearly from a full system to a filling ratio of 9% (Fig. 6). This evolution is mainly due to the decrease in the condenser thermal resistance. For lower filling ratios, the thermal resistance decreases abruptly until f_r =3.5%, for which its value is minimum and 3.7 times lower than that of the empty system. This abrupt variation is most likely due to the thinning of the liquid film in the grooves at the evaporator and especially to the very thin film at the junction between the meniscus and the wall where most of the heat flux is dissipated. This result shows that the filling of the system has to be optimized to obtain the best thermal performance. Furthermore, one should notice that a small underestimation of the filling ratio can lead abruptly to the drying of the evaporator (f_r=2.4%) and consequently to very poor performance.

4 Measurements of the Liquid Film Thickness Inside the Capillary Structure

In this part, we present liquid film thickness measured by means of confocal microscopy in the grooves and on the fins.

4.1 Measurements by Confocal Microscopy. Figure 7(*a*) presents an example of measurement obtained at r=13.7 mm for a methanol filling ratio of 4.7%, a heat flux equal to 8.4 W/cm²,

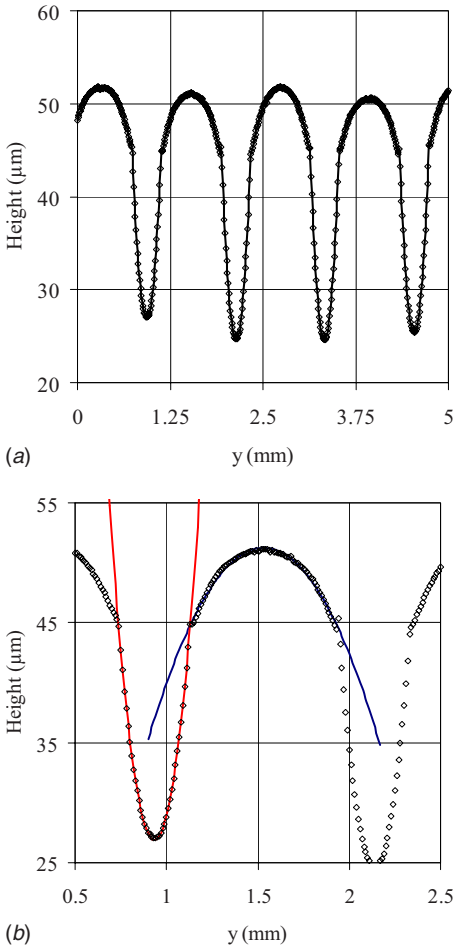

Fig. 7 (a) Meniscus curvature radii measured inside the grooves by confocal microscopy (T_{work}=30°C, f_r=4.7%, q=8.4 W/cm^2) and (b) comparison between experimental measurements and fitted circles (T_{work}=30°C, f_r=4.7%, q=8.4 W/cm^2)

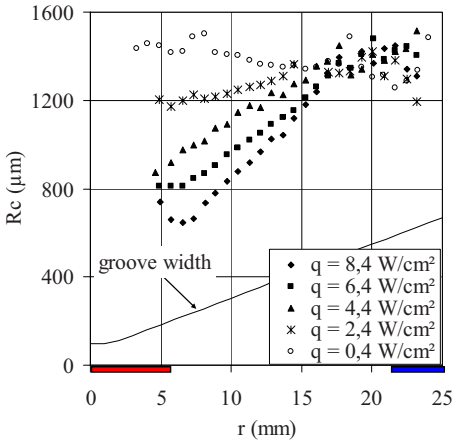

Fig. 8 Measured meniscus curvature radii along the FPHP for different heat fluxes (T_{work}=30°C, f_r=4.7%)

and a working temperature equal to 30°C. Four grooves are visualized. The width of the grooves and the fins are about 400 μm and 800 μm, respectively. One has to notice that the scale on the y axis is 100 times lower than that on the x axis. This figure shows that it is possible to measure both the meniscus curvature radius inside the grooves and the condensate film on the fins. According to our knowledge, this film thickness has never been measured before in a heat pipe. This information is fundamental to understand the distribution of the liquid film on the fins, which has an important consequence on the heat pipe temperature. In our previous experimental works [2], the confocal microscope was not useful to measure this thin film; the FPHP was made of copper and the reflection of white light on a copper surface is larger than on silicon surface. As a result, the intensity of the reflected light is so high compared with that of the light reflected on the liquid-vapor interface that the focalization on the liquid film is not accurate enough for proper measurements. With silicon, the intensity of the reflected light is lower, which allows this measurement. In this example the thin condensate film thickness is lower than 5 μm.

Figure 7(b) presents a zoom of Fig. 7(a) with the circles that fit the experimental data, so as to determine the film radii of curvature. The radius of curvature is found to be 1.08 mm in the grooves and 12.4 mm on the fins. In addition, the curvatures between these zones are reversed. Therefore, because of the Young–Laplace law, the liquid pressure is higher than the vapor pressure on the fins and lower than the vapor pressure in the grooves. In the condenser section, as the liquid film is present in both the grooves and the fins, the solid-liquid interface is not visible. The exact location is obtained in nonworking conditions or the silicon can be viewed with the confocal microscope if the liquid refractive index is known. In that case, the optical system analyzes two reflected lights, one from the liquid-vapor interface and one from the solid-liquid interface.

The connection between the condensate film and the film in the grooves is of great importance. Indeed, the grooves are mostly filled by the vapor that condensates on the fins. As a result, a connection between the two films shall exist to allow the condensate to flow from the fins to the grooves. Nevertheless, the transition between the two films looks abrupt from our measurements. Thus, a very small region shall be present where the curvature changes from a constant positive value to a constant negative value. Furthermore, in this very small region, condensation shall be intense because this thin liquid film will result in a very low thermal resistance. A microcondensation model has to be developed for this microzone. This task could be analogous to that performed for micro-evaporation at the contact line (e.g., Refs. [7,8], and all the subsequent literature on that issue). It has to be noticed that the optical sensor is not useful to measure such small films perhaps because its measuring range is too wide (350 μm).

4.2 Results for a Fixed Filling Ratio of Methanol. Measurements with the confocal microscope have been performed on the entire surface in steady-state conditions. Figure 8 presents the meniscus curvature radii R_c measured all along the grooves for different heat fluxes (q=0.4 to 8.4 W/cm^2 by step of 2 W/cm^2). These results correspond to a filling ratio of 4.7% and can be associated to the temperature measurements presented in Fig. 4. The meniscus curvature radii obtained by confocal microscopy are averaged over ten grooves located at a same radial position. The average standard deviation of these measurements is about 50 μm. Thus, the major uncertainty is not due to the measurement apparatus but to some dispersion of the meniscus curvature between the different grooves. In the evaporator area, the microscope is not useful to measure the menisci. Indeed the slope of the meniscus at the junction with the grooves is higher than the maximum measuring angle of the optical sensor, which is equal to 27.4 deg for specular reflection. Nevertheless, the measurements show that even in the evaporator section, the meniscus is always attached to the top of the grooves for the observed zones.

For a heat flux of 0.4 W/cm^2, the system is nearly in nonworking conditions. As a result, R_c is constant all along the grooves and is equal to 1.4 mm. When the heat flux increases, the meniscus curvature radius remains constant at the condenser but de-

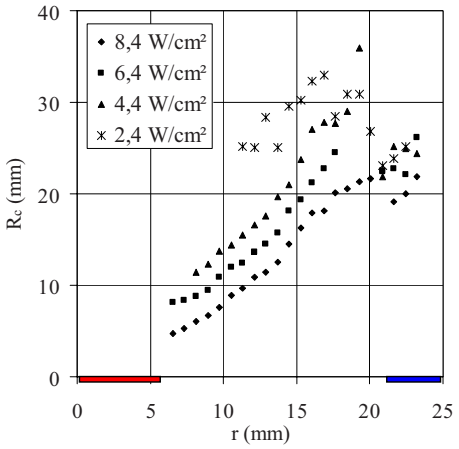

Fig. 9 Measured meniscus curvature radii on the fins for different heat fluxes (T_{work}=30°C, f_r=4.7%)

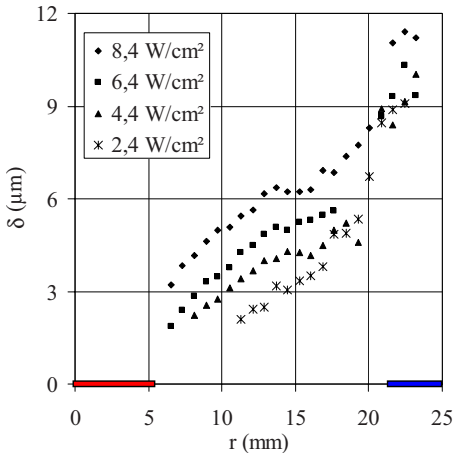

Fig. 10 Thin film thickness at the middle of the fins for different heat fluxes (T_{work}=30°C, f_r=4.7%)

creases elsewhere due to the flow of liquid from the condenser to the evaporator, which creates a pressure drop inside the grooves. Indeed, a pressure difference exists between the liquid and the vapor due to the Young–Laplace law:

$$P_v - P_l = \frac{\sigma}{R_c}$$

where σ is the surface tension and, P_v and P_l are the vapor and liquid pressure, respectively. In the present experiment, as the vapor space is high, the vapor pressure can be considered as constant all along the grooves. Thus, the pressure drop in the liquid can be expressed as follows:

$$\Delta P_l = \sigma\left(\left.\frac{1}{R_c}\right|_{\max} - \left.\frac{1}{R_c}\right|_{\min}\right)$$

The system works while the meniscus curvature radius is higher than half the width of the grooves. Then, the capillary limit is reached and dry out occurs at the evaporator. As we can see on Fig. 8, even for the maximum heat flux applied during this experiment, this limit is not reached. But, as it was explained in Sec. 3, boiling occurs for higher heat fluxes, which prevents the measurements of the menisci for higher heat fluxes.

Figure 9 presents the meniscus curvature radii measured on the fins for different heat fluxes (q=2.4–8.4 W/cm^2 by step of 2 W/cm^2). The dispersion of the measurements is noticeable for radii higher than 20 mm. This is especially true for the smallest heat flux (q=2.4 W/cm^2). Nevertheless, for radii lower than 20 mm, the standard deviation of these measurements is lower than 1 mm. Figure 9 shows that a condensate film exists until the extremity of the evaporator at r=5.7 mm. One part of the liquid is drained from the evaporator to the condenser by the capillary forces. Indeed, on the fins, the meniscus curvature radius decreases from the condenser to the evaporator which creates a small capillary pressure difference. For example, the capillary pressure difference reaches about 3 Pa for a heat flux of 8.4 W/cm^2. Nevertheless, this capillary pressure difference remains small compared with that inside the grooves (e.g., 14 Pa for a heat flux of 8.4 W/cm^2) and the condensate films are very thin compared with the thickness of the liquid in the grooves. As a result, the liquid flow on the fins is small compared with that in the grooves.

The radius of curvature is used to calculate the liquid film thickness δ at the middle of a fin (Fig. 10). For the different heat fluxes, it is possible to determine film thicknesses higher than 2 μm. The microscope fails to reach smaller thicknesses. In the condenser the liquid thickness is relatively independent from the heat flux. At high heat fluxes, the thickness of the condensate film is higher due to higher rates of condensation.

4.3 Results Obtained With FC72. Figure 11 presents meniscus curvature radii obtained with FC-72 as working fluid and a working temperature of 50°C. Two heat fluxes were applied to the system: 4.6 W/cm^2 and 8 W/cm^2. FC-72 has very bad thermal properties (small surface tension, latent heat of vaporization, and thermal conductivity). However, these properties are interesting in the present experiment because they lead to very high variation in the meniscus curvature radius inside the grooves. These results are interesting for future works to validate hydrodynamic model of liquid flow inside radial microgrooves.

5 Conclusion

A flat plate heat pipe made of silicon including a radially grooved capillary structure has been characterized experimentally. For that purpose, a confocal microscope has been used to measure both the meniscus curvature radius in the grooves and the condensate films on the fins. Using this optical method allows measuring condensate films of very small thickness (down to 2 μm) for such a silicon wall. The measurements show that this condensate film forms a circle whose curvature radius decreases from the condenser to the evaporator like the meniscus radius in the grooves. As a result, a small part of the liquid is drained from the evaporator to the condenser by the fins. Such experimental results are

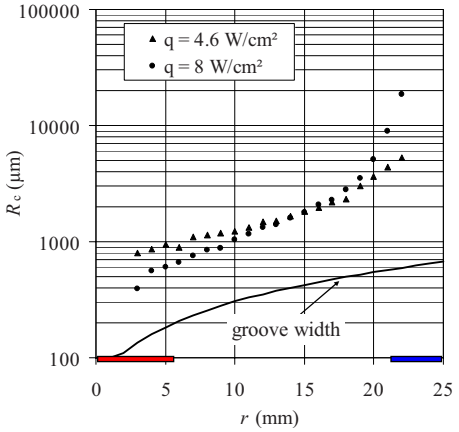

Fig. 11 Measured meniscus curvature radii along the FPHP for two heat fluxes (T_{work}=50°C, f_r=13.4%)

not available in the heat pipe literature and constitute a database to analyze and validate thermal and hydrodynamic models of these systems. The measurements show that a microcondensation model has to be developed to take into account the transition between the condensate film and the meniscus in the grooves.

Acknowledgment

This work was supported by the GIP-ANR in the frame of the nonthematic project "INTENSIFILM" under Grant No. ANR-06-BLAN-0119-03.

Nomenclature

f_r = filling ratio
P = pressure, Pa
q = heat flux, W m^{-2}
r = radial coordinate, m
R_c = meniscus curvature radius, m
R_{th} = thermal resistance, K W^{-1}

Subscripts

cond = condenser
evap = evaporator
max = maximum
min = minimum
l = liquid
v = vapor
w = wall
work = working

Greek Symbols

σ = surface tension, N m^{-1}
δ = liquid film thickness, m
T = temperature, K

References

[1] Lallemand, M., and Lefèvre, F., 2004, "Micro/Mini Heat Pipes for the Cooling of Electronic Devices," 13th International Heat Pipe Conference, Shanghai, China, pp. 12–22.
[2] Rullière, R., Lefèvre, F., and Lallemand, M., 2007, "Prediction of the Maximum Heat Transfer Capability of Two-Phase Heat Spreaders—Experimental Validation," Int. J. Heat Mass Transfer, **50**, pp. 1255–1262.
[3] Hopkins, R., Faghri, A., and Khrustalev, D., 1999, "Flat Miniature Heat Pipes With Micro Capillary Grooves," ASME J. Heat Transfer, **121**, pp. 102–109.
[4] Lips, S., Lefèvre, F., and Bonjour, J., 2008, "Nucleate Boiling in a Flat Grooved Heat Pipe," Int. J. Therm. Sci., **48**, pp. 1273–1278.
[5] Badran, B., Gerner, F. M., Ramada, P., Henderson, T., and Baker, K. W., 1997, "Experimental Results for Low-Temperature Silicon Micromachined Micro Heat Pipe Arrays Using Water and Methanol as Working Fluids," Exp. Heat Transfer, **10**, pp. 253–272.
[6] Le Berre, M., Launay, S., Sartre, V., and Lallemand, M., 2003, "Fabrication and Experimental Investigation of Silicon Heat Pipes for Cooling Electronics," J. Micromech. Microeng., **13**, pp. 436–441.
[7] Das Gupta, S., Schonberg, J. A., and Wayner, P. C., 1993, "Investigation of an Evaporating Extended Meniscus Based on the Augmented Young–Laplace Equation," ASME J. Heat Transfer, **115**, pp. 201–208.
[8] Stephan, P. C., and Busse, C. A., 1992, "Analysis of the Heat Transfer Coefficient of Grooved Heat Pipe Evaporator Walls," Int. J. Heat Mass Transfer, **35**, pp. 383–391.
[9] Ichikawa, N., Hosokawa, K., and Maeda, R., 2004, "Interface Motion of Capillary-Driven Flow in Rectangular Microchannel," J. Colloid Interface Sci., **280**, pp. 155–164.
[10] Gokhale, S. J., Plawsky, J. L., and Wayner, P. C., 2003, "Experimental Investigation of Contact Angle, Curvature, and Contact Line Motion in Dropwise Condensation and Evaporation," J. Colloid Interface Sci., **259**, pp. 354–366.
[11] Mederic, B., Miscevic, M., Platel, V., Lavieille, P., and Joly, J.-L., 2004, "Experimental Study of Flow Characteristics During Condensation in Narrow Channels: The Influence of the Diameter Channel on Structure Patterns," Superlattices Microstruct., **35**, pp. 573–586.
[12] Jones, B. J., Lee, P.-S., and Garimella, S. V., 2008, "Infrared Micro-Particle Image Velocimetry Measurements and Predictions of Flow Distribution in a Microchannel Heat Sink," Int. J. Heat Mass Transfer, **51**, pp. 1877–1887.

Flow Boiling Visualization of R-134a in a Vertical Channel of Small Diameter

Claudi Martín-Callizo
e-mail: claudi@energy.kth.se

Björn Palm
e-mail: bpalm@energy.kth.se

Wahib Owhaib
e-mail: wahib@energy.kth.se

Rashid Ali
e-mail: rashid.ali@energy.kth.se

Applied Thermodynamics and Refrigeration,
Royal Institute of Technology, KTH,
SE100-44 Stockholm, Sweden

The present work reports on flow boiling visualization of refrigerant R-134a in a vertical circular channel with an internal diameter of 1.33 mm and 235 mm in heated length. A quartz tube with a homogeneous Indium Tin Oxide coating is used to allow heating and simultaneous visualization. Flow patterns have been observed along the heated length with the aid of high-speed complementary metal oxide semiconductor (CMOS) digital camera. From the flow boiling visualization, seven distinct two-phase flow patterns have been observed: isolated bubbly flow, confined bubbly flow, slug flow, churn flow, slug-annular flow, annular flow, and mist flow. Two-phase flow pattern observations are presented in the form of flow pattern maps. The effects of the saturation temperature and the inlet subcooling degree on the two-phase flow pattern transitions are elucidated. Finally, the experimental flow pattern map is compared with models developed for conventional sizes as well as to a microscale map for air-water mixtures available in literature, showing a large discrepancy.
[DOI: 10.1115/1.4000012]

Keywords: flow boiling, two-phase, flow patterns, microchannel, refrigerant R-134a

1 Introduction

With the rapid development of microelectronic devices and micromanufacturing technology, boiling heat transfer in minichannels and microchannels has become increasingly important. Previous studies reported higher heat transfer capability in microchannels than in ordinary sized large tubes [1]. However, the governing phenomena are not yet well understood.

Two-phase vapor-liquid flow can take on many geometrical configurations according to the spatial distribution of the vapor and liquid phases in the channel. These configurations are known as flow patterns. Although the flow pattern classification is not yet clear from literature, four main flow patterns seem to exist: *bubbly*, *intermittent*, and *annular*; for horizontal flow, it is *stratified flow*. Good knowledge on the actual bubble dynamics is fundamental for the understanding and prediction of flow boiling heat transfer in small channels.

No satisfactory method has been developed to predict the correct flow pattern for any specified local flow conditions. One simple method, however, is to present the flow patterns in the form of so-called flow pattern maps, plotting the transition boundary lines on two-dimensional graphs. The difficulty of identifying flow regimes and their transitions comes mainly from the lack of agreement in the description and classification of the flow patterns and from the subjectivity of the observer.

The earliest flow pattern map for two-phase gas-liquid flow was proposed by Baker [2] based on observations on cocurrent flow of gases and condensate petroleum products in horizontal pipes. Many more flow pattern maps were presented since then; among them, the most commonly accepted, are perhaps those of Mandhane et al. [3] for horizontal flow and Hewitt and Roberts [4] for vertical channels. Most of these flow pattern maps, however, result from experimental observations and are limited to conditions near those of the measurements. Taitel and co-workers [5,6], for horizontal flow and vertical flow, suggested a generalized model to predict flow patterns based on a momentum balance. In their model, each flow pattern transition is defined by a separate transition criterion using a set of nondimensional parameters. The model was validated using the available experimental data taken in horizontal, vertical, and inclined pipes ranging in size from 13 mm to 60 mm in diameter and with air-water at low pressure. Mishima and Ishii [7] argued that traditional flow regime criteria based on the gas and liquid superficial velocities is not sufficient to the two-fluid model formulation and that geometrical parameters such as the void fraction should be used. From this point of view, a new flow regime model was developed. They are in good agreement with the existing data for atmospheric air-water flow, for steam-water, and for boiling flow. A large comprehensive review of available flow pattern maps and predictive models for conventional sizes can be found in Spedding and Spence [8].

The flow pattern transition mechanisms in small channels are not yet generally agreed. However, most researchers agree that when the dimension of the channel is reduced, the surface tension becomes an increasingly important parameter [9–15]

One of the first studies on flow patterns in small channels is that of Marchessault and Mason [16], where they considered the hydrodynamics of the liquid film surrounding an air bubble in a capillary tube.

Suo and Griffith [17] studied the flow of gas and liquid in horizontal tubes of 0.5 mm and 0.7 mm diameter. They distinguished three different flow patterns, namely, *slug*, *slug-bubbly*, and annular. No stratified flow was observed in their experiments.

Oya [18] experimentally investigated the effects of the entrance section and the liquid properties on the flow patterns in upward two-phase flow in tubes of 2 mm, 3 mm, and 6 mm diameter. He found the transition lines in the flow pattern maps to be only slightly affected by the tube size both for vertical and horizontal flows.

Barnea et al. [9] conducted visual observations of air-water flow patterns in glass pipes with diameters ranging from 4.0 mm to 12.3 mm both for horizontal and vertical flows. The experimental data were found to be in good agreement with the predictive models by Taitel and co-workers [5,6] with the exception of the *stratified nonstratified* transition boundary in horizontal flow. It is claimed that in small pipes the surface tension effect becomes the

Contributed by the Heat Transfer Division of ASME for publication in the JOURNAL OF HEAT TRANSFER. Manuscript received February 13, 2008; final manuscript received September 1, 2008; published online January 7, 2010. Assoc. Editor: Yogesh Jaluria.

dominant mechanism for the stratified-intermittent transition, while for larger pipe sizes, the Kelvin–Helmholtz instability is the dominant factor. Finally, they proposed a modification to the semi-analytical model by Taitel and Dukler [5] for small sized pipes that takes into account the surface tension effect.

Damianides and Westwater [19] investigated air-water flow pattern for horizontal glass tubes of inner diameters from 1 mm to 5 mm. They found that the model of Taitel and Dukler [5] satisfactorily predict their bubbly-slug transition but not the other transition lines.

Fukano and Kariyasaki [10] investigated air-water flow patterns in horizontal and vertical tubes of inner diameters from 1 mm to 9 mm. No stratified flow was seen in the smaller tubes. The critical pipe diameter at which the surface tension force exceeds gravity force was found to be between 5 mm and 9 mm. They also reported a poor agreement with the flow map of Mandhane et al. [3]. Similar results were obtained by Mishima and Hibiki [20] who performed experiments with air-water mixtures in vertical tubes of 1 mm to 4 mm internal diameter. Their flow pattern transitions could be well predicted by the Mishima and Ishii [7] model.

Using water and air, Triplett et al. [21] performed experiments in circular (1.1 mm and 1.45 mm diameter) and semitriangular (1.09 mm and 1.49 mm hydraulic diameter) microchannels. The resulting flow pattern maps were similar for all the test sections and mostly covered by the slug and slug-annular flow patterns. They also claim that since the channel diameter are about equal to or smaller than the Laplace length scale, the hydrodynamic interfacial processes that are governed by Taylor instability, crucial in larger channels, do not apply to capillaries.

Serizawa et al. [22] investigated the two-phase flow patterns in a 20 μm, 25 μm, and 100 μm (air-water) and in a 50 μm (steam-water) microchannel with a quite similar general trends. A number of flow patterns were identified, some of them not previously observed for capillary tubes of 1 mm in diameter, namely, *dispersed bubbly*, *gas slug*, *skewered slug*, *liquid ring*, *frothy annular*, *annular*, *liquid lump*, and *rivulet* and for the steam-water, the *liquid droplet flow*.

Kawahara et al. [23] conducted visual observations of nitrogen-water two-phase flow patterns in a silica capillary tube of 100 μm. They did not observe bubbly and *churn flow*. A flow pattern map was developed based on the probability of appearance of each type of flow.

Most of the studies on flow patterns in small channels dealt with adiabatic air-water mixtures, whose characteristics differ extensively from that of refrigerants in a boiling process, as highlighted by Hetsroni et al. [24].

Yang and Shieh [25] performed an experimental investigation on flow patterns in small channels (1.0–3.0 mm diameter) using both refrigerant R-134a and air-water two-phase flow. When comparing the resulting flow pattern maps, they found the slug to annular transition to occur at lower gas velocity for R-134a. Surface tension force, larger for water than for the refrigerant, tends to keep the liquid holdup between the tube walls and thus retard the transition from slug to annular. The surface tension force also makes the bubbles to retain its circular shape making the intermittent to bubbly transition to occur earlier for air-water than for R-134a.

Garimella et al. [26] studied flow patterns during condensation of R-134a in circular channels of 0.5 mm to 4.9 mm internal diameter, and proposed a correlation to determine the transition between intermittent and nonintermittent flow.

Huo et al. [27] experimentally investigated the flow patterns and heat transfer of R-134a flow boiling inside vertical tubes with internal diameters of 4.26 mm and 2.01 mm. The reduction in the diameter was seen to shift the slug to churn and the churn to annular transitions to higher values of gas velocity. Chen et al. [28,29] extended the visualization study by using 2.88 mm and 1.10 mm diameter tubes at three different pressures. Twelve flow pattern maps were drawn and compared with existing models for normal size tubes indicating significant differences in the 4.26 mm tube and more so for the smaller tubes. An increase in the pressure resulted in earlier (i.e., lower vapor velocity) transition from slug to churn and churn to annular flow.

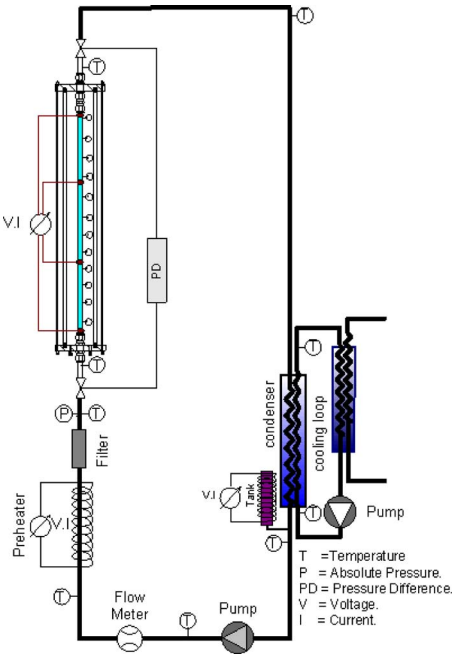

Fig. 1 Microscale heat transfer and visualization test rig

Flow patterns of two-phase R-134a and R-245fa in horizontal microtubes of 0.5 mm and 0.8 mm diameter were investigated by Revellin and Thome [30]. The two-phase flow transitions did not compare well to a macroscale flow map for refrigerants or to a microscale map for air-water flow. The diameter effect was limited to the bubbly to slug transition and all transitions seemed to be less influenced by the mass flux when using R-245fa.

In all these flow boiling experiments, the flow patterns were observed at an adiabatic glass section placed, in the best case, immediately after the heated section due to the difficulty of visualization through the metal heating wall. The present work reports new *sui generis* data on two-phase flow patterns of refrigerant R-134a under nonadiabatic conditions in a single vertical transparent tube of 1.33 mm internal diameter.

2 Experimental Facility and Data Reduction

The two-phase flow boiling rig was designed and constructed as schematically illustrated in Fig. 1. In the apparatus, system pressure, heat flux, mass flux, and inlet subcooling degree can be adjusted independently.

Circulation of the fluid is driven by a magnetic gear pump with microprocessor control and is measured with a Coriolis mass flow meter. The system pressure is adjusted by fixing the cooling water flow rate in the condenser and further set within $\pm 2\%$ by controlling the electrical heat input to a tank connected to the main loop. The liquid level in the condenser defines the system pressure. Subcooling degree at the inlet of the test section is adjusted with an electrical preheater. The circuit also includes a 7 μm filter to prevent the flow blocking from small particles.

The test section consists of a vertical quartz glass tube with internal diameter of 1.33 mm, coated on the outside by a transparent resistive coating of Indium Tin Oxide (ITO). The test section is heated using an electrical dc power supply applying a potential difference directly over the resistive coating. In the experiments the heated length was 235 mm. The test section is

Table 1 Operating conditions and uncertainties

Parameter	Operating range	Uncertainty
D (mm)	1.33	±0.003
P_{in} (bar)	7.70 and 8.87	±0.01
T_{sat} (°C)	30 and 35	±0.1
G (kg m^{-2} s^{-1})	100–500	±0.5%–2%
q'' (kW m^{-2})	5–45	±2%
$\Delta T_{sub,in}$ (°C)	3–8	±0.2
x_{th}	−0.05 to 0.97	±0.015

placed inside a sealed 60 mm diameter glass tube to which vacuum was supplied, while the entire test rig is clad with a thermal insulation layer.

The experimental facility is instrumented with an absolute pressure transducer (0–20 bar absolute) to measure the test section inlet pressure and the corresponding saturation temperature. A differential pressure transducer (0–350 mbar differential) to measure the pressure drop through the test section and 0.1 mm diameter T-type thermocouples to measure the bulk fluid temperature at the locations indicated in Fig. 1. Temperatures, system and differential pressures, and mass flow and test section dc voltage and current are recorded using a data logger connected to a computer. All tests are performed under steady-state conditions. Thermodynamic properties for R-134a including density, enthalpy, viscosity, saturation temperature, and thermal conductivity are calculated with the computer code REFPROP 7.0 developed by the U.S. National Institute of Standards and Technology [31]. The experimental conditions and maximum associated uncertainties [32] are summarized in Table 1.

Flow patterns have been observed and recorded with a high-speed CMOS digital camera with a recording speed up to 100,000 frames per second (fps) and tungsten lightning (Fig. 2). For the actual experiments, recording speeds from 3000 fps to 10,000 fps were used. A still digital camera (3 megapixel) with automatic synchronized flash and close-up lens has been used in parallel. The use of a transparent heated tube enabled flow pattern visualization along the whole heated length.

For a given test point, the heat flux added to the test section q'' is calculated as

$$q'' = \frac{I \cdot V}{A} \tag{1}$$

where V and I are, respectively, the current and voltage intensity applied to the test section and A the heat transfer area. Even the distribution of the heat flux across the whole surface is assumed.

The thermodynamic vapor quality at any axial location $x_{th}(z)$ is defined from the heat transferred to the fluid as

$$x_{th}(z) = \frac{q''\pi D(z - z_{sat})}{AGi_{lg}} \tag{2}$$

where i_{lg} is the latent heat of vaporization and z_{sat} is the position at which saturated condition would be reached [33] and calculated as

$$z_{sat} = \frac{\dot{m}_{R\text{-}134a} c_p (T_{sat} - T_i)}{q''\pi D} \tag{3}$$

3 Results and Discussion

3.1 Flow Pattern Classification. The classification of flow patterns in vertical channels is not yet generally agreed. However, most of the researchers seem to agree to categorize their observations by three main flow patterns: bubbly flow, intermittent flow, and annular flow. Each main class could then be divided into subclasses. In the current study, the following seven distinct flow patterns were identified from the experimental flow visualization.

1. Isolated bubbly flow is characterized by distinct and essentially spherical bubbles and, in general, considerably smaller in diameter than the channel.
2. Confined bubbly flow is with distinct but distorted (nonspherical) bubbles, which is of characteristic size comparable to the channel diameter.
3. Slug flow is characterized by elongated, bullet-shaped bubbles with spherical cap and flat tail (slugs) that occupy most of the cross section. In this regime, the liquid flow is mainly contained in liquid plugs, which separate successive vapor slugs. These liquid plugs may or may not contain smaller bubbles.
4. Churn flow is formed when the vapor slugs become unstable and disrupted. The vapor flows in a more or less chaotic manner through the liquid, which is mainly displaced to the channel wall.
5. Slug-annular flow is characterized by the collision of neighboring slugs leading to a wavy-annular flow pattern with deep waves that interrupt the annular flow.
6. Annular flow is where the gas flows continuously in the tube center while the liquid flows in a film along the channel wall.
7. Mist flow is with the majority of the flow entrained in the gas core and dispersed as liquid droplets.

3.2 Experimental Flow Pattern Map. All experiments were performed by changing the wall heat flux while refrigerant mass flux (G=100–500 kg m^{-2} s^{-1}), inlet subcooling degree ($\Delta T_{sub,i}$ =3–8 °C), and inlet pressure (P_i=7.70 bar and 8.87 bar) were kept constant. For each given set of conditions (inlet pressure,

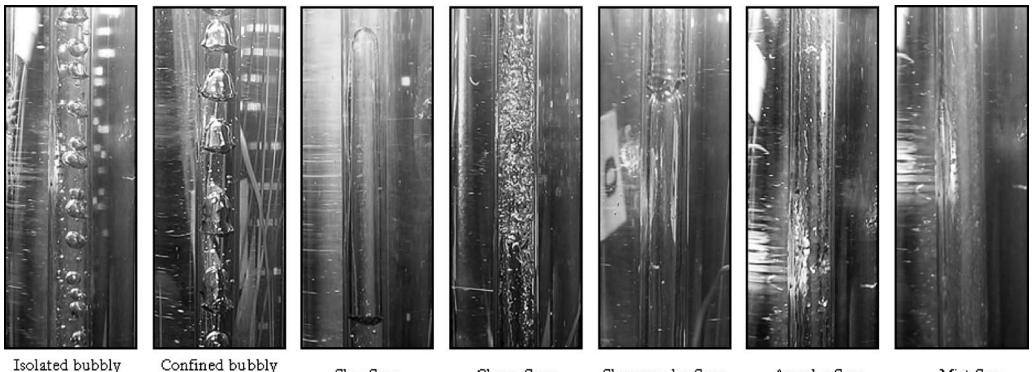

Fig. 2 Representative photographs of the different two-phase flow patterns observed

Table 2 Axial location for flow pattern inspection

Pos. No.	1	2	3	4	5	6	7	8
z (mm)	13	42	72.5	103	132.5	162.5	192	215

inlet subcooling, mass flux, and heat flux), the flow patterns were identified at eight different positions along the heated section (see Table 2) in order to investigate the flow pattern evolution with quality.

In the experiments, the fluid enters under subcooled liquid conditions and is heated to the saturation temperature. A thermal boundary layer forms at the wall and a radial temperature profile is set up. If the heat flux is high enough, the liquid temperature close to the wall will become superheated and, eventually, vapor nucleation will occur. Vapor bubbles grow from activated nucleation sites on the surface of the tube, slide, and finally detach to form a bubbly flow. After detachment these bubbles continue to grow and coalesce with other bubbles [34] to form vapor slugs separated by liquid plugs in slug flow. Further vapor formation occurs mainly by evaporation at the interface between the liquid film and the vapor; vapor slugs become more elongated and liquid plugs narrower. At higher vapor qualities the neighboring slugs collide and ultimately form the annular flow. Further vapor formation occurs mainly by evaporation at the interface between the liquid film and the vapor; vapor slugs become more elongated and liquid plugs narrower. At higher vapor qualities the neighboring slugs collide and ultimately form the annular flow.

The increase in velocities in the vapor core will cause entrainment of liquid in the form of droplets (mist flow). The reduction in the liquid film caused by entrainment and evaporation at the interface between the liquid film and the vapor results, ultimately, in the complete dry out of the surface [33]. A schematic representation of the flow patterns inside the vertical heated tube is shown in Fig. 3.

Two-phase flow pattern observations from the present study are presented in Fig. 4 in terms of mass flux and vapor quality and in terms of superficial liquid velocity versus superficial vapor velocity.

Except for $G=500\ \mathrm{kg\,m^{-2}\,s^{-1}}$, it is clear that the higher the mass flux, the earlier the transitions between the different flow patterns. The mist flow was only observed for the lowest mass flux at $q''=28\ \mathrm{kW\,m^{-2}}$ for vapor qualities above 0.9.

The transition from intermittent (slug) flow to nonintermittent (annular) flow has been seen to occur in two different ways: through a slug-annular flow or through a churn flow. When the liquid velocity is low and the flow laminar (e.g., for $G=100\ \mathrm{kg\,m^{-2}\,s^{-1}}$), the surface tension force is able to maintain the slugs in their shape while growing longer and eventually reach another existing slug. Neighboring slugs will then coalesce into a slug-annular flow, creating a thicker liquid ring at the merging point. On the other hand, if the liquid velocity is high (e.g., for $G=500\ \mathrm{kg\,m^{-2}\,s^{-1}}$) turbulence and agitation of the gas-liquid interface will result in a much more chaotic regime, termed as churn flow. For $G=500\ \mathrm{kg\,m^{-2}\,s^{-1}}$, the churn flow is the dominant flow pattern for the range of experimental conditions.

For the intermediate mass fluxes of the investigation ($G=200-400\ \mathrm{kg\,m^{-2}\,s^{-1}}$) slug-annular flow and churn flow seem to coexist for $0.1<x_{\mathrm{th}}<0.25$. This can be explained by the fact that given a fixed mass flux, a certain vapor quality will be reached at different axial positions for different values of heat flux. It is well known that since the density of the vapor is much smaller than that of the liquid, the evaporation process provokes an acceleration of the flow. Higher heat fluxes lead to higher evaporation rates, which in turn, lead to higher velocity and turbulence of the flow. In consequence, for high heat fluxes the transition from slug to annular flow tends to be through churn flow, while for low values of the heat flux the transition is by annular-slug flow, as illustrated in Fig. 5.

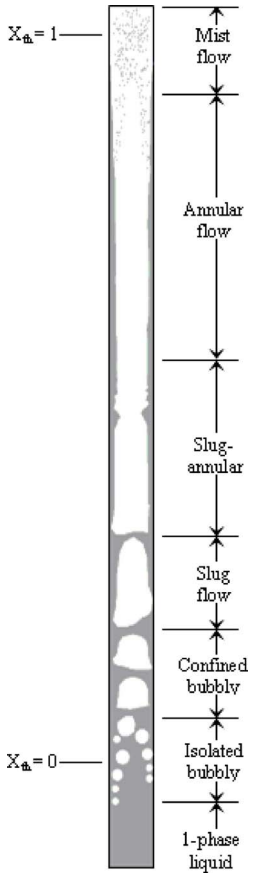

Fig. 3 Flow patterns inside the heated tube

It can also be seen from Fig. 5 that in the low to moderate heat flux range ($q''=5-15\ \mathrm{kW\,m^{-2}}$ for $G=200\ \mathrm{kg\,m^{-2}\,s^{-1}}$) when the heat flux is increased the boiling front shifts upstream (i.e., downwards) close to the inlet of the test section.

3.3 Effect of System Pressure and Inlet Subcooling Degree. The effect of the saturation temperature on the flow patterns is shown in Fig. 6 for tests at inlet saturation temperatures of 30°C and 35°C (corresponding to 7.70 bar and 8.87 bar saturation pressure, respectively). As seen in the figure, an increase in the saturation temperature shifts all transition boundaries toward higher vapor qualities. At higher pressure the density ratio ρ_l/ρ_g is lower and in consequence, the bubbles become smaller and more energy is needed for coalescence to occur.

Figure 7 shows the experimental transition boundaries for three different inlet subcooling degrees, namely, 3°C, 5°C, and 8°C. No significant difference in the position of the transition boundaries has been observed between inlet subcooling of 5°C and 8°C. However, for $\Delta T_{\mathrm{sub,in}}=3$°C the transition boundaries of isolated bubbly to confined bubbly, confined bubbly to slug, and slug to slug-annular or churn flow seem to move to higher values of vapor quality. Subcooled boiling implies the existence of bubbles at negative vapor quality. It is thus reasonable to believe that a larger subcooling degree would shift the transition boundaries in the early vapor quality region to lower values. The experimental data, however, is not conclusive.

3.4 Comparison to Exiting Flow Pattern Maps. The present flow pattern maps of Fig. 4 are here compared with the existing

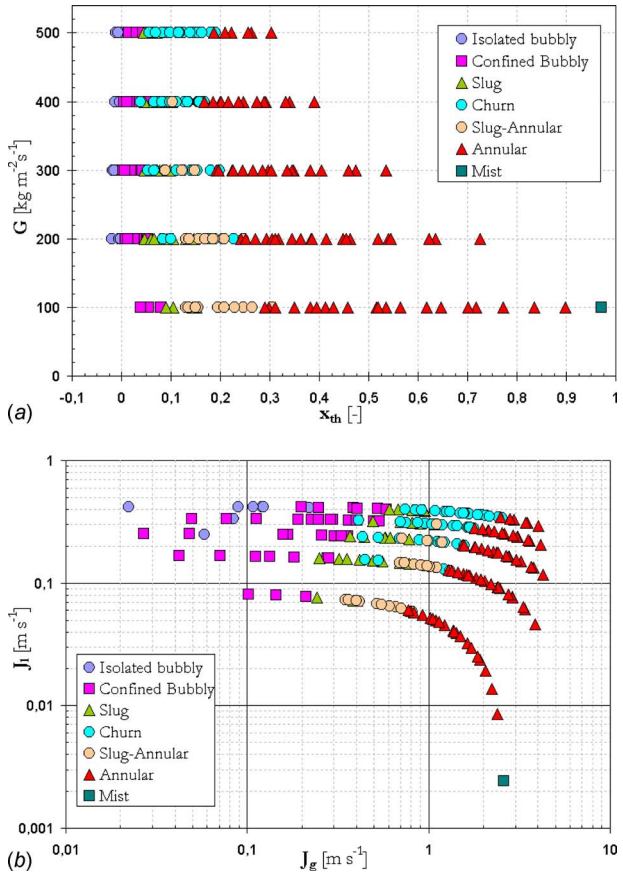

Fig. 4 Flow pattern maps for R-134a: D=1.33 mm, L_{hs} =235 mm, T_{sat}=30°C, and $\Delta T_{sub,i}$=5°C

models and experimental transition lines for vertical upward flow in normal sized tubes and in microchannels.

As mentioned in Sec. 1, one of the earliest flow pattern maps available for vertical flows is that of Hewitt and Roberts [4]. This flow map was based on their observations on low pressure air-

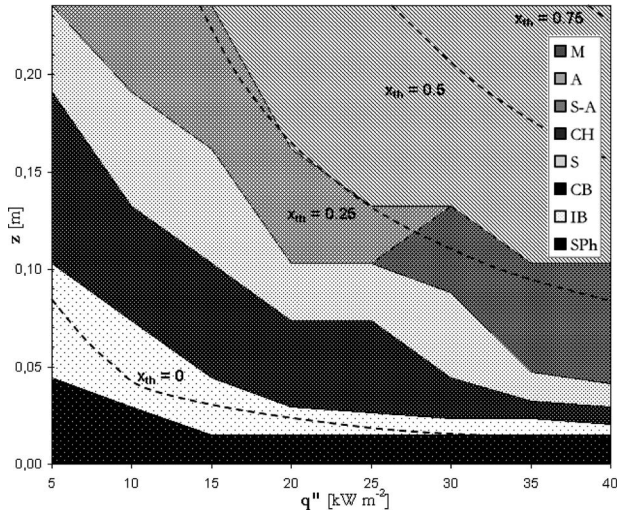

Fig. 5 Effect of heat flux on flow patterns of R-134a along the heated length (G=200 kg m^{-2} s^{-1}, T_{sat}=30°C, and $\Delta T_{sub,i}$ =5°C): SPh is the single-phase flow, IB is the isolated bubbly flow, CB is the confined bubbly flow, S is the slug flow, CH is the churn flow, S-A is the slug-annular flow, A is the annular flow, M is the mist flow

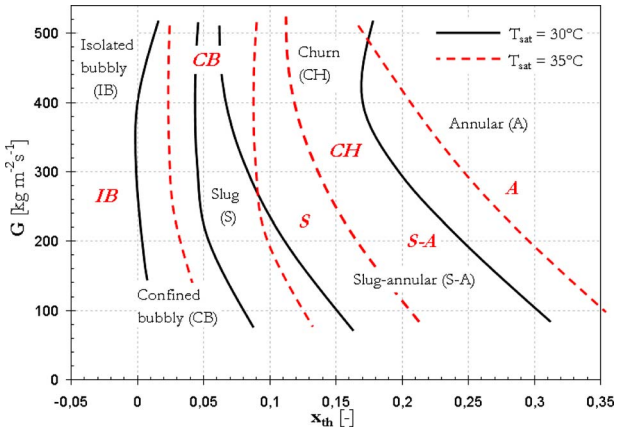

Fig. 6 Effect of saturation temperature on transition boundaries (R-134a: D=1.33 mm, L_{hs}=235 mm, and $\Delta T_{sub,i}$=5°C)

water and high-pressure steam-water flow in vertical tubes with diameters ranging from 10 mm to 30 mm. The axes represent the superficial momentum fluxes of the liquid $\rho_l J_l^2$ and vapor phases $\rho_g J_g^2$, respectively.

As shown in Fig. 8, this flow pattern map presents a very poor agreement with the present experimental data both with respect to the significant trends of the curves and their absolute locations.

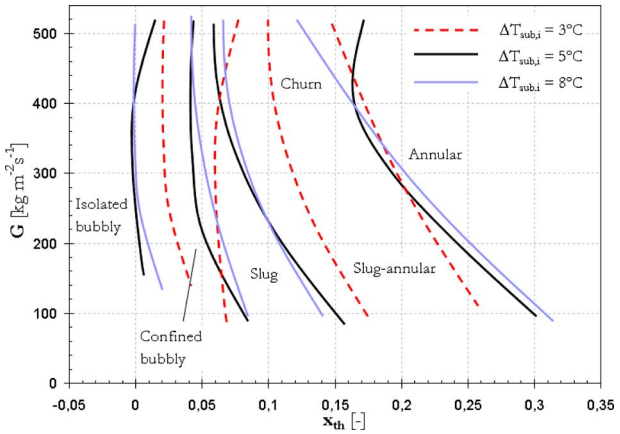

Fig. 7 Effect of inlet subcooling degree on transition boundaries (R-134a: D=1.33 mm, L_{hs}=235 mm, and T_{sat}=30°C)

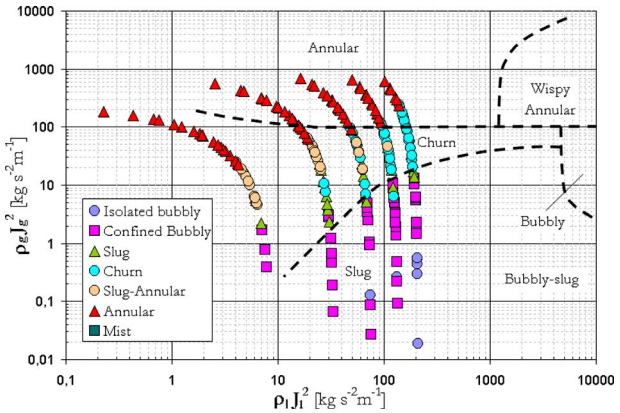

Fig. 8 Comparison between the present flow pattern map (R-134a: D=1.33 mm, L_{hs}=235 mm, T_{sat}=30°C, and $\Delta T_{sub,i}$=5°C) and the experimental transition lines of Hewitt and Roberts [4] for low pressure air-water and high-pressure steam-water flow in vertical tubes of 10–30 mm diameter

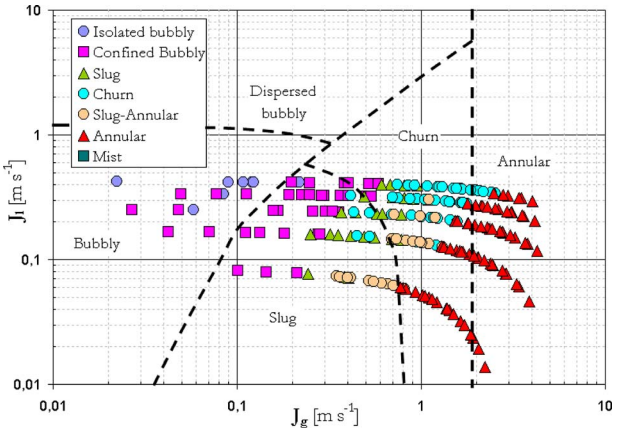

Fig. 9 Comparison between the present flow pattern map (R-134a: D=1.33 mm, L_{hs}=235 mm, T_{sat}=30°C, and $\Delta T_{sub,i}$=5°C) and transition lines predicted with the model by Taitel et al. [6] evaluated at the experimental conditions

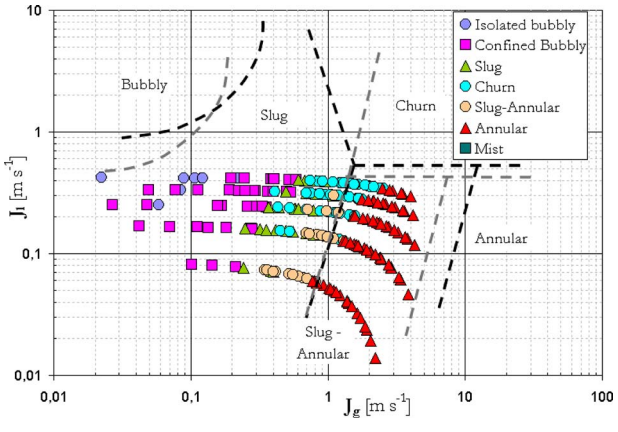

Fig. 11 Comparison between the present flow pattern map (R-134a: D=1.33 mm, L_{hs}=235 mm, T_{sat}=30°C, and $\Delta T_{sub,i}$=5°C) and the experimental transition lines of Triplett et al. [21] for air-water flow in 1.097 mm and 1.45 mm tubes, respectively

Figures 9 and 10 show the present flow pattern map compared with predictions using the semi-analytical models for upward two-phase flow in conventional size vertical tubes of Taitel et al. [6] and Mishima and Ishii [7], respectively. From the figures, neither of them is able to predict any of the flow regime transitions. For instance, the experimental transition boundary from churn to annular is dependent on both vapor and liquid velocities while in the model of Taitel et al. [6], it is independent of the liquid velocity and the churn zone predicted by the model of Mishima and Ishii [7] shrinks to a very small area in the low liquid velocity range while in the experiments it is a main flow pattern, specially at high mass fluxes (i.e., liquid superficial velocities).

Figure 11 shows a comparison between the present experimental data and the transition lines of Triplett et al. [21] obtained for air-water in circular microchannel of 1.097 mm and 1.45 mm internal diameter. As expected, although the trends of the transition lines are somewhat similar, the agreement is not satisfactory. The thermophysical properties of R-134a differ significantly from those of water, in particular, the surface tension of water is about ten times that of R-134a (72.80 mN m^{-1} and 8.76 mN m^{-1}, respectively at 20°C). Furthermore, the bubble formation of an air-water mixture is not necessarily the same as that in a boiling process.

On the other hand, in spite of being developed for a condensing process, the agreement between the present data and the correlation proposed by Garimella et al. [26] is surprisingly good (Fig. 12). The predicted boundary line for intermittent and nonintermittent flow transition overlaps precisely with the experimental transitions from slug-annular to annular and churn to annular flow. In small diameters, where the Bond number (Bo) approaches unity, surface tension forces grow to be dominant and the two-phase characteristics of flow boiling and condensation processes become similar.

Finally, the experimental data are presented in Figs. 13 and 14 against the transition lines of Chen et al. [28] for flow boiling of R-134a in a vertical tube of 1.10 mm. Except for the fact that no churn flow was identified for the lower mass fluxes in the present observations, there is much resemblance between the two flow maps; although the transitions from slug to churn and from churn to annular seem to occur earlier in the present results. Chen et al. [28] proposed the coordinate group of the Lockhard–Martinelli parameter and the mass flux (Fig. 14) as the appropriate to deduce a general correlation to predict the transition boundaries.

4 Conclusions

Two-phase flow patterns in convective boiling of refrigerant R-134a through a vertical circular channel with internal diameter of 1.33 mm have been investigated.

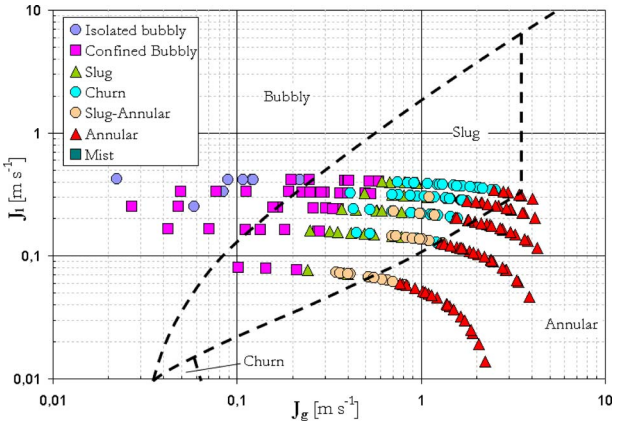

Fig. 10 Comparison between the present flow pattern map (R-134a: D=1.33 mm, L_{hs}=235 mm, T_{sat}=30°C, and $\Delta T_{sub,i}$=5°C) and transition lines predicted with the model by Mishima and Ishii [7] evaluated at the experimental conditions

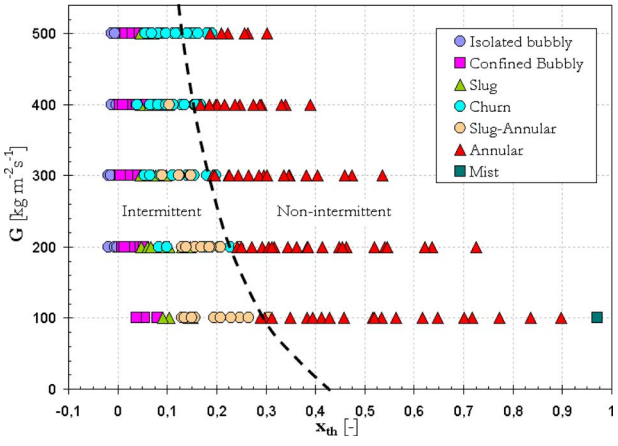

Fig. 12 Comparison between the present flow pattern map (R-134a: D=1.33 mm, L_{hs}=235 mm, T_{sat}=30°C, and $\Delta T_{sub,i}$=5°C) and the transition line predicted with the correlation by Garimella et al. [26] evaluated for D=1.33 mm

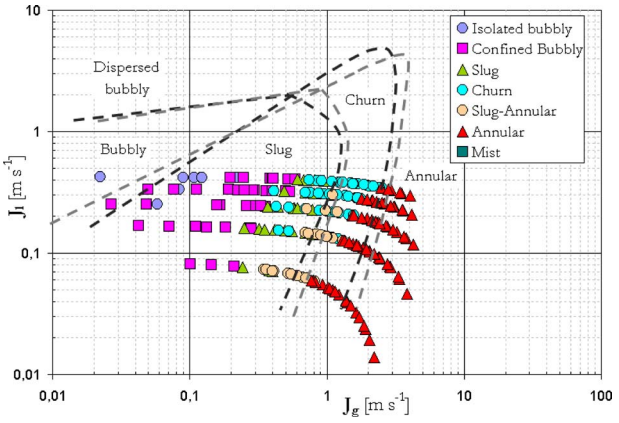

Fig. 13 Comparison between the present flow pattern map (R-134a: D=1.33 mm, L_{hs}=235 mm, T_{sat}=30°C, and $\Delta T_{sub,i}$=5°C) and the experimental transition lines of Chen et al. [28] for two-phase flow of R-134a in a 1.10 mm vertical tube and pressures of 6 bar and 8 bar, respectively

A unique test section consisting of a quartz tube with a homogeneous ITO coating, allowing heating and simultaneous visualization, has been used to visualize the flow in nonadiabatic conditions. From flow boiling visualization seven distinct two-phase flow patterns have been observed: isolated bubbly flow, confined bubbly flow, slug flow, churn flow, slug-annular flow, annular flow, and mist flow. Two-phase flow pattern observations are presented in the form of flow pattern maps. Annular-type flow patterns are dominant for $x_{th}>0.2$.

An increase in the saturation temperature shifts all transition boundaries toward higher vapor qualities. No significant influence of the inlet subcooling degree has been observed on the slug-annular/churn to annular flow (intermittent to nonintermittent) transition. However, larger inlet subcooling seems to move all other transitions to earlier vapor qualities.

The experimental flow pattern maps are compared with models developed for conventional sizes available in literature and a microscale map developed for air-water showing a large discrepancy. On the other hand, the results are consistent with other studies using refrigerants in minichannels.

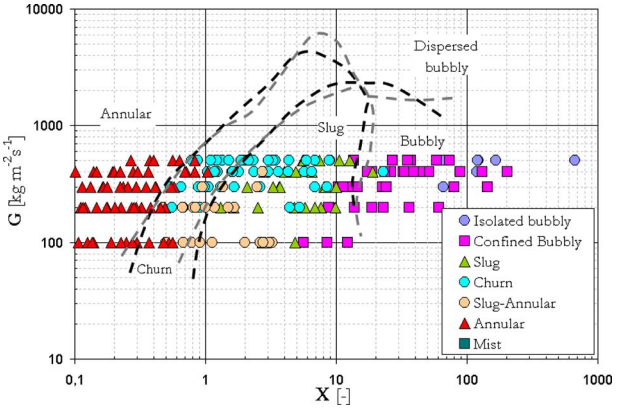

Fig. 14 Comparison between the present flow pattern map (R-134a: D=1.33 mm, L_{hs}=235 mm, T_{sat}=30°C, and $\Delta T_{sub,i}$=5°C) and the experimental transition lines of Chen et al. [28] for two-phase flow of R-134a in a vertical tube of 1.10 mm and 2.01 mm diameter, respectively

Acknowledgment

This work was supported in part by the European Community's Human Potential Programme under Contract No. HPRN-CT-2002-00204 (HMTMIC).

Nomenclature

A = heat transfer area (m^2)
C_p = specific heat (J kg^{-1} K^{-1})
D = diameter [m]
G = mass flux (kg m^{-2} s^{-1})
I = current (A)
i_{lg} = latent heat of vaporization (J kg^{-1})
J_l = superficial liquid velocity, $G(1-x)/\rho_l$ (m s^{-1})
J_g = superficial vapor velocity, Gx/ρ_v (m s^{-1})
L = length (m)
$\dot{m}_{R\text{-}134a}$ = mass flow of refrigerant (kg s^{-1})
P = pressure (Pa)
ΔP = pressure drop (Pa)
q'' = heat flux (W m^{-2})
T = temperature (°C)
ΔT_{sub} = subcooling degree, T_{sat}-T (°C)
V = voltage (V)
x_{th} = thermodynamic vapor quality
X = Lockhart–Martinelli parameter, $(\Delta P_{ls}/\Delta P_{gs})^{1/2}$
z = axial position (m)

Subscripts

in = inlet
l = liquid
ls = based on the superficial liquid velocity
g = gas
gs = based on the superficial gas velocity
sat = saturation

References

[1] Owhaib, W., Martin-Callizo, C., and Palm, B., 2004, "Evaporative Heat Transfer in Vertical Circular Microchannels," Appl. Therm. Eng., **24**, pp. 1241–1253.
[2] Baker, O., 1954, "Simultaneous Flow of Oil and Gas," Oil & Gas J., **53**, pp. 185–190.
[3] Mandhane, J. M., Gregory, G. A., and Aziz, K., 1974, "A Flow Pattern Map for Glass-Liquid Flow in Horizontal Pipes," Int. J. Multiphase Flow, **1**, pp. 537–553.
[4] Hewitt, G. F., and Roberts, D. N., 1969, "Studies of Two-Phase Flow Patterns by Simultaneous X-Ray and Flash Photography," Paper No. AERE-M 2159.
[5] Taitel, Y., and Dukler, A. E., 1976, "A Model for Predicting Flow Regime Transitions in Horizontal and Near Horizontal Gas-Liquid Flow," AIChE J., **22**(1), pp. 47–55.
[6] Taitel, Y., Barnea, D., and Dukler, A. E., 1980, "Modeling Flow Pattern Transitions for Steady Upward Gas-Liquid Flow in Vertical Tubes," AIChE J., **26**(3), pp. 345–354.
[7] Kaichiro, M., and Ishii, M., 1984, "Flow Regime Transition Criteria for Upward Two-Phase Flow in Vertical Tubes," Int. J. Heat Mass Transfer, **27**, pp. 723–737.
[8] Spedding, P. L., and Spence, D. R., 1993, "Flow Regimes in Two-Phase Gas-Liquid Flow," Int. J. Multiphase Flow, **19**(2), pp. 245–280.
[9] Barnea, D., Luninski, Y., and Taitel, Y., 1983, "Flow Pattern in Horizontal and Vertical Two Phase Flow in Small Diameter Pipes," Can. J. Chem. Eng., **61**, pp. 617–620.
[10] Fukano, T., and Kariyasaki, A., 1993, "Characteristics of Gas-Liquid Two-Phase Flows in a Capillary Tube," Nucl. Eng. Des., **141**, pp. 59–68.
[11] Coleman, J. W., and Garimella, S., 1999, "Characterization of Two-Phase Flow Patterns in Small Diameter Round and Rectangular Tubes," Int. J. Heat Mass Transfer, **42**, pp. 2869–2881.
[12] Sheng, C. H., 2001, "Some Two-Phase Flow and Boiling Heat Transfer Characteristics in Small Diameter Tubes," Licentiate thesis, Royal Institute of Technology, KTH, Sweden.
[13] Satitchaicharoen, P., and Wongwises, S., 2004, "Two-Phase Flow Pattern Maps for Vertical Upward Gas-Liquid Flow in Mini-Gap Channels," Int. J. Multiphase Flow, **30**, pp. 225–236.
[14] Chung, P. M., and Kawaji, M., 2004, "The Effect of Channel Diameter on Adiabatic Two-Phase Flow Characteristics in Microchannels," Int. J. Multiphase Flow, **30**, pp. 735–761.
[15] Ide, H., Kariyasaki, A., and Fukano, T., 2007, "Fundamental Data on Gas—Liquid Two-Phase Flow in Minichannels," Int. J. Therm. Sci., **46**, pp. 519–

530.
[16] Marchessault, R. N., and Mason, S. G., 1960, "Flow Entrapped Bubbles Through a Capillary," Ind. Eng. Chem., **52**, pp. 79–84.
[17] Suo, M., and Griffith, P., 1964, "Two-Phase Flow in Capillary Tubes," ASME J. Basic Eng., **86**(3), pp. 576–582.
[18] Oya, T., 1971, "Upward Liquid Flow in Small Tube Into Which Air Streams (1st Report, Experimental Apparatus and Flow Patterns)," Bull. JSME, **14**(78), pp. 1320–1329.
[19] Damianides, D. A., and Westwater, J. W., 1988, "Two-Phase Flow Patterns in Compact Heat Exchanger and in Small Tubes," *Proceedings of the Second UK National Conference on Heat Transfer*, Glasgow, UK, Vol. 2, pp. 1257–1268.
[20] Mishima, K., and Hibiki, T., 1996, "Some Characteristics of Air-Water Two-Phase Flow in Small Diameter Vertical Tubes," Int. J. Multiphase Flow, **22**, pp. 703–712.
[21] Triplett, K. A., Ghiaasiaan, S. M., Abdel-Khalil, S. I., and Sadowski, D. L., 1999, "Gas-Liquid Two-Phase Flow in Micro-Channels Part I: Two-Phase Flow Patterns," Int. J. Multiphase Flow, **25**, pp. 377–394.
[22] Serizawa, A., Feng, Z., and Kawara, Z., 2002, "Two-Phase Flow in Micro-channel," Exp. Therm. Fluid Sci., **26**, pp. 703–714.
[23] Kawahara, A., Cheng, P. M.-Y., and Kawaji, M., 2002, "Investigation of Two-Phase Flow Pattern, Void Fraction and Pressure Drop in a Microchannel," Int. J. Multiphase Flow, **28**, pp. 1411–1435.
[24] Hetsroni, G., Mosyak, A., Segal, Z., and Pogrebnyak, E., 2003, "Two-Phase Flow Patterns in Parallel Micro-Channels," Int. J. Multiphase Flow, **29**, pp. 341–360.
[25] Yang, Ch.-Y., and Shieh, Ch.-Ch., 2001, "Flow Pattern of Air-Water and Two-Phase R-134a in Small Circular Tubes," Int. J. Multiphase Flow, **27**, pp. 1163–1177.
[26] Garimella, S., Killion, J. D., and Coleman, J. W., 2002, "An Experimental Validated Model for Two-Phase Pressure Drop in the Intermittent Flow Regime for Circular Channel," ASME J. Fluids Eng., **124**, pp. 205–214.
[27] Huo, X., Chen, L., Tian, Y. S., and Karayiannis, T. G., 2004, "Flow Boiling and Flow Regimes in Small Diameter Tubes," Appl. Therm. Eng., **24**, pp. 1225–1239.
[28] Chen, L., Tian, Y.S., and Karayiannis, T.G., 2005, "Vertical Upward Flow Patterns in Small Diameter Tubes," *Proceedings of the Sixth World Conference on Experimental Heat Transfer, Fluid Mechanics and Thermodynamics*, Matsushima, Japan, Paper No. 9-b-4.
[29] Chen, L., Tian, Y. S., and Karayiannis, T. G., 2006, "The Effect of Tube Diameter on Vertical Two-Phase Flow Regimes in Small Tubes," Int. J. Heat Mass Transfer, **49**, pp. 4220–4230.
[30] Revellin, R., and Thome, J. R., 2007, "Experimental Investigation of R-134a and R-245fa Two-Phase Flow in Microchannel for Different Flow Conditions," Int. J. Heat Mass Transfer, **28**, pp. 63–71.
[31] NIST, 2002, National Institute of Standard and Technology, REFRPROP Version 7.0, Boulder, CO.
[32] Kline, S. J., and McClintock, F. A., 1953, "Describing Uncertainties in Single-Sample Experiments," Mech. Eng. (Am. Soc. Mech. Eng.), **75**, pp. 3–8.
[33] Collier, J. G., and Thome, J. R., 1994, *Convective Boiling and Condensation*, 3rd ed., Oxford Science, New York, pp. 1–33 and 184.
[34] Owhaib, W., Palm, B., and Martín-Callizo, C., 2007, "A Visualization Study of Bubble Behavior in Saturated Flow Boiling Through a Vertical Mini-Tube," Heat Transfer Eng., **28**(10), pp. 852–860.

Convection Calibration of Schmidt–Boelter Heat Flux Gauges in Stagnation and Shear Air Flow

A. Gifford

A. Hoffie

T. Diller
Fellow ASME

S. Huxtable

Department of Mechanical Engineering,
Virginia Tech,
Blacksburg, VA 24061

Experiments were performed to characterize the performance of Schmidt–Boelter heat flux gauges in stagnation and shear convective air flows. The gauges were of a standard design (25.4 mm and 38 mm in diameter), using a copper heat sink with water cooling channels around the active sensing element. A simple model of the gauges using an internal thermal resistance between the sensor surface and the heat sink is used to interpret the results. The model predicts a nonlinear dependence of the gauge sensitivity as a function of the heat transfer coefficient. Experimental calibration systems were developed to simultaneously measure the heat flux gauge response relative to a secondary standard under the same flow and thermal conditions. The measured gauge sensitivities in the stagnation flow matched the model, and were used to estimate the value of the internal thermal resistance for each of the four gauges tested. For shear flow, the effect of the varying gauge surface temperature on the boundary layer was included. The results matched the model with a constant factor of 15–25% lower effective heat transfer coefficient. When the gauge was water cooled, the effect of the internal thermal resistance of the gauge was markedly different for the two flow conditions. In the stagnation flow, the internal resistance further decreased the apparent gauge sensitivity. Conversely, in shear flow, the resistance was effectively offset by the cooler heat sink of the gauge, and the resulting sensitivities were nearly the same as, or larger than, for radiation.
[DOI: 10.1115/1.3211866]

Keywords: heat flux gauge, sensor calibration, convection effects

1 Introduction

As energy becomes increasingly costly, the importance of efficiency in energy systems becomes more important. One tool for analyzing and controlling energy intensive processes is the measurement of heat flux. The use of heat flux gauges along with temperature measurements gives a more complete understanding of energy systems because of the additional information about energy transfer and heat paths that are provided.

Although a number of heat flux gauges are commercially available, they are usually only calibrated in radiation. Consequently, if they are used for convective heat flux measurements, there are questions about their accuracy. Because the gauge can cause a disruption of the thermal conditions at the surface where it is mounted [1], it is important to calibrate heat flux gauges in environments close to their use. The present research investigates the operation of heat flux gauges in convection, and the difference between radiation and convection calibration. A unique convection calibration facility was developed to calibrate four Schmidt–Boelter heat flux gauges, and compare the results with the usual radiation calibrations. The implications for the measurement of convective heat flux are discussed.

2 Heat Flux Measurement

Most methods for measuring heat flux are based on either the application of a sensor onto a surface, or insertion through a hole in the material to a position flush with the surface. Either method can cause a physical and/or thermal disruption of the surface. The measurement goal is to minimize these disruptions to measure the actual heat flux at the surface. This requires an understanding and analysis of the gauge system.

The present work considers an insert heat flux gauge, as shown in Fig. 1. In general, three modes of energy transfer act on the gauge. Assuming that the material is opaque, an energy balance at the surface relates the different modes of heat transfer as

$$q_{\text{cond}} = q_{\text{conv}} + q_{\text{rad}} \tag{1}$$

Conduction through the gauge and the plate provides the pathway for the energy transfer by convection and radiation at the surface. The convection heat transfer can be expressed in terms of the difference in temperature between the fluid and the surface of the gauge as

$$q''_{g_{\text{conv}}} = h_g(T_\infty - T_g) \tag{2}$$

Because the gauge surface temperature may be different than the plate temperature, the convection to the gauge may be different than that to the plate as expressed by

$$q''_{p_{\text{conv}}} = h_p(T_\infty - T_p) \tag{3}$$

The difference in surface temperature may also affect the heat transfer coefficient, as indicated by the different subscripts in Eqs. (2) and (3).

For radiation, if the radiator surrounds the gauge, and appears black, the flux to the gauge is simply

$$q''_{\text{rad}} = \varepsilon\sigma(T_r^4 - T_g^4) \tag{4}$$

where ε is the gray body emissivity of the gauge, and the temperatures are absolute. If the temperature of the radiator (T_r) is

Contributed by the Heat Transfer Division of ASME for publication in the JOURNAL OF HEAT TRANSFER. Manuscript received December 1, 2008; final manuscript received July 6, 2009; published online December 22, 2009. Review conducted by Minking Chyu.

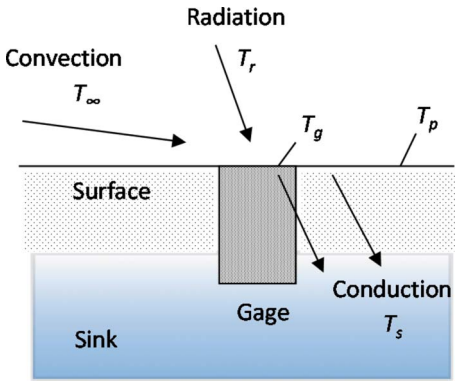

Fig. 1 Heat flux sensor with the three modes of energy transfer

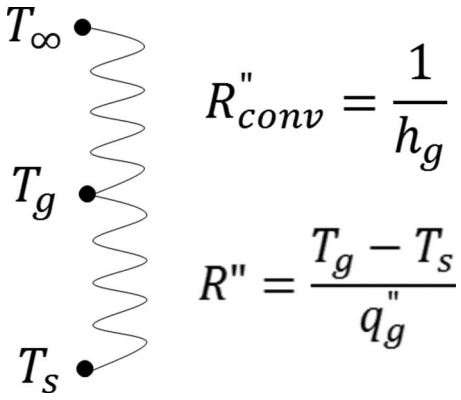

Fig. 2 Heat flux gauge resistance network for convection

much higher than the temperature of the gauge (T_g), the last term in Eq. (4) is negligible.

3 General Thermal Model of the Heat Flux Gauge

As shown in Fig. 1, the heat flux gauge measures the net convection and radiation at its surface. At steady state, the thermal energy is necessarily transferred through the gauge to a heat sink, which is usually the mounting plate or water cooling channels. An overall thermal resistance R'' from the surface of the gauge to the heat sink can, therefore, be defined as

$$R'' = \frac{T_g - T_s}{q''_g} \tag{5}$$

where T_g is the average surface temperature of the gauge, T_s represents the temperature of the heat sink, and q''_g is the conduction through the gauge. All of the thermal resistances between the gauge surface and the heat sink are included, whether one-dimensional or three-dimensional effects. Examples of the thermal resistances are: solid material, contact resistances, air gaps, paint, thermal paste, potting material, and glue layers.

At the surface of the gauge, the net convection and radiation must equal the conduction through the gauge, as expressed by Eq. (1). For the combined convection and radiation heat transfer case, the heat flux to the gauge is matched with the conduction expressed in Eq. (5)

$$q''_g = h_g(T_\infty - T_g) + \varepsilon\sigma(T_r^4 - T_g^4) = \frac{(T_g - T_s)}{R''} \tag{6}$$

The corresponding heat flux to the plate is different because the gauge temperature is generally different than the plate temperature

$$q''_p = h_p(T_\infty - T_p) + \varepsilon\sigma(T_r^4 - T_p^4) \tag{7}$$

Because the plate is usually either directly cooled or is the heat sink, there is assumed to be no conduction resistance between the plate and the heat sink $T_p = T_s$.

In a purely convective environment with negligible radiation, as used in this paper, the ratio of Eqs. (6) and (7) (with $T_p = T_s$) reduces to

$$\frac{q''_g}{q''_p} = \frac{h_g(T_\infty - T_g)}{h_p(T_\infty - T_s)} \tag{8}$$

The gauge surface temperature T_g, which is generally unknown, may be found using Eq. (6) without radiation as

$$T_g = \frac{T_s/R'' + T_\infty h_g}{1/R'' + h_g} \tag{9}$$

This appears as the center temperature of a resistance network, as shown in Fig. 2. Using Fig. 2, the corresponding heat flux through the gauge can be expressed in terms of the sink temperature, using only the conduction resistance R'' and the convection resistance $1/h_g$ as

$$q''_g = \frac{(T_\infty - T_s)}{\frac{1}{h_g} + R''} \tag{10}$$

Substitution of Eq. (10) into Eq. (8) gives, after simplification, the desired ratio of heat fluxes

$$\frac{q''_g}{q''_p} = \frac{1}{\frac{h_p}{h_g} + h_p R''} \tag{11}$$

The ratio of the heat flux to the gauge and to the plate is then only a function of the two dimensionless parameters h_p/h_g and $h_p R''$. These relate flow parameters and gauge parameters to a systematic error in the resulting measurement. Kuo and Kulkarni [2] used a similar model for the internal resistance of a Gardon gauge without the h_p/h_g term.

4 Heat Flux Gauges

Two styles of heat flux gauges already available on the market are the heat flux microsensor (HFM) and the Schmidt–Boelter (SB). The HFM is a thin-film thermopile, model 7E/L made by Vatell Corp. (Christiansburg, VA), which is less than 2 μm thick [1]. It is deposited on a ceramic base of aluminum nitride (k = 175 W/m K), which is press fit into a 6.3 mm diameter metal housing. The use of high temperature thermocouple materials allow operating temperatures of over 800°C for short times, and heat flux from 1 kW/m^2, with no practical upper limit. Because of the thin sensor design, the thermal response time is less than 10 μs so that the frequency response is well above 10 kHz [3]. The high temperature and fast time response capabilities are useful for aerodynamic applications, including combusting flows and high speed events such as shock waves. Because of the very thin design on a high conductivity base, it has a minimal thermal resistance, which is assumed to be negligible. Consequently, the HFM is used as the standard for the convection calibrations, and is assumed to be at the same temperature and heat flux as the plate. This was confirmed by direct thin-film temperature measurements on the HFM surface and calibrations in conduction, convection, and radiation [3,4].

The Schmidt–Boelter gauge is the major emphasis of this work. The active element of a Schmidt–Boelter gauge is a bare constantan wire, usually about 0.05 mm in diameter, which is wrapped around the thermal resistance layer, or wafer [1]. Consequently, the sensor is sometimes called a "wire-wound" gauge. The wafer is usually made of anodized aluminum with the geometry illustrated in Fig. 3. The wire/wafer assembly is electroplated with copper on one side. After plating, the wafer with the wire is placed

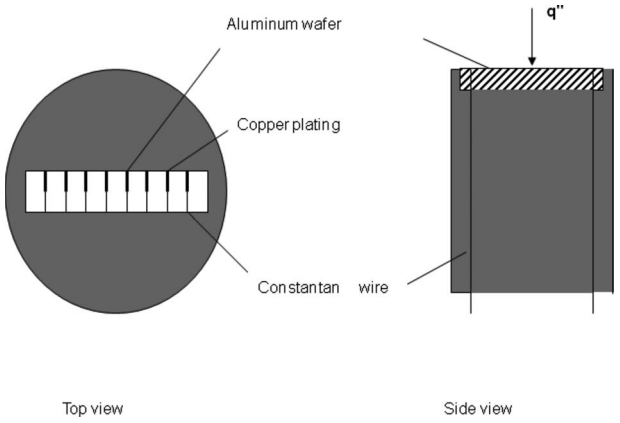

Fig. 3 Schematic diagram of the Schmidt–Boelter gauge

into the gauge body, which works as a heat sink for the sensor. The entire wafer is then surrounded by a potting material to give a smooth surface to the top of the gauge.

The basic heat flux sensing mechanism uses the temperature gradient developed between the top and the bottom surface of the wafer. The sensitivity is directly proportional to the number of turns of constantan wire wound around the wafer, although the output is less than that for an actual thermopile with separate thermocouple wire and junctions [5]. The thermoelectric signal is produced with what appears to be a constantan wire in electrical series with a parallel combination of constantan and copper. Four different Schmidt–Boelter gauges were examined, including two 1 in. (25 mm) in diameter and two 1.5 in. (38 mm) in diameter. Although they appear to be large, most of each gauge consists of a copper body that is used for water cooling. The actual sensor that is mounted into the body is much smaller: 9.5 mm for the 1 in. gauge and 5.0 mm for the 1.5 in. gauge. They were manufactured by Medtherm Corp. (Huntsville, AL) and supplied by Sandia National Lab (Albuquerque, NM).

5 Radiation Calibration

Heat flux gauges are almost always calibrated based on an incident radiation source. The narrow-angle method focuses a beam of radiation from a blackbody cavity onto the gauge surface, which sits outside of the cavity. The insert method actually puts the gauge into a graphite-tube cylindrical cavity. Murthy et al. [6] described these two radiation calibration methods as used at the National Institute of Standards and Technology (NIST). For the in-cavity calibrations, an optical pyrometer is used to measure the center partition temperature of the graphite tube, and control the power supply to maintain the cavity temperature at the set point. The NIST narrow-angle method uses an electrical substitution radiometer (ESR) as the standard. The heat flux gauge to be calibrated and the transfer standard radiometer are alternately substituted at the same position to receive equal radiant heat flux from the blackbody cavity. The heat flux gauge manufacturers use variations of these methods to calibrate the gauges that are used commercially. They usually provide calibrations, based on the incident radiation, but may also include the effect of the gauge absorptivity (assumed equal to the emmisivity) for an absorbed sensitivity

$$S_{\text{abs}} = \frac{S_{\text{inc}}}{\varepsilon} = \frac{E_g}{q_g''} \tag{12}$$

where E_g is the voltage output of the gauge, and q_g'' is the net heat flux through the gauge. The absorbed sensitivity includes any combination of convection and radiation, and will be used throughout this paper. Because the manufacturers of the HFM and Schmidt–Boelter gauges use different calibration methods, the radiation calibration of the HFM was adjusted to about 10% to match that of the Schmidt–Boelter gauges. This provides internal consistency to the heat flux measurements in our facility.

The cavity temperatures for radiation calibration usually range from 1100°C to 2500°C [6]. This corresponds to radiation heat fluxes up to 3300 kW/m^2. Because the gauge is maintained at close to room temperature (300 K) during calibration, the contribution of the T_g^4 term in Eq. (4) is negligible ($<0.2\%$). In addition, convection effects are designed to be negligible. Consequently, during radiation calibration, there is no effect of the gauge temperature on the heat flux, and the gauge heat flux is the same as the plate heat flux $q_g''=q_p''$. The sensitivity corresponding to the plate heat flux is the same

$$S_{\text{abs},p} = \frac{E_g}{q_p''} \tag{13}$$

6 Convection Calibration

Because the internal conduction pathway for measuring heat flux within most heat flux gauges is the same for convection or radiation, the convection sensitivity for the heat flux that passes through the gauge is the same as that for the absorbed radiation S_{abs}. Unlike for the radiation calibration, however, the convection heat transfer to the gauge surface is dependent on the surface temperature of the gauge. Consequently, any temperature difference relative to the plate will cause a difference in the measured heat transfer, and the influence of Eq. (11) must be considered when interpreting convection results. It is desired to have a convection sensitivity S_{conv}, defined in the same form as Eq. (13) in terms of the plate heat transfer

$$S_{\text{conv}} \equiv \frac{E_g}{q_p''} = \frac{S_{\text{abs}}}{\dfrac{h_p}{h_g} + h_p R''} \tag{14}$$

where S_{abs} is the calibrated gauge sensitivity from Eq. (12). This equation represents the two major effects on the apparent sensitivity of heat flux gauges in convection: changes in the heat transfer coefficient and internal thermal resistance. It is the major theoretical assumption of this research, and will be used to help interpret the experimental results.

7 Convection Calibration Facility

A convection calibration facility has been developed to calibrate heat flux gauges for heat transfer in both shear and stagnation flow. In shear flow, there is an upstream thermal boundary layer influence on the heat transfer coefficient at the gauge, which means that $h_g \neq h_p$. Conversely, for stagnation flow, there is no upstream boundary layer, so that $h_g=h_p$.

The basic apparatus is the same for both shear and stagnation flow, as illustrated in Fig. 4. A compressed air supply with a maximum pressure of about 400 kPa is connected to the facility with a pressure gauge (PG) to set the supply pressure. The air flows directly into an air heater, consisting of a copper tube with a high temperature heater tape wrapped around the tube, and a power controller to adjust the exit air temperature. A series of valves (V1–V4) directs the air flow to the stagnation stand or through the nozzles (N1 and N2) of the shear stand. The electrical power of about 2 kW is sufficient to heat the air to over 150°C. An aluminum box was constructed around the copper tubing, and packed with glass-fiber insulation. One data acquisition unit (DAQ2) was used to record the heater temperature and pressure. A second 24-bit DAQ (DAQ1) was an NI TBX-68T, used to measure the two heat fluxes and temperatures. Data sampling was carried out with LABVIEW®.

7.1 Stagnation Stand. The stagnation stand was designed to provide the same convective heat flux to the reference standard and to the test gauge. This was realized by simply putting a tee

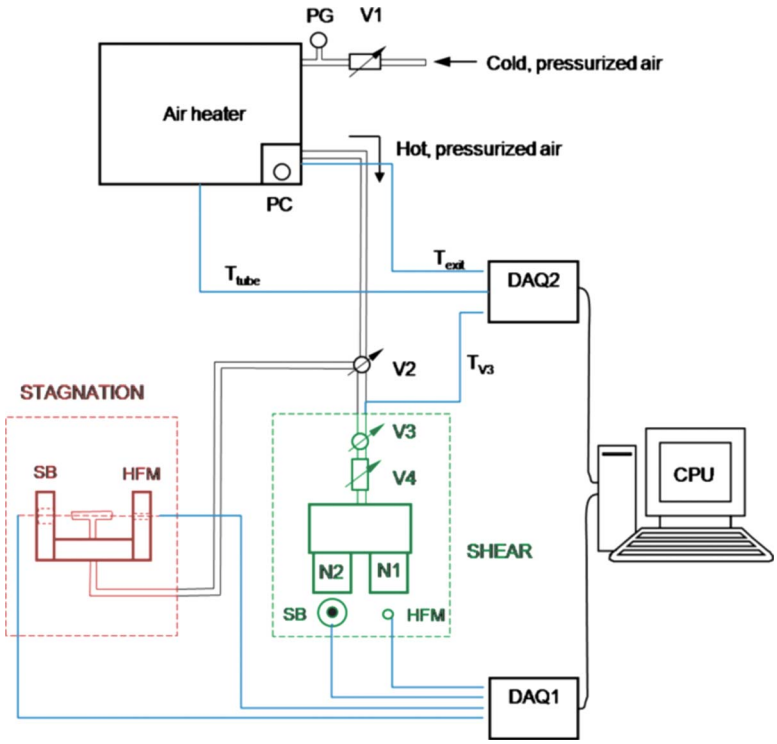

Fig. 4 Schematic of the convection calibration facility

junction in the air supply line with a 6.3 mm orifice at each end, creating equal impinging jets on each surface. Figure 5 shows the basic design of the stagnation stand. The gauges were mounted in vertically aligned 10 cm by 12 cm plates, which were connected to the main support plate, forming a U-shape, and holding the tee nozzle in position. The distance between orifices and plates was set at 50 mm, to provide maximum and consistent convection heat flux. The inlet heated air from the air heater was directed into the tee nozzle from the bottom side of the stand.

A type K thermocouple was mounted in the air supply of the nozzles, immediately before the tee junction, to measure the incoming air temperature. Thermocouples were also press fit into the aluminum plates flush with the surface. They were located right next to the heat flux gauges to measure the plate temperature at the gauge location. The gauges were mounted into the plate, and aligned with the centerline of the nozzle. The 25-mm diameter Schmidt–Boelter gauges have a large flange that was connected to the back of the 19-mm thick plate with three screws. A washer between the flange and the plate aligns the gauge surface flush with the plate surface. The 38-mm diameter Schmidt–Boelter gauges did not have a flange, and were held into the plate by using one plastic set screw. To close the air gaps between gauges and the plate, and to better align the gauge and plate surface, a high thermal conductivity paste was used ("Omega Therm 201"). The HFM was mounted into the 19-mm thick plate with a special screw assembly to provide good thermal contact with the plate, as illustrated in Fig. 6.

The calibration test started with the sensors blocked by a cover to divert the air jets until a steady-state condition was reached (constant air temperature through the tee nozzle). At this point, the data acquisition was started, and a few seconds of data was taken to establish the reference zero for each gauge in each test run before the cover was removed, allowing the jets to impinge on the sensors. The measurements with flow were taken for 20 s. After the test was done, the stand was allowed to cool down to room temperature again, which took approximately 20 min.

Several tests were performed to confirm that the heat flux from each of the impinging jets was the same. These consisted of a series of measurements that switched the sensors from one side to the other. The results showed no difference due to the location on the calibration values of the gauges within the three percent uncertainty of the measurements. The ratio of the sensor size to the jet diameter could also affect the relative heat flux experienced by

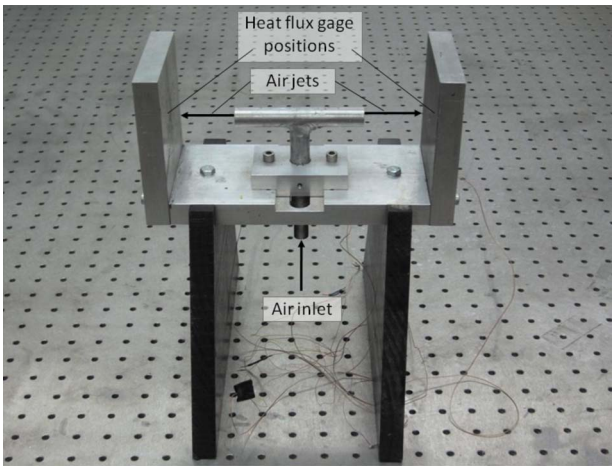

Fig. 5 Stagnation calibration stand

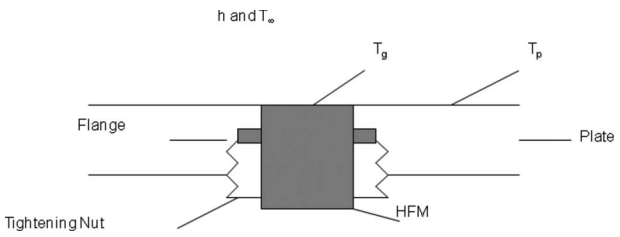

Fig. 6 HFM mounting in a plate

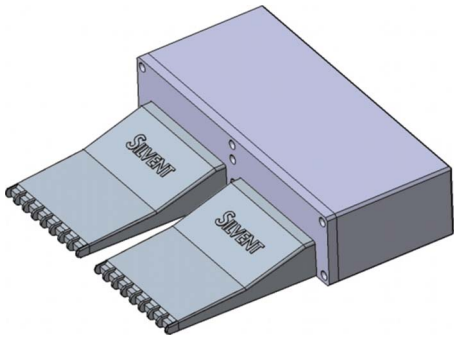

Fig. 7 Shear stand nozzles

the two gauges. As described earlier, however, the sizes of the sensing elements of the three different gauge styles were nearly the same.

7.2 Shear Stand. The shear stand provided turbulent convective air flow parallel to a plate surface. Heated air was directed to a plenum, and then through two identical flat nozzles over the plate. The exit dimensions of the nozzles were 12 cm by 2.4 cm, as illustrated in Fig. 7.

The plenum and nozzles were mounted to the 17 cm by 19 cm plate, as pictured in Fig. 8, creating a wall jet along the plate. The heat flux gauges were mounted in the 19-mm thick plate by the same procedure as for the stagnation stand. They were placed about 20 mm from the exit of the nozzle, side-by-side. In Fig. 8, the nozzles are labeled "N1" and "N2," with the HFM mounted with nozzle N2, and a 38-mm diameter Schmidt–Boelter gauge mounted with nozzle N1. The flow characteristics from the nozzles were measured with particle-image velocimetry (PIV), and were shown to be typical of a well developed wall jet at the gauge locations [7].

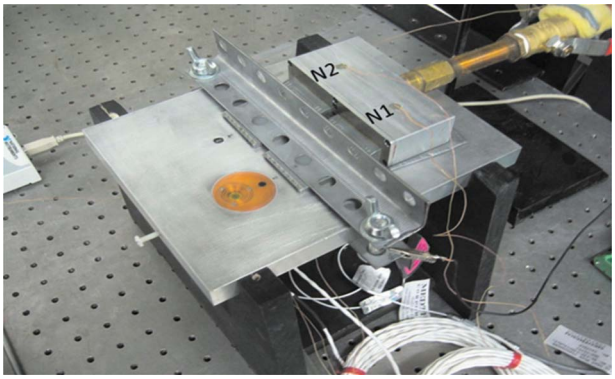

Fig. 8 Picture of the assembled shear stand

The plenum assembly was designed to provide the same air flow through both nozzles. To improve uniformity, a flow resistance made of copper foam was mounted inside of the plenum, and attached to the nozzle inlets. Total pressure measurements were made to quantify the uniformity of flow from the nozzles. Small tubes were aligned with the flow, and connected to MKS (Andover, MA) model 223BD differential pressure transducers. The results are shown in Fig. 9 in terms of the corresponding velocities at few positions across the nozzles at the gauge locations. Notice that near the centerline of the nozzles, the velocity is identical to about 4%. The effect on the heat flux measurements is discussed later.

All of the thermocouples used were type K. There were two thermocouples placed inside of the box to measure the air temperature in the middle of each nozzle entrance. There were two thermocouples press fit into the plate. They were located near the corresponding heat flux gauge, at identical distances from the nozzle along the nozzle centerlines. If water cooling was used, there was also a thermocouple for measuring the water temperature.

The sampling frequency for all of the temperatures and heat fluxes was set to 1 Hz. Data sampling that began 10 s before the flow was initiated to establish the reference zero values for the heat flux gauges. Data were taken until the air temperature in the plenum reached steady-state conditions. This took approximately 10 min (for lower pressures) to 7 min (for higher pressures). Once the steady-state temperature was achieved, data were taken for another 30 s. After a test was completed, the entire assembly was cooled down to room temperature in order to start from the same initial conditions.

8 Data Analysis

The heat transfer coefficient was determined from the HFM standard measurements of heat flux and temperature, which were assumed to match those of the plate, as previously discussed

$$h_p = \left[\frac{q''_p}{(T_\infty - T_p)} \right]_{\text{HFM}} \tag{15}$$

Radiation effects were neglected because the plate and gauges were near room temperature, and the same small effect acts on both gauges. The corresponding heat flux that should be measured at the position of the Schmidt–Boelter gauge is

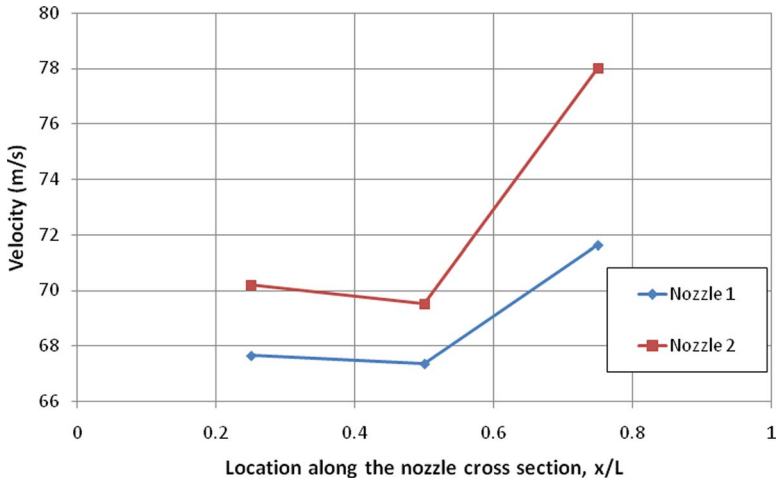

Fig. 9 Exit nozzle velocities from total pressure measurements

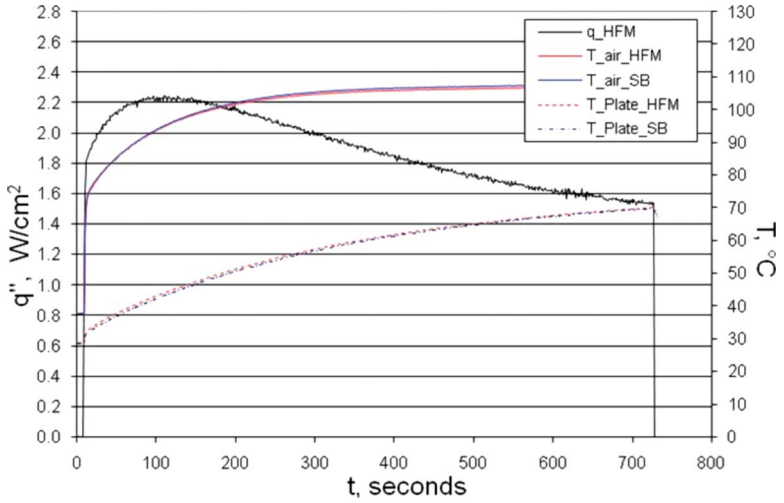

Fig. 10 Typical heat flux and temperature data for the shear stand

$$q''_{SB} = h_p(T_\infty - T_s)_{SB} \tag{16}$$

with the value of the sink temperature T_s representing the mounting plate temperature or the cooling water temperature. This is the heat flux for an ideal gauge with $R''=0$ and $T_g=T_s$. The resulting convection sensitivity

$$S_{conv} = \frac{E_g}{q''_{SB}} = \frac{E_g}{h_p(T_\infty - T_s)_{SB}} \tag{17}$$

gives the gauge output, relative to the supplied heat flux.

A typical set of test data for the shear stand is shown in Fig. 10. The air temperatures are shown at each side of the plenum box, before the air enters the nozzles. The values on each side are nearly identical over the entire length of the test. The plate temperatures start from about 28°C room temperature, and rise until they reach 70°C at the end of the test on both sides with negligible differences. The heat flux signal shows a maximum at around 100 s, and then decreases as the air to plate temperature difference decreases over the duration of the test of about 730 s. The sensitivity was averaged in the range of 500–600 s for the shear stand. Figure 11 shows the resulting heat transfer coefficient, which remains essentially constant over this time span, as expected. The stagnation tests are similar, except that the temperature changes are smaller because of the shorter run time (about 30 s) of these tests.

To minimize a nozzle-to-nozzle bias error of up to 20% on the shear stand, the Schmidt–Boelter gauge and HFM were switched and tested under both nozzles. The resulting sensitivity was averaged between the tests on both sides of the shear stand. This was not necessary for the stagnation tests because the heat flux matched within experimental uncertainty from side-to-side.

9 Calibration Results

The measured sensitivities were plotted for each gauge over a range of air pressures, giving different heat transfer coefficients. An example of the results is shown in Fig. 12 for one of the four Schmidt–Boelter gauges in the stagnation flow calibration stand. The average experimental uncertainty was estimated to be 6.6% for the measured sensitivities. This was obtained from the combined standard error of all of the associated bias and precision uncertainties [8]. The largest contribution was the radiation calibration uncertainty between the two gauges, which was estimated to be 5%.

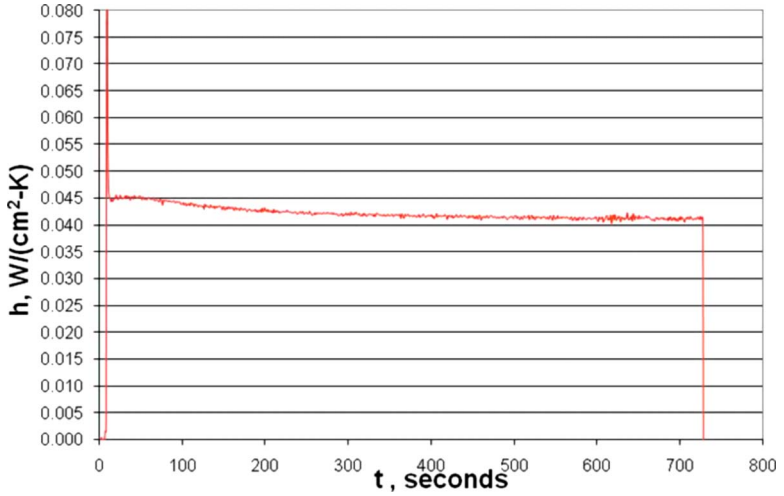

Fig. 11 Typical progression of the heat transfer coefficient for the shear stand

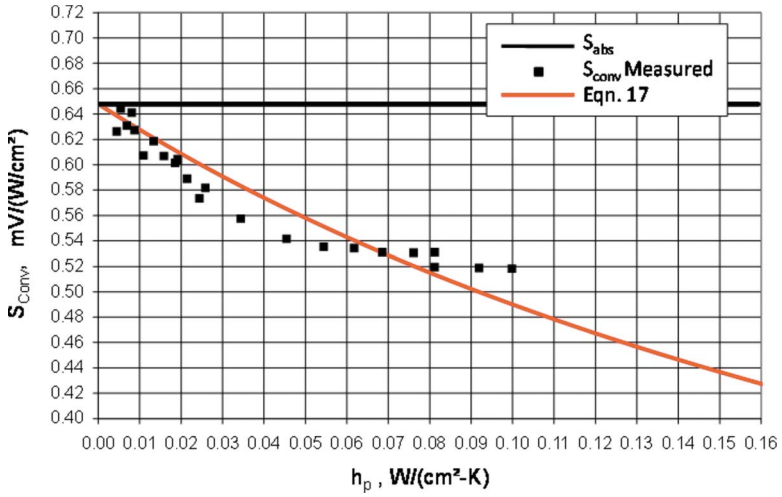

Fig. 12 Stagnation calibration sensitivities for SB 137861 in stagnation flow

The assumption for the stagnation flow is that the heat transfer coefficient is the same for the two gauges and the plate $h_g = h_p$ because there is no boundary layer development along the plate leading to the gauge. Equation (14) then reduces to

$$S_{\text{conv}} = \frac{S_{\text{abs}}}{1 + h_p R''} \tag{18}$$

The red line in Fig. 12 represents the least-squares curve fit of this equation for R'' while forcing the curve through the radiation calibration point at $h_p = 0$. The corresponding values of R'' for all of the gauges are listed in Table 1, along with the associated uncertainties. The uncertainty values are rather large because R'' is obtained from a curve fit of the sensitivity data, which amplifies the individual uncertainties. As expected, the gauge with the lowest radiation sensitivity has the smallest internal resistance R''. In addition, the physically larger gauges have higher internal resistance. The values reported are consistent with the expected thermal resistances of the aluminum wafer and potting material in the Schmidt–Boelter gauges [5]. They are of the same form, but generally lower than the values for comparable Gardon gauges [9].

Table 1 Summary of stagnation calibration results

Sensor	S_{abs} (mV/W/cm^2)	R'' (cm^{2}K/W)	R'' uncertainty (%)
1.0 in. SB 137861	0.648	3.22	56
1.0 in. SB 137864	0.428	2.65	66
1.5 in. SB 142781-T	0.681	5.78	34
1.5 in. SB 142782-T	0.782	5.42	36

The results for shear flow were done to observe the effects of the gauge temperature distribution on the heat transfer coefficient. As discussed in the introduction, this is an important effect in boundary layer flows. It is anticipated that the effective heat transfer coefficient over the gauge will be decreased by the smaller difference in the gauge temperature, relative to that of the surrounding plate. To observe this effect, the theoretical curve in Eq. (14) was used to fit the data, assuming that the value of R'' remained the same as for the stagnation tests. The equation was then fit to the data using h_p/h_g as the variable parameter. Figure 13 shows an example of the results for the same gauge, as shown in the stagnation flow in Fig. 12. The average experimental uncertainty of the measured sensitivity values was estimated to be 11.6%. The largest contribution to the uncertainty was an estimated 10% uncertainty in the heat transfer coefficient between the two nozzles.

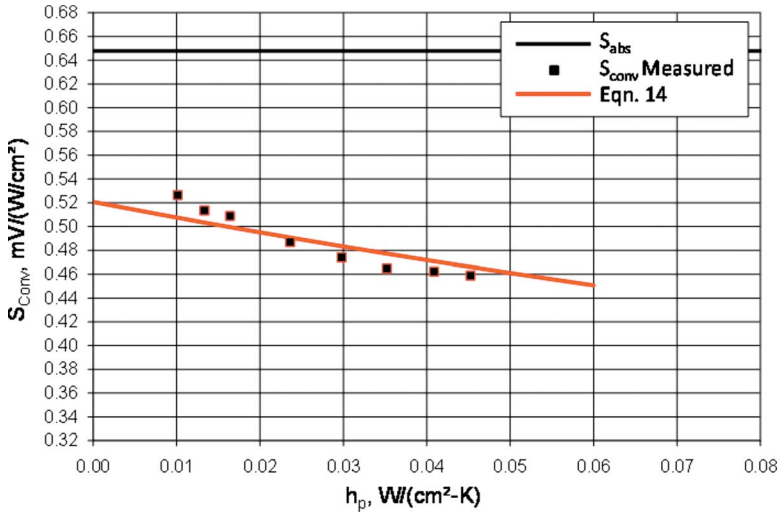

Fig. 13 Calibration sensitivities for SB 137861 in shear flow

Table 2 Ratio of heat transfer coefficient for shear flow

Sensor	S_{abs} (mV/W/cm^2)	h_p/h_g	h_p/h_g uncertainty (%)
1.0 in. SB 137861	0.648	1.24	17
1.0 in. SB 137864	0.428	1.14	16
1.5 in. SB 142781-T	0.681	1.20	18
1.5 in. SB 142782-T	0.782	1.16	17

The values of h_p/h_g obtained for all four gauges are listed in Table 2, with the corresponding values of estimated uncertainty. The largest contribution to the uncertainty is from the measured gauge sensitivity. As expected, the lowest value (smallest temperature effect) is for the gauge with the lowest sensitivity. All of the values are not far from 1, which is typical of turbulent boundary layers over the relatively small dimensions of the heat flux gauges [10].

The ratio h_p/h_g was assumed constant for each gauge, even though a wide range of h_p values was used. Because the value of this ratio is probably a combination of gauge geometry and flow effects, there may be a second-order effect of h_p on h_p/h_g. The constant value assumption, however, is validated by the good fit of the curve with the data, certainly within experimental uncertainty.

10 Effects of Water Cooling

Schmidt–Boelter heat flux gauges are often operated with water cooling when used in hot environments. This alters the internal heat transfer pathways, and could affect the apparent thermal resistances and heat flux measured by the gauge. Therefore, the calibration tests were repeated with water cooling to further characterize the gauge response.

Figure 14 shows the sensitivities for the stagnation flow, both with and without water cooling for comparison. Moreover, when water cooling is introduced, the water temperature is another possible sink temperature for reducing the data, in addition to the plate temperature. Therefore, the data are shown in Fig. 14 for both possible heat sink temperatures. Because the water temperature was constant at room temperature (30°C), the results generally straddle the uncooled case. The actual sensor temperature is now lower than the plate temperature because of the lower temperature water cooling, but always higher than the water temperature itself. Consequently, because of the larger actual temperature difference, the heat flux and corresponding sensitivity will be higher than the uncooled case when using the plate temperature. The opposite is true when using the water temperature as the heat sink. The gauge temperature difference $T_\infty - T_g$ is then smaller than $T_\infty - T_s$, giving a smaller gauge heat flux and lower apparent gauge sensitivity.

The corresponding results for shear flow are shown in Fig. 15. The trends are quite different. When using the water temperature to define the heat flux, the sensitivity is close to the uncooled case. The sensitivities when using the plate temperature, however, are much higher. In fact, the results for water cooling using the plate temperature actually appear to match the radiation sensitivity! The water-cooled copper casing around the blackened sensor can be seen in Fig. 8. As the heated flow first goes over the aluminum plate, then the water-cooled copper gauge, the temperature difference is increasing, which increases the heat flux and apparent sensitivity. This is somewhat balanced by the effect on the boundary layer of the varying temperatures. The result is a sensitivity using the plate temperature that is higher than the uncooled case, and nearly that of the radiation calibration. For the case of the 38-mm diameter gauges, the water cooling is higher than the radiation line by up to 10%. It is important to note that the sensitivity for water cooling is dependent on the temperature of the cooling water among other variables, and would not be the same for other conditions. In summary, it appears that the matched sensitivities with the radiation calibration are more by chance of the test conditions than a characteristic of the gauge.

11 Conclusions and Recommendations

A convective heat flux calibration system that provides measurements in both stagnation and shear flows was developed and tested. This was used to show that Schmidt–Boelter heat flux gauge sensitivities obtained in convection are different from those obtained by the standard radiation calibration. A model equation, based on internal and external thermal resistances, provides a good explanation for the dependence of the apparent gauge sensitivity on the heat transfer coefficient. The internal resistance R'' in this model is based on the material properties of the gauge, as measured in the stagnation flow. Additional thermal effects of the gauge on the boundary layer were measured in shear flow, and characterized by the ratio h_p/h_g. The experimental results matched

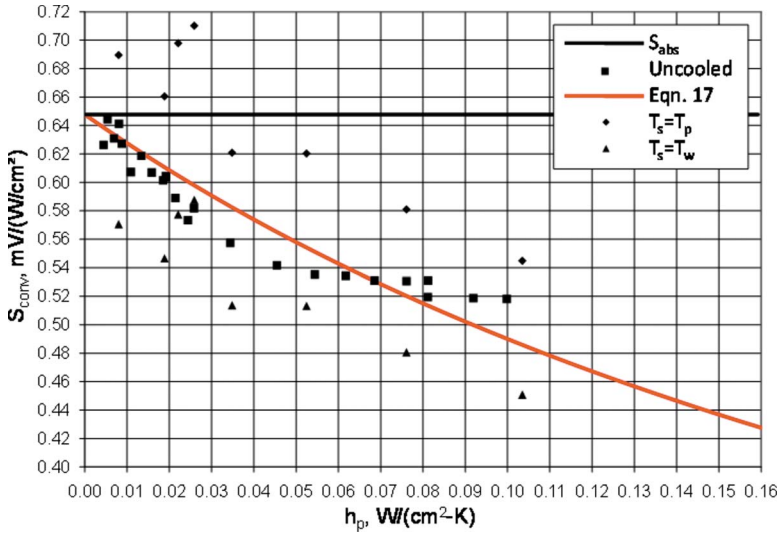

Fig. 14 Stagnation calibration sensitivities for SB 137861 in stagnation flow with water cooling

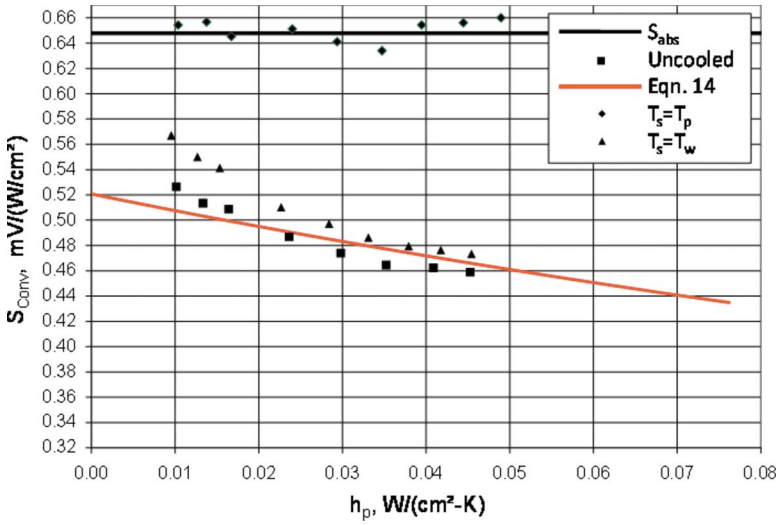

Fig. 15 Calibration sensitivities for SB 137861 in shear flow with water cooling

the model, and were used to estimate values of these two parameters for the four Schmidt–Boelter gauges tested, although the uncertainties were high for R''.

Differences between the calibrations with stagnation and shear flow were further amplified when water cooling of the gauge was introduced. This factor complicates the interpretation of the results for convective flows. A detailed understanding of the temperature distribution around the gauge would be helpful to obtain an understanding of the gauge operation. For example, this could be achieved with 3-D computational modeling and an experimental surface temperature mapping system.

Acknowledgment

Funding for this work was provided by Sandia National Laboratories through program managers Jim Nakos and Tom Blanchat.

Nomenclature

E_g = gauge voltage output (mV)
h = heat transfer coefficient ($W/m^2\,K$)
L = nozzle width (mm)
q = heat transfer (W)
q'' = heat flux (W/m^2)
R'' = thermal resistance ($m^2\,K/W$)
S = gauge sensitivity ($mV/(W/m^2)$)
T = temperature (K)
ε = surface emissivity
σ = Stefan–Boltzmann constant (5.67×10^{-8} $W/m^2\,K^4$)

Subscripts

abs = absorbed
cond = conduction
conv = convection
g = gauge
inc = incident
p = plate
r = radiation source
rad = radiation
s = sink
w = water
∞ = air

References

[1] Diller, T. E., 1993, "Advances in Heat Flux Measurements," Adv. Heat Transfer, **23**, pp. 279–368.
[2] Kuo, C. H., and Kulkarni, A. K., 1991, "Analysis of Heat Flux Measurement by Circular Foil Gages in Mixed Convection/Radiation Environment," ASME J. Heat Transfer, **113**, pp. 1037–1040.
[3] Holmberg, D. G., and Diller, T. E., 1995, "High-Frequency Heat Flux Sensor Calibration and Modelling," ASME J. Fluids Eng., **127**, pp. 502–506.
[4] Hager, J. M., Terrell, J. P., Sivertson, E., and Diller, T. E., 1994, "In-Situ Calibration of a Heat Flux Microsensor Using Surface Temperature Measurements," *Proceedings of the 40th International Instrumentation Symposium, ISA*, Research Triangle Park, NC, ISA Paper No. 94-1034, pp. 261–270.
[5] Kidd, C. T., and Nelson, C. G., 1995, "How the Schmidt-Boelter Gage Really Works," *Proceedings of the 41st International Instrumentation Symposium, ISA*, Research Triangle Park, NC, pp. 347–368.
[6] Murthy, A. V., Fraser, G. T., and De Witt, D. P., 2006, "Experimental In-Cavity Radiative Calibration of High-Heat-Flux Meters," J. Thermophys. Heat Transfer, **20**, pp. 327–335.
[7] Hoffie, A., 2006, "Convection Calibration of Schmidt-Boelter Heat Flux Gages in Shear and Stagnation Air Flows," MS thesis, Virginia Tech, Blacksburg, VA.
[8] Taylor, B. B., and Kuyatt, C. E., 1994, "Guidelines for Evaluating and Expressing the Uncertainty of NIST Measurement Results," NIST Technical Note 1297.
[9] Borell, G. J., and Diller, T. E., 1987, "A Convection Calibration Method for Local Heat Flux Gages," ASME J. Heat Transfer, **109**, pp. 83–89.
[10] Mukerji, D., Eaton, J. K., and Moffat, R. J., 2004, "Convective Heat Transfer Near One-Dimensional and Two-Dimensional Steps," ASME J. Heat Transfer, **126**, pp. 202–210.

A Hybrid Method for Measuring Heat Flux

David O. Hubble
Department of Mechanical Engineering,
AEThER Laboratory,
Virginia Polytechnic Institute and State University,
114R Randolph Hall,
Blacksburg, VA 24061

Tom E. Diller
Professor
Fellow ASME
Department of Mechanical Engineering,
Virginia Polytechnic Institute and State University,
114R Randolph Hall,
Blacksburg, VA 24061

The development and evaluation of a novel hybrid method for obtaining heat flux measurements is presented. By combining the spatial and temporal temperature measurements of a heat flux sensor, the time response, accuracy, and versatility of the sensor is improved. Sensors utilizing the hybrid method are able to make heat flux measurements on both high and low conductivity materials. It is shown that changing the thermal conductivity of the backing material four orders of magnitude causes only an 11% change in sensor response. The hybrid method also increases the time response of heat flux sensors. The temporal response is shown to increase by up to a factor of 28 compared with a standard spatial sensor. The hybrid method is tested both numerically and experimentally on both high and low conductivity materials and demonstrates significant improvement compared with operating the sensor as a spatial or temporal sensor alone.
[DOI: 10.1115/1.4000051]

Keywords: heat flux gauge, thermal time response, slug calorimeter

1 Introduction

Modeling of thermal systems requires a combination of temperatures and energy fluxes for prediction of their performance. Temperatures are commonly measured by a variety of standard methods, but the measurement of heat flux is a particular challenge because it is an energy flux normal to a plane of material rather than a property of a material. Therefore, sensors that measure the heat flux must be usually mounted onto a material that provides a good heat sink so that the energy flow is not impeded. This makes it very difficult to use heat flux gauges to measure the heat flux on materials that are not good thermal conductors. The purpose of this paper is to present a new method, which allows heat flux gauges to make accurate measurements on any type of backing material. Applications include furnaces to thermal protection systems for spacecraft.

2 Background

Two of the most common modes of heat flux measurement are that of a differential heat flux sensor and that of a slug calorimeter [1]. A differential heat flux sensor measures the temperature difference over a spatial distance with a known thermal resistance, as illustrated in Fig. 1. The temperature difference is used to calculate the heat flux through the sensor from the steady-state version of Fourier's law, wherein T_1 is the temperature of the exposed face while T_2 is the temperature at the back of the sensor.

$$q''_{\text{differential}} = k\frac{T_1 - T_2}{\delta} \tag{1}$$

Under steady-state conditions the heat flux entering the sensor q_1'', as shown in Fig. 1, is equal to that leaving q_2''. Hager [2] calculated the 98% response time to a step change in the heat flux at the surface in terms of the sensor's thickness and thermal diffusivity. This is often considered as steady-state.

$$t_{ss} = 1.5\frac{\delta^2}{\alpha} \tag{2}$$

The analysis of Hager [2] was performed on the ideal case of a sensor mounted on a perfect heat sink, where the backside temperature T_2 remains constant.

In a slug calorimeter the amount of thermal energy absorbed by the sensor is measured as a function of time. The rate of change in the sensor's temperature is measured and its thermal capacitance is known. As illustrated in Fig. 1, conservation of energy for a control volume surrounding the sensor "slug" yields

$$q''_{\text{slug}} = \rho C\delta\frac{dT_{\text{ave}}}{dt} = q_1'' - q_2'' \tag{3}$$

where $\rho C\delta$ is the thermal mass of the slug per sensor area. The heat loss (q_2'') is minimized by insulating all sensor surfaces except for the sensor face. If the average temperature within the slug were known, Eq. (3) would perfectly measure the net heat flux into the slug. However, since it is not possible to measure the average temperature, the slug is typically made from a high conductivity material and the temperature at the back surface is used to approximate the slug's average temperature. Therefore, for a short time after the heat flux is applied to the slug, thermal energy is absorbed by the slug (the slug's average temperature increases) before any heat reaches the back surface. This causes a delay before the slug accurately measures the actual net heat flux. The 99% response time to a step change in the heat flux at the surface is given as

$$t_{ss} = 0.54\frac{\delta^2}{\alpha} \tag{4}$$

by Hightower et al. [3]. This analysis was performed assuming a perfectly insulated backside surface ($q_2''=0$).

While these two modes of operation can be used for specific measurement applications, they both have serious limitations. For example, for a differential gauge to have a fast time response, it must be very thin. This is difficult to achieve in harsh environments, where sensors must be typically made with a substantial thickness to survive. Also, since a differential sensor only measures heat flowing through it, it must be provided with a good heat sink. This necessitates its mounting on or in a high conductivity material, not an insulator. The main problems encountered when using a slug calorimeter include adequately insulating the slug to minimize losses as well as noise amplification due to the differential operation. Also, since the output of a slug is proportional to the rate at which its temperature is changing, it is unable to measure the heat flux at steady-state. It is worth noting that the design criteria for these two types of sensors are opposite. A differential gauge more accurately measures q_1'' when q_2'' is maximized with

Manuscript received February 15, 2009; final manuscript received July 20, 2009; published online December 28, 2009. Editor: Yogesh Jaluria.

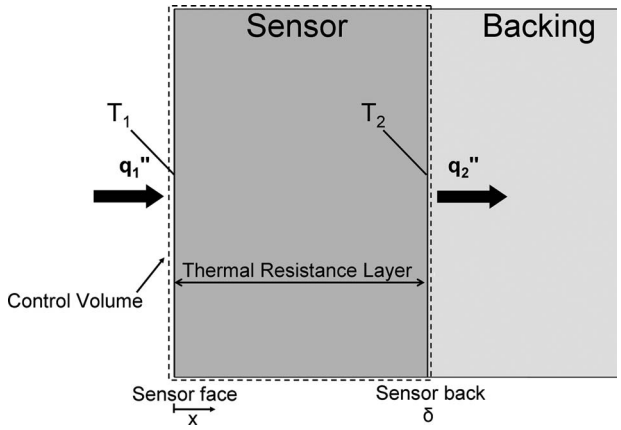

Fig. 1 Sensor-backing system

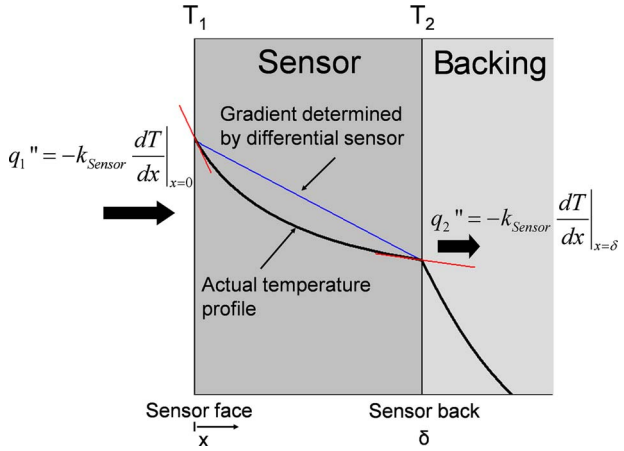

Fig. 2 Temperature profile with sensor-backing system

minimal heat storage in the gage. Conversely, a slug calorimeter needs to minimize q_2'' and maximize the stored thermal energy.

A number of papers have reported using a combination of the spatial and temporal changes in temperature to infer or improve heat flux measurements. Kidd and Adams [4] used finite element analysis to determine the response function for their Schmidt–Boelter heat flux gauges. This was used to compensate for the energy deficit caused by the thermal capacitance of this differential style gauge. They were able to substantially increase the time response of the heat flux measurements for their transient tests in high-speed wind tunnels. A complete analysis of a simpler thin polyimide differential gauge mounted on a metal heat sink was performed by Epstein et al. [5]. This enabled measurements from steady-state to 100 kHz on metal turbine blades, but required solution of the equations for one-dimensional transient conduction for a particular mounting material. A "plug-type" heat flux gauge was developed by Liebert [6] to account for the combination of conduction and storage in the post normal to the surface. Four temperatures were measured along the post as a function of time and compared with transient temperature solutions to determine the surface heat flux. Experimental results were obtained for metal turbine blade models. Unfortunately, the method did not work well when the sensor was mounted in a low thermal conductivity material [7].

A popular variation in the slug calorimeter uses a single temperature measurement at the surface of the material and a semi-infinite solution to the transient thermal field. The results can be used only over a short time span before the thermal front reaches the backside of the material, which corresponds to the time *before* results from a slug calorimeter can be used. The data reduction procedure involves inverse solution methods because the measured surface temperature is the known boundary condition that is used to solve for the corresponding heat flux. Several digital and analog processing methods have been developed in efforts to minimize the effect of noise in the resulting heat flux signal [8–10]. There are a number of methods available for measuring the transient surface temperature. Point measurements can be made with resistance temperature sensors (RTDs) [11] or coaxial thermocouples [12]. Optical methods include liquid crystals [13], infrared thermography [14], and thermographic phosphors [15] that can be used with high-speed imaging cameras to scan over an entire surface. The biggest limitations are as follows: (1) the initial temperature distribution throughout the material must be known, (2) there are no steady-state results, and (3) the test time is limited.

Clearly, there are advantages to including both the differential and transient slug type responses in measuring the heat flux. It would be beneficial to design a simple sensor and analysis scheme, which could utilize the advantages of these two sensor types together while minimizing their negative characteristics. It is with this goal in mind that the following analysis was performed on a simple one-dimensional sensor for such a hybrid heat flux (HHF) method.

3 HHF Methodology

3.1 Differential Term. Figure 1 shows the schematic of a one-dimensional heat flux sensor. The majority of differential heat flux sensors is designed to minimize the 2D effects and can therefore be treated as one-dimensional. The quantity q_1'' represents the heat flux into the sensor face, which is the desired measurement. Figure 2 depicts a typical temperature profile resulting from the heat flux applied at the sensor face, which diffuses through the sensor and into the backing material. These profiles will be nonlinear until the entire system reaches steady-state, at which point both curves will become linear. Using Fourier's law

$$q'' = -k\frac{dT}{dx} \tag{5}$$

the heat flux at any point can be calculated from the gradient of the temperature profile if the thermal conductivity is known.

A differential heat flux sensor measures the temperature at the front and back surfaces of the sensor and indicates the heat flux based on the thickness and thermal conductivity. Figure 2 shows, however, that when the sensor is not at steady-state, the gradient (and therefore the heat flux) that the differential sensor is measuring (Eq. (1)) is different from the gradient at the sensor face. However, once the temperature profile within the sensor is sufficiently developed, the gradient determined by the differential sensor equals the *average* of the gradients at the two surfaces. For example, it can be shown that this is true for any quadratic temperature profile ($T(x)=ax^2+bx+c$), that is

$$\underbrace{\frac{1}{2}\left(\left.\frac{dT}{dx}\right|_{x=x_1} + \left.\frac{dT}{dx}\right|_{x=x_1+\delta}\right)}_{\text{Average of two surface gradients}} = \underbrace{\frac{T(x_1+\delta)-T(x_1)}{\delta}}_{\text{Gradient determined by differential sensor}} = 2ax_1 + a\delta + b \tag{6}$$

Once the gradient measured by the differential sensor equals the average of the gradients at the two surfaces to within 2%, the temperature profile is considered fully developed. The time required for the temperature profile to develop can be calculated in a variety of ways. For example, Eq. (7) utilizes the exact analytical solution for the case of a sensor mounted on a perfect heat sink, subjected to a step change in surface temperature to calculate the gradients.

$$\left(\left.\frac{\partial T}{\partial x}\right|_{x=x_1} + \left.\frac{\partial T}{\partial x}\right|_{x=x_1+\delta} \right) = \frac{-2(T_1 - T_2)}{\delta} + \sum_{n=1}^{\infty} \frac{-2(T_1 - T_2)}{\delta} \exp\left(\frac{-n^2\pi^2}{\delta^2} \alpha t \right) (1 + (-1)^n) \tag{7}$$

The gradients at the two sensor surfaces are then compared with the gradient determined from the two surface temperatures $(T_2 - T_1)/\delta$ to see when they agree to within 2%. For the analytical case described by Eq. (7), a time corresponding to a Fourier number (nondimensional time $\mathrm{Fo} = t \cdot \alpha / \delta^2$) of 0.12 is required. The Fourier number required for the temperature profile to become fully developed was also calculated analytically for a step change in the heat flux on a perfect heat sink and was found to be 0.91. Numerical simulations of cases other than a perfect heat sink show that a step change in the heat flux on a perfect heat sink requires the longest time to become fully developed. For a typical ceramic gauge [16] with a thickness of 500 μm and thermal diffusivity of 1.0×10^{-5} m^2/s, a Fo of 0.91 corresponds to a time of 22.8 ms. For a metallic sensor such as the high temperature heat flux sensor (HTHFS) [17] with a thickness of 3.2 mm and thermal diffusivity of 5.5×10^{-6} m^2/s, a Fo of 0.91 corresponds to a time of 1.69 s.

Once the temperature profile is fully developed, Eq. (6) can be used to relate the heat fluxes q_1'' and q_2''. The temperature gradients at the sensor face and back surfaces represent the heat flux in and out of the sensor, respectively, and the differential sensor heat flux is proportional to the total temperature difference $T_1 - T_2$. Substituting the corresponding heat fluxes into Eq. (6) gives

$$\frac{q_1'' + q_2''}{2} = q''_{\text{differential}} = k\frac{T_1 - T_2}{\delta} \tag{8}$$

3.2 Slug Term. A slug calorimeter measures heat flux by measuring the rate at which heat is absorbed by the slug. The absorbed flux represents the net heat flux in the control volume $q_1'' - q_2''$, as shown in Fig. 2. Equation (3) states that this net heat flux can be measured using a slug calorimeter, which measures the time rate of change of the slug's average temperature. As mentioned, the standard method for measuring this average temperature is to measure the temperature at the back of the sensor and assume that this approximates the actual average temperature. This is a valid assumption once enough time has passed for the heat that enters the sensor face to reach the sensor back. However, for the sensor shown in Fig. 1, both surface temperatures are known. By utilizing the temperature measurement at the sensor face, a more accurate measure of the absorbed heat flux can be made. Subsequently, the sensor can be operated as a slug calorimeter in three different modes; the sensor's average temperature can be approximated by the face temperature, the back temperature, or an average of the two. The response of a slug calorimeter to a step change in the heat flux while mounted on a perfect insulator using these three methods is shown in Fig. 3. The sensor properties and the numerical method are discussed in Sec. 4.

Figure 3 shows that utilizing only the surface temperature offers no advantages compared with only using the back temperature, as it takes just as long for an accurate measurement to be made. On the other hand, utilizing the average of the two surface temperatures has advantages and drawbacks. By utilizing both the sensor face and back temperatures, the time response is more than a factor of three faster compared with using only T_2 but this temporal increase is accompanied by a large overshoot. The overshoot associated with using T_1 in the slug measurement is a result of the $\sqrt{t}$ dependence of the surface temperature since the sensor acts as a semi-infinite solid before heat has had a chance to reach its back surface. Since the surface temperature history is a function of $\sqrt{t}$, it has an infinite temporal derivative at $t=0$. While the overshoot

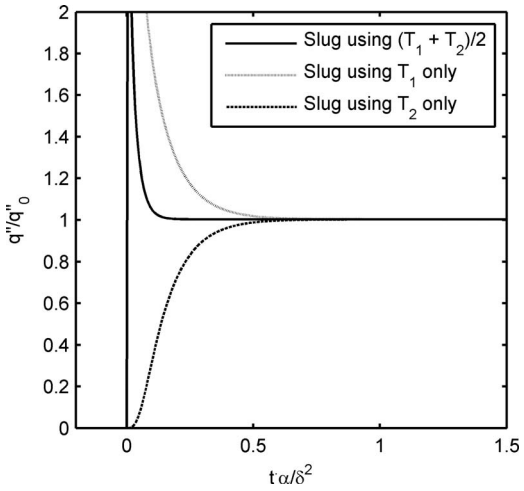

Fig. 3 Comparison of slug calorimeter response using different temperature measurements

associated with using the average of the two surface temperatures is initially large, it measures the applied heat flux more accurately than the standard method (curve is closer to one) for all Fourier numbers greater than 0.02. Therefore, in many situations, it is advantageous to utilize the average of the two surface temperatures in order to increase the temporal response of the sensor. From this point on, q''_{slug} will denote a slug calorimeter that utilizes the average of T_1 and T_2 unless specified otherwise.

$$q''_{\text{slug}} = \rho C \delta \frac{d}{dt}\left(\frac{T_1 + T_2}{2} \right) = q_1'' - q_2'' \tag{9}$$

3.3 Hybrid Heat Flux. To combine the spatial and temporal responses of a heat flux sensor, only Eqs. (8) and (9) are needed, as repeated here.

$$q_1'' + q_2'' = 2q''_{\text{differential}} \tag{10}$$

$$q_1'' - q_2'' = q''_{\text{slug}} \tag{11}$$

Combining Eqs. (10) and (11), and solving for the desired q_1'' yields the HHF method.

$$q_1'' = q''_{\text{differential}} + \frac{1}{2} q''_{\text{slug}} \tag{12}$$

Equation (12) shows how the differential and slug calorimeter outputs of a sensor can be combined. While this represents a simple model, it was derived from basic thermal energy conservation.

The validity of Eq. (12) can be supported by examining two limiting cases. First, consider the limit of a perfectly insulating backing material. For this case, the one-dimensional heat equation within the sensor simplifies to

$$\frac{d^2T}{dx^2} = \text{Const.} \tag{13}$$

once the temperature profile is fully developed. The solution to this equation yields a temperature profile within the sensor that is quadratic with a gradient of zero at $x = \delta$ since $q_2'' = 0$. Using Eq. (6), this means that the differential sensor will measure exactly half the heat flux entering the sensor. Also, since q_2'' is zero for this case, the slug calorimeter will measure the heat flux perfectly, i.e., $q''_{\text{slug}} = q_1''$. Therefore, the hybrid method described in Eq. (12) will measure the correct heat flux for this case.

Another limiting case occurs when the entire system is at steady-state on a perfect heat sink ($d^2T/dx^2 = 0$). For this case, the temperature profile within the sensor is linear. Consequently, the

Table 1 Parameters used in numerical simulation

Parameter	Value	Units
Sensor thermal conductivity	22	W/m K
Sensor density	7278	kg/m^3
Sensor specific heat	548	J/kg K
Sensor thickness	3.175	mm
Backing thickness	9.525	mm
Backing thermal conductivity	0.22–2200	W/m K
Spatial step	0.03175	mm
Time step	0.5	ms

differential sensor will measure the exact heat flux $q''_{\text{differential}} = q_1''$. Also, since the system is at steady-state, the time derivative of the temperature everywhere in the sensor is zero and the slug calorimeter will measure zero heat flux. Once again, the HHF method (Eq. (12)) handles this limiting case.

The HHF method requires that a sensor be designed such that T_1, T_2, and ΔT are measured. However, accurately measuring any two of these allows the third to be calculated since $\Delta T = T_1 - T_2$. For the two sensors already mentioned [16,17] the hybrid method can be used without any change in the design since these two sensors already measured the required temperatures.

4 HHF Numerical Validation

In order to validate the HHF method, 1D transient conduction through the sensor-backing system (Fig. 1) was modeled using finite difference computations. This was accomplished using an in-house developed code, which utilizes an implicit discretization of the 1D heat equation in MATLAB. The derivation of this discretization can be found in Ref. [18]. Table 1 summarizes the parameters used in the numerical simulations. The boundary conditions at the sensor face allowed any thermal condition to be applied including time varying fluxes and convective or radiative conditions. Temporal and spatial steps were kept sufficiently small to eliminate any grid and time step dependence. This was verified for the parameters shown in Table 1 by increasing both the temporal and spatial resolutions by a factor of ten over the values in Table 1 and comparing the results to those obtained using the lower resolution. In both cases, the discrepancy was less than 0.1%. Changing the material properties as well as the thickness of the sensor allowed for any sensor design to be tested. Also, the material properties and thickness of the backing material could be varied to investigate how this affected the sensor performance. For all numerical simulations shown, the HTHFS [17] (described in Sec. 5) was modeled mounted on a backing material three times thicker than the sensor. It was verified that the baking material thickness did not significantly affect the analysis. This was done by varying the thickness from one to ten times the thickness of the sensor, which caused less than a 3% change in the sensor performance. For all tests, the boundary condition at the back surface of the backing material was held at a constant temperature.

At each time step in the code, the temperatures at the face and back of the sensor (T_1 and T_2) were recorded. This allowed the sensor's performance in all three modes of operation to be evaluated using only these two temperature histories along with the sensor's properties. The sensor's response to a step heat flux of q_0'' is plotted against the Fourier number (dimensionless time) in Fig. 4. A step change in the heat flux is used in all the numerical simulations because it allows for the most direct comparison between different modes of sensor operation and backing conditions.

In the analysis shown in Fig. 4, the properties of the backing material were identical to the properties of the sensor. The accuracy as a slug calorimeter decreases with time while the differential sensor's accuracy increases with time. As the temperature of the sensor increases, more heat is conducted through the sensor into the backing material (q_2'' is increasing). If steady-state conditions were reached, the differential sensor would measure the exact heat flux. Because the backing material in this case is identical to the sensor, the entire system acts as a semi-infinite solid, which never reaches a steady-state. Figure 4 shows the speed and accuracy of the HHF method. Not only does the HHF capture the transient heat flux better than the slug calorimeter, it quickly settles to the proper steady-state value.

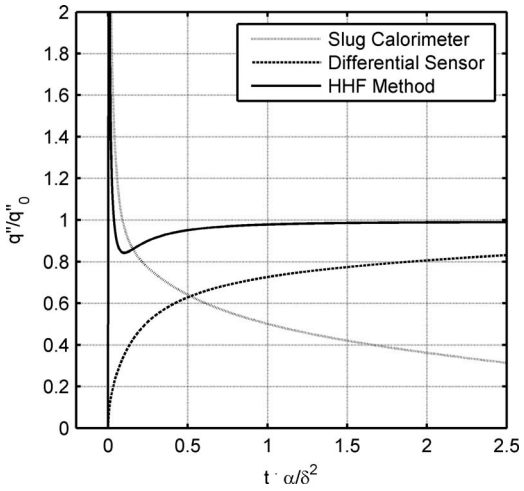

Fig. 4 Simulated response of sensor in three modes of operation

The analysis was extended to a wide range of backing materials in Fig. 5. The error of the three methods for a step heat flux input is shown as a function of time and backing material thermal conductivity. In these tests, the backing material's thermal conductivity was stepped from 100 times lower than that of the sensor to 100 times greater. Specific regions are shown for each mode of sensor operation. The differential region is bounded by the high conductivity backing case above and the low conductivity case below while the slug calorimeter region is bounded by the low conductivity case above and the high conductivity case below. The large size of these regions indicates the sensitivity of the slug calorimeter and differential sensor to backing material conductivity. The much smaller region of the HHF in Fig. 5 indicates that its performance is far less dependent on the properties of the backing material. In fact, although the backing material thermal conductivity is varied by four orders of magnitude, at no point does this cause more than an 11% change in the response of the HHF method.

The results in Fig. 5 can also be used to show the sensor response time as a function of the backing material properties. The HHF region is bounded by the low conductivity case above and

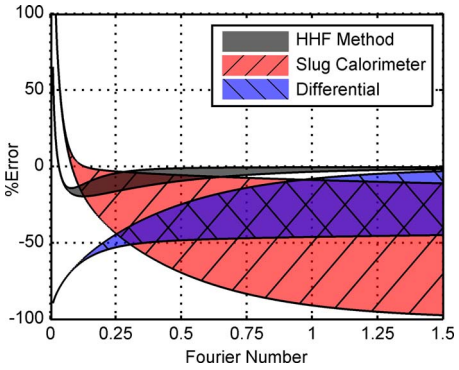

Fig. 5 Error as a function of time and backing material thermal conductivity

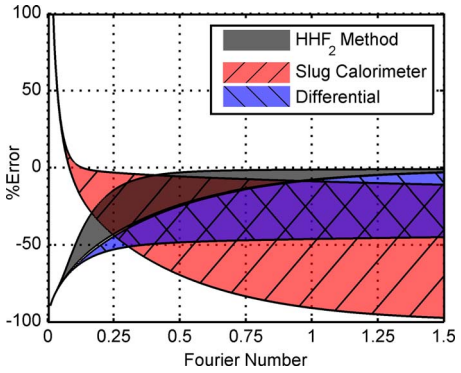

Fig. 6 Error of HHF_2 using only T_2 in slug calorimeter term of HHF compared with standard methods

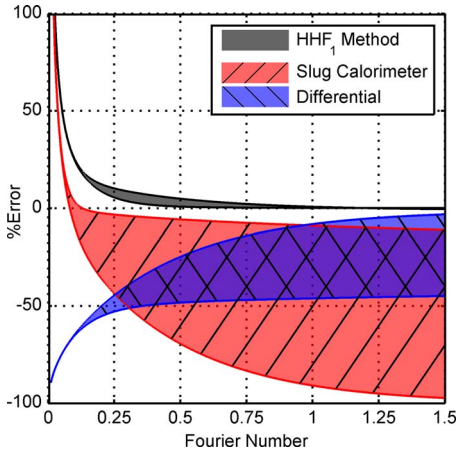

Fig. 7 Error of HHF_1 using only T_1 in slug calorimeter term of HHF compared with standard methods

the high conductivity case below and obtains accuracy to within 2% at a Fourier number of 0.33 on an insulator and 1.40 on a conductor. Even on a highly conductive material, which is the best case scenario for a differential sensor, the HHF is faster (Fo =1.4 versus 1.5). Finally, it is worth noting that for all Fourier numbers greater than 0.02, the error of the HHF is never more than $\pm 20\%$ regardless of the backing material. For comparison, a differential sensor requires a Fourier number greater than 0.57 to measure the heat flux to within $\pm 20\%$ on a perfect conductor, which is 28 times slower than the HHF method.

The primary limitation with the HHF method is the large overprediction in the heat flux at Fourier numbers less than 0.02. As discussed previously, this is because the face temperature is used in the slug calorimeter term (Eq. (9)). In certain situations, it would be desirable to eliminate the overshoot of the HHF method. This can be accomplished by using only the back temperature (T_2) in the slug calorimeter term, as shown in Fig. 6. Hereafter, if the slug term of the hybrid method only includes the back temperature (T_2), it will be referred to as the HHF_2 method. Figure 6 shows that there is no overshoot and the HHF_2 method still accurately measures the steady-state heat flux regardless of the backing material. The only drawback to this method compared with the standard HHF method is its slower response time. While the time required to reach an accuracy of 2% is essentially unchanged, the time required for accuracy within 20% is drastically increased. For any Fourier number greater than 0.02 the HHF is within 20% while the HHF_2 method requires a Fourier number greater than 0.57, the same as for a differential sensor on a conductor. This implies that if the sensor is attached to a perfect heat sink, the HHF_2 method offers no advantages compared with a standard differential sensor. For all real materials, however, the HHF_2 method is superior to either the differential sensor or the slug calorimeter. As in Fig. 5, the top of the HHF region in Fig. 6 is the low conductivity case while the bottom of the region is the high conductivity case.

At the other extreme, the hybrid method was analyzed with the slug term only containing T_1 (HHF_1). This response is shown in Fig. 7 and demonstrates the versatility of the hybrid method. By simply changing the weights of T_1 and T_2 in the slug term the response can be changed drastically. Figures 5–7 show that as the ratio of T_1/T_2 in the slug term of the hybrid method increases, the overshoot increases and the response time decreases. In this case, accuracy within 2% is obtained at a Fourier number of 0.75, which represents a significant improvement compared with the value of 1.40 for the standard hybrid method shown in Fig. 5. On the other hand, accuracy within 20% does not occur until a Fourier number of 0.125 is reached instead of the value of 0.02 reported from Fig. 5. With this in mind, it is worth noting that Figs. 6 and 7 represent two extremes for implementing the hybrid method. Which method is best must be determined on a case by case basis. If no overshoot can be tolerated, T_2 should be heavily weighted. On the other hand, if response time is critical and some overshoot can be tolerated, T_1 should be more heavily weighted. The case where the two temperatures are weighted evenly (Fig. 5) is shown as a good tradeoff between the overshoot and response time.

5 HHF Experimental Validation

To further validate the hybrid method, it was experimentally tested using a HTHFS [17]. The HTHFS, as shown in Fig. 8, consists of a thermopile, which directly measures the temperature difference across the sensors, as well as two thermocouples, which measure the face and back surface temperatures. When operated as a differential sensor, the HTHFS has a sensitivity of 579 ± 29 $\mu V/W/cm^2$. The HTHFS is made from materials that are thermally conductive to ensure that the heat flow is primarily one-dimensional.

The HTHFS was tested using two backing conditions: water cooled and insulated. The testing was performed in a stagnating jet convection stand, which was fully characterized by Gifford et al. [19]. This stand, as shown in Fig. 9, consists of a fully adjustable T-nozzle, which directs a 6 mm diameter jet of heated air at both the test sensor and a Vatell Corp. (Christiansburg, VA) HFM-7® reference sensor located 14 diameters away. The heat flux microsensor (HFM) is a differential sensor, which measures both the heat flux and surface temperature and has a time response faster than 100 kHz [20], but it can only be used on high conductivity materials. The jet velocity was measured at the sensor location with a pitot-static tube and was found to be 55 ± 2 m/s. By switching the HFM from one side to the other of the calibration stand, the heat transfer coefficient on each side of the T-nozzle was shown to be identical to within approximately 3% at the stagnation point. Because the hot free jet entrains ambient air and

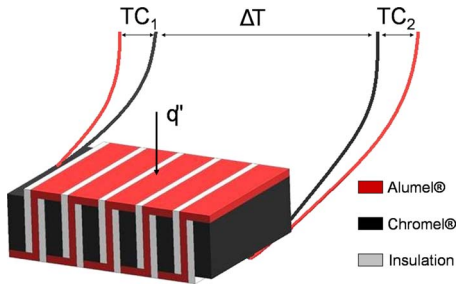

Fig. 8 HTHFS design overview

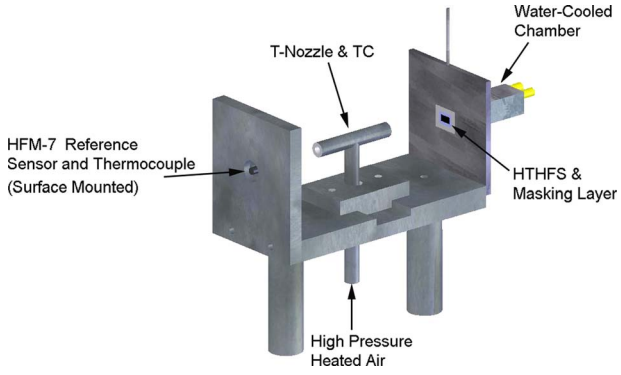

Fig. 9 Stagnation flow convection calibration facility

cools before it reaches the sensor location, the jet recovery temperature (T_r) at the sensor location is needed. Recovery temperatures were measured by 36 gauge K-type thermocouples, which were stretched 1 mm above the stagnation point. The recovery temperatures relative to the room temperature ($T_r - T_\infty$) from one side to the other were identical to within 4%. It was verified that the thermocouples were measuring the recovery temperature by allowing the HTHFS to reach steady-state on an adiabatic backing. The discrepancy between the thermocouple's recovery temperature and the HTHFS' recovery temperature was less than 0.5°C.

Using the heat flux and surface temperature measured by the HFM with the measured jet recovery temperature, the convective heat transfer coefficient was calculated as

$$h = \frac{q''_{\text{HFM}}}{T_r - T_{S_{\text{HFM}}}} \tag{14}$$

The heat transfer coefficient is shown as a function of time in Fig. 10 and is constant on the mean to within 2% throughout the test. With the convective heat transfer coefficient determined, the heat flux to the test sensor was calculated using the recovery temperature and the measured surface temperature of the HTHFS.

$$q''_{\text{HTHFS}} = h(T_r - T_{S_{\text{HTHFS}}}) - q''_{\text{radiation}} \tag{15}$$

The radiation term was included to account for any net radiation leaving the sensor face. Since the HTHFS is painted using Krylon™ ultra flat black spray paint, the emissivity was assumed to be 0.97 [21]. The surroundings were treated as a black body at room temperature. For all tests, the radiative flux was less than

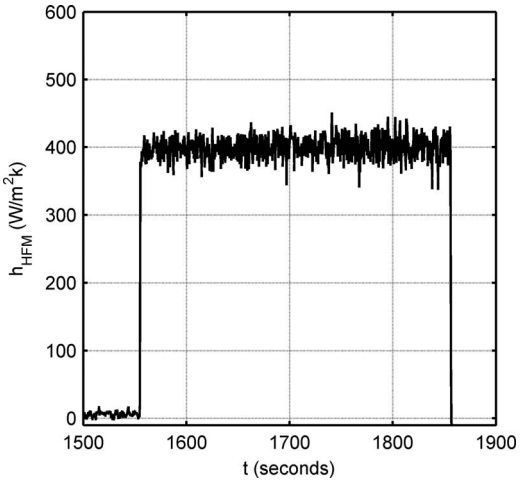

Fig. 10 Convective heat transfer coefficient

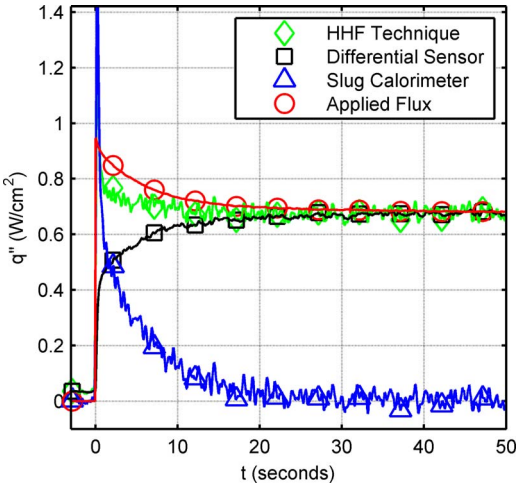

Fig. 11 Sensor on water cooled backing

2% of the convective flux, indicating that a more thorough radiation analysis would not significantly affect the results.

The calculated heat flux is shown with the output of the HTHFS in Figs. 11–14. Figure 11 shows the response of the sensor operated as a differential sensor, a slug calorimeter, and using the HHF method while mounted on a water cooled backing. The limitations of the slug calorimeter and differential sensor are obvious. Since the backing is water cooled, this represents the best case scenario for a differential sensor. Although the differential method performs well at steady-state, it has a slow time response. The slug calorimeter does not give an accurate measurement and as the sensor reaches steady-state, the slug calorimeter's output trends to zero. This is as expected and demonstrates why slug calorimeters cannot be used on conductive materials or to measure steady-state heat fluxes. The HHF method eliminates these problems and performs just as predicted numerically (Fig. 5). The HHF has the fast time response of the slug calorimeter, and then trends to the steady-state heat flux more quickly than the differential sensor.

Figure 12 shows the same test as in Fig. 11 except that the HHF_2 method was applied. As expected, the overshoot at the beginning of the test is eliminated for the HHF_2 method at the expense of a slower response time. As predicted in Fig. 6, an accurate measurement of the steady-state heat flux is still made.

Figures 13 and 14 show the response of the sensor mounted on a block of low conductivity, fibrous alumina insulation. Here, the

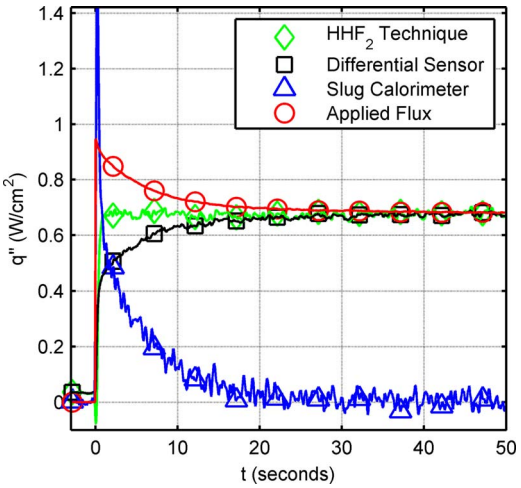

Fig. 12 Sensor on water cooled backing using only T_2 in slug and hybrid methods

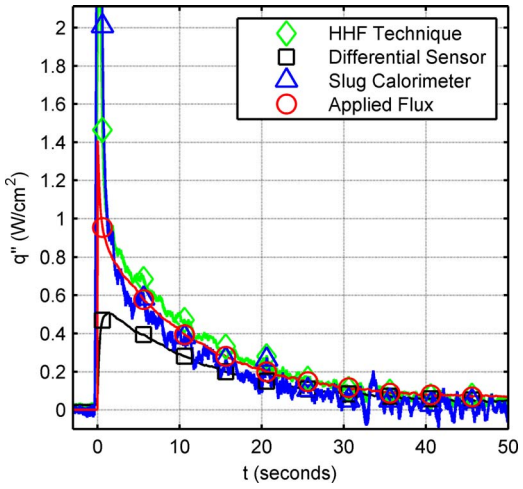

Fig. 13 Sensor on insulated backing

curves appear much different than for the water cooled case. In this test, the heat flux quickly trends to zero. This is because the HTHFS surface temperature quickly warms to the recovery temperature since very little heat leaves the sensor. Therefore, the temperature difference driving the heat flux trends to zero, causing the heat flux to trend to zero. Although the test time is short, the advantages of the HHF method are still apparent. This time, the differential sensor is unable to accurately measure the heat flux. This is because q_2'' is much less than q_1'', which implies that the average of q_2'' and q_1'' is not an accurate measure of q_1''. On the other hand, since q_2'' is small, the slug calorimeter works relatively well in this case. As stated previously, in the limit, as the backing material becomes a perfect insulator, the HHF method and the slug calorimeter will give identical results once the temperature profile is fully developed. Therefore, for any real insulator with nonzero thermal conductivity, the HHF method will outperform the slug calorimeter. This is shown in Fig. 13. Even on this very low conductivity substance, there is still enough heat leaving the back surface of the sensor that the HHF method more accurately measures the heat flux compared with the slug calorimeter.

Figure 14 shows the same test as Fig. 13 except the only T_2 is used in the slug and hybrid analyses. Once again, the HHF_2 method accurately measures the heat flux with a much smaller

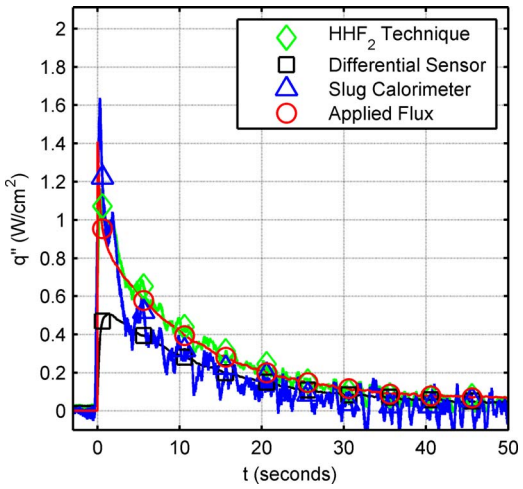

Fig. 14 Sensor on insulated backing using only T_2 in slug and hybrid methods

initial overshoot. Here, it is more difficult to see any slower time response. This is reasonable because, as shown in Fig. 6, as the backing material thermal conductivity is reduced, the time response of the HHF_2 improves. More experimentation is needed to fully examine the time response characteristics of sensors utilizing the various forms of the hybrid method.

6 Conclusions

This paper outlines a hybrid method for obtaining surface heat flux measurements. It is shown that by combining both spatial and temporal temperature measurements in a hybrid method, the time response and accuracy of heat flux sensors can be improved. More importantly, the HHF method causes the sensor's response to be much less dependent on the properties of the material to which it is mounted. In addition, it is shown that by adjusting how the temperatures used in the HHF method are weighted, the method can be specifically tailored to a particular test. The HHF method was validated by performing numerical simulations, which were supported by experimentation. These results show significant improvements compared with operating the sensor as a solely spatial or temporal heat flux sensor.

Acknowledgment

The authors would like to acknowledge the support of NASA Dryden Flight Research Center through Tao of Systems Integration Inc. and contract monitor Larry Hudson.

Nomenclature

C = specific heat
Fo = Fourier number, $t\alpha/\delta^2$
k = thermal conductivity
h = convective heat transfer coefficient
q'' = heat flux
q_0'' = step change heat flux for simulation
q_1'' = heat flux into sensor face
q_2'' = heat flux out of sensor back
$q''_{\text{differential}}$ = heat flux measured by differential sensor
q''_{HFM} = heat flux measured by HFM reference sensor
q''_{slug} = heat flux measured by slug calorimeter
T = time
t_{ss} = time to reach steady-state
T_1 = temperature at sensor face
T_2 = temperature at sensor back
T_{ave} = average sensor temperature
T_r = measured jet recovery temperature
$T_{S\ \text{HFM}}$ = HFM surface temperature
$T_{S\ \text{HTHFS}}$ = HTHFS surface temperature
T_∞ = room temperature
x = distance from sensor face
α = thermal diffusivity of sensor, $k/\rho C$
ΔT = time between temperature measurements, inverse of sampling frequency
δ = thickness of sensor
ρ = density

References

[1] Diller, T. E., 1993, "Advances in Heat Flux Measurement," *Advances in Heat Transfer*, Academic, Boston, pp. 279–368.
[2] Hager, N. E. J., 1965, "Thin Foil Heat Meter," Rev. Sci. Instrum., **36**, pp. 1564–1570.
[3] Hightower, T. M., Olivares, R. A., and Philippidis, D., 2008, "Thermal Capacitance (Slug) Calorimeter Theory Including Heat Losses and Other Decaying Processes," NASA Report No. TM-200-TM-0215364.
[4] Kidd, C. T., and Adams, J. C., 2001, "Fast-Response Heat-Flux Sensor for Measurement Commonality in Hypersonic Wind Tunnels," J. Spacecr. Rockets, **38**(5), pp. 719–729.
[5] Epstein, A. H., Guenette, G. R., Norton, R. J. G., and Yuzhang, C., 1986, "High-Frequency Response Heat-Flux Gauge," Rev. Sci. Instrum., **57**(4), pp. 639–649.

[6] Liebert, C. H., 1992, "High Temperature Plug-Type Heat Flux Gauges," NASA Report No. TM-105403.
[7] Rooke, S., Fralick, G., and Liebert, C., 1998, "Heat Transfer Analysis of a Plug-Type Heat Flux Gauge," J. Thermophys. Heat Transfer, **12**(4), pp. 536–542.
[8] Walker, D. G., and Scott, E. P., 1998, "Evaluation of Estimation Methods for High Unsteady Heat Fluxes From Surface Measurements," J. Thermophys. Heat Transfer, **12**(4), pp. 543–551.
[9] George, W. K., Rae, W. J., and Woodward, S. H., 1991, "An Evaluation of Analog and Numerical Techniques for Unsteady Heat-Transfer Measurements With Thin-Film Gauges in Transient Facilities," Exp. Therm. Fluid Sci., **4**(3), pp. 333–342.
[10] Schultz, D. L., and Jones, T. V., 1973, "Heat Transfer Measurements in Short Duration Hypersonic Facilities," AGARDograph No. 165.
[11] Anthony, R. J., Jones, T. V., and LaGraff, J. E., 2005, "High Frequency Surface Heat Flux Imaging of Bypass Transition," ASME J. Turbomach., **127**(2), pp. 241–250.
[12] Kidd, C. T., Nelson, C. G., and Scott, W. T., 1994, "Extraneous Thermoelectric EMF Effects Resulting From the Press-Fit Installation of Coaxial Thermocouples in Metal Models," 40th International Instrumentation Symposium, pp. 317–335.
[13] Wang, Z., Ireland, P. T., and Jones, T. V., 1995, "An Advanced Method of Processing Liquid-Crystal Video Signals From Transient Heat-Transfer Experiments," ASME J. Turbomach., **117**(1), pp. 184–189.
[14] Nasir, H., Ekkad, S. V., and Bunker, R. S., 2007, "Effect of Tip and Pressure Side Coolant Injection on Heat Transfer Distributions for a Plane and Recessed Tip," ASME J. Turbomach., **129**(1), pp. 151–163.
[15] Bizzak, D. J., and Chyu, M. K., 1995, "Use of a Laser-Induced Fluorescence Thermal Imaging-System for Local Jet Impingement Heat-Transfer Measurement," Int. J. Heat Mass Transfer, **38**(2), pp. 267–274.
[16] Oishi, T., Gorbunov, S., Fu, J., and Martinez, E., 2006, "Thermal Sensor Development and Testing for NASA Entry Probe Thermal Protection Systems," AIAA Aerospace Sciences Meeting and Exhibit, Reno, NV.
[17] Gifford, A. R., Hubble, D. O., Pullins, C. A., Diller, T. E., and Huxtable, S. T., 2009, "A Durable Heat Flux Sensor for Extreme Temperature and Heat Flux Environments," J. Thermophys. Heat Transfer, in press.
[18] Incropera, F., and DeWitt, D., 2002, *Introduction to Heat Transfer*, 5th ed., Wiley, New York.
[19] Gifford, A. R., Hoffie, A., and Diller, T. E., 2009, "Convection Calibration of Schmidt–Boelter Heat Flux Gages in Shear and Stagnation Air Flow," ASME J. Heat Transfer, in press.
[20] Holmberg, D. G., and Diller, T. E., 1995, "High-Frequency Heat Flux Sensor Calibration and Modeling," ASME J. Fluids Eng., **117**(4), pp. 659–664.
[21] Kidd, C., 1983, "Determination of the Uncertainty of Experimental Heat-Flux Calibrations," AEDC Report No. TR-83-13.

Fluorescence and Fiber-Optics Based Real-Time Thickness Sensor for Dynamic Liquid Films

T. W. Ng

A. Narain
ASME Fellow
e-mail: narain@mtu.edu

M. T. Kivisalu

Department of Mechanical Engineering-Engineering Mechanics,
Michigan Technological University,
Houghton, MI 49931

To overcome the limitations/disadvantages of many known liquid film thickness sensing devices (viz. conductivity probes, reflectance based fiber-optics probes, capacitance probes, etc.), a new liquid film thickness sensor that utilizes fluorescence phenomena and fiber-optic technology has been developed and reported here. Measurements from this sensor are expected to facilitate better understanding of liquid film dynamics in various adiabatic, evaporating, and condensing film flows. The sensor accurately measures the instantaneous thickness of a dynamically changing liquid film in such a way that the probe does not perturb the flow dynamics in the proximity of the probe's tip. This is achieved by having the probe's exposed surface embedded flush with the surface over which the liquid film flows, and by making arrangements for processing the signals associated with the emission and collection of light (in distinctly different wavelength windows) at the probe's flush surface. Instantaneous film thickness in the range of 0.5–3.0 mm can accurately (with a resolution that is within ±0.09 mm over 0.5–1.5 mm range and within ±0.18 mm over 1.5–3.0 mm range) be measured by the sensor described in this paper. Although this paper only demonstrates the sensor's ability for dynamic film thickness measurements carried out for a doped liquid called FC-72 (perfluorohexane or C_6F_{14} from 3M Corporation, Minneapolis, MN), the approach and development/calibration procedure described here can be extended, under similar circumstances, to some other liquid films and other thickness ranges as well.
[DOI: 10.1115/1.4000045]

Keywords: liquid film thickness measurements, real-time liquid thickness sensor, fiber-optic sensor, dynamic liquid film, liquid-vapor interface, fluorescence probe

1 Introduction

Over the last few decades, measurement of a dynamic liquid film's thickness has become increasingly important in numerous research and development fields. This paper focuses on a sensor, which may be used to obtain interfacial wave characteristics—such as the amplitude, frequency, and propagation velocity—by postprocessing and analyzing dynamic, local film thickness data at known locations. Need for such measurements based information exists for two-phase systems that involve film flows under adiabatic, evaporating, or condensing conditions. Many techniques have been developed to satisfy the objectives of measuring liquid film thickness values (instantaneous or time-averaged) within the experimental goals, constraints, and equipment restrictions imposed by the specific needs of the application of interest.

Direct mechanical measurements involving needle contact [1] have been used very early on for scientific studies where the intrusion of the probe in the film does not lead to significant alteration of the flow, unlike many two-phase flows of scientific interest.

Conductivity and capacitance measurements based approaches for a liquid film's thickness are the most popular among the nonintrusive techniques. These techniques [2–4] measure the conductance and/or capacitance [4,5] of a certain volume of the liquid film in the vicinity of the probe. Even inductive probes have been used [3,6]. A well known distance measuring principle has also been used [7] in the present context by identifying and measuring the total transit time of a sound wave as it travels from a flush ultrasound probe to the film interface and back after its first reflection. However, a major limitation of these [2–4,7] approaches are their insufficient spatial resolution for dynamically resolving spatially nonuniform and time-varying film thickness.

Use of optical reflection from the liquid film's interface [6,8–12], optical interference [13–15] of illuminating and reflecting lights, optical ellipsometry [16,17], optical absorption/transmission [18–20] characteristics, optical fluorescence imaging [21–24] of the liquid film, and the approach of measuring the amount of fluorescent light (see Refs. [5,25–28] as well as the approach described in this paper) typically require a transparent liquid film. Methods based on optical absorption, interference, and reflection techniques depend on the exciting light's reflection from the liquid interface; hence they do not work well when instantaneous thickness is desired in the presence of waves on the liquid's interface. These techniques are useful for thickness measurements of very thin films (within nano- to microscale) with negligible wave effects (as in Refs. [5,27]), or when only the peaks and troughs of the interface are of interest (as in Ref. [9]), or in systems employing an appropriate multifiber collection technique similar to the one presented here (as in Ref. [11]). The calibration curves in Ref. [11] are not linear, and they require a double ring of receiving optical fibers in their probe. Other fluorescence techniques used in the literature apply to applications in which a liquid-vapor interface is not present, as in Ref. [25]. The absorbance methods require optical access on both sides of the liquid-vapor interface and sometimes require a dye [20,29]. According to Mouza et al. [19], the settling time of the photo detector diode may impair the temporal resolution of their sensor, and interface reflection and refraction in the presence of waves with interface angles greater than 20 deg may introduce errors. The fluorescence-based film thickness measurements recorded by Ting [30] require an optical window (which must be corrected for refraction); they were not calibrated, and the calibration method suggested in Ref. [30] is not representative of liquid-vapor inter-

Contributed by the Heat Transfer Division of ASME for publication in the JOURNAL OF HEAT TRANSFER. Manuscript received September 12, 2007; final manuscript received August 15, 2009; published online December 30, 2009. Assoc. Editor: Yogesh Jaluria.

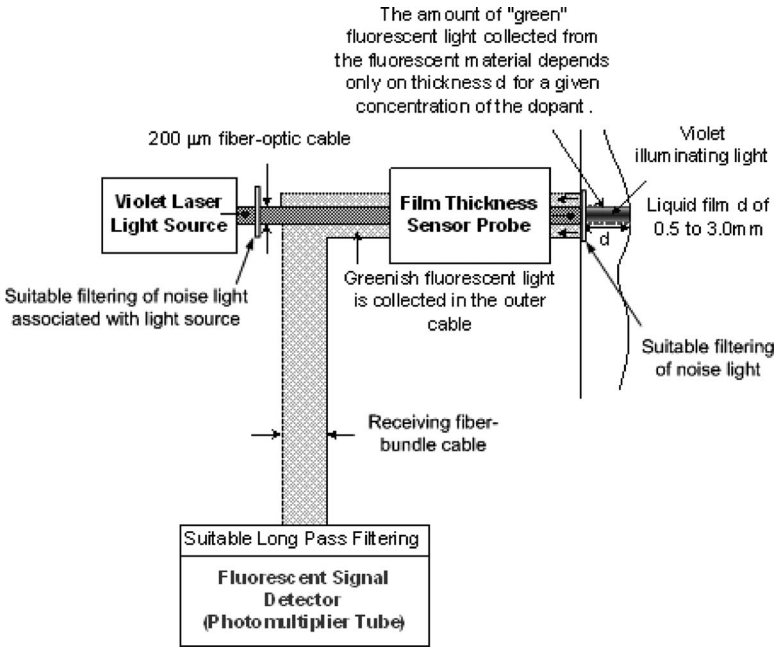

Fig. 1 Operating principle of a fluorescence sensor

faces of the type encountered in condensing flows. A method employed by Driscoll et al. [28] (a refinement of an earlier method introduced by Schmidt et al. [31]) is of considerable complexity with regard to access to the liquid film (it uses the insertion of a "purge cone" in the gaseous space of an annular flow). Furthermore, its accuracy in measuring dynamic film thickness with a wavy interface is suspected because their calibration method employs a smooth, planar interface of constant angle for the liquid film (unlike the wavy interfaces associated with dynamic films) and they indicate the need for changes in their electronics for use of their approach for dynamic film thickness measurements.

The only currently available viable alternative to our technology for accurately determining annular flow morphology in condensing and boiling flows is the laser focus displacement (LFD) method of Takamasa et al. [32,33], which has been used by Hazuku et al. [34] and Ebner et al. [29] for film thickness measurements in horizontal adiabatic flows. This method requires optical windows, and unlike the approach of this paper, must be nonempirically corrected for refraction effects through the transparent window material [32–34]. It measures the film thickness indirectly via the displacement of a lens, the movement of which is correlated with a laser focus point as it sweeps through the liquid film from wall to interface. The LFD method was found to be valid for interface angles up to 33 deg in Ref. [34]; however, Ebner et al. [29] noted an 8.0 deg interface angle limitation in their LFD measurements of oil flows in horizontal rectangular ducts. The LFD method in Ref. [34] requires neither dopant nor darkness in the sensing region, rendering it useful in combined thickness and visualization studies.

In summary, many liquid film thickness measuring techniques have been developed, each with its own range of applicability, advantages, disadvantages, and limitations. However, for characterizing wave motions on dynamic liquid films of thickness in the range of 0.2–5 mm, available sensors show limitations and/or a need for additional enhancements/modifications toward simplifying the calibration process and reducing the cost.

2 Principle of the Sensor

The above-stated goal is to have the sensing probe accurately measure the instantaneous thickness of a dynamically changing liquid film in such a way that the probe does not perturb the flow phenomenology in the proximate distance to the probe's tip. This is achieved by having the probe's exposed surface embedded flush with the flow surface (the surface on which the liquid film flows or moves) and processing the signals associated with light emission and light collection at the probe's flush surface itself. A thickness range between 0.5 mm and 3.0 mm is resolved by the developed sensor.

Film thickness measurements are carried out for stationary and dynamic films of a liquid called FC-72 (perfluorohexane or C_6F_{14} made by 3M Corporation). The liquid film shown in Fig. 1 is fluoresced by exciting it with a suitable light source. A portion of the fluorescent light, which has a different and distinct wavelength spectrum than the spectrum of the excitation light, falls back (after possibly reflecting once or more times from the interface) on a designated collection area of the flush probe. As shown in Fig. 2, the flush probe in Fig. 1 has an arrangement of illumination (marked by *I*) and collection (marked by *R*) locations, and at these

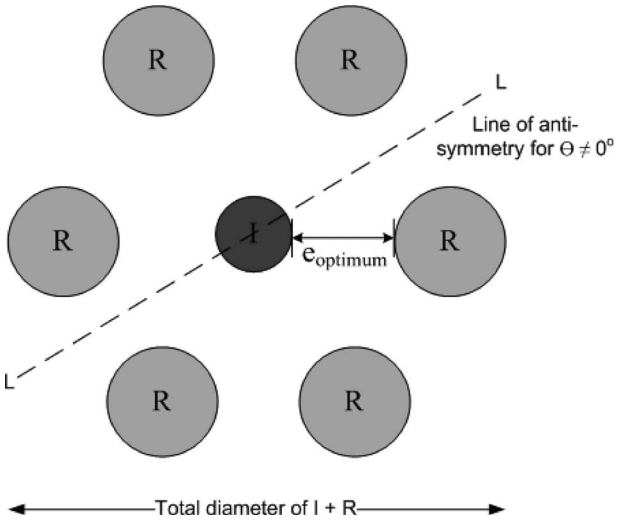

Fig. 2 Symmetrical arrangement of *R* probes around an *I* probe

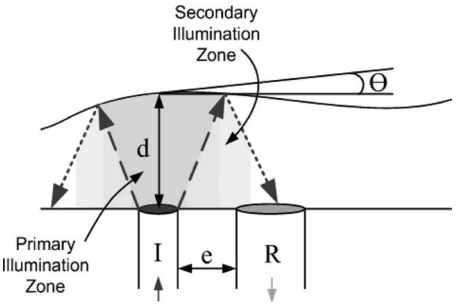

Fig. 3 Greater detail on the neighborhood of illuminating (*I*) and receiving (*R*) fiber tips

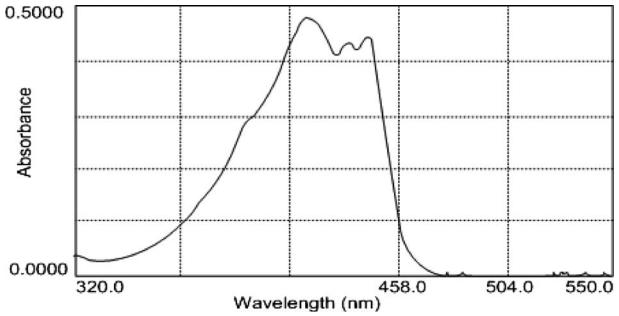

Fig. 4 Absorbance spectrum of a bi-acetyl doped FC-72 solution (*C*=0.121%)

locations, suitably small and thin optical filters are placed on the tips of their respective fiber-optic cables and are flush with the sensor's probe area. The amount of collected/detected fluorescent light depends, among other variables, on the instantaneous film thickness to be measured. For the new calibration technique described and proposed here, the measured value of the detected fluorescent light correlates directly to the instantaneous film thickness, even in the presence of interfacial waves.

To fluoresce the liquid film, the FC-72 is slightly doped (concentration = mass of dopant $*$ 100/mass of total solution = 0.20%) by a suitably chosen fluorescent additive (bi-acetyl or $C_4H_6O_2$ in this case). The excitation of this doped liquid film at shorter wavelengths of light (400–410 nm) leads to sufficient absorption of this light. This, in turn, induces sufficient fluorescent emission at longer wavelengths (460–600 nm). In other words, molecular absorption of shorter wavelength photons triggers emission of lower energy photons with longer wavelengths. The wavelength spectrum of the emitted fluorescent light (460–600 nm) is separated and identified for detection because light in this spectrum—as it traverses its way out of the film—is not self-quenched or absorbed by the doped liquid film. The excitation light is arranged to be minuscule in order to excite the film mostly through the primary illumination cone in Fig. 3 (i.e., to minimize presence of secondary illumination cones resulting from interfacial reflection of the excitation light in the primary illumination cone). As a result of the minuscule excitation, the light in the fluorescent range, as detected at the receiving fibers (after filtering out any reflected excitation light) after its first reflection from a nearly planar interface (see Fig. 3), is also minuscule and is detected by a sensitive photomultiplier tube (PMT). The *predominant* amount of detected light should come directly from the fluorescent light originating in the primary illumination cone in Fig. 3, and a much smaller amount should come indirectly through fluorescence caused by illuminating light reflected from the interface and then absorbed in secondary illumination cones, as shown in Fig. 3. This predominant component of detected light correlates directly with instantaneous film thickness and is made precisely known (and deterministic) by sorting and identifying this portion of the total detected light with the help of a paired set of calibration experiments especially developed for this purpose. The results of the calibration experiments, as well as experimental demonstration of the sensor's dynamic measurement capabilities, are reported in this paper. Note that if the working fluid is sufficiently fluorescent as for some oils [27], the use of a dopant may be avoided without significant hardware alterations, and only minor changes to the calibration procedure may be needed.

2.1 Choice of Dopant. The pure working liquid FC-72 is a clear, colorless, and odorless dielectric liquid with high density, low viscosity, low surface tension, and low boiling point (56°C at one atmosphere of pressure). It is commonly used as an electronic cooling fluid due to its low boiling point, high convective heat transfer coefficient, and its clean, safe, and easy-to-use characteristics. It has a spectral absorptivity of nearly zero over the visible range. Here, FC-72 is doped by dissolving a small amount of bi-acetyl, $C_4H_6O_2$ (henceforth called dopant).

The doped FC-72 solution, when excited by a 408 nm laser source, results in significant absorbance and sufficient fluorescence of the bi-acetyl molecules. The solution's absorbance and fluorescence characteristics are shown in Figs. 4 and 5, respectively. In Fig. 4, absorbance = 0 has been set for pure FC-72. The measurements reported in Fig. 4 were done with a 10 mm light path cuvette in a Beckman spectral photometer. The mass concentration of the doped solution was 0.121%. It is seen through the absorbance spectrum (see Fig. 4) that the detected fluorescent light (460 nm $\leq \lambda \leq$ 600 nm), when making its way out of the liquid film, will see zero absorbance and hence will not be self-quenched or absorbed by the liquid film.

For an excitation light of $\lambda = 425$ nm, as shown in Fig. 5, the dotted curve indicates the level of fluorescence (dominant over 460–600 nm range) that the doped solution yields. This curve was obtained by a fluorescence meter when a doped solution ($C = 0.054\%$) was excited by a 425 nm light source.

The solid curve plots the "factor" ($0 \leq$ factor ≤ 1.02) at various wavelengths of excitation light, by which the fluorescent spectrum's intensity, when excited at $\lambda = 425$ nm (dashed curve, photon counts over instrument's specified interval of time), may be multiplied to estimate fluorescent light intensity.

3 Requirements

Based on the above discussions of the sensor principle, and our experience with the sensor, this film thickness sensor can be used whenever the following requirements are met:

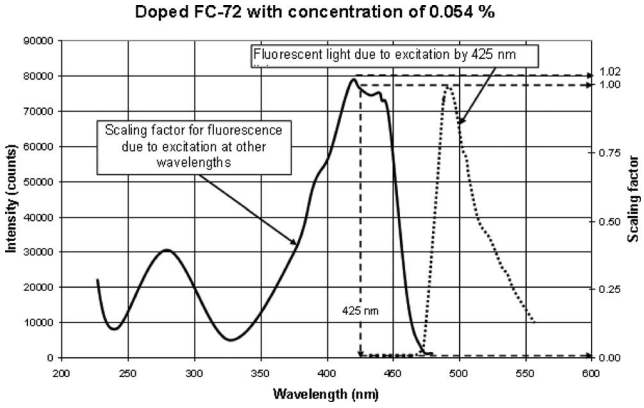

Fig. 5 Fluorescent intensity versus wavelength curves of a bi-acetyl doped FC-72 solution for an excitation light of λ = 425 nm and concentration of 0.054% (scaling factor is proportional to the absorbance)

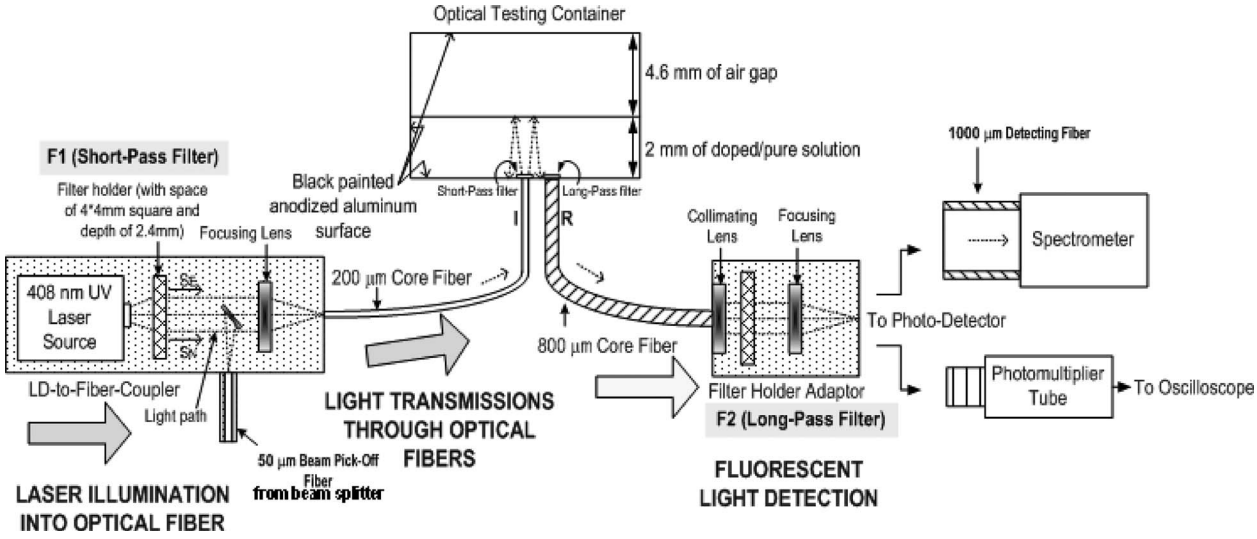

Fig. 6 Schematic of the experimental setting for the developed sensor

- The liquid film whose thickness is to be measured transmits light and can, if needed, be doped by a fluorescent chemical. The absorbance and fluorescence spectrum of the doped liquid must meet the criteria discussed under "choice of dopant."
- The measurement can take place either in a dark environment with no ambient light or only under an ambient light illumination at selected and allowable wavelengths that do not interfere with wavelengths associated with excitation or collection lights (e.g., $\lambda \gg 600$ nm).
- The inner walls of the container, within which flow of the film takes place, must be close to a "black surface" to minimize reflection of the excitation light.
- The components of the sensor and the sensing environment must be clean to avoid autoflouroscence (caused by excitation light) from impurities that can corrupt the signal in the spectrum of the light to be sensed.
- The liquid film thickness should be within a certain well defined range for any chosen excitation light illumination level (which is 0.5–3.0 mm for the reported light level situation). A wider range of measurements is possible if the sensor arrangement and excitation light levels are suitably modified. For different ranges of film thickness all one has to do is to prescribe a different "small amount" of excitation light for which the calibration in that specific range (say 2.5–5 mm) will work with different estimates on the resolution of the thickness and the spatial resolution with regard to the locality of the measurements.

4 Sensor Schematic, Hardware, and Experimental Procedure

4.1 Schematic. The schematic of the experimental setting of the developed sensor is depicted in Fig. 6. In general, illuminating light from a 408 nm violet laser source is transmitted through fiber I with a core diameter of 200 μm. A much smaller core diameter for fiber I can be used for better spatial resolution of the measurements. The light coming out of the fiber I illuminates a nearly cylindrical primary cone (Fig. 3) within a stationary or dynamic film (made up of a bi-acetyl doped FC-72 liquid) inside a cylindrical anodized aluminum container (optical testing container in Fig. 6). Absorption of the violet photons by the dopant molecules is followed in less than 1 ns by an emission of photons in longer wavelengths, which are within the range of 470–600 nm. It should be noted that previous spectrofluorometer experiments have confirmed that no fluorescence is yielded if pure FC-72 liquid is subjected to this excitation. The doped solution's fluorescent light ranging within 470–600 nm is channeled through a set of other optical fibers *R* (which are chosen to have a bigger core diameter of 800 μm and are arranged as in Fig. 2) into a photo detector of choice. The detector in Fig. 6 indicates use of either a photomultiplier tube (for measurement and calibration) or a spectrometer (for evaluation of system performance).

Along the optical paths, installation of the optical filters is needed to minimize the presence of noise light within the detected fluorescent range of interest. For instance, a short-pass (SP) filter, which allows transmission of light with wavelengths shorter than a specific wavelength λ, is installed at filter holder F1 in Fig. 6. This SP filter allows wavelengths below 415 nm to pass and blocks the very small noise light in the range of 420–700 nm, which typically accompanies the violet excitation laser light's spectrum (see Ref. [35] for details). For the sensor principle to be effective, reduced noise light and reflection of illuminating light from the interface is required. For this, calibration at very low excitation light levels (near 0–1 mW) are employed. One important reason for very low excitation light level (close to the zero light output threshold for the laser) is that our experience shows that the magnitude of unwanted laser emission in the fluorescent zone (470–600 nm) of interest, as well as other unwanted signals described later on in this paper, increases more rapidly with increased laser light than does the collected fluorescent light from the doped liquid.

In addition to the above, between F1 and the exit of the laser diode (LD)-to-fiber coupler, more ultrathin SP filters are placed to further improve the ability to block any undesired noise light arising from autofluorescence of the optical components inside the coupler. A short-pass filter (blocks everything above $\lambda \geq 420$ nm) is again employed at the tip of the illuminating fiber I in Fig. 6. This filter is to reduce noise light that goes through, despite the presence of the filter at F1, and, also, to eliminate some noise light that is created by the autofluorescence of the illuminating fiber I. Long-pass (LP) filters, which allow transmission of light of wavelengths longer than a specific wavelength $\lambda = 470$ nm, are placed on the tips of each of the receiving fibers *R* to block/reduce the amount of 408 nm excitation laser light that would otherwise enter *R* due to reflection of the laser illuminating light from the interface. An identical LP filter, which blocks wavelengths below 470 nm, is installed at filter holder F2 right before the photo detector to block possible autofluorescence light (in the spectrum of interest) from certain materials between *R* and the detector that would otherwise enter the detector. It was necessary to specify fused

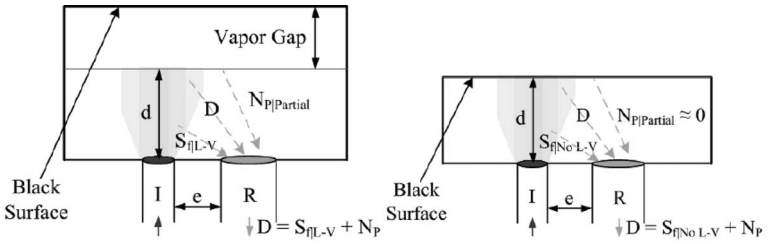

Fig. 7 (*a*) Calibration experimental configuration with liquid-vapor interface and associated nomenclature; (*b*) calibration experimental configuration without liquid-vapor interface and associated nomenclature

silica as the substrate of all optical filters to minimize problems with autofluorescence of the filter material into the wavelength range of the desired fluorescent signal.

4.2 Hardware Implementation. A system consisting of optical, electrical, and mechanical subsystems has been developed for the sensor. This section gives an overall picture of how hardware components are integrated into three optical subsystems, which are as follows: laser diode-to-fiber coupler used for laser illumination and focusing onto the illuminating fiber (with its associated filter and adapter), illuminating (laser light) and receiving fibers with their associated filters and fittings, and photo detector for sensing the amount of fluorescent light (with its associated filter and adapter). Figure 6 presents the schematic design. Pictures of the actual physical assemblies of the overall system and additional details of all the pieces of hardware, including optical, electrical, and mechanical components, are given in Ref. [35].

A violet LD is installed in a laser-to-fiber coupler. The filtered light is focused by an aspheric lens into a 200 μm core fiber (Fig. 6). LD current is controlled through a precise potentiometer. To monitor laser power of the LD so as to ensure constancy of the light output, some 4–8% of the laser light is captured through a beam splitter and channeled through a 50 μm core multimode (MM) fiber connected to the side path, as shown in Fig. 6 as beam pickoff fiber, of the laser-to-fiber coupler. A photodiode and an oscilloscope are used to detect the light coming out of this beam sampler. In addition, one thermoelectric cooler is connected to the photodiode and one to the laser-to-fiber coupler to maintain each one of them at specified constant temperatures of 20°C. This ensures the stability and consistency of the device performance. A fan acting on a finned heat sink is also attached onto the laser-to-fiber coupler to allow better heat dissipation during the LD and thermoelectric cooler operation.

Laser light illuminated from the LD is coupled through a straight-tip (ST) optical fiber connector into a fiber cable with a core diameter of 200 μm. After transmitting the light to a distance of about 1 m in the fiber, the fiber tip is housed inside a 1.1 mm diameter stainless steel distal tip, which is mounted in the bottom of the calibrating container with a nonfluorescent black silicon. This illuminating tip touches a short-pass filter, which is mounted flush with the calibrating container's bottom surface and exposed to a doped FC-72 liquid film. Light yielded by fluorescence of the bi-acetyl in the solution is collected through six or more fiber cables mounted at offset locations (R) from the illuminating fiber cable (see Figs. 2 and 3).

Fluorescent light exiting the receiving fiber cable(s) is collimated by a collimating lens (see Fig. 6). The collimated light passes through a cylindrical barrel (1 in., or 25.4 mm inner diameter), which works as a filter holder adapter (see F2 in Fig. 6). After filtering, the light passes through a suitable lens that focuses it on the active area of the photo detector. When the PMT is used for actual calibrations and measurements, an oscilloscope is connected to the PMT with a coaxial cable. A resistor at the output end of the PMT converts the detected and amplified signals from amperes to voltage values before the signal reaches the oscilloscope. It should be noted that the rise times of PMT and spectrometer are 2.5 ns and 3 ms, respectively.

4.3 Procedures. To improve the amount of fluorescent light collected, the doped solution is prepared at close to its highest allowable mass concentration, which is 0.20% dopant since the limit of bi-acetyl solubility in FC-72 at room temperature is found to be about 0.22% by mass. Clean, pure FC-72 solution is used throughout the tests to minimize the possibility of unwanted particles fluorescing under violet laser excitation. Although oxygen and other atmospheric gases are highly soluble in FC-72 according to 3M datasheets, it is assumed here that they will reach an equilibrium concentration at standard temperature and pressure, which is the same for all tests and calibrations conducted for this paper. It has been verified by dipping probe spectroscopy that the doped liquid FC-72 achieves repeatable fluorescent properties. Spectral analysis is employed by using a spectrometer whenever the characteristics of noise light need to be ascertained toward improvement of signal-to-noise ratio or better understanding of the system.

Optimal offset distance e in Fig. 3 for these tests were experimentally found to be best, with regard to signal-to-noise ratio, at 1.7 mm. Total height of the container in Fig. 6 is 1 in. or 25.4 mm. However, the top of this container also has a movable black disk, whose lower surface is initially at 6.6 mm from the bottom of the container. This movable disk can be lowered to effectively reduce the gap between the liquid-vapor interface and the top wall. As described later, it is this movable disk that allows a change between the configurations depicted in Figs. 7(a) and 7(b).

During the tests, pure or doped solution is added into the calibrating container, which is designed such that a stationary and horizontal liquid film's thickness corresponds directly to the added liquid volume. At least two measurements are taken for each film thickness. Proper choice of the best signal scaling on the detector's oscilloscope helps in reducing the measurement errors. Values smaller than the oscilloscope analog-digital conversion (ADC) errors are discarded and the corresponding thickness/light levels determine the lower limits of the sensor's capabilities. All measurements need to be taken within 1 min of laser illumination to prevent photo/thermal degradation of the doped solution. LD degradation is also minimized by turning off the LD driver in between experimental runs.

All electrostatic discharge (ESD) sensitive electronics are placed on top of a grounded, antistatic table mat. Any electrical and optical cables, which are sensitive to physical arrangement and/or movement, are properly secured.

Additional detail on the calibrating container designed for the tests, experimental precautions, and procedures can be found in Ref. [35].

5 Calibration Experiments, Parameter Definitions, and Governing Relationships

5.1 Calibration Experiments. Calibration is performed by the proposed novel paired set of experimental configurations (with and without liquid-vapor interface for a stationary horizontal liquid film) shown in Figs. 7(*a*) and 7(*b*) below. The experiments are carried out with the help of the entire system indicated in Fig. 6.

The purpose of a pair of calibration experiments for the same stationary and horizontal liquid film—first in the experimental configurations in Fig. 7(*a*), followed by measurements in the experimental configuration in Fig. 7(*b*)—is to develop a calibration curve that fulfills the requirement of having achieved a certain one-to-one correspondence among various signals. To discuss this further, it is essential that these signals and issues associated with their measurements be defined first. This is done in Sec. 5.2.

5.2 Important Definitions of Relevant Quantities. N_P (unit: mV, measured on the detector) is the amount of noise light (i.e., light other than the fluorescent light) that is received at the PMT despite all the earlier described filtering, when either of the two configurations in Fig. 7 is used to provide the liquid film shown in the system in Fig. 6. This N_P is measured as the amount of detected light—from the entire system (Fig. 6)—when the liquid film used in the configuration shown in Fig. 7(*a*) or Fig. 7(*b*) is not doped, so there is no fluorescence of the film. As needed, N_P for the experimental configuration in Fig. 7(*a*) is denoted as $N_{P|L\text{-}V}$ because of the presence of a liquid-vapor (*L*-*V*) interface and N_P for the experimental configuration in Fig. 7(*b*) is denoted as $N_{P|\mathrm{No}\ L\text{-}V}$ because of an absence of a *L*-*V* interface. Unless otherwise stated, N_P denotes $N_{P|L\text{-}V}$. Ideally, if it was not for limitations imposed by the requirements underlying the principle of the sensor, technology, and cost, one would try to achieve $N_P \approx 0$ relative to the signal of interest. In reality a nonzero value for N_P arises from the following sources: (i) some feeble noise light (that is predominantly in the fluorescent range of interest and is from the LD or autofluorescence in the LD housing) that gets out of the *I*-tip, reflects off from the liquid-vapor interface and/or enclosure, and enters the *R*-tip, (ii) some feeble noise light that gets generated by autofluorescence in the illuminating and receiving fibers' interaction with the illuminating light (typically the 408 nm excitation light), and (iii) some noise signal readings that arise from some inherent electrical noise in the electronics.

$S_{f|L\text{-}V}$ (unit: mV, measured on the detector) is the fluorescent signal that is received through the receiving fibers when the liquid film is in the configuration in Fig. 7(*a*)—a configuration in which the film has a liquid-vapor interface. This signal $S_{f|L\text{-}V}$ is due to (i) direct collection (by the *R*-tips in Fig. 2) of fluorescent light from the primary illumination cone in Fig. 3[1], (ii) reception of fluorescent light (also from primary illumination) at *R*-tip after its reflection from the liquid-vapor interface[2], and (iii) additional reception of fluorescent light at *R*-tip due to fluorescence in the secondary illumination zone (i.e., the zone formed by reflection of the illuminating light from the liquid-vapor interface; see Fig. 3). Note that the intensity of the light fluorescing in secondary illumination zones is expected to be quite weak compared with the intensity of the light fluorescing in the primary illumination zone due to the very low level of illuminating laser light, the absorption of the illuminating light in the film in the primary illumination cone, the loss of light due to the transmission of illuminating light through the interface, and the fact that the fluorescent light will still be orders of magnitude smaller than the feeble reflected illuminating light.

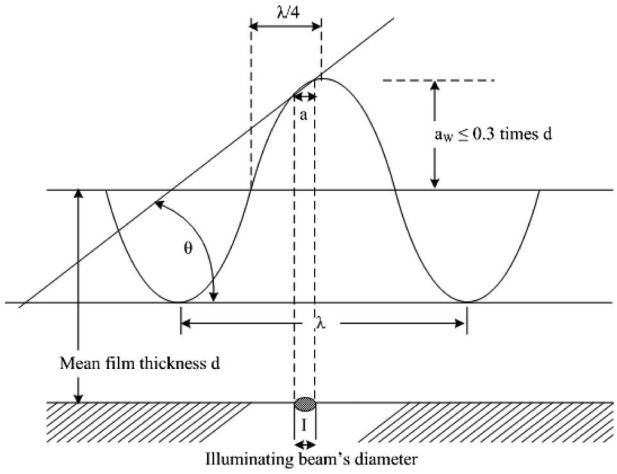

Fig. 8 Relationship of interfacial wavelength λ to the angle of the illuminated portion of the interface

D (unit: mV, measured on the detector) is the total detected light from the entire system (see Fig. 6) for a doped film in the configuration in Fig. 7(*a*) or Fig. 7(*b*). Ideally, for the configuration in Fig. 7(*a*), one should have $D = S_{f|L\text{-}V}$. However, because of a nonzero noise light component N_P, $D = S_{f|L\text{-}V} + N_P$.

N_P/D (unit: dimensionless) is the noise-to-detected light ratio (also called noise ratio). It is desirable that this ratio be made as small as possible. The smaller the value of N_P/D, the closer is the value of *D* to $S_{f|L\text{-}V}$ and the greater is the possibility of bringing it close to the desired signal $S_{f|\mathrm{No}\ L\text{-}V}$ defined below.

$S_{f|\mathrm{No}\ L\text{-}V}$ (unit: mV, measured on the detector), or the fluorescent signal ($S_{f|\mathrm{No}\ L\text{-}V} = D - N_P$), is computed from the measured values of *D* and N_P for this configuration when the doped film is in the experimental configuration, as depicted in Fig. 7(*b*). In this configuration, there is a complete absence of liquid-vapor interface as it is replaced by a liquid-solid (black surface) interface, and hence, there is a nearly complete absence of any reflection of light from the wetted top surface. Therefore, $S_{f|\mathrm{No}\ L\text{-}V}$ is the measure of the signal associated with collection of fluorescent light from the primary illumination zone. This is because the liquid-solid interface that replaces the liquid-vapor interface absorbs almost all of the illuminating and fluorescent light reaching the solid black surface.

Other terms and definitions are as follows: *C* is the solution concentration = (mass of dopant/mass of total solution) * 100% (%), *d* is the local liquid film thickness (mm) (see Fig. 7), *e* is the distance between the edges of illuminating and receiving fibers (mm) (see Fig. 7), E_{LD} is the excitation light that transmits out of the illuminating fiber, including any noise light (mA), *T* is the temperature of liquid film (°C), θ is the local interface angle with respect to the horizontal (deg) (see Fig. 3 or Fig. 9).

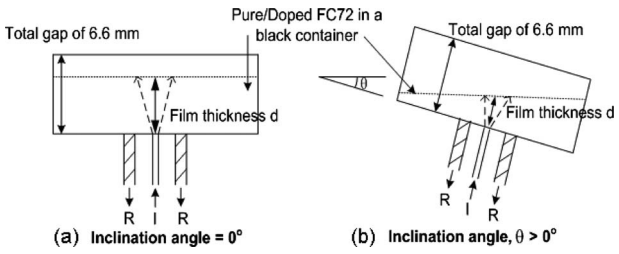

Fig. 9 (*a*) Interface angle test, 0 deg inclination angle; (*b*) interface angle test, nonzero inclination angle $\theta > 0$ deg

[1]In the current design, this light is due to fluorescent light incident on the *R*-tips at the solid-liquid interface scattering into the acceptance cone of the receiving fibers or by transmission of light incident on the *R*-tips at an angle outside of the acceptance cone of the receiving fibers through cladding modes in the fiber.

[2]This light may be comparable in intensity to the directly collected fluorescent light because, as in Fig. 3, the "acceptance cone" of the *R*-fibers may not overlap the primary illumination zone that emits diffuse fluorescent light in all directions.

5.3 Governing Relationships Among Relevant Parameters and Factors. The following relationships highlight the principles underlying the calibration of the sensor through the film configurations recommended in Figs. 8(*a*) and 8(*b*). These relationships show the dependent factors associated with various signals collected by the sensor as follows:

Equation (1): Experimentally detected light D for doped film and factors influencing it in the configurations (Figs. 7(*a*) and 7(*b*)) of interest

$$D = S_{f|L\text{-}V}(\text{or } S_{f|\text{No } L\text{-}V}) + N_P$$

= Function (N_P, C, d, e, E_{LD}, T, θ, etc.[3]);
= Function (N_P, d, θ) if concentration C and system settings are constant; and
= Function (d) if concentration C and system settings are constant, and specially designed receiving fiber arrangement (Fig. 2) and hardware improvements allow insensitivity of D and N_P values to changes in interface angle θ. This follows from the assumption that N_P is constant in intensity for the same hardware arrangement, consistent with the definition of N_P. (1)

Equation (2): Fluorescent signal $S_{f|L\text{-}V}$ in the presence of direct and reflected fluorescent light (due to primary illumination) from liquid-vapor interface and some fluorescent light from secondary illumination (see Figs. 3 and 7(*a*))

$$S_{f|L\text{-}V} = D - N_{P|L\text{-}V}$$

= Function (C, d, e, E_{LD}, T, θ, etc.[3]);
= Function (d, θ) if concentration C and system settings are constant; and
= Function (d) if concentration C and system settings are constant, and specially designed receiving fiber arrangement (Fig. 2) and hardware improvement allow insensitivity to changes in interface angle θ. (2)

Equation (3): True fluorescent signal $S_{f|\text{No } L\text{-}V}$ of interest in the absence of liquid-vapor interface (see Fig. 7(*b*) arrangement implying negligible reflected illuminating light and very low intensity reflected fluorescent light, and hence, near θ independence when the receiving fibers are symmetrically arranged)

$$S_{f|\text{No } L\text{-}V} = D - N_{P|\text{No } L\text{-}V}$$

= Function (C, d, e, E, T, etc.[3]); and
= Function (d) if concentration C and system settings are constant. (3)

6 Challenges

There were three main challenges associated with the development of the proposed sensor. The challenges are related to the elimination of effects associated with the presence of noise light, elimination/containment of effects associated with the expected changes in the liquid film's interface angle θ under conditions of a dynamic film, and reduction in errors by minimizing variations in the so-called fixed system settings and hence, improving repeatability of data at fixed levels of N_P and a range of θ values.

6.1 Noise Light Challenge. For both the configurations in Fig. 7, reduction in noise light N_P is very important. If N_P is not sufficiently small with respect to detected light D, it may not be possible to correlate the detected light D to the illuminated liquid film thickness that characterizes the volume of the primary illumination cone in Fig. 3. Under these high N_P/D conditions, the required one-to-one correspondence between D and the fluorescent signals $S_{f|L\text{-}V}$ and $S_{f|\text{No } L\text{-}V}$ typically either does not exist or the correspondence is unsatisfactory. As a result, for large N_P/D values, measurement of liquid thickness may not be possible over a range of thicknesses of interest. All these problems associated with large N_P/D are exemplified by a representative experimental result shown later in Fig. 13 of this paper and in figures 31 and 32 in Ref. [35].

Even if, say on a detector, a noise light level of $N_P \approx 10^{-6}$ times the illuminating light intensity is achieved through good filtering at various locations, the fluorescent signal $S_{f|L\text{-}V}$ remains very small—typically only about 2–11 times N_P. This is because of the ultrasmall level of fluorescent light $S_{f|L\text{-}V}$ yielded by the ultrasmall primary illumination (see Fig. 3) in comparison to the level of noise light N_P associated with various noise sources in the system. As a result, there are practical limitations on significantly increasing signal-to-noise ratio ($S_{f|\text{No } L\text{-}V}/N_P$) or detected light-to-noise ratio D/N_P. These practical limitations, despite the employment of state-of-the-art technology involving high quality optical filtering, photomultiplier tube detection (for very low level of light), high quality fiber-optic cables, and very high quality optics and electronics for the remaining system required development of a novel and effective calibration procedure. To address this problem, use of the proposed paired set of calibration experiments indicated in Figs. 7(*a*) and 7(*b*) led to a situation that does not require complete elimination of N_P or very significant enhancement of $S_{f|L\text{-}V}/N_P$ or D/N_P values. The novel calibration technique developed here can be effective despite an unavoidable presence of a nonzero N_P, provided that it is within certain bounds (e.g., $S_{f|L\text{-}V}/N_P$ is between 2–10 and the required one-to-one correspondence among D, $S_{f|L\text{-}V}$, and $S_{f|\text{No } L\text{-}V}$ is achieved).

6.2 Interface Angle Challenge. In addition to the calibration with stationary films addressing challenges associated with noise light N_P, there is a need for local film thickness measurement even in the presence of waves. The measurement principles are highlighted by Eqs. (1) and (2) in Sec. 5.3. From there it is known that the θ dependence in the collected signal is largely due to the component of fluorescent and noise lights that are collected after their reflections from a potentially wavy interface. This requires development of a measurement approach that minimizes the dependence of detected signals D and $S_{f|L\text{-}V}$ on the interface angle θ.

For most wavy situations, one only needs θ independence over $-\theta_{\max} \le \theta \le \theta_{\max}$. The maximum interface angle $\theta = \theta_{\max}(d)$ in Fig. 8 depends on the maximum amplitude a_w of the waves (assumed here to be less than 30% of the film thickness d). Let the minimum wavelength $\lambda_{\min}$ be such that, for $\lambda \ge \lambda_{\min}$, the wave energy in the dynamic film cannot be ignored. This gives, through Fig. 8, a simple estimate of $\theta_{\max}(d) \approx \arctan(4a_w/\lambda_{\min})$. For 0.5 mm $\le d \le 3.0$ mm and typical FC-72 waves of $\lambda \ge \lambda_{\min} \approx 1$ cm, this gives a $\theta_{\max}$ of approximately 3–20 deg. This type of sensor's range of applicability is determined by the experimentally determined value of $\theta_{\max}(d)$ for which θ independence can be confirmed. For a known θ independence in a range determined by $\theta_{\max}(d)$, the sensor can resolve, within certain bounds, instantaneous thickness for waves with minimum wavelength $\lambda_{\min}$ (i.e., all $\lambda \ge \lambda_{\min}$) and maximum amplitude a_w, provided that the criterion $\{\lambda_{\min} > 8a\}$ (where $a = 200$ μm is the base diameter of the illuminating beam at the interface) for planar approximation of the interface, and the criterion $\{\arctan(4a_w/\lambda_{\min}) \le \theta_{\max}\}$ for staying within an experimentally verified zone of θ independence ($-\theta_{\max} \le \theta \le \theta_{\max}$) are met. The experimental values of $\theta_{\max}$ were obtained by tilting the horizontal flat interface in Fig. 9(*a*) to other interface angles (to the extent possible by the available arrangements of the type indicated in Fig. 9(*b*)), which are $\theta = 0$ deg, 5 deg, 10 deg, etc., to study the effect of θ on signal D while

[3]Examples of other factors are as follows: photo detector's area, type, and number of optical filters in the system, opposite wall reflectivity, indices of refraction of the doped liquid and vapor, reflectivity and diffusivity of nearby surfaces, time duration of solution excitement by laser, ambient light (dark room, day, night, etc.), location and size of *I* and *R* fibers, etc. Also see "Other terms and definitions" in Sec. 5.2 for variables such as E_{LD}, T, etc.

holding the mean value of film thickness d the same. The desired θ independence for D and $S_{f|L\text{-}V}$ has been nearly achieved by a combination of the following two approaches.

The first approach is to use optimal location (distance e in Fig. 2), optimal (which is minimal) laser excitation current, and optimal filter settings so as to reduce the reflected light component of $S_{f|L\text{-}V}$ by minimizing $|S_{f|L\text{-}V} - S_{f|\text{No } L\text{-}V}|$. That is, the first approach is to operate the calibration experiment in the actual configuration in Fig. 7(*a*) such that this configuration's results are as close as possible to the results obtained from the associated calibration experiment in Fig. 7(*b*). The second approach consists of using an array of receiving fibers R (number ≥ 6) in the symmetrical arrangement shown in Fig. 2. For $\theta = 0$ deg, the illumination zone in Fig. 3 is symmetric with respect to any line LL passing through the center of the illuminating fiber in the plane of the probe (see Fig. 2). For two or three dimensional wave motions for which the interface can be approximated as some locally inclined plane of $\theta \neq 0$ deg, there exists some instantaneous line LL in the plane of the probes, as shown in Fig. 2, with respect to which the collected fluorescent light (directly or indirectly emanating from the primary and secondary illumination zones) has an antisymmetric distribution. The total signal collected from the symmetrical arrangement of receiving fibers cancels signal increases over half of the receiving fibers on one side of LL with signal decreases over the remaining half of the receiving fibers on the other side of LL.

By combining the two approaches described above, suitable θ independence in the values of D has been experimentally verified for -10 deg $\leq \theta \leq +10$ deg (see definition of θ in Fig. 3). The resulting variations in D are within $\pm 5.0\%$ and because of the slope of the "D versus d" curve, these variations still lead to a good resolution of the film thickness d (± 0.09 mm for 0.5 mm $\leq d \leq 1.5$ mm and ± 0.18 mm for 1.5 mm $\leq d \leq 3.0$ mm) over the thickness range of interest.

6.3 Fixing System Settings and Hardware Response. Several methods were used to ensure that variations in hardware configuration were not significantly affecting the response of the sensor. The fiber installations within the distal tip were carefully done, as per our specifications, by professionals (Myriad Fiber Imaging, Dudley, MA) who know the importance of care needed in fiber installation. The rigidity of the installed distal tip itself in the test section was also insured. Great care was taken in placing filters over the fiber tips so as not to scratch or apply silicon over the tips of the fibers. Standard sub miniature version A (SMA-905) and straight tip (ST) connectors were used to attach the fibers to the filter housings on the laser diode and photomultiplier tube. Other methods through which the repeatability of the reported results were insured include taking measurements shortly after the laser diode has been turned on (after 30 s to allow the photomultiplier tube to stabilize), removing or covering all potential sources of noise light in the room (indicator lights, monitor, etc.), levelling the calibration chamber, rinsing the calibration chamber with undoped FC-72 between calibration tests, using a syringe to meter out the volume of liquid for each test, using a mass balance to mix the doped solution, and using commercially available thermoelectric coolers to hold the laser diode and photodiode at fixed and repeatable temperatures. Additional details are given in Ref. [35].

6.4 Addressing Spatial Resolution Concerns. The optimal offset distance e was 1.7 mm because of physical constraints on filtering in the design, which prevented closer spacing between illuminating and receiving fibers. It has since been discovered that the use of this offset, considered with the fiber core diameters and numerical aperture values of the fiber used, did not allow an intersection between the acceptance angle of the receiving fibers (defined by their numerical aperture) and the primary illumination cone (defined by the numerical aperture of the illuminating fiber) in Fig. 3. However, it has been verified that our eight-receiving fiber probe assembly still allows weak transmission of light even

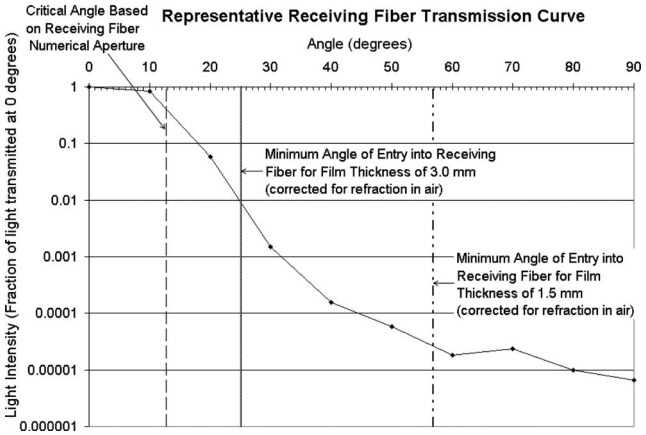

Fig. 10 Variation in transmitted light through receiving fiber of incident red laser light at angles from 0 deg to 90 deg from the receiving fiber tip as measured with a photomultiplier tube

outside of this acceptance angle (see Fig. 10). For establishing this fact, a red laser at a constant offset distance of approximately 0.8 m from the receiving fiber tip was used and the laser beam was tilted through 90 deg from pointing directly at a receiving fiber (0 deg in Fig. 10) to pointing perpendicular to the receiving fiber tip (90 deg in Fig. 10). A photomultiplier tube, shunt resistor, and a personal computer (PC) oscilloscope were used to record the intensity of the transmitted light. It may be seen from Fig. 10 that the "tails" on the transmission spectrum extend well beyond the acceptance angle defined by the numerical aperture of the receiving fiber (marked on Fig. 10), into the region necessary for transmission of light emanating directly from the primary illumination cone (also marked on Fig. 10) defined by the numerical aperture of the illuminating fiber. Although the transmissibility in this region is quite low (approximately two or more orders of magnitude lower than the peak, where the laser light is shining directly on the receiving fiber tip, it is nonetheless too large to be ignored. It must therefore be concluded that a significant portion of the light entering the receiving fibers, at least for experiments conducted with this probe, came directly from the primary illumination cone without reflection from the interface, as defined in condition (i) for the definition of $S_{f|L\text{-}V}$ in Sec. 5.2. There is thus a competition between attenuations due to reflection of fluorescent light and fluorescence of reflected illumination light from the interface and the attenuation of the fluorescent light coming directly from the primary illumination zone due to its wide angle of incidence on the receiving fibers. We currently do not have a good estimate on the ratio of reflected fluorescence to direct fluorescence. Whether or not it is already good, the following proposed modifications and experiments will improve it further and quantify it.

Additionally, the spatial resolution of the sensor for $e = 1.7$ mm may be impaired by the spread angle of the primary illumination cone in Fig. 11. However, the planned modifications (including hardware) depicted in Fig. 11 allow $e < 1.7$ mm and, therefore, the spatial resolution is expected to become nearly equal to the area of the illuminated spot on the interface where it passes over the primary illumination cone. Incidentally, a suitable gradient refractive index (GRIN) lens on the tip of the illuminating fiber can make the illuminating cone quite cylindrical—this may be desirable for adapting this method to a larger range of film thicknesses. As may be seen in Fig. 11, even without a GRIN lens, the spread angle of the primary illumination cone is quite small (11.3 deg from normal) due to the low numerical aperture of the illuminating fiber (0.22) and the relatively high index of refraction of the doped liquid (1.251 at 25°C).

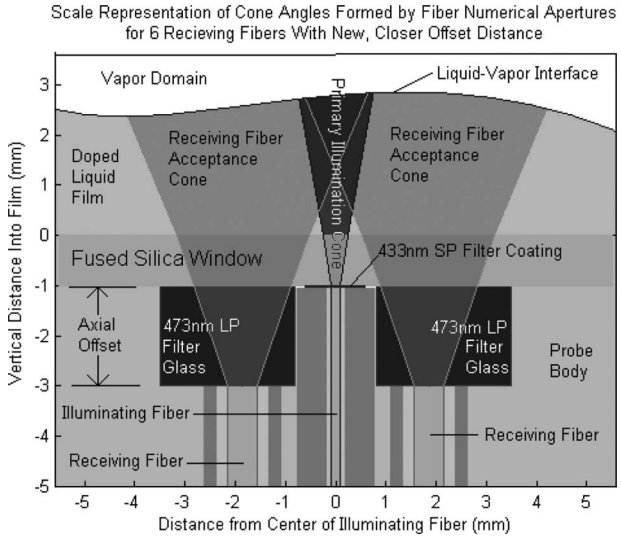

Fig. 11 Scaled schematic of preliminary concept probe. Note that the zones within the primary illumination cone from which fluorescent light is able to enter one or more receiving fibers directly within their acceptance cones (dark regions where the primary illumination cone and receiving fiber acceptance cone(s) intersect).

7 Calibration Results, Errors, and Sensor's Resolutions

7.1 Calibration Results. One of the three curves shown in Fig. 12(*a*) gives the principal D versus d calibration curve for a film that should remain valid even for dynamic films under environmental conditions similar to the one in Fig. 7(*a*). The other curves in Figs. 12(*b*)–12(*d*) demonstrate the attainment of the required one-to-one correspondence between "D versus $S_{f|L\text{-}V}$," "$S_{f|L\text{-}V}$ versus $S_{f|\text{No } L\text{-}V}$," and "$S_{f|\text{No } L\text{-}V}$ versus d" relationships. For cases with high N_P/D, such as the one in Fig. 13, D versus $S_{f|L\text{-}V}$ fails to achieve one-to-one correspondence and the calibration principle is not satisfied. The reported results are from experiments for the paired set of calibration described in Sec. 5.1 for stationary horizontal films with interface angle of 0 deg. In fact the linearity of $S_{f|\text{No } L\text{-}V}$ versus d curves, as shown in Figs. 12(*a*) and 12(*d*), is theoretically expected. Although, in principle, this straight line fit should pass through $S_{f|\text{No } L\text{-}V}=0$ when $d=0$; the experimental results show an offset not only in Figs. 12(*a*) and 12(*d*), but also in other experimental results (e.g., see figures 64–67 in Ref. [35]). This is, in all likelihood, due to some nonlinear behavior over $0 \text{ mm} \le d \le 0.5$ mm that arises from the fact that for very small d, for which e/d (e is offset in Fig. 3) is large, the absorption of the interface and black surfaces in the calibration

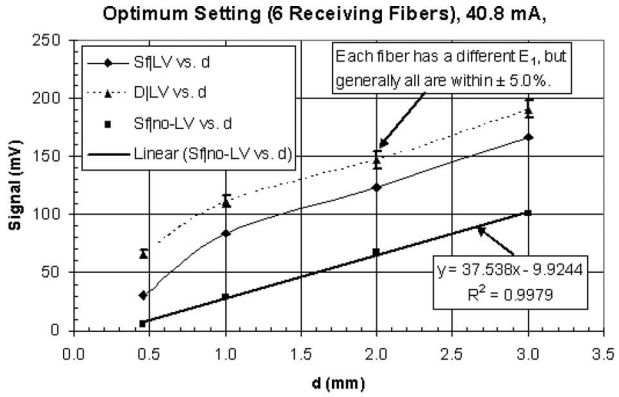

(a) Interface Angle Error, E_1

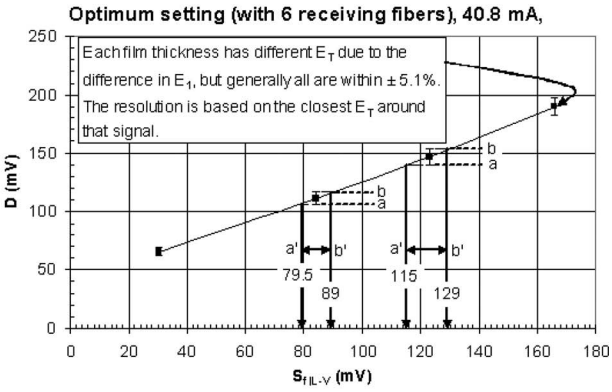

(b) Total Error in Detected Light, E_T

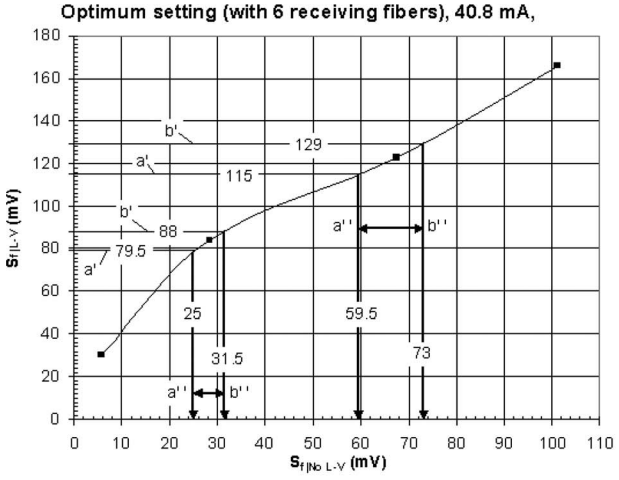

(c) Effect of Liquid-Vapor Interface

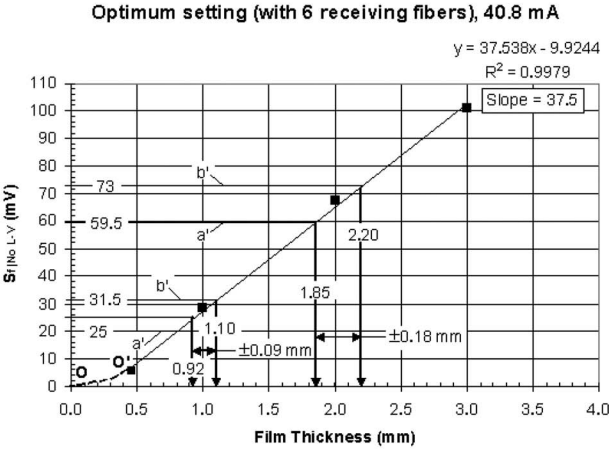

(d) Sensor Resolution

Fig. 12 (*a*) Errors E_1 of the developed sensor for interface angle of ±10 deg; (*b*) correspondence of estimated error E_T for D and error for $S_{f|L\text{-}V}$; (*c*) correspondence of estimated errors between $S_{f|L\text{-}V}$ and $S_{f|\text{No } L\text{-}V}$ for this calibration; and (*d*) resolutions of the developed sensor displayed on the $S_{f|\text{No } L\text{-}V}$ versus film thickness curve

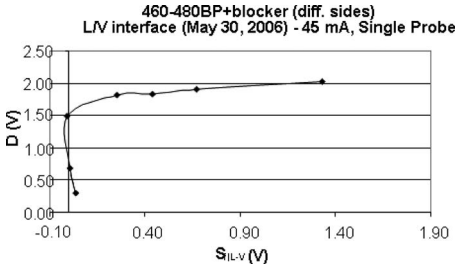

Fig. 13 Appearance of a nonmonotonic $D-S_{f|L\text{-}V}$ curve if N_P is not sufficiently small with respect to D. This test was done under conditions of a higher LD excitation current. The filtering is described in Ref. [35].

chamber quenches all the fluorescent light. The nature of this part of the curve is not experimentally understood but is schematically estimated in Fig. 12(*d*) as a dashed curve O−O′.

The one-to-one correspondence obtained in Figs. 12(*a*)–12(*d*) establish the functionality of the proposed calibration principle, which allows use of this sensor without requiring $N_P \approx 0$ or $D \approx S_{f|\text{No } L\text{-}V}$. All that is required is that the departure amounts of $N_P \neq 0$ and $D-S_{f|\text{No } L\text{-}V} \neq 0$ must be such that the one-to-one correspondence of the types shown in Figs. 12(*a*)–12(*d*) be achievable.

Once the in situ calibration curve of D versus d of the type shown in Fig. 12(*a*) is available and it satisfies the one-to-one correspondence principle of the type shown in Figs. 12(*b*)–12(*d*), one can use the calibration curve in Fig. 12(*a*) to convert experimentally measured values of time-varying signal D—in an actual sensor application involving a dynamic film (in a configuration similar to the one described in Fig. 7(*a*))—to obtain the corresponding time-varying values of film thickness d. The time-varying values simply follow from associating the instantaneous values of signal D with instantaneous thickness d—through the type of D versus d curve shown in Fig. 12(*a*).

7.2 Errors and Resolution. The developed sensor has errors in the detected light D and these calibration errors need to be related to the error or resolution in the measurement of film thickness d. The errors are of types E_1, E_2, and E_3 described below.

7.2.1 E_1. E_1 are errors associated with the fact that experimentally detected light D does not achieve perfect θ independence.

In real applications of the developed sensor, to find the film thickness d, a calibrated $S_{f|\text{No } L\text{-}V}$ versus d curve should ideally be used instead of an experimentally obtained D versus d curve. However, using the experimentally obtained D values alone is practical because experimental measurements only give the D signals and any use of the underlying calibration curves must come from separately performed calibration experiments. Errors E_1 associated with the measurements in D are the variations in D due to changes in θ. A maximum error of $E_1 = \pm 5.0\%$ times D were achieved for the reported results (for $\theta_{\max} = 10$ deg) and these are shown as vertical bars in D versus d curve in Fig. 12(*a*). The reported errors E_1 have been obtained from calibration experiments performed for $\theta = 0$ deg and various angles up to $\theta_{\max} = 10$ deg.

It is expected that when hardware changes to facilitate experiments over $-20 \text{ deg} \leq \theta \leq 20$ deg becomes available, θ independence over a much larger range will be experimentally verified. Even for waves with θ in the larger range, the sensor's resolution can be further improved without sacrificing its range of applicability as far as its ability to resolve instantaneous film thickness are concerned. For example, if it is found that, for a larger $\theta_{\max}$, E_1 can only be contained within $\pm 7-9\%$ of D, then the sensor's resolution (see definition in Eq. (4) below) can still be further improved because increasing the number of symmetrically placed receiving fibers in Fig. 2 improves resolution by increasing $\partial D/\partial d$ values (more ΔD for same Δd) in Eq. (4) below.

It is important to note that the current calibration equipment allows only the investigation of interface angles that are planar over the entire area of the calibration chamber. This means that the symmetrical placement of the receiving fibers would still yield relative θ independence in the current calibration configuration in Fig. 9, even if the fluorescent light reflected from the interface reduces the effective spatial resolution of the sensor to an averaged film thickness value over an area between the area illuminated by the primary illumination cone and the perimeter defined by the inside edges of the receiving fiber cores. The planned new probe design represented in Fig. 11 is expected to yield superior performance by ensuring that the fluorescent light directly received from the primary illumination cone significantly dominates any reflected fluorescent light or light fluorescing in secondary illumination cones, improving the spatial resolution such that the sensing area is defined only by the volume of the primary illumination zone in Fig. 3, allowing larger amplitudes and shorter wavelengths to be effectively resolved. Modified calibration arrangements to test the probe's response are under consideration and would be implemented if and when the new probe design is implemented. This new design would allow quantification of the effects of further reducing the offset distance e such that light from the primary illumination cone enters the receiving fibers within the acceptance angle defined by their numerical aperture (0.44 for the new probe design) and the index of refraction of the doped FC-72 film.

7.2.2 E_2. E_2 are errors due to variations in concentration and temperature of the doped solution from those at reference concentration and reference temperature employed in obtaining the temperature curves. This type of error can be minimized by picking the most suitable reference concentration and reference temperature.

If one expects a deviation in concentration or temperature, and it is possible to in situ measure or otherwise know their values in the measurement application, one may generate a series of calibration curves at various temperatures and concentrations, which cover the range of conditions actually experienced in the measurement situation (see results reported in Ref. [35]).

7.2.3 E_3. E_3 are errors associated with imperfect variations in fixed system settings (e.g., rigidity of optical connectors, quality of temperature and current control of laser light source, resolutions of various electronic instruments, etc.). These errors have been found, through repetition of experiments for the reported data set, to be within $\pm 1.1\%$ of D.

7.2.4 E_T. Total error E_T associated with the detected light D from the developed sensor is computed from $E_T = [E_1^2 + E_2^2 + E_3^2]^{1/2}$. This definition of E_T is valid as long as the underlying assumptions of causal independence among E_1, E_2, and E_3 and the assumption of Gaussian distribution of each of the error components (if sufficient and large number of experiments were performed) are considered to be reasonable.

Due to variations in E_1 with film thickness, each film thickness value has, in general, different E_T associated with its D. Over the entire range of $0.5 \text{ mm} \leq d \leq 3 \text{ mm}$, E_T is calculated to be within $\pm 5.1\%$ of D. E_T for $S_{f|L\text{-}V}$ and $S_{f|\text{No } L\text{-}V}$ are similarly obtained through the indicated use of associated error bars in Figs. 12(*b*) and 12(*c*) (see lines *a*-*b*, *a*′-*b*′, and *a*″-*b*″). In any graph, the horizontal error bar (e.g., line *a*′-*b*′ in Fig. 12(*b*)) is obtained by dividing the associated vertical error bar (line *a*-*b*) by the mean local slope of the curve in the figure (i.e., D versus $S_{f|L\text{-}V}$ curve's slope in Fig. 12(*b*)).

7.2.5 Sensor Resolution. The sensor's resolution at any measured film thickness d is given by

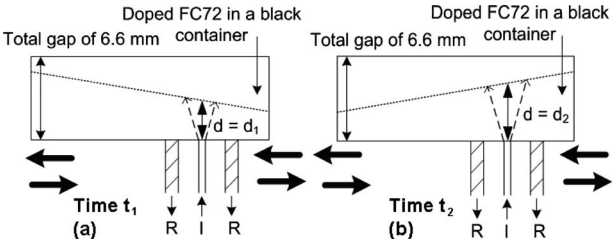

Fig. 14 Dynamic liquid film measurement test that yields time-varying thicknesses, where the static thickness (not shown) is designated as d_0: (*a*) with dynamic response $d(t_1)=d_1<d_0$, and (*b*) with dynamic response $d(t_2)=d_2>d_0$

$$\Delta d \cong \left\{ 1/\frac{\partial D}{\partial d} \right\} \cdot E_T \tag{4}$$

where E_T is the total error and $\partial D/\partial d$ is the slope of the D versus d calibration curve in Fig. 12(*a*). The overall resolution Δd_o of the sensor is defined to be the maximum of Δd values obtained, over a range of d values, from Eq. (4).

8 Capability Verification of the Calibrated Sensor

The developed sensor has been used in a proof-of-concept experiment that has a time-varying film thickness at the measurement location.

Under forced (0–2 Hz) horizontal oscillations of the container (see Ref. [35] to note that the container forms a cylindrical hollow space of 2 in. diameter and height of 1 in. (25.4 mm)) in Fig. 14, local thickness measurements at an off-center location were performed. The oscillations caused the initially horizontal liquid film of 1.5 mm thickness to become dynamic, yielding a dynamic film of time-varying thickness at the offset location (see, in Fig. 14, suggested but simplified interface configurations at different times), where the film thickness is measured by the newly invented sensor. Note that the thickness oscillations at any point is not expected to be sinusoidal for two reasons as follows: (i) somewhat nonsinusoidal nature of the forced oscillations, and (ii) sloshing, i.e., the long term nature of the waves being detected result from a superposition of the forced waves and its continuous reflections off the container's walls.

The horizontal vibration ranging from 0 Hz to 2 Hz was applied to the container by an Accel Shaker from Labworks, Inc., Costa Mesa, CA. The film thickness measurements were found by signals D collected through the sensor. Under identical forcing conditions, independent film thickness measurements were also obtained by a direct mechanical measurement technique for the wave's amplitude. The wave's principal frequency was assumed to be the same as the shaker frequency. The separate and independent mechanical measurements were obtained at the same off-center location, where the I-tip (Fig. 2) of the sensor was in the experiment employing the sensor. The maximum wave amplitude was measured by placing a thin vertical needle directly above the off-center measuring location and by measuring the distance between the initial (prior to shaking) and final wetted lengths. The measurements yielded the amplitude of the oscillations whereas the time period T $(=1/f)$ of oscillations was determined by the shaker's frequency of 1 Hz.

The frequency and amplitude of the film thickness, as obtained by the newly invented sensor, are shown in Figs. 15(*a*) and 15(*b*). These measurements agree very well with independent measurements (marked by x in Figs. 15(*a*) and 15(*b*)) of the time-varying film thickness amplitude and period of oscillations. This establishes that the sensor is able to resolve both the amplitude and the frequency of the dynamic film. More sophisticated comparison experiments (not available at this time) are planned and they are likely to show very good agreement at all intermediate times—times between the crests and troughs—as well. The electronic and other noises of frequency greater than 10 Hz were filtered out for signal D, reported for dynamic films in Fig. 15(*c*) and reported for static films in Fig. 15(*d*). These filtered signals more accurately represent the actual waves for this validation experiment.

9 Conclusions

- Development and calibration of a fluorescence and fiber-optics based real-time film thickness sensor have been com-

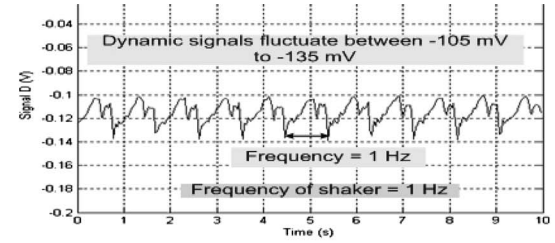

(a) Signal D (volts) vs. Time (s)

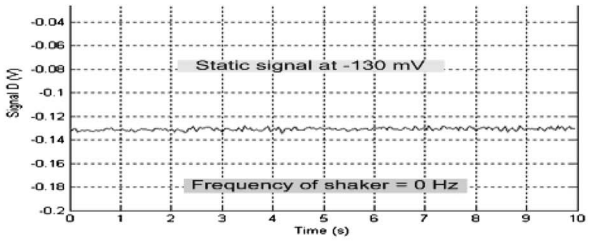

(b) Stationary Film Signal D (volts) vs. Time (s)

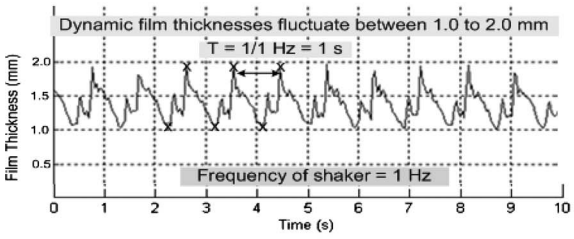

(c) Dynamic Thickness (mm) vs. Time (s)

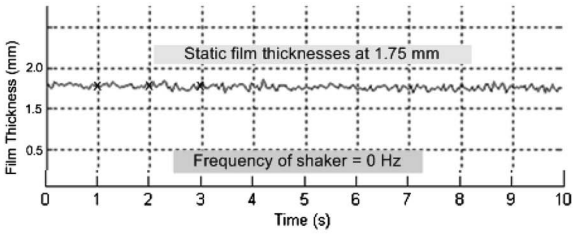

(d) Static Thickness (mm) vs. Time (s)

Fig. 15 (*c*) Signal D obtained for dynamic films at a fixed location in the calibration chamber in Fig. 14; (*d*) signal D obtained for stationary films of the same mean thickness at the same measurement location as in Fig. 15(*c*); (*a*) dynamic film thicknesses measured from the calibrated signal in Fig. 15(*c*) and its comparisons with alternative measurements (marked by x); and (*b*) stationary film thicknesses measured from the calibrated signal in Fig. 15(*d*) and its comparisons with alternative measurements (marked by x)

pleted. The verified and developed measurement principle and the calibration experiments are of more general value and can be used for fabricating any other sensor on this principle. Results for the sensor developed here show that the detected light D and fluorescent light $S_{f|L\text{-}V}$ increase with increasing liquid film thickness over a measurable range of 0.5–3.0 mm.

- The calibration strategy presented here is able to extract relevant information from experiments that show the presence of an unavoidable, nonzero amount of noise light N_P. This N_P is mostly due to the presence of noise light in the illuminating light and due to optical components' autofluorescence under excitation from the illuminating light. Signal improvement tests, noise source analyses, and hardware modifications have been implemented that ensure extraction, from D, the relevant signal $S_{f|\mathrm{No}\ L\text{-}V}$ associated with fluorescent light under minimized presence of noise light N_P, and minimized sensitivity of $S_{f|L\text{-}V}$ to the inclination angle θ of the liquid-vapor interface.
- Developed sensor reaches a near θ independence for D and N_P by combining two approaches. The first approach is to use optimal location of fiber mounting, optimal laser excitation current, and optimal filter settings to reduce the reflected light component of $S_{f|L\text{-}V}$ by minimizing $|S_{f|L\text{-}V} - S_{f|\mathrm{No}\ L\text{-}V}|$. The second approach is to use an array of six or more receiving fibers in a symmetrical arrangement surrounding an illuminating fiber.
- After taking into consideration issues related to repeatability of experimental data, errors of $\pm 1.1\%$ of D were found to be a good estimate. The total error E_T associated with measurements of D can be minimized to within $\pm 5.1\%$. This leads to a reasonable film thickness resolution of ± 0.09 mm (over 0.5–1.5 mm) and ± 0.18 mm (over 1.5–3.0 mm).
- The developed sensor has also been used in a proof-of-concept experiment that has a time-varying film thickness at the measurement location. The frequency and amplitude measurements of the film thickness obtained by the sensor agree very well with independent measurements of amplitude and frequency of the time-varying film thickness.
- An improved design for the next generation of this sensor has been reported. The improved probe's schematic is demonstrated in Fig. 11.

Acknowledgment

This work was supported by NSF and NASA under Grant Nos. CTS-0086988 and NNC04GB52G. We thank Dr. A. E. Smart for his initial guidance at the beginning of this project. We also thank Ralph Swafford and Oz Optics, Canada; and John Gauvin and Myriad Fiber Imaging for their advice and effort in making most of the custom optical components.

References

[1] Alekseenko, S. V., 1994, *Wave Flow of Liquid Films*, Begell House, New York.
[2] Kumar, R., Gottmann, M., and Sridhar, K. R., 2002, "Film Thickness and Wave Velocity Measurements in a Vertical Duct," ASME J. Fluids Eng., **124**, pp. 634–642.
[3] Tihon, J., 2004, "Hydrodynamics of the Solitary Waves Travelling Down a Liquid Film," XXI International Congress of Theoretical and Applied Mechanics, Warsaw, Poland, Aug. 15–21.
[4] Gorse, P., Busam, S., and Dullenkopf, K., 2006, "Influence of Operating Condition and Geometry on the Oil Film Thickness in Aeroengine Bearing Chambers," ASME J. Eng. Gas Turbines Power, **128**(1), pp. 103–110.
[5] Ghandhi, J. B., 2000, "Single- and Dual-Fiber Fluorescence Probes: Application to Oil-Film Measurements in an Internal Combustion Engine," Appl. Opt., **39**(30), pp. 5456–5464.
[6] Zaitsev, D. V., Kabov, O. A., and Evseev, A. R., 2003, "Measurement of Locally Heated Liquid Film Thickness by a Double-Fiber Optical Probe," Exp. Fluids, **34**, pp. 748–754.
[7] Lu, Q., 1992, "An Experimental Investigation of Heat Transfer With Condensation in a Horizontal Rectangular Duct," Ph.D. thesis, MEEM Department, Michigan Technological University, Houghton, MI.
[8] Shedd, T. A., and Newell, T. A., 2004, "Characteristics of the Liquid Film and Pressure Drop in Horizontal, Annular, Two-Phase Flow Through Round, Square and Triangular Tubes," ASME J. Fluids Eng., **126**, pp. 807–817.
[9] Than, C. F., Tee, K. C., Low, K. S., and Tso, C. P., 1993, "Optical Measurement of Slope, Thickness and Velocity in Liquid Film Flow," Smart Mater. Struct., **2**, pp. 13–21.
[10] Shedd, T. A., and Newell, T. A., 1998, "Automated Optical Liquid Film Thickness Measurement Method," Rev. Sci. Instrum., **69**(12), pp. 4205–4213.
[11] Perron, A., Kiss, L., and Verreault, R., 2006, "A Multifibre Optic Sensor to Meausre the Liquid Film Thickness Between a Moving Bubble and an Inclined Surface," Meas. Sci. Technol., **17**, pp. 1594–1600.
[12] Ohba, K., Takada, H., Kawakami, N., and Nagae, K., 1992, "Twin Fiber Optic Liquid Film Sensor for Simultaneous Measurement of Local Film Thickness and Velocity in Two-Phase Annular Flow," *Proceedings of the 6th International Symposium for Application of Laser Techniques to Fluid Mechanics*, Lisbon, Portugal, Vol. 39, No. 1, pp. 1–6.
[13] Qiu, H., Wang, X., and Hong, F., 2005, "Measurements of Interfacial Film Thickness for Immiscible Liquid-Liquid Slug/Droplet Flows," Meas. Sci. Technol., **16**, pp. 1374–1380.
[14] Wang, X., and Qiu, H., 2005, "Fringe Probing of Liquid Film Thickness of a Plug Bubble in a Micropipe," Meas. Sci. Technol., **16**, pp. 594–600.
[15] Nozhat, W. M., 1997, "Measurement of Liquid-Film Thickness by Laser Interferometry," Appl. Opt., **36**(30), pp. 7864–7869.
[16] Liu, A., Wayner, P. C., Jr., and Plawsky, J. L., 1994, "Image Scanning Ellipsometry for Measuring the Transient, Film Thickness Profiles of Draining Liquids," Phys. Fluids, **6**(6), pp. 1963–1971.
[17] Jones, G., Markvart, T., and Greef, R., 2001, "Deposition and Characterisation of Sensitising Dye Layers," *Proceedings of the Post Graduate Conference in Engineering Materials*, University of Southampton, Southampton, UK.
[18] Wu, X. L., Levine, R., Rutgers, M., Kellay, H., and Goldburg, W. I., 2001, "Infrared Technique for Measuring Thickness of a Flowing Soap Film," Rev. Sci. Instrum., **72**(5), pp. 2467–2471.
[19] Mouza, A. A., Vlachos, N. A., Paras, S. V., and Karabelas, A. J., 2000, "Measurement of Liquid Film Thickness Using a Laser Light Absorption Method," Exp. Fluids, **28**, pp. 355–359.
[20] Wittig, S., Himmelsbach, J., Noll, B., Feld, H. J., and Samenfink, W., 1992, "Motion and Evaporation of Shear-Driven Liquid Films in Turbulent Gasses," ASME J. Eng. Gas Turbines Power, **114**(2), pp. 395–400.
[21] Giroud-Garapon, S., Heid, G., and Lavergne, G., 2003, "Thin Wall Liquid Film Thickness Measurement: A Video Optical Technique," *Proceedings of PSFVIP-4*, Chamonix, France, Jun. 3–5.
[22] Cho, H., and Min, K., 2003, "Measurement of Liquid Fuel Film Distribution on the Cylinder Liner of a Spark Ignition Engine Using the Laser-Induced Fluorescence Technique," Meas. Sci. Technol., **14**(7), pp. 975–982.
[23] Jeremy, M. C., Noel, T., and Doherty, W. G., 2004, "Laser Induced Fluorescence Measurements of the Thickness of Fuel Films on the Combustion Chamber Surface of a Gasoline SI Engine," The Calouste Gulbenkian Foundation, 12th International Symposium, Lisbon, Portugal, Jul. 12–15.
[24] Hidrovo, C. H., and Hart, D. P., 2001, "Emission Reabsorption Laser Induced Fluorescence Film Thickness Measurement," Meas. Sci. Technol., **12**, pp. 467–477.
[25] Smart, A. E., and Ford, R. A. J., 1974, "Measurement of Thin Liquid Films by a Fluorescence Technique," Wear, **29**, pp. 41–47.
[26] Hentschel, W., Grote, A., and Langer, O., 1997, "Measurement of Wall Film Thickness in the Intake Manifold of a Standard Production SI Engine by a Spectroscopic Technique," SAE Paper No. 972832.
[27] Richardson, D. E., and Borman, G. L., 1991, "Using Fiber Optics and Laser Fluorescence for Measuring Thin Oil Films With Application to Engines," SAE Paper No. 912388.
[28] Driscoll, D. I., Schmitt, R. L., and Stevenson, W. H., 1992, "Thin Flowing Liquid Film Thickness Measurement by Laser Induced Fluorescence," ASME J. Fluids Eng., **114**, pp. 107–112.
[29] Ebner, J., Gerendas, M., Schafer, O., and Wittig, S., 2002, "Dropplet Entrainment From a Shear-Driven Liquid Wall Film in Inclined Ducts: Experimental Study and Correlation Comparison," ASME J. Eng. Gas Turbines Power, **124**(4), pp. 874–880.
[30] Ting, L. L., 1980, "Development of a Laser Fluorescence Technique For Measuring Piston Ring Oil Film Thickness," ASME J. Lubr. Technol., **102**, pp. 165–171.
[31] Schmitt, R. L., Stevenson, W. H., and Simmons, H. C., 1982, "Optical Measurement of Liquid Film Thickness," *Proceedings of the Technical Program—Electro-Optics/Laser Conference and Exposition*, Vol. 33, pp. 31–35.
[32] Takamasa, T. and Hazuku, T., 2000, "Measuring Interfacial Waves on Film Flowing Down a Vertical Plate Wall in the Entry Region Using Laser Focus Displacement Meters," Int. J. Heat Mass Transfer, **43**, pp. 2807–2819.
[33] Takamasa, T. and Kobayashi, K., 2000, "Measuring Interfacial Waves on Film Flowing Down Tube Inner Wall Using Laser Focus Displacement Meter," Int. J. Multiphase Flow, **26**, pp. 1493–1507.
[34] Hazuku, T., Fukamachi, N., Takamasa, T., Hibiki, T., and Ishii, M., 2005, "Measurement of Liquid Film in Microchannels Using a Laser Focus Displacement Meter," Exp. Fluids, **38**, pp. 780–788.
[35] Ng, T. W., 2006, "Development and Calibration of a Fluorescence and Fiber-Optics Based Real-Time Thickness Sensor for Dynamic Liquid Films," Ph.D. thesis, MEEM Department, Michigan Technological University, Houghton, MI.

On the Mach Number Invariance of Gas Jets Expanding Into Hot or Cold Environments

R. Sambasivam
Technology Group (Global Wires and Longs),
Tata Steel Ltd.,
Jamshedpur 831 001, India
e-mail: rsambasivam@tatasteel.com

F. Durst
FMP Technology GmbH,
Am Weichselgarten 34,
D-91058 Erlangen, Germany

Gas jet flows expanding into a space containing the same medium but at a significant temperature difference are of concern in many fields of engineering. One such example is the expansion of supersonic oxygen jets in the basic oxygen furnace (BOF) steelmaking process. While studying the characteristics of such gas jets, an interesting invariance of the local Mach number with the change in the surrounding temperature was found. The velocity and temperature of the jet at any given location increased with the increasing ambient temperature. However, the local Mach number remained the same for all ambient temperatures. This interesting result was further studied since there is no mention of it in any published literature. The reasons for these characteristics of the jet are analyzed in this paper. It is stressed that this finding is of practical importance and can be used in experimental studies of submerged gas jets expanding into environments with different ambient temperatures. [DOI: 10.1115/1.3222735]

1 Introduction and Aim of Work

The theory of submerged gas jets expanding in spaces containing the same medium is considered to be well developed. Numerous theories and experimental studies on various characteristics of expanding gas jets are available [1–16], and the results are summarized in the books by Abramovich [11] and Pai [12]. It is generally believed on the basis of the numerous studies available on this subject [1–16] that all the characteristics of the submerged gas jets are well understood. However, the authors found an interesting behavior of submerged gas jets, which is the so-called local Mach number invariance, while studying supersonic oxygen jets expanding into high temperature surroundings in the basic oxygen furnace (BOF) or Linz–Donawitz (LD) steelmaking process. Since there is no mentioning of these characteristics in any published literature to the best of the authors' knowledge, a detailed study was carried out numerically, and the results are presented in this paper.

While studying the expansion of a supersonic oxygen jet of Mach number 2.3 at the nozzle exit into its surroundings maintained at 300 K and 1000 K, the authors found out the Mach number invariance with the ambient temperature, as shown in Fig. 1. It is easy to observe in this figure that the velocity and temperature profiles along the axis of the jet change significantly with the change in ambient temperature, whereas the local Mach number remains the same, i.e., displays a characteristic independent of the ambient temperature. It seems that the temperature and the velocity profiles of the gas jet adjust themselves with the change in ambient temperature to maintain its local Mach number at any given location. Hence, the local Mach number profiles are governed only by the inlet conditions at the nozzle exit, and not by the ambient conditions of the space the jet expands into. It is stressed in this paper that this result has physical significance, and can be used in experimental studies of gas jets. A detailed analysis was carried out to understand this invariance better, and the results are summarized here.

The physical reasoning for the Mach number invariance with the change in ambient temperature is given in Sec. 2. Numerical simulations were performed to validate the conclusions drawn from some theoretical reasoning made in Sec. 2 using the commercially available computational fluid dynamics software, FLUENT 6.3. The results are presented in Sec. 3. In Sec. 4, the physical significance of this result and the possible use of the Mach number invariance in practical applications are stated. Finally, Sec. 5 presents a detailed summary, some final remarks, and conclusions.

2 Theoretical Considerations of the Mach Number Invariance

The authors considered it worthwhile to explore whether there exists some theoretical basis, experimental evidence or references for the observed Mach number invariance of expanding jet flows [1–17]. To the best of the authors' knowledge, there is no literature available on the influence of the ambient temperature on the Mach number characteristics of expanding gas jets. There are some analytical solutions available for the development of velocity and temperature profiles of submerged jets [11,12,17]. It was not possible to analyze the Mach number invariance with these solutions. One of the well known characteristics of submerged gas jets is that the integral momentum of the jet remains constant [9,17] at any cross section of the jet. This can be mathematically expressed as

$$\text{Momentum of the jet at any cross section,} \quad 2\pi\int_0^\infty \rho(x,r)U(x,r)^2 r\,dr = \text{const} \tag{1}$$

In Eq. (1), ρ is the local density of the jet, U is the local velocity, and x and r are the axial and radial coordinates, respectively. It is well known that the pressure p can be assumed to be constant in submerged gas jets [17]. Hence, from the ideal gas law, the density can be written as follows:

$$\rho(x,r) = \frac{p}{RT(x,r)} = \frac{A}{T(x,r)} \tag{2}$$

where A is a constant and given by $A=p/R$, where R is the gas constant, and T is the local temperature in K. It is interesting to note that any change in temperature will influence only the density since the pressure remains a constant throughout the domain. By substituting Eq. (2) in Eq. (1), one can obtain the momentum characteristics in terms of local Mach number M, as given below:

Contributed by the Heat Transfer Division of ASME for publication in the JOURNAL OF HEAT TRANSFER. Manuscript received September 16, 2008; final manuscript received August 6, 2009; published online December 22, 2009. Review conducted by Yogesh Jaluria

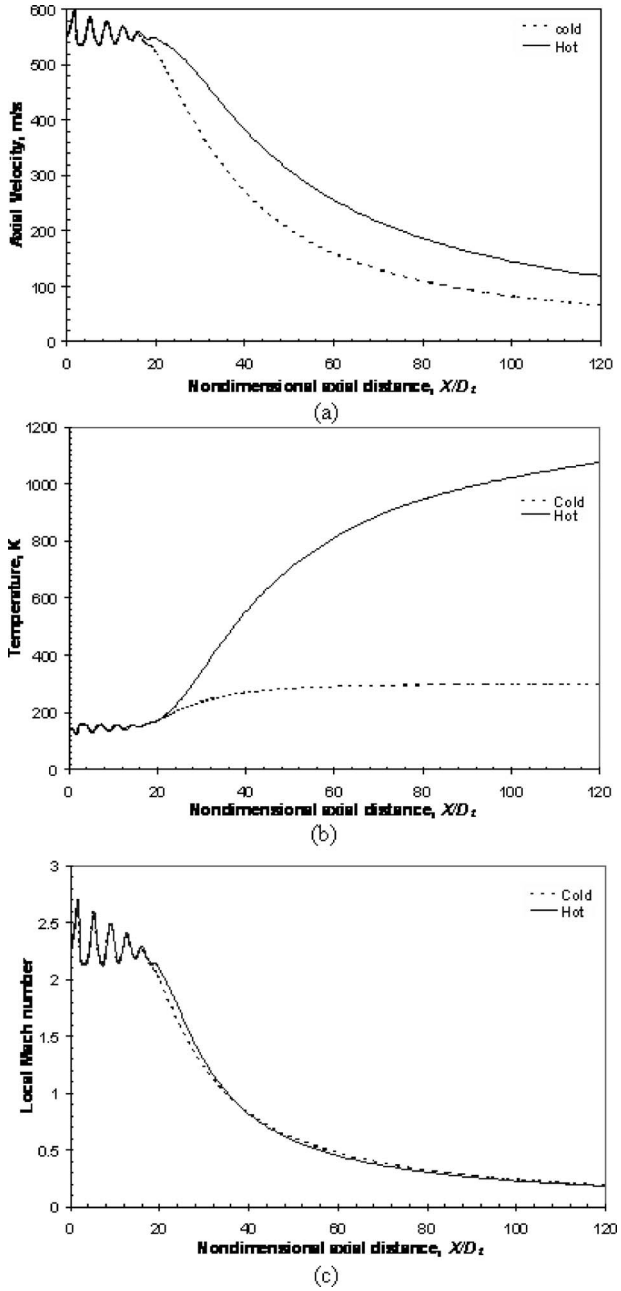

Fig. 1 Mach number invariance of a supersonic oxygen jet expanding into environments of 300 K and 1000 K: (*a*) axial velocity along the axis of the jet (*b*) temperature along the axis of the jet, and (*c*) local Mach number along the axis

$$2\pi B\int_0^\infty M(x,r)^2 r dr = \text{const} \tag{3}$$

where $B=A\gamma R$, and γ is the ratio of specific heats. The local Mach number M is defined as

$$M(x,r) = \frac{U(x,r)}{\sqrt{\gamma RT(x,r)}} \tag{4}$$

From Eq. (3), one can deduce that the integral Mach number at every axial location, x, remains constant for all temperatures. However, it is not possible to claim from Eq. (3) that the local Mach number at every axial and radial location also remains invariant with the ambient temperature. Hence, further analysis was necessary to establish this special property of submerged gas jets.

Since the submerged jet falls into the category of free shear layer flows, the axial gradients of the flow quantities are, in general, much smaller than their radial counterparts. Hence, it is possible to use the boundary layer form of the governing equations to analyze the flow theoretically [10,17]. It was felt that one could explore theoretically the fundamental reasons for the Mach number invariance with the change in ambient temperature with such simplified equations. Further, the viscous dissipation terms were also neglected in the energy equation for the theoretical analysis.

The equations in cylindrical coordinates in boundary layer form are as follows:

$$\text{Continuity equation} \quad \frac{\partial(\rho U_x)}{\partial x} + \frac{1}{r}\frac{\partial(r\rho U_r)}{\partial r} = 0 \tag{5}$$

$$\text{Axial momentum equation} \quad \frac{\partial(\rho U_x U_x)}{\partial x} + \frac{1}{r}\frac{\partial(\rho r U_x U_r)}{\partial r} = \frac{1}{r}\frac{\partial}{\partial r}\left(r\mu_{\text{eff}}\frac{\partial U_x}{\partial r}\right) \tag{6}$$

$$\text{Energy equation} \quad \frac{\partial(\rho U_x C_p T)}{\partial x} + \frac{1}{r}\frac{\partial(r\rho U_r C_p T)}{\partial r} = \frac{1}{r}\frac{\partial}{\partial r}\left(r\lambda_{\text{eff}}\frac{\partial T}{\partial r}\right) \tag{7}$$

where x and r are the axial and radial coordinates, respectively, U_x and U_r are the axial and radial velocity components, respectively, and T is the local temperature of the jet. μ_{eff} and λ_{eff} are the local effective viscosity and thermal conductivity, respectively, and these are defined as

$$\mu_{\text{eff}} = \mu + \mu_t \quad \text{and} \quad \lambda_{\text{eff}} = \lambda + \lambda_t \tag{8}$$

where μ and μ_t are the local dynamic viscosity and eddy viscosity, respectively. Similarly, λ and λ_t represent the local and eddy thermal conductivities of the flow, respectively. The turbulent viscosity and thermal conductivity are related through the turbulent Prandtl number Pr_t

$$\text{Pr}_t = \frac{\mu_t C_p}{\lambda_t} \tag{9}$$

In turbulent round jets, the turbulent viscosity μ_t can be modeled as constant [17] within the shear layer. It is generally assumed that the turbulent Prandtl number is close to unity. For a perfect gas, the variation of specific heat capacity C_p with the temperature is negligible. Therefore, from Eq. (9), one can deduce easily that the eddy thermal conductivity can be approximated to be a constant within the shear layer. Thus, Eqs. (6) and (7) can be rewritten as

$$\frac{\partial(\rho U_x U_x)}{\partial x} + \frac{1}{r}\frac{\partial(\rho r U_x U_r)}{\partial r} = \mu_{\text{eff}}\frac{1}{r}\frac{\partial}{\partial r}\left(r\frac{\partial U_x}{\partial r}\right) \tag{10}$$

$$\frac{\partial(\rho U_x T)}{\partial x} + \frac{1}{r}\frac{\partial(r\rho U_r T)}{\partial r} = \frac{\lambda_{\text{eff}}}{C_p}\frac{1}{r}\frac{\partial}{\partial x}\left(r\frac{\partial T}{\partial r}\right) \tag{11}$$

By substituting Eq. (2), Eqs. (10) and (11) can be rewritten as follows:

$$\frac{\partial\left(\frac{A}{T}U_x U_x\right)}{\partial x} + \frac{1}{r}\frac{\partial\left(\frac{A}{T}r U_x U_r\right)}{\partial r} = \mu_{\text{eff}}\frac{1}{r}\frac{\partial}{\partial r}\left(r\frac{\partial U_x}{\partial r}\right) \tag{12}$$

$$\frac{\partial(AU_x)}{\partial x} + \frac{1}{r}\frac{\partial(rAU_r)}{\partial r} = \frac{\lambda_{\text{eff}}}{C_p}\frac{1}{r}\frac{\partial}{\partial x}\left(r\frac{\partial T}{\partial r}\right) \tag{13}$$

By substituting Eq. (4), Eqs. (12) and (13) become

$$B\left[\frac{\partial(M_x M_x)}{\partial x} + \frac{1}{r}\frac{\partial(rM_x M_r)}{\partial r}\right] = \mu_{\text{eff}}\frac{1}{r}\frac{\partial}{\partial r}\left(r\frac{\partial U_x}{\partial r}\right) \tag{14}$$

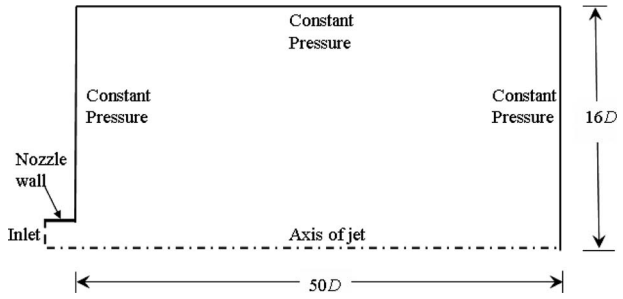

Fig. 2 Schematic representation of the geometry and the boundary conditions

$$A\left[\frac{\partial(U_x)}{\partial x}+\frac{1}{r}\frac{\partial(rU_r)}{\partial r}\right]=\frac{\lambda_{\text{eff}}}{C_p}\frac{1}{r}\frac{\partial}{\partial x}\left(r\frac{\partial T}{\partial r}\right) \tag{15}$$

Since the effective Prandtl number, as defined in Eq. (9), is close to unity, the values of the coefficients on the right-hand sides of Eqs. (14) and (15) are identical, i.e., the diffusive transports of the momentum and thermal energy in the turbulent shear layer of the jet are similar. It is also interesting to note in Eq. (15) that the temperature is dropped from the left-hand side of the energy equation, i.e., the convective transport of enthalpy is zero. Any change in temperature is balanced by an equivalent change in density. Hence, the net influence of the convective heat fluxes in the energy equation at any location can be neglected completely. Further, as observed in Eq. (14), the convective terms of the momentum equation can be written in terms of the local Mach number.

The above mentioned arguments can be summarized as follows. (a) It is clear that there is a unique balance between the diffusive transport of heat and momentum in the shear layer. Further, the net influence of convective transport of thermal energy is zero. (b) From the classical theory of submerged jets, it can be stated that the integral Mach number at every cross section remains constant, as shown in Eq. (3). (c) All the above findings point toward a possibility of the local Mach number to be invariant of the surrounding temperature. (d) However, the above stated arguments cannot be considered to be a conclusive proof. Therefore, it was decided to carry out more numerical simulations to analyze this invariance thoroughly.

3 Numerical Investigations

Since the purpose of numerical simulations was to establish the invariance of the local Mach number of the jet with the surrounding temperature, the simulations were done for subsonic jets only. The commercial computational fluid dynamics software, FLUENT 6.3, was used to carry out the simulations.

Table 1 Boundary conditions used in the simulations

Nozzle inlet conditions for subsonic flow simulations	
Gas velocity	125 m/s
Stagnation temperature	300 K
Density	1.177 kg/m^3
Speed of sound	347.2 m/s
Inlet Mach number	0.36
Nozzle diameter	0.03 and 0.06 m
Inlet turbulent intensity	10%
Medium used in simulations	Air
Ambient conditions	
Ambient temperatures studied	300, 400, 500, 600, 700, 800, and 1000 K
Ambient pressure	Standard atmosphere (101.325 kPa)

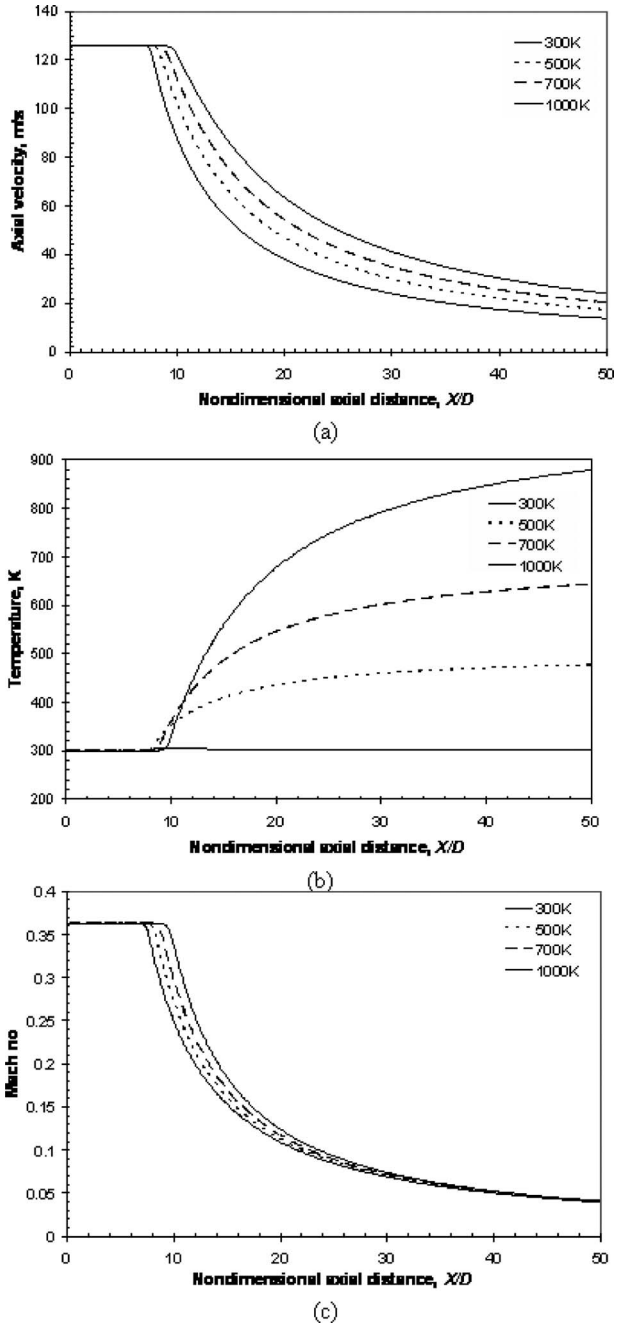

Fig. 3 Mach number invariance of a subsonic jet expanding into environments of different temperatures: (*a*) axial velocity along the axis of the jet, (*b*) temperature along the axis of the jet, and (*c*) local Mach number along the axis of the jet

3.1 Geometry and Boundary Conditions. The geometry and boundary conditions used in the simulations are shown schematically in Fig. 2. The jet was assumed to be axisymmetric, and the dimensions of the entire flow geometry were chosen to be 50*D* and 16*D* in the axial and radial directions, respectively, where *D* is the diameter of the nozzle. Two nozzle diameters were studied, as shown in Table 1. Air was chosen as the working fluid. The variations of the thermodynamic fluid properties with temperature were taken completely into account. The ideal gas law was used to calculate the local density of the gas. The pressure in the domain was chosen to be that of the standard atmosphere. The standard $k-\varepsilon$ turbulence model was used in the simulations to close the system of equations for turbulent flows. All calculations were car-

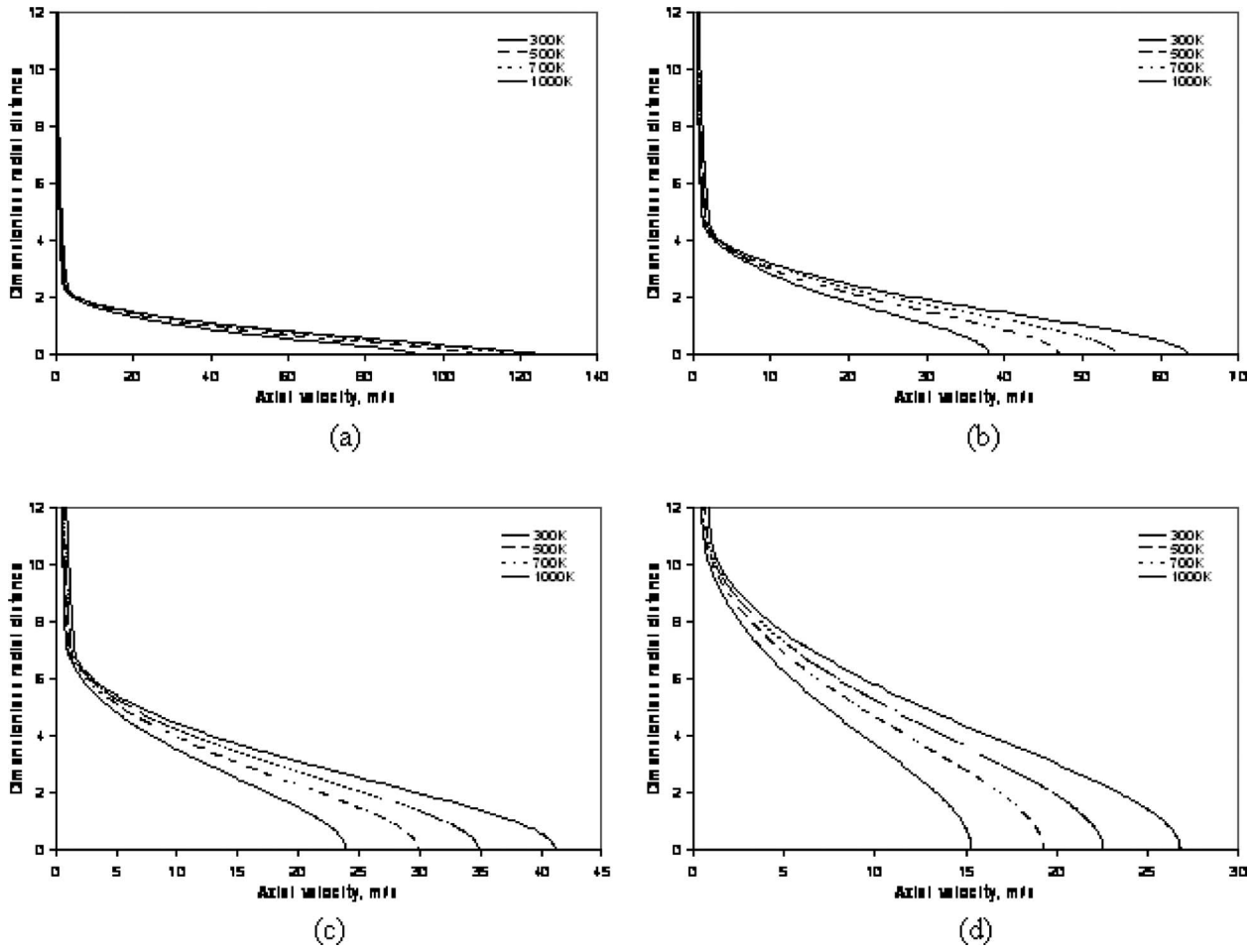

Fig. 4 Comparison of axial velocity profiles of the subsonic jet expanding into surroundings of different temperatures at *x*/*D*: (*a*) 10, (*b*) 20, (*c*) 30, and (*d*) 45

ried out with the second-order discretization scheme, and the PISO algorithm was employed for pressure-velocity coupling.

The boundary conditions applied in the numerical simulations are summarized in Table 1. The nozzle exit Mach number was fixed to be 0.36. The ambient temperature was varied over a wide range to study its influence on the jet characteristics. A grid independence study was carried out, and the velocity and temperature profiles at different axial locations obtained with different grid levels were compared. Based on these studies, the final grid chosen had 350 cells and 160 cells in the axial and radial directions, respectively. The solutions were considered converged after the residuals dropped several orders of magnitude, i.e., when the residuals reached a value close to 10^{-6}.

3.2 Results and Discussion. The high intensity turbulent interactions between the jet and its surroundings result in transports of momentum and thermal energy, and hence, the jet influences a wider cross section of the surroundings as it travels in the axial direction. The exchange of momentum between the jet and its surroundings leads to a decrease in the jet velocity, and a gradual increase in the net mass flow rate of the jet in the axial direction. One can easily comprehend that as the temperature of the surrounding increases, the density of the ambient fluid decreases, and hence, the mass entrained by the jet from the surroundings is also decreased. This leads to a reduced exchange of jet momentum with the environment. Therefore, it is expected that the velocity at all locations in the jet will increase when the ambient temperature is raised. This can be clearly observed in Fig. 3(*a*), where the axial velocity along the axis of the jet is shown for various ambient temperatures. From this figure, it is evident that the jet retains higher velocities while expanding in hotter environments.

It is obvious that the temperature along the axis of the jet will increase as it travels through the hot environment, as shown in Fig. 3(*b*). The heat transfer from the surroundings to the jet is enhanced by the presence of intense turbulence mixing in the shear layer. This helps the jet to approach the temperature of the surroundings as it moves in the axial direction. However, it is interesting to note that there exists a near-perfect balance in the development of the velocity and temperature profiles so as to retain the local Mach number profile constant, irrespective of the temperature of the surroundings, as shown in Fig. 3(*c*). As stated before, there is no mentioning of this feature of the submerged gas jet in the published literature, to the best of our knowledge. From the classical theory of submerged jets, it is only possible to state that the integral Mach number at every cross section remains constant, with change in the surrounding temperature, as explained in Sec. 2. However, it is evident that the local Mach number also remains invariant with the change in the surrounding temperature, as described here. Furthermore, it is worth notingthe deviations in the local Mach number profiles at small dimensionless axial distance values as shown in Fig. 3(*c*). A detailed error analysis is presented to explain this, later in this paper.

Figures 4–6 present the local axial velocity, temperature, and Mach number profiles, respectively, as a function of the dimensionless radial coordinate at various nondimensional axial loca-

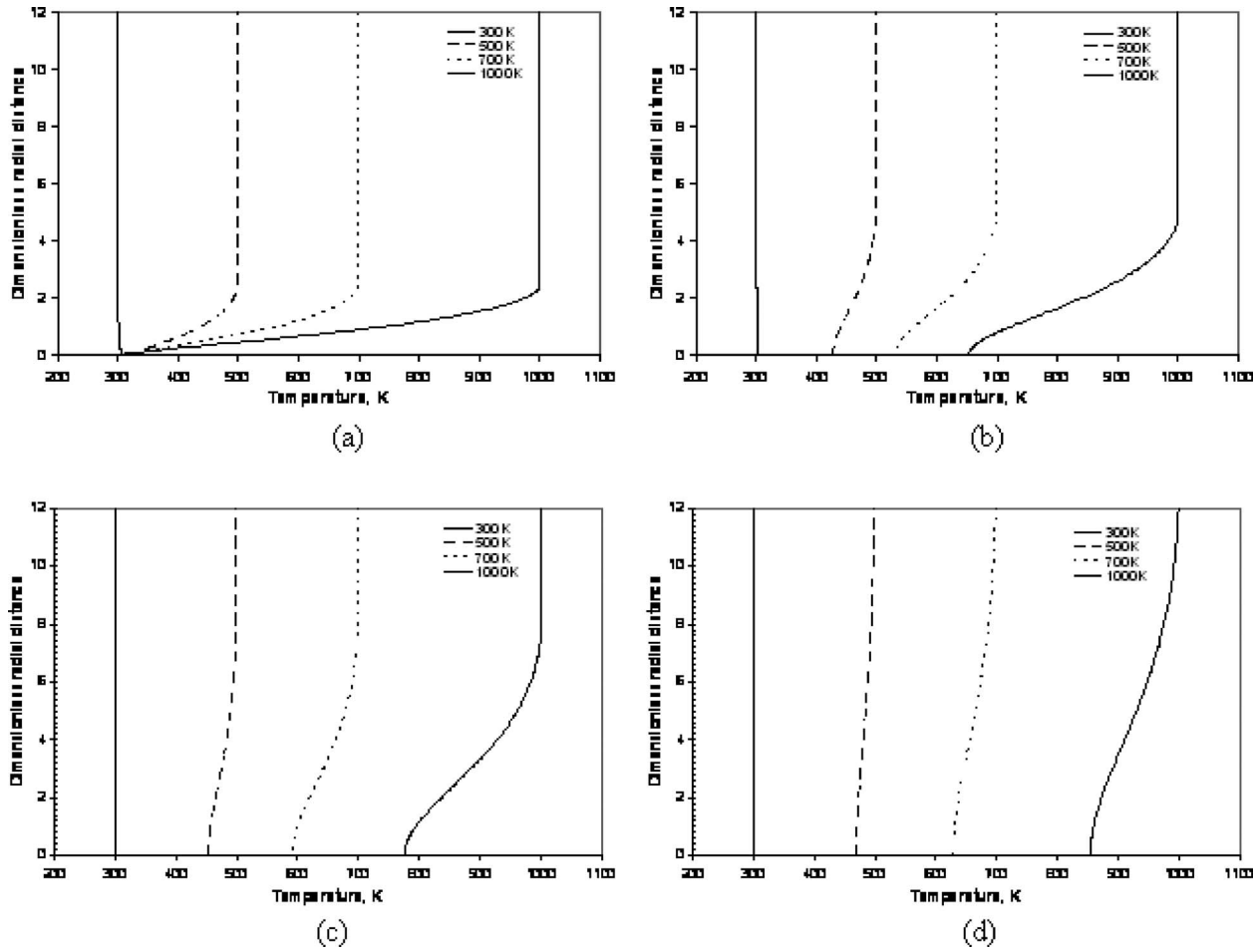

Fig. 5 Comparison of temperature profiles of the subsonic jet expanding into surroundings of different temperatures at *x*/*D*: (*a*) 10, (*b*) 20, (*c*) 30, and (*d*) 45

tions and surrounding temperatures. As observed in Fig. 4, the axial velocity increases with the increasing ambient temperature due to the reduced mass entrainment into the jet. Further, the temperature profiles in the radial direction are also significantly influenced by the ambient temperature, as shown in Fig. 5. However, as shown in Fig. 6, the local Mach number profiles remain nearly insensitive to the change in the ambient temperature, and converge to a single Mach number profile. These results point toward the balance between the transports of momentum and heat between the surroundings and the jet to ensure the Mach number invariance with the ambient temperature, as described earlier in Sec. 2. As shown in Eqs. (1) and (3), it is possible to state that the integral momentum of the jet remains constant at all cross sections. However, in the present analysis, it has been shown that the local momentum also remains constant for different surrounding temperatures.

3.3 Further Analysis of Mach Number Profiles. As discussed in Sec. 3.2, it is evident that an invariance of the Mach number, with respect to the ambient temperature, exists. However, the computed local Mach number profiles do not match perfectly, as shown in Figs. 3(*c*) and 6, whereas the local Mach number profiles obtained for the supersonic jet, as shown in Fig. 1(*c*), are identical for different ambient temperatures. Hence, it is necessary to estimate the deviations observed in the Mach number profiles, and also to find the exact reasons for this behavior. In Fig. 7, the deviations in the local Mach number profiles along the axis of the subsonic jet, in comparison with the average profile calculated over the ambient temperature range considered in this study, are shown for various ambient temperatures. Further, the mean Mach number profile is also plotted in this figure for reference.

As observed in Fig. 7, the maximum deviations occur near the end of the potential core region, i.e., the region where the velocity at the axis of the jet starts decreasing from the value at the exit of the nozzle. It is evident from Fig. 3(*a*) that the length of the potential core of the jet changes with the ambient temperature. As the ambient temperature increases, the length of the potential core also increases due to the decrease in momentum transfer from the jet to the surroundings because of less entrainment of ambient mass into the jet. As stated earlier, for the local Mach number profiles to be invariant with the surrounding temperature, the heat and momentum transfer have to be in balance. It is argued that in the downstream parts of the jet, this balance is achieved through strong turbulent mixing. To substantiate this argument, it is required to analyze the structure of a submerged gas jet, as shown schematically in Fig. 8.

As soon as the jet leaves the nozzle into the surroundings, a high intensity turbulent shear layer engulfs the core of the jet through which the momentum and heat transfer occur between the jet and its surroundings. Because of this intense momentum transfer, the velocity of the jet along the axis decreases quickly in the downstream direction. Downstream of the potential core region, the high intensity turbulent region occupies the whole of the cross section of the jet. The potential core region is the least turbulent region of the whole jet. It is well known that the transport of

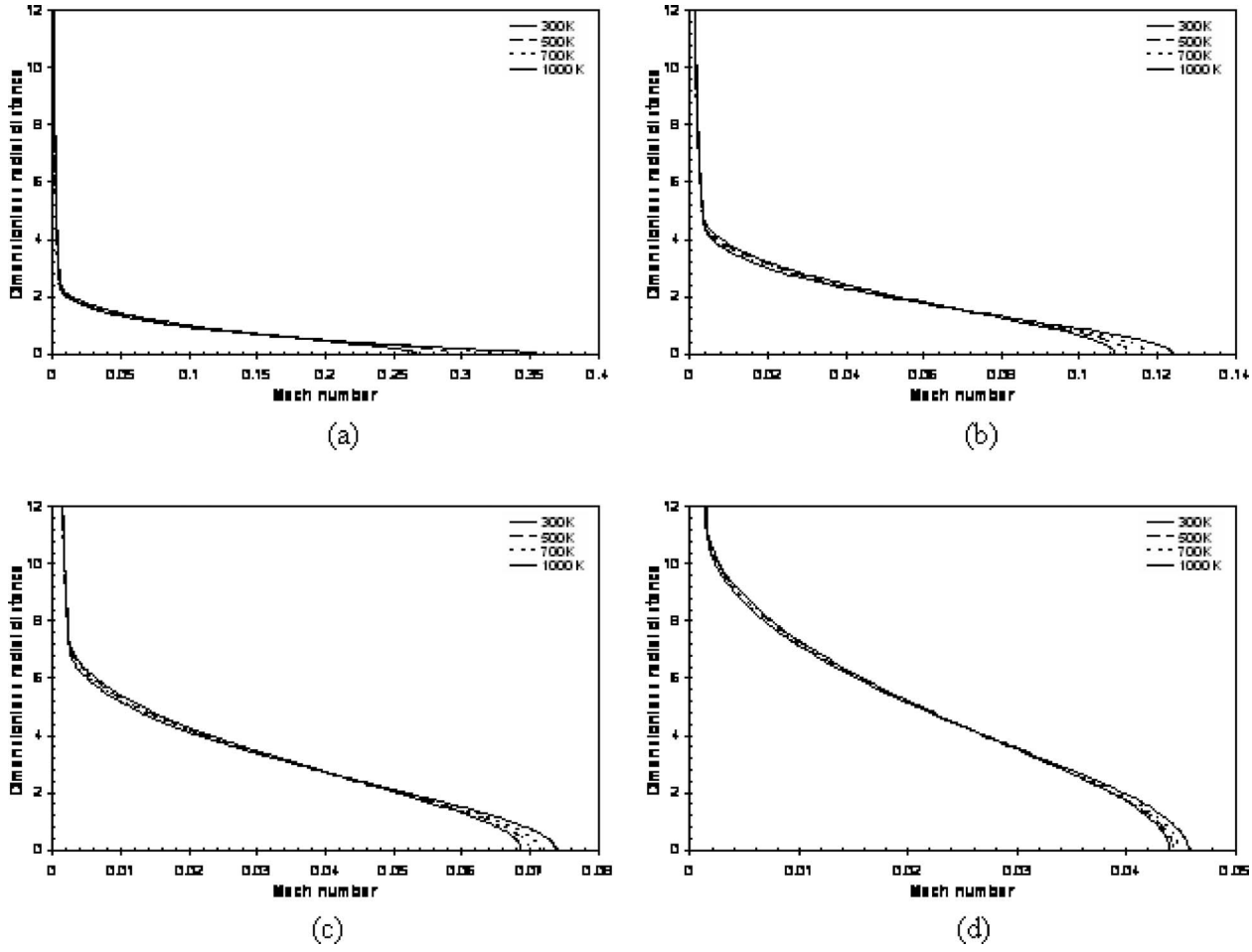

Fig. 6 Comparison of Mach number profiles of the jet expanding into surroundings of different temperatures at x/D: (*a*) 10, (*b*) 20, (*c*) 30, and (*d*) 45

momentum and heat are almost similar in the turbulent region of the jet because of the turbulent Prandtl number being close to unity. However, the potential core of the jet is less turbulent, and therefore, the molecular transport properties of momentum and heat also determine the rate of transport in this region. This can be seen clearly in Fig. 9, where the effective viscosity profiles of the jet expanding into various ambient temperatures are shown at different axial locations. As observed in this figure, the effective viscosity in the potential core region, i.e., at $x/D=10$, is much smaller near the axis of the jet than in the turbulent shear layer region. However, farther downstream the jet becomes fully turbulent, and the peak of the effective viscosity profiles shifts toward the axis. The effective thermal conductivity profiles display a similar behavior, and they are omitted here for brevity.

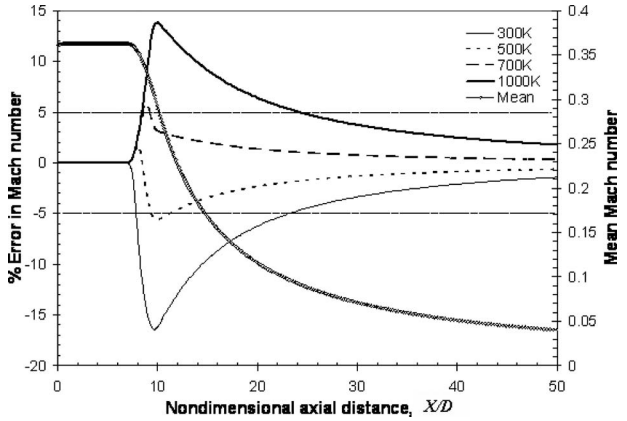

Fig. 7 Deviation of Mach number profiles from the mean along the axis of the subsonic jet for different ambient temperatures

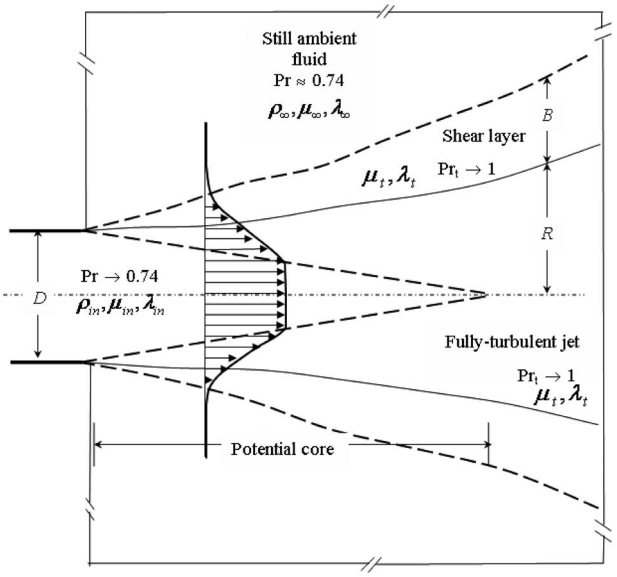

Fig. 8 Schematic representation of the structure of a submerged gas jet

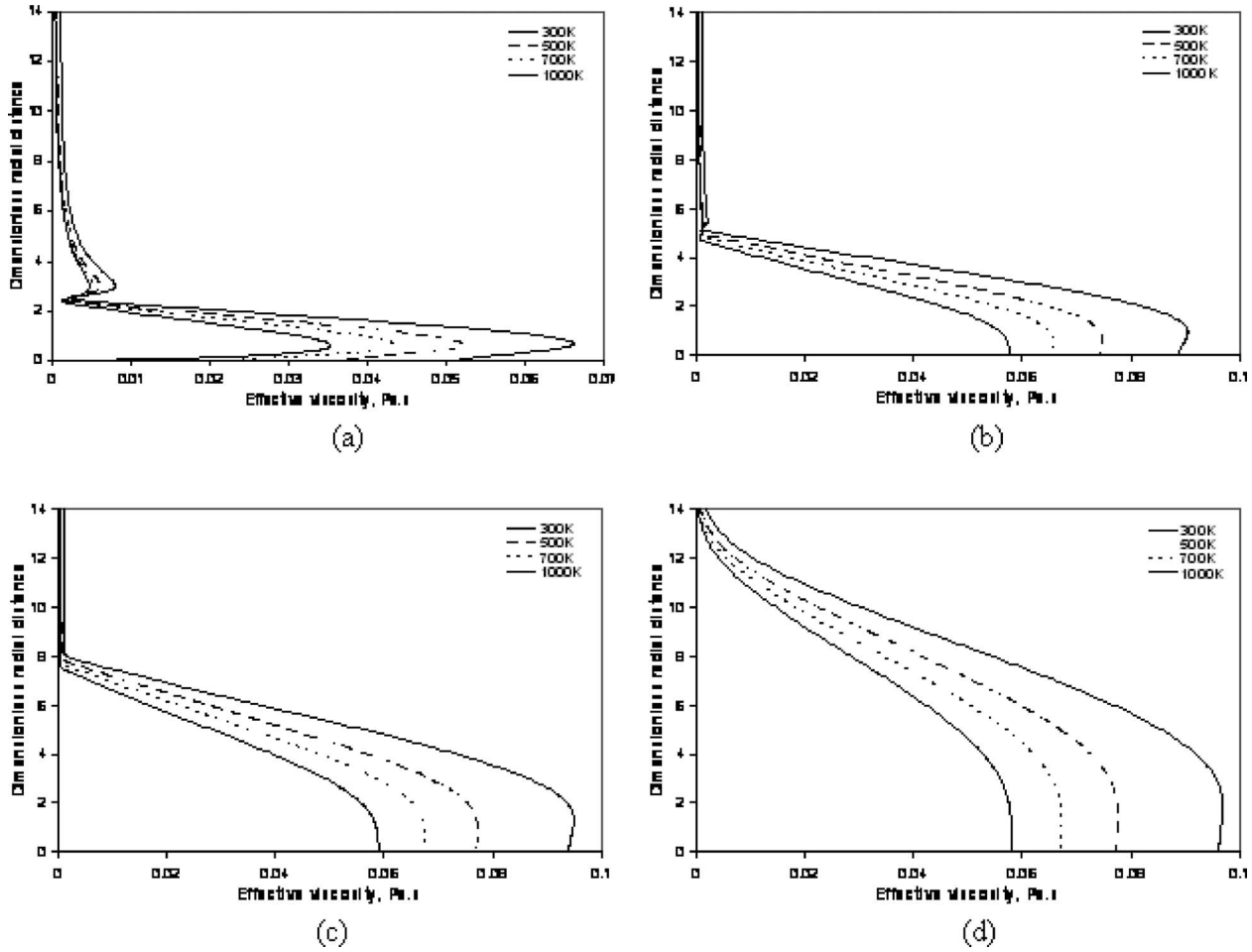

Fig. 9 Comparison of effective viscosity profiles of the jet expanding into surroundings of different temperatures at *x*/*D*: (*a*) 10, (*b*) 20, (*c*) 30, and (*d*) 45

The low turbulence intensity in the potential core region results in a difference in the transports of momentum and heat in this region, and hence, the jet expanding into the hotter environment retains more momentum, as seen in Fig. 3(*a*). As the jet becomes fully turbulent, the heat and momentum transports become balanced, and the local Mach number profiles become increasingly identical, as seen in Fig. 7. When the flow becomes fully turbulent earlier such as for the supersonic jet shown in Fig. 1, the balance between heat and momentum transports occurs earlier, and the local Mach number profiles converge faster to a single profile.

4 Implications of the Mach Number Invariance

In the LD-steelmaking process, cold supersonic oxygen jets are expanded into surroundings at temperatures above 1500 K. On the contrary, in aerospace and defense applications, high temperature gas jets expand into environments that are at a relatively low temperature. There are other applications as well, where the Mach number invariance stated above can be of practical importance. The analysis in Secs. 2 and 3 showed conclusively that the local Mach number is independent of the ambient temperature downstream of the potential core region where the jet is fully turbulent. If experiments were to be carried out to study the characteristics of jets expanding into environments of different temperatures, up to now, it would have been considered necessary to measure both the velocity and temperature profiles accurately at different locations. When the Mach number invariance is taken into account, the number of experiments can be reduced significantly. By measuring the temperature profiles at other surrounding temperatures, one can obtain all the characteristics of the jet by employing the local Mach number invariance. The experimenter benefits in two ways: Tedious velocity measurements at high temperature conditions are avoided, and the number of experiments is also reduced. Further, the stated Mach number invariance is also of academic value as it reveals an important, and so far, an apparently unknown characteristic of the jet.

5 Summary and Conclusions

Submerged gas jets are in widespread use in many fields of engineering, and it is, in general, believed that they are understood thoroughly. However, based on the analytical and numerical analysis, a unique ambient temperature independence of the local Mach number profiles was identified. The following major conclusions can be drawn from this study.

1. When a gas jet expands through a gaseous medium at different temperatures, the velocity at any location of the jet increases with the increasing ambient temperature, due to the reduced mass entrainment from the surroundings because of the lower ambient density. Similarly, the temperatures in the jet also increase when the ambient temperature is raised.
2. The local Mach number at any location of the jet remains independent of the ambient temperature.
3. Small deviations of the local Mach number profiles were observed near the potential core region, which is less turbulent. These deviations were less pronounced for supersonic jets.

4. The observed Mach number invariance is of practical importance, and can be used in experimental studies of jets expanding into different ambient temperatures.

Nomenclature

C_p = specific heat at constant pressure (J/kg K)
M = local Mach number
p = local static pressure (Pa)
Pr_t = turbulent Prandtl number
R = gas constant
r = radial coordinate (m)
T = local temperature (K)
U_r = radial velocity component (m/s)
U_x = axial velocity component (m/s)
x = axial coordinate (m)

Greek Symbols

ρ = local density ($\mathrm{kg/m^3}$)
γ = ratio of specific heats
λ = local molecular thermal conductivity (W/m K)
λ_{eff} = local effective thermal conductivity (W/m K)
λ_t = local turbulent thermal conductivity (W/m K)
μ = local molecular dynamic viscosity (Pa s)
μ_{eff} = local effective viscosity (Pa s)
μ_t = local turbulent viscosity (Pa s)

References

[1] Bickley, W., 1937, "The Plane Jet," Phil. Mag., **23**, pp. 727–731.
[2] Schlichting, H., 1933, "Laminare Strahlenausbreitung," Z. Angew. Math. Mech., **13**, pp. 260–263.
[3] Squire, H. B., 1951, "The Round Laminar Jet," Q. J. Mech. Appl. Math., **4**, pp. 321–329.
[4] Squire, H. B., 1955, "Radial Jets," *Fifty Years of Boundary Layer Research*, W. Tollmien and H. Görtler, eds., Vieweg, Braunschweig, Germany, pp. 47–54.
[5] Krzywoblocki, M. Z., 1949, "On Steady, Laminar Round Jets in Compressible Viscous Gases for Behind the Mouth," Oesterr. Ing.-Arch., **3**, pp. 373–383.
[6] Pack, D. C., 1954, "Laminar Flow in an Axially Symmetrical Jet of Compressible Fluid Far From the Orifice," Proc. Cambridge Philos. Soc., **50**, pp. 98–104.
[7] Goertler, H., 1954, "Decay of Swirl in an Axially Symmetrical Jet Far From the Orifice," Rev. Mat. Hisp.-Am., **14**, pp. 143–178.
[8] Howarth, L., 1938, "Concerning the Velocity and Temperature Distributions in Plane and Axially Symmetrical Jets," Proc. Cambridge Philos. Soc., **34**, pp. 185–203.
[9] Durst, F., 2006, *Theorie and Praxis der Stroemungsmechanik – eine Einfuehrung*, Springer-Verlag, Berlin.
[10] Schlichting, H., 1979, *Boundary Layer Theory*, McGraw-Hill, New York.
[11] Abramovich, G. N., 1963, *The Theory of Turbulent Jets*, Massachusetts Institute of Technology, Cambridge, MA.
[12] Pai, S. L., 1954, *Fluid Dynamics of Jets*, Van Nostrand, New York.
[13] Prandtl, L., 1935, "The Mechanics of Viscous Fluids," *Aerodynamic Theory*, Vol. 1W. F. Durand, ed., pp. 16–208.
[14] Görtler, H., 1942, "Berechnung von Aufgaben der freien Turbulenze auf Grund eines neuen Naherungsansatzes," Z. Angew. Math. Mech., **22**, pp. 244–254.
[15] Hinze, J. O., and van der H Zijnon, B. G., 1948, "Transfer of Heat and Matter in the Turbulent Mixing Zone of an Axially Symmetric Jet," *Proceedings of the 7th International Congress for Applied Mechanics*, Vol. 2, pp. 286–299.
[16] Reichardt, H., 1941, "Ueber eine neue Theorie der freien Turbulenz," Z. Angew. Math. Mech., **21**, pp. 257–264.
[17] Bejan, A., 1995, *Convection Heat Transfer*, 2nd ed., Wiley, New York, Chap. 8.

Boris Schilder
Department of Mechanical Engineering,
Technische Universitaet Darmstadt,
Petersenstrasse 30,
64287 Darmstadt, Germany

Simon Yu Ching Man
School of Mechanical and Aerospace Engineering,
Nanyang Technological University,
50 Nanyang Avenue,
Singapore 639798, Singapore

Nobuhide Kasagi
Department of Mechanical Engineering,
University of Tokyo,
Tokyo 113-8656, Japan

Steffen Hardt
Center of Smart Interfaces,
Technische Universitaet Darmstadt,
Darmstadt D-64287, Germany

Peter Stephan[1]
Department of Mechanical Engineering,
Technische Universitaet Darmstadt,
Petersenstrasse 30,
64287 Darmstadt, Germany
e-mail: p.stephan@ttd.tu-darmstadt.de

Flow Visualization and Local Measurement of Forced Convection Heat Transfer in a Microtube

The pressure drop and the convective heat transfer characteristics of ethanol and water in a circular tube with a diameter of 600 μm with and without phase change have been studied experimentally. The test section consists of a glass tube coated with a transparent indium tin oxide heater film. For single-phase liquid flow (including superheated liquid) it was found that the measured Nusselt numbers and friction factors are in good agreement with the theoretical values expected from Poiseuille flow. Subsequently, the boiling heat transfer of ethanol was studied. It was found that boiling with bubble growth in both upstream and downstream directions leaving behind a thin evaporating liquid film on the tube wall is the dominant phase change process. Wavy patterns on the film surface indicate shear forces between vapor and liquid phase during slug flow. Temporary dryout phenomena occur even at a low mean vapor quality due to film rupture as a result of film instabilities. Local Nusselt numbers are calculated for the two-phase flow at different heat fluxes and Reynolds numbers. Compared with single-phase flow the heat transfer is enhanced by a factor of 3–8. [DOI: 10.1115/1.4000046]

1 Introduction

Heat and mass transfer in microchannels have been in the focus of intense research activities in the past decade due to their relevance in fields such as electronic equipment cooling and lab-on-a-chip technology. With regard to electronics, the heat flux density in microelectronic circuits has been constantly increasing, demanding more efficient cooling technologies. In this context, boiling heat transfer in microchannels or microtubes has been identified as a method for removing high heat fluxes.

Despite the amount of research work in this area, still numerous unexplained phenomena exist and conflicting results have been reported by different researchers around the globe. For example, the Nusselt numbers for single-phase flow were found to vary from values less than the corresponding value for the Poiseuille flow [1] to values three times higher than that. The friction factors for microchannels and tubes have also shown scattering results, and many researchers attributed the effects to the surface conditions of the channels. A good summary of the topic can readily be found in the papers by Sobhan and Garimella [2], Palm [3], and more recently Morini [4]. The scatter of the experimental results may be, in part, due to difficulties associated with the experimental setup and the quantifications of uncertainty levels, the temperature measurements, in particular. Due to the size of the tubes considered, direct temperature measurements on the inner wall and in the liquid were not possible; they were normally derived from the measurements of the outer wall temperature. Lelea et al. [5] and Celata et al. [6] are among the few who have shown results that are close to the predictions of the classical theory. Their experiments were conducted in a vacuum chamber to minimize heat losses.

For experiments involving phase change, one of the prime interests has been on the visualization of the bubble formation process. In many of the experiments previously conducted, nucleate boiling, plug flow, slug flow, and annular flow were identified as common flow patterns for microchannels and microtubes [7,8]. In contrast to macrosize tubes, in microtubes these flow patterns typically alternate with one another even at constant heat and mass fluxes. Besides these, unique microchannel flow patterns have also been described. Hetsroni et al. [9] found a rapid bubble growth phenomenon and called it explosive evaporation due to the short timescales observed. Zhang et al. [10] postulated different boiling mechanisms depending on the channel size. For channels larger than 100 μm in diameter, they expect nucleate boiling to be the major heat transfer process. In channels smaller than 50 μm, they identified explosive boiling without bubble nucleation as being dominant. Hardt et al. [11] observed explosive boiling processes with subsequent film evaporation in channels with $d_h = 50$ μm and assumed bubble nucleation to trigger this process. In the present investigation, an indium tin oxide (ITO) coated microglass tube has been used for heat and mass transfer studies. The arrangement can effectively generate a uniform heat flux along the outer surface of the tube without providing optical obstruction to the test section. By employing a high speed camera, the phase change at high heat fluxes could be visualized clearly.

2 Experimental Arrangement and Procedure

Figure 1 shows a schematic view of the experimental setup used in the present investigation. Distilled and degassed water and degassed ethanol are used as the working fluids for the convective heat transfer experiments. The working fluid is delivered to the test section via a HPLC Pump (GL Sciences, PU 714). The flow

[1]Corresponding author.

Contributed by the Heat Transfer Division of ASME for publication in the JOURNAL OF HEAT TRANSFER. Manuscript received October 20, 2008; final manuscript received July 31, 2009; published online January 4, 2010. Assoc. Editor: Yogesh Jaluria.

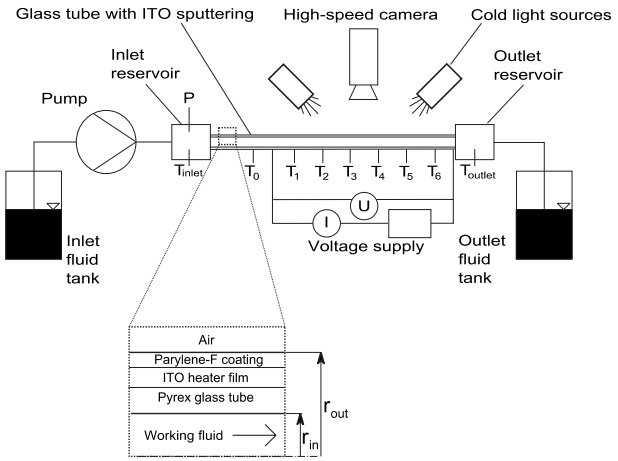

Fig. 1 Schematic view of the experimental setup

rate is accurate to within +/−1%. Experiments have been carried out in an inlet Reynolds number range of 25–202.

The fluid temperatures before and after the glass tube (T_{in} and T_{out}) are measured by 0.5 mm diameter K-type thermocouples in the inlet and outlet reservoir. The volume of the reservoirs is 3.5 cm^3 each. K-type thermocouples with a diameter of 25 μm are used for the measurement of the temperatures along the tube (T_0-T_6). These thermocouples are glued by silicone adhesive with a thermal conductivity of 1.53 W/m K to the outer wall of the tube. All thermocouples are calibrated for the experimental temperature range and have an accuracy of +/−0.1 K.

Pressure measurements are performed by a Sokken Pz-77 pressure transducer with an accuracy of +/−98.1 Pa. The flow visualization is conducted via a high speed camera (VISION RESEARCH PHANTOM V5.0) operated at a frame rate of up to 8100 per second with an interrogation area of 1024×1024 pixels. The glass tube test section is a 600 μm internal diameter tube (outer diameter 1000 μm) with a rather smooth inner surface; only shallow cavities with a diameter of 2–5 μm could be identified. The outer surface of the glass tube is coated with a 2 μm ITO/Ag film in such a way that Joule heating can be applied uniformly along the coated surface, which remains transparent. The uniformity of the electric resistance of the ITO film is within +/−5%. Silver paste with a specific electric resistance of 5×10^{-5} Ω cm is used to connect the copper wires to the ITO film to supply electric current.

It became evident that the ITO film is sensitive to oxidation. Figure 2 shows the electric resistance over time for the unprotected ITO film in the presence of air. Without heating the electric resistance monotonously increases; but if the film is exposed to external heating or Joule heating is applied, it decreases. Therefore, we protected the ITO film from the environmental oxygen by a 0.42 μm Parylene-F coating to avoid oxidation. A constant heat flux is created along the outer surface of the tube by applying a constant voltage between the two wires connected to the test section. The heating is stable to within +/−2% over a period of 6 h. The total length of the glass tube is 200 mm, of which a section of 110 mm is heated. The entry section in front of the heated section is 85 mm long to ensure hydrodynamically developed flow.

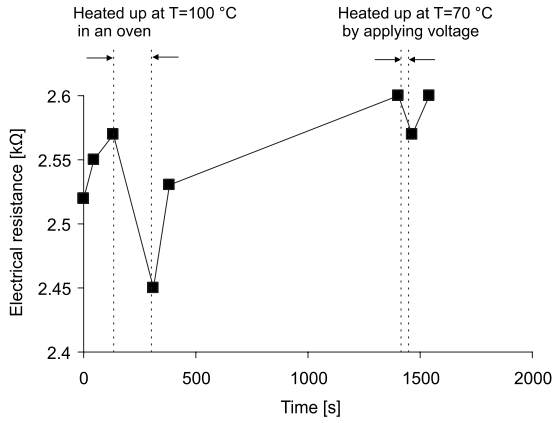

Fig. 2 Change of electric resistance of an unprotected ITO film

The experiments were conducted as follows. The working fluid is fed to the test section at room temperature ($T=23°C$). The flow rate of the working fluid and the heating voltage were adjusted to the desired values. To ensure quasisteady-state conditions, the measurement data were taken after a waiting time of 20 min. Temperature and pressure data were recorded every 464 ms. The recorded data of 40 measurement cycles were averaged for calculating the Nusselt number and friction factor.

3 Data Reduction and Uncertainties

3.1 Estimation of Heat Losses. In the present study the test section is not surrounded by a vacuum chamber to allow for flow visualization by a high speed camera. As a consequence special efforts need to be made to account for heat losses. Preliminary experiments with an empty test section were conducted to estimate heat losses due to free convection, conduction, and radiation. The heat transfer coefficient of the heat losses is defined as

$$h_{loss} = \frac{\dot{q}_{loss}}{T_{wall,out} - T_{amb}} \tag{1}$$

Due to the fact that no working fluid is employed in this case, the Joule heat is transferred to the ambience

$$\dot{q}_{loss} = \dot{q}_{heat} = \frac{VI}{\pi d_{out} l_{heat}} \tag{2}$$

where V and I are the voltage and the current measured at the copper wires connected to the tube, d_{out} is the outer diameter of the tube, and l_{heat} is the heated length. The experimentally estimated h_{loss} has been compared with calculations following the Nusselt number correlations for natural convection at the wall of a horizontal cylinder [12]. Depending on the tube temperature, the experimentally derived h_{loss} is up to 40% higher than the theoretical value for convection only. Additional heat losses due to radiation and conduction (axial along the tube and via the thermocouple and heater wires) are the likely reasons for this discrepancy. Nevertheless, it was found that the heat losses are less than 10% of the total heat input for all experiments with working fluid.

A second order polynomial is used to provide a continuous relationship for q_{loss} depending on $T_{wall,out}-T_{amb}$

$$\dot{q}_{loss} = (T_{wall,out} - T_{amb})^2 c_1 + (T_{wall,out} - T_{amb}) c_2 + c_3 \tag{3}$$

c_1, c_2, and c_3 are the coefficients that fit the experimental data best in a least-squares sense.

3.2 Calculation of Local Heat Transfer Performance. The local heat transfer performance for single-phase and two-phase flow between the inner wall of the tube and the working fluid is expressed by the dimensionless Nusselt number. The local Nusselt number is calculated for all thermocouple positions at the heated length of the tube

$$\mathrm{Nu}_{loc} = \frac{h_{loc} d_{in}}{\lambda_{liquid}} \tag{4}$$

The thermal conductivity of the pure liquid λ_{liquid} and the inner diameter of the tube have been used for calculating Nu_{loc} both for single-phase and two-phase flows.

The local heat transfer coefficient is given as

$$h_{\mathrm{loc}} = \frac{\dot{q}_{\mathrm{loc}}}{T_{\mathrm{wall,in}} - T_{\mathrm{bulk}}} \tag{5}$$

When pumping a working fluid through the tube, a part of the heat is transferred to the working fluid and another part to the ambience. The heat transferred to the working fluid is calculated as follows:

$$\dot{q}_{\mathrm{loc}} = \dot{q}_{\mathrm{heat}} - \dot{q}_{\mathrm{loss}} \tag{6}$$

$$\dot{q}_{\mathrm{loc}} = \frac{VI}{\pi d_{\mathrm{in}} l_{\mathrm{heat}}} - \dot{q}_{\mathrm{loss}} \tag{7}$$

$\dot{q}_{\mathrm{loss}}$ is calculated depending on the measured temperatures using Eq. (3). Due to the constant electric resistance of the ITO film along the tube, $\dot{q}_{\mathrm{heat}}$ is constant over the total heated area. The heat loss $\dot{q}_{\mathrm{loss}}$ is a function of the temperature difference $T_{\mathrm{wall,out}} - T_{\mathrm{amb}}$, which changes along the heated tube because of the heat transferred to the working fluid. Therefore, $\dot{q}_{\mathrm{loss}}$ and $\dot{q}_{\mathrm{loc}}$ are functions of the axial distance x.

The temperature at the inner wall of the tube at each thermocouple position is computed using the one-dimensional heat conduction equation in cylindrical coordinates

$$T_{\mathrm{wall,in}} = T_{\mathrm{wall,out}} - \frac{\dot{q}_{\mathrm{loc}} d_{\mathrm{in}}}{2\lambda_{\mathrm{tube}}} \ln \frac{d_{\mathrm{out}}}{d_{\mathrm{in}}} \tag{8}$$

The axial conduction number introduced by Maranzana et al. [13] has been calculated to find out whether the assumption of purely radial heat transfer is reasonable

$$\mathrm{Ma} = \frac{\dot{Q}_{\mathrm{cond,axial}}}{\dot{Q}_{\mathrm{conv,axial}}} = \frac{\frac{\lambda_{\mathrm{tube}}}{l_{\mathrm{heat}}} A_{\mathrm{cond}}}{\dot{M} c_p} \tag{9}$$

According to Maranzana axial conduction can be neglected if the conduction number Ma is lower than 10^{-2}. Depending on the flow rate, we found values ranging between 4.0×10^{-6} and 4.8×10^{-5}.

The average fluid temperature, referred to as bulk temperature, is calculated for each thermocouple position by taking the energy balance

$$T_{\mathrm{bulk}} = T_{\mathrm{in}} + \frac{1}{x} \int_0^{x_{\mathrm{th}}} \dot{q}_{\mathrm{loc}} dx \frac{\pi d_{\mathrm{in}} x_{\mathrm{th}}}{\dot{M} c_p} \tag{10}$$

where x_{th} is the axial distance of the thermocouple measured from the starting point of the heated length. For the evaluation of the integral, the heated length of the tube has been discretized by 110 cylindrical elements with an increment of 1 mm. For experiments where boiling has been observed, the maximum bulk temperature is specified as the saturation temperature of the liquid. The saturation pressure inside the tube is calculated by linear interpolation between the pressure in the inlet reservoir and the ambient pressure.

The heat transferred from each cylindrical element to the working fluid is then calculated in the same way as the local heat flux (Eq. (7)). The heat losses from the elements are estimated by using Eq. (3).

The mean outside wall temperature of the elements is interpolated by a third order polynomial. The coefficients of the polynomial are found by fitting the polynomial to the temperatures measured by the microthermocouples at the outside wall of the tube.

The local vapor quality for each measurement point is calculated by the energy balance

$$\chi = \frac{1}{x} \int_0^{x_{\mathrm{th}}} \dot{q}_{\mathrm{loc}} dx \frac{\pi d_{\mathrm{in}} x_{\mathrm{th}}}{\dot{M} \Delta h_{\mathrm{lv}}} - \frac{c_p (T_{\mathrm{sat}} - T_{\mathrm{in}})}{\Delta h_{lv}} \tag{11}$$

The temperature dependent fluid properties, such as viscosity, density, thermal conductivity, and specific heat, are calculated by polynomials provided in Ref. [12]. Due to a lack of physical properties for superheated liquid ethanol, data for higher pressure at the same temperature have been used. The database has been extrapolated to obtain liquid properties at temperatures higher than 100°C.

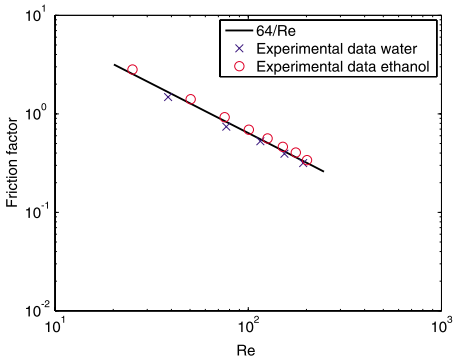

Fig. 3 Friction factor compared with theory for laminar flow

The equivalent wall heat flux due to heating of the liquid by viscous dissipation has been calculated to be less than 40 $\mathrm{W/m^2}$, which is in all cases less than 1% of the Joule heating and, thus, has been neglected.

The standard deviation of the Nusselt number due to the measurement uncertainties is calculated following the Gaussian error propagation formula to be less than $\Delta \mathrm{Nu}/\mathrm{Nu} = \pm 20\%$ for all test runs.

4 Results and Discussion

4.1 Single-Phase Flow. The pressure drop for water and ethanol was measured at room temperature ($T_{\mathrm{liquid}} = 23°\mathrm{C}$). The derived friction factor is well in agreement with the theory for laminar flow (friction factor $= 64/\mathrm{Re}$) for both liquids (Fig. 3). The secondary pressure losses due to hydrodynamically developing flow and the tube inlet/exit losses have been estimated and were found to be marginal (see the Appendix).

Figure 4 shows the typical temperature distribution for a single-phase flow heat transfer test run. The wall temperatures and the bulk temperatures are almost on parallel lines, indicating that the heat flux generated is uniformly distributed along the surface, and heat losses are marginal.

Figure 5 shows the local Nusselt numbers for two Reynolds numbers and six different heat fluxes. They converge toward the classical value for constant heat flux and Poiseuille flow (Nu $= 4.36$) at about 80% of the heated tube length. Higher Nusselt numbers at the entrance to the heated section are a consequence of

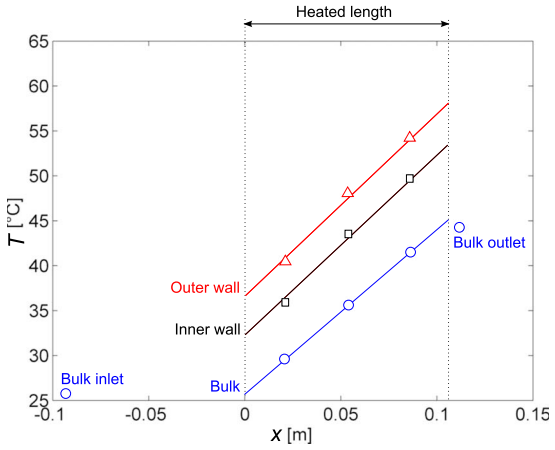

Fig. 4 Outer wall, inner wall, and bulk temperature

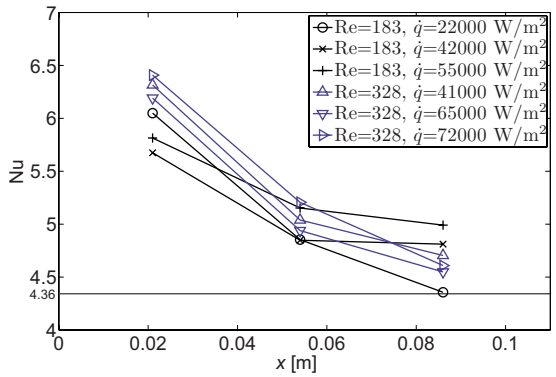

Fig. 5 Nusselt number variation in flow direction for single-phase heat transfer

thermal entrance effects. Grigull and Tratz [14] investigated the thermal entrance problem for laminar flow with constant heat flux numerically and evaluated the Nusselt number as a function of the dimensionless axial distance ($x/(d\ \mathrm{Re}\ \mathrm{Pr})$). In Fig. 6 the data of multiple test runs using water and ethanol are compared with the correlation of Grigull and Tratz. The liquid ethanol could be significantly superheated without observing phase change inside the tube. Using Eq. (10) a maximum liquid bulk superheat of about 40 K at the end of the heated length of the tube has been calculated. The data referring to superheated ethanol represent the local measured Nusselt numbers for liquid ethanol at temperatures above saturation. If the experimental uncertainties are accounted for, the present measurements for subcooled and superheated liquids agree with the classical theory. The measured Nusselt numbers for superheated ethanol seem to be slightly higher than predicted by the correlation. This may be a consequence of the extrapolation of physical properties described in Sec. 3.

A large number of investigations regarding single-phase flow in microtubes have been executed. Some authors found that the friction factor and the Nusselt number agree with the conventional predictions for macrosize tubes. Lelea et al. [5] found good agreement with the conventional results for tubes, including the entrance region, testing 0.1 mm, 0.3 mm, and 0.5 mm inner diameter microtubes. Celata et al. [6] presented results of the heat transfer in tubes with diameters ranging from 528 μm down to 120 μm. For the largest tube a good agreement of the global Nusselt number with the theory accounting for thermally developing flow has been found. For the smaller tubes, lower Nusselt numbers were measured. The authors assume that heat losses by peripheral conduction away from the test section are the reason for the deviations. In many other cases researchers found that the experimental data for the friction factor and the Nusselt number disagree with the predictions for macrosize channels. In the reviews of Morini [4], Sobhan and Garimella [2], and Palm [3], the experimental data of numerous studies are summarized. For laminar single-phase flow, the reported friction factors and Nusselt numbers lie both above and below the predictions of the classical theory. Suggested reasons for these deviations are rarefaction, viscous dissipation, electroosmosis, property variation effects, and channel surface conditions. Our results imply that momentum and heat transfer during single-phase flow in 600 μm diameter microtubes are well described by the standard correlations. Nusselt numbers for superheated liquid flow in a microtube are, to our knowledge, reported for the first time.

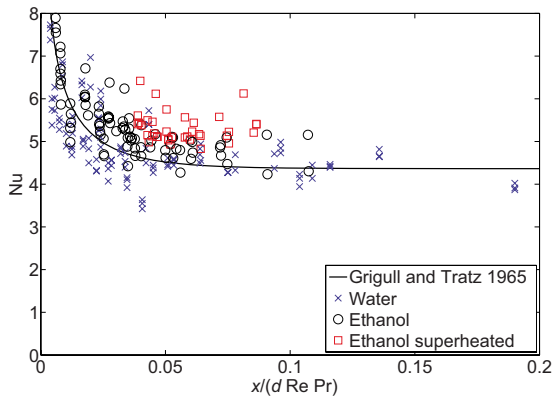

Fig. 6 Nusselt number as a function of dimensionless length and experimental results compared with correlation of Grigull and Tratz for single-phase heat transfer

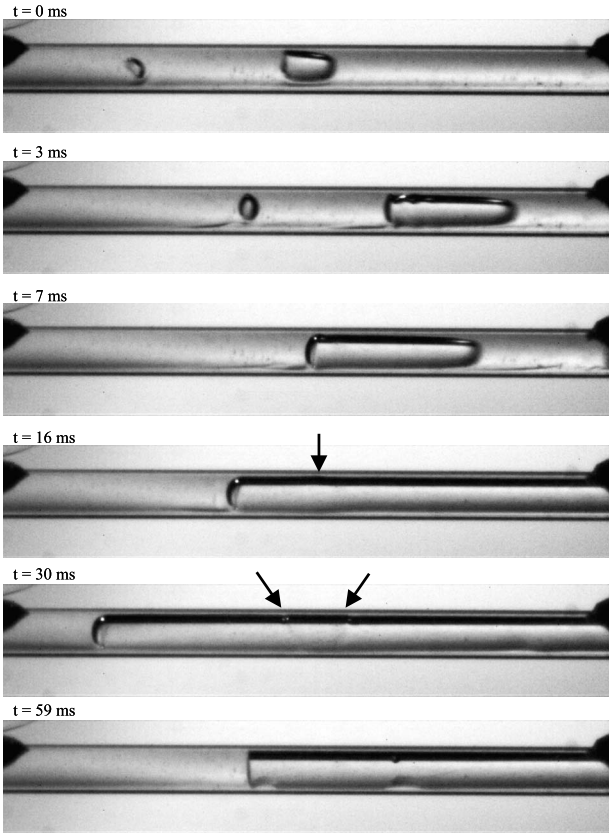

Fig. 7 Evolution of flow pattern during a boiling cycle, part 1: bubble nucleation in the camera's field of view

4.1.1 Boiling. Boiling experiments have been conducted with ethanol as a working fluid. Alternating flow patterns with a defined temporal sequence have been observed. Photographic images of the evaporation process are displayed in Figs. 7 and 8. Both sequences were taken at a mass flux density of 158 kg/m^2 s and a heat flux of 66,000 W/m^2 between the fourth and the fifth thermocouple in the heated area with a frame rate of 1000 frames per second. In Fig. 7 a typical evaporation cycle starting with a bubble nucleation event in the camera's field of view is shown as follows.

- $t=0$ ms: two vapor bubbles have detached from the heated wall and are transported with the liquid.
- $t=3$ ms: the bubbles grow. Since the diameter of the right bubble equals the channel diameter, it grows faster than before.
- $t=7$ ms: the left bubble has reached the channel diameter and expands in the streamwise direction. Liquid is pressed to the channel wall due to the fast bubble growth, forming a

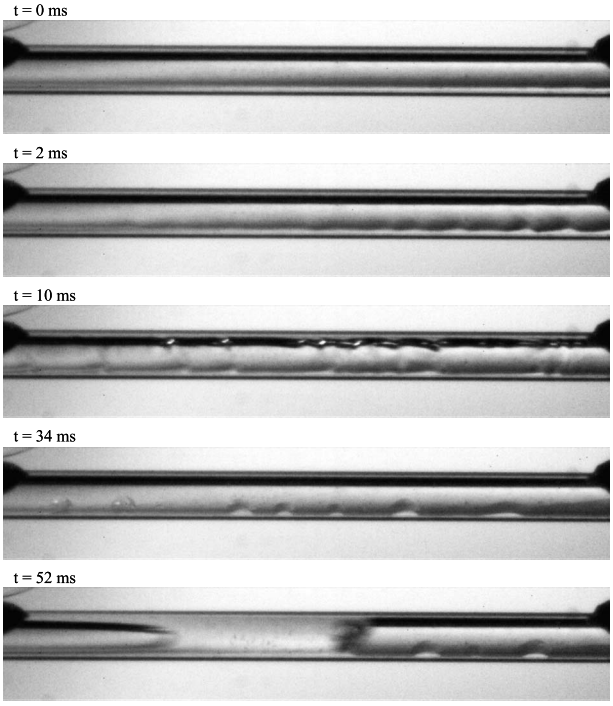

Fig. 8 Evolution of flow pattern during a boiling cycle, part 2: bubble nucleation upstream of the camera's field of view

thin liquid film between the bubble and wall. The right bubble has left the camera's view field.

- $t=16$ ms: the bubble starts to grow in the counterstreamwise direction as well. The smallest liquid film thickness is found at the location of first contact of the bubble with the wall of the tube (indicated by an arrow).
- $t=30$ ms: during the growth in the counterstreamwise direction, the liquid film thickness decreases, and a film rupture takes place (indicated by arrows).
- $t=59$ ms: liquid refills the tube and pushes the elongated bubble out of the camera's field of view in the streamwise direction.

The second sequence shown in Fig. 8 has been taken 100 ms after the first sequence. It shows the typical flow patterns in case of a bubble nucleation upstream of the camera's field of view.

- $t=0$ ms: an elongated bubble surrounded by a thin liquid film with a uniform thickness is inside the studied tube section.
- $t=2$ ms: wavy patterns start to develop on the liquid film surface at the bottom of the tube while the bubble moves downstream. The motion of the waves is in flow direction.
- $t=10$ ms: the liquid film along the full circumference of the inner tube wall displays wavy patterns, and the amplitude of the waves increases, while the liquid film thickness decreases.
- $t=34$ ms: a film rupture has occurred, the remaining liquid has coalesced to isolated droplets at the bottom of the tube. The droplets move in the downstream direction with decreasing velocity and finally become immobile.
- $t=52$ ms: a liquid plug rewets the tube wall, and another vapor bubble approaches.

By utilizing flow visualization, thin film evaporation triggered by single bubble nucleation has been identified as the dominant phase change process. At first the bubble grows comparatively slowly, but once the bubble diameter reaches the inner diameter of the tube, the bubble growth rate is strongly enhanced. Constricted

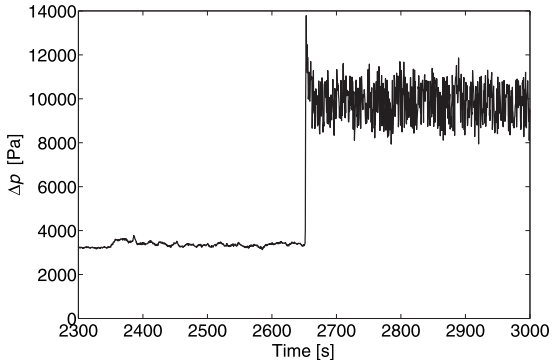

Fig. 9 Pressure drop, transition from single-phase flow to boiling, $\dot{m}=237$ kg/m^2 s, and $\dot{q}=79{,}000$ W/m^2

by the tube wall, the bubble grows in the streamwise, as well as in the counterstreamwise direction. Depending on the heat flux and the inlet Reynolds number, even the tube area upstream of the heated section is affected by two-phase flow patterns because of counterstreamwise bubble growth. The vapor bubble shrinks and splits into several smaller bubbles due to condensation upstream of the heated section. Before being totally condensed liquid pushes the bubbles downstream, back into the heated section. It has been observed that these bubbles periodically trigger the successive evaporation cycle. This could mean that once boiling has been initiated, active nucleation sites inside the heated area of the tube are no longer necessary to maintain boiling.

A liquid film is formed between the growing bubble and the tube wall. At the beginning when the vapor bubble is comparatively short, the film has a uniform thickness but with increasing bubble length it becomes unstable. Wavy patterns, moving in the downstream and upstream directions could be observed on the liquid film surface. Shear stress between the vapor and the liquid phase is expected to be the reason for the observed wavy patterns on the liquid film surface. Due to evaporation, the film thickness decreases. If the time period prior to the arrival of the next liquid plug is long enough, the liquid film ruptures and dryout occurs.

Assuming a nonexpanding bubble, shear forces act on the liquid surface in the direction of bubble motion, and the relative velocity between vapor and liquid phase is constant along the bubble length. For an expanding bubble, the velocity of the upstream meniscus is different from the velocity of the downstream meniscus, indicating that the relative velocity between the vapor and liquid phase at the front of the bubble is different from that at the bubbles's end. Hence the shear stress acting on the liquid surface and thereby the amplitude and the motion of the wavy patterns change along the bubble length. For a bubble expanding in both directions, flow visualization has shown that even the direction of wave motion in the left part of a bubble can be different from that in its right part.

Flow reversal has already been observed during flow boiling in multichannel setups [15,16], as well as in single microchannels and microtubes [17,8]. Shear induced waves have been observed during annular flow in microtubes [18], but wave motion in the streamwise and counterstreamwise directions during elongated bubble flow has to our knowledge not been reported before. The images (Fig. 8) prove that the stability of the liquid film surrounding a vapor bubble can be an important issue during flow boiling in microtubes. In our experiments temporary dryout phenomena occur even at a low mean vapor quality due to film rupture as a result of film instabilities.

Significant pressure fluctuations induced by the unsteady evaporation process have been measured. Figure 9 shows the change of pressure drop for the transition from single-phase flow to boiling at $t=2652$ s in a test run. The pressure drop suddenly jumps from a virtually constant value of 3300 Pa for single-phase

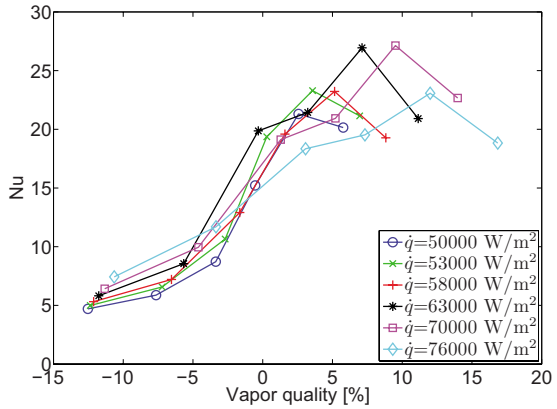

Fig. 10 Nusselt numbers for boiling, $\dot{m}$=158 kg/m^2 s

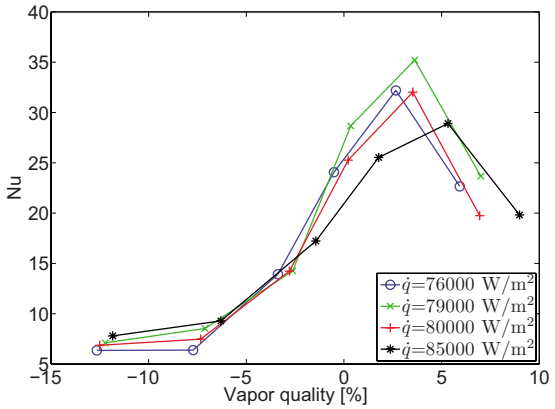

Fig. 11 Nusselt numbers for boiling, $\dot{m}$=237 kg/m^2 s

flow to a fluctuating value of 8000–12,000 Pa for the previously described boiling process. The cyclic flow pattern, especially the upstream bubble growth, appears to be the reason for the strong pressure fluctuations. According to Kandlikar [19] the high heat transfer coefficient in microchannels leads to a superheated liquid environment around a nucleating bubble. The successive pressure increase inside the bubble introduces a pressure spike in the microchannel. This pressure spike may overcome the inertia of the incoming liquid and the pressure inside the inlet reservoir and thus cause a flow reversal. The data of the present study support this assumption.

Wang et al. [20] studied the stability of flow boiling in microchannels and found three distinguished flow boiling modes depending on the heat flux to mass flux density ratio. For a single microchannel stable flow boiling existing for $\dot{q}/\dot{m} < 0.96$ kJ/kg, unstable flow boiling with long-period oscillation mode for $0.96 \text{ kJ/kg} < \dot{q}/\dot{m} < 2.14$ kJ/kg, and unstable flow boiling with a short-period oscillation mode for $\dot{q}/\dot{m} > 2.14$ kJ/kg. The investigated range for flow boiling in our study is $0.28 \text{ kJ/kg} < \dot{q}/\dot{m} < 0.49$ kJ/kg, or in terms of the dimensionless boiling number $\text{Bo} = 3.2 \times 10^{-4} - 5.7 \times 10^{-4}$. Contrary to Wang et al. pressure and temperature oscillations have been observed in all cases. For a ratio lower than $\dot{q}/\dot{m} = 0.28$ kJ/kg, boiling could not be established, supposably because of the rather smooth tube wall, instead superheated or subcooled single-phase flow was found.

In another study Wang et al. investigated flow boiling in a single trapezoidal microchannel having a hydraulic diameter of 155 μm. They suggest the exit vapor quality as a measure to distinguish stable and unstable flow boiling [21]. For an exit vapor quality less than 1.3%, stable boiling was present, while for higher vapor qualities unstable boiling was identified. For unstable flow boiling, bubble expansion in the upstream direction was observed. In the experiments presented here, boiling at a vapor quality of less than 3% at the tube exit could not been established. This might be an explanation of the fact that no stable boiling condition was found in this investigation. Wang et al. measured oscillatory flow boiling modes with long-period temperature and pressure fluctuations on a time scale of 100 s and more. Contrary to these findings, only oscillations on a time scale of less than 1 s (short-period oscillations) could be identified in the present study (see Fig. 9).

It has been shown that flow instabilities in microchannels can be minimized by employing flow barriers and artificial nucleation sites [22]. For the stabilized flow a reduction in the channel wall temperatures has been observed indicating an improved heat transfer. Nevertheless, employing flow barriers generally increases the required pumping power. Further studies need to prove whether an artificially stabilized flow leads to a higher ratio of transferred heat over required pumping power than unstable flow.

Figures 10–12 show the time-averaged local Nusselt numbers as a function of vapor quality for three different mass flux densities. The vapor quality is calculated by the energy balance (Eq. (11)), hence, negative values indicate that the bulk temperature is lower than the saturation temperature. Compared with the single-phase experiments, the heat transfer is enhanced for all thermocouple positions, also for those measuring a time-averaged temperature below saturation temperature, which defines the negative vapor qualities. The reason for this heat transfer enhancement at positions with negative quality might be explained by the temporal flow reversal when bubbles grow in the counterstreamwise direction, as shown and discussed above (Fig. 7).

For $\dot{m}$=158 kg/m^2 s the local Nusselt numbers for boiling are about 22 and seem to be rather independent of the vapor quality and the heat flux in the tested range (Fig. 10). For a higher mass flux density higher local Nusselt numbers were measured. At $\dot{m}$=237 kg/m^2 s and $\dot{m}$=317 kg/m^2 s, the average local Nusselt numbers are about 27, and the dependence on the vapor quality is more pronounced. While at the last thermocouple the local Nusselt number is between 17 to 24 in all cases, the Nusselt numbers increase with increasing mass flux density for the other thermocouples at lower vapor quality. Dryout phenomena could be the reason for the reduced heat transfer performance at the end of the tube in Figs. 11 and 12, although the vapor qualities are lower than for $\dot{m}$=158 kg/m^2 s (Fig. 10). Alternating flow patterns may trigger a long dryout time fraction even at a low mean vapor quality if, for example, the time fraction for which liquid plugs are present is also comparatively long. As a consequence, the two-phase flow pattern responsible for the high heat transfer performance might be largely suppressed. Investigations at a higher average vapor quality than 17% were not conducted due to thermal

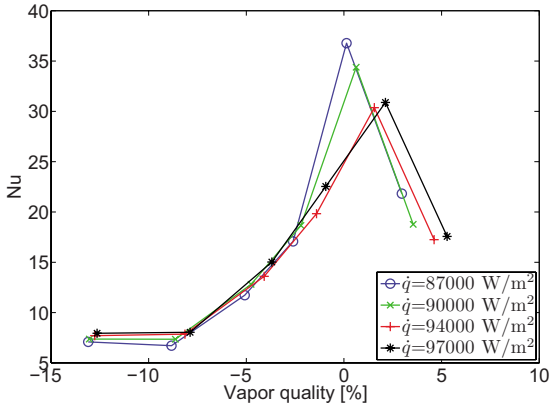

Fig. 12 Nusselt numbers for boiling, $\dot{m}$=317 kg/m^2 s

stress and limitations in heat flux. Beyond this condition, assuming a similar flow pattern, a decreasing Nusselt number can be expected as a consequence of dryout.

No clear tendency of the Nusselt number dependence on the heat flux could be identified in Figs. 10–12. In common flow boiling models, the heat transfer is divided into two parts: nucleate boiling heat transfer and convective boiling heat transfer. The nucleate boiling heat transfer performance is known to be a function of heat flux, since the active nucleation site density increases with increasing heat flux. The convective heat transfer performance is found to be rather independent of the heat flux, but it is a function of mass flux density [23]. Thus, the behavior of the local Nusselt numbers supports the impression obtained by flow visualization, namely, that nucleate boiling is not the dominant heat transfer process in our experiments. Many experimental studies have concluded that nucleate boiling controls microchannel evaporation, whereas the convective evaporation contribution is negligible [7,24]. Some authors assumed that nucleate boiling is dominant at low vapor qualities, while convective boiling is dominant at high vapor qualities [8,25]. We found that convective thin film evaporation is dominant throughout the tested range of vapor quality.

Qu and Mudawar [26] studied flow boiling of water in parallel microchannels and concluded that forced convection boiling is the dominant heat transfer mechanism in their heat sink. Comparable to our studies, they found that the saturated flow boiling heat transfer coefficient is a function of mass flux and only a weak function of heat flux. However, in our experiments an increase in the mass flux only partially enhances the heat transfer performance. While Qu and Mudawar employed water in their boiling experiments, we used ethanol, which has a higher viscosity. The lower fluidity of ethanol may weaken the dependence of the heat transfer performance on the mass flux.

Thome et al. [27] developed a model to predict the heat transfer performance of boiling processes in microchannels and found rather good agreement with the experimental database [28]. In their model, counterstreamwise bubble growth is not considered, and the heat transfer performance is a function of the heat flux. Our results indicate that refined models are needed to account for the observed phenomena.

We compared our data for flow boiling with the results of other researchers using similar setups with single circular tubes and direct current heating. The heat transfer coefficients published by these authors have been used to calculate the Nusselt numbers. In microtube flow boiling heat is transported from the tube wall through a thin liquid film to the liquid/vapor interface where the phase change takes place. The thermal resistance of the film depends on the thermal conductivity of the liquid and the film thickness. By employing the dimensionless Nusselt number, the heat transfer performance is related to the thermal resistance of the liquid film, enhancing the comparability of different data referring to various fluids. We based the Nusselt number on the inner diameter of the tube instead of the liquid film thickness because quantitative information about film geometries is not available. The amount of liquid remaining on the wall of a capillary tube in which a liquid slug is transported has been the focus of several studies. According to the results of Taylor [29], the thickness of the remaining film is, among other things, proportional to the tube diameter. More recent investigations show deviations from Taylor's law for high capillary numbers [30,31]. Nevertheless, using the diameter for calculating the Nusselt number seems to be reasonable to express the dependence of the liquid film thickness on the microtube size.

Figure 13 shows the averaged data for each mass flux density of our measurements ($\dot{m}=158$, 237 and 317 $\mathrm{kg/m^2\,s}$) compared with the data of Yen et al. [24,8] and Lin et al. [25]. Yen et al. [24] tested HCFC123 in a steel tube with an inner diameter of 510 μm in 2003 and tested the same fluid in a transparent Pyrex glass tube of 210 μm in 2006 [8]. Cavities having diameters of about

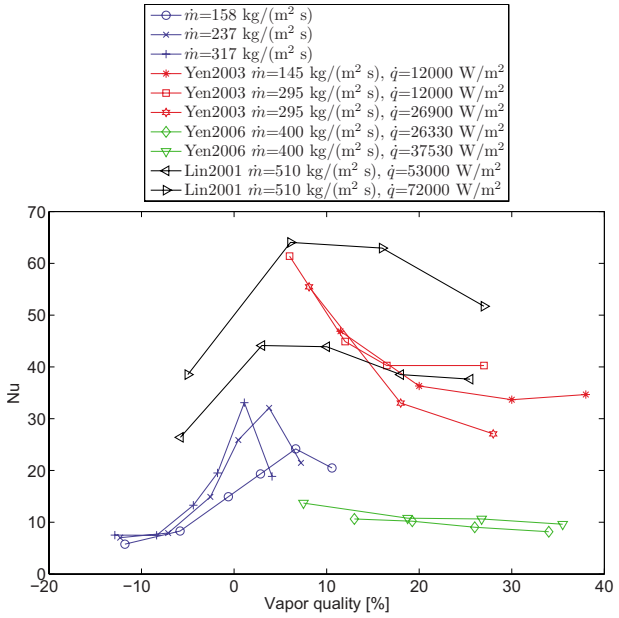

Fig. 13 Average Nusselt numbers for boiling at different mass flux densities compared with data of Yen et al. [24,8] and Lin et al. [25]

3–4 μm have been found for the steel tube, whereas the surface of the glass tube was reported to be very smooth. Lin et al. [25] used R141b in a 1.1 mm tube without providing information about material and surface topography. The Nusselt numbers of Yen et al. regarding the glass tube (Yen2006 in Fig. 13) are about 10 and decrease with increasing χ; a dependence on $\dot{q}$ could not be measured, and the mass flux was not varied. We measured Nusselt numbers of up to 37 for a vapor quality between 0% and 10%, but similar to Yen et al. the data shows a decreasing trend for higher χ. For the highest mass flux density of 317 $\mathrm{kg/m^2\,s}$, the Nusselt number is about 19 at a vapor quality of 4.1%, while we calculated for Yen et al. Nu=13.7 at $\chi=7.5\%$ and a slightly higher mass flux density of 400 $\mathrm{kg/m^2\,s}$. Yen et al. observed periodically alternating bubbly flow, capillary flow, annular flow, and dryout inside the glass tube. Similar to our observations bubble growth in the upstream direction has been found. In addition to the flow patterns reported by Yen et al., we also found single-phase liquid flow as a periodically occurring important flow pattern during boiling. This may be a consequence of the working fluid we used. Due to the good wetting characteristics of ethanol, it fills the cavities in the tube wall [32], and a high degree of liquid superheat is needed in each evaporation cycle to restart the nucleation process.

Compared with the glass tube, the heat transfer is considerably enhanced for the steel tube (Yen2003 in Fig. 13) and—similarly as for the glass tube—monotonically decreases with increasing vapor quality in the saturated flow boiling regime. The heat transfer is independent of mass flux density and decreases with increasing heat flux. This is the opposite of what could be expected, since heat transfer is found to be independent of heat flux in convective boiling and increases with heat flux in nucleate boiling [12]. Yen et al. concluded that annular flow prevails in microtubes and that the effect of nucleate boiling is dominant, whereas that of the convection boiling is assumed to be of minor importance. Flow visualization was not performed.

The Nusselt numbers of Lin et al. (Lin2001 in Fig. 13) are similar to what Yen et al. found for the steel tube. Unlike Yen et al. they found an increase in the heat transfer coefficient for increasing heat flux, indicating that nucleate boiling is dominant. Comparable to our studies, Lin et al. found a considerably higher heat transfer performance for a vapor quality less than zero as

what could be expected for single-phase flow (Nu=4.36). In our experiments flow visualization shows that the enhancement of the heat transfer performance could be related to counterstreamwise bubble growth.

In total, the data seem to indicate that different heat transfer mechanisms are found for boiling in microtubes, depending on whether or not the surface properties promote nucleate boiling. However, the data are not fully conclusive, since Yen et al. measured a decreasing heat transfer performance with increasing heat flux.

5 Summary and Conclusions

Experiments were conducted to determine friction factors and local Nusselt numbers in a microtube with an inner diameter of 600 μm. Distilled water and ethanol were used as the working fluids. The major findings from the study are summarized as follows.

- The friction factor and the Nusselt number for single-phase liquid flow with constant heating agree with the classical theories for laminar flow (friction factor=64/Re and Nu =4.36 for constant heat flux). Slightly higher Nusselt numbers were derived for superheated liquid flow. This might be due to inaccuracies of required physical properties.
- For boiling, alternating flow patterns with a defined temporal sequence have been observed. Evaporation of a thin liquid film covering the tube wall seems to be the dominant heat transfer mechanism. Wavy patterns on the film surface moving in the upstream and downstream directions indicate shear forces between the vapor and the liquid phase. The photographic images prove that the stability of the liquid film surrounding a vapor bubble could be an important issue during flow boiling in microtubes. Temporary dryout phenomena occur even at a low mean vapor quality due to film rupture as a result of film instabilities. The influence of these instabilities on the heat transfer performance needs to be investigated in further studies.
- Once the boiling process has been initiated, small vapor bubbles left over from the previous evaporation cycle serve as nuclei for the bubble growth during the successive cycle.
- The mean pressure drop for flow boiling is about three times higher than that for single-phase flow. Due to the fast alternating flow patterns the pressure drop fluctuates in a range of about $\pm$10%.
- The Nusselt number for boiling is independent of the heat flux, increases with increasing mass flux density, and up to eight times higher than that for single-phase heat transfer.

Acknowledgment

We thank Professor Y. Suzuki for valuable discussions, and Messrs. Y. Hamana and S. Hayashi, and Dr. J. Miwa for their technical assistance. B. Schilder received support for this project as a JSPS Scientific Visitor to Turbulence and Heat Transfer Laboratory at the University of Tokyo.

Nomenclature

A = cross-sectional area (m^2)
bo = boiling number
c_p = specific heat (J/kg K)
d = tube diameter (m)
h = heat transfer coefficient (W/m^2 K)
Δh_{lv} = latent heat of vaporization (J/kg)
I = electric current (A)
l = length (m)
$K(\infty)$ = Hagenbach's factor
$\dot{M}$ = mass flux (kg/s)
Ma = axial conduction number
$\dot{m}$ = mass flux density (kg/m^2 s)
Nu = Nusselt number
Pr = Prandtl number
Δp = pressure drop (Pa)
$\dot{Q}$ = heat transfer rate (W)
$\dot{q}$ = heat flux (W/m^2)
Re = Reynolds number
r = tube radius (m)
T = temperature [°C]
t = time (s)
U = mean flow velocity (m/s)
V = electric voltage (V)
x = axial distance (m)
χ = vapor quality (%)
κ = loss coefficient
λ = thermal conductivity [W/m K]
μ = contraction coefficient
ρ = density (kg/m^3)

Subscripts

amb = ambient
axial = in the axial direction
bulk = bulk fluid property
cond = conduction
conv = convection
dev = developing flow
elem = element
ex = exit
h = hydraulic
heat = heated
in = inner
inl = inlet
loc = local
loss = heat loss
out = outer
re = reservoir
sat = saturation
th = thermocouple
wall, in = inner tube wall
wall, out = outer tube wall

Appendix: Estimation of Secondary Pressure Losses

The main factors that contribute to the overall pressure drop for liquid flow in microchannels are the friction of the hydrodynamically developing flow at the entrance of the tube, the following fully developed flow, and the tube inlet and exit losses. The contribution of the pressure losses due to hydrodynamically developing flow and the inlet/exit losses to the total measured pressure drop have been estimated. The increase in the pressure drop due to hydrodynamically developing flow can be calculated using Hagenbach's factor [33] as

$$\Delta p_{dev} = K(\infty)\frac{\rho}{2}U^2 \tag{A1}$$

Hagenbach's factor $K(\infty)$ can be calculated as proposed by Chen [34]

$$K(\infty) = 1.20 + (38/\mathrm{Re}) \tag{A2}$$

The inlet and exit pressure losses due to sudden contraction of the flow entering the tube and sudden expansion of the flow at the tube exit have been estimated according to Ref. [35]. The loss coefficient for the tube inlet has been calculated as

$$\kappa_{inl} = \left(\frac{1-\mu}{\mu}\right)^2 \tag{A3}$$

where μ is the contraction coefficient depending on the ratio of the cross-sectional area in front of and inside the microtube. For the cross sectional area ratio in our experiments (A_{tube}/A_{re} =0.06), a value of μ=0.60–0.61 is listed in the literature [35].

The loss coefficient for the tube exit has been calculated as

$$\kappa_{ex} = \left(1 - \frac{A_{tube}}{A_{re}}\right)^2 \tag{A4}$$

The inlet/exit pressure losses are then calculated as

$$\Delta p_{inl,ex} = \frac{\rho}{2} U^2 (\kappa_{inl} + \kappa_{ex}) \tag{A5}$$

The fraction of pressure drop due to hydrodynamically developing flow as well as inlet and exit losses of the measured total pressure drop increases with increasing flow velocity. According to the formulas above, the secondary pressure losses amount to 3.2% of the overall pressure drop at the highest mean flow velocity of 0.29 m/s (Re=202). Hence, these contributions have been neglected in calculating the friction factor.

References

[1] Shah, R. K., and London, A. L., 1978, *Laminar Flow Forced Convection in Ducts: A Source Book for Compact Heat Exchanger Analytical Data*, Academic, New York.

[2] Sobhan, C. B., and Garimella, S. V., 2001, "A Comparative Analysis of Studies on Heat Transfer and Fluid Flow in Microchannels," Microscale Thermophys. Eng., **5**(4), pp. 293–311.

[3] Palm, B., 2001, "Heat Transfer in Microchannels," Microscale Thermophys. Eng., **5**(3), pp. 155–175.

[4] Morini, G. L., 2004, "Single-Phase Convective Heat Transfer in Microchannels: A Review of Experimental Results," Int. J. Therm. Sci., **43**(7), pp. 631–651.

[5] Lelea, D., Nishio, S., and Takano, K., 2004, "The Experimental Research on Microtube Heat Transfer and Fluid Flow of Distilled Water," Int. J. Heat Mass Transfer, **47**(12–13), pp. 2817–2830.

[6] Celata, G. P., Cumo, M., Marconi, V., McPhail, S. J., and Zummo, G., 2006, "Microtube Liquid Single-Phase Heat Transfer in Laminar Flow," Int. J. Heat Mass Transfer, **49**(19–20), pp. 3538–3546.

[7] Gasche, J. L., 2006, "Carbon Dioxide Evaporation in a Single Microchannel," J. Braz. Soc. Mech. Sci. Eng., **28**, pp. 69–83.

[8] Yen, T. H., Shoji, M., Takemura, F., Suzuki, Y., and Kasagi, N., 2006, "Visualization of Convective Boiling Heat Transfer in Single Microchannels With Different Shaped Cross-Sections," Int. J. Heat Mass Transfer, **49**(21–22), pp. 3884–3894.

[9] Hetsroni, G., Mosyak, A., Pogrebnyak, E., and Segal, Z., 2005, "Explosive Boiling of Water in Parallel Micro-Channels," Int. J. Multiphase Flow, **31**(4), pp. 371–392.

[10] Zhang, L. A., Wang, E. N., Goodson, K. E., and Kenny, T. W., 2005, "Phase Change Phenomena in Silicon Microchannels," Int. J. Heat Mass Transfer, **48**(8), pp. 1572–1582.

[11] Hardt, S., Schilder, B., Tiemann, D., Kolb, G., Hessel, V., and Stephan, P., 2007, "Analysis of Flow Patterns Emerging During Evaporation in Parallel Microchannels," Int. J. Heat Mass Transfer, **50**(1–2), pp. 226–239.

[12] Verein Deutscher Ingenieure, 2006, *Wärmeatlas, erw. aufl*, Vol. 10, VDI-Verlag, Düsseldorf.

[13] Maranzana, G., Perry, I., and Maillet, D., 2004, "Mini- and Micro-Channels: Influence of Axial Conduction in the Walls," Int. J. Heat Mass Transfer, **47**(17–18), pp. 3993–4004.

[14] Grigull, U., and Tratz, H., 1965, "Thermischer einlauf in ausgebildeter laminarer rohrströmung," Int. J. Heat Mass Transfer, **8**(5), pp. 669–678.

[15] Hetsroni, G., Mosyak, A., Segal, Z., and Pogrebnyak, E., 2003, "Two-Phase Flow Patterns in Parallel Micro-Channels," Int. J. Multiphase Flow, **29**(3), pp. 341–360.

[16] Li, H. Y., Tseng, F. G., and Pan, C., 2004, "Bubble Dynamics in Microchannels. Part II: Two Parallel Microchannels," Int. J. Heat Mass Transfer, **47**(25), pp. 5591–5601.

[17] Lee, P. C., Tseng, F. G., and Pan, C., 2004, "Bubble Dynamics in Microchannels. Part I: Single Microchannel," Int. J. Heat Mass Transfer, **47**(25), pp. 5575–5589.

[18] Pettersen, J., 2004, "Flow Vaporization of CO_2 in Microchannel Tubes," Exp. Therm. Fluid Sci., **28**(2–3), pp. 111–121.

[19] Kandlikar, S. G., 2006, "Nucleation Characteristics and Stability Considerations During Flow Boiling in Microchannels," Exp. Therm. Fluid Sci., **30**(5), pp. 441–447.

[20] Wang, G., Cheng, P., and Wu, H., 2007, "Unstable and Stable Flow Boiling in Parallel Microchannels and in a Single Microchannel," Int. J. Heat Mass Transfer, **50**(21–22), pp. 4297–4310.

[21] Wang, G. D., and Cheng, P., 2008, "An Experimental Study of Flow Boiling Instability in a Single Microchannel," Int. Commun. Heat Mass Transfer, **35**(10), pp. 1229–1234.

[22] Kandlikar, S. G., Kuan, W. K., Willistein, D. A., and Borrelli, J., 2006, "Stabilization of Flow Boiling in Microchannels Using Pressure Drop Elements and Fabricated Nucleation Sites," ASME J. Heat Transfer, **128**(4), pp. 389–396.

[23] Thome, J. R., and Collier, J. G., 1996, *Convective Boiling and Condensation*, 3rd ed., Clarendon, Oxford.

[24] Yen, T. H., Kasagi, N., and Suzuki, Y., 2003, "Forced Convective Boiling Heat Transfer in Microtubes at Low Mass and Heat Fluxes," Int. J. Multiphase Flow, **29**(12), pp. 1771–1792.

[25] Lin, S., Kew, P. A., and Cornwell, K., 2001, "Two-Phase Heat Transfer to a Refrigerant in a 1 mm Diameter Tube," Int. J. Refrig., **24**(1), pp. 51–56.

[26] Qu, W., and Mudawar, I., 2003, "Flow Boiling Heat Transfer in Two-Phase Micro-Channel Heat Sinks—I. Experimental Investigation and Assessment of Correlation Methods," Int. J. Heat Mass Transfer, **46**(15), pp. 2755–2771.

[27] Thome, J. R., Dupont, V., and Jacobi, A. M., 2004, "Heat Transfer Model for Evaporation in Microchannels. Part I: Presentation of the Model," Int. J. Heat Mass Transfer, **47**(14–16), pp. 3375–3385.

[28] Dupont, V., Thome, J. R., and Jacobi, A. M., 2004, "Heat Transfer Model for Evaporation in Microchannels. Part II: Comparison With the Database," Int. J. Heat Mass Transfer, **47**(14–16), pp. 3387–3401.

[29] Taylor, G. I., 1961, "Deposition of a Viscous Fluid on the Wall of a Tube," J. Fluid Mech., **10**(2), pp. 161–165.

[30] Aussillous, P., and Quere, D., 2000, "Quick Deposition of a Fluid on the Wall of a Tube," Phys. Fluids, **12**(10), pp. 2367–2371.

[31] Han, Y., and Shikazono, N., 2008, "Thickness of Liquid Film Formed in Slug Flow in Micro Tube," ECI International Conference on Heat Transfer and Fluid Flow in Microscale, Sept. 21–26.

[32] Dupont, V., Miscevic, M., Joly, J. L., and Platel, V., 2003, "Boiling Incipience of Highly Wetting Liquids in Horizontal Confined Space," Int. J. Heat Mass Transfer, **46**(22), pp. 4245–4256.

[33] Kandlikar, S. G., 2006, *Heat Transfer and Fluid Flow in Minichannels and Microchannels*, 1st ed., Elsevier, New York.

[34] Chen, R. Y., 1973, "Flow in Entrance Region at Low Reynolds-Numbers," ASME J. Fluids Eng., **95**(1), pp. 153–158.

[35] Kuhlmann, H. C., 2007, *Stroemungsmechanik*, Pearson Sudium, München.

Computational Analysis of Pin-Fin Arrays Effects on Internal Heat Transfer Enhancement of a Blade Tip Wall

Gongnan Xie

Bengt Sundén
e-mail: bengt.sunden@energy.lth.se

Department of Energy Sciences,
Division of Heat Transfer,
Lund University,
P.O. Box 118,
SE-221 00 Lund, Sweden

Esa Utriainen

Lieke Wang

Siemens Industrial Turbomachinery AB,
SE-612 83 Finspong, Sweden

Cooling methods are strongly needed for the turbine blade tips to ensure a long durability and safe operation. Improving the internal convective cooling is therefore required to increase the blade tip life. A common way to cool the tip is to use serpentine passages with 180-deg turns under the blade tip cap. In this paper, enhanced heat transfer of a blade tip cap has been investigated numerically. The computational models consist of a two-pass channel with a 180-deg turn and various arrays of pin fins mounted on the tip cap, and a smooth two-pass channel. The inlet Reynolds number is ranging from 100,000 to 600,000. The computations are 3D, steady, incompressible, and nonrotating. Details of the 3D fluid flow and heat transfer over the tip walls are presented. The effects of pin-fin height, diameter, and pitches on the heat transfer enhancement on the blade tip walls are observed. The overall performances of ten models are compared and evaluated. It is found that due to the combination of turning, impingement, and pin-fin crossflow, the heat transfer coefficient of the pin-finned tip is a factor of 2.67 higher than that of a smooth tip. This augmentation is achieved at the expense of a penalty of pressure drop around 30%. Results show that the intensity of heat transfer enhancement depends upon pin-fin configuration and arrangement. It is suggested that pin fins could be used to enhance the blade tip heat transfer and cooling. [DOI: 10.1115/1.4000053]

Keywords: tip wall, pin fins, enhancement, computation, gas turbine cooling

1 Introduction

It is a well-known fact that one way to increase the power output and thermodynamic efficiency of a gas turbine engine is to increase the turbine inlet temperature. Thus, the turbine inlet temperature for industrial and aircraft gas turbines has been continuously increased to improve power and efficiency. However, the heat transferred to the blade is increased significantly with the increase in the turbine inlet temperature, but the allowable melting temperature of materials has only increased much less. This indicates that the turbine blade inlet temperature may exceed the material melting temperature by more than 500°C. As a result, turbine blades must be cooled for a safe and long-lasting operation. Various internal and external cooling techniques are employed to decrease the blade material temperature below the melting point. Figure 1 depicts a typical cooling technology for internal and external zones. The leading edge is cooled by jet impingement with film cooling, the middle portion is cooled by internal serpentine ribbed-turbulators passages, and the trailing edge is cooled by pin fins with ejection. In internal cooling, the relatively cold air, bypassed/discharged from the compressor, is directed into the coolant passages inside the turbine blade. In external cooling, the bypassed air is ejected through cooling holes, which are located on the turbine blade discretely. Most recent developments in the increase in the turbine inlet temperature have been achieved by better cooling of the turbine blade and improved understanding of the heat transfer mechanisms in the turbine passages. Several recent publications reviewing the gas turbine heat transfer and cooling technology research are available [1–4].

Cooling of the blade should include the cooling of all regions exposed to high temperature gas and thermal load. Among such regions, the blade tip area is a region of particular interest in high pressure turbines. Gas turbine blades usually have a clearance gap between the blade tip and the stationary casing, or the shroud for the blade rotation and for its mechanical and thermal expansion. The hot gas leaks through the gap because of the pressure difference between the pressure side and suction side. The hot leakage flow increases the thermal load on the blade tip, leading to high local blade temperature. It is therefore very essential to cool the turbine blade tip and the region near the tip. However, it is difficult to cool such regions and seal against the hot leakage flow. The blade tip operates in an environment between the rotating blade and the stationary casing, and experiences the extremes of the fluid-thermal conditions within the turbine [5,6]. A very common way to cool the blade tip is to adopt internal cooling by designing serpentine (two-pass, three-pass, or multipass) channels with a 180-deg turn/bend inside the blade (as shown in Fig. 2). Taking advantage of impinging and turning effects, the tip can be cooled to some certain extent. During recent years, several studies concerned turbulent heat transfer in various two-pass channels [7–21]. For example, Ekkad et al. [7] measured the detailed heat transfer distributions inside straight and tapered two-pass channels with and without rib turbulators. It was found that the tapered channel with ribs provided 1.5–2.0 times higher Nusselt number ratios over the tapered smooth channel in the first pass, while in the after-turn region of the second pass, the ribbed and smooth channels provided similar Nusselt number ratios. Fu et al. [13,14] and Liu et al. [15] reported heat transfer coefficients and friction factors in two-pass rectangular channels with rib turbulators placed on the leading and trailing surfaces. Five kinds of ribs were considered: 45-deg angled, V-shaped, discrete 45-deg angled, discrete V-shaped, and crossed V-shaped. It was found that due to the significant secondary flow effects generated in the turn, the rota-

Contributed by the Heat Transfer Division of ASME for publication in the JOURNAL OF HEAT TRANSFER. Manuscript received February 25, 2009; final manuscript revised May 29, 2009; published online December 30, 2009. Assoc. Editor: Yogesh Jaluria.

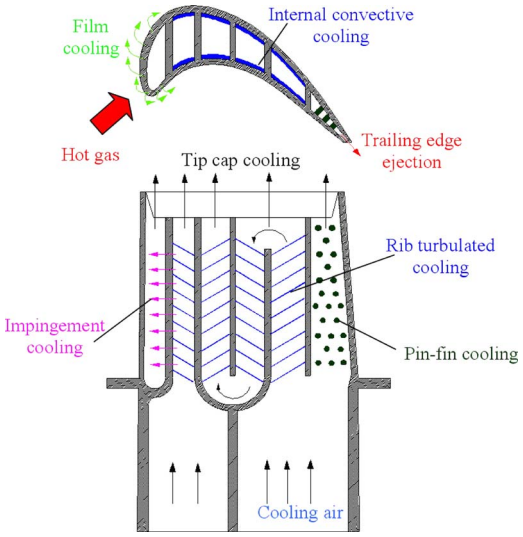

Fig. 1 Typical cooling techniques for a turbine blade

tion effect was greater on heat transfer in the first pass than in the second pass. Kim et al. [16,17] measured the detailed heat/mass transfer and pressure drop in a rotating two-pass duct with transverse ribs. It was found that due to the rotation of the duct, the Sherwood number ratios and pressure coefficients were high on the trailing surface in the first pass and on the leading surface in the second pass. In the turn region of the stationary duct, two Dean vortices were transformed into one large asymmetric vortex cell, which changed the heat/mass transfer and pressure drop characteristics. Very recently, Lucci et al. [19], Jenkins et al. [20], and Shevchuk et al. [21] studied turbulent flow and heat transfer inside internal cooling channels with a varying aspect ratio. The effect of the divider wall-to-tip wall distance was investigated. Results showed that decreasing the distance can increase the tip heat transfer in the bend region and near the bend region of the second pass, but with an increased pressure drop.

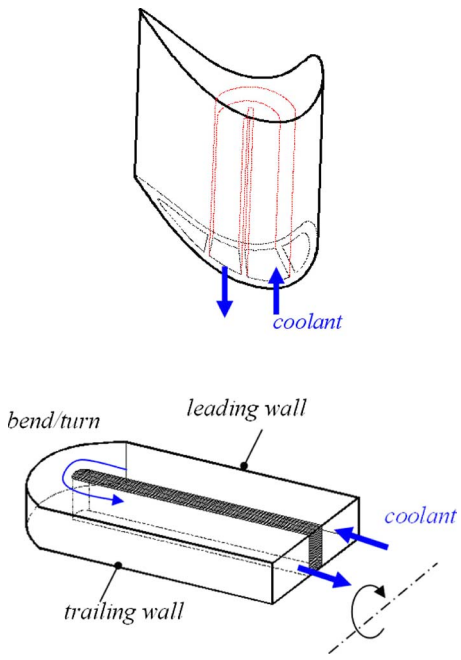

Fig. 2 A typical serpentine cooling passage inside a blade

On the other hand, many investigations have proven that pin fins can improve the cooling in low aspect ratio channels for gas turbines, typically at the trailing edges. The application of pin fins has received much attention for enhancing heat transfer in cooling channels, e.g., turbine blades, heat sinks, and compact heat exchangers. Pin fins are commonly employed in turbine blades where higher heat transfer enhancement is required while higher pressure drop is tolerated. Metzger et al. [22] studied the developing heat transfer in rectangular ducts having short pin-fin arrays. They found that the heat transfer coefficient was gradually increased to the first three or four rows, followed by a gradual decrease through the remaining rows. Lau et al. [23] experimentally studied the effect of several pin configurations on the local endwall heat/mass transfer in pin-fin channels. They observed that the decrease in the streamwise pin spacing leads to an increase in the endwall heat/mass transfer. Chyu et al. [24] reported that the pin-fin heat transfer is 10–20% higher than the endwall heat transfer. Goldstein et al. [25] found that the stepped-diameter circular pin-fin array provides a higher mass transfer coefficient and a smaller pressure loss than a uniform-diameter circular pin-fin array. Other recent investigations can be found in Refs. [26–30]. Previous works showed that the increase in the pin-fin heat transfer is always accompanied by a substantial increase in pressure loss. Most recently, Bunker [31] presented a method to provide substantially increased convective heat flux on the internally cooled tip cap of a turbine blade, where arrays of discrete shaped pins were fabricated and placed. The detailed heat transfer distribution over the internal tip cap was obtained, based on a large-scale model of a sharp 180-deg tip turn. Five tip cap surfaces were tested. It was found that the effective heat transfer coefficient could be increased by up to a factor of 2.5, due to the combination of impingement and crossflow convection around the pins. The tip turn pressure drop was negligibly greater than that of a smooth surface.

Although a similar trend of the averaged heat transfer results in two-pass channels with pin fins can be found in the experimental work by Bunker [31], only limited details of the heat transfer and fluid flow on the pin fins and endwalls are available. Furthermore, most previous studies were concerned about the heat transfer on the leading and trailing walls of the two-pass channels, and thus, very limited information is available for the tip walls. For these reasons, it is desirable to investigate more details of the heat transfer enhancement over tip walls, and to improve understanding of three-dimensional flow and heat transfer for pin-finned blade tips. The objective of the present paper is to investigate heat transfer enhancement over tips in a rectangular two-pass channel with pin-fin arrays on the tip at high Reynolds numbers. Detailed flow field and heat transfer results are presented, and a parametric study of pin-fin arrays on the tip-wall heat transfer enhancement is conducted. The overall performances of pin-finned tip two-pass channels are compared and evaluated.

2 General Description of Physical Models

A schematic diagram of the geometrical models used in this paper is shown in Fig. 3. The two-pass channels have a rectangular cross section with an aspect ratio of 1:2, where the shorter walls are the turbine pressure side and suction side, respectively. Each channel has lengths of 139.7 mm and 69.9 mm, with a hydraulic diameter of 93.13 mm. The lengths of the inlet channels (first pass) and the outlet channels (second pass) are about ten hydraulic diameters, and both the inlet and outlet channels are smooth without any turbulators. The internal separation rib (divider) is assumed to be 25.4 mm thick so that the full tip-wall cap section is 139.7×165.1 mm^2. A distance of 88.9 mm is used for the flow gap between the divider and the tip wall. Figure 3(*a*) shows the smooth-tip two-pass channel. It is used for performance comparison with the pin-finned tip two-pass channels (a typical model is shown in Fig. 3(*b*)). The geometries of the numerical models of the rectangular two-pass channels are similar to those in

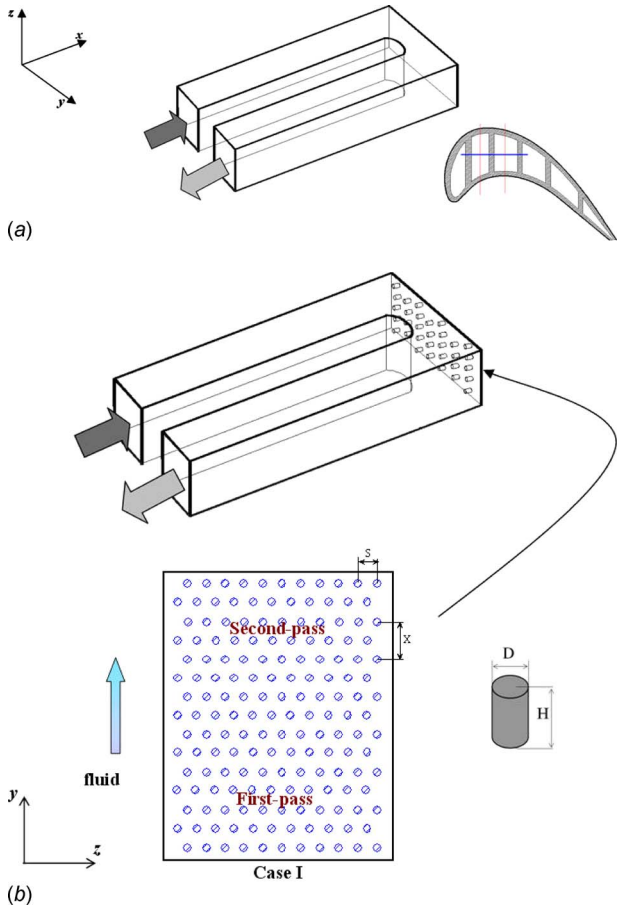

Fig. 3 Schematics of the numerical model

the experiments by Bunker [31], but the pin-fin configurations and arrangements in the present paper and the experiments are different.

In Fig. 3(*b*), pin-fin arrays are mounted on the internal tip cap. The pin fins are perfect circular straight cylinders, and are placed in a staggered arrangement. In all simulations, the pin fins are assumed to be made of aluminum. Nine models with different pin-fin parameters (height H and diameter D) and layouts (pitches X and S) are considered in this paper. The parameters of the nine models are listed in Table 1. For the pin-finned tip two-pass channels, the tip consists of the endwall (smooth tip wall is substracted by cylinder bottom surfaces) and pin-finned surfaces (cylinder side surfaces and top surfaces).

3 Computational Details

3.1 Overview. Application of computational fluid dynamics (CFD) techniques to predict the flow field and heat transfer coefficient distribution in turbomachineries and related applications attracted many researchers of different fields in recent years [32–42]. For example, Chen et al. [35], Jang et al. [36], and Al-Qahtani et al. [37] calculated the 3D flow and heat transfer in rotating two-pass square channels with smooth walls or with 45 deg and 60 deg angled ribs by a second-moment closure model and a two-layer k-ε isotropic eddy viscosity model. Good agreement with experimental data was achieved. The comparison of the results showed that the near-wall second-moment closure model provided accurate predictions of the complex 3D flow and heat transfer, resulting from the rotation and strong wall curvatures. Also, it was observed that angled ribs with high blockage ratio and a 180 deg sharp turn produced strongly nonisotropic turbulence and heat flux, which significantly affected the flow field and heat transfer coefficient. From the above-mentioned references, it is indicated that heat transfer and cooling in gas turbine channels might be predicted decently accurate by CFD simulations with various turbulence models.

To investigate the three-dimensional turbulent flow field and temperature in a rectangular two-pass channel, with or without staggered pin-fin arrays, the k-ε turbulence model is used. When solving a practical engineering problem, eddy viscosity based turbulence models have been found to be more effective than the large eddy simulation (LES) and direct numerical simulation (DNS) methods because of less demand on the number of cells, less computer memory, and the computational results may meet the engineering requirement with acceptable accuracy. In the present paper, the finite volume modeling was conducted by the simulation software FLUENT version 6.3.26. This code uses the finite volume method to solve the governing equations of fluid flow and heat transfer with appropriate boundary conditions. The pressure and velocity fields are linked by the semi-implicit method for pressure linked equations consistent (SIMPLEC) algorithm. Another commercial software, GAMBIT version 2.4.6, providing geometry generation, geometry import, and mesh generation capabilities, was used to generate the ten models. This paper examined turbulent flow (for high Reynolds numbers) and heat transfer characteristics over smooth or pin-finned tip walls.

3.2 Governing Equations. Initially, six different turbulence models, i.e., the standard k-ε model, the renormalization group (RNG) k-ε model, the realizable k-ε model, the shear stress transport (SST) k-ω model, the v^2f model, and an Reynolds stress model (RSM) model were considered for simulation of the turbulent heat transfer in the smooth two-pass channel (as shown in Fig. 3(*a*)). It was found that the RNG k-ε model results approach the experimental data better than the other five turbulence models, even though the results predicted by the three kinds of k-ε models are similar. Compared with the experimental data [31], the maxi-

Table 1 Parameters of pin-fin arrays of pin-finned tip two-pass channels

Model	Diameter D (mm)	Streamwise pitch X (mm)	Spanwise pitch S (mm)	Height H (mm)	Number of pin-fins N	Increased area ratio A/A_s
Case 1	4.064	21.117	6.096	8.128	165	1.739
Case 2	4.064	12.192	10.559	8.128	162	1.727
Case 3	4.064	12.192	10.559	4.064	162	1.370
Case 4	4.064	7.62	6.599	8.128	389	2.745
Case 5	4.064	7.62	6.599	4.064	389	1.873
Case 6	6.096	18.288	15.838	8.128	68	1.458
Case 7	3.048	12.192	10.559	8.128	162	1.545
Case 8	6.096	12.192	10.559	8.128	175	2.099
Case 9	3.048	12.192	10.559	4.064	162	1.272

mum difference 14.7% is found by the k-ε RNG model. Based on these calculations, the RNG k-ε turbulence model is selected for all final computations. More details can be found in Ref. [43].

The idea behind the RNG in turbulence is that the small scales of turbulence are removed systematically to a point where the large scales are resolvable. A more comprehensive description of the RNG theory and its application to turbulence can be found in Ref. [44]. The equations for k and ε are

$$\frac{\partial}{\partial x_j}(\rho U_j k) = \frac{\partial}{\partial x_j}\left[\sigma_k(\mu + \mu_\tau)\frac{\partial k}{\partial x_j}\right] + P_k - \rho\varepsilon \tag{1}$$

$$\frac{\partial}{\partial x_j}(\rho U_j \varepsilon) = \frac{\partial}{\partial x_j}\left[\sigma_\varepsilon(\mu + \mu_\tau)\frac{\partial \varepsilon}{\partial x_j}\right] + C_{\varepsilon 1}\frac{\varepsilon}{k}P_k - C_{\varepsilon 2}\rho\frac{\varepsilon^2}{k} - \Re \tag{2}$$

where $\sigma_k = 1.0$, $\sigma_\varepsilon = 1.3$, $C_{\varepsilon 1} = 1.42$, and $C_{\varepsilon 2} = 1.68$.

The production term P_k is expressed as

$$P_k = \tau_{ij} S_{ij} = -\rho\overline{u_i u_j} S_{ij} \tag{3}$$

where

$$S_{ij} = \frac{1}{2}\left(\frac{\partial U_i}{\partial x_j} + \frac{\partial U_j}{\partial x_i}\right)$$

and $\Re$ is defined as

$$\Re = \rho\frac{C_\mu \eta^3(1 - \eta/\eta_0)}{1 + \beta\eta^3}\frac{\varepsilon^2}{k} \tag{4}$$

where $\eta = k/\varepsilon\sqrt{2S_{ij}S_{ij}}$, $\eta_0 = 4.38$, and $\beta = 0.012$. The turbulent eddy viscosity is calculated as

$$\mu_\tau = \rho C_\mu \frac{k^2}{\varepsilon} \tag{5}$$

where $C_\mu = 0.085$. It should be pointed out that the RNG model cannot be used with damping functions, i.e., as a low-Reynolds k-ε model, since the small scales are removed. For a long time, the accuracy of the ε-equation has been regarded as the critical thing in the standard k-ε model. The RNG k-ε model is interesting because the ε-equation contains a strain-dependent correction through the variable $\Re$, which may avoid the limitation of the standard k-ε model for complex flows. Furthermore, rather than using an RSM model, the RNG k-ε model may decrease the number of grid points, and thereby less computational resources are required.

3.3 Boundary Conditions. Although the heat transfer on the leading and trailing walls are important for gas turbine blade design, the heat transfer enhancement of a pin-finned tip wall over that of a smooth tip wall is the major concern of this paper. Therefore, except for the tip walls, the remaining walls, i.e., leading walls, trailing walls, inner walls, and outer walls, are assumed to be adiabatic. A constant heat flux is prescribed on the tip walls. For the smooth-tip two-pass channel, only the smooth tip wall is heated. For the pin-finned tip two-pass channels, only the endwalls and pin-fin surfaces are heated by an identical heat flux. This implies that the fin efficiency for the pin fins is assumed to be equal to unity. No-slip velocity conditions are applied on all walls. Uniform inlet velocity and temperature are assumed at the inlet, and an outflow condition is chosen for the outlet.

The fluid is assumed to be incompressible with constant thermal physical properties, and the flow is assumed to be three-dimensional, turbulent, steady, and nonrotating. The working fluid is dry air. In this paper, standard wall functions of the RNG k-ε model are applied for the near-wall treatment because of the high Reynolds numbers and complicated computational model. Most $y+$ values lie between 10 and 30. The minimum convergence criterion for continuity, momentum quantities error, and k and ε equations are 10^{-4} and 10^{-9} for the energy equation.

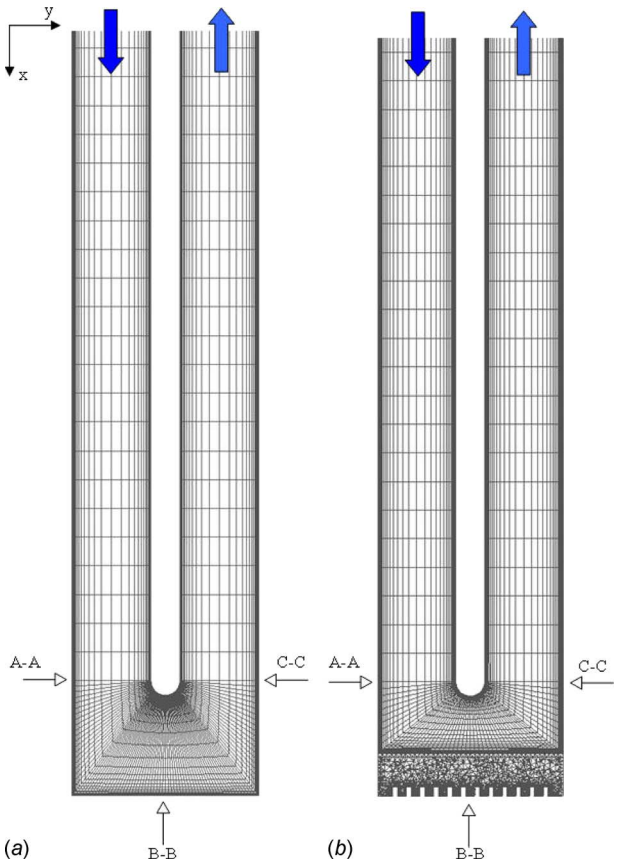

Fig. 4 Typical cross sections of the grids for computations

The preprocessor software GAMBIT is used to generate the computational grids. Figure 4 shows typical cross sections of the grids of the two models. Because of the complex geometries, a multiblock grid technique is employed to generate grids by dividing the whole domain into several subdomains. Especially for the pin-finned tip two-pass channel, an additional subdomain is introduced near the tip wall. Due to the large amount of small circular pin fins on the tip wall, an unstructured grid (T-grid) has to be filled into such subdomain. A careful check of the grid independence of the numerical solutions has been carried out by considering several grid systems with a large number of grid points (about 1.2～2.1 million cells). The grid system with around 1.5 million cells is chosen for all the computations. More details can be found in Ref. [43]. These simulations are performed on a PC with two CPUs having a frequency of 3.0 GHz, and a core memory of 8 G. The typical running time for the computation of a case is about 12 h for the smooth tip channel, and 20 h for the pin-finned tip channel.

4 Results and Discussion

4.1 Parameter Definitions. Before analyzing and comparing the fluid flow and heat transfer characteristics between the smooth tip two-pass channel and the pin-finned tip two-pass channels, the Nusselt number and friction factor definitions are presented. First, the Fanning friction factor f is defined as

$$f = \frac{\Delta p}{2\rho u_i^2}\cdot\frac{D_h}{L} \tag{6}$$

where u_i is the inlet velocity, and L is the two-pass channel total length.

Table 2 Comparison of Nusselt number and pressure drop of the smooth two-pass channel

		Re=200,000	Re=310,000	Re=440,000
Nu	This work	412.12	574.26	761.50
	Bunker [31]	483.34	620.82	770.85
	Deviation (%)	14.73	7.50	1.21
Δp (Pa)	This work	1005.63	2344.69	4656.32
	Bunker [31]	1186.44	2758.47	4998.82
	Deviation (%)	15.24	15.01	6.83

The overall/averaged Nusselt number can be calculated in the following way. The local Nusselt number of every cell is first calculated as

$$\mathrm{Nu}(i) = \frac{q_w}{T(i) - T_f} \cdot \frac{D_h}{k} \tag{7}$$

where T_f is the mass-weighted average temperature between the inlet and outlet fluid temperatures, $T(i)$ is the local surface temperature, and q_w is the wall heat flux. The pin-fin surfaces and endwall surface Nusselt numbers are then calculated by averaging the local Nusselt numbers included in the corresponding surfaces. The overall Nusselt number is determined by averaging all local Nusselt numbers of all cells included on both the pin-fin surfaces and endwall surface. It is noted that for the smooth two-pass channel, there is only the endwall surface heat transfer coefficient or Nusselt number.

4.2 Model Validation. Prior to conducting the aimed computations, it is necessary to validate the computational model. The turbulent heat transfer in the smooth-tip two-pass channel is computed. The averaged Nusselt numbers and inlet-to-outlet pressure drop are also compared and listed in Table 2. It is found that the maximum deviation of the averaged Nusselt number between the simulated results by the RNG k-ε turbulence model and the experimental data is less than 15%, and the minimum deviation is 2%. In the work by Bunker [31], the experimental uncertainty in the heat transfer coefficient is between 8% and 15%. The good agreement between the predicted and tested results shows the reliability of the physical model. Thus, the validation and reliability of the present paper are ensured. More details can be found in Ref. [43].

4.3 Velocity and Temperature Fields. In order to provide a better understanding of the enhanced heat transfer over the tips, the velocity vectors and temperature contours are presented. Figure 5 shows the cross-sectional velocity vectors of the two channels. From Fig. 5, it can be seen that for both channels, high momentum fluid enters the turn from the inlet channel, and impinges on the outer walls. Before the sharp turn, the velocity profiles are flat. Upon entering the turn, the flow accelerates near the inner wall while it decelerates near the outer wall. This distribution is reversed at the beginning of the second channel. When the coolant travels through the 180-deg turn of the two-pass channels, areas of impingement, separation, and recirculation are created. Due to the inability of the flow to follow the turn, a separation bubble occurs downstream of the divider tip, followed by a reattachment. The two circulating regions occur at the first pass channel corner and the second pass corner. As the fluid flows through the 180-deg turn, the centrifugal forces arising from the curvature and pressure difference (low pressure at inner wall while high pressure at outer wall) produces a pair of counter-rotating vortices in the turn. These vortices are significant in strength, and are responsible for the transport of cold fluid from the core towards the outer wall. For the smooth tip channel, only vortices remain upstream of the second pass. For the pin-finned tip channel (only Case 7 is used to describe the flow mechanisms), the cores of the pair of counter-rotating vortices in the turn move downwards, close to the pin fins, and the zone of separation is larger than that of the smooth tip channel. At the upstream side of the second pass, both the vortices and the separation bubble exist. The vortices force the cold fluid to impinge toward the pin fins, and then induce turbulent mixing of the approaching cold fluid with the hot fluid near the pin fins and endwall. At this point, the heat transfer over the tip wall is increased due to the continuous mixing.

Figure 6 shows typical tip-wall temperature contours of the smooth tip and a pin-finned tip channel, Case 1. It can be observed

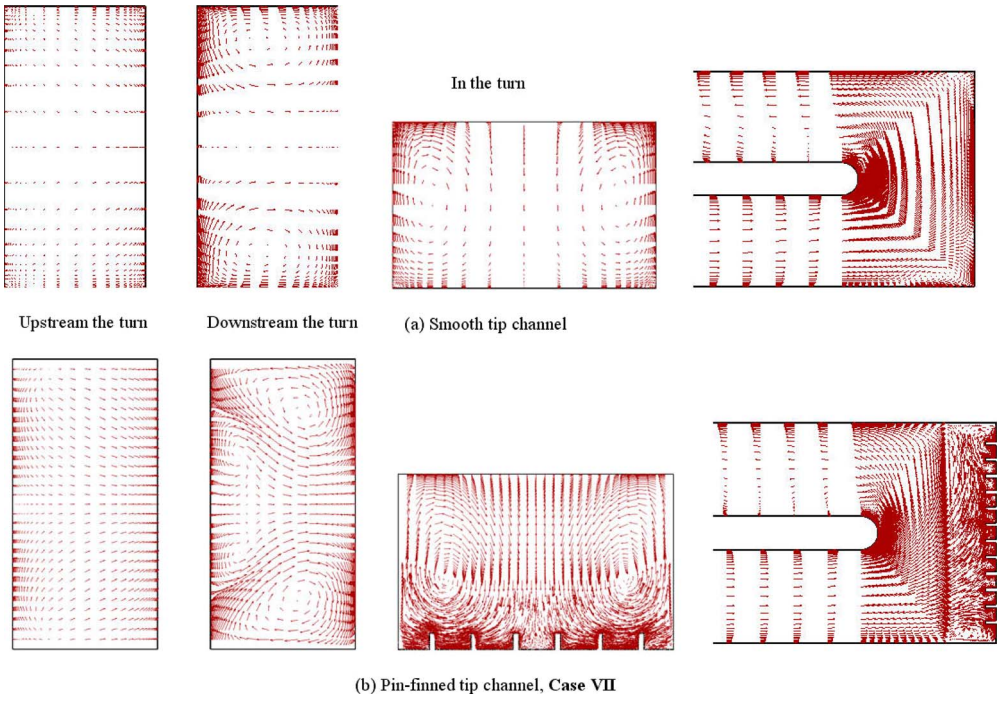

Fig. 5 Flow fields (upper: smooth tip; lower: pin-finned tip, Case 7)

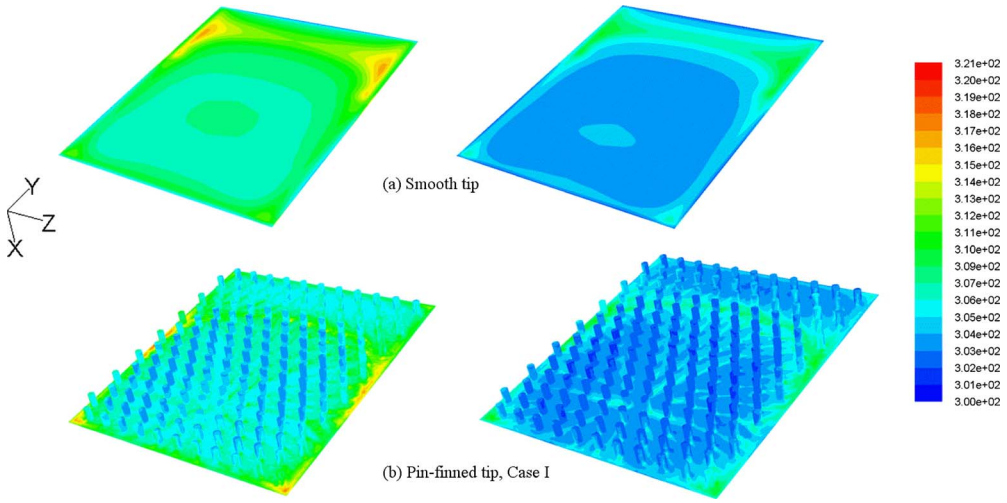

Fig. 6 Temperature contours (left: Re=200,000; right: Re=440,000)

that, due to the cold fluid impinging toward the tip wall, the temperature of the first tip part is lower than that of the second tip part. By comparing Figs. 6(*a*) and 6(*b*), it is found that a low temperature region occurs at the pin-finned surfaces, due to the cold fluid impingement and pin-fin crossflow. Especially for the pin fins, the temperature of the leading surfaces is lower than those of the rear surfaces. This might be because the staggered arrangement of pin-fins forces the impinging flow to accelerate in the gap upstream the front surfaces, and boundary layer flow separation occurs behind the pins. As an effect, higher temperature is found on the rear surfaces.

4.4 Friction and Heat Transfer

4.4.1 Effect of Pin-Fin Height. The averaged Nusselt number and inlet-outlet pressure drop for Case 2 and Case 3 are presented in Fig. 7. The pin-fin height of Case 3 is half of the pin-fin height of Case 2. For the heat transfer, the overall Nusselt numbers of the two pin-finned tip channels are 1.1 ~ 1.7 times higher than those of the smooth-tip channel. The overall heat transfer of Case 2 is slightly higher (about 2–4%) than that of Case 3, below a Reynolds number of 350,000. Beyond a Reynolds number of 350,000, Case 3 provides slightly higher heat transfer. This might be because the pin fins considered in this paper are relatively short, and then the pin-fin height has no significant effect on the tip-wall heat transfer enhancement. Similar local Nusselt number distribution can be observed from Figs. 8(*b*) and 8(*c*). From Fig. 7(*b*), the pressure drops of the two pin-finned tip channels are about 10–35% higher than those of the smooth-tip channel. The pressure drop of Case 3 is higher than that of Case 2, especially at high Reynolds numbers, i.e., 600,000.

4.4.2 Effect of Pin-Fin Diameter. The averaged Nusselt number and pressure drop for Case 2 and Case 7 are presented in Fig. 9. The pin-fin diameter of Case 7 is three-fourth (75%) of the pin-fin diameter of Case 2. From Fig. 9(*a*), it can be clearly found that the overall Nusselt numbers of the two pin-finned tip channels are 1.1–2.1 times higher than those of the smooth-tip channel. The overall heat transfer of Case 7 is about 10–18% higher than that of Case 2. From Figs. 8(*b*) and 8(*d*), it is found that the larger region with a high local Nusselt number is provided by Case 7, compared with that of Case 2. This indicates that for the short small pin fins considered in the present paper, the pin-fin diameter has an evident effect on the tip-wall heat transfer enhancement. From Fig. 9(*b*), the pressure drops of the two pin-finned tip channels are 10–36% higher than those of the smooth-tip channel. The pressure drop of Case 7 is slightly higher than that of Case 2. At the highest Reynolds numbers of 600,000, Case 7 produced about 10% higher pressure drop, compared with Case 2.

4.4.3 Effect of Pin-Fin Pitches. Figure 10 presents the averaged Nusselt number for Case 1 and Case 2. From Fig. 10(*a*), it is found that the heat transfer of the pin-finned tip channels is 12–84% higher than that of the smooth-tip channel. For the pressure loss, as in Fig. 10(*b*), the pressure drops of the pin-finned tip

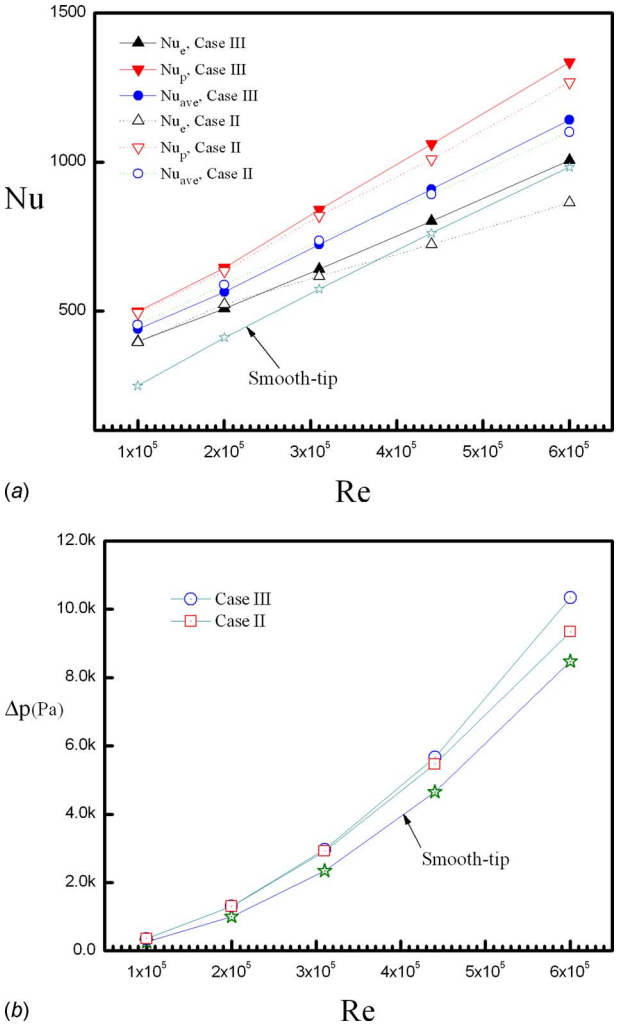

Fig. 7 Effect of pin-fin height on Nusselt number and pressure drop

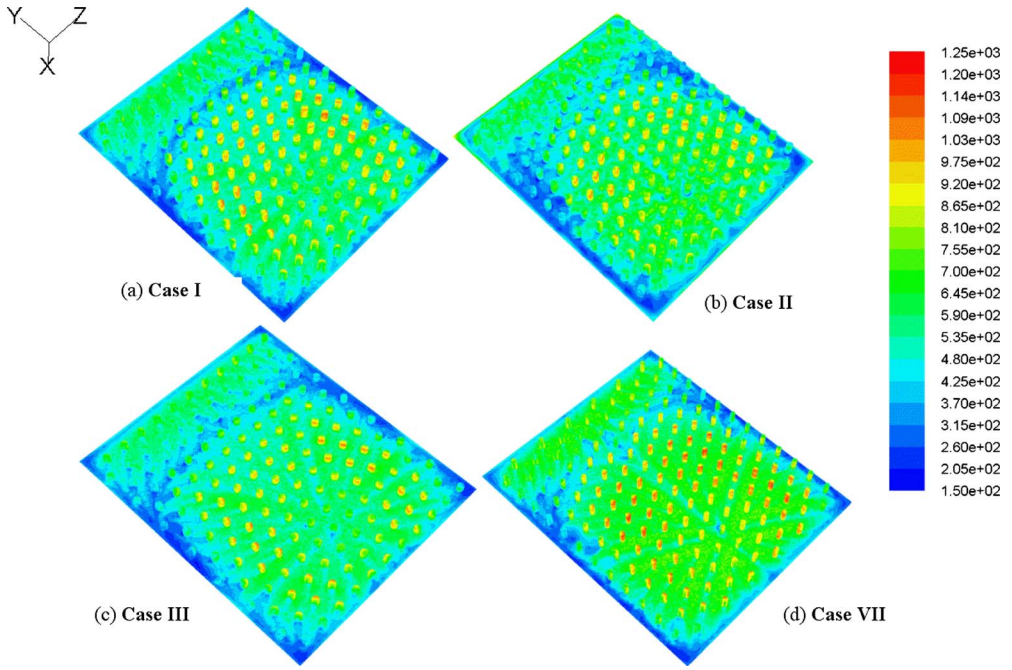

Fig. 8 Local Nusselt numbers (Case I, Case II, Case III, Case VII, Re=200,000)

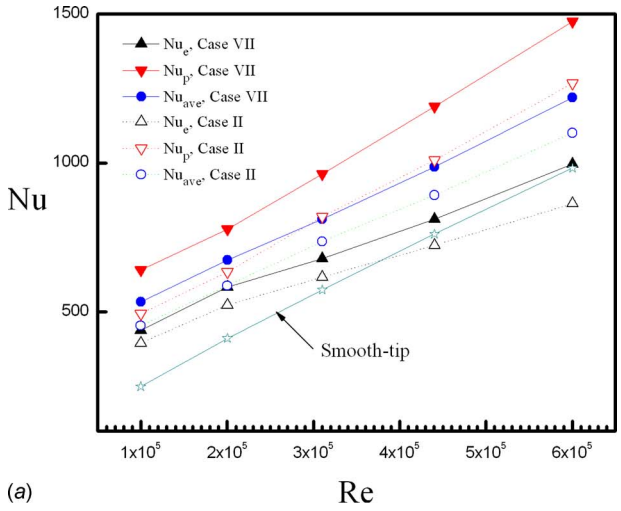

(*a*)

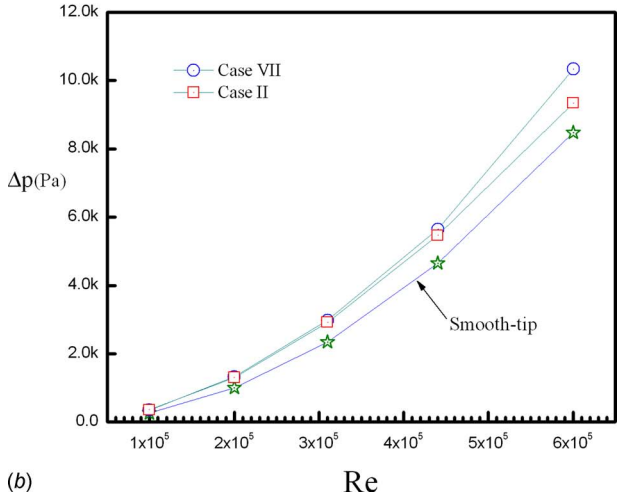

(*b*)

Fig. 9 Effect of pin-fin diameter on Nusselt number and pressure drop

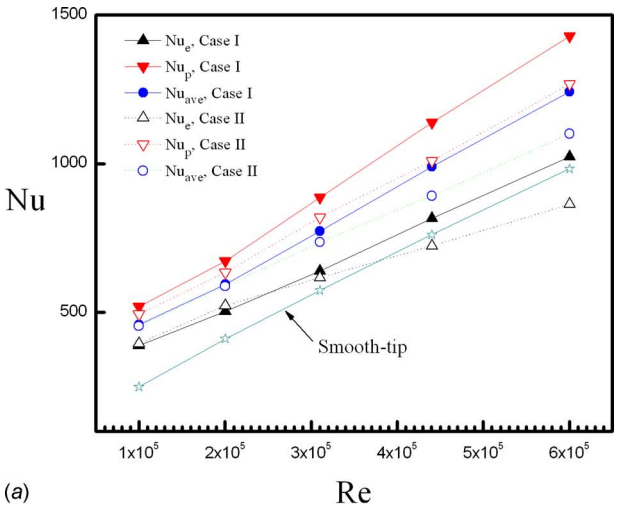

(*a*)

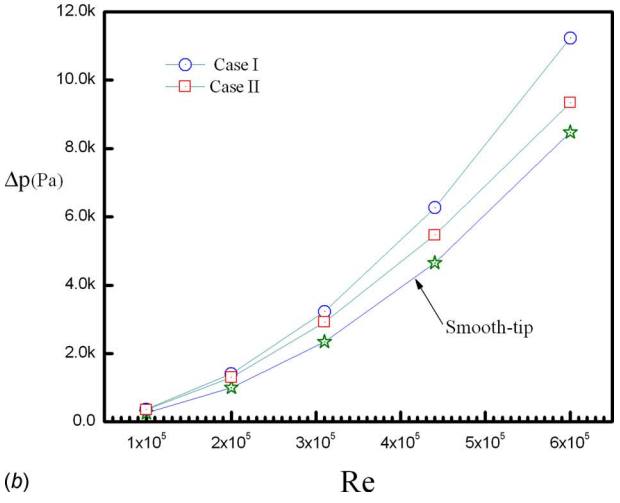

(*b*)

Fig. 10 Effect of pin-fin pitches on Nusselt number and pressure drop

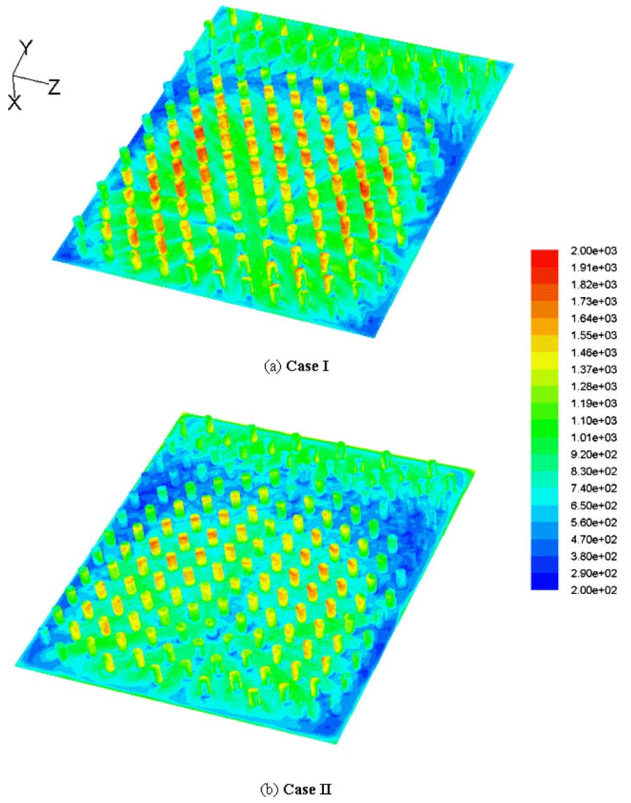

Fig. 11 Local Nusselt numbers of Case 1 and Case 2 at Re =440,000

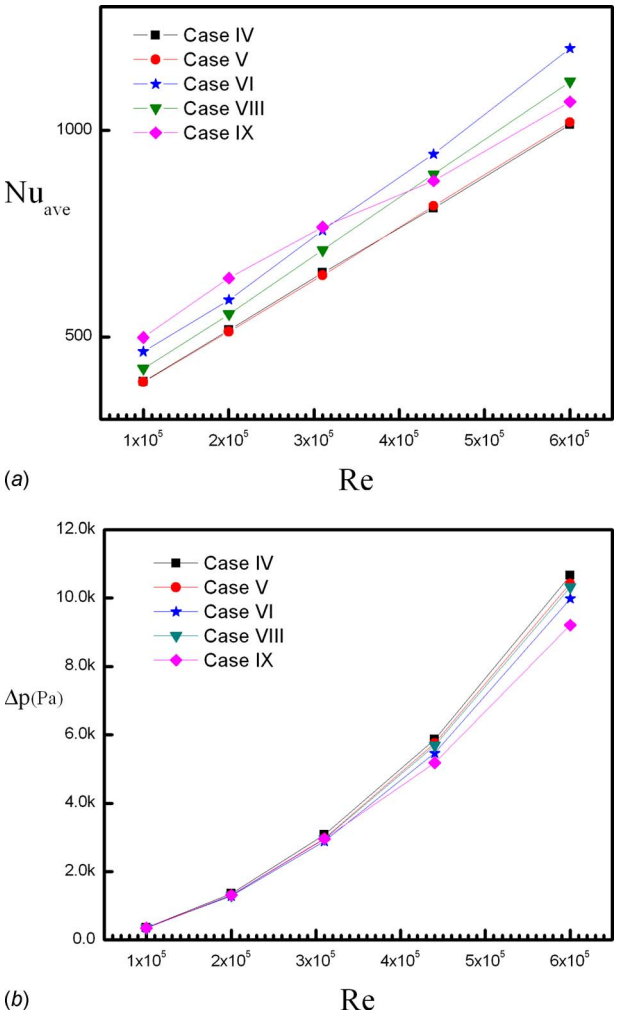

Fig. 12 Combination effect of pin-fin parameters on Nusselt number and pressure drop

channels are 10–42% higher than those of the smooth tip channel. This means that the increase in pressure drop is lower than that of the heat transfer. The pressure drop of Case 1 is 4–20% higher than that of Case 2. At the highest Reynolds number of 600,000, Case 1 produces about 20% higher pressure drop. From Figs. 8(*a*) and 8(*b*), it can be clearly seen that at a Reynolds number of 200,000, the tip surface local Nusselt number distributions for Case 1 and Case 2 are similar, while at Reynolds number of 440,000, as shown in Fig. 11, the local Nusselt number distribution of Case 1 is evidently different at most regions. Compared with Case 2, the larger surface regions of Case 1 have higher local Nusselt numbers, resulting in a higher overall heat transfer.

4.4.4 Combined Effect of Pin-Fin Parameters. The averaged Nusselt number and inlet-outlet pressure drop for the remaining cases, i.e., Case 4, Case 5, Case 6, Case 8, and Case 9, are summarized in Fig. 12. The heat transfer of the pin-finned tip channels is 12–84% higher than that of the smooth-tip channel. For the pressure loss, the pressure drops of the pin-finned tip channels are about 20–28% higher than those of the smooth tip channel. Case 9 provides the highest heat transfer among these cases below a Reynolds number of 320,000, while beyond that Reynolds number, the increased level of heat transfer of Case 9 is decreased so that the corresponding heat transfer is lower than those of Case 6 and Case 8 (additional calculations at Re=440 K and Re=600 K have verified these similar trends). Case 4 and Case 5 offer similar heat transfer performance, while Case 6 and Case 8 take second place and third place between Reynolds numbers 100 K and 450 K, respectively.

Figure 13 provides the averaged Nusselt number and friction factor, as normalized by the corresponding values for the turbulent flow and heat transfer inside the smooth-tip channel, based on inlet channel conditions (identical Reynolds numbers). From this figure, as expected with an increase in the Reynolds number, it is obvious that the value of Nu/Nu_s is decreased while the value of f/f_s is increased. The heat transfer enhancement ratios of the pin-finned tip two-pass channels over the smooth-tip channel lie between 1.1 and 2.1, while the increased friction factor ratios lie between 1.08 and 1.42. Case 4 and Case 5 provide the lowest heat transfer enhancement, while Case 7 provides the largest heat transfer enhancement below the Reynolds number of about 450,000. The results indicate that increasing the number of pin fins does not mean an increased heat transfer enhancement. By summarizing Fig. 13, the conclusion can be drawn that the heat transfer and pressure drop of the pin-finned tip two-pass channel are higher than those of the smooth tip two-pass channel. The benefit of heat transfer enhancement is substantial, even though the additional pressure loss is taken into account. Adopting pin fins increases the tip heat transfer, and hence, improves the cooling of the blade tip being exposed to high thermal load.

A comparison of Nusselt numbers between this work and the experimental data by Bunker [31] is plotted in Fig. 14. Three cases, i.e., Case 1, Case 2, and Case 7 are used for examples. The reason for this selection is that the pin fins of Case 1 and Case 2 have the same geometry as those in the experiments, and for the experimental data, the case with the highest Nusselt number is chosen. Since the present definition of Nusselt number is different from the definition by Bunker [31], the overall Nusselt number should be modified into that like Bunker's definition through the following transformation, based on energy conservation:

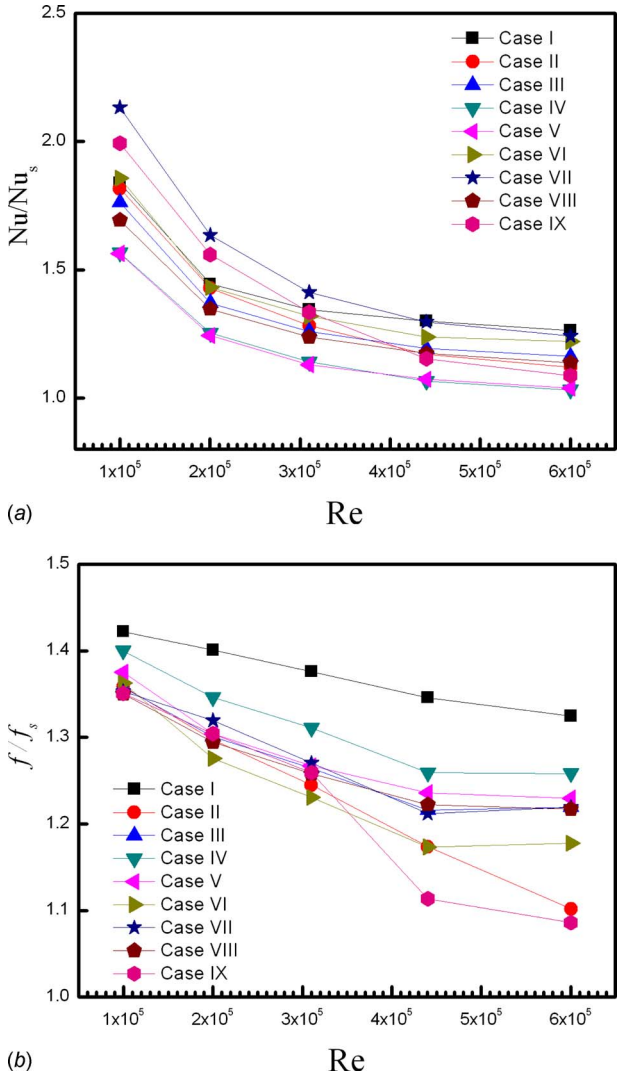

Fig. 13 Normalized Nusselt number and friction factor based on smooth-tip channel

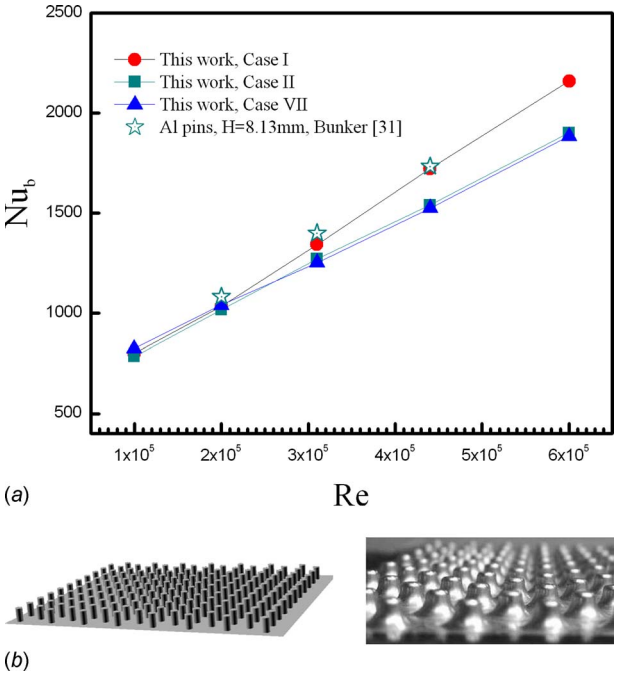

Fig. 14 Comparison of Nusselt number between simulation and experimental data by Bunker [31]

$$\mathrm{Nu}_b(i) = \frac{Q_w/A_s}{T(i) - T_f} \cdot \frac{D_h}{k} = \frac{(A_p + A_e)}{A_s} \cdot \frac{q_w}{T(i) - T_f} \cdot \frac{D_h}{k} = \frac{A}{A_s} \cdot \mathrm{Nu}(i) \tag{8}$$

where A/A_s is the increased area ratio, which is listed in Table 1, and $\mathrm{Nu}(i)$ is obtained by Eq. (7). It is found that good agreement of Nusselt numbers between of Case 1 and that case in Ref. [31] is achieved. At high Reynolds numbers, Nusselt numbers of that case in Ref. [31] are about 4–12% higher than those of the present: Case 2 and Case 7. This might partly be due to the fact that a difference is present in the geometries of the experimental samples and the numerical models. In the work by Bunker [31], shaped pins having base fillet and tip radius were tested, as shown in Fig. 14(*b*), while in the present paper, constant cross section (straight) circular pins have been assumed for simplicity. Since the casting process does not make a perfect cylinder pin, a fillet needs to be placed at the endwall. The pins tested by Bunker [31] seem to be of a stepped-diameter type, having the largest diameter at the base, and then a gradually reduced diameter along the pin height until the pin tip. With the different layout of the various shaped pin fins, the augmented area factors are different. As described in a previous section, the augmented area factors of the present cases are around 1.7, while the maximum augmented area factor in the experiments [31] is 2.1. Another reason might be the heat flux boundary condition. In the experiments by Bunker [31], a uniform heat flux was created for the external tip cap by applying a heater under the endwall surface, while for simplicity in the present numerical study, and as the details of the profiled pin surface heat flux could not be acquired, a uniform heat flux boundary condition is prescribed on both the pin-fin surfaces and the endwall surface. The imperfection of the heat flux boundary condition may therefore contribute to the difference between the simulated results and the experimental data, since in practice, the pin-fin surfaces do not have a uniform heat flux. These reasons probably explain why the enhanced heat transfer of the present pin-finned tip is not similar as those of Bunker's pin-finned tips [31]. On the other hand, since the clear details of pressure measurement and location point could not be picked in Bunker's experiments [31], the comparisons of profiled pressure are not presented in this paper.

5 Overall Comparisons

As mentioned above, the two-pass channel with pin-finned tip provides a higher Nusselt number associated with a higher pressure drop. Accordingly, it is essential to compare the heat transfer enhancement performance of the two-pass channels. In the present paper, two criteria are used to evaluate the overall performance of the two-pass channels with various pin-fin arrays.

Figure 15 presents a comparison of the averaged Nusselt number ratio divided by the normalized friction factor ratio for all the channels. The $\mathrm{Nu}/\mathrm{Nu}_0/(f/f_0)$ parameter is referred to as the Reynolds analogy performance parameter, and the $\mathrm{Nu}/\mathrm{Nu}_0/(f/f_0)^{1/3}$ parameter provides a heat transfer augmentation quantity. It relates the heat transfer augmentation $\mathrm{Nu}/\mathrm{Nu}_0$ and the friction factor increase f/f_0 for the same ratio of mass flux in a channel with augmentation devices to a channel with smooth surfaces. From Fig. 15(*a*), it is found that higher values of the parameter $\mathrm{Nu}/\mathrm{Nu}_0/(f/f_0)$ are produced by Case 2, Case 6, Case 7, and Case 9. Among these cases, Case 7 offers the highest values. Below the Reynolds number of 300,000, the values of $\mathrm{Nu}/\mathrm{Nu}_0/(f/f_0)$ of Case 1, Case 3, and Case 8 are higher than those of the smooth-tip channels. Beyond the Reynolds number of 200,000, the values of $\mathrm{Nu}/\mathrm{Nu}_0/(f/f_0)$ of the smooth-tip channels are higher than those of Case 4 and Case 5. From Fig. 15(*b*), it can be clearly seen that

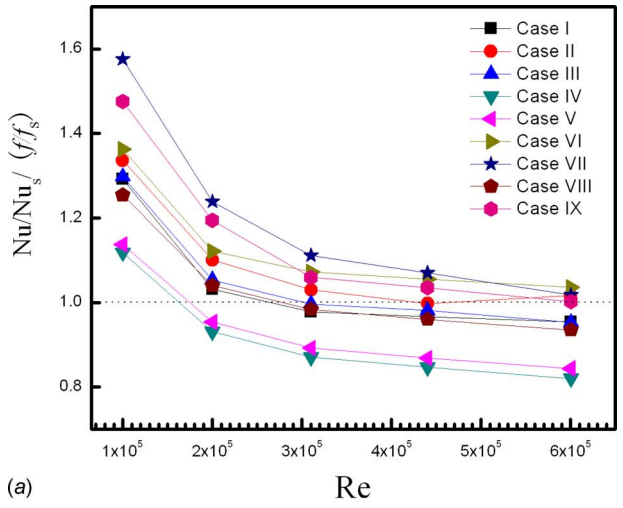

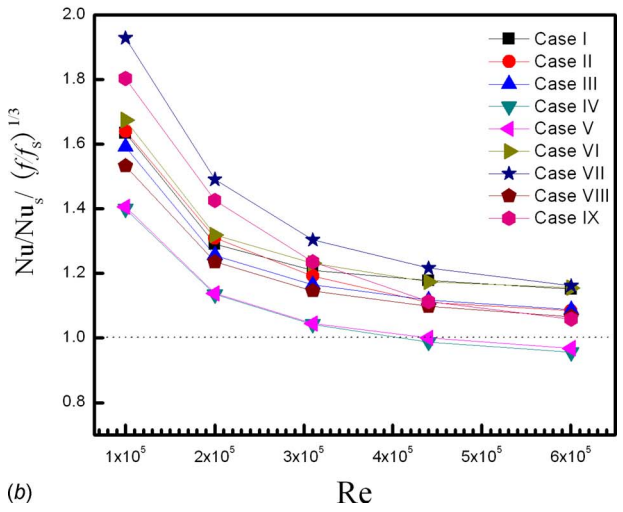

Fig. 15 Performance comparison of various tips under Case 1

the highest values of the parameter $\mathrm{Nu}/\mathrm{Nu}_0/(f/f_0)^{1/3}$ are also produced by Case 7. Except for Case 4 and Case 5 at Reynolds numbers being larger than about 450,000, all cases provide higher values of $\mathrm{Nu}/\mathrm{Nu}_0/(f/f_0)^{1/3}$ than that of the smooth-tip channel. Summarizing from this figure, it is suggested, based on the two criteria, that Case 7 exhibits the best performance, followed by Case 9 and Case 6.

Figure 16 presents a comparison of the heat transfer coefficients subject to the required pumping powers for all the channels. From this figure, it is found that at identical required pumping power, the pin-finned tip channels (except for the Case 4 and Case 5 at pumping power being larger than about 5,000 W) offer a higher heat transfer coefficient, and thereby higher heat transfer enhancement. This indicates that the application of pin fins on the tip could substantially increase the heat transfer intensity associated with low additional pressure loss. Therefore, from Figs. 15 and 16, the pin-finned tip two-pass channels (especially for Case 7) provide good performance for gas turbine blade tip cooling.

6 Conclusions

A parametric study of the three-dimensional turbulent flow and convective heat transfer over a blade tip has been performed. Nine models of pin-finned tip channels are considered. The overall performance of all the channels is evaluated. The main conclusions from this paper can be summarized as follows.

(1) The pin fins are very effective heat transfer enhancement devices for gas turbine blade tips due to combination of turn, impingement, and pin-fin crossflow. The pin fins force the vortices toward the tip wall, and thereby improve the turbulent mixing of the approaching cold and hot fluids near the tip.

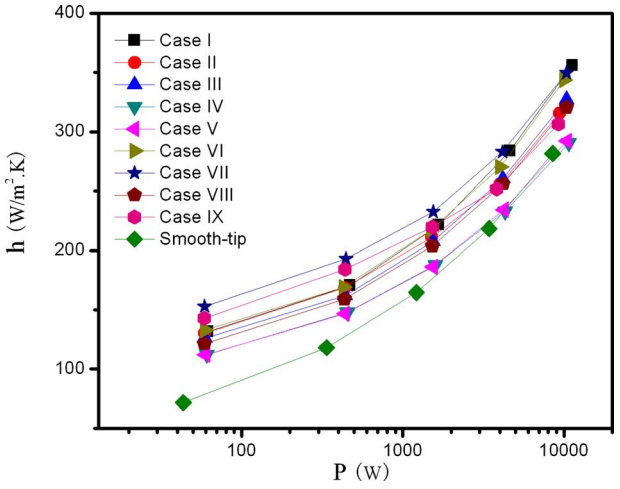

Fig. 16 Performance comparison of various tips under Case 2

(2) Compared with the smooth-tip channel, the heat transfer enhancement of the pin-finned tip channels is up to 2.67. The pin-fin heat transfer is about 30–40% higher than the endwall heat transfer.

(3) For the short small pin fins studied in the present paper, the heat transfer enhancement is influenced slightly by the pin-fin height, but is affected clearly by the pin-fin diameter and pin-fin pitches. The performance of heat transfer enhancement on the pin-finned tip depends on the pin-fin configurations and arrangements.

(4) By applying two criteria, it is found that the pin-finned tip channels provide good overall performance. It is suggested that application of pin fins for tip cooling is effective with a high heat transfer enhancement at a moderate additional pressure loss.

Acknowledgment

The research has been funded by the Swedish Energy Agency, Siemens Industrial Turbomachinery AB, and Volvo Aero Corporation through the Swedish research program TURBO POWER. The support of which is gratefully acknowledged.

Nomenclature

A = wall surface area
D = pin-fin diameter
D_h = hydraulic diameter
f = Fanning friction factor
H = pin-fin height
h = heat transfer coefficient
k = fluid-thermal conductivity
N = number of pin fins
Nu = Nusselt number
p = pressure
P = pumping power
q_w = wall heat flux
Re = Reynolds number ($\mathrm{Re}=\rho u_i D_h/\mu$)
S = spanwise/transverse pin-fin pitch
T = temperature
u_i = inlet velocity
X = streamwise/longitudinal pin-fin pitch

Greek Symbols

Δp = pressure drop
μ = fluid dynamic viscosity
ρ = fluid density

Subscripts

0 = fully developed flow channel
ave = averaged/overall
b = defined by Bunker [31]
e = endwall of tip
i = inlet
o = outlet
p = pin fin
s = smooth-tip channel
w = wall

References

[1] Han, J. C., Dutta, S., and Ekkad, S. V., 2000, *Gas Turbine Heat Transfer and Cooling Technology*, Taylor & Francis, New York.
[2] Goldstein, R. J., 2001, *Heat Transfer in Gas Turbine Systems*, New York Academy of Sciences, New York.
[3] Sundén, B., and Faghri, M., 2001, *Heat Transfer in Gas Turbines*, WIT, UK.
[4] Han, J. C., 2004, "Recent Studies in Turbine Blade Cooling," Int. J. Rotating Mach., **10**(6), pp. 1–15.
[5] Bunker, R. S., 2000, " A Review of Turbine Blade Tip Heat Transfer," *Annals of the New York Academy of Sciences*, R. J. Goldstein, ed., New York Academy of Sciences, New York, pp. 64–79.
[6] Bunker, R. S., 2006, "Axial Turbine Blade Tips: Function, Design and Durability," J. Propul. Power, **22**(2), pp. 271–285.
[7] Ekkad, S. V., Pamula, G., and Shantiniketanam, M., 2000, "Detailed Heat Transfer Measurements Inside Straight and Tapered Two-Pass Channels With Rib Turbulators," Exp. Therm. Fluid Sci., **22**, pp. 155–163.
[8] Son, S. Y., Kihm, K. D., and Han, J. C., 2002, "PIV Flow Measurements for Heat Transfer Characterization in Two-Pass Square Channels With Smooth and 90° Ribbed Walls," Int. J. Heat Mass Transfer, **45**, pp. 4809–4822.
[9] Al-Hadhrami, L., Griffith, T., and Han, J. C., 2003, "Heat Transfer in Two-Pass Rotating Rectangular Channels (AR=2) With Five Different Orientations of 45-deg V-Shaped Rib Turbulators," ASME J. Heat Transfer, **125**, pp. 232–242.
[10] Astarita, T., Cardone, G., and Carlomagno, G. M., 2002, "Convective Heat Transfer in Ribbed Channels With a 180° Turn," Exp. Fluids, **33**, pp. 90–100.
[11] Liou, T. M., Chen, M. Y., and Wang, Y. M., 2003, "Heat Transfer, Fluid Flow and Pressure Measurements Inside a Rotating Two-Pass Duct With Detached 90-deg Ribs," ASME J. Turbomach., **125**, pp. 565–574.
[12] Liou, T. M., Hwang, Y. S., and Li, Y. C., 2006, "Flowfield and Pressure Measurements in a Rotating Two-Pass Duct With Staggered Rounded Ribs Skewed 45-deg to the Flow," ASME J. Turbomach., **128**, pp. 340–348.
[13] Fu, W. L., Wright, L. M., and Han, J. C., 2005, "Heat Transfer in Two-Pass Rotating Rectangular Channels (AR=1:2 and AR=1:4) With 45-deg Angled Rib Turbulators," ASME J. Turbomach., **127**, pp. 164–174.
[14] Fu, W. L., Wright, L. M., and Han, J. C., 2006, "Heat Transfer in Two-Pass Rotating Rectangular Channels (AR=1:2) With Discrete Ribs," J. Thermophys. Heat Transfer, **20**(3), pp. 569–582.
[15] Liu, Y. H., Wright, L. M., Fu, W. L., and Han, J. C., 2007, "Rib Spacing Effect on Heat Transfer in Rotating Two-Pass Ribbed Channel," J. Thermophys. Heat Transfer, **21**(3), pp. 582–595.
[16] Kim, K. M., Lee, D. H., Rhee, D. H., and Cho, H. H., 2006, "Local Heat/Mass Transfer Phenomena in Rotating Passage, Part 1: Smooth Passage," J. Thermophys. Heat Transfer, **20**(2), pp. 188–198.
[17] Kim, K. M., Lee, D. H., Rhee, D. H., and Cho, H. H., 2006, "Local Heat/Mass Transfer Phenomena in Rotating Passage, Part 2: Angled Ribbed Passage," J. Thermophys. Heat Transfer, **20**(2), pp. 199–210.
[18] Lee, S. W., Ahn, H. S., and Lau, S. C., 2007, "Heat (mass) Transfer Distribution in a Two-Pass Trapezoidal Channel With a 180-deg Turn," ASME J. Heat Transfer, **129**, pp. 1529–1537.
[19] Lucci, J. M., Amano, R. S., and Guntur, K., 2007, "Turbulent Flow and Heat Transfer in Variable Geometry U-Bend Blade Cooling Passage," ASME Paper No. GT2007-27120.
[20] Jenkins, S. C., Zehnder, F., and Shevchuk, I. V., 2008, "The Effect of Ribs and Tip Wall Distance on Heat Transfer for a Varying Aspect Ratio Two-Pass Ribbed Internal Cooling Channel," ASME Paper No. GT2008-51270.
[21] Shevchuk, I. V., Jenkins, S. C., and Zehnder, F., 2008, "Validation and Analysis of Numerical Results for a Varying Aspect Ratio Two-Pass Internal Cooling Channel," ASME Paper No. GT2008-51219.
[22] Metzger, D. E., Berry, R. A., and Bronson, J. P., 1982, "Developing Heat Transfer in Rectangular Ducts With Staggered Arrays of Short Pin Fins," ASME J. Heat Transfer, **104**, pp. 700–706.
[23] Lau, S. C., Kim, Y. S., and Han, J. C., 1987, "Local Endwall Heat/Mass Distributions in Pin Fin Channels," AIAA J. Thermophys. Heat Transfer, **1**(4), pp. 365–372.
[24] Chyu, M. K., Hsing, Y. C., Shih, T. I. P., and Natarajan, V., 1999, "Heat Transfer Contributions of Pins and Endwall in Pin-Fin Arrars: Effect of Thermal Boundary Condition Modeling," ASME J. Turbomach., **121**, pp. 257–263.
[25] Goldstein, R. J., Jabbari, M. Y., and Chen, S. B., 1994, "Convective Mass Transfer and Pressure Loss Characteristics of Staggered Short Pin-Fin Arrays," Int. J. Heat Mass Transfer, **37**(1), pp. 149–160.
[26] Wright, L. M., Lee, E., and Han, J. C., 2004, "Effect of Rotating on Heat Transfer in Rectangular Channels With Pin Fins," J. Thermophys. Heat Transfer, **18**(2), pp. 263–272.
[27] Ames, F. E., Dvorak, L. A., and Morrow, M. J., 2005, "Turbulent Augmentation of Internal Convection Over Pins in Staggered-Pin Fin Arrays," ASME J. Turbomach., **127**, pp. 183–190.
[28] Sahiti, N., Lemouedda, A., Stojkovic, D., Durst, F., and Franz, E., 2006, "Performance Comparison of Pin Fin In-Duct Flow Arrays With Various Pin Cross-Section," Appl. Therm. Eng., **26**, pp. 1176–1192.
[29] Su, G. G., Chen, H. C., and Han, J. C., 2007, "Computation of Flow and Heat Transfer in Rotating Rectangular Channels (AR=4:1) With Pin-Fins by a Reynolds Stress Turbulence Model," ASME J. Heat Transfer, **129**, pp. 685–696.
[30] Chang, S. W., Yang, T. L., Huang, C. C., and Chiang, K. F., 2008, "Endwall Heat Transfer and Pressure Drop in Rectangular Channels With Attached and Detached Circular Pin-Fin Array," Int. J. Heat Mass Transfer, **51**, pp. 5247–5259.
[31] Bunker, R. S., 2008, "The Augmentation of Internal Blade Tip-Cap Cooling by Arrays of Shaped Pins," ASME J. Turbomach., **130**, p. 041007.
[32] Saha, A., and Acharya, S., 2004, "Unsteady Simulation of Turbulent Flow and Heat Transfer in a Channel With Periodic Array of Cubic Pin-Fins," Numer. Heat Transfer, Part A, **46**(8), pp. 731–763.
[33] Etemad, S., and Sundén, B., 2006, "Numerical Investigation of Turbulent Heat Transfer in a Rectangular-Sectioned 90° Bend," Numer. Heat Transfer, Part A, **49**(4), pp. 323–343.
[34] Kim, K. Y., and Lee, Y. M., 2007, "Design Optimization of Internal Cooling Passage With V-shaped Ribs," Numer. Heat Transfer, Part A, **51**(11), pp. 1103–1118.
[35] Chen, H. C., Jang, Y. J., and Han, J. C., 2000, "Computation of Heat Transfer in Rotating Two-Pass Square Channels by a Second-Moment Closure Model," Int. J. Heat Mass Transfer, **43**, pp. 1603–1616.
[36] Jang, Y. J., Chen, H. C., and Han, J. C., 2001, "Computation of Flow and Heat Transfer in Two-Pass Channels With 60-deg Ribs," ASME J. Heat Transfer, **123**, pp. 563–575.
[37] Al-Qahtani, M., Jang, Y. J., Chen, H. C., and Han, J. C., 2002, "Flow and Heat Transfer in Rotating Two-Pass Rectangular Channels (AR=2) by Reynolds Stress Turbulence Model," Int. J. Heat Mass Transfer, **45**, pp. 1823–1838.
[38] Jia, R., Sunden, B., and Faghri, M., 2005, "Computational Analysis of Heat Transfer Enhancement in Square Ductrs With V-shaped Ribs—Turbine Blade Cooling," ASME J. Heat Transfer, **127**, pp. 425–433.
[39] Jia, R., Sunden, B., and Faghri, M., 2007, "A New Low Reynolds Stress Transport Model for Heat Transfer and Fluid in Engineering Applications," ASME J. Heat Transfer, **129**, pp. 434–440.
[40] Yang, C. S., Jeng, D. Z., Yih, K. A., Gau, C., Aung, W., 2009, "Numerical and Analytical Study of Reversed Flow and Heat Transfer in a Heated Vertical Duct," ASME J. Heat Transfer, **131**, p. 072501.
[41] Zhou, F., Lagrone, J., and Acharya, S., 2007, "Internal Cooling in 4:1 AR Passages at High Rotation Numbers," ASME J. Heat Transfer, **129**, pp. 1666–1675.
[42] Liu, Y.H., Huh, M., Han, J.C., Chopra, S., 2008, "Heat Transfer in a Two-Pass Rectangular Channel (AR=1:4) Under High Rotation Numbers," ASME J. Heat Transfer, **130**, p. 081701.
[43] Xie, G. N., Sundén, B., Wang, L. K., and Utriainen, E., 2009, "Enhanced Internal Heat Transfer on the Tip-wall in a Rectangular Two-pass Channel by Pin-Fin Arrays," Numer. Heat Transfer, Part A, **55**, pp. 739–761.
[44] Choudhury, D., 1993, "Introduction to the Renormalization Group Method and Turbulence Modeling," Fluent Inc. Technical Paper No. TM-107.

Equilibrium Molecular Dynamics Study of Lattice Thermal Conductivity/Conductance of Au-SAM-Au Junctions

Tengfei Luo
Department of Mechanical Engineering,
Michigan State University,
2555 Engineering Building,
East Lansing, MI 48824
e-mail: luotengf@msu.edu

John R. Lloyd[1]
ASFC 1.316.C RRMC,
Rapid Response Manufacturing Center,
University of Texas Pan American,
Edinburg, TX 78539
e-mail: lloyd@egr.msu.edu

In this paper, equilibrium molecular dynamics simulations were performed on Au-SAM (self-assembly monolayer)-Au junctions. The SAM consisted of alkanedithiol ($-S-(CH_2)_n-S-$) molecules. The out-of-plane (z-direction) thermal conductance and in-plane (x- and y-direction) thermal conductivities were calculated. The simulation finite size effect, gold substrate thickness effect, temperature effect, normal pressure effect, molecule chain length effect, and molecule coverage effect on thermal conductivity/conductance were studied. Vibration power spectra of gold atoms in the substrate and sulfur atoms in the SAM were calculated, and vibration coupling of these two parts was analyzed. The calculated thermal conductance values of Au-SAM-Au junctions are in the range of experimental data on metal-nonmetal junctions. The temperature dependence of thermal conductance has a similar trend to experimental observations. It is concluded that the Au-SAM interface resistance dominates thermal energy transport across the junction, while the substrate is the dominant media in which in-plane thermal energy transport happens. [DOI: 10.1115/1.4000047]

Keywords: molecular dynamics, thermal energy transport, interface

1 Introduction

Molecular electronic devices have become more and more important nowadays, and among them, the self-assembly monolayer (SAM) on metal or semiconductor substrates has drawn much attention. There were intensive works focused on the electronic and structural properties of SAM-solid junctions [1–4]. However, the studies of thermal properties of such junctions are limited, and knowledge of thermal transport in these junctions is very important to the growing fields of molecular electronics and small molecule organic thin film transistors. Ge et. al [5] measured the transport of thermally excited vibrational energy across planar interfaces between water and solids that have been chemically functionalized with the SAM using the time-domain thermoreflectance. Wang et. al [6] studied heat transport through the SAM of long-chain hydrocarbon molecules anchored to a gold substrate by ultrafast heating of the gold. Patel et. al [7] studied the interfacial thermal resistance of water-surfactant-hexane systems by nonequilibrium molecular dynamics.

There are two typical kinds of SAM-solid junctions, one of them is the SAM-metal junction, which was studied a lot [8,9]. The other kind is the SAM-semiconductor junction, which is relatively new, but became very popular [10]. In this work, thermal transport in Au-SAM-Au junctions with alkanedithiols ($-S-(CH_2)_n-S-$) being the SAM molecules is studied using molecular dynamics (MD). The reason such junctions are chosen is that the structural properties, including the absorption site, tilt angle, coverage, etc., were studied thoroughly [8,9,11,12], and a set of reliable classical potentials for MD simulation is available [13]. In such metal-SAM-metal junctions, the SAM-metal interfaces play important roles in thermal energy transport across the junctions, especially when the system sizes are in the nanoscale [14].

In solid materials, there exist two kinds of heat carriers in thermal energy transport: phonons and electrons. Phonons are the quanta of the lattice vibrational field [15]. Phonons dominate the thermal energy transport in semiconductors and insulators, while electrons play important roles in energy transport in metals. In this work, where the metal-SAM junction exists, it is difficult for electrons in the metal to tunnel through the SAM molecules, and thus, electron transport is largely depressed by the nonmetal SAM layer. As a result, the primary goal of this work is to calculate the lattice thermal conductivities/conductance in both in-plane directions (*x*- and *y*-directions) and out-of-plane direction (*z*-direction) of the junctions. Some physical insight of the thermal energy transport mechanism is done by analyzing vibration coupling between different groups of atoms. A more detailed analysis of the thermal transport mechanism across the junctions is being done in a follow-on work, which uses nonequilibrium MD.

For lattice thermal conductivity calculations, classical MD with appropriate potential functions was demonstrated to be a powerful method [16–23]. However, to our knowledge, no work has been done to investigate the thermal transport properties of metal-SAM-metal junctions by MD simulation. The equilibrium MD with the Green–Kubo [24] method was applied successfully to heterogeneous systems such as superlattices [21] and solid-liquid interfaces [22,23]. As a result, in the present work, equilibrium MD is chosen to simulate Au-SAM-Au junctions, and thermal transport properties are calculated using the Green–Kubo method. Thermal conductivities and conductance are calculated versus simulation cell size, temperature, junction thickness, molecular chain length, molecule coverage (number of molecules on Au substrates), and simulated normal pressure.

[1]Corresponding author.

Contributed by the Heat Transfer Division of ASME for publication in the JOURNAL OF HEAT TRANSFER. Manuscript received November 13, 2008; final manuscript received August 14, 2009; published online December 22, 2009. Editor: Yogesh Jaluria.

2 Theory and Simulation

Classical MD is a computational method that simulates the behavior of a group of atoms by simultaneously solving Newton's second law of motion (Eq. (1)) for the atoms with a given set of potentials, that is

$$-\nabla\phi = \vec{F} = m\frac{d^2\vec{r}}{dt^2} \tag{1}$$

where ϕ is the potential energy, $\vec{F}$ is the force, m is the atomic mass, $\vec{r}$ is the position vector, and t is the time. By processing the trajectory obtained from an MD simulation using different statistical techniques, transport properties such as diffusion coefficient and thermal conductivity can be calculated.

MD was proven to be a powerful tool in nanoscale thermal energy transport studies [25–27]. There are two different MD approaches to study thermal transport in solid systems: equilibrium method and nonequilibrium method (also called direct method). The nonequilibrium method is like an experiment. By applying a heat bath to a system, the thermal conductivity is calculated by the Fourier's law of conduction [7,28]. In the equilibrium method, a system is simulated in an equilibrium state. It relies on small statistical temperature fluctuations to drive instantaneous heat fluxes. The thermal conductivity of the system can be calculated from the heat current autocorrelation (HCAC) function, according to the Green–Kubo formula [24]. This method was used widely, and was shown to give good results [29,30].

According to Green–Kubo relation, the thermal conductivity tensor k can be calculated with the following equation:

$$k = \frac{1}{Vk_BT_m^2}\int_0^\infty \langle\vec{J}(\tau)\vec{J}(0)\rangle d\tau \tag{2}$$

where $\vec{J}(\tau)$ is the instantaneous heat current, $\langle\vec{J}(\tau)\vec{J}(0)\rangle$ is the HCAC function, V is the volume of the simulated system, k_B is the Boltzmann constant, and T_m is the mean temperature during the production period of a MD simulation. Heat current $\vec{J}$ is given by

$$\vec{J} = \frac{\partial}{\partial t}\left(\sum_j \vec{r}_j E_j\right) \tag{3}$$

where the subscript j refers to the index of atoms, and E_j is the total energy including potential and kinetic energy of atom j. Since Eq. (3) produces heat current vectors, thermal conductivities in the x-, y-, and z-directions can then be calculated by one single simulation.

It needs to be noted that in this work, the Green–Kubo method is used towards the whole junction and calculated lumped thermal conductivities of the whole junction. The calculated thermal conductivity in the z-direction is a combination of thermal conductivities of the materials making up the junction. It should not be considered as a material property, and its value varies when the system configuration changes.

In any MD simulation, potential functions are critical. In this work, the well established Hautman–Klein model [13] is employed. In this model, the light hydrogen atoms of the hydrocarbon molecules are not simulated explicitly, but incorporated into the carbon backbone. Their masses are added to the carbon atoms, which they bond to, and forming pseudo carbon atoms. The reason for such treatment is that the high frequency vibrational motions of light hydrogen atoms in the hydrocarbon groups are less important than the lower frequency movements of the carbon backbone [13]. Such treatment was demonstrated to be a valid approach to simplify simulations, and to give good results [30,31]. Bond stretching, bond bending, and the Ryckaert–Bellemans torsion potentials are used in alkanedithiol molecules for the bonded interactions. Morse type interactions are used to simulate the interaction between sulfur atoms and gold substrates [32,33], and the interaction among gold atoms [34]. The Lennard-Jones potentials, together with the Lorentz–Berthelot mixing rule [35], $\varepsilon_{ab} = \sqrt{\varepsilon_a\varepsilon_b}$, $\sigma_{ab} = 1/2(\sigma_a + \sigma_b)$, are used to simulate long distance and intermolecular interactions. The potential function and parameters are listed in Table 1. All the parameters are from Refs. [13,32], or as otherwise specified in the table. In our simulations, a neighborlist with cutoff of less than 12.00 Å is used to speed up the calculation (in our code, the neighborlist cutoff radius is compared with dimensions of the system, and it is adjusted automatically to avoid double counting). This neighborlist is not updated after the structure is optimized, due to the fact that there should not be large atomic displacements other than vibrations about the equilibrium positions in the solid phase system. For every simulation, five separate runs with different random initial conditions were performed. The resulting values are averaged over the five runs.

Table 1 Potential functions with parameters used in the simulations

Potential	Function forms and parameters	
Bond stretching S–C C–C	$U_s = \frac{1}{2}k_s(r - r_o)^2$ where $k_s = 14.00224$ eV/Å^2, $r_o = 1.523$ Å (for C–C), and $r_o = 1.815$ Å (for S–C)	(4)
Bond bending S–C–C C–C–C	$U_\theta = \frac{1}{2}k_\theta(\theta - \theta_o)^2$ where $k_\theta = 5.388$ eV/rad^2, $\theta_o = 109.5$ (for C–C–C), and $\theta_o = 114.4$ (for S–C–C)	(5)
Ryckaert–Bellemans torsion S–C–C–C C–C–C–C	$U_t = \sum_{i=0}^{5} a_i \cos^i(\varphi)$ where φ is the dihedral angle $a_0 = 0.09617$ eV, $a_1 = 0.125988$ eV, $a_2 = -0.13598$ eV, $a_3 = -0.0317$ eV, $a_4 = 0.27196$ eV, $a_5 = -0.32642$ eV	(6)
Lennard-Jones with Lorentz–Berthelot mixing rule	$U_{L\text{-}J} = 4\varepsilon\left[\left(\frac{\sigma}{r}\right)^{12} - \left(\frac{\sigma}{r}\right)^{6}\right]$ where ε and σ are determined by mixing rule [35] for C: $\varepsilon = 0.00513$ eV, $\sigma = 3.914$ Å for S that interact with other atoms other than S: $\varepsilon = 0.01086$ eV, $\sigma = 3.550$ Å for Au: $\varepsilon = 0.001691$ eV, $\sigma = 2.934$ Å [36] for S–S interaction: $\varepsilon = 0.01724$ eV, $\sigma = 4.250$ Å	(7)
Morse Au–Au Au–S	$U_M = De[(1 - e^{-a(r-r_{mo})})^2 - 1.0]$ where $De = 0.475$ eV (for Au–Au) [34], $De = 0.380$ eV (for Au–S) [33], $a = 1.583$ Å^{-1} (for Au–Au), $a = 1.470$ Å^{-1} (for Au–S), $r_{mo} = 3.0242$ Å (for Au–Au), and $r_{mo} = 2.650$ Å (for Au–S)	(8)

The structures of Au-SAM-Au junctions studied in this work are shown in Fig. 1. The junctions consist of two gold substrates with the SAM in between. $-S-(CH_2)_8-S-$ is used as the SAM molecule for all simulations except those in Sec. 3.7. Figure 1 shows systems with different cell sizes in the x- and y-directions. In this figure, Fig. 1(a) is a system with four molecules, Fig. 1(b) is a system with 16 molecules, and Fig. 1(c) contains 36 molecules. In all these systems, each substrate contains 12 layers of gold atoms. The procedures to prepare the junctions are as follows. First, 1 Au(111) substrate is optimized using the Morse potential (Figure 2(a)). Then, a number of SAM molecules are implanted on the gold substrate with the sulfur heads placed in the

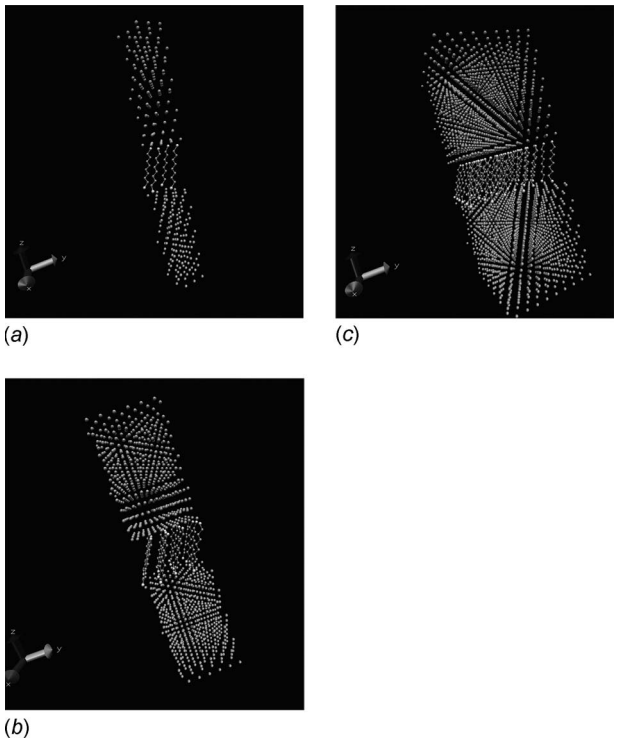

Fig. 1 Simulated Au-SAM-Au systems of different sizes: (*a*) a 1×1 system of 328 atoms (4 alkanedithiol molecules and 288 gold substrate atoms), (*b*) a 2×2 system of 1312 atoms (16 alkanedithiol molecules and 1152 gold substrate atoms), and (*c*) a 3×3 system of 2952 atoms (36 alkanedithiol molecules and 2592 gold substrate atoms)

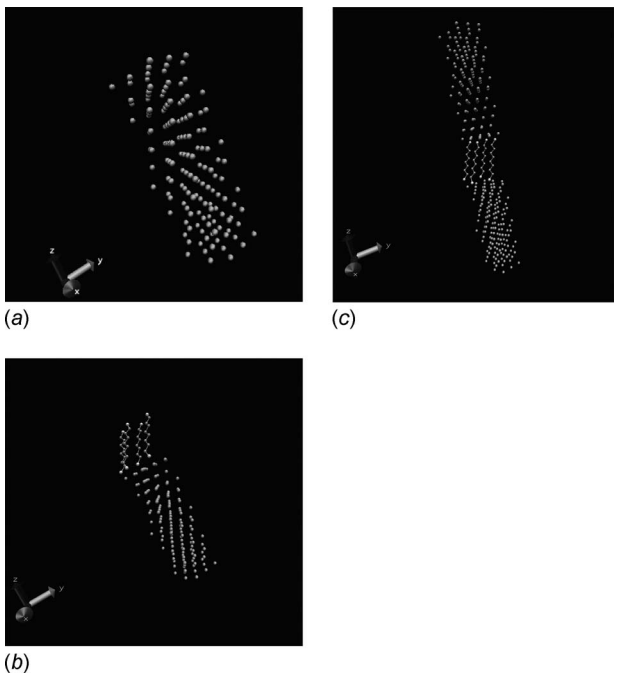

Fig. 2 Procedures of preparing the Au-SAM-Au simulation system: (*a*) one gold substrate is optimized by Morse potential, (*b*) alkanedithiol molecules are implanted on the substrate and the whole system is relaxed using the potentials specified in Table 1, and (*c*) the other optimized substrate is imposed on top of the alkanedithiol molecules

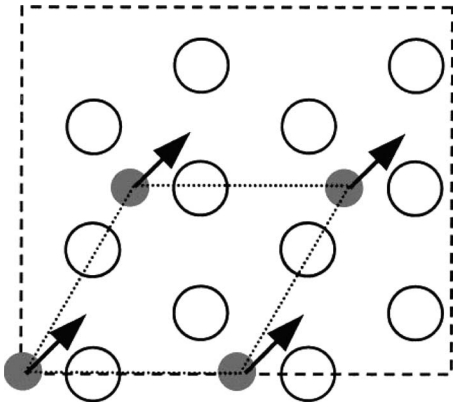

Fig. 3 Absorption sites and tilt directions of SAM molecules on Au(111) surface [37]. Open circles are gold atoms on the surface of substrate. Filled circles are sulfur heads which are absorbed on the substrate surface. Arrows represent tilt directions of SAM molecules. Dashed lines form the boundary of the simulation system and dotted lines represent SAM lattice constants.

threefold hollow sites of the Au(111) surface, thus forming a lattice with lattice constant of 4.99 Å [8,12,37] (Figure 3). The threefold site was reported to be the most stable site for SAM molecules absorption [8,37]. The molecules are then relaxed at 100 K until all molecule atoms attained their equilibrium positions (Fig. 2(*b*)). Finally, the other optimized gold substrate is imposed on top of the SAM (Fig. 2(*c*)). The equilibrium cell dimension in the *z*-direction was found to be about 68.10 Å. It was reported that the tilt angle does not change much at a temperature range from 50 K to 300 K [37]. In this work, the temperature effect on the tilt angle was ignored so that the simulation cell size in the *z*-direction remains unchanged throughout the temperature range (50–350 K).

In MD simulations, there is a limitation on the number of atoms that can be handled, due to the capability of the computing hardware. Thus, the thickness of the gold substrate must be limited to tens of angstroms. However, in reality, the gold substrates are often thick (several hundred microns), and their properties are close to bulk solids. The periodic boundary condition (PBC) in the *z*-direction was used to compensate the thickness limit in our simulations. The validation of this treatment is discussed in Sec. 3.2. Besides the PBC, the free boundary condition is also used in some simulations for comparison. PBCs are used in the *x*- and *y*-directions with no exception. A simulation system, which contains 4 SAM molecules and 12 gold atoms in each substrate layer, is defined as a unit cell (see Fig. 1(*a*)). It has a dimension of 9.99 Å in the *x*-direction, and 8.652 Å in the *y*-direction. The unit cell is expanded in the *x*- and *y*-directions to obtain the simulation supercells. Supercells with sizes of 1×1, 2×2, and 3×3 unit cells, which correspond to systems with 328, 1312, and 2952 atoms, are presented in Fig. 1.

The simulation procedure is as follows. (1) All atoms started moving from their equilibrium positions with random initial velocities. (2) Nose–Hoover thermostats were applied to the system for a long time (>25 ps) to make sure that the system reached the target temperature. (3) Thermostats were then released, and an equilibration period of 150 ps was performed. (4) A production run was performed, in which the HCAC function was calculated. (5) The HCAC function was integrated, and the resulted thermal conductivity was plotted to find a convergence value.

3 Results

3.1 Defining the Value of Thermal Conductivity. A typical normalized HCAC function profile is presented in Fig. 4. It can be seen that fast fluctuations are imposed on the overall profile,

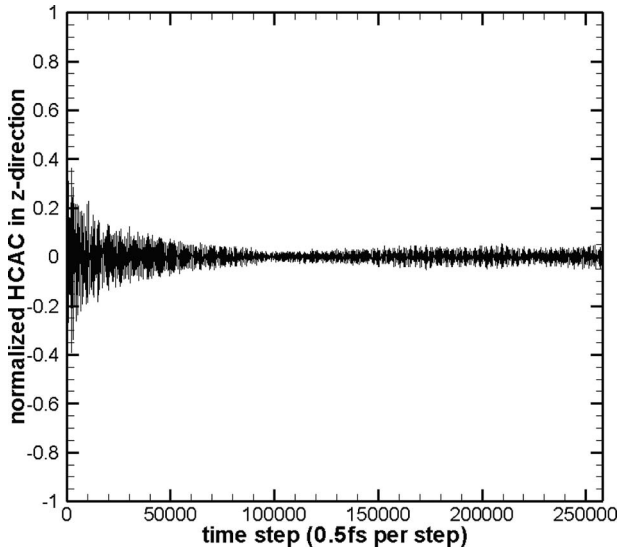

Fig. 4 A typical normalized HCAC function

which make the integration in Eq. (2) nontrivial. The fast fluctuations are believed to be from the optical phonons [19,30]. Since the bulk gold will have only acoustic phonons [38], the optical phonons are the result of the presence of SAM molecules, which have optical branches in the phonon dispersion [39]. The calculated thermal conductivity profiles are different in different simulations (see Fig. 5). For thermal energy transport in the out-of-plane direction with free boundary conditions, phonons traveling across the junction will be scattered at two Au-SAM interfaces, and they will also be scattered at the free Au surfaces at the ends of the simulation cell. Then this will further reduce the out-of-plane thermal conductivity [40]. However, in the in-plane directions, no such scattering exists, and the thermal conductivity exhibits a smoother profile in these directions. To extract the thermal conductivity from different profiles, three methods were used to find the convergence areas. The thermal conductivity profile in Fig. 5(*a*), where a flat area exists, is encountered in some integrations for *z*-direction thermal conductivities. Similar thermal conductivity profiles were also found by McGaughey and Kaviany [19], who used a running average to define the convergence region. In the present study, since the flat area is obvious, we define the convergent thermal conductivity values by directly averaging the values over the flat area. For profiles like Fig. 5(*b*), which

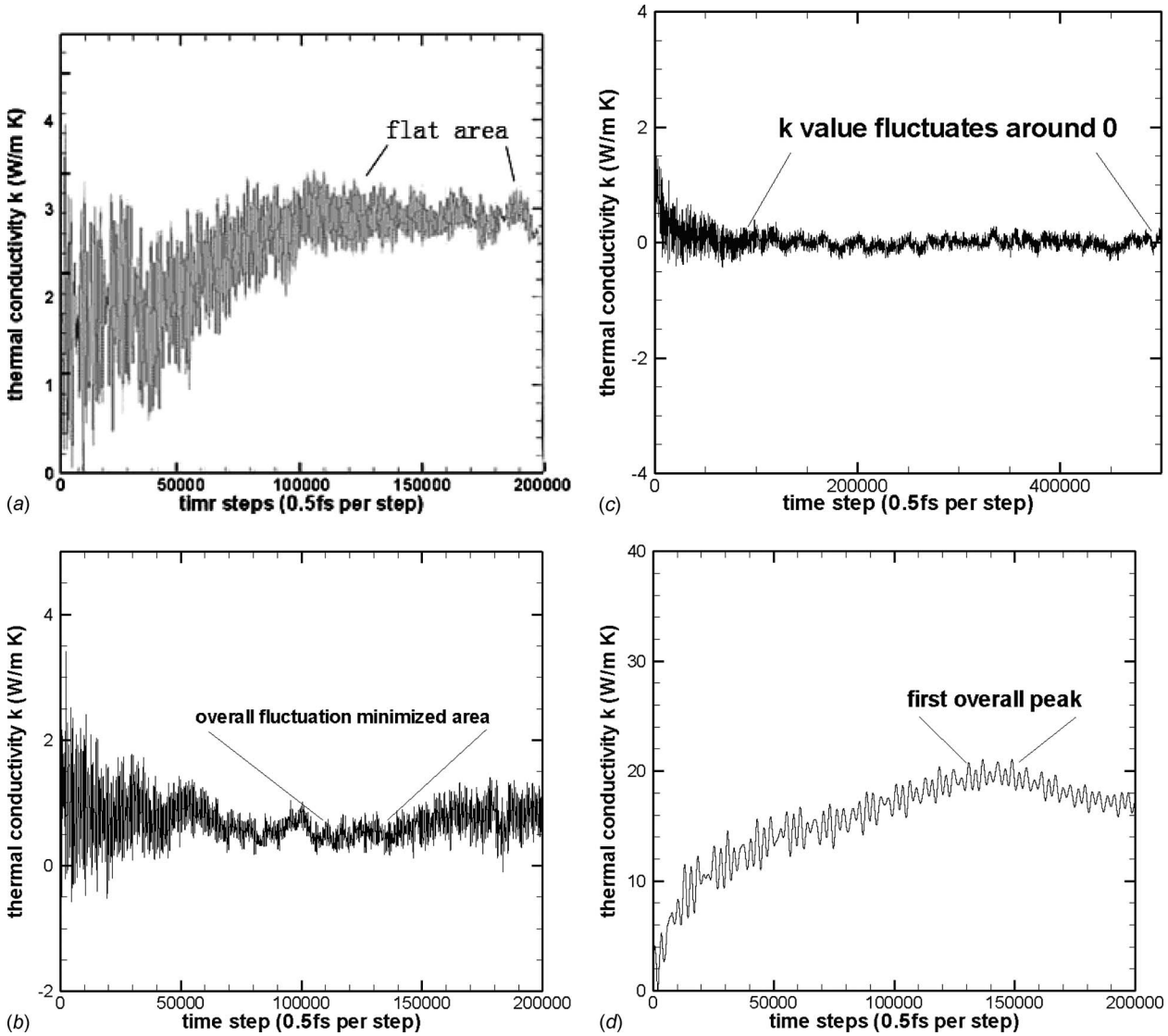

Fig. 5 Thermal conductivity profiles obtained from the calculations: (*a*) profile that has a flat area, (*b*) profile that has an overall fluctuation minimized area, (*c*) profile whose value fluctuates about 0, and (*d*) profile with a first overall peak

Table 2 Finite size effect on thermal conductivities

System size	1×1	2×2	3×3	2×2	3×3
Boundary condition in *z*-direction	PBC	PBC	PBC	Free	Free
No. of atoms	328	1312	2952	1312	2952
k_x (W/m K)	4.9±1.0	17.6±3.0	22.5±7.4	12.5±2.7	13.8±2.7
k_y (W/m K)	4.6±1.0	19.4±3.4	14.6±3.3	10.8±1.6	9.5±1.7
k_z (W/m K)	1.2±0.2	1.8±0.3	1.8±0.4		

appeared in many *z*-direction integrations, a convergence area is chosen, where the overall profile fluctuates around a mean value, and the overall fluctuation (overall fluctuation refers to the fluctuation with lower frequency, compared to the high frequency fluctuations) magnitude becomes a minimum. Such convergence area was similar to the "neck region" seen in Ref. [19]. Thermal conductivities are found by averaging values over the convergence area. For systems with free boundary conditions in the *z*-direction, the integration profiles are shown to be like Fig. 5(*c*), where the value converges to 0. For profiles seen in Fig. 5(*d*), which are found in most integrations in the *x*- and *y*-directions, the averaged value around the first overall peak is used. Such a method is similar to the "first-dip" method [20], which was found valid for the thermal conductivity calculation for crystalline β–SiC. In all the different profiles except Fig. 5(*c*), the data is averaged over no less than 5000 steps, which equals to 2.5 ps.

3.2 Boundary Conditions. As seen in Fig. 5(*c*), the simulation with the free boundary condition gave thermal conductivities, which were approximately 0. There are two possible reasons for such results: (1) The free boundaries add very large boundary resistance to the entire Au-SAM-Au junction, which makes the conductivity of the junction very small; or (2) the ultra thin (2–5 nm) substrates depressed the excitation of many phonon modes, so there were only very limited modes available for thermal energy transport. However, in practice, the substrates are not as thin as several tens of nanometers. To make our simulation reflect greater reality, PBC is used in the *z*-direction. With the PBC in the *z*-direction, and an appropriate neighborlist cutoff (less than 12 Å in this work), the gold atoms in one substrate can interact with the image gold atoms of the other substrate, while they do not interact with the image SAM molecule atoms if the interaction cutoffs are smaller than the substrate thickness. In this sense, the gold substrates are not isolated thin layers with free surfaces at the junction ends, but rather, they work as thick chunks of gold.

3.3 Finite Size Effect. In MD simulations, the sizes of the simulation cells usually affect the results. To investigate the finite size effects in the *x*- and *y*-directions, thermal conductivity calculations were performed at 100 K on 1×1, 2×2, and 3×3 systems, with 12 layers of gold atoms on each substrate. Both the PBC and free boundary condition were used in the *z*-direction. PBCs are used in the *x*- and *y*-directions for all cases. The results are listed in Table 2. The results from 2×2 and 3×3 systems do not differ from each other significantly when the errors are taken into account. This means that, in the *x*- and *y*-directions, the 2×2 system is sufficient for our simulations. In the rest of the work, all simulations use the 2×2 system.

3.4 Substrate Thickness Effect. In the simulations, the *z*-direction is a special direction since it is the cross direction of the Au-SAM-Au junction. Energy transport has to cross two Au-SAM interfaces in this direction. In order to investigate thermal transport across the interfaces, the influence from the limited thicknesses of the substrates should be minimized. The substrate thickness effect on thermal conductivities/conductance for a 2×2 system was studied by changing the number of gold layers in the substrates. All the following cases have PBCs in all three directions, and all simulations are carried out at 100 K. To investigate the effect of SAM molecules on the substrate in-plane thermal conductivities, the system without SAM molecules is studied. The results are presented in Table 3.

To compare the *z*-direction results, thermal conductance should be the property to be compared, as it is mentioned in Sec. 2 that the thermal conductivity k_z is structural dependent rather than an intrinsic property of the junctions. Thermal conductance G is defined by $q = G \cdot \Delta T$, where q is the heat flux normal to the junction interfaces, and ΔT is the temperature difference across the junction. G is related to k_z by

$$G = k_z/L \tag{9}$$

where L is the thickness of the junction. In Table 3, the thermal conductance does not exhibit monotonic decrease when the substrates are thickened from 6 layers to 36 layers of gold, as one would intuitively expect. It is believed that the discrepancies of thermal conductance among systems with different Au thicknesses are not from the thickness size effect but from other factors such as the difficulty of defining the convergence thermal conductivity value and the limited number of runs used to get the mean values. The effects of these factors are reflected in the error bars. The total thermal resistance of the junction can be written as a serial combination of resistances of different parts that make up the junction

$$R_{\text{total}} = 2 \times R_{\text{substrate}} + 2 \times R_{\text{interface}} + R_{\text{SAM}} \tag{10}$$

Consider the relation between resistance and conductance

$$G = 1/R \tag{11}$$

Eq. (10) becomes

Table 3 Substrate thickness effect on thermal conductivities and thermal conductance

No. of gold layers	6	12	18	24	36	12 (no SAM)
Thickness L of the whole junction (Å)	39.42	68.10	96.73	125.67	182.90	68.10
k_x (W/m K)	9.1±1.5	17.6±3.0	23.9±5.6	27.9±4.3	36.3±8.3	18.6±1.6
k_y (W/m K)	7.8±1.1	19.4±3.4	23.5±4.5	19.8±6.2	25.3±7.4	19.8±4.7
k_z (W/m K)	1.3±0.2	1.8±0.3	2.5±0.6	3.8±1.2	4.9±0.5	0
G (MW/m^2 K)	327±58	261±46	258±66	302±95	268±30	

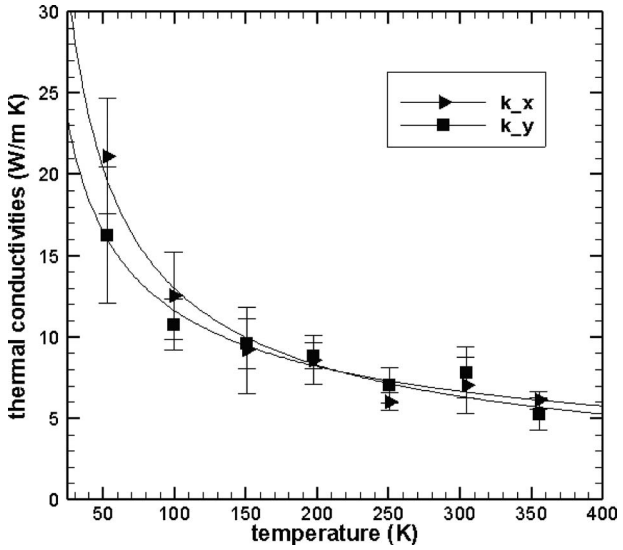

Fig. 6 Temperature dependence of in-plane thermal conductivities of systems with free boundary condition in *z*-direction

$$\frac{1}{G_{\text{total}}} = 2 \times \frac{1}{G_{\text{substrate}}} + 2 \times \frac{1}{G_{\text{interface}}} + \frac{1}{G_{\text{SAM}}} \tag{12}$$

Due to the large conductance of gold substrates, the first term $1/G_{\text{substrate}}$ becomes negligibly small (in reality, bulk gold has a thermal conductivity of 318 W/m K, which leads to a conductance G of about 1.2×10^5 MW/m^2 K for a substrate with thickness of 26.2 Å. The corresponding resistance R is 8.3×10^{-6} m^2 K/MW, and it is negligible compared to other terms. As stated in Sec. 1, the electron transport contribution to the thermal transport is ignored since it is hard for electrons to tunnel through the SAM molecules. Due to this and the substrate thickness effects, the Au lattice thermal conductivity should be smaller than 318 W/m K. However, even if the calculated thermal conductivities (~20 W/m K) in the *x*- and *y*-directions are used, the resistance comes out to be $\sim1.3\times10^{-4}$ m^2 K/MW, which contributes only 3% of the total resistance. Wang et. al [6] found that the energy transport along the SAM molecule chains was ultrafast (0.95 nm/ps), which suggests that the thermal resistance inside the molecule itself is very small. Henry and Chen [39], using an equilibrium MD simulation with the Green–Kubo formula, also found that a single polyethylene molecule has a thermal conductivity higher than 100 W/m K along the chain. As a result, the total thermal resistance of the junction is way larger than the resistances of the Au substrate and SAM molecules. Therefore, the junction thermal resistance is dominated by the SAM-Au interfaces. Since there are no strong intermolecular interactions among the discrete SAM molecules, the energy transport from one molecule to another should be weak. Comparing the results of the systems with and without SAM molecules (the sixth case in Table 3), one can see that the existence of SAM molecules does not affect the in-plane thermal transport. It is also found that for the system without SAM molecules connecting the two Au substrates, the out-of-plane thermal conductance becomes 0, as expected. We then believe that the in-plane (*x*- and *y*-direction) thermal transport mostly happens in the crystalline gold substrates, and SAM molecules present channels for out-of-plane thermal conduction. From Table 3, it can be seen that in the *x*- and *y*-directions, the supercell with thickness of 68.10 Å still suffers from the finite size effect for the in-plane thermal transport. However, if the dimension in the *z*-direction is too large, the calculation becomes too demanding to handle with the current code. For the junctions in our work, what is really important is the out-of-plane (*z*-direction) thermal transport, and the 12 layer substrates have shown to be thick enough to ignore the thickness effect on the thermal conductance in the *z*-direction (see Table 3). As a result, substrates with 12 gold layers are used in all the simulations.

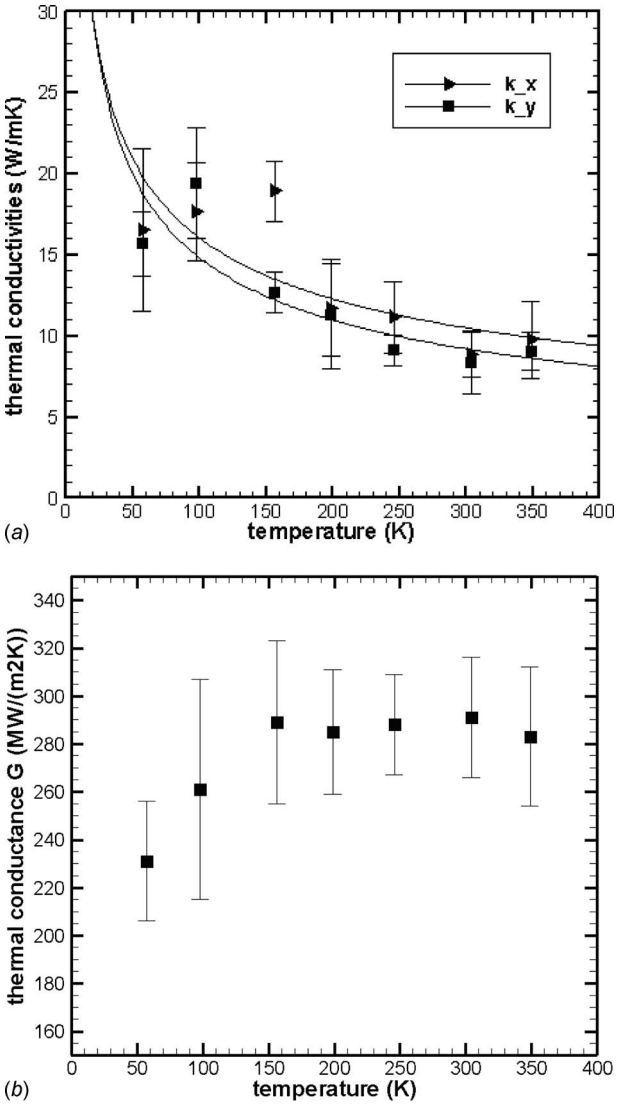

Fig. 7 Temperature dependence of thermal conductivities and conductance of systems with PBC in *z*-direction: (*a*) thermal conductivities in *x*-, *y*-, and *z*-directions, and (*b*) thermal conductance of the Au-SAM-Au junction

3.5 Temperature Effect. One of the topics investigated in this work is the temperature dependence of thermal conductivity/conductance. Figure 6 shows the in-plane results of a system with free boundary conditions. The solid lines are power fits to the discrete data. Data for simulations that use PBC in the *z*-direction are shown in Fig. 7. From the fitted line, the temperature dependence of the calculated lattice thermal conductivities in the in-plane directions (*x*- and *y*-directions) shows the same trend as that found in simulations with free boundary conditions (Fig. 6), which declines with increased temperature, and the same trend is found in thermal conductivities of crystalline solids [20,41]. For thermal conductance in the out-of-plane direction (Fig. 7(*b*)), a comparison with the experimental data of Wang et al. [42] on Au-SAM-GaAs junctions was done (see Fig. 10). In the work of Wang et. al [42], Au-alkanedithiols-GaAs junctions were studied, which are different from the Au-alkanedithiols-Au junctions studied here. In practical experiments, the alkanedithiols lattice on the GaAs substrate is not as perfect as that on the Au substrate in our

Table 4 Simulated pressure dependence of thermal conductivities/conductance in *x*-, *y*-, and *z*-directions

Thickness (Å)	k_x (W/m K)	k_y (W/m K)	k_z (W/m K)	G (W/m K)
68.10	22.2 ± 3.4	16.4 ± 3.0	1.8 ± 0.3	265 ± 44
67.90	14.5 ± 4.8	21.8 ± 10.2	2.0 ± 0.6	295 ± 88
67.70	15.9 ± 3.2	21.7 ± 6.5	2.1 ± 0.4	310 ± 59
67.50	14.7 ± 6.6	18.1 ± 6.3	2.2 ± 0.3	326 ± 44
67.30	18.1 ± 4.6	17.3 ± 4.0	2.3 ± 0.2	342 ± 30
67.10	18.3 ± 8.0	18.1 ± 7.2	2.2 ± 0.2	328 ± 30

work, and the molecules are not always upstraight, while some of them lay down. As a result, the effective molecule-substrate contacts are not as good as the ones studied in this paper, which are perfect contacts [43]. So, it is not a surprise that our data are much larger than the experimental data of Wang et. al [42]. Although the absolute values are not comparable, the trend of the discrete data is similar. The mean thermal conductance increases at low temperatures as the temperatures rises, and becomes almost unchanged at higher temperatures (>150 k). We are not aware of any experimental thermal conductance data on the exact same junction that is studied here at a temperature range from 50 K to 350 K. However, for metal-nonmetal interfaces, the experimental thermal conductance is reported to be $8 < G < 700$ MW/(m^2 K) [44–46]. In our work, as can be seen in Fig. 7(*b*), the thermal conductance ranges from 200 MW/m^2 K to 300 MW/m^2 K, which falls in the above range. Ge et. al [5] reported the Au-(hydrophobic SAM)-water interface to have thermal conductance of 50 ± 5 MW/(m^{2}K), and a conductance of 100 ± 20 MW/(m^2 K) for the Au-(hydrophilic SAM)-water interface. Wang et. al. [6] reported a thermal conductance of 220 ± 100 MW/(m^2 K) for a Au-SAM junction. It can be seen that our data is on the same order of available experimental data.

3.6 Simulated Normal Pressure Effect. The external normal pressure effect on the thermal conductivity/conductance was simulated by decreasing the dimension of the simulation cell in the *z*-direction at 100 K because there is no way to apply forces on the free surfaces of the Au substrates when the PBC is used in the *z*-direction. In this way, the junction would feel "pressure" as the junction is compressed by the decreased cell dimension in the *z*-direction. The *z*-direction dimension was decreased by 1 Å with an interval of 0.2 Å. The Young's modulus, calculated using GULP [47], ranged from 3.5 GPa to 118 GPa as the *z*-direction dimension decreases. According to the GULP calculations, the Young's modulus of pure Au was 341 GPa in the *z*-direction (111 direction). It was the presence of SAM, which resulted in a lower Young's modulus of the junction, compared to pure Au (Note: The calculated bulk modulus of Au using GULP is 173.2 GPa, which is identical to the experimental result of 173 GPa. However, the calculated Young's modulus of 341 GPa in the *z*-direction is much higher than that of the bulk Au (78 GPa) from experiments. A possible reason is that the calculated Young's modulus is in a specified crystal axis, which is a more rigid direction.) The 0.2 Å decrease in dimension thus corresponds to pressure increases ranging from 10 MPa to 350 MPa, which are very large pressure changes. The calculated results are shown in Table 4 and Fig. 8. In Fig. 8, where the *z*-direction thermal conductance is presented, no pressure dependence was observed when error bars are considered. The reason for such a result could be that the SAM-Au interface resistances are the dominate factors, which impeded the thermal energy transport across the junction (detailed discussions were presented in Sec. 3.4). Although the junction is under pressure, due to the flexibility of the chain-like alkanedithiol molecules, the structure will adapt itself to the small dimension change in the *z*-direction, and thus, the local dynamics around the SAM-Au interface does not change much. As a result, the interface resistance is not much affected. The thermal conductivities in the *x*- and *y*-directions do not show any pressure dependence (see Table 4).

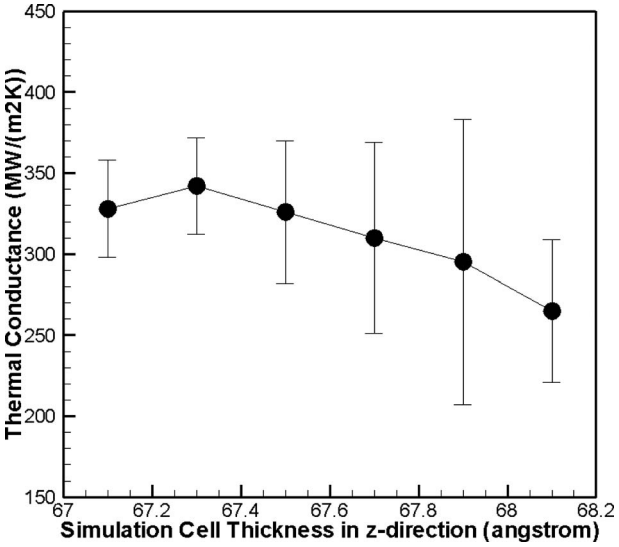

Fig. 8 Out-of-plane thermal conductance vs. simulation cell thicknesses

3.7 Chain Length Effect. Systems with different alkanedithiol molecule chain lengths were also studied. The thermal conductivities of junctions with $-S-(CH_2)_8-S-$, $-S-(CH_2)_9-S-$, and $-S-(CH_2)_{10}-S-$ were calculated at temperatures ranging from 50 K to 350 K. The in-plane thermal conductivities at 100 K are tabulated in Table 5, and they do not exhibit any chain length

Table 5 Chain length effect on thermal conductivities in *x*- and *y*-directions at 100 K

Chemical formula	$S_2(CH)_8$	$S_2(CH)_9$	$S_2(CH)_{10}$
k_x (W/m K)	17.6 ± 3.0	14.9 ± 4.1	22.1 ± 8.2
k_y (W/m K)	19.4 ± 3.4	19.3 ± 3.4	16.3 ± 1.7

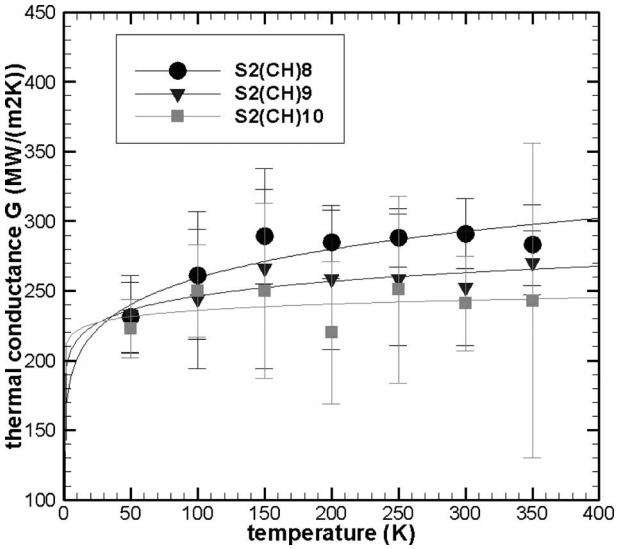

Fig. 9 Temperature dependence of Au-SAM-Au junction thermal conductance with different alkanedithiol chain lengths

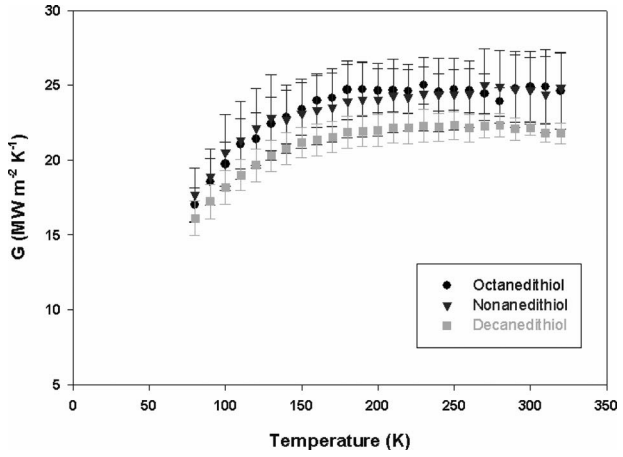

Fig. 10 Experimental data of temperature dependence of Au-SAM-GaAs junction thermal conductance with different alkanedithiol chain lengths [42]

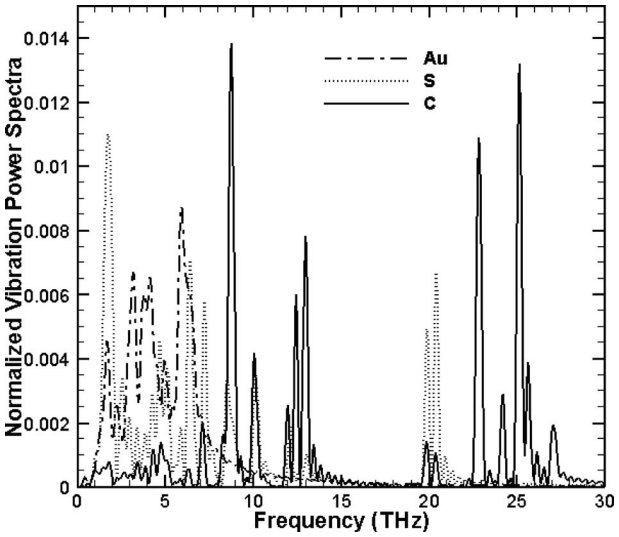

Fig. 11 Normalized vibrational power spectra of Au substrate, sulfur heads, and carbon atoms

dependence. The out-of-plane thermal conductance is plotted in Fig. 9. Solid lines are power fits of discrete data.

Considering the errors, the thermal conductance values of junctions with different chain lengths are not very different from each other. However, the mean values revealed weak chain length dependence: As the chain become longer, the out-of-plane thermal conductance decreased slightly. This makes sense if one considers the extreme cases of chain lengths equal to 0 and infinity. The thermal conductance should decrease from the maximum value for junctions with no SAM to 0 when the substrates are separated by infinitely long chains. Such a trend coincides with the experimental measurements of Wang et. al [42] on Au-SAM-GaAs junctions (see Fig. 10). The reason that there is no obvious thermal conductance change should still be that the SAM-Au interface resistance dominates the energy transport ability in the *z*-direction, while the chain-like molecules themselves have very small resistances. It can be concluded that the limited chain length change (from $-S-(CH_2)_8-S-$ to $-S-(CH_2)_{10}-S-$) does not have a significant effect on thermal transport ability of the junctions.

3.8 SAM Molecule Coverage Effect. To change the molecule coverage on the Au substrate, the number of molecules attached to the substrate surface was changed. With PBCs in the *x*- and *y*-directions, every alkanedithiol molecule is equivalent. Molecules were deleted symmetrically so as to keep symmetries. Thermal conductivities/conductance of systems with 16, 14, 12, 10, and 8 alkanedithiol molecules were calculated and presented in Table 6.

From Table 6, no trend of in-plane thermal conductivities is found. The mean value of out-of-plane thermal conductivities/conductance decreases with the decrease in coverage as expected. In Au-SAM-Au junctions, thermal energy is transported from one substrate to another through the discrete alkanedithiol molecules.

Table 6 Molecule coverage (refers to the number of alkanedithiols in a 2×2 simulation cell) dependence of thermal conductivities and thermal conductance

Coverage (No. of thiols/simulation cell)	k_x (W/m K)	k_y (W/m K)	k_z (W/m K)	G (MW/(m^2 K))
16	17.6 ± 3.0	19.4 ± 3.4	1.8 ± 0.3	261 ± 46
14	13.1 ± 1.6	10.6 ± 2.2	1.8 ± 0.3	257 ± 48
12	20.9 ± 4.0	13.7 ± 4.8	1.6 ± 0.2	233 ± 26
10	14.5 ± 4.7	15.8 ± 4.1	1.3 ± 0.2	185 ± 26
8	17.3 ± 6.5	17.8 ± 4.2	1.0 ± 0.1	148 ± 19

These molecules are like channels through which energy passes. When the number of molecules decreases, energy transport channels are decreased. As a result, thermal energy transport becomes more difficult, and conductance becomes smaller.

3.9 Vibration Coupling Analysis. To investigate how efficiently the thermal energy is transported from the substrate to the discrete molecules, the vibrational power spectra of Au atoms in the substrate, sulfur atoms, and carbon atoms in the alkanedithiol molecules were calculated (see Fig. 11). The calculations were done by performing Fourier transforms of the velocity autocorrelation functions. Two layers of Au atoms and 16 sulfur heads, which form an interface, were chosen as the samples from which the velocity autocorrelation functions were calculated. Trajectories of 16 carbon atoms bonded to the sulfur heads were sampled to calculate the vibration power spectra of the carbon atoms. It can be seen that both the Au atoms and the S atoms have largely populated low frequency modes (<10 THz), which results in large spectra overlap. Compared to some interfaces with almost no overlap in vibration spectra [48], the coupling is regarded to be strong. It is believed that the relatively large coupling is due to the strong Morse interaction between the Au and S atoms. Although the vibration coupling between Au and S appears to be strong, the discrete SAM molecules limit the number of channels available for thermal energy transport, and thus, they significantly influence the heat transfer efficiency. As a result, the Au-SAM interface presents a large resistance to the junction. It also can be seen that the overlap of S and C spectra spans over frequencies up to about 22 THz, which facilitate the thermal transport inside the molecule chains. The calculated thermal conductance values in this work are close to those of the interface conductance values of water-surfactant heads (300 ± 40 MW/(m^2 K)), hexane-surfactant tails (370 ± 40 MW/(m^2 K)), and benzene-surfactant tails (200 ± 30 MW/(m^2 K)), which also have large vibration coupling [7]. The C84-organic solvent interface thermal conductance found by Huxtable et. al. [48] (10–20 MW/(m^2 K)) has almost no vibration spectra overlap, and is much lower than our data.

4 Summary and Conclusion

The present work calculated thermal conductivity/conductance of Au-SAM (alkanedithiol)-Au junctions using equilibrium classical MD with the Green–Kubo method. PBCs were used in the *x*- and *y*-directions. Both the free boundary condition and PBC were used in the *z*-direction. The effect of the simulation finite size was

investigated. Vibration coupling was analyzed to explore the mechanism of thermal energy transport between Au substrates and SAM molecules. Due to the limited thermal transport channels presented by the discrete SAM molecules, thermal energy transport across the interface is not efficient even though the Au–S vibration coupling appears to be strong, and thus, the interface resistance is large. From the phononic point of view, the Au-SAM interfaces present scattering sites, which scatter and reflect the phonon wave packets. Only a part of the phonon energy is transmitted through the interfaces, and this leads to interface resistance. Temperature dependence, molecule chain length dependence, substrate thickness dependence, pressure dependence, and alkanedithiol molecule coverage dependence of thermal conductivities/conductance were studied. The results show that the thermal conductance in the out-of-plane direction (z-direction) increases with temperature increase at temperatures below 150 K, and remains almost unchanged at temperatures above 150 K. The in-plane thermal conductivity displayed a bulk crystal lattice thermal conductivity behavior, which decreases with the increase in temperature. It was also observed that the junction thermal conductance does not have obvious molecule chain length dependence (chain length from $-S-(CH_2)_8-S-$ to $-S-(CH_2)_{10}-S-$). Substrate thickness does not seem to affect the thermal conductance across the junction. Pressure dependence is also not obvious in Au-SAM-Au junctions. These three observations demonstrate that it is the Au-SAM interface that dominates the thermal transport across the junction. The alkanedithiol molecule coverage has an effect on the out-of-plane direction thermal transport. The thermal conductance decreases obviously with coverage decrease, due to the reduced number of energy transport channels. All the calculated thermal conductance values are between 200 MW/(m^2 K) and 300 MW/(m^2 K), which is inside the experimentally measured range of metal-nonmetal interfaces.

Acknowledgment

The authors gratefully acknowledge the support of NSF under Grant No. 0522594 to enable this work to be performed. The project is in collaboration with Professor Arun Majumdar in UC Berkeley.

Nomenclature

ΔT = temperature difference across the junction
ε, σ = parameters for Lennard-Jones potential
φ = dihedral angle of four body group
ϕ = potential energy
$a_0, a_1, a_2, a_3, a_4, a_5$ = parameters for torsion potential
De, a, r_{mo} = parameters for Morse potential
E_j = total energy of atom j
$\vec{F}$ = force vector
G = thermal conductance
$J(\tau)$ = heat current at instant τ
k = thermal conductivity
k_B = Boltzmann constant
k_s, r_o = parameters for bond stretching potential
L = junction thickness
m = atomic mass
q = heat flux normal to the junction interfaces
$\vec{r}$ = position vector
R = thermal resistance
t = time
T_m = mean temperature of a simulation
$U_{\mathrm{L\text{-}J}}$ = potential energy of Lennard-Jones potential
U_M = potential energy of Morse potential
U_s = potential energy of bond stretching potential
U_t = potential energy of torsion potential
V = volume of simulation system

References

[1] Loo, Y., Hsu, J. W. P., Willett, R. L., Baldwin, K. W., West, K. W., and Rogers, J. A., 2002, "High-Resolution Transfer Printing on GaAs Surfaces Using Alkane Dithiol Monolayers," J. Vac. Sci. Technol. B, **20**, pp. 2853–2856.

[2] Nakagawa, O. S., Ashok, S., Sheen, C. W., Martensson, J., and Allara, D. L., 1991, "GaAs Interface With Octadecyl Thiol Self-Assembled Monolayer," Jpn. J. Appl. Phys., Part 1, **30**, pp. 3759–3762.

[3] Koike, A., and Yoneya, M., 1996, "Molecular Dynamics Simulations of Sliding Friction of Langmuir-Blodgett Monolayers," J. Chem. Phys., **105**, pp. 6060–6067.

[4] McGuiness, C. L., Shaporenko, A., Mars, C. K., Uppili, S., Zharnikov, M., and Allara, D. L., 2006, "Molecular Self-Assembly at Bare Semiconductor Surfaces: Preparation and Characterization of Highly Organized Octadecanethiolate Monolayers on GaAs(001)," J. Am. Chem. Soc., **128**, pp. 5231–5243.

[5] Ge, Z., Cahill, D. G., and Braum, P. V., 2006, "Thermal Conductance of Hydrophilic and Hydrophobic Interfaces," Phys. Rev. Lett., **96**, p. 186101.

[6] Wang, Z., Carter, J. A., Lagutchev, A., Koh, Y. K., Seong, N. H., Cahill, D. G., and Dlott, D. D., 2007, "Ultrafast Flash Thermal Conductance of Molecular Chains," Science, **317**(5839), pp. 787–790.

[7] Patel, H. A., Garde, S., and Keblinski, P., 2005, "Thermal Resistance of Nanoscopic Liquid-Liquid Interfaces: Dependence on Chemistry and Molecular Architecture," Nano Lett., **5**, pp. 2225–2231.

[8] Yourdshahyan, Y., Zhang, H. K., and Rappe, A. M., 2001, "N-Alkyl Thiol Head-Group Interactions With the Au(111) Surface," Phys. Rev. B, **63**, p. 081405.

[9] Gronbeck, H., Curioni, A., and Andreoni, W., 2000, "Thiols and Disulfides on the Au(111) Surface: The Headgroup-Gold Interaction," J. Am. Chem. Soc., **122**, pp. 3839–3842.

[10] Sheen, C. W., Shi, J., Martensson, J., Parikh, A. N., and Allara, D. L., 1992, "A New Class of Organized Self-Assembled Monolayers: Alkane Thiols on GaAs(100)," J. Am. Chem. Soc., **114**, pp. 1514–1515.

[11] Andreoni, W., Curioni, A., and Gronbeck, H., 2000, "Density Functional Theory Approach to Thiols and Disulfides on Gold: Au(111) Surface and Clusters," Int. J. Quantum Chem., **80**, pp. 598–608.

[12] Reese, S., and Fox, M. A., 1998, "Self-Assembled Monolayers on Gold of Thiols Incorporating Conjugated Terminal Groups," J. Phys. Chem. B, **102**, pp. 9820–9824.

[13] Hautman, J., and Klein, M. L., 1989, "Simulation of a Monolayer of Alkyl Thiol Chains," J. Chem. Phys., **91**, pp. 4994–5001.

[14] Cahill, D. G., Ford, W. K., and Goodson, K. E., 2003, "Nanoscale thermal transport," J. Appl. Phys., **93**(2), pp. 793–818.

[15] Ziman, J. M., 1960, *Electrons and Phonons*, Oxford University Press, New York.

[16] Volz, S., Saulnier, J. B., Lallemand, M., Perrin, B., Depondt, P., and Mareschal, M., 1996, "Transient Fourier-Law Deviation by Molecular Dynamics in Solid Argon," Phys. Rev. B, **54**, pp. 340–347.

[17] Poetzsch, R. H. H., and Böttger, H., 1994, "Interplay of Disorder and Anharmonicity in Heat Conduction: Molecular Dynamics Study," Phys. Rev. B, **50**, pp. 15757–15763.

[18] Crocombette, J. P., Dumazer, G., and Hoang, N. Q., 2007, "Molecular Dynamics Modeling of the Thermal Conductivity of Irradiated SiC as a Function of Cascade Overlap," J. Appl. Phys., **101**, p. 023527.

[19] McGaughey, A. J. H., and Kaviany, M., 2004, "Thermal Conductivity Decomposition and Analysis Using Molecular Dynamics Simulations, Part II. Complex Silica Structures," Int. J. Heat Mass Transfer, **47**, pp. 1799–1816.

[20] Li, J., Porter, L., and Yip, S., 1998, "Atomistic Modeling of Finite-Temperature Properties of Crystalline β–SiC, II. Thermal Conductivity and Effects of Point Defects," J. Nucl. Mater., **255**, pp. 139–152.

[21] McGaughey, A. J. H., and Li, J., 2006, "Molecular Dynamics Prediction of the Thermal Resistance of Solid-Solid Interfaces in Superlattices," ASME Paper No. IMECE2006-13590.

[22] Barrat, J. L., and Chiaruttini, F., 2003, "Kapitza Resistance at the Liquid-Solid Interface," Mol. Phys., **101**, pp. 1605–1610.

[23] Puech, L., Bonfait, G., and Castaing, B., 1986, "Mobility of the ^{3}He Solid-Liquid Interface: Experiment and Theory," J. Low Temp. Phys., **62**, pp. 315–327.

[24] Kubo, R., Yokota, M., and Nakajima, S., 1957, "Statistical-Mechanical Theory of Irreversible Processes. II. Response to Thermal Disturbance," J. Phys. Soc. Jpn., **12**, pp. 1203–1211.

[25] Lukes, J. R., and Zhong, H., 2007, "Thermal Conductivity of Individual Single-Wall Carbon Nanotubes," ASME J. Heat Transfer, **129**, pp. 705–716.

[26] Xu, X., Cheng, C., and Chowdhury, I. H., 2004, "Molecular Dynamics Study of Phase Change Mechanisms During Femtosecond Laser Ablation," ASME J. Heat Transfer, **126**, pp. 727–734.

[27] Pan, H., Ko, S. H., and Grigoropoulos, C. P., 2008, "The Solid-State Neck Growth Mechanisms in Low Energy Laser Sintering of Gold Nanoparticles: A Molecular Dynamics Simulation Study," ASME J. Heat Transfer, **130**, p. 092404.

[28] Stevens, R. J., Norris, P. M., and Zhigilei, L. V., 2004, "Molecular-Dynamics

Study of Thermal Boundary Resistance: Evidence of Strong Inelastic Scattering Transport Channels," *Proceeding of the IMECE04*.
[29] Tien, C. L., Lukes, J. R., and Chou, F. C., 1998, "Molecular Dynamics Simulation of Thermal Transport in Solids," Microscale Thermophys. Eng., **2**, pp. 133–137.
[30] Huang, B. L., McGaughey, A. J. H., and Kaviany, M., 2007, "Thermal Conductivity of Metal-Organic Framework 5 (MOF-5): Part I. Molecular Dynamics Simulations," Int. J. Heat Mass Transfer, **50**, pp. 405–411.
[31] Leach, A. R., 1996, *Molecular Modeling Principles and Applications*, Addison-Wesley, Reading, MA.
[32] Sung, I. H., and Kim, D. E., 2005, "Molecular Dynamics Simulation Study of the Nano-Wear Characteristics of Alkanethiol Self-Assembled Monolayers," Appl. Phys. A: Mater. Sci. Process., **81**, pp. 109–114.
[33] Mahaffy, R., Bhatia, R., and Garrison, B. J., 1997, "Diffusion of a Butanethiolate Molecule on a Au(111) Surface," J. Phys. Chem. B, **101**, pp. 771–773.
[34] Lincoln, R. C., Koliwad, K. M., and Ghate, P. B., 1967, "Morse-Potential Evaluation of Second- and Third-Order Elastic Constants of Some Cubic Metals," Phys. Rev., **157**, pp. 463–466.
[35] Rieth, M., 2003, *Nano-Engineering in Science and Technology*, World Scientific, Singapore.
[36] Rappe, A. K., Casewit, C. J., Colwell, K. S., Goddard, W. A., and Skiff, W. M., 1992, "UFF, A Full Periodic Table Force Field for Molecular Mechanics and Molecular Dynamics Simulations," J. Am. Chem. Soc., **114**, pp. 10024–10035.
[37] Zhang, L., Goodard, W. A., and Jiang, S., 2002, "Molecular Simulation Study of the c(4×2). Superlattice Structure of Alkanethiol Self-Assembled Monolayers on Au(111)," J. Chem. Phys., **117**, pp. 7342–7349.
[38] Gohel, V. B., Acharya, C. K., and Jani, A. R., 1985, "On Phonon Dispersion in Noble Metals," J. Phys. F: Met. Phys., **15**, pp. 279–285.
[39] Henry, A., and Chen, G., 2008, "High Thermal Conductivity of Single Polyethylene Chains Using Molecular Dynamics Simulations," Phys. Rev. Lett., **101**, p. 235502.
[40] Gomes, C. J., Madrid, M., Goicochea, J. V., and Amon, C. H., 2006, "In-Plane and Out-of-Plane Thermal Conductivity of Silicon Thin Films Predicted by Molecular Dynamics," ASME J. Heat Transfer, **128**, pp. 1114–1121.
[41] Kaburaki, H., Li, J., and Yip, S., 1999, "Thermal Conductivity of Solid Argon by Classical Molecular Dynamics," Mater. Res. Soc. Symp. Proc., **538**, pp. 503–508.
[42] Wang, R. Y., Segalman, R. A., and Majumdar, A., 2006, "Room Temperature Thermal Conductance of Alkanedithiol Self-Assembled Monolayers," Appl. Phys. Lett., **89**, p. 173113.
[43] Wang, R., private communication.
[44] Stoner, R. J., and Maris, H. J., 1993, "Kapitza Conductance and Heat Flow Between Solids at Temperatures From 50 to 300 K," Phys. Rev. B, **48**, pp. 16373–16387.
[45] Costescu, R. M., Wall, M. A., and Cahill, D. G., 2003, "Thermal Conductance of Epitaxial Interfaces," Phys. Rev. B, **67**, p. 054302.
[46] Smith, A. N., Hostetler, J. L., and Norris, P. M., 2000, "Thermal Boundary Resistance Measurements Using a Transient Thermoreflectance Technique," Nanoscale Microscale Thermophys. Eng., **4**, pp. 51–60.
[47] Gale, J. D., 1997, "GULP—A Computer Program for the Symmetry Adapted Simulation of Solids," J. Chem. Soc., Faraday Trans., **93**, pp. 629–637.
[48] Huxtable, S. T., Cahill, D. G., Shenogin, S., and Keblinski, P., 2005, "Relaxation of Vibrational Energy in Fullerene Suspensions," Chem. Phys. Lett., **407**, pp. 129–134.

J. Alvarez-Quintana

Ll. Peralba-Garcia

Department of Physics,
Nanomaterials and Microsystems Group,
Universitat Autònoma de Barcelona,
08193 Bellaterra, Spain

J. L. Lábár

Research Institute for Technical Physics and Materials Science,
P.O. Box 49,
Budapest 114 H-1525, Hungary

J. Rodríguez-Viejo[1]

Department of Physics,
Nanomaterials and Microsystems Group,
Universitat Autònoma de Barcelona,
08193 Bellaterra, Spain;
MATGAS Research Center,
Campus Universitat Autònoma de Barcelona,
08193 Bellaterra, Spain
e-mail: javirod@gnam.uab.es

Ultra-Low Thermal Conductivity in Nanoscale Layered Oxides

The cross-plane thermal conductivity of several nanoscale layered oxides SiO_2/Y_2O_3, SiO_2/Cr_2O_3, and SiO_2/Al_2O_3, synthesized by e-beam evaporation was measured in the range from 30 K to 300 K by the 3ω method. Thermal conductivity attains values around 0.5 W/m K at room temperature in multilayer samples, formed by 20 bilayers of 10 nm SiO_2/10 nm Y_2O_3, and as low as 0.16 W/m K for a single bilayer. The reduction in thermal conductivity is related to the high interface density, which produces a strong barrier to heat transfer rather than to the changes of the intrinsic thermal conductivity due to the nanometer thickness of the layers. We show that the influence of the first few interfaces on the overall thermal resistance is higher than the subsequent ones. Annealing the multilayered samples to 1100°C slightly increases the thermal conductivity due to changes in the microstructure. These results suggest a route to obtain suitable thermal barrier coatings for high temperature applications. [DOI: 10.1115/1.4000052]

Keywords: dielectric oxides, ultra-low thermal conductivity, multilayers

1 Introduction

Decreased efficiencies in energy conversion systems, turbine blade protection, and failure in power microelectronic circuits are the driving forces toward the development of new thermal protective and insulating materials as part of the operating components. Thermal barrier coatings (TBC), based on ceramic insulators, was used for the past 3 decades to protect and extend the life of metallic superalloys, which need to withstand high temperature loads during turbine operation [1]. The selection of TBC materials is restricted by several requirements such as chemical inertness, low thermal conductivity, high melting point, thermal expansion match with the substrate, and phase stability. A very low thermal conductivity is necessary to protect the bulk material from high temperatures that will degrade it [2]. For a long time, it was considered that the thermal conductivity of amorphous oxides or strongly disordered crystalline oxides represented a lower limit to the thermal conductivity, with values lying in the range $1.3 < \kappa < 4.0$ W/m K at room temperature [3,4]. Therefore, amorphous oxides such as fused Silica and Yttria stabilized Zirconia (YSZ) are still currently used as TBC materials [5–9].

Recently, nanostructured coatings have emerged as alternative candidates, and have received widespread attention, because of their improved properties with respect to simpler structures. For instance, the thermal conductivity of YSZ as a function of grain size, which is 10 nm to 100 nm, was measured by Yang et al. [10] up to 500 K. The thermal conductivity of the 10 nm size nanostructured sample is reduced to half that of the coarse-grained structure in the whole temperature range. Although a large variety of multilayer, nanostructured, fluorite, and pyrochlore oxides materials were analyzed [11–13], none of them exhibits thermal conductivities below the amorphous limit of the disordered oxides at room temperature. On the other hand, it is well known that in a region of joining two solids exists a thermal boundary resistance (TBR) or Kapitza resistance that produces a temperature discontinuity, in response to impede the flow of heat of an applied heat flux. Experimental values of the TBR typically span from 10^{-7} m^2 K/W^{-1} to 10^{-9} m^2 K/W^{-1}. These values have only a small influence on the thermal conductivity of bulk materials; however, as the system becomes of nanometer size, the interfacial effect may become significant, and heavily influence the effective thermal conductivity [14,15]. Thus, it is expected that materials engineered with high interface densities by alternating nanolayers of dissimilar materials may effectively reduce the perpendicular thermal conductivity below the amorphous limit. A first attempt was pursued by Cahill et al. [16] by growing multilayers of SiO_2/YSZ of different thickness. They found that the thermal conductivity in the perpendicular direction was not significantly reduced, compared with single layers with values around 1.3 W/m K at room temperature. The authors concluded that the thermal resistance associated to the interface between the two materials was in the low 10^{-9} m^2 K/W^{-1} range, and therefore, the impact on the effective thermal conductivity was negligible. Other reports have addressed the achievement of very low thermal conductivities by growing thin film multilayers of dissimilar materials. Costescu et al. [17] were the first to report a very low value of 0.6 W/m K at 300 K for 3 nm thick W/Al_2O_3 nanolaminates. More recently, an ultra-low value of 0.05 W/m K was achieved in multilayers of crystalline WSe_2, a material with weak bonding interactions in the perpendicular direction between W and Se planes [18]. However, these layers may not be adequate for high temperature applications precluding a potential use as thermal barrier coatings.

In the present paper, we exploit the presence of a high-density of interfaces between several types of oxides including SiO_2/Y_2O_3, SiO_2/Cr_2O_3, and SiO_2/Al_2O_3, to achieve ultra-low thermal conductivity values in nanostructured layered materials with sufficient thermal stability to be potential candidates for thermal barrier coatings.

[1]Corresponding author.

Manuscript received February 21, 2009; final manuscript received July 27, 2009; published online December 28, 2009. Editor: Yogesh Jaluria.

Table 1 Nomenclature, individual layer thickness, and number of bilayers for the different samples

Group-Sample	Bilayer	Layer thickness (nm)	N deg bilayers
1-SA20–5	SiO_2/Al_2O_3		
1-SC20–5	SiO_2/Cr_2O_3	5/5	20
1-SY20–5	SiO_2/Y_2O_3		
2-SY20–6	SiO_2/Y_2O_3	3/6	
2-SY20–10	SiO_2/Y_2O_3	5/10	20
2-SY20–20	SiO_2/Y_2O_3	10/20	
3-SY1–10	SiO_2/Y_2O_3		1
3-SY3–10	SiO_2/Y_2O_3		3
3-SY5–10	SiO_2/Y_2O_3		5
3-SY7–10	SiO_2/Y_2O_3	10/10	7
3-SY15–10	SiO_2/Y_2O_3		15
3-SY20–10	SiO_2/Y_2O_3		20
3-SY30–10	SiO_2/Y_2O_3		30

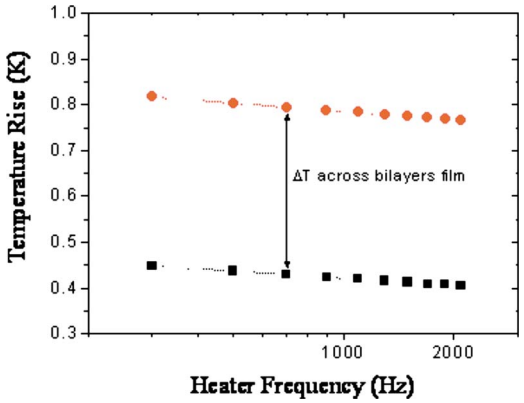

Fig. 1 Amplitude of the temperature oscillations of the heater versus heater frequency. Closed squares and circles represent the measured thermal oscillations for the reference sample (Si substrate plus SiO_2 insulating layer) and the SiO_2/Y_2O_3 sample (Si substrate plus SiO_2 insulating layer plus nanolaminate film), respectively. The dot lines represent the calculated thermal oscillations.

2 Experimental Section

Multilayer samples of SiO_2/Al_2O_3, SiO_2/Cr_2O_3, and SiO_2/Y_2O_3, with different modulation lengths, were prepared by alternate electron beam physical vapor deposition (EB-PVD) from pure pellets on thermally oxidized Si (001) substrates. EB-PVD is the technique of choice for TBC components, since in spite of their higher thermal conductivity, they have a longer life, and are more reliable than plasma-sprayed coatings [1]. The substrates were cleaned in running deionized water, and rinsed with 5% HF; this procedure was repeated 3–5 times to ensure the cleanliness of the Si surface prior to the growth of a 100 nm thick thermal oxide. Before introduction in the high-vacuum deposition chamber, the substrates were cleaned again with deionized water, and dried with N_2. The deposition rate of the different oxides was fixed at around 0.25 nm/s, by using a previously calibrated quartz crystal monitor. Multilayers composed by 20 bilayers of 5 nm/5 nm nominal thicknesses of SiO_2/Al_2O_3, SiO_2/Cr_2O_3, and SiO_2/Y_2O_3 (group 1, see Table 1) were grown with a total thickness of 200 nm. In addition, multilayers of SiO_2/Y_2O_3 formed by 20 bilayers of 3 nm/6 nm, 5 nm/10 nm, and 10 nm/20 nm (group 2) were also deposited, in order to study the influence of the bilayer thickness on the thermal conductivity while keeping the number of interfaces constant. We also changed the number of SiO_2/Y_2O_3 multilayers from 1 to 30, maintaining the bilayer thickness constant at 20 nm (group 3), to analyze the influence of the number of interfaces on the effective thermal conductivity.

Table 1 summarizes the different samples. Thickness was measured by cross-sectional scanning or transmission electron microscopy images. In all cases, deposition started with Yttria, and finished with a SiO_2 layer. Samples of group 1: 1-SA20–5T, 1-SC20–5T, and 1-SY20–5T, were heat treated at 1100°C during 2 h in nitrogen atmosphere, to analyze the impact of a high temperature treatment on the thermal conductivity. The pairs of materials, SiO_2/Al_2O_3, SiO_2/Cr_2O_3, and SiO_2/Y_2O_3, were chosen, due to their immiscibility up to 1200°C to avoid the formation of intermediate phases upon heating and/or to reduce grain growth that could adversely affect the thermal behavior [19–21]. Thicker films of 200 nm of amorphous SiO_x grown by electron beam and 200 nm of nanocrystalline Y_2O_3, to be used as reference for the behavior of the "bulk" material, were also deposited by EB-PVD in the same conditions as the nanolaminates.

The cross-plane thermal conductivities were measured with the differential 3ω method [22] for as-deposited and heat treated samples. We used 100 nm thick Al wires with a 5 nm Cr adhesion layer for the 3ω sensor. The thin film heater is defined by photolithography and liftoff. All measurements were carried out in the temperature range of 30–300 K in a vacuum of 2.5×10^{-7} mbar. Joule heating was produced by applying an AC current to the 35 μm width and 2 mm long Al strip using a Keithley 6221 source on the current pads of the sensor. The 3ω voltage was measured using a Stanford Research 830 lock-in amplifier in the range of 300–3000 Hz. The one-dimensional steady-state heat conduction model was used to extract the cross-plane thermal conductivity values from the temperature rise of the films. Cross section TEM images were acquired in a 300 kV JEOL 3010, equipped with LaB_6, GATAN Tridiem electron energy loss spectroscopy, and elemental mapping. We used low-temperature glue (60°C) for mechanical preparation, and a 6 kV Ar-ion beam with 1 mA beam current to prevent ion-beam or heat damage during sample preparation.

3 Results and Discussion

The temperature drop across the as-deposited 5 nm SiO_2/5 nm Y_2O_3 20 bilayer sample (1-SY20–5) measured at 300 K in the frequency range of 300–2100 Hz is shown in Fig. 1. The presence of the multilayer simply adds a frequency independent temperature rise, which is used to derive the effective thermal conductivity of the nanolayered film. The value of κ obtained from any slope of the lines for the undoped Si substrate is 148 W/m K at 300 K, which closely agrees with literature values [23].

The thermal conductivity data for the nanolaminate samples of group 1 are shown in Fig. 2. Most of the data exhibit the typical dependence of an amorphous film with temperature, i.e., a gradual increase with increasing temperature, similarly to what was reported for cross-plane measurements on thin films of SiO_2, Si_3N_4, a-Si or a-Ge [24–28], or other multilayer systems [16–18]. The three lower curves show the thermal conductivity of the as-deposited films with values around 0.5 W/m K at 300 K. The three upper curves correspond to the samples heat treated during 2 h at 1100°C with κ values ranging from 0.8 W/m K to 1.4 W/m K at 300 K.

The annealed samples exhibit higher values of the thermal conductivity compared with as-grown samples. In general, thermal annealing in quasidisordered/nanocrystalline structures is accompanied by coarsening, grain growth, and densification of the material [29]. In our case, the differences are mainly attributed to changes in the microstructure. X-ray diffraction of the as-deposited stacks (not shown here) shows the absence of crystalline peaks, which is compatible with the disordered/nanocrystalline nature of the layers. However, after annealing at 1100°C, the SiO_2/Y_2O_3 stack shows well defined Bragg peaks

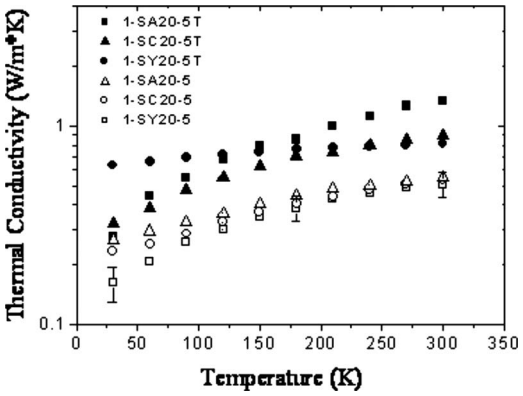

Fig. 2 Thermal conductivity as a function of temperature for SiO_2/Al_2O_3, SiO_2/Cr_2O_3, and SiO_2/Y_2O_3 nanolayered samples with a modulation length of 5 nm/5 nm. The solid symbols represent the data from the heat treated samples, whereas the open symbols are for the as-deposited samples. Representative error bars are only shown for the 1-SY20–5 sample.

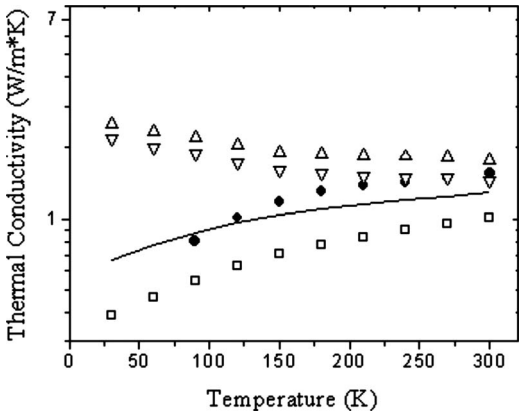

Fig. 3 Thermal conductivity as a function of temperature for oxide layers of 10 nm (down triangle) and 200 nm (up triangle) of Y_2O_3 and 200 nm SiO_x (square). Also, it is shown for comparison data from Cahill et al. [16] on 1 μm thick disordered Yttria (solid circle). The continuous line represents the value of the intrinsic thermal conductivity of the layers κ_{layers}, i.e., without considering the contribution of the thermal boundary resistance.

that correspond to both cubic Yttria and an unknown phase that may be probably attributed to some sort of metastable ternary compound. We infer that grain growth and channeling through the SiO_2 layer has occurred during the thermal treatment. These microstructural changes may be at the origin of the lower slope in the low-temperature region of the SiO_2/Y_2O_3 sample compared with a typical disordered structure. The other two stacks, SiO_2/Cr_2O_3 and SiO_2/Al_2O_3, show no clear XRD peaks after annealing. However, it seems reasonable to argue that the higher κ values in the annealed samples are also related to an increase in the grain size.

Next, we analyze the reduction in the thermal conductivity of the nanolaminates compared with that of their component materials. We focus on the SiO_2/Y_2O_3 multilayer system. The effective thermal conductivity k_{eff} for a stack of alternating layers with thickness t is written as

$$\kappa_{\text{eff}} = \frac{\kappa_{\text{layers}}}{1 + \kappa_{\text{layers}} \dfrac{R_{\text{th}}}{t}} \tag{1}$$

where $\kappa_{\text{layers}}^{-1} = 0.5 \cdot (\kappa_{SiO_2}^{-1} + \kappa_{Y_2O_3}^{-1})$ is the thermal conductivity from individual layers of identical thickness, and R_{th} is the overall interfacial resistance considered as the sum of the thermal resistance of the SiO_2/Y_2O_3 interfaces.

Figure 3 shows the measured thermal conductivities of single layers of Yttria (10 nm and 200 nm) and SiO_2 (200 nm) as a function of temperature, along with data on a 1 μm Yttria layer measured by Cahill et al. [16]. SiO_2 exhibits the typical behavior of a highly disordered material, and at room temperature, the thermal conductivity of the 200 nm electron beam SiO_x thin film is 1.1 W/m K. However, the thermal conductivity of both Yttria layers increases with decreasing temperature, which is characteristic of crystalline materials. This is in contrast to the temperature dependence of the 1 μm Yttria layer previously reported in Ref. [16], and exemplifies the strong influence of the grain size and the particular microstructure on the thermal properties. The value for Yttria depends on the thickness of the layers, whereas we measured 1.78 W/m K at 300 K for the 200 nm layer, we obtained a value of 1.30 W/m K for the 10 nm film. The measured values for Yttria are smaller than previously reported data for bulk samples, which is 14 W/m K, and also smaller than the values obtained for nanocrystalline Yttria films grown by magnetron sputtering [14]. The diffraction patterns of the as-deposited Yttria film are consistent with the cubic equilibrium structure with symmetry Ia3 (JCPDS-43–1036). The 200 nm film is polycrystalline and highly oriented along the [222] direction, which is the only reflection observed in the $\theta-2\theta$ scan. $\theta_{(222)}$ is 28.49 deg, which is associated with a lattice parameter of 10.852 Å, whereas for standard Y_2O_3 is 10.604 Å. This result means a 2.3% increase in the lattice parameter in the direction normal to the surface of the substrate, which may be related to the existence of some residual stress in the films.

However, as mentioned above, as-deposited SiO_2/Y_2O_3 multilayers do not show distinctive diffraction peaks, which is indicative of its quasidisordered/nanocrystalline structure. Cross-sectional TEM is used to inspect the microstructure of the 2-SY20–20 multilayer, which is representative of the as-deposited samples. The multilayer is nicely seen, as in Fig. 4, due to the combined effect of mass thickness contrast and diffraction contrast. Whereas the silicon oxide layer is fully disordered, the Yttria layer is composed of nanograins, which occasionally slightly grow into the amorphous SiO_2 at the interfaces.

Consequently, in the case of the Y_2O_3 layers, we may expect an intrinsic thermal conductivity with a value between the thermal conductivity of a disordered oxide layer, i.e., 1.5 W/m K at 300 K [16], and the experimental value of the 200 nm layer, which is 1.8 W/m K (this work). In the case of SiO_2, as the mean free path of the phonons in amorphous oxides is around 0.5 nm at 300 K and remains relatively constant with temperature from 30 K to 300 K [30], and our individual layer film thickness are a factor of ten larger, we expect that size effects should not influence the

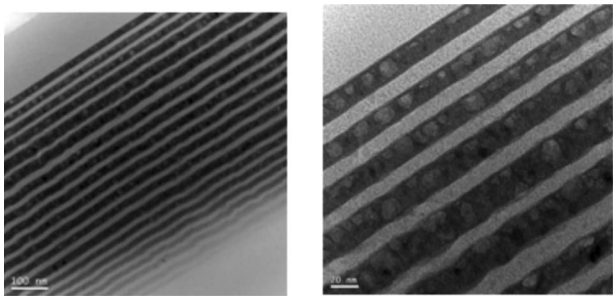

Fig. 4 Cross-sectional TEM images of the as-deposited 20 bilayer 10/20 SiO_2/Y_2O_3 sample at several magnifications. Dark layers correspond to Yttria.

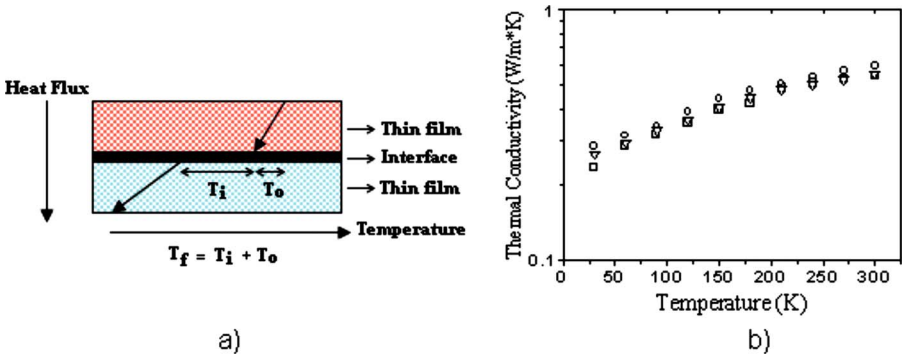

Fig. 5 (*a*) One-dimensional temperature profile across a thin film in response to an applied heat flux. The temperature drop across an interior region of film is denoted by T_o. T_i indicates the temperature discontinuity resulting from the interfacial resistance. (*b*) Effective thermal conductivity for sample of group 2: 2-SY20–6 (squares), 2-SY20–10 (down triangle), and 2-SY20–20 (circles).

intrinsic thermal conductivity of the layer. Therefore, using the limiting values of the thermal conductivity for the Yttria film, the combined thermal conductivity of the individual layers ranges from 1.26 W/m K $< k_{\text{layers}} <$ 1.4 W/m K, which disagrees with the experimental value of 0.5 W/m K. Solving Eq. (2) for R_{th}, we obtain the overall TBR for the 1-SY20–5 sample, which is 2.4×10^{-7} m^2 K/W $< R_{\text{th}} < 2.7 \times 10^{-7}$ m^2 K/W. The averaged thermal resistance associated to each interface has a value of the order of $6-7 \times 10^{-9}$ m^2 K/W, and produces a non-negligible effect on the effective thermal conductivity of the nanolayered system. This value is below the thermal boundary resistance value obtained by Yang et al. [14] for the interface between Yttria and Al_2O_3, 3×10^{-8} m^2 K/W^{-1}, and is almost an order of magnitude higher than the value reported by Cahill et al. [16] on YSZ/SiO_2 multilayers. The effect of the interfaces on the thermal conductivity can be qualitatively understood by drawing the temperature profile across a thin film having an interface with another film, as shown in Fig. 5(*a*). The temperature drop across the structure consists on the temperature difference in the interior region of the film T_o and temperature discontinuity at an interface T_i. Thermal resistances reduce the flow of heat due to the differences in elastic properties and densities of vibrational states, rendering more difficult the transfer of thermal energy across interfaces between dissimilar materials.

The three curves in the plot of Fig. 5(*b*) show the effective thermal conductivity against temperature obtained for the set of multilayers composed by 20 bilayers of SiO_2/Y_2O_3 with thickness 3 nm/6 nm, 5 nm/10 nm, and 10 nm/20 nm (group 2, Table 1). There is only a small difference by altering the effective thickness of the component nanolayers, which confirms that the intrinsic thermal conductivity of the films remain unaltered due to their quasidisordered structure. In fact, the difference is within the experimental uncertainty but could also arise from small variations in the void density of the films. Although no favorable changes were observed in the effective thermal conductivity value around 0.5 W/m K by keeping the number of interfaces and changing the thickness of the individual component materials, the value obtained is lower than those reported by other researchers for similar nanostructured materials [16,17]. To gain further insight into the role of the interfaces onto the effective thermal conductivity, we prepared several samples (group 3 in Table 1) with identical bilayer thickness, but with varying number of interfaces ranging from 2 to 60.

Figure 6 shows the effective thermal conductivity for the different samples, and reveals that κ_{eff} increases with the number of bilayers, which at first sight seems to be contrary to expectations. The effective thermal conductivity of sample 3-SY1–10, which contains only 1 bilayer, shows an ultralow value of 0.16 W/m K. Considering that the intrinsic thermal conductivity for the Yttria layer is constant, and lies within the minimum value for a disordered media and the value of the 200 nm film, we plot in Fig. 7 the overall thermal resistance as a function of the number of interfaces n. The observed trend confirms that as n increases, the thermal resistance also increases. However, the curve does not follow a linear behavior with n, as should be expected, if all the interfaces contribute similarly to the scattering of phonons, and therefore, to the thermal barrier. Instead, the curve approaches an asymptotic value when n is large. This was already observed in other multilayer systems where the contribution to the overall thermal barrier is higher for the first few interfaces [31,32]. This is better seen by plotting the interfacial resistivity R_{th}/t (solid circles, right axis of Fig. 7). If the contribution to the effective thermal conductivity of the multilayer system was identical from all interfaces, the resistivity should be independent of the number of interfaces. However, Fig. 7 clearly shows that this is not the case. The thermal boundary resistance of the sample with two interfaces is six times lower than the one obtained for the sample with 60 interfaces. The variation in the thermal boundary resistance is at the origin of the reduction in the effective thermal conductivity measured for samples with identical period thickness, but with only few interfaces. The figure also includes the overall TBR values deduced for samples with 20 bilayers from group 1 (1-SY20–5) and group 2 (2-SY20–6, 10, 20). Also, when the thermal resistance of samples containing 40 interfaces is di-

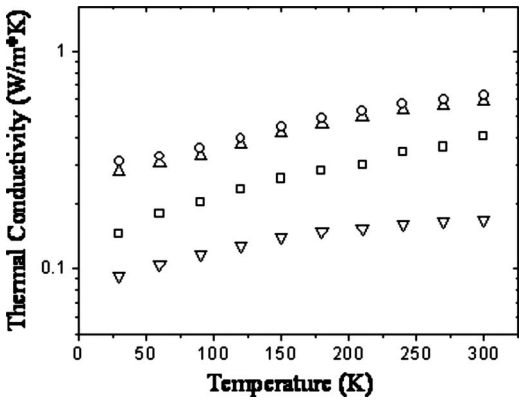

Fig. 6 Effective thermal conductivity of SiO_2/Y_2O_3 multilayers of group 3, with identical period thickness of 20 nm but with varying number of interfaces (total thickness): 3-SY1–10 (down triangle), 3-SY5–10 (square), 3-SY20–10 (up triangle), and 3-SY30–10 (circle)

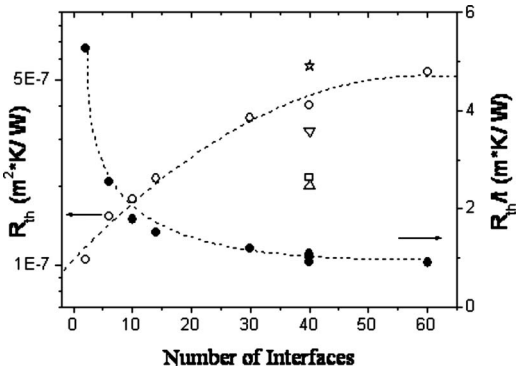

Fig. 7 (a) Overall thermal boundary resistance (open symbols, left axis) and interface resistivity (closed symbols, right axis) of the SiO_2/Y_2O_3 multilayer system (group 3) versus the number of interfaces. The lines are only guides to the eye. Data of the overall TBR from 1-SY20–5 (square) and 2-SY20–6 (up triangle), and 2-SY20–10 (down triangle) and 2-SY20–20 (star), is included for comparison.

vided by the total thickness of each sample, they converge to a single value of the interface resistivity of 1 ± 0.1 m K/W^{-1}.

In Fig. 8, we plot the temperature dependence of the averaged interfacial thermal resistance, defined as the overall TBR, divided by the number of interfaces, and associated to each interface for sample 2-SY20–6. Symbols represent the experimental interfacial resistance of the SiO_2/Y_2O_3 interfaces, and the solid line represents the predicted interfacial resistance by using the diffusive mismatch model (DMM) approach [33]. The DMM model assumes that the correlations between incident and scattered phonons are lost at the interface. The acoustic properties of a-SiO_2 and Y_2O_3 used in the DMM approximation are taken from Refs. [34,35], respectively. The experimental values of the averaged thermal resistance per interface in the high temperature region are slightly above predictions from the DMM. However, at low temperatures, the experimental data does not follow the observed trend in the DMM, mainly because the intrinsic conductivity of the Yttria film is assumed to increase with decreasing temperature, as observed for a single layer of Yttria.

4 Conclusions

Multilayers of SiO_2/Al_2O_3, SiO_2/Cr_2O_3, and SiO_2/Y_2O_3 have values of the effective thermal conductivity at room temperature, significantly below the thermal conductivity of the component materials. We have shown that the interface between SiO_2 and Yttria plays a significant role in the reduction in the thermal conductivity, and conversely, the influence of the thickness of the layers in between 3 nm and 10 nm is negligible. By comparing samples with identical modulation length but different number of interfaces, we demonstrate that the first interfaces influence the thermal resistance much more than subsequent interfaces. Whereas measurements at high temperatures were not performed in this work, the apparent high thermal stability of these materials, together with the low thermal conductivity achieved at room temperature, indicates its potentiality as thermal insulators for high temperature applications.

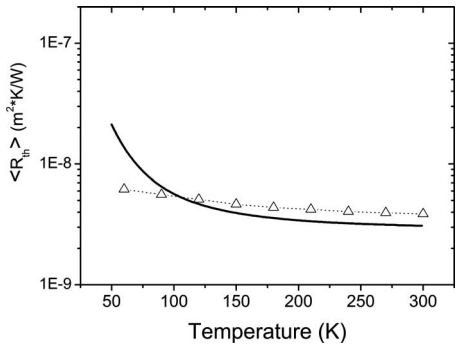

Fig. 8 Averaged thermal boundary resistance associated to each interface for sample 2-SY20–6 as a function of temperature. The continuous line represents the interfacial resistance predicted by the DMM.

Acknowledgment

We thank Andrea Jakab for TEM sample preparation. J. A. Q. acknowledges Conacyt Mexico for fellowship. This work was supported in part by the Spanish Ministerio de Educación y Ciencia through Grant No. MAT2007-61521, and by Direcció General de Recerca of the Generalitat of Catalonia through Grant No. 2009SGR01225.

Nomenclature

κ = thermal conductivity (W/m K)
κ_{eff} = effective thermal conductivity (W/m K)
R_{th} = overall thermal boundary resistance (m^2 K/W)
$\langle R_{\text{th}} \rangle$ = average thermal boundary resistance (m^2 K/W)
t = thickness (nm)
θ = Bragg angle (deg)
n = number of interfaces

References

[1] Beele, W., Marijnissen, G., and Van Lieshout, A., 1999, "The Evolution of Thermal Barrier Coatings-Status and Upcoming Solutions for Today's Key Issues," Surf. Coat. Technol., **120-121**(799), pp. 61–67.
[2] Cao, X. Q., Vassen, R., and Stover, D., 2004, "Ceramic Materials for Thermal Barrier Coatings," J. Eur. Ceram. Soc., **24**, pp. 1–10.
[3] Hasselman, D. P. H., Johnson, L. F., Bentsen, L. D., Syed, R., and Lee, H. L., 1987, "Thermal Diffusivity and Conductivity of Dense Polycrystalline ZrO_2 Ceramic," J. Am. Ceram. Soc., **66**(5), pp. 799–806.
[4] Clarke, D. R., 2003, "Materials Selection Guidelines for Low Thermal Conductivity Thermal Barrier Coatings," Surf. Coat. Technol., **163-164**, pp. 67–74.
[5] Schlichting, K. W., Padture, N. P., and Klemens, P. G., 2001, "Thermal Conductivity of Dense and Porous Yttria-Stabilized Zirconia," J. Mater. Sci., **36**(12), pp. 3003–3010.
[6] Gao, P., Meng, L. J., Dos Santos, P. M., Teixeira, V., and Andritschky, M., 2002, "Study of ZrO_2/Al_2O_3 Multilayers," Vacuum, **64**(3-4), pp. 267–273.
[7] Winter, M. R., and Clarke, D. R., 2007, "Oxide Materials With Low Thermal Conductivity," J. Am. Ceram. Soc., **90**(2), pp. 533–540.
[8] Soyez, G., Eastman, J. A., Thompson, L. J., Bai, G. R., Baldo, P. M., Dimelfi, R. J., Elmustafa, A. A., Tambwe, M. F., and Stone, D. S., 2000, "Grain-Size-Dependent Thermal Conductivity of Nanocrystalline Yttria-Stabilized Zirconia Films Grown by Metal-Organic Chemical Vapor Deposition," Appl. Phys. Lett., **77**(8), pp. 1155–1157.
[9] Clarke, D. R., and Levi, C. G., 2003, "Materials Design for the Next Generation of Thermal Barrier Coatings," Annu. Rev. Mater. Res., **33**, pp. 383–417.
[10] Yang, H. S., Bai, G. R., Thomson, L. J., and Eastman, J. A., 2002, "Interfacial Thermal Resistance in Nanocrystalline Yttria-Stabilized Zirconia," Acta Mater., **50**(9), pp. 2309–2317.
[11] Zeng, T., and Chen, G., 2001, "Phonon Heat Conduction in Thin Films: Impacts of Thermal Boundary Resistance and Internal Heat Generation," ASME J. Heat Transfer, **123**(2), pp. 340–347.
[12] Stoner, R. J., and Maris, H. J., 1993, "Kapitza Conductance and Heat Flow Between Solids at Temperatures From 50 to 300 K," Phys. Rev. B, **48**(22), pp. 16373–16387.
[13] Clarke, D. R., and Phillpot, S. R., 2005, "Thermal Barrier Coatings Materials," Mater. Today, **8**(6), pp. 22–29.
[14] Yang, H. S., Kim, J. W., Park, G. H., Kim, C. S., Kihm, K., Kim, S. R., Kim, K. C., and Hong, K. S., 2007, "Interfacial Effect on Thermal Conductivity of Y_2O_3 Thin Films Deposited on Al_2O_3," Thermochim. Acta, **455**(1-2), pp. 50–54.
[15] Padture, N. O., Gell, M., and Jordan, E. H., 2002, "Thermal Barrier Coatings for Gas Turbine Engine Applications," Science, **296**, pp. 280–284.
[16] Cahill, D. G., Bullen, A., and Lee, S. M., 2000, "Interface Thermal Conductance and the Thermal Conductivity of Multilayer Thin Films," High Temp. - High Press., **32**, pp. 135–142.
[17] Costescu, R. M., Cahill, D. G., Fabreguette, F. H., Sechrist, Z. A., and George, S. M., 2004, "Ultra-Low Thermal Conductivity in W/Al_2O_3 Nanolaminates," Science, **303**, pp. 989–990.

[18] Chiritescu, C., Cahill, D. G., Nguyen, N., Johnson, D., Bodapati, A., Keblinski, P., and Zschack, P., 2007, "Ultralow Thermal Conductivity in Disordered, Layered WSe_2 Crystals," Science, **315**, pp. 351–353.
[19] Kumar, S., and Drummond, C. H., 1992, "Crystallization of Various Compositions in the Y_2O_3–SiO_2 System," J. Mater. Res., **7**(4), pp. 997–1003.
[20] Welch, J. H., 1960, "A New Interpretation of the Mullite Problem," Nature (London), **186**, pp. 545–546.
[21] Levin, E. M., Robbins, C. R., and Mcmurdie, H. F., 1974, *Phase Diagrams for Ceramists*, Vol. 1, M. K. Reser, ed., The American Ceramic Society, Columbus, OH, pp. 130–131.
[22] Cahill, D. G., 1990, "Thermal Conductivity Measurement From 30 to 750 K: The 3ω Method," Rev. Sci. Instrum., **61**, pp. 802–808.
[23] MacConnell, A. D., and Goodson, K. E., 2005, "Thermal Conduction in Silicon Micro- and Nanostructures," Annu. Rev. Heat Transfer, **14**, pp. 129–168.
[24] Lee, S. M., and Cahill, D. G., 1997, "Heat Transport in Thin Dielectric Films," J. Appl. Phys., **81**(6), pp. 2590–2595.
[25] Cahill, D. G., Katiyar, M., and Abelson, J. R., 1994, "Thermal Conductivity of a-Si:H Thin Films," Phys. Rev. B, **50**(9), pp. 6077–6081.
[26] Yamane, T., Nagai, N., Takayana, S., and Tokodi, M., 2002, "Measurement of Thermal Conductivity of Silicon Dioxide Thin Films Using a 3ω Method," J. Appl. Phys., **91**(12), pp. 9772–9976.
[27] Griffin, A. J., Jr., Brotzen, F. R., and Loos, P. J., 1994, "The Effective Transverse Thermal Conductivity of Amorphous Si_3N_4 Thin Films," J. Appl. Phys., **76**(7), pp. 4007–4011.
[28] Alvarez-Quintana, J., and Rodriguez-Viejo, J., 2008, "Interfacial Effects on the Thermal Conductivity of *a*-Ge Thin Films Grown on Si Substrates," J. Appl. Phys., **104**(7), p. 074903.
[29] Mengucci, P., Barucca, G., Caricato, A. P., Di Cristoforo, A., Leggieri, G., Lunches, A., and Maijnia, G., 2005, "Effects of Annealing on the Microstructure of Yttria-Stabilised Zirconia Thin Films Deposited by Laser Ablation," Thin Solid Films, **478**(1-2), pp. 125–131.
[30] Cahill, D. G., and Pohl, R. O., 1988, "Lattice Vibrations and Heat Transport in Crystals and Glasses," Annu. Rev. Phys. Chem., **39**, pp. 93–121.
[31] Zhang, W., Fisher, T. S., and Mingo, N., 2007, "Simulation of Interfacial Phonon Transport in Si–Ge Heterostructures Using an Atomistic Green's Function Method," ASME J. Heat Transfer, **129**(4), pp. 483–491.
[32] Abramson, A., Tien, C., and Majumdar, A., 2002, "Interface and Strain Effects on the Thermal Conductivity of Heterostructures: A Molecular Dynamics Study," ASME J. Heat Transfer, **124**(5), pp. 963–970.
[33] Swartz, E. T., and Pohl, R. O., 1989, "Thermal Boundary Resistance," Rev. Mod. Phys., **61**, pp. 605–668.
[34] Bogardus, E. H., 1965, "Third-Order Elastic Constants of Ge, MgO, and Fused SiO_2," J. Appl. Phys., **36**(8), pp. 2504–2513.
[35] Palko, J. W., Kriven, W. M., Sinigeiking, S. V., Bass, J. D., and Sayir, A., 2001, "Elastic Constants of Yttria (Y_2O_3) Monocrystals to High Temperatures," J. Appl. Phys., **89**(12), pp. 7791–7796.

Investigations on Multimode Heat Transfer From a Heated Vertical Plate

R. Krishna Sabareesh

S. Prasanna
Research Scholar

S. P. Venkateshan[1]
Professor
e-mail: profspv@gmail.com

Department of Mechanical Engineering,
Heat Transfer and Thermal Power Laboratory,
IIT Madras,
Chennai 600036, India

The interaction of surface radiation and conduction with natural convection heat transfer from a vertical flat plate assembly, with an embedded heater, has been investigated, both experimentally (using differential interferometer) and numerically (using FLUENT), in the present work. In the absence of radiation, the asymptotic limits that can be attained by the heated plate are isothermal and isoflux conditions. High values of plate thermal conductivity tend to make the surface isothermal, where as, lower values of thermal conductivity tend to make it isoflux. Irrespective of the thermal conductivity of the plate, an increase in the emissivity reduces the average temperature of the plate and brings the plate toward isothermal condition. A new methodology has also been proposed to determine the thermophysical properties, emissivity and thermal conductivity, the consistency of which is tested by carrying out experiments for various heat inputs and comparing the estimated values with those available in literature. [DOI: 10.1115/1.4000055]

Keywords: multimode heat transfer, interferometer, thermal conductivity, emissivity, asymptotic limits

1 Introduction

Laminar buoyancy induced flow over vertical flat surfaces has an important position in heat transfer research due to its practical importance in many applications. In most of the studies, either isothermal or isoflux conditions have been assumed at the surface of the wall. But, in many practical applications such as fins, heat exchangers, etc., there exists a thermal balance between more than one modes of heat transfer. For example, if a heated wall of a finite thermal conductivity and thickness with a high emissivity coating is exposed to an ambient, equilibrium is established under the influence of all the three modes of heat transfer. Depending on the problem under consideration, particular mode(s) of heat transfer may be dominant. Conjugate heat transfer classically refers to heat transfer which involves interaction between conduction in the solid and convection to the fluid surrounding it. In addition to this, for high values of emissivity the effect of surface radiation should also be taken into account in order to ensure temperature and heat flux continuity at the solid-fluid interface. The classical example of heat transfer from an isothermal vertical flat plate is given by Ostrach [1]. He gave an analytical solution for the local heat transfer coefficient. Sparrow and Gregg [2] considered heat transfer from a vertical flat plate with constant heat flux condition. Analytical solutions for prescribed nonuniform temperature or prescribed nonuniform heat flux are also found in the literature. One of the first works on conjugate heat transfer is due to Kelleher and Yang [3], who obtained analytical solutions for a semi-infinite vertical flat slab with internal heat generation. Zinnes [4] investigated, both experimentally and numerically, conjugate heat transfer effects from a flat plate of finite thickness with a localized heating on its surface. Miyamoto et al. [5] studied conjugate heat transfer from a vertical flat plate for isothermal and isoflux boundary conditions at the outside surface of the flat plate, using the method of local similarity. They also performed experiments and found the pertinent parameter which could explain the effect of the axial conduction on the interfacial temperature. Pozzi and Lupo [6] developed analytical solution for a thin vertical slab to ensure one dimensional heat conduction within the solid. Lee and Yovanovich [7] developed a simple analytical model to predict the heat transfer characteristics with arbitrary surface heat flux distribution. Vynnycky and Kimura [8] proposed a model, which does not assume any interfacial boundary temperature profile, to predict the local and average heat transfer coefficients when a vertical plate is maintained at constant temperature at the backside. Kimura et al. [9] experimentally validated their previous observations [8] and proposed conjugate Nu-Ra correlations. Mendez and Trevino [10] studied conjugate heat transfer from a vertical plate with nonuniform internal heat generation for both thin and thick wall regimes. Yadav and Kant [11] have verified experimentally their analytical solution for natural convection from a heated thin walled plate, with the surface partly subjected to constant heat flux and partly to uniform temperature.

One of the first works, which addresses the interaction of surface radiation with natural convection, has been reported by Webb [12]. He experimentally and theoretically investigated the interaction of radiation with natural convection from a single, isolated vertical flat plate with uniform heat flux boundary condition and found that radiation tends to make the surface temperature more uniform. Venkateshan and Balaji [13] discussed the interaction of surface radiation with natural convection and conduction for different geometries like closed cavity, open cavity, and *L* shaped corner, and concluded that radiation plays an important role even at low temperature levels (room temperature to 100°C). It was also found that radiation suppresses natural convection while increasing the overall heat transfer. To the best of the authors' knowledge, the interaction of both conduction and radiation with natural convection from a vertical flat plate has not been addressed to date in the heat transfer-literature. The objective of the present work is to bring out the importance of thermal conductivity and surface emissivity on natural convection heat transfer from a heated vertical flat plate, and hence determine the appropriate boundary condition. Therefore both experiments and numerical simulations have been carried out to understand the physics underlying the interaction process.

[1]Corresponding author.

Contributed by the Heat Transfer Division of ASME for publication in the JOURNAL OF HEAT TRANSFER. Manuscript received March 27, 2009; final manuscript received August 7, 2009; published online December 29, 2009. Editor: Yogesh Jaluria.

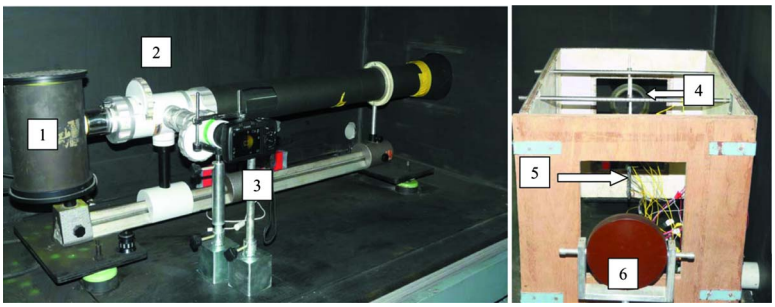

Fig. 1 Photograph of the DI used in the present study

2 Experimental Setup

The experimental setup consists of a differential interferometer (DI) assembly and the test section, placed inside a long enclosure as shown in Fig. 1, free from external disturbance. The DI head is separated from the test section by means of a wooden partition whose purpose is to avoid disturbances to the test plate assembly while adjustments to the interferometer are being done.

2.1 Differential Interferometer. The schematic of the DI used for measuring the local heat transfer coefficient is shown in Fig. 2 (Spindler and Hoyer GmbH, Germany) [14]. The core element of the DI is the Wollaston prism, the shearing element. The Wollaston prism consists of two birefringent quartz prisms, whose optical axes are perpendicular to each other, cemented together at the base. The prism splits the polarized incident wave front into two orthogonal wave fronts, which are separated by a definite angle. The biconvex lens-plane mirror combination is used to make the two rays, the ordinary and the extraordinary rays, to traverse the test section with a small and constant spacing. So, when the two wave fronts are superposed onto one another, the difference in optical paths due to the gradient of refractive index, are recorded. The second Wollaston prism (WP2) is introduced into the path of the light to make quantitative heat transfer measurements. When a heated object is introduced into the path of the light, the otherwise parallel fringes tend to deflect in the vicinity of the object. The amount of deflection of the fringes from the normal position is directly proportional to the *convective* heat transfer from the surface. In the present study, yellow light (wavelength, $\lambda = 584$ nm) is chosen for analyzing the heat transfer phenomena. The interferograms are captured using a computer controlled digital camera (Canon SX 110 IS). The field of view of the present optical setup is approximately a circle of diameter equal to 9.5 cm.

2.2 Test Section. The test section is a wooden box which houses the test plate assembly. The top and the bottom of the test section are open and distance between the sidewalls and the test plate is about 25 cm, and hence will not affect the flow field near the heated test plate. The vertical plate assembly is suspended freely from two parallel stainless steel rods using two Teflon rods as depicted in Fig. 3. The test plate assembly used in the experiments consists of two plates of dimensions $150 \times 250 \times 3$ mm, with a flat heater sandwiched between them. The flat heater is formed by winding a Nichrome wire over a mica sheet and the same is electrically insulated from the unexposed side of the test plates by using mica sheets. The two halves of the test plate are fastened together using screws and nuts that are seated in countersunk holes to avoid disturbances to flow due to protrusion. The chamfering operation done at the bottom of the test plates ensures smooth flow of air. The experiments are carried out with test plates of different materials such as aluminum, mild steel, titanium, and bakelite to cover a large range of thermal conductivities. The various surface emissivities are obtained by buffing (low emissivity), coating the surface with metallic aluminum paint (medium emissivity), red oxide paint, and blackboard paint (high emissivity) (All paints used are manufactured by Asian Paints, India.) As it is difficult to carry out the buffing operation on titanium, the surface is wrapped with pure aluminum foil pasted on the surface using a commercially available thermal paste. A perfect contact, free of air pockets and wrinkles, is ensured between the foil and the surface. Similarly, the experiments on bakelite are conducted for "no coating" and also wrapping the surface with aluminum foil as explained above.

The temperatures at different locations are recorded using calibrated K-type 36AWG stainless steel sheathed thermocouples, which are seated in milled grooves on the plate and attached using a highly conducting copper cement. The ambient temperature is

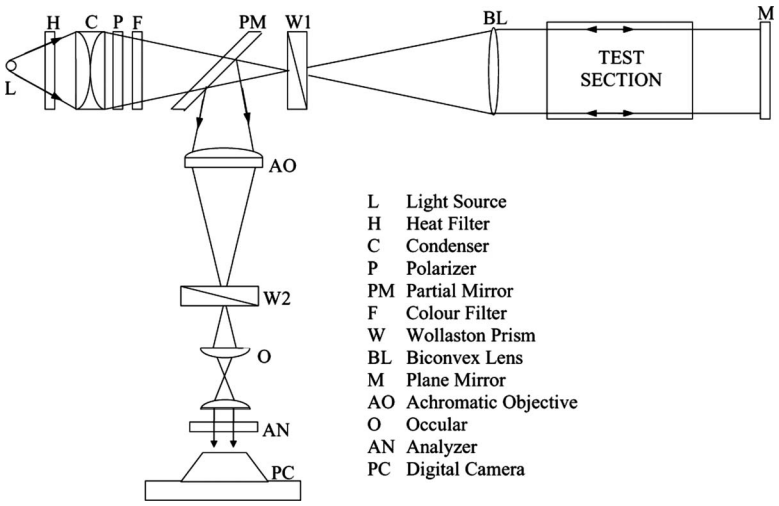

Fig. 2 Schematic diagram of the DI

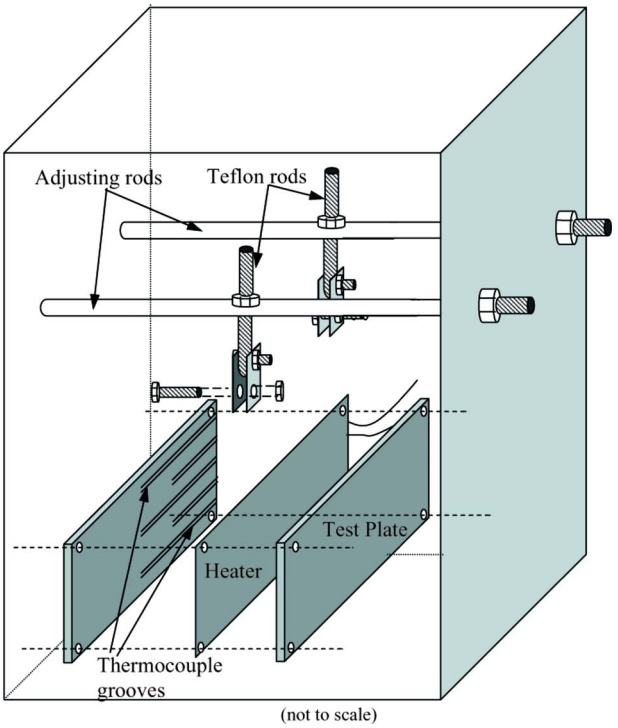

Fig. 3 Schematic of test setup

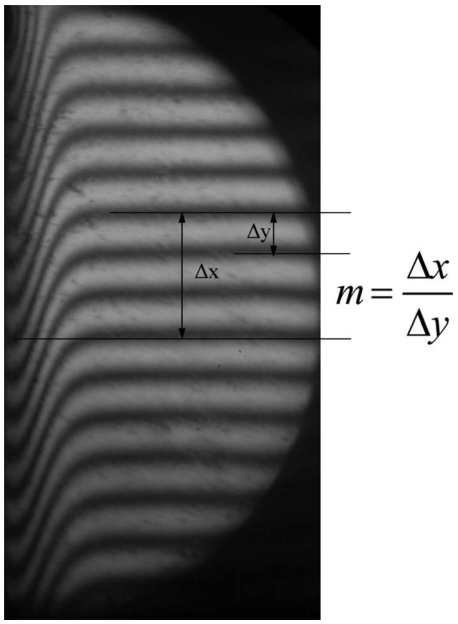

Fig. 4 A typical interference fringe pattern along a heated vertical flat plate

measured using a separate calibrated thermocouple, which is kept inside the large chamber and is placed sufficiently far away from the zone of influence of the heated plate assembly. All thermocouples are connected to a personal computer based data acquisition system (Model 2700, Integra Series, Keithley Instruments, Inc.) through compensating wires. The power input to the heater is supplied from a regulated dc power source (Densei-Lambda GEN 1500 W). Spirit level is used to ensure the verticality of the plate. The surface of the plate is adjusted such that it is parallel to the optical axis of the interferometer. Steady state experiments, simulating natural convection environment inside the test section, are carried out for various power inputs and plate temperatures ranging from 50°C to 120°C. Steady state is achieved when the variation in the temperature readings of all the thermocouples is within 0.1°C over a period of 10 min.

2.3 Digital Image Processing and Fringe Analysis. One sample interferogram captured using the digital camera is shown in Fig. 4. The interferograms captured contain Gaussian noise, which is random in nature and has spatially high frequency compared with the fringes. Therefore by suitably selecting a low pass filter in the frequency domain, the high frequency noise can be eliminated from the interferogram. The interferogram after removing the noise is used for determining the fringe shift factor m, which is defined as the ratio of the amount of deflection ΔX to the fringe width ΔY, as shown in Fig. 4. The points corresponding to the fringe minima at the wall are determined for both undeformed and deformed fringes by row-wise scanning of the pixels. A code has been written in MATLAB 7 for this purpose.

2.4 Measurement of Heat Transfer. Since a good review of heat transfer measurement using DI is available in Ref. [15], only a brief explanation is provided here. If the flow field is assumed to be two dimensional, the optical path difference of the light rays traveling through the test section of length L would be

$$2L\Delta n = m\lambda \tag{1}$$

The lateral shear produced due to the Wollaston prism [15] is

$$\Delta y = 0.0182d \tan \delta \tag{2}$$

Combining Eqs. (1) and (2), the gradient of the refractive index can be approximated as

$$\frac{\partial n}{\partial y} \sim \frac{\Delta n}{\Delta y} = \frac{m\lambda}{2L\Delta y} \tag{3}$$

By using Lorenz–Lorentz relationship between density and refractive index for air and assuming air to be an ideal gas, the temperature gradient can be expressed as

$$\frac{\partial T}{\partial y} = -\frac{2}{3}\frac{RT_w^2}{CP}\frac{m\lambda}{2L\Delta y} \tag{4}$$

After further simplifications, the local heat transfer coefficient can be expressed as

$$h = \frac{q''}{T_w(x) - T_\infty} = \frac{2}{3}\frac{RT_w^2}{CP}\frac{m\lambda}{2L\Delta y}\frac{k_{fw}}{[T_w(x) - T_\infty]} \tag{5}$$

3 Numerical Formulation

3.1 Modeling. The physical model and the coordinate system considered are as shown in Fig. 5. The thickness of the plate considered in the present study is very small compared with the height of the plate so that the Biot number (Bi) in the lateral direction is always less than 0.1. Considering the plate to be lumped in the lateral direction, heat flux can be modeled as an equivalent heat generation as shown in Fig. 5. Radiation is assumed to be diffuse and gray, which is a good approximation for the surfaces considered. The volume ratio of the test plate to the test section is about 9×10^{-5}, and therefore the test plate can be treated as a small object placed in a large enclosure. The steady state governing equation can be written as

$$k_s t\frac{d^2T}{dx^2} + h(T_\infty - T_w) + \varepsilon\sigma(T_\infty^4 - T_w^4) + Q_{\text{gen}}t = 0 \tag{6}$$

which is that of a heat generating fin losing heat to the ambient by radiation and convection. The experimental conditions are simulated using the commercially available computational fluid dynamics (CFD) package FLUENT 6.3. In order to simulate natural convection, an extended domain, whose temperature and static

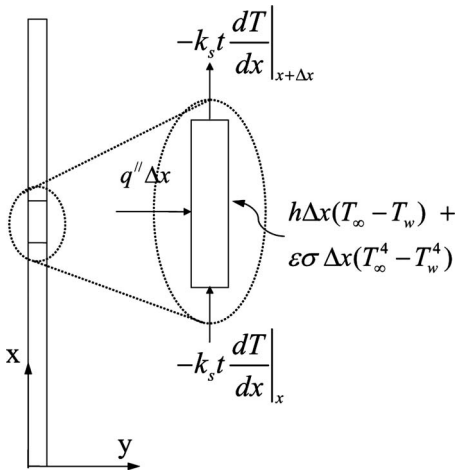

Fig. 5 Sketch of the physical geometry showing energy balance for a wall element

pressure is the same as that of the ambient, is considered around the heat generating plate. This is achieved using pressure outlet boundary condition available in FLUENT. Radiation is modeled using the discrete ordinates model (DOM). Detailed validation for the use of DOM has been given in Ref. [16]. All the faces of the test plate are given *coupled* boundary conditions, i.e., conduction within the solid is balanced by convection and radiation to the ambient. The computational domain with proper mesh considered in the present study is shown in Fig. 6. The mesh is finer close to the solid surfaces to capture the boundary layer and coarser far away from them, for computational efficiency. The proper mesh has been selected after carrying out extensive grid independence study, the details of which are given in Table 1.

Two dimensional conduction equation with heat generation is solved within the solid domain and temperature gradient in the lateral direction is found to be very small. Hence, modeling the

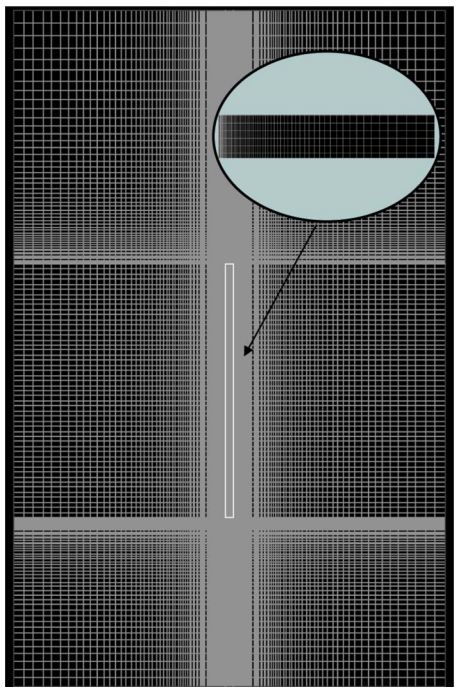

Fig. 6 Sketch of the mesh used. The gradual variation in the fineness of the mesh is also shown.

Table 1 Grid independence study

No. of cells	$T_{w,\text{avg}}$	% deviation
12,075	358.43	
24,300[a]	359.02	0.164
49,200	359.11	0.025

[a]Chosen grid size.

constant heat flux as an internal heat generation is a valid assumption. Natural convection is laminar and the solution is obtained by solving the Navier–Stokes equations by the finite volume method.

The purpose of the numerical simulations is two-fold. In the first stage it has been used to propose a new method to determine the thermophysical properties, the thermal conductivity of the material, and the surface emissivity [17]. In the second stage, the numerical simulations are used for understanding the interaction phenomena occurring between the various modes of heat transfer.

In the parlance of the inverse methodology used for parameter estimation, the forward model refers to determining the temperature distribution in a material with all the thermophysical properties of the material known. Similarly, the inverse method refers to determining the various properties, given the temperature distribution in the material. In the present parameter retrieval process, the result obtained from the numerical simulation is used as the forward model which involves obtaining the temperature distribution along the plate for different combinations of surface emissivity and thermal conductivity, and for various heat inputs. The important observations from the numerical study can be summarized as follows. For a fixed heat input and emissivity, as the thermal conductivity of the material increases, the temperature gradient along the plate decreases. Therefore, the isothermal assumption is strictly valid for materials having high thermal conductivity, such as aluminum. Table 2 shows the variation in the average temperature of the plate for a thermal conductivity of 200 W/m K, for different values of emissivity. It is seen that the average temperature of the plate decreases with increase in emissivity. It is also seen that the average heat transfer coefficient decreases with increase in emissivity, which is in accordance with the observations made by Venkateshan and Balaji [13]. Table 3 shows the dependence of the average temperature of the plate on the thermal conductivity, for a given emissivity and power input. It is *clear* that for a given emissivity, the average plate temperature is independent of thermal conductivity for a fixed heat input.

Table 2 Effect of emissivity on the average plate temperature and average convective heat transfer coefficient (numerical)

k (W/m^2 K)	ε	T_{avg} (K)	$\overline{h}$ (W/m^2 K)	$\overline{h}_{\text{tot}}$ (W/m^2 K)
200	0	338.8	5.0	5.0
	0.5	324.8	4.5	8.4
	1	318.3	4.2	11.5

Table 3 Effect of thermal conductivity on the average plate temperature (numerical)

ε	k (W/m^2 K)	T_{avg} (K)
0.5	0.1	324.4
	1	324.5
	50	324.7
	200	324.8

Table 4 List of emissivities retrieved

Surface condition	Emissivities				
	Present method	[18]	[19]	[20]	[14]
Buffed aluminum	0.09		0.04	0.05	0.05
Buffed mild steel	0.12				
Aluminum foil	0.04				0.05
Aluminum paint	0.39	0.31	0.21	0.47	
Red oxide paint	0.69				
Bakelite	0.72				
Blackboard paint	0.85	0.85	0.81	0.85	0.85

3.2 Inverse Method. Since the parameter retrieval process is considered in detail in Ref. [17], only a brief description is presented here.

3.2.1 Retrieval of Emissivity. A database of simulated average plate temperatures is created for different values of emissivity for a fixed value of heat input. The thermal conductivity independence ensures that even if a paint, whose emissivity is to be retrieved, is applied on a material of unknown thermal conductivity, the database can be generated using any value of thermal conductivity in the forward model. A cubic polynomial is then fit to the database and the root of the cubic equation corresponding to the experimentally obtained average plate temperature gives the desired emissivity. The list of emissivities retrieved using the above method is compared with the literature as shown in Table 4. The small differences in the emissivity values could be attributed to the difference in the surface condition of the test plate, paints used, and the thickness of the paint coating applied in the respective studies. Thus, this method of retrieving the emissivity of the coating is superior to other methods [18,19] as it does not require the knowledge of any other thermophysical property. All the values of emissivities, which are used in the present study, are estimated based on the above methodology.

3.2.2 Retrieval of Thermal Conductivity. Once the emissivity and heat input are fixed, the temperature distribution along the plate depends only on the thermal conductivity. So the forward model is run with the retrieved value of the emissivity obtained by the previous method, for different values of thermal conductivity. The thermal conductivity is retrieved by minimizing the sum of the squares of the differences between the numerically simulated and the experimentally obtained temperatures, which is

$$R = \sum_{i=1}^{n} (T_i - T_{\exp})^2 \tag{7}$$

The thermal conductivity values of bakelite and titanium determined using the above method are shown in Fig. 7. For bakelite, the thermal conductivity value was obtained as 0.22 ± 0.01 W/m K, while that of titanium was obtained as 9.95 ± 0.84 W/m K. It is seen that the value of emissivity and thermal conductivity determined using the present methodology are in very good agreement with the values mentioned in the literature [17].

4 Results and Discussion

Experiments have been carried out for five different heat inputs for all the surface conditions of each material. However, only a few results have been described here to bring out the physics involved in the interaction phenomena. Moreover, error analysis has been carried out for all the cases considered and it is found that the maximum error in the convective heat transfer coefficient is about $\pm 5\%$ for higher thermal conductivity materials like aluminum, where as it is about $\pm 10\%$ for bakelite whose thermal conductivity is very small. A detailed error analysis for one of the experiments has been provided in the Appendix. All the results obtained have been compared with Ostrach's [1] and Sparrow and Greg's [2] solutions which give, respectively, the variation in local Nusselt number for an isothermal and isoflux surface.

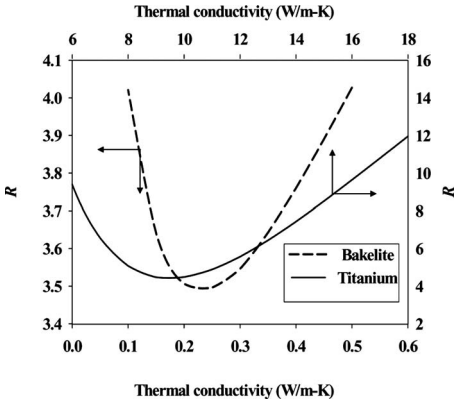

Fig. 7 Least square residual plots for determining the thermal conductivity of titanium and bakelite

4.1 Effect of Thermal Conductivity. Figure 8 represents the results obtained using the numerical simulations for three different values of thermal conductivity when the surface emissivity of the plate is set as zero. It is clear that, as the thermal conductivity increases, the solution approaches the Ostrach's solution and as the thermal conductivity decreases the solution approaches the Sparrow's solution. This implies that the constant heat generation condition used in the numerical simulations for simulating the experiments, is a realistic thermal condition, and that the plate asymptotically approaches the isothermal condition for large values of thermal conductivity and the isoflux condition for small values of thermal conductivity. The solutions for all the other values of thermal conductivity fall in between these two asymptotic limits.

Figure 9 represents the experimental results obtained for four different materials: aluminum, mild steel, titanium, and bakelite, with the surfaces being buffed for aluminum and mild steel, and the surfaces being wrapped with aluminum foil for titanium and bakelite. Though the fringe analysis does not require any knowl-

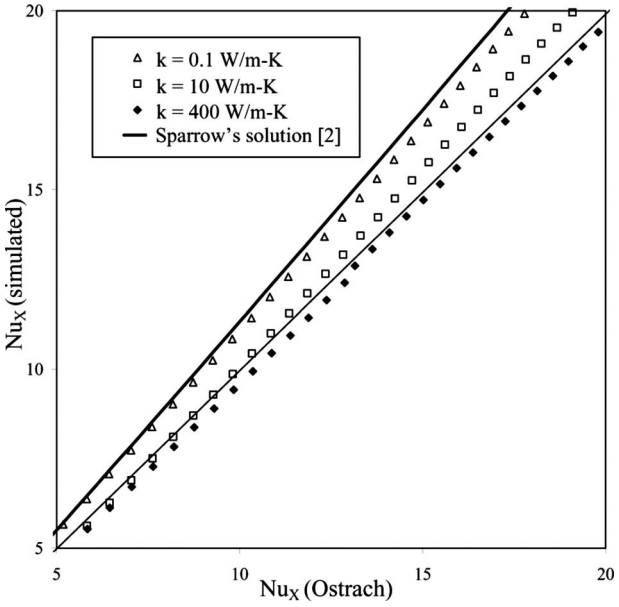

Fig. 8 Effect of thermal conductivity for $\varepsilon = 0$ (numerical)

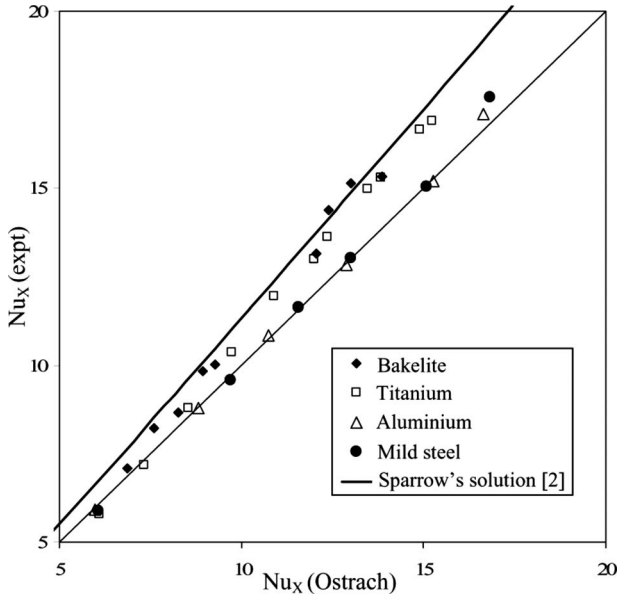

Fig. 9 Effect of thermal conductivity for low emissivity (experimental)

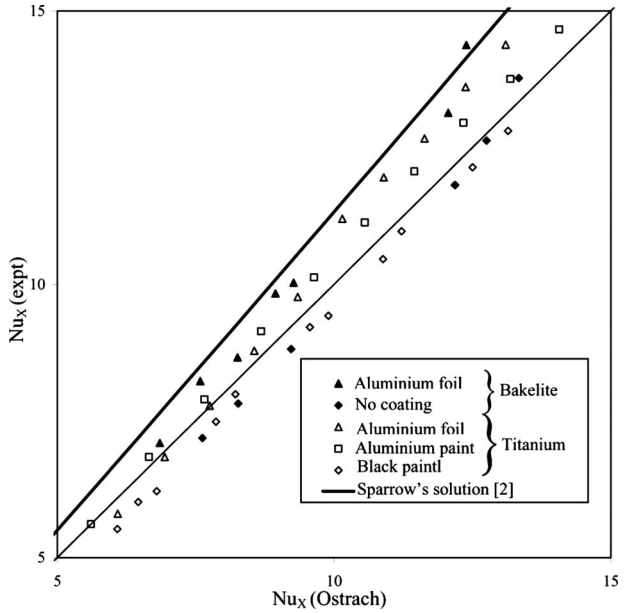

Fig. 11 Effect of surface emissivity for bakelite and titanium (experimental)

edge of the surface emissivity, they are found out using the method mentioned earlier, to ensure that the observations found in the numerical simulations are in agreement with the experiments.

4.2 Effect of Emissivity. Figure 10 represents the numerical results obtained for different values of emissivity for thermal conductivity of 1 W/m K and 200 W/m K. For lower thermal conductivity material, it is found that as the surface emissivity increases, the solution moves toward the Ostrach's solution from the Sparrow's solution. This implies that the surface of the plate is tending to become isothermal as the value of the emissivity increases. As the emissivity of the surface increases, though the convection heat transfer coefficient decreases, the net rate of heat transfer increases. This leads to a reduction in the average temperature of the plate. From this we can conclude that the role of the emissivity is to equilibrate the system. Another important observation from the numerical simulation is that there is not much of an effect for emissivity other than reducing the average temperature of the plate, for higher values of thermal conductivity as seen in Fig. 10. This points to the fact that the isothermal condition is the limiting condition that can be attained by a system for a given value of heat input. So if the system is having a thermal conductivity such that Ostrach solution is satisfied even when the emissivity is zero, the increase in emissivity will just decrease the average temperature of the plate and it will not make much deviation to the solution obtained without radiation.

Figure 11 represents the results obtained from the experiments for bakelite for two different surface conditions and for titanium plate for three different surface conditions. There exists a very good agreement between the results obtained from the experiments and the numerical simulations.

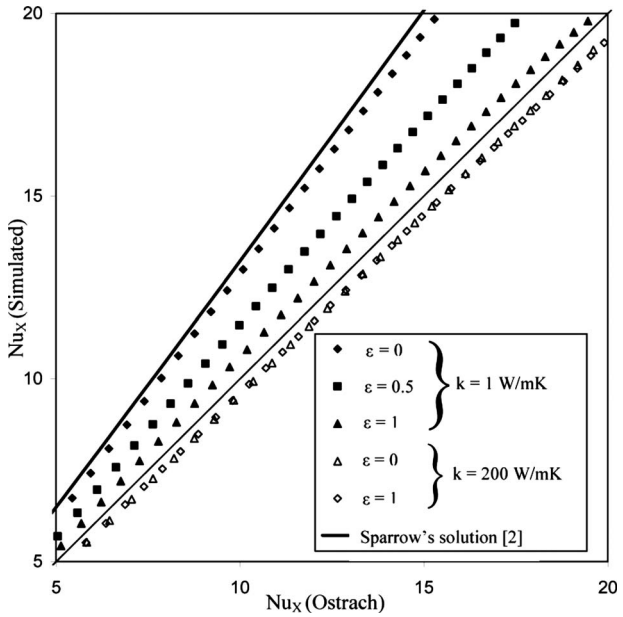

Fig. 10 Effect of surface emissivity for k=1 and 200 W/m K (numerical)

4.3 Scale Analysis. It is possible to qualitatively explain the asymptotic limits of isothermal and isoflux situations by applying scaling arguments to the governing equation. For easy explanation consider the case with no radiation i.e., $\varepsilon = 0$.

Case 1. When the thermal conductivity is very high such that the Biot number criteria ($\mathrm{Bi} < 0.1$) is satisfied, all the terms on the left hand side of Eq. (6) becomes very small compared with the first term. So the equation reduces to

$$k_s t \to \infty, \quad \frac{d^2T}{dx^2} \approx 0 \tag{8}$$

This implies that there exists no temperature gradient along the axial direction.

Case 2. Similarly, when the thermal conductivity of the plate is very small within the limit of the Biot number criteria, the conductive term on the left hand side becomes very small and there exists a balance between the convective term and the heat generation term. This implies that as the thermal conductivity decreases, the asymptotic limit of constant heat flux condition is reached.

$$k_s t \to 0, \quad k_s t \frac{d^2T}{dx^2} \to 0, \quad h(T_\infty - T_w) + Q_{\mathrm{gen}} t \approx 0 \tag{9}$$

Case 3. If now the effect of radiation is considered for case 2, i.e., $\varepsilon \neq 0$, the equation can be written as

$$k_s t \to 0, \quad k_s t \frac{d^2T}{dx^2} \to 0, \quad h(T_\infty - T_w) + \varepsilon\sigma(T_\infty^4 - T_w^4) + Q_{\text{gen}} t \approx 0 \tag{10}$$

Radiation suppresses convection. The underlying physics can be explicitly understood by linearizing the radiation term (linearization is a good approximation for the range of temperatures involved in the present study).

$$(T_w - T_\infty) = \frac{Q_{\text{gen}} t}{(\overline{h} + \overline{h_R})} \tag{11}$$

For a given heat generation rate, as the emissivity increases, the average convective heat transfer coefficient $\overline{h}$ decreases slightly, but the average radiative heat transfer coefficient $\overline{h_R}$ increases, such that the denominator of Eq. (11) increases much more and hence the average wall temperature decreases. Moreover, the temperature gradient within the plate also decreases. This means that for large values of emissivity, the radiation term plays a significant role in heat balance and hence it drives the system toward constant temperature case.

5 Conclusion

The present study has considered the role played by plate conductivity and surface emissivity in the interaction between radiation and natural convection from a heated vertical plate. In general, radiation decreases the average temperature of the plate irrespective of its thermal conductivity. For materials having low thermal conductivity, the radiation tends to drive the system away from isoflux case toward isothermal case. For a given surface emissivity, lowering the thermal conductivity drives the plate toward constant flux case. Effect of surface radiation has a basic role in determining the nature of the boundary condition that is achieved, for a heated vertical plate losing heat by natural convection. A novel method which involves a judicious combination of experiments and numerical simulations has also been proposed in this study to estimate the values of thermal conductivity and emissivity.

Nomenclature

- Bi = Biot number, $\text{Bi} = h_{\text{tot}} t / k_s$
- C = Gladstone–Dale constant, m^3/kg. For air, $C = 0.1506 \times 10^{-3}$ m^3/kg.
- d = distance of the biconvex lens from the Wollaston prism in the differential interferometer, m
- Gr_x = local Grashof number, $\text{Gr}_x = g\beta(T_w(x) - T_\infty)x^3/\nu^2$
- h = local convective heat transfer coefficient, $\text{W}/\text{m}^2\,\text{K}$
- $\overline{h}$ = average convective heat transfer coefficient, $\text{W}/\text{m}^2\,\text{K}$
- $\overline{h_R}$ = average radiative heat transfer coefficient, $\text{W}/\text{m}^2\,\text{K}$
- k = thermal conductivity, W/m K
- L = length of the test plate, m
- m = fringe shift factor, defined in the text
- Nu_x = local Nusselt number, $\text{Nu}_x = hx/k_f$
- n = refractive index
- P = atmospheric pressure, Pa
- Q_{gen} = volumetric heat generation rate, W/m^3
- q'' = heat flux, W/m^2
- R = gas constant, J/kg K. For air $R = 287$ J/kg K
- T = temperature, K
- t = thickness of the plate, m
- x = distance in the axial direction, m
- y = distance in the lateral direction, m

Greek Symbols

- δ = angle of the Wollaston prism, deg
- ε = total hemispherical emissivity
- λ = wavelength, m
- σ = Stefan–Boltzmann constant, 5.67×10^{-8} $\text{W}/\text{m}^2\,\text{K}^4$

Subscripts

- avg = average
- exp = experiment
- fw = fluid at wall condition
- i = index of thermocouple
- s = solid
- tot = total, i.e., (convection+radiation)
- w = wall
- ∞ = ambient

Appendix: Uncertainty Analysis

It has been found that the maximum error occurring in ΔX and ΔY, i.e., $\sigma_{\Delta X}$ and $\sigma_{\Delta Y}$ is ± 2 pixels. Consider a case where $\Delta X = 50$ pixels and $\Delta Y = 37$ pixels. The fringe shift factor, $m = 1.351$. The uncertainty in m, σ_m can be obtained as

$$\frac{\Delta m}{m} = \left\{ \left(\frac{\sigma_{\Delta X}}{\Delta X} \right)^2 + \left(\frac{\sigma_{\Delta Y}}{\Delta Y} \right)^2 \right\}^{0.5} \tag{A1}$$

On substituting the values on Eq. (A1), σ_m is obtained as ± 0.091.

The differential interferometer, being an optical instrument, is generally fabricated with high precision and is assumed to be error free. It is assumed that the error in the heat transfer coefficient is *only* due to the uncertainties in the temperature measurement and fringe shift factor. The uncertainty in wall temperature, σ_{T_w} and ambient temperature, σ_{T_∞} is taken as ± 0.1 K. Data of a typical experiment on aluminum for a particular heat input is considered here: $T_w = 344$ K, $T_\infty = 301.5$ K, $k_w = 2.5 \times 10^{-2}$ W/m K, $R = 287$ J/kg K, $\lambda = 584$ nm, $C = 1.506 \times 10^{-4}$ m^3/kg, $P = 101325$ Pa, $L = 0.25$ m, $d = 1.25$ m, and $\delta = 1$ deg.

The uncertainty in the heat transfer coefficient can be written as

$$\sigma_h = \left\{ \left(\frac{\partial h}{\partial T_w} \sigma_{T_w} \right)^2 + \left(\frac{\partial h}{\partial T_\infty} \sigma_{T_\infty} \right)^2 + \left(\frac{\partial h}{\partial m} \sigma_m \right)^2 \right\}^{0.5} \tag{A2}$$

Substituting the numerical values in Eq. (5), the local convective heat transfer coefficient is obtained as 3.47 $\text{W}/\text{m}^2\,\text{K}$ and from Eq. (A2), the uncertainty in the determination of local convective heat transfer coefficient is, $\sigma_h = 0.145$ $\text{W}/\text{m}^2\,\text{K}$, which is less than 5%.

References

[1] Ostrach, S., 1952, "An Analysis of Laminar Free-Convection Flow and Heat Transfer About a Flat Plate Parallel to the Direction of the Generating Body Force," NACA Technical Report No. NACA-TN-2635.

[2] Sparrow, E., and Gregg, J., 1956, "Laminar Free Convection From a Vertical Plate With Uniform Surface Heat Flux," ASME J. Heat Transfer, **78**(43), pp. 5–440.

[3] Kelleher, M., and Yang, K., 1967, "A Steady Conjugate Heat Transfer Problem With Conduction and Free Convection," Appl. Sci. Res., **17**(4), pp. 249–269.

[4] Zinnes, A., 1970, "The Coupling of Conduction With Laminar Natural Convection From a Vertical Flat Plate With Arbitrary Surface Heating," ASME J. Heat Transfer, **92**, pp. 528–535.

[5] Miyamoto, M., Sumikawa, J., Akiyoshi, T., and Nakamura, T., 1980, "Effects of Axial Heat Conduction in a Vertical Flat Plate on Free Convection Heat Transfer," Int. J. Heat Mass Transfer, **23**, pp. 1545–1553.

[6] Pozzi, A., and Lupo, M., 1988, "The Coupling of Conducting With Laminar Natural Convection Along a Flat Plate," Int. J. Heat Mass Transfer, **31**(9), pp. 1807–1814.

[7] Lee, S., and Yovanovich, M., 1992, "Linearization of Natural Convection From a Vertical Plate With Arbitrary Heat-Flux Distributions," ASME J. Heat Transfer, **114**, pp. 909–916.

[8] Vynnycky, M., and Kimura, S., 1996, "Conjugate Free Convection Due to a Heated Vertical Plate," Int. J. Heat Mass Transfer, **39**(5), pp. 1067–1080.

[9] Kimura, S., Okajima, A., and Kiwata, T., 1998, "Conjugate Natural Convection From a Vertical Heated Slab," Int. J. Heat Mass Transfer, **41**(21), pp.

3203–3212.
[10] Mendez, F., and Trevino, C., 2000, "The Conjugate Conduction-Natural Convection Heat Transfer Along a Thin Vertical Plate With Non-Uniform Internal Heat Generation," Int. J. Heat Mass Transfer, **43**(15), pp. 2739–2748.
[11] Yadav, V., and Kant, K., 2008, "Experimental Validation of Analytical Solutions for Vertical Flat Plate of Finite Thickness Under Natural-Convection Cooling," ASME J. Heat Transfer, **130**(3), p. 032503.
[12] Webb, B., 1990, "Interaction of Radiation and Free Convection on a Heated Vertical Plate-Experiment and Analysis," J. Thermophys. Heat Transfer, **4**, pp. 117–121.
[13] Venkateshan, S. P., and Balaji, C., 2006, "Experimental and Numerical Studies on Interaction of Radiation With Other Modes of Heat Transfer," International Heat Transfer Conference, IHTC 13, KN-06, Sydney, Australia.
[14] Ramesh, N., and Venkateshan, S. P., 2001, "Experimental Study of Natural Convection in a Square Enclosure Using Differential Interferometer," Int. J. Heat Mass Transfer, **44**(6), pp. 1107–1117.
[15] Rammohan Rao, V., Sobhan, C. B., and Venkateshan, S. P., 1990, "Differential Interferometry in Heat Transfer," Sadhana: Proc., Indian Acad. Sci., **15**(2), pp. 105–128.
[16] Sudhakar, T. V. V., Balaji, C., and Venkateshan, S. P., 2008, "Optimal Configuration of Discrete Heat Sources in a Vertical Duct Under Conjugate Mixed Convection Using Artificial Neural Networks," Int. J. Therm. Sci., **48**, pp. 881–890.
[17] Krishna Sabareesh, R., Prasanna, S., and Venkateshan, S. P., 2009, "Estimation of Thermal Conductivity and Emissivity Using Conjugate Heat Transfer Experiments," Seventh World Conference on Experimental Heat Transfer, Fluid Mechanics and Thermodynamics, HMT-6, Krakow, Poland, pp. 1215–1222.
[18] Krishnan, A., Balaji, C., and Venkateshan, S. P., 2003, "A Synergistic Approach to Parameter Estimation in Multimode Heat Transfer," Int. Commun. Heat Mass Transfer, **30**(4), pp. 515–524.
[19] Venugopal, G., Deiveegan, M., Balaji, C., and Venkateshan, S. P., 2008, "Simultaneous Retrieval of Total Hemispherical Emissivity and Specific Heat From Transient Multimode Heat Transfer Experiments," ASME J. Heat Transfer, **130**, p. 061601.
[20] Rammohan Rao, V., 1992, "Interferometric Study of Interaction Between Radiation and Free Convection in Fins and Fin Arrays," Ph.D. thesis, Department of Mechanical Engineering, IIT Madras, Chennai, India.

Zuo Lei

Sukang Zhu

Institute of Physics of Fibrous Soft Matters,
Donghua University,
Shanghai 200051, China

Ning Pan

Institute of Physics of Fibrous Soft Matters,
Donghua University,
Shanghai 200051, China;
Department of Biological and Agricultural Engineering,
University of California,
Davis, CA 95616

Transient Methods of Thermal Properties Measurement on Fibrous Materials

Fibrous material is a complex porous medium and steady test methods are the main test approaches we currently depend on to study the heat transfer properties. The application of unsteady test methods on fibrous material is still not mature. In this paper, some systematic studies are taken to investigate this problem. By analyzing the main factors impacting the test results, it is found that the local heat convection potentially excited by imposing test temperature can be avoided by limiting the internal temperature gradient and the so-called dual-phase lagging effects are negligible so that the feasibility of the unsteady test method is verified via both theoretical analysis and experimental data. [DOI: 10.1115/1.4000049]

1 Introduction

Fibrous material has excellent thermal insulation property in addition to its flexibility, low density, and formability [1]. As a result, their applications are no longer limited in apparel, but also increasingly in various engineering heat insulation areas.

The basic constituents of a fibrous material include fiber and often-moistured air forming an intricate multiphase and multiscale system. The fiber were arranged in the space by certain porous forms yielding numerous interconnected voids that are filled by the air. Once the heat flow passing through the material, a complex thermal transfer process will take place in the material. From the microview, the heat flow is delivered alternately between the air and the fiber. The microheat flows seem to be random and even chaotic. But at macrosystem level, the heat flow transferring from one side to the other side is both regular and continuous, which are the so-called effective behaviors [2–8].

Therefore, for practical engineering applications, the complex microthermal processes are often not the major interest when we describe the material heat transfer performance. Instead, we focus chiefly on the effective thermal behavior with the macroview.

Over the years, lots of researches have been reported investigations on heat transport in porous fibrous materials. As in many other cases, such investigations largely follow two tracks either theoretical prediction or experimental examination or both, which generated a rich body of knowledge in the effective thermal behaviors of fibrous material [2,3,6,7,9–17]. Needless to say, much remains to be done.

In terms of instrumental measurement, the effective thermal conductivity of fibrous sheets (fabrics) is tested by the guarded hot plate method as recommended by the ASME Standard [18,19]. However the guarded hot plate is based on the principle of thermal equilibrium and it works best when the tested specimen can reach the steady-state quickly. For porous materials such as fabrics, where the multiphase renders the heat equalizing process slow and unstable, the conventional steady-state techniques become ineffective and even inaccurate. Since 1987, Martin and Lamb [20], Schneider and Hoschke [21], and Jirsak et al. [22] successively explored the application of unsteady transient methods to fibrous materials.

However, researchers held controversial opinions on whether fibrous material can be tested through the unsteady method. Jirsak et al. [22] pointed out in his paper that the test result of effective thermal conductivity (by using unsteady method) was unreliable due to the heat convection inside the material invoked by the temperature gradient applied during testing. All such transient methods are based on thermal conduction theories and, hence, unable to deal with the coupling of conduction and convection [23–25] and lead to non-negligible testing errors. Another recent issue has to do with the so-called dual-phase lagging (DPL) effects in porous materials [26,27], i.e., temperature change and heat wave flow both take time yet the classic Fourier's law implies an instantaneous local thermal equilibrium (zero transfer time). Based on a new testing scheme we developed recently [28], the aim of this paper is to examine the influences of such issues so as to establish the unsteady methods as a viable and preferred testing approach to fibrous materials.

2 The Hypothesis of Local Thermal Equilibrium

Fibrous material is a two-phase system with solid and gas composition. If the assumption of *local thermal equilibrium* is valid, then we can use the one-equation model in Eq. (1) to express the heat transfer process [26,27]

$$\langle \rho \rangle c \frac{\partial \langle T \rangle}{\partial t} = \nabla \cdot [k_{\text{eff}} \cdot \nabla \langle T \rangle] \tag{1}$$

where k_{eff} is the equivalent (or effective) thermal conductivity. This one-equation model is necessary for analyzing the thermal properties testing. The factors affecting the hypothesis of local thermal equilibrium include the difference in physical properties of the two phases, the volume fraction of each phase, the heat transfer coefficient, and the heat exchange area between the two phases. According to the research of Minkowycz et al. [29], the local thermal equilibrium, if the *Sp* number $\text{Nu}_{r_h}(k_f/k_{\text{eff}})(L/r_h)^2$ is great than 100, the condition of the local thermal equilibrium is satisfied for all practical applications where h, L, and r_h are the interstitial heat transfer coefficient, porous layer thickness, and the hydraulic radius, respectively. The Nusselt number Nu_{r_h} is nearly constant: $\sim$10 for conduction case and $\sim$0.9 for incompressible laminar flow in the pores. For most fibrous materials, the ratio of $k_{\text{air}}/k_{\text{eff}}$ is usually greater than 1/4, so if the test is designed in such that $L/r_h > 20$ the local thermal equilibrium will be valid in fibrous material.

3 Selection of Transient Method

Among the unsteady thermal tests, transient method is the most preferred in which a thermal perturbation is imposed at a given location of the measured material; the thermal response to this

Contributed by the Heat Transfer Division of ASME for publication in the JOURNAL OF HEAT TRANSFER. Manuscript received February 13, 2009; final manuscript received July 28, 2009; published online December 23, 2009. Editor: Yogesh Jaluria.

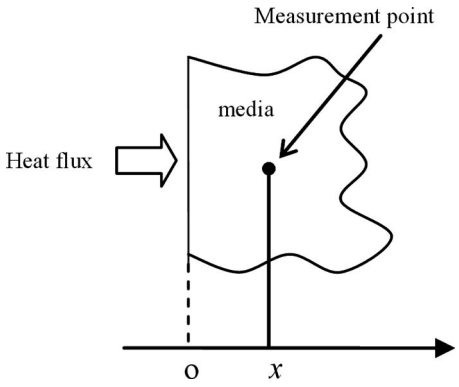

Fig. 1 Measuring principle of stepwise transient method

disturbance is recorded in another designated location. The corresponding thermal properties parameters can thus be calculated using the established theoretical law. According to the form of the heat source, it can be subdivided into a variety of testing methods so we must choose a testing method suitable to fibrous materials.

In terms of the heat source type, linear and surface heat source shapes are usually the available options in transient method. The linear option offers a very large aspect ratio in order to reduce the influence of heat loss at both ends. The thin slender shape however often causes the heat probe to bend just under its own weight. If we apply a tension to maintain a straight state, there may form a local stress concentration at the interface between the heat source and the material. Fibrous materials are very soft and easily deform under a small press themselves; the linear heat probe may not be a good choice and the testing probe in planner shape would at least alleviate such problems.

The heating mode of the heat source is also an important parameter. The pores inside the fibrous material are connected together. If the heating rate is too abrupt, it will cause a dramatic expansion of air in the material so as to generate forced local convection, which will alter the property of the material. Therefore, we selected the stepwise mode, a relatively smooth way, over other pulse profiles.

In summary, this study chose the stepwise transient heating mode with a metal foil probe to form the measurement apparatus for testing the fibrous materials. The stepwise transient method was examined in several studies [30,31] for its several advantages: In theory at least, the stepwise transient method can measure the thermal conductivity and thermal diffusivity of the materials simultaneously. It used a thin surface heat source, which can generate constant heat flow in testing. Furthermore, the stepwise transient method brings much less impact on the sample tested, compared to other unsteady methods [5,32–41].

4 Measurement Principle

The measuring principle for the stepwise transient method is shown in Fig. 1. Assuming the local thermal equilibrium, and a specimen with infinite size and uniform initial temperature T_0 when a constant heat flux starts at $x=0$ and $t>0$, the temperature distribution inside any point in the sample will depend only on the distance x between the measurement point and the heat source and the time t, and can thus be treated as a one-dimensional problem. Equation (1) will reduce into the classic Fourier's law with the solution for the prescribed boundary and initial conditions as

$$T(x,t) = T_0 + \frac{q}{k}\left\{\left(\frac{at}{\pi}\right)^{1/2}\exp\left(-\frac{x^2}{4at}\right) - \frac{x}{2}erfc\left(\frac{x}{\sqrt{4at}}\right)\right\} \quad (2)$$

$$k\left.\frac{\partial T}{\partial x}\right|_{x=0} = \begin{cases} q & t>0 \\ 0 & t\le 0 \end{cases} \quad (3)$$

where $T(x,t)$ is the temperature at position x and time t, q is the flux of heat source, k is the thermal conductivity, and a is the thermal diffusivity.

The temperature profile $T(x,t)$ in Eq. (2) is a time-domain function, which can be measured by the thermometer and recorded by a computer. The thermal conductivity k and the thermal diffusivity a of the sample can be found by superimposing Eq. (2) on the recorded temperature-time curve using appropriate fitting techniques.

5 The Test Apparatus

The schematic diagram shown in Fig. 2 is the test apparatus we recently developed [28]. The main framework of the testing apparatus consists of two plates with guard-bars. These guard-bars are fixed on *plate B* and *plate A* can be moved up and down along with the guard-bars. Multiple specimens are required in one test to form two stacks of the same thickness, which are placed between the plate A and plate B with the heat source located at the center as shown. The sheet heat source made of metal foil with 17.3 Ω electric resistance. The size of the heat source is 90×90 mm^2 and thickness less than 0.1 mm. Owing to the tiny thickness of the heat source, its volume heat capacity can be ignored so that the output power of the heat source can be considered as equal to the input electric power. Given the symmetry of the system, the thermal flow generated from the heat source will be uniformly distributed to the up and down sample stacks provided that, first, the buoyant influence is small and only takes place after a certain time.

The sample temperature response is measured and recorded by a computer data acquisition modules through the temperature sensor placed inside the sample in the figure. In our testing, the sampling frequency is four times per second.

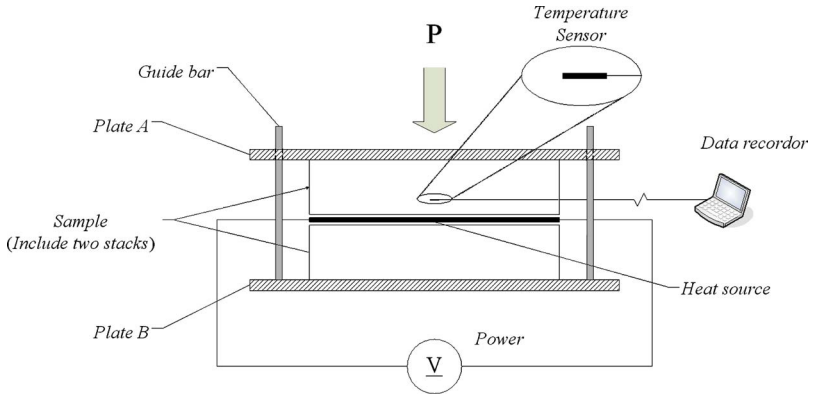

Fig. 2 The schematic diagram of test apparatus

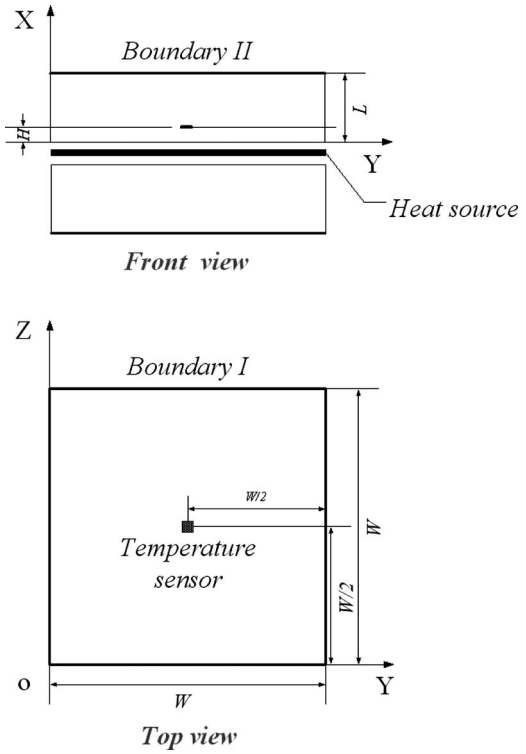

Fig. 3 The actual sample in the experiment

The test specimens are all in sheet form and are stacked up to make up the required total thickness up to 3.5 cm to fill the space. Furthermore, additional air residing in between the fabric layers poses collectively as a potential error source. Still, due to the porous and flexible nature of the fabrics, the density and thus the thermophysical properties of the fibrous material are closely related to the external pressure [23]. As a result, an appropriately defined pressure has to be applied on the sample stacks to stabilize/standardize the thickness of the sample piles. A constant pressure P of 792 Pa is exerted onto the samples uniformly through plate A for all tests in this study.

6 Estimating the Measurement Time

The sample size in establishing Eq. (2) of heat conduction is assumed to be infinite and, obviously, this assumption cannot be realized in an actual experiment. Comparing with the theory, the actual sample with limited size has additional boundaries (*boundary I* and *boundary II*), as illustrated in Fig. 3. For easier treatment without losing generality, we assume the *YZ* plane as the actual square sample of equal sides W with sensor located at the center and the *XZ* plane represents the thickness L with sensor at distance H from the heat source. Because of the planer symmetry, all the edges in the *YZ* plane will be of the boundary I type and in the thickness direction, the boundary II type.

Because of its limited size, the temperature distribution in an actual sample cannot be described by Eq. (2). However, it is easily conceivable that upon heating, it will take some time t_m before the heat can reach the boundaries for the influence caused by limited sample size to realize. That is to say, if we take the measurement within the period $t < t_m$, the difference Δ_f between the actual experiment and theory will be small enough to be negligible and then Eq. (2) becomes valid to use in estimating the sample thermal properties k and a.

In general, the difference Δ_f is a function related to sample type, size, testing time, etc., as expressed in Eq. (4).

$$\Delta_f = (T_E - T_T)/(T_T - T_0) = f(L, W, H, k, a, q, \beta_I, \beta_{II}, t) \quad (4)$$

where T_E is the temperature in the actual sample and T_T is the corresponding temperature in infinite medium defined in Eq. (2), at given (x,t), β_I and β_{II} are the heat transfer coefficients at boundary I and boundary II, respectively. When $|\Delta_f|$ is small enough than a critical value Δ_{fa}, T_E will be close enough to T_T such that we can use Eq. (2) in the test. Therefore $|\Delta_{fm}| < \Delta_{fa}$ is a logical criterion to be used for the t_m determination, where $|\Delta_{fm}|$ is the maximum value of $|\Delta_f|$ at time $t = t_m$ and Δ_{fa} is the allowable testing error.

In calculation of Δ_{fm}, T_T and T_E must be obtained first. T_T can be calculated from Eq. (2) and T_E can be estimated here by numerical approaches as the following. For heat transfer in a finite sample in 3D mode, the temperature field will be governed by Eq. (5), which can be solved under certain boundary conditions using either the finite difference method (FDM) or the finite element method (FEM) to obtain T_E. Once the temperature field is solved and Δ_{fm} value can be calculated from Eq. (4) at $t = t_m$

$$\frac{\partial T}{\partial t} = \frac{\partial^2 T}{\partial x^2} + \frac{\partial^2 T}{\partial y^2} + \frac{\partial^2 T}{\partial z^2} \quad (5)$$

Boundary I leads to the heat transfer between sample and air and according to the natural convection conditions, we can take the convective heat transfer coefficient as 10 $\mathrm{W\,m^{-2}\,C^{-1}}$ [42]. Boundary II reflects the heat transfer between the sample and the plates as the plate is made of metal, which has much greater thermal conductivity and heat capacity than the polymeric samples tested, so it can be considered that there is no temperature gradient at the interface between the sample and the plate, i.e., sample has little disturbance on the temperature field of the plate.

However the distance between the sensor and heat source has to be carefully chosen, for the farther away the sensor from heat source, the greater impact is caused by boundary II on temperature measured. In this article the distance between sensors and heat source will not be more than 5 mm. So in the calculations we assume that the distance between the sensor and the heat source $H = 5$ nm in order to ensure that the calculation result can be valid on all tests. The thickness for each stack of the samples is $L = 35$ nm.

The value of T_E in 3D heat transfer mode can be calculated by using ANSYS finite element software and the impact of material thermal properties on system Δ_{fm} is analyzed and shown in Fig. 4. From the results, the smaller the thermal conductivity and/or the greater the thermal diffusion coefficient, the greater the deviation of $|\Delta_{fm}|$. According to the range of fiber thermophysical parameters, we use $k = 0.025$ $\mathrm{W/m\,^\circ C}$ and $a = 5 \times 10^{-7}$ $\mathrm{m^2\,s^{-1}}$ in the calculation of t_m in order to suit most fibrous samples tested.

Next we are to determine the maximum testing time t_m, which will allow $|\Delta_{fm}| < \Delta_{fa}$. As shown in Fig. 5, we calculated $|\Delta_f|$ versus time according to the chosen k and a. The flux of the heat source used in the calculation is $q = 20.0$ $\mathrm{wm^{-2}}$. From Fig. 5, we know as expected that $|\Delta_f|$ increases monotonically with the measurement time. If we take $\Delta_{fa} = 0.05\%$, then t_m will be about 202 s.

The next question is whether the magnitude of q has any impact on t_m, so we again conducted the abovementioned numerical analysis by using different q values. Based on the result in Fig. 5, we used the value of $|\Delta_f|$ at time point 202 s in Fig. 6 and see that the impact of q on $|\Delta_f|$ is very limited that it can be ignored. From $q = 20$ $\mathrm{W\,m^{-2}}$ to 20 $\mathrm{W\,m^{-2}}$, all the calculated results of $|\Delta_f|$ are less than the given threshold Δ_{fa}. We thus come to the conclusion that t_m can be treated as independent of the power of the heat source in our test conditions. In order to simplify the test, we used $t_m = 200$ s for all the samples in the study.

7 The Accuracy of Test Apparatus

In order to check the reliability of the test apparatus, we chose perspex as a standard sample for the validation. The size of per-

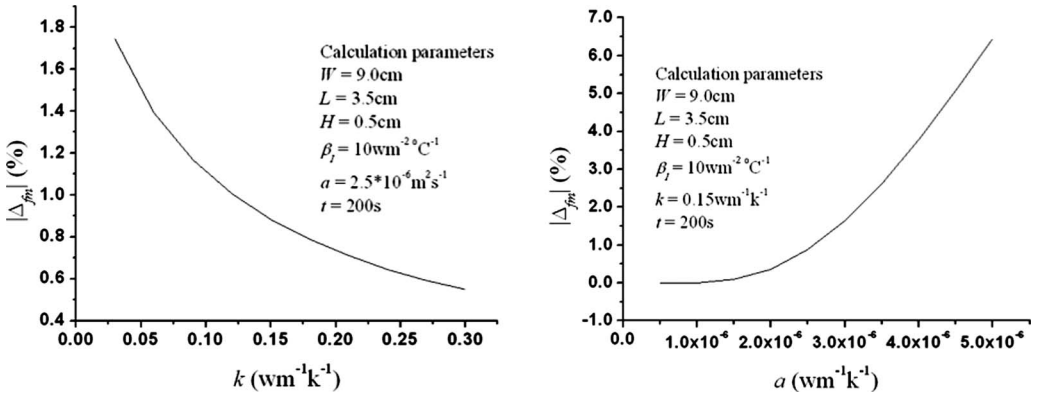

Fig. 4 The impact of material thermophysical properties on Δ_{fm}

spex is $90\times90\times35$ mm^3 and the distance H is 4.53 mm. Through the fitting method mentioned in Ref. [30], we obtained the thermal property parameters of the perspex samples as shown in Table 1.

Both thermal properties for the perspex samples from our tests agree well with the reference values from literature and the errors range from 2% to 3.94%. The reliability of our test device for solid sheets materials are thus confirmed.

8 Apply Stepwise Transient Method on Fiber Materials

The additional difficulty in measuring the thermal properties of fibrous materials or any porous media with interconnected pores, lies in the fact that a fibrous material is a mixed multiphase system of fiber and air residing in the pores. Once the temperature gradient gets large enough in the testing process, the air inside the fibrous material will begin to move around and the convective heat transfer takes place, which completely changes the nature of the heat transfer and renders Eq. (2) for thermal conductivity only no longer valid [25]. In other words, two issues have to be dealt with in testing a fibrous material—the boundary influence and convective heat loss.

In this paper, three kinds of fibrous material (nonwoven, twill, and knit velvet) are used in the testing. All samples are balanced for 24 h under standard environment with temperature of 20°C and relative humidity of 65%.

For the thickness of the fabrics is very small, in order to achieve the required thickness for testing, fabric samples must be stacked together to 35 mm on both sides of the heat source and the temperature sensor is placed inside the upper stack as discussed before. The samples and test parameters are shown in Table 2.

To further examine the potential convective heat transfer, we tested the samples under two different temperature gradients. If there is no convection, then the parameters k and a, as derived by fitting Eq. (2), should remain constant with time. We used two different flux values of heat source in the testing of the nonwoven fabric samples as shown in Fig. 7. Since the sample resistant is given, different heat flux will generate different temperature gradients, in this case by nine times. When the heat density q $=20.6$ W m^{-2}, both effective thermal conductivity and thermal diffusivity, largely remain the same with some random fluctuation around the mean value in different fitting time sections $\bar{t}$. Note that each fitting time is $t<t_m$ so as to eliminate the boundary influ-

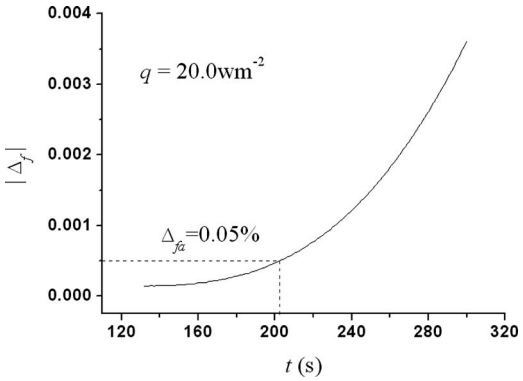

Fig. 5 The influence of t on $|\Delta_f|$

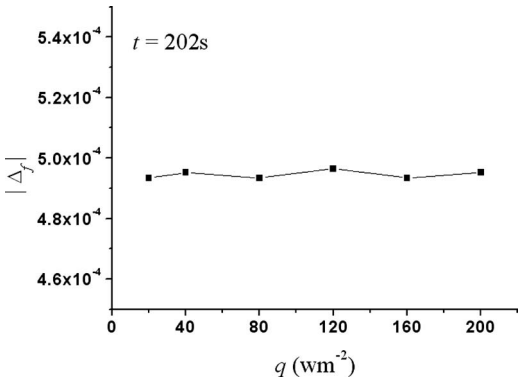

Fig. 6 The influence of q on $|\Delta_f|$

Table 1 Results comparison of thermal property parameters for perspex

	k (W m^{-1} K^{-1})	c_v (J g^{-1} K^{-1})	a (m^2 s^{-1})
Measured value	0.195	1.37	1.22×10^{-7}
Reference value[1]	0.191	1.35	1.22×10^{-7}
Relative error (%)[2]	2.09	1.71	3.94

(1) Reference value is under 20°C from Ref. [43].
(2) Relative error=|measured value−reference value|/reference value (%). The atmosphere temperature is 18°C.

Table 2 The samples and test parameters

Sample	Fabric weight (g/m^2)	H[1] (mm)
Nonwoven	4.852	3.38
Twill	143.1	3.08
Knit velvet	203.5	3.30

(1) H is the distance in Fig. 3, averaged over several measurements.

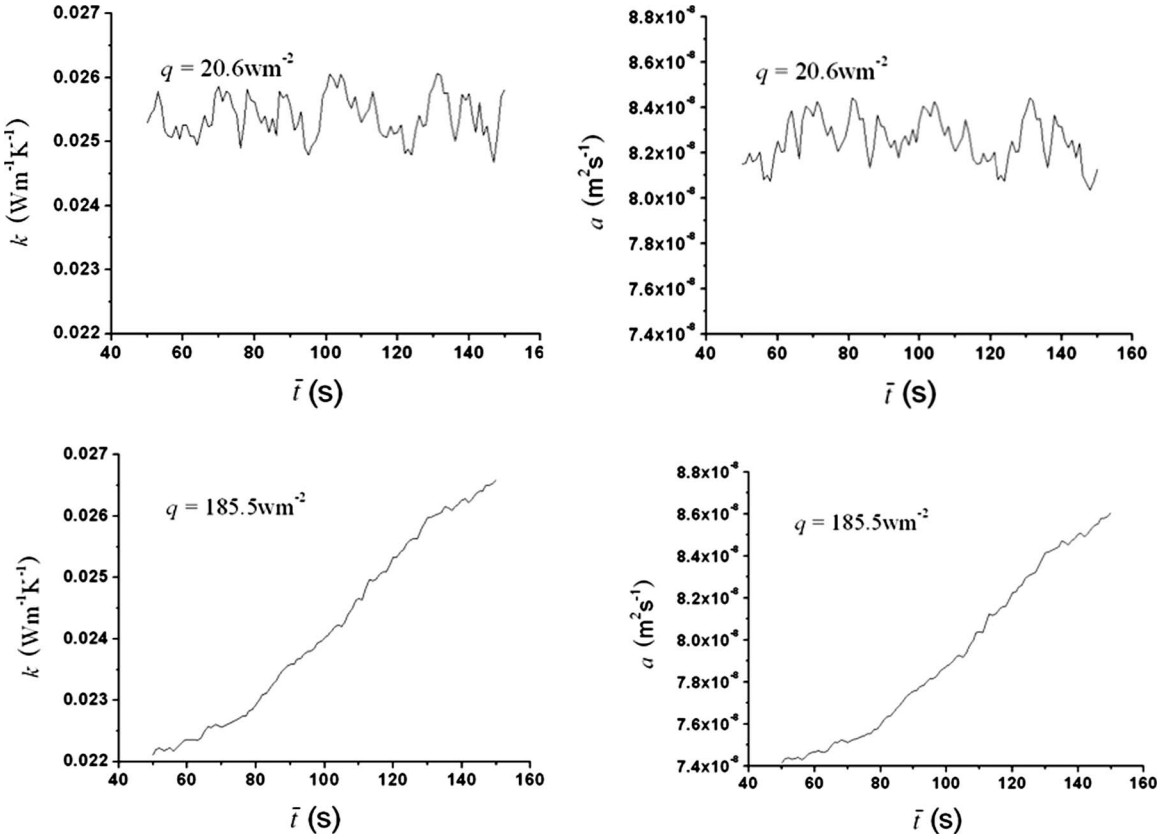

Fig. 7 The testing results for nonwoven fabric under different heat source power

ence. However, these properties now increase monotonously and exceed those at low heat load under a much higher heat load $q = 185.5\ \text{wm}^{-2}$ showing an increase in heat loss due ostensibly to convection. It is interesting that the initial values of the properties in this case would be smaller than those at low heat flux: This may reveal that when the sample is still at room temperature, which is too high a heat impact that actually impedes the heat transfer until the sample temperature rises to a certain level.

In conclusion, to avoid both the sample boundary and heat convection influence, the testing conditions for fibrous materials include appropriately low heat flux $q = 20.6\ \text{W m}^{-2}$ and within a time limit $t < t_m$.

The test results of all three fibrous samples are given in Fig. 8 and each data point is a result of five repeats. From the results we can see the nonwoven fabric has the smallest effective thermal conductivity k and thermal diffusivity a among the three fabrics. Whereas the twill fabric exhibits higher effective thermal conductivity k yet lower thermal diffusion coefficient a than the knit velvet. Parameter k describes the medium's thermal conduction performance under the steady-state condition but $a = k/c_v$ describes the temperature diffusion ratio under the unsteady-state condition, so these two parameters have different application fields. In our test, both k and a are simultaneously measured, which can completely describe the fabric sample thermal performance in all cases.

Different fabric samples have different dispersion of test results. In effective thermal conductivity aspect, the coefficient of variation (CV) value for nonwoven fabric and knitting velvet are 12.0% and 6.9%, respectively, which are bigger than twill fabric (CV = 3.2%). However in the thermal diffusion coefficient aspect, the CV value for nonwoven fabric and knitting velvet are larger than twill fabric with 9.8%, 9.5%, and 4.3%, respectively, which explains twill fabric has better uniform structure and stability than nonwoven fabric and knitting velvet.

9 Conclusion

In this paper, we have studied the application of unsteady thermal properties methods on fiber material. We first demonstrated that the local heat convection potentially excited by imposing test temperature can be avoided by controlling the heat density q and the DPL effects are normally negligible in practical measurements of fibrous materials. By both numerical analysis and experimental validation, we have demonstrated that our unsteady measurement approach, the stepwise transient heating mode with a metal foil probe, can be used to test the effective thermal conductivity and thermal diffusion coefficient of various fibrous materials.

Nomenclature

a = thermal diffusivity, $\text{m}^2\ \text{s}^{-1}$
β = heat transfer coefficient
c = heat capacity, $\text{J kg}^{-1}\ \text{C}^{-1}$
c_v = volume heat capacity, $\text{J m}^{-3}\ \text{C}^{-1}$
h = heat transfer coefficient, $\text{W m}^{-2}\ \text{C}^{-1}$
k = thermal conductivity, $\text{W m}^{-1}\ \text{C}^{-1}$
k_{air} = thermal conductivity of air, $\text{W m}^{-1}\ \text{C}^{-1}$
k_{eff} = equivalent (or effective) thermal conductivity, $\text{W m}^{-1}\ \text{C}^{-1}$
H = distance between the sensor and the heat source, m
L = thickness, m
Nu_{r_h} = Nusselt number
ρ = density, kg m^{-3}
q = heat flux, W m^{-2}
r_h = hydraulic radius, m
T = temperature, C
T_0 = initial temperature, C
T_E = temperature in the actual sample

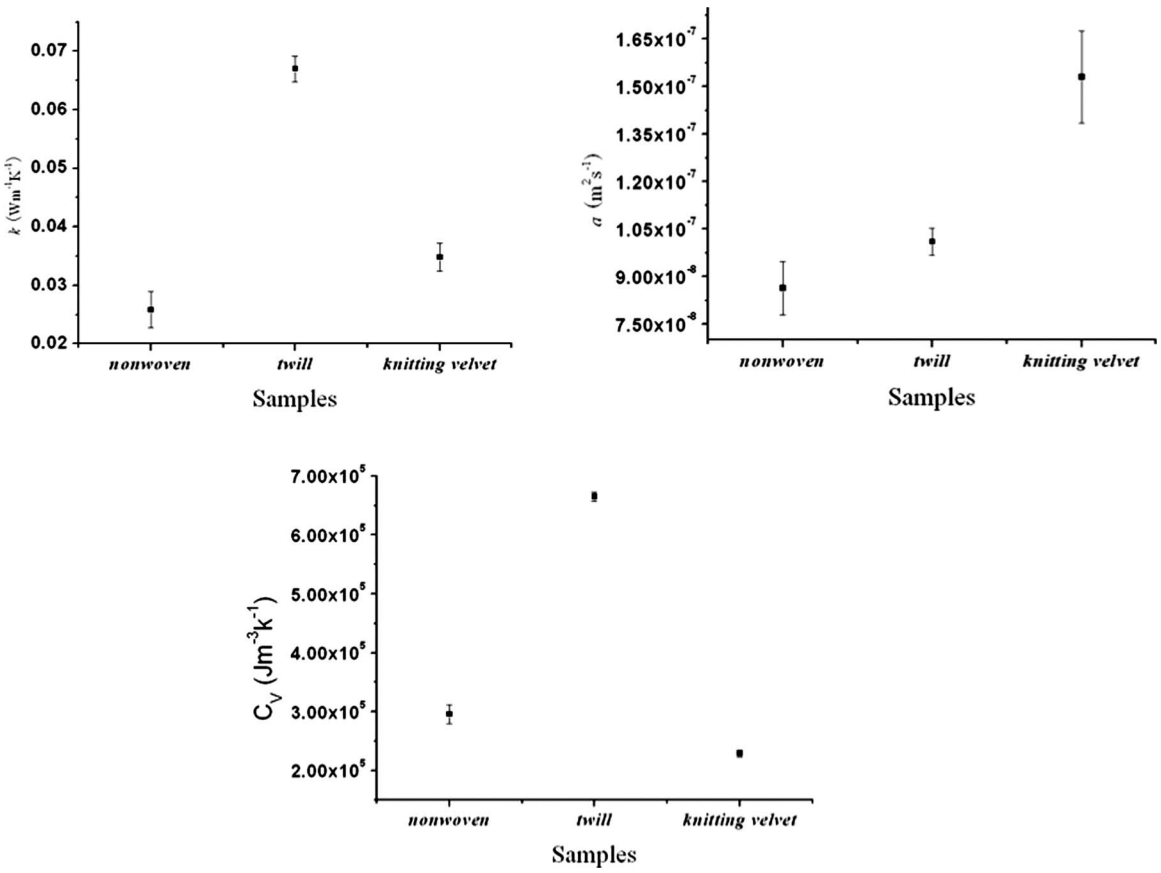

Fig. 8 The test result of fiber materials (the range is +/− standard deviation of the test result)

T_T = temperature in infinite medium
t = time, s
t_m = maximum test time, s
$\bar{t}$ = mean value in different fitting time sections
x = distance between the measurement point and the heat source, m
Δ_f = difference between the actual experiment and theory
Δ_{fa} = critical value of Δ_f
$|\Delta_{fm}|$ = maximum value of $|\Delta_f|$

References

[1] Pan, N., He, J., and Yu, J., 2007, "Fibrous Materials as Soft Matter," Text. Res. J., **77**(4), pp. 205–213.
[2] Layeghi, M., 2008, "Numerical Analysis of Wooden Porous Media Effects on Heat Transfer From a Staggered Tube Bundle," ASME J. Heat Transfer, **130**(1), p. 014501.
[3] Sakamoto, H., and Kulacki, F. A., 2008, "Effective Thermal Diffusivity of Porous Media in the Wall Vicinity," ASME J. Heat Transfer, **130**(2), p. 022601.
[4] Rencz, M., 2003, "New Possibilities in the Thermal Evaluation, Offered by Transient Testing," Microelectron. J., **34**(3), pp. 171–177.
[5] Li, C. H., Williams, W., Buongiorno, J., Hu, L.-W., and Peterson, G. P., 2008, "Transient and Steady-State Experimental Comparison Study of Effective Thermal Conductivity of Al_2O_3/Water Nanofluids," ASME J. Heat Transfer, **130**(4), p. 042407.
[6] Wang, M., and Pan, N., 2008, "Modeling and Prediction of the Effective Thermal Conductivity of Random Open-Cell Porous Foams," Int. J. Heat Mass Transfer, **51**(5–6), pp. 1325–1331.
[7] Wang, M., Wang, J., Pan, N., and Chen, S., 2007, "Mesoscopic Predictions of the Effective Thermal Conductivity for Microscale Random Porous Media," Phys. Rev. E, **75**(3), p. 036702.
[8] Wang, M., and Pan, N., 2008, "Predictions of Effective Physical Properties of Complex Multiphase Materials," Mater. Sci. Eng. R., **63**(1), pp. 1–30.
[9] Christon, M., Burns, P. J., and Sommerfeld, R. A., 1994, "Quasi-Steady Temperature Gradient Metamorphism in Idealized Dry Snow," Numer. Heat Transfer, Part A, **25**(3), pp. 259–278.
[10] Wang, J., Carson, J. K., North, M. F., and Cleland, D. J., 2006, "A New Approach to Modelling the Effective Thermal Conductivity of Heterogeneous Materials," Int. J. Heat Mass Transfer, **49**, pp. 3075–3083.
[11] Rocha, R. P. A., and Cruz, M. E., 2001, "Computation of the Effective Conductivity of Unidirectional Fibrous Composites With an Interfacial Thermal Resistance," Numer. Heat Transfer Part A, **39**(2), pp. 179–203.
[12] Fu, S., and Mai, Y., 2003, "Thermal Conductivity of Misaligned Short-Fiber-Reinforced Polymer Composites," J. Appl. Polym. Sci., **88**, pp. 1497–1505.
[13] Zou, M. Q., Yu, B., Zhang, D., and Ma, Y., 2003, "Study on Optimization of Transverse Thermal Conductivities of Unidirectional Composites," ASME J. Heat Transfer, **125**(6), pp. 980–987.
[14] Ning, Q. G., and Chou, T. W., 1995, "Closed-Form Solutions of the Inplane Effective Thermal-Conductivities of Woven-Fabric Composites," Compos. Sci. Technol., **55**(1), pp. 41–48.
[15] Dasgupta, A., Agarwal, R. K., and Bhandarkar, S. M., 1996, "Three-Dimensional Modeling of Woven-Fabric Composites for Effective Thermo-Mechanical and Thermal Properties," Compos. Sci. Technol., **56**(3), pp. 209–223.
[16] Woo, S. S., Shalev, I., and Barker, R. L., 1994, "Heat and Moisture Transfer Through Nonwoven Fabrics. I. Heat Transfer," Text. Res. J., **64**(3), pp. 149–162.
[17] Wang, M., He, J., Yu, J., and Pan, N., 2007, "Lattice Boltzmann Modeling of the Effective Thermal Conductivity for Fibrous Materials," Int. J. Therm. Sci., **46**, pp. 848–855.
[18] Huang, J., 2006, "Sweating Guarded Hot Plate Test Method," Polym. Test., **25**, pp. 709–716.
[19] Mathis, N., and Chandler, C., 2000, "Orientation and Position Dependant Thermal Conductivity," J. Cellular Plastics, **36**(4), pp. 327–336.
[20] Martin, J. R., and Lamb, G. E. R., 1987, "Measurement of Thermal Conductivity of Nonwovens Using a Dynamic Method," Text. Res. J., **57**(12), pp. 721–727.
[21] Schneider, A. M., and Hoschke, B. N., 1992, "Heat Transfer Through Moist Fabrics," Text. Res. J., **62**(2), pp. 61–66.
[22] Jirsak, O., Gok, T., Ozipek, B., and Pan, N., 1998, "Comparing Dynamic and Static Methods for Measuring Thermal Conductive Properties of Textiles," Text. Res. J., **68**(1), pp. 47–56.
[23] Jirsak, O., Sadikoglu, T. G., Ozipek, B., and Pan, N., 2000, "Thermo-Insulating Properties of Perpendicular-Laid Versus Cross-Laid Lofty Nonwoven Fabrics," Text. Res. J., **70**(2), pp. 121–128.
[24] Pakdee, W., and Rattanadecho, P., 2006, "Unsteady Effects on Natural Convective Heat Transfer Through Porous Media in Cavity Due to Top Surface

Partial Convection," Appl. Therm. Eng., **26**, pp. 2316–2326.
[25] Sun, G., Yoo, H. S., Zhang, X. S., and Pan, N., 2000, "Radiant Protective and Transport Properties of Fabrics Used by Wildland Firefighters," Text. Res. J., **70**(7), pp. 567–573.
[26] Tzou, D., 1995, "A Unified Field Approach for Heat Conduction From Macro- to Micro-Scales," ASME J. Heat Transfer, **117**(1), pp. 8–16.
[27] Wang, L., and Wei, X., 2008, "Equivalence Between Dual-Phase-Lagging and Two-Phase-System Heat Conduction Processes," Int. J. Heat Mass Transfer, **51**(7–8), pp. 1751–1756.
[28] Zuo, L., Zhu, S., and Pan, N., 2009, "Determination of Sample Size for Step-Wise Transient Thermal Tests," Polym. Test., **28**, pp. 307–314.
[29] Minkowycz, W., Haji-Sheikh, A., and Vafai, K., 1999, "On Departure From Local Thermal Equilibrium in Porous Media Due to a Rapidly Changing Heat Source: The Sparrow Number," Int. J. Heat Mass Transfer, **42**(18), pp. 3373–3385.
[30] Kubicár, L., and Bohác, V., 2000, "A Step-Wise Method for Measuring Thermophysical Parameters of Materials," Meas. Sci. Technol., **11**, pp. 252–258.
[31] Kubičár, L., Boháč, V., and Vretenár, V., 2002, "Transient Methods for the Measurement of Thermophysical Properties: The Pulse Transient Method," High Temp. - High Press., **34**(5), pp. 505–514.
[32] Milano, G., Scarpa, F., Righini, F., and Bussolino, G. C., 2001, "Ten Years of Parameter Estimation Applied to Dynamic Thermophysical Property Measurements," Int. J. Thermophys., **22**(4), pp. 1227–1240.
[33] Papa, J., Albano, C., Baré, W., Navarro, O., Galárraga, D., and Zannin, F., 2002, "An Unsteady State Method for the Measurement of Polymer Thermal Diffusivity I. Development of a Cell," Eur. Polym. J., **38**(10), pp. 2109–2117.
[34] Hammerschmidt, U., 2004, "Quasi-Steady State Method: Uncertainty Assessment," Int. J. Thermophys., **25**(4), pp. 1163–1185.
[35] Kalogiannakis, G., Hemelrijck, D. V., and Assche, G. V., 2004, "Measurements of Thermal Properties of Carbon/Epoxy and Glass/Epoxy Using Modulated Temperature Differential Scanning Calorimetry," J. Compos. Mater., **38**(2), pp. 163–175.
[36] Boháč, V., Dieška, P., and Kubičár, L., 2007, "The Heat Loss Effect at the Measurements by Transient Pulse Method," Measurement, **7**(3), pp. 24–27.
[37] Gutierrez, G., and Rodriguez, R., 2007, "Conductivity Measurement of Ferrofluid Using Transient Hot Wire Method," ASME International Mechanical Engineering Congress and Exposition, Seattle, WA.
[38] Bai, S.-Y., Tang, Z.-A., Huang, Z.-X., Yu, J., and Wang, J.-Q., 2008, "Thermal Conductivity Measurement of Submicron-Thick Aluminium Oxide Thin Films by a Transient Thermo-Reflectance Technique," Chin. Phys. Lett., **25**(2), pp. 593–596.
[39] Solorzano, E., Rodriguez-Perez, M. A., and de Saja, J. A., 2008, "Thermal Conductivity of Cellular Metals Measured by the Transient Plane Sour Method," Adv. Eng. Mater., **10**(4), pp. 371–377.
[40] Sabuga, W., and Hammerschmidt, U., 1995, "A New Method for the Evaluation of Thermal Conductivity and Thermal Diffusivity From Transient Hot Strip Measurements," Int. J. Thermophys., **16**(2), pp. 557–565.
[41] Bohac, V., Kubicar, L., and Vretenar, V., 2003, "Use of the Pulse Transient Method to Investigate the Thermal Properties of Two Porous Materials," High Temp. - High Press., **35–36**(1), pp. 67–74.
[42] Holman, J. P., 1997, *Heat Transfer*, McGraw-Hill, New York.
[43] Tye, R. P., Kubičár, L., and Lockmuller, N., 2005, "The Development of a Standard for Contact Transient Methods of Measurement of Thermophysical Properties," Int. J. Thermophys., **26**(6), pp. 1917–1938.

Natural Convection From a Porous Cavity With Sublayers of Nonuniform Thickness: A Lumped System Analysis

R. L. Marvel III
Research Assistant

F. C. Lai
Professor
Fellow ASME

School of Aerospace and Mechanical Engineering,
University of Oklahoma,
Norman, OK 73019

A numerical study has been performed to further investigate the flow and temperature fields in layered porous cavity. The geometry considered is a two-dimensional square cavity comprising of three or four vertical sublayers with nonuniform thickness and distinct permeability. The cavity is subjected to differential heating from the vertical walls. The results obtained are used to further evaluate the capacity of the lumped-system analysis in the prediction of heat transfer results of layered porous cavities. It has been found that predictions by the lumped-system model are reasonably good for the range of Rayleigh numbers encountered in engineering applications. In addition, the predictions improve when the number of sublayers increases as well as the sublayer thickness becomes more uniform. Thus, it proves that the lumped-system analysis can offer a quick estimate of heat transfer result from a layered porous cavity with reasonable accuracy.
[DOI: 10.1115/1.3213527]

Keywords: natural convection, heat transfer, porous media, numerical method

1 Introduction

Heat transfer in porous media has received considerable attention in the last few decades because of its important applications in engineering. However, previous studies have mostly focused on homogenous porous media while layered porous media, although encountered quite frequently in applications, have receive rather little attention. For stability analysis, Masuoka et al. [1] made the first study on the onset of thermal convection in a two-layer porous system. Their work was later extended by McKibbin and O'Sullivan [2] to multilayer systems. Rees and Riley [3] further extended the classical stability problem into a three-dimensional domain. Most recently Nield et al. [4] developed a numerical code based on the algorithm that they proposed earlier [5] to predict the critical Rayleigh number for the onset of convection in a saturated porous medium with strong heterogeneity in permeability, thermal conductivity, and applied temperature gradient in both vertical and horizontal directions. For heat transfer analysis, Donaldson [6] reported the first numerical result of heat convection in a multilayer system. This was followed by Rana et al. [7] in a numerical simulation of a geothermal reservoir using a layered porous model. Their results compared favorably with the field data obtained. For horizontal layers, heat transfer results have been presented by McKibbin and coworker [8–10]. For vertical layers, Poulikakos and Bejan [11] as well as Lai and Kulacki [12] studied the effects of permeability contrast and thermal conductivity ratio on natural convection in two- or three-layer porous systems.

Earlier studies [12–14] have also shown that numerical results for heat transfer in layered porous media are usually obtained with great efforts. The solution process is further complicated by the need to implement interface conditions between two neighboring sublayers. Therefore, it is highly desirable to have a simple model for engineering applications, which can accurately predict the heat transfer results without laborious computational effort. Recently, a lumped-system model has been proposed by Leong and Lai [13,14] to determine the heat transfer rate by natural convection in a layered porous system. The proposed lumped-system model uses an effective permeability to represent a layered porous medium and treat the medium as if it was homogeneous. As they suggested, an effective permeability defined by the arithmetic average should be used when the sublayers are oriented parallel to the primary heat flow direction. On the other hand, an effective permeability based on the harmonic mean should be used when the sublayers are perpendicular to the primary heat flow. They have shown that the lumped-system model works quite well for layered porous cavities of various aspect ratios with uniform sublayer thickness [13,14].

The objective of the present study is to further examine the capacity of the lumped-system model in the prediction of heat transfer result for layered porous systems. To this end, the present study considers a porous cavity with three or four vertical sublayers with nonuniform thickness. Numerical calculations are first performed using the actual layered model. The heat transfer results thus obtained are then compared with those predicted by the lumped-system model. In addition, the results will be used in the comparison with those obtained from homogeneous anisotropic model in the subsequent study.

2 Formulation and Numerical Method

The geometry considered is a square cavity ($L=H$) (Fig. 1). It consists of three or four sublayers of nonuniform thickness and distinct permeability. The permeabilities of these sublayers are alternating among the sublayers (i.e., $K_1=K_3$ and $K_2=K_4$). The sublayers are assumed to be saturated with the same fluid. The cavity walls are impermeable. The top and bottom walls are insulated while the vertical walls are differentially heated at constant temperatures T_h and T_c ($T_h>T_c$). The governing equations based on Darcy's law as given by Leong and Lai [13,14] are

$$\frac{\partial u_i}{\partial x}+\frac{\partial v_i}{\partial y}=0 \tag{1}$$

$$u_i=-\frac{K_i}{\mu}\frac{\partial p_i}{\partial x} \tag{2}$$

Contributed by the Heat Transfer Division of ASME for publication in the JOURNAL OF HEAT TRANSFER. Manuscript received December 9, 2008; final manuscript received July 2, 2009; published online December 30, 2009.

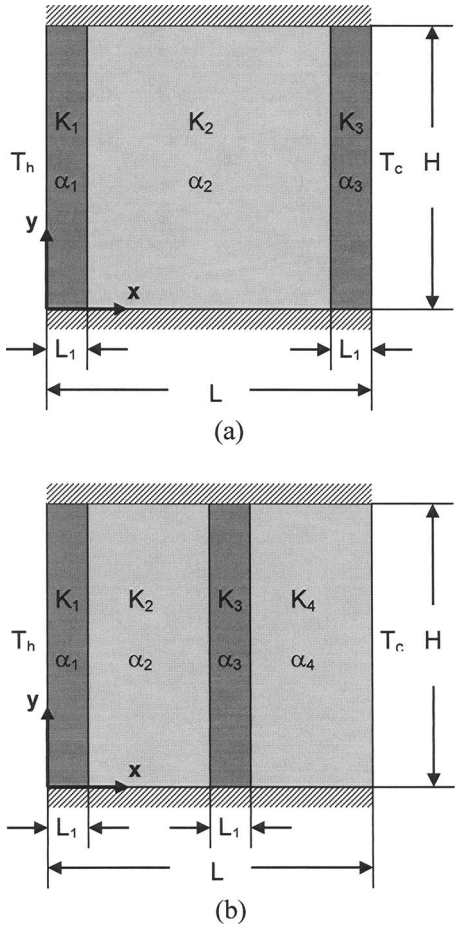

Fig. 1 Layered porous cavities subject to differential heating from two vertical walls: (*a*) three sublayers and (*b*) four sublayers

$$v_i = -\frac{K_i}{\mu}\left(\frac{\partial p_i}{\partial y} + \rho_i g\right) \tag{3}$$

$$u_i\frac{\partial T_i}{\partial x} + v_i\frac{\partial T_i}{\partial y} = \alpha_i\left(\frac{\partial^2 T_i}{\partial x^2} + \frac{\partial^2 T_i}{\partial y^2}\right) \tag{4}$$

where the subscript i refers to the individual sublayer in the cavity. In addition to the boundary conditions, interface conditions are required for the solution of the flow and temperature fields in the cavity. The interface conditions imposed are the continuity of mass, pressure, temperature, and heat flux across the interface. McKibbin and O'Sullivan [2] as well as Rana et al. [7] justified the use of these conditions. For brevity, the boundary and interface conditions are presented here only for a three-layer cavity, but can be extended to a four-layer case in a similar fashion, as follows:

$$x = 0, \quad u_1 = 0, \quad T_1 = T_h \tag{5a}$$

$$x = L, \quad u_3 = 0, \quad T_3 = T_c \tag{5b}$$

$$x = L_1, \quad u_1 = u_2, \quad p_1 = p_2$$

$$T_1 = T_2, \quad k_1\frac{\partial T_1}{\partial x} = k_2\frac{\partial T_2}{\partial x} \tag{5c}$$

$$x = L - L_1, \quad u_2 = u_3, \quad p_2 = p_3$$

$$T_2 = T_3, \quad k_2\frac{\partial T_2}{\partial x} = k_3\frac{\partial T_3}{\partial x} \tag{5d}$$

$$y = 0, \quad x < L_1, \quad v_1 = 0, \quad \frac{\partial T_1}{\partial y} = 0$$

$$L_1 < x < L - L_1, \quad v_2 = 0, \quad \frac{\partial T_2}{\partial y} = 0$$

$$L - L_1 < x < L, \quad v_3 = 0, \quad \frac{\partial T_3}{\partial y} = 0 \tag{5e}$$

$$y = H, \quad x < L_1, \quad v_1 = 0, \quad \frac{\partial T_1}{\partial y} = 0$$

$$L_1 < x < L - L_1, \quad v_2 = 0, \quad \frac{\partial T_2}{\partial y} = 0$$

$$L - L_1 < x < L, \quad v_3 = 0, \quad \frac{\partial T_3}{\partial y} = 0 \tag{5f}$$

Equations (1)–(4) and (5*a*)–(5*f*) can be simplified by introducing the stream function. In dimensionless form, they are given by

$$\frac{\partial^2 \Psi_i}{\partial X^2} + \frac{\partial^2 \Psi_i}{\partial Y^2} = -\mathrm{Ra}_i\frac{\partial \theta_i}{\partial X} \tag{6}$$

$$\frac{\partial \Psi_i}{\partial Y}\frac{\partial \theta_i}{\partial X} - \frac{\partial \Psi_i}{\partial X}\frac{\partial \theta_i}{\partial Y} = \frac{\partial^2 \theta_i}{\partial X^2} + \frac{\partial^2 \theta_i}{\partial Y^2} \tag{7}$$

where

$$\alpha_i = \frac{k_i}{(\rho c_p)_f}, \quad \mathrm{Ra}_i = \frac{K_i g\beta(T_h - T_c)L}{\alpha_i \nu_i} \tag{8}$$

Since the porous layers are saturated with the same fluid (thus, $\nu_1 = \nu_2$ and $\alpha_1 = \alpha_2$), the ratio of Rayleigh numbers can be obtained as

$$\frac{\mathrm{Ra}_1}{\mathrm{Ra}_2} = \frac{K_1}{K_2} \tag{9}$$

The corresponding boundary and interface conditions are expressed as follows:

$$X = 0, \quad \Psi_1 = 0, \quad \theta_1 = 1 \tag{10a}$$

$$X = 1, \quad \Psi_3 = 0, \quad \theta_3 = 0 \tag{10b}$$

$$X = \frac{L_1}{L}, \quad \Psi_1 = \frac{\alpha_2}{\alpha_1}\Psi_2, \quad \theta_1 = \theta_2$$

$$\frac{\partial \Psi_1}{\partial X} = \frac{K_1}{K_2}\frac{\alpha_2}{\alpha_1}\frac{\partial \Psi_2}{\partial X}$$

$$\frac{\partial \theta_1}{\partial X} = \frac{k_2}{k_1}\frac{\partial \theta_2}{\partial X} \tag{10c}$$

$$X = 1 - \frac{\mathrm{L}_1}{\mathrm{L}}, \quad \Psi_2 = \frac{\alpha_3}{\alpha_2}\Psi_3, \quad \theta_2 = \theta_3$$

$$\frac{\partial \Psi_2}{\partial X} = \frac{K_2}{K_3}\frac{\alpha_3}{\alpha_2}\frac{\partial \Psi_3}{\partial X}$$

$$\frac{\partial \theta_2}{\partial X} = \frac{k_3}{k_2}\frac{\partial \theta_3}{\partial X} \tag{10d}$$

$$Y = 0, \quad X < \frac{L_1}{L}, \quad \Psi_1 = 0, \quad \frac{\partial \theta_1}{\partial Y} = 0$$

$$\frac{L_1}{L} < X < 1 - \frac{L_1}{L}, \quad \Psi_2 = 0, \quad \frac{\partial \theta_2}{\partial Y} = 0$$

$$1 - \frac{L_1}{L} < X < 1, \quad \Psi_3 = 0, \quad \frac{\partial \theta_3}{\partial Y} = 0 \tag{10e}$$

$$Y = 1, \quad X < \frac{L_1}{L}, \quad \Psi_1 = 0, \quad \frac{\partial \theta_1}{\partial Y} = 0$$

$$\frac{L_1}{L} < X < 1 - \frac{L_1}{L}, \quad \Psi_2 = 0, \quad \frac{\partial \theta_2}{\partial Y} = 0$$

$$1 - \frac{L_1}{L} < X < 1, \quad \Psi_3 = 0, \quad \frac{\partial \theta_3}{\partial Y} = 0 \tag{10f}$$

The interface conditions have been implemented using imaginary nodal points as described by Rana et al. [7]. The equations for the dimensionless stream function and temperature at the first interface are given below and they can be obtained for other interfaces in a similar manner.

$$\Psi^1_{N,j} = \frac{1}{2}\frac{\tilde{K}}{\tilde{K}+1}\Psi^1_{N-1,j} + \frac{1}{2}\frac{1}{\tilde{K}+1}\Psi^2_{N+1,j} + \frac{1}{4}(\Psi^1_{N,j-1} + \Psi^1_{N,j+1}) + \frac{1}{8}\frac{\tilde{K}}{\tilde{K}+1}\mathrm{Ra}_1(\theta^1_{N-2,j} - 4\theta^1_{N-1,j} + 4\theta^2_{N+1,j} - \theta^2_{N+2,j})\Delta X \tag{11a}$$

$$\theta^1_{N,j} = \theta^2_{N,j} = \frac{1}{3}\frac{4(\theta^1_{N-1,j} + \theta^2_{N+1,j}) - (\theta^1_{N-2,j} + \theta^2_{N+2,j})}{2} \tag{11b}$$

where $\tilde{K} = K_2/K_1$ is the permeability ratio and N is the nodal number along the interface.

The governing equations with the boundary and interface conditions were solved using a finite difference method. This method has been successfully employed by the authors for similar studies [13,14]. For the present study, various sublayer thicknesses have been considered ($L_1/L = 1/13$, 2/13, 3/13, 4/13, 5/13, and 6/13 for the case of three sublayers and $L_1/L = 1/16$, 1/8, 3/16, 5/16, 3/8, and 7/16 for the case of four sublayers). In addition, computations have covered a wide range of base Rayleigh number ($10 \leq \mathrm{Ra}_1 \leq 1000$) as well as permeability ratio ($K_1/K_2 = 0.1$, 1, 10, and 100). Uniform grids (1561×1561) with under- and over-relaxation are used for most of the calculations to ensure the accuracy of the numerical results. It should be noted that the grid used is denser than those of the previous studies to ensure that there are sufficient nodes in the thinnest sublayer considered. It should also be pointed out that solution for cavities with $K_1/K_2 < 1$ is more difficult to converge than those with $K_1/K_2 > 1$ at a given base Rayleigh number. This can be seen from Eq. (9) that the Rayleigh number for the even-number sublayer is K_2/K_1 times higher than the base Rayleigh number. As a result, local convection is much stronger than that implied by the base Rayleigh number for cavities with $K_1/K_2 < 1$. Nevertheless once the solution converges, it is noticed that further refinement of the grid does not significantly improve the results. An overall energy balance has been performed in each calculation to further evaluate the accuracy of the results obtained. For the present study, the results are satisfied within 3% (most are within 1%). The overall heat transfer is expressed in terms of the average Nusselt number at each vertical wall as given by

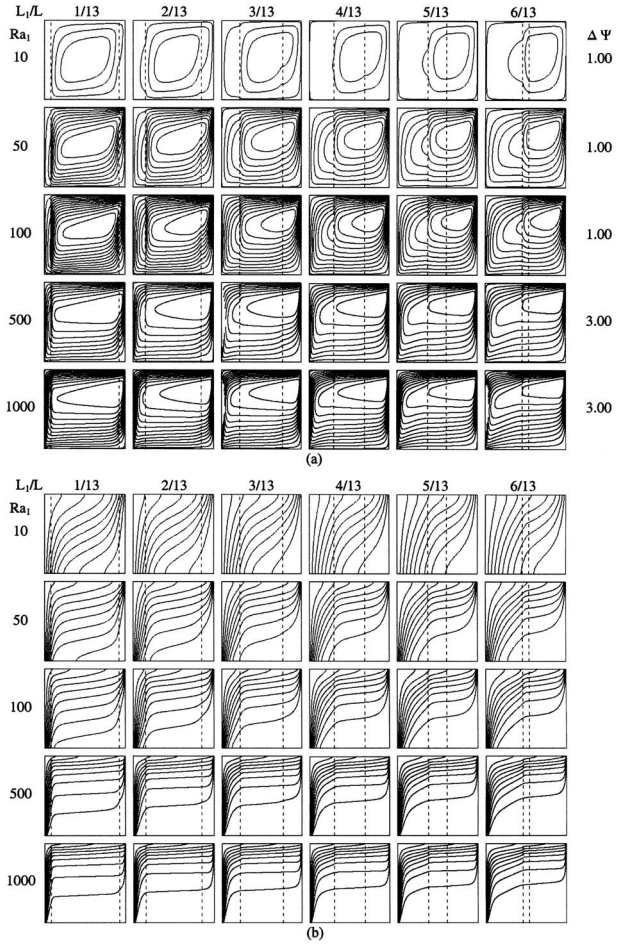

Fig. 2 Flow and temperature fields in a porous cavity with three sublayers ($K_1/K_2 = 0.1$): (*a*) flow field ($\Delta\Psi$ as indicated in the figure) and (*b*) temperature field ($\Delta\theta = 0.1$)

$$\mathrm{Nu} = -\int_0^1 \left.\frac{\partial \theta}{\partial X}\right|_{X=0,1} dY \tag{12}$$

To validate the code thus developed, results have been tested against those reported in the literature for a homogeneous porous cavity by setting the permeability ratio K_1/K_2 to unity. The agreement is very good and is documented in Ref. [15].

3 Results and Discussion

For natural convection in a homogeneous porous cavity, the flow development with increase in the Rayleigh number has been classified by Prasad and Kulacki [16] into four regimes: conduction, asymptotic flow, pseudo boundary layer flow, and boundary layer flow. While the conduction regime is characterized by a moderate circulatory parallel flow structure and a temperature profile linearly distributed in the *x*-direction, the asymptotic flow regime is identified by gradual temperature stratification in the core region and an increase in heat transfer by convection near the walls. Further increase in the Rayleigh number leads to the boundary layer flow regime. These classifications are very useful for the discussion that follows.

The flow and temperature fields in a cavity with three sublayers and a permeability ratio of $K_1/K_2 = 0.1$ are shown in Fig. 2 (in terms of streamlines and isotherms) for various base Rayleigh numbers and sublayer thicknesses. In general, the flow structure for a cavity with three sublayers is similar to that with two sublayers [12], only more complicated by the presence of additional

sublayers. Because of the difference in the permeability between two neighboring sublayers, the location of the interface can be easily identified by the abrupt change in the slope of streamlines.

For the present case ($K_1/K_2=0.1$), the two outer sublayers are less permeable than the one in the middle. As such, when the base Rayleigh number increases, convection is more prominent in the middle sublayer than that in the outer sublayers. Also it is noticed that the direction of the convective flow becomes nearly horizontal in the middle sublayer while it runs mostly vertical in the outer sublayer. As the sublayer thickness ratio (L_1/L) increases, one observes that the strength of the convective flow becomes weaker because of an increase in the flow resistance from the less permeable outer sublayers. Thus the outer sublayers can be considered as a damper that significantly weakens the convective flow when their thickness increases. It is also interesting to note that the presence of the less permeable outer sublayers forces the convective flow to run faster in the upper half of the middle sublayer than that in the lower half, which produces a significant effect on the temperature distribution in the cavity. As observed from Fig. 2(*b*), the cavity is thermally stratified when the base Rayleigh number increases. However, the thermal stratification observed here is different from that of a homogeneous cavity [16]. The stratification for the present case is not uniform but confined mostly to the upper half of the cavity due to the disparity in the convective flow velocity mentioned earlier. As the base Rayleigh number increases, the largest temperature gradient (heat flux) occurs at the lower left corner of the cavity while the eye of the convective cell shifts to the upper right corner of the cavity.

The flow and temperature fields for a cavity with three sublayers and a permeability ratio of $K_1/K_2=10$ are shown in Fig. 3 for various base Rayleigh numbers and sublayer thicknesses. In this case, the two outer sublayers are more permeable than the middle one. It is clearly observed that the flow and temperature profiles for the present case are very different from those of $K_1/K_2=0.1$ (Fig. 2). For the present case, convection always starts in the more permeable outer sublayer near the hot wall and penetrates the less permeable middle sublayer as the base Rayleigh number increases. In addition, the strength of the convective flow increases as the sublayer thickness ratio increases. The heat transfer mode in each sublayer can be easily identified from the isotherm contours (Fig. 3(*b*)). The linear distribution of isotherms at a low base Rayleigh number (e.g., $Ra_1=10$) indicates that heat transfer is driven by conduction. An increase in the base Rayleigh number leads to a transition of the heat transfer mode from conduction to convection. In contrast to the case of $K_1/K_2=0.1$, it is noticed that the eye of the convective cell is now shifted to the lower left corner of the cavity as the base Rayleigh number increases.

For cavities with four sublayers, the flow and temperature fields are shown in Figs. 4 and 5 for $K_1/K_2=0.1$ and 10, respectively. For a given permeability ratio, it is observed that the temperature field in the first two sublayers of a four-sublayer cavity bears some similarity to that in a three-layer cavity. For a given base Rayleigh number, the presence of the middle less permeable sublayer has created additional flow resistance that has to be overcome by the buoyancy-induced flow in order to sustain convection in the second more permeable sublayers. This suggests that an increase in the number of sublayers suppresses the convection within the cavity. For $K_1/K_2=0.1$, the added flow resistance due to additional sublayer has greatly reduced the strength of convection (Fig. 4). For $K_1/K_2=10$, the penetration of convective flow to the right most sublayer is considerably reduced. In addition, the breakdown of the primary cell to two secondary cells due to the presence of the less permeable sublayer that was observed in the three-layer case is even more obvious in the present case (Fig. 5). For $K_1/K_2=10$, it is clear that conduction remains the dominant heat transfer mode at low base Rayleigh numbers. This is confirmed by the presence of evenly distributed isotherms throughout the cavity (Fig. 5). An increase in the base Rayleigh number causes only slight distortion of isotherms in the more permeable sublayer. The distortion of isotherms is an indication of weak convection.

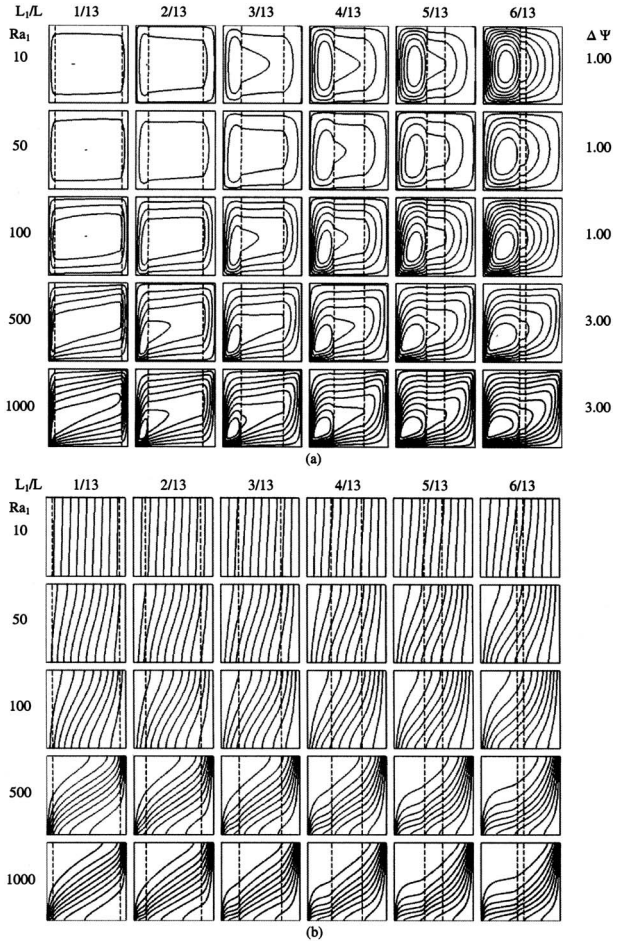

Fig. 3 Flow and temperature fields in a porous cavity with three sublayers ($K_1/K_2=10$): (*a*) flow field ($\Delta\Psi$ as indicated in the figure) and (*b*) temperature field ($\Delta\theta=0.1$)

With an increase in the permeability contrast (i.e., $K_1/K_2=0.01$ or 100), the less permeable sublayer behaves almost like an impermeable wall. The penetration of convective flow to these sublayers is only possible at a higher Rayleigh number, leaving convection mainly in the more permeable sublayer. This has led to conduction heat transfer in the less permeable sublayer(s) and convective heat transfer in the more permeable sublayer(s).

For heat transfer results, it is found that the average Nusselt number for $K_1/K_2<1$ is always greater than that of a homogeneous one while it is always less than that of a homogeneous one for $K_1/K_2>1$. This is consistent with the results reported in the previous studies [12–14]. To verify if the lumped-system analysis is applicable for the present problem, the heat transfer results obtained are expressed as a function of the Rayleigh number based on the effective permeability. For the present study, the sublayers are oriented vertically. Since the cavity is differentially heated from the vertical side walls, the sublayers are perpendicular to the heat flow direction. According to the lumped-system theory [13,14], an effective permeability based on the harmonic mean should be employed, which is given by

$$\frac{1}{\overline{K}_H}=\frac{2L_1/L}{K_1}+\frac{(1-2L_1/L)}{K_2} \tag{13}$$

Clearly, the lumped-system analysis is based on a concept similar to thermal resistance. Since the resistance to convective heat

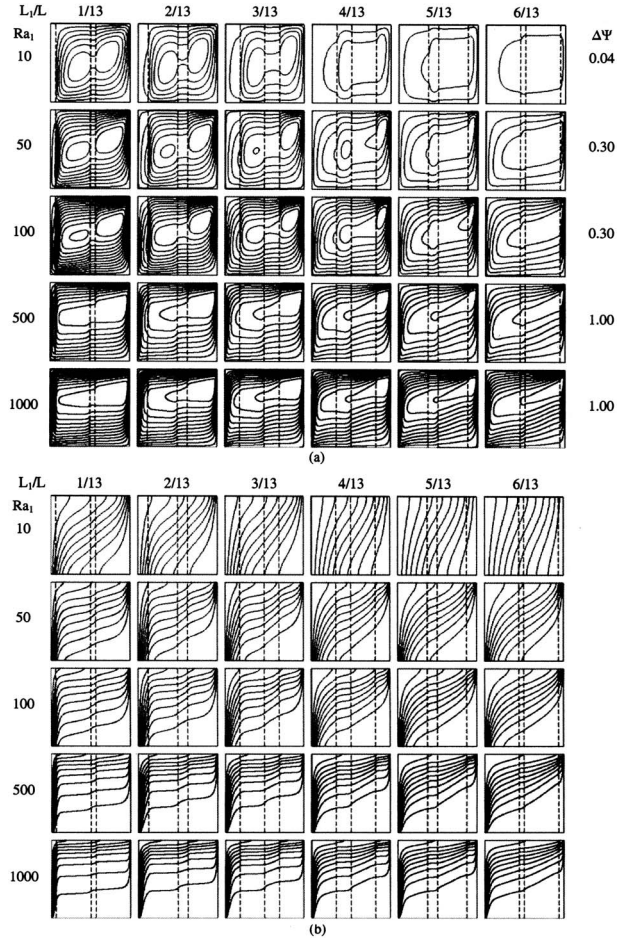

Fig. 4 Flow and temperature fields in a porous cavity with four sublayers ($K_1/K_2=0.1$): (*a*) flow field ($\Delta\Psi$ as indicated in the figure) and (*b*) temperature field ($\Delta\theta=0.1$)

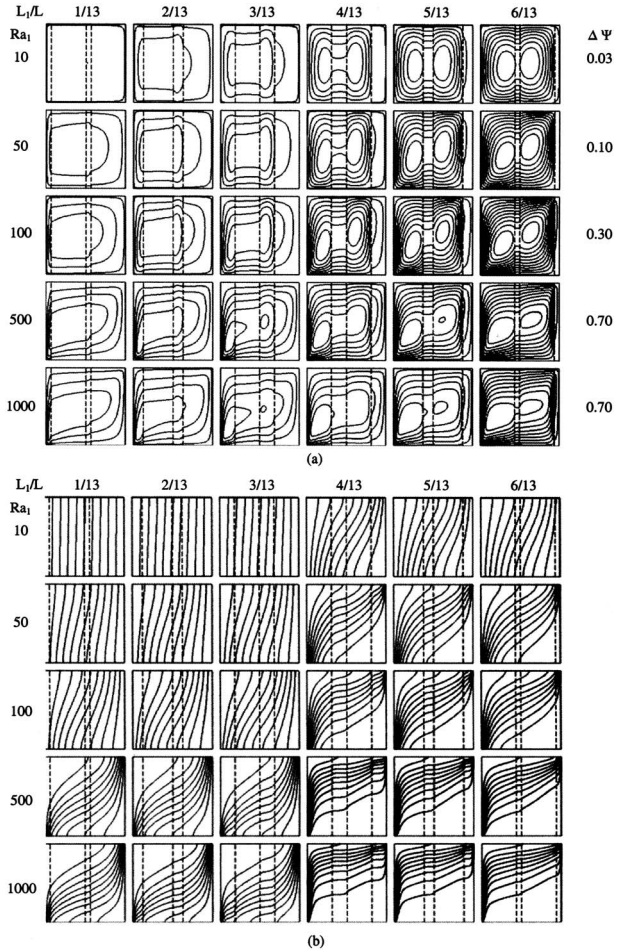

Fig. 5 Flow and temperature fields in a porous cavity with four sublayers ($K_1/K_2=10$): (*a*) flow field ($\Delta\Psi$ as indicated in the figure) and (*b*) temperature field ($\Delta\theta=0.1$)

transfer is inversely proportional to the sublayer permeability, the above expression represents a thermal circuit in series.

The heat transfer results are shown in Fig. 6 as a function of the effective Rayleigh number. For comparison, the results for a homogeneous cavity are also included (as solid lines) in the figures. For cavities with three sublayers, Fig. 6(*a*) reveals that all data nearly collapse to the curve representing the heat transfer result for a homogeneous cavity. But there is some discrepancy between the actual Nusselt number and that predicted by the lumped-system analysis. The discrepancy is initially negligible at small Rayleigh numbers but grows to a maximum (about 50%) when the Rayleigh number becomes large (i.e., $\mathrm{Ra}_H > 600$). Similarly, for cavities with four sublayers (Fig. 6(*b*)), it is observed that the data collapse to the curve even better than those with three sublayers, which is consistent with the observation that the model would work best when the number of sublayers increases [9]. Also it is noticed that the lumped-system analysis give a better prediction for cavities with sublayers of nearly uniform thickness (e.g., $L_1/L=3/13$ and 4/13 for three-sublayer and 3/16 and 5/16 for four-sublayer). From the above observations, one concludes that the lumped-system analysis with an effective permeability based on the harmonic mean can provide a fairly good prediction in heat transfer for cavities with nonuniform sublayers.

The findings from the present study are consistent with that of Leong and Lai [13,14]. Therefore, we can assert that the direction of heat flow relative to the sublayer orientation is crucial in the determination of the effective permeability of a layered porous cavity to be used in the lumped-system analysis. Particularly, the present study showed that the effective permeability based on the harmonic mean provides a fairly good prediction in heat transfer for a layered system, in which the sublayers are oriented perpendicular to the direction of heat flow. It is further demonstrated that heat transfer in a layered porous cavity is analogous to an electric circuit, where the effective permeability plays the same role as the equivalent electrical resistance.

4 Conclusions

Natural convection in layered porous cavities differentially heated from two vertical walls has been numerically examined in this study as an extension to several earlier studies [12–14]. In addition, the present study has further examined the capacity of the lumped-system approach in the prediction of heat transfer results in layered porous cavities. The agreement between the actual results and those predicted by the lumped system is generally acceptable in the range of Rayleigh numbers of practical interest. From this aspect, one can say that the present results have confirmed the applicability of the lumped-system analysis for layered porous media. In particular, it shows that the lumped system analysis can provide a quick estimate of heat transfer result for a layered system without massive computations. That is, to use this model, one only needs to calculate the corresponding Rayleigh number based on the effective permeability and then use a proper correlation of the heat transfer results for the homogeneous cavity. Since the latter is already well documented in the literature, the

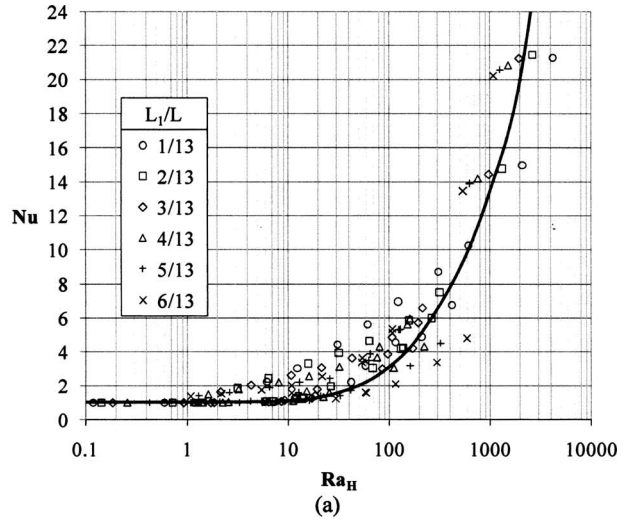

Fig. 6 Heat transfer results for a layered porous cavity: (*a*) three sublayers and (*b*) four sublayers

calculation of heat transfer results for a layered cavity is simple and quick, and its accuracy is generally acceptable for most engineering applications.

Nomenclature

A = aspect ratio, $A=H/L$
c_p = heat capacity (J/kg K)
g = gravitational acceleration (m/s^2)
H = height of cavity (m)
h = heat transfer coefficient (W/m^2 K)
K = permeability (m^2)
$\tilde{K}$ = permeability ratio $\tilde{K}=K_2/K_1$
K_H = effective permeability of vertical layers (m^2)
k = effective thermal conductivity of porous medium (W/m K)
L = width of cavity (m)
L_1 = location of the interface of vertical sublayers (m)
N = nodal number of the layer interface
Nu = average Nusselt number, $Nu=hL/k$
p = pressure (Pa)
Ra_1 = base Rayleigh number, $Ra=K_1 g\beta(T_h-T_c)H/\alpha\nu$
T = temperature (K)
U_i = dimensionless velocity in the x-direction, $U_i=\partial\Psi_i/\partial Y$
u_i = Darcy velocity in the x-direction, $u_i=\alpha_1 U_i/L$ (m/s)
V_i = dimensionless velocity in the y-direction, $V_i=-\partial\Psi_i/\partial X$
v_i = Darcy velocity in the y-direction, $v_i=\alpha_1 V_i/L$ (m/s)
X,Y = dimensionless Cartesian coordinates
x,y = Cartesian coordinates (m)
α = effective thermal diffusivity of porous medium $\alpha=k/(\rho c_p)_f$ (m^2/s)
β = thermal expansion coefficient, $(-1/\rho)(\partial\rho/\partial T)_p$ (K^{-1})
θ = dimensionless temperature, $(T-T_c)/(T_h-T_c)$
μ = dynamic viscosity of fluid (kg/m s)
ν = kinematic viscosity of fluid (m^2/s)
ρ = fluid density (kg/m^3)
Ψ = dimensionless stream function

Subscripts

c = cold wall
f = fluid
h = hot wall
i = index of the sublayer (1,2,…)

References

[1] Masuoka, T., Katsuhara, T., Nakazono, Y., and Isozaki, S., 1978, "Onset of Convection and Flow Patterns in a Porous Layer of Two Different Media," Heat Transfer-Jpn. Res., **7**, pp. 39–52.
[2] McKibbin, R., and O'Sullivan, M. J., 1980, "Onset of Convection in a Layered Porous Medium Heated From Below," J. Fluid Mech., **96**, pp. 375–393.
[3] Rees, D. A. S., and Riley, D. S., 1990, "The Three-Dimensional Stability of Finite-Amplitude Convection in a Layered Porous Medium Heated From Below," J. Fluid Mech., **211**, pp. 437–461.
[4] Nield, D. A., Kuznetsov, A. V. K., and Simmons, C. T., 2009, "The Effects of Strong Heterogeneity on the Onset of Convection in a Porous Medium—Non-Periodic Global Variation," Transp. Porous Media, **77**, pp. 169–186.
[5] Nield, D. A., and Simmons, C. T., 2007, "A Discussion on the Effect of Heterogeneity on the Onset of Convection in a Porous Medium," Transp. Porous Media, **68**, pp. 413–421.
[6] Donaldson, I. G., 1962, "Temperature Gradients in the Upper Layers of the Earth's Crust Due to Convective Water Flows," J. Geophys. Res., **67**, pp. 3449–3459.
[7] Rana, R., Horne, R. N., and Cheng, P., 1979, "Natural Convection in a Multi-Layered Geothermal Reservoir," ASME J. Heat Transfer, **101**, pp. 411–416.
[8] McKibbin, R., 1982, "Some Effects of Non-Homogeneity in the 'Water-Saturated Porous Layer' Model of a Geothermal Field," *Mathematics and Models in Engineering Science*, DSIR, Wellington, New Zealand, pp. 139–148.
[9] McKibbin, R., and Tyvand, P. A., 1983, "Thermal Convection in a Porous Medium Composed of Alternating Thick and Thin Layers," Int. J. Heat Mass Transfer, **26**, pp. 761–780.
[10] McKibbin, R., and Tyvand, P. A., 1984, "Thermal Convection in a Porous Medium With Horizontal Cracks," Int. J. Heat Mass Transfer, **27**, pp. 1007–1023.
[11] Poulikakos, D., and Bejan, A., 1983, "Natural Convection in Vertically and Horizontally Layered Porous Media Heated From the Side," Int. J. Heat Mass Transfer, **26**, pp. 1805–1814.
[12] Lai, F. C., and Kulacki, F. A., 1988, "Natural Convection Across a Vertical Layered Porous Cavity," Int. J. Heat Mass Transfer, **31**, pp. 1247–1260.
[13] Leong, J. C., and Lai, F. C., 2001, "Effective Permeability of a Layered Porous Cavity," ASME J. Heat Transfer, **123**, pp. 512–519.
[14] Leong, J. C., and Lai, F. C., 2004, "Natural Convection in Rectangular Layered Porous Cavities," J. Thermophys. Heat Transfer, **18**, pp. 457–463.
[15] Marvel, R. L., 2008, Comparison of Two Predictive Methods for Natural Convection in Layered Porous Cavities With Non-Uniform Sublayer Thickness, M.S. thesis, University of Oklahoma, Norman, OK.
[16] Prasad, V., and Kulacki, F. A., 1984, "Convective Heat Transfer in a Rectangular Porous Cavity—Effect of Aspect Ratio on Flow Structure and Heat Transfer," ASME J. Heat Transfer, **106**, pp. 158–165.

Optimization of a Pin Fin With Variable Base Thickness

H. S. Kang
Department of Mechanical Engineering,
Kangwon National University,
Chuncheon 200-701, Korea
e-mail: hkang@kangwon.ac.kr

A pin fin with variable fin base thickness is optimized using a two-dimensional analytic method. The values of the inner wall temperature and fin volume are given as constants. The fin base temperature varies with variation in the fin base thickness, fin outer radius, fin length, and convection characteristic number. Under these conditions, the optimum heat loss, the corresponding optimum fin effectiveness, fin length, and fin outer radius are presented as functions of the fin base thickness, fin volume, and convection characteristic number. One of the results shows that both the optimum heat loss and optimum fin length decrease linearly with increase in the fin base thickness. [DOI: 10.1115/1.4000048]

Keywords: convection characteristic number, fin base thickness, heat loss, pin fin, optimization

1 Introduction

Extended surfaces or fins play an important role by enhancing heat transfer in many engineering applications. Many studies about fin problems have been reported [1–7]. The most commonly studied fins include rectangular, triangular, trapezoidal, and annular fins. For example, Aziz and Lunardini [4] reviewed the literature on multidimensional heat conduction in single fins and fin assemblies including rectangular and triangular fins. Kang and Look [5] analyzed trapezoidal fins of various slopes using an analytical method. Look [6] demonstrated two-dimensional effects by comparing the results of one- and two-dimensional analyses of a rectangular fin on a pipe. Also, Campo and Cui [7] presented an elementary analytic procedure for solving approximately the quasi-1D heat conduction equation governing the annular fin of hyperbolic profile.

The pin fin is also a popular shape of fin and many studies on it have been reported. For example, Irey [8] presented the relative error of heat loss between 1D and 2D analyses for a pin fin while Laor and Kalman [9] presented a theoretical-numerical analysis of spine fins with a temperature-dependent heat transfer coefficient. Su and Hwang [10] developed analytic transient solutions for a two-dimensional pin fin using the Laplace transformation and the separation of variables methods.

Optimizing fins is also an interesting area of study for fin problems. One representative optimization procedure is to find the maximum heat loss for a given fin material. For this kind of optimization, Kang and Look [11] presented the optimum procedure for a thermally asymmetric convective and radiating annular fin. Yu and Chen [12] discussed the optimization of rectangular profile circular fins with variable thermal conductivity and convective heat transfer coefficients. Kang [13] analyzed and optimized a rectangular fin with fluid on the inside wall using a two-dimensional analytic method.

To optimize a pin fin, Yeh [14] investigated analytically the optimum dimensions of cylindrical pin fins, considering temperature-dependent heat transfer coefficients. Chung and Iyer [15] presented an extended integral approach to determine the optimum dimensions for pin fins by incorporating traverse heat conduction. In these papers, for a pin fin optimization, the pin fin base temperature is given as a constant.

In this two-dimensional optimization of a pin fin for fixed fin volumes, the inner wall temperature is given and the fin base temperature varies with variation in the fin base thickness and fin radius, fin length, and convection characteristic number. Under these conditions, the optimum heat loss, fin effectiveness, fin length, and outer radius are presented as functions of the fin base thickness, fin volume, and convection characteristic number.

2 2D Analysis

For a pin fin under steady state condition as shown in Fig. 1, two-dimensional governing equation and four boundary conditions can be written in dimensionless form as

$$\frac{\partial^2\theta}{\partial R^2}+\frac{1}{R}\frac{\partial\theta}{\partial R}+\frac{\partial^2\theta}{\partial X^2}=0 \tag{1}$$

$$\left.\frac{\partial\theta}{\partial R}\right|_{R=0}=0 \tag{2}$$

$$-\left.\frac{\partial\theta}{\partial X}\right|_{X=L_b}=\frac{1-\theta|_{X=L_b}}{L_b} \tag{3}$$

$$\left.\frac{\partial\theta}{\partial X}\right|_{X=L_e}+M\cdot\theta|_{X=L_e}=0 \tag{4}$$

$$\left.\frac{\partial\theta}{\partial R}\right|_{R=R_o}+M\cdot\theta|_{R=R_o}=0 \tag{5}$$

Fin base boundary condition is presented by Eq. (3) and it means that heat conduction from the inner wall to the fin base and heat conduction through the fin base are the same. Solving Eq. (1) with the boundary conditions (Eqs. (2)–(4)), the dimensionless temperature distribution within the fin is

$$\theta(X,R)=\sum_{n=1}^{\infty}\frac{R_o f_1(X) f_2(R)}{2\lambda_n\{g_1(\lambda_n)+g_2(\lambda_n)\}g_3(\lambda_n)} \tag{6}$$

where

$$f_1(X)=\cos h(\lambda_n X)+g_4(\lambda_n)\sin h(\lambda_n X) \tag{7}$$

$$f_2(R)=J_1(\lambda_n R_o)\cdot J_0(\lambda_n R) \tag{8}$$

$$g_1(\lambda_n)=\{1-\lambda_n L_b g_4(\lambda_n)\}\cos h(\lambda_n L_b) \tag{9}$$

$$g_2(\lambda_n)=\{g_4(\lambda_n)-\lambda_n L_b\}\sin h(\lambda_n L_b) \tag{10}$$

$$g_3(\lambda_n)=J_0^2(\lambda_n R_o)+J_1^2(\lambda_n R_o) \tag{11}$$

$$g_4(\lambda_n)=-\frac{\lambda_n\tan h(\lambda_n L_e)+M}{\lambda_n+M\tan h(\lambda_n L_e)} \tag{12}$$

The eigenvalues λ_n can be calculated using Eq. (13), which is arranged from Eq. (5), as follows:

$$M=\frac{\lambda_n J_1(\lambda_n R_o)}{J_0(\lambda_n R_o)} \tag{13}$$

Dimensionless heat loss from the pin fin is given by

$$Q=q/(kl_c\phi_i)=-\sum_{n=1}^{\infty}\frac{4\pi g_7(\lambda_n)\{J_1(\lambda_n R_o)\}^2}{\lambda_n\{g_1(\lambda_n)+g_2(\lambda_n)\}g_3(\lambda_n)} \tag{14}$$

where

Manuscript received January 15, 2009; final manuscript received July 7, 2009; published online December 23, 2009. Editor: Yogesh Jaluria.

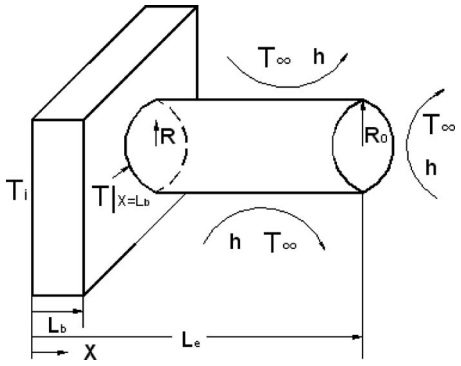

Fig. 1 Schematic diagram of a cylindrical pin fin

$$g_7(\lambda_n) = \sin h(\lambda_n L_b) + g_4(\lambda_n)\cos h(\lambda_n L_b) \tag{15}$$

In the case of bare wall, the energy balance equation and two boundary conditions are denoted by

$$\frac{d^2\theta}{dX^2} = 0 \tag{16}$$

$$\theta|_{X=0} = 1 \tag{17}$$

$$\left.\frac{\partial\theta}{\partial X}\right|_{X=L_b} + M\cdot\theta|_{X=L_b} = 0 \tag{18}$$

The dimensionless temperature distribution between $X=0$ and $X=L_b$ in the bare wall case is written by

$$\theta = -\frac{M}{1+M\cdot L_b}X + 1 \tag{19}$$

The dimensionless form of heat loss from the outer bare wall can be expressed as

$$Q_w = \frac{q_w}{kl_c\phi_i} = \frac{\pi R_o^2 M}{1+ML_b} \tag{20}$$

The fin effectiveness is defined as the ratio of heat loss from the fin to heat loss from the outer bare wall (i.e., $\varepsilon = Q/Q_w$).

3 1D Analysis

The one-dimensional energy balance equation for the pin fin and two boundary conditions are

$$\frac{d^2\theta}{dX^2} - \frac{2M}{R_o}\theta = 0 \tag{21}$$

$$-\left.\frac{\partial\theta}{\partial X}\right|_{X=L_b} = \frac{1-\theta|_{X=L_b}}{L_b} \tag{22}$$

$$\left.\frac{\partial\theta}{\partial X}\right|_{X=L_e} + M\cdot\theta|_{X=L_e} = 0 \tag{23}$$

Then, the dimensionless temperature distribution in a pin fin is written by

$$\theta(X) = \frac{C_3\cos h(mX) - C_4\sin h(mX)}{C_1C_3 + C_2C_4} \tag{24}$$

where

$$C_1 = \cos h(mL_b) - mL_b\sin h(mL_b) \tag{25}$$

$$C_2 = mL_b\cos h(mL_b) - \sin h(mL_b) \tag{26}$$

$$C_3 = m\cos h(mL_e) + M\sin h(mL_e) \tag{27}$$

Table 1 Relative error of heat loss between 1D and 2D analyses for $L_e = 0.5 + L_b$

		$(Q_1-Q_2)/Q_2$ (%)	
R_o	M	$L_b=0.0001$	$L_b=0.1$
0.4	0.1	0.571	0.608
	0.2	1.077	1.125
1	0.1	0.769	0.890
	0.2	1.467	1.677

$$C_4 = m\sin h(mL_e) + M\cos h(mL_e) \tag{28}$$

$$m = (2M/R_o)^{1/2} \tag{29}$$

The dimensionless heat loss from the fin is given by

$$Q = \frac{\pi R_o^2 m\{C_4\cos h(mL_b) - C_3\sin h(mL_b)\}}{C_1C_3 + C_2C_4} \tag{30}$$

4 Results

Table 1 lists the relative error of heat loss between 1D and 2D analyses with variation in the fin outer radius, convection characteristic number, and fin base thickness. The relative error increases as all given variables increase. The effect of the fin base thickness can be ignored when $L_b=0.0001$ and then the condition for $R_o=1$, $M=0.1$, and $L_e=0.5001$ in this table becomes the condition for Bi=0.1 and $L/a=0.5$ given by Irey [8] (i.e., $\text{Bi}=(h\cdot r_o)/k=\{(h\cdot l_c)/k\}\cdot(r_o/l_c)=M\cdot R_o$, $L=L_e-L_b$ and $a=R_o$). So, in the case of $L_b=0.0001$ and $M=0.1$ in this Table, the relative errors for $R_o=0.4$ and $R_o=1$ are 0.571% and 0.769%, respectively, which agree well with the results for Bi=0.04, $L/a=1.25$ and Bi=0.1, $L/a=0.5$ shown by Irey [8].

Figure 2 presents the variation in the optimum heat loss and the corresponding optimum fin effectiveness, optimum fin length, and optimum outer radius as a function of the fin base thickness for a pin fin when the fin's dimensionless volume is fixed at 0.3. The optimum heat loss is defined as the maximum heat loss at the practical fin length, and the corresponding optimum values are defined as the values when the heat loss becomes optimum. This figure indicates that the optimum heat loss corresponding optimum fin effectiveness and optimum fin length decrease linearly, but the optimum outer radius increases linearly as the fin base thickness increases. It should be noted that the existing range of the optimum values for $M=0.05$ is less than that for $M=0.01$.

The dimensionless fin volume V was arbitrarily selected to be 0.3 in the previous discussion. The variation in the optimum values as a function of V is shown in Fig. 3. As expected, an increase in V enhances the optimum heat loss. The corresponding optimum

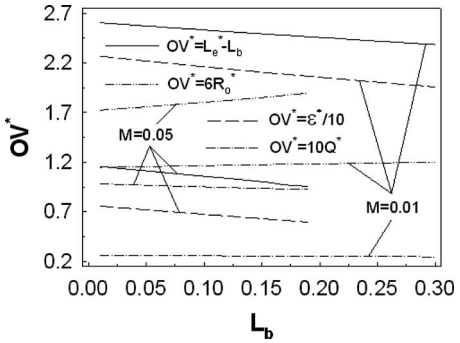

Fig. 2 Optimum values versus the fin base thickness for $V=0.3$

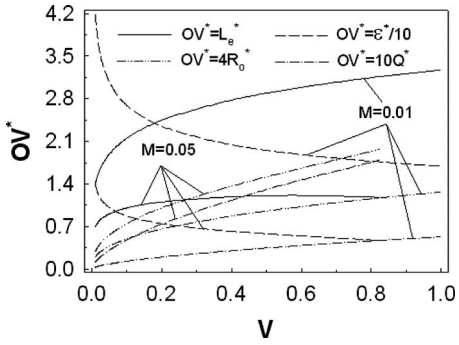

Fig. 3 Optimum values versus the fin volume for L_b=0.1

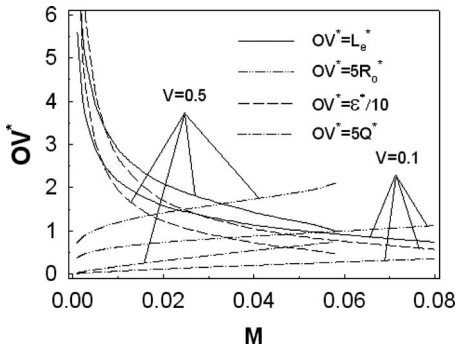

Fig. 4 Optimum values versus the convection characteristic number for L_b=0.1

effectiveness decreases rapidly at first, and then decreases slowly with increase in the fin volume. It shows that both the optimum fin length and outer radius increase rapidly at first and then level off as the fin volume increases. Note that the increasing rate of the optimum outer radius is larger than that of the optimum fin length. Physically, the optimum pin fin's shape becomes "fatter" with increase in the fin volume.

The effect of convection characteristic number M on the optimum values is depicted in Fig. 4. It shows that the optimum heat loss increases linearly, whereas the corresponding optimum effectiveness decreases very rapidly first and then decreases slowly with increase in the convection characteristic number. The optimum fin length decreases remarkably at first, and then decreases slowly, and the optimum outer radius increases because of the fixed fin volume as the convection characteristic number increases.

5 Conclusions

Optimum values of a pin fin for fixed fin volumes are presented as a function of the fin base thickness, fin volume, and convection characteristic number. These optimum values may be used to design a practical pin fin. Both the optimum heat loss and the optimum fin length decrease linearly as the fin base thickness increases. Even though the optimum heat loss increases, the corresponding optimum fin effectiveness decreases as the fin volume and convection characteristic number increase. This is either because the optimum fin length decreases, whereas the optimum outer radius increases, with increase in the convection characteristic number, or because the increasing rate of the fin length is less than that of the fin outer radius with increase in the fin volume.

Acknowledgment

The author thanks Professor Look for his suggestions and revisions, which improved this paper's quality and presentation.

Nomenclature

Bi = Biot number, $M \cdot R_o$
h = heat transfer coefficient, $W/m^2 \cdot C$
J_0 = Bessel function of the first kind with zero order
J_1 = Bessel function of the first kind with first order
k = thermal conductivity, $W/m \cdot C$
l_b = fin base thickness (m)
l_c = characteristic length (m)
l_e = fin tip length (m)
L_b = dimensionless fin base thickness, l_b/l_c
L_e = dimensionless fin tip length, l_e/l_c
M = convection characteristic number, $(hl_c)/k$
q = heat loss from a pin fin (W)
Q = dimensionless heat loss from a pin fin, $q/(kl_c\phi_i)$
q_w = heat loss from the bare outer wall (W)
Q_w = dimensionless form of q_w, $q_w/(kl_c\phi_i)$
r = pin fin radius directional coordinate (m)
R = dimensionless form of r, r/l_c
r_o = outer radius of a pin fin (m)
R_o = dimensionless outer radius of a pin fin, r_o/l_c
T = temperature (°C)
T_i, T_∞ = inner wall and ambient temperature (°C)
v = fin volume (m^3)
V = dimensionless fin volume, $v/l_c^3 = \pi R_o^2(L_e - L_b)$
x = fin length directional coordinate (m)
X = dimensionless form of x, x/l_c
ε = fin effectiveness, Q/Q_w
θ = dimensionless temperature, $(T-T_\infty)/(T_i-T_\infty)$
ϕ_i = adjusted inner wall temperature, (T_i-T_∞)
λ_n = eigenvalues, $n=1,2,3,\ldots$

Subscripts

1, 2 = one- and two-dimensional analyses
b = fin base
c = characteristic
e = fin tip
i = inner wall
o = outer radius
w = bare outer wall
∞ = ambient

Superscripts

* = optimum

References

[1] Kundu, B., 2007, "Performance and Optimization of Flat Plate Fins of Different Geometry on a Round Tube: A Comparative Investigation," ASME J. Heat Transfer, **129**(7), pp. 917–926.
[2] Kang, H. S., 2008, "Optimization of a Reversed Trapezoidal Fin Using a 2-D Analytic Method," J. Mech. Sci. Technol., **22**(3), pp. 556–564.
[3] Sommers, A. D., and Jacobi, A. M., 2006, "An Exact Solution to Steady Heat Conduction in a Two-Dimensional Annulus on a One-Dimensional Fin: Application to Frosted Heat Exchangers With Round Tubes," ASME J. Heat Transfer, **128**(4), pp. 397–404.
[4] Aziz, A., and Lunardini, V. J., 1995, "Multidimensional Steady Conduction in Convecting, Radiating, and Convecting-Radiating Fins and Fin Assemblies," Heat Transfer Eng., **16**(3), pp. 32–64.
[5] Kang, H. S., and Look, D. C., Jr., 1997, "Two Dimensional Trapezoidal Fins Analysis," Comput. Mech., **19**(3), pp. 247–250.
[6] Look, D. C., Jr., 1999, "Fin (on a Pipe) Effectiveness: One Dimensional and Two Dimensional," ASME J. Heat Transfer, **121**(1), pp. 227–230.
[7] Campo, A., and Cui, J., 2008, "Temperature/Heat Analysis of Annular Fins of Hyperbolic Profile Relying on the Simple Theory for Straight Fins of Uniform Profile," ASME J. Heat Transfer, **130**(5), p. 054501.
[8] Irey, R. K., 1968, "Errors in the One-Dimensional Fin Solution," ASME J. Heat Transfer, **90**(1), pp. 175–176.

[9] Laor, K., and Kalman, H., 1996, "Performance and Optimum Dimensions of Different Cooling Fins With a Temperature-Dependent Heat Transfer Coefficient," Int. J. Heat Mass Transfer, **39**(9), pp. 1993–2003.
[10] Su, R. J., and Hwang, J. J., 1998, "Analysis of Transient Heat Transfer in a Cylindrical Pin Fin," J. Thermophys. Heat Transfer, **12**(2), pp. 281–283.
[11] Kang, H. S., and Look, D. C., Jr., 2007, "Optimization of a Thermally Asymmetric Convective and Radiating Annular Fin," Heat Transfer Eng., **28**(4), pp. 310–320.
[12] Yu, L. T., and Chen, C. K., 1999, "Optimization of Circular Fins With Variable Thermal Parameters," J. Franklin Inst., **336B**, pp. 77–95.
[13] Kang, H. S., 2007, "Optimum Performance and Design of a Rectangular Fin," Int. J. Automotive Technology, **8**(6), pp. 705–711.
[14] Yeh, R.-H., 1997, "An Analytical Study of the Optimum Dimensions of Rectangular Fins and Cylindrical Pin Fins," Int. J. Heat Mass Transfer, **40**(15), pp. 3607–3615.
[15] Chung, B. F. T., and Iyer, J. R., 1993, "Optimum Design of Longitudinal Rectangular Fins and Cylindrical Spines With Variable Heat Transfer Coefficient," Heat Transfer Eng., **14**(1), pp. 31–42.

Inverse Heat Conduction in a Composite Slab With Pyrolysis Effect and Temperature-Dependent Thermophysical Properties

Jianhua Zhou
Research Assistant Professor
Mem. ASME

Yuwen Zhang[1]
Professor
Fellow ASME
e-mail: zhangyu@missouri.edu

J. K. Chen
William & Nancy Thompson Professor
Fellow ASME

Z. C. Feng
Professor
Fellow ASME

Department of Mechanical and Aerospace Engineering,
University of Missouri,
Columbia, MO 65211

The inverse heat conduction problem (IHCP) in a one-dimensional composite slab with rate-dependent pyrolysis chemical reaction and outgassing flow effects is investigated using the iterative regularization approach. The thermal properties of the composites are considered to be temperature-dependent. A nonlinear conjugate gradient method formulation is developed and applied to solve the IHCP in an organic composite slab whose front-surface is subjected to high intensity periodic laser heating.
[DOI: 10.1115/1.4000050]

Keywords: composite, inverse heat conduction, pyrolysis, temperature-dependent thermal properties

1 Introduction

To defeat the invasion of the enemy military object, high energy laser (HEL) weapons can be employed because they offer the advantages of remote delivery of energy at the speed of light onto a small spot of military target. It is critical to know the temperature at the heated front target surface in order to accurately understand the damage mechanism in laser-irradiated composite materials. However, the heated front-surface is either inaccessible or too hot so that it is unsuitable for attaching a sensor. Therefore, the heated (front) surface temperature has to be determined indirectly by solving an inverse heat conduction problem (IHCP) [1,2] based on the transient temperature and/or heat flux measured at the back-surface.

Although IHCPs were extensively studied for different applications in the past (e.g., Refs. [3–6]); little work was done for periodic laser irradiation to a remote surface. The laser energy is delivered to the surface in a periodic way due to target-spinning or atmosphere variation. Recently, the authors proposed a low-error IHCP algorithm to reconstruct the front-surface heating condition with back-surface measurement data [7]. It was demonstrated that high-accuracy solutions can be obtained by choosing the front-surface heat flux as the unknown function and using the back-surface temperature measurement data as the boundary condition while the back-surface heat flux measurement data are employed in the objective function. However, the applicability of the authors' work is limited to pure conduction cases. To the best of the authors' knowledge, little is done for the inverse problem in composite materials subjected to laser heating, although Aviles-Ramos et al. [8] developed an exact solution for the IHTPs in a two-layer composite material, the pyrolysis effect is not considered in their model.

2 Inverse Problem and Solution Method

Consider a 1D composite slab with a thickness of L, as shown in Fig. 1. The two parts, fiber and matrix, are depicted on a microscale size level. The black regions represent fibers; the gray regions denote the matrix. Initially, the slab is uniformly at temperature T_0 and is subjected to a high intensity laser heating from time $t>0$ at its front-surface ($x=0$). Before the pyrolysis occurs, only pure conduction takes place in the composite. When the temperature of the composite is elevated to the pyrolysis temperature, the composite material undergoes chemical decomposition. Meanwhile, the decomposing process gives off gaseous byproducts that flow outward from the pyrolysis zone to the composite surface (the white regions in Fig. 1 represent the gas flow channels).

The inverse problem can be mathematically described as

$$C(T)\frac{\partial T}{\partial t} = \frac{\partial}{\partial x}\left[k(T)\frac{\partial T}{\partial x}\right] + Q(x,t) + G(x,t) \tag{1}$$

$$T = T_0 \quad \text{for} \quad 0 \le x \le L, \quad t = 0 \tag{2}$$

$$T(L,t) = 2 \cdot Y_{TL}(t) - T_g \quad \text{for} \quad x = L, \quad t > 0 \tag{3}$$

where T is the temperature of the solid part during pyrolysis, C and k are the volume specific heat and thermal conductivity of the solid part, respectively, $Q(x,t)$ is the heat generation arising from the thermal decomposition, $G(x,t)$ is the heat source due to the convective heat exchange between the pyrolysis gas and the solid part, $Y_{TL}(t)$ is the average solid-gas temperature measured at back-surface, and T_g is the temperature of pyrolysis gas, which is calculated based on pyrolysis kinetics simulation [9].

The purpose of the IHCP is to reconstruct the heat flux $q_1(t)$ and temperature $T_1(t)$ at the front-surface of the composite material based on the measured temperature $Y_{TL}(t)$ and heat flux $Y_{qL}(t)$ at the back-surface and the temperature readings $Y_{T1}(t)$ at an interior position.

The thermal conductivity k is considered to be temperature-dependent and will change as pyrolysis progresses [10]. The volume specific heat C, is pyrolysis process dependent and is computed based on a 3D porous structure using the local volume averaging method [11].

The conjugate gradient method (CGM) [2] is applied to solve the inverse problem formulated as above. The inverse solution is obtained by minimizing the objective function

$$S[q_1(t)] = \int_0^{t_f} \{Y_{qL}(t) - q[L,t;q_1(t)]\}^2 dt + \int_0^{t_f} \{Y_{T1}(t) - T[x_1,t;q_1(t)]\}^2 dt \tag{4}$$

where t_f is the final simulation time, $q[L,t;q_1(t)]$ is the estimated heat flux at the back-surface, and $T[x_1,t;q_1(t)]$ is the estimated average temperature at the interior position x_1.

[1]Corresponding author.

Contributed by the Heat Transfer Division of ASME for publication in the JOURNAL OF HEAT TRANSFER. Manuscript received February 17, 2009; final manuscript received July 14, 2009; published online December 28, 2009. Editor: Yogesh Jaluria.

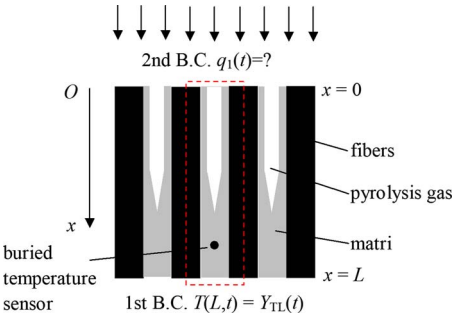

Fig. 1 Physical model

The CGM mathematical formulations and solution procedure for nonlinear inverse problems are similar to those in Ref. [7].

3 Results and Discussion

3.1 Generation of Simulated Measurement Data. Instead of conducting actual experiment, the measurement data of temperature and heat flux are generated numerically by solving a direct problem with radiation and convection boundary conditions. To account for the measurement error, one extra term is added to heat flux measurement $Y_{qL\text{exact}}(t)$

$$Y_{qL}(t) = Y_{qL\text{exact}}(t) + \omega\delta_q \tag{5}$$

where $Y_{qL\text{exact}}(t)$ is the simulated measurement data from the direct problem, δ_q is the standard deviation of the heat flux measurement and is set as a percentage of the highest heat flux value at the back-surface, and ω is a random variable between −1 and 1.

It is assumed that the temperature readings at back-surface and interior locations contain no errors since temperature can be measured with much less uncertainty compared with the heat flux [12].

3.2 Results of IHCP. The temperature-dependent thermal conductivities of the composites can be found in Ref. [10]. The thermal properties of fiber and matrix are the same as those in Ref. [9]. The thickness and initial temperature of the composite are $L=2.5$ mm and $T_0=300$ K, respectively. The front-surface heat flux is assumed to be uniform and can be expressed as $q=q_c+0.1q_c \sin(2\pi ft)$ (W/m^2), where q_c is a constant heat flux and f is the frequency of the sinusoidal component. Unless specified otherwise, $q_c=200$ W/cm^2, $\delta_q=5\%\cdot[Y_{qL\text{exact}}(t)]_{\max}$ and $\delta_b=3\%\cdot[Y_{qL\text{exact}}(t)]_{\max}$.

The thermal properties of the pyrolysis gas are considered to be those of CO_2 [13]. The pyrolysis kinetics parameters are from Ref. [9].

Figure 2 displays the inverse heat conduction results for the case where the frequency of the periodic laser heat flux is $f=2$ Hz and the interior temperature sensor is located at $x_1=1/3L$. Figures 2(*a*) and 2(*b*) show the heat sources $Q(0, t)$ and $G(0, t)$ due to decomposition chemical reaction and pyrolysis gas flow, respectively. As can be seen, the peak value of heat source $Q(x, t)$ due to chemical reaction takes place at about 0.1 s while the gas flow heat source peak occurs at some later time (about 0.3 s). In Fig. 2(*b*), the wiggles near time 0.3 s is due to the finite time step used in the simulations. It is seen in Fig. 2(*c*) that the recovered front-surface temperature agrees well with the exact solution obtained by solving the direct problem.

Our numerical experiments show that the frequency of the periodic laser heating flux f plays a dominant role in the inverse solution accuracy. As the frequency of the periodic laser heating flux increases, a convergent inverse solution can only be obtained when the interior temperature sensor is moved closer toward the laser heating surface. The positions of the interior temperature

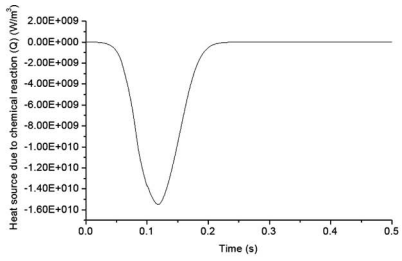

(a) Heat source $Q(0, t)$ due to decomposition chemical reaction

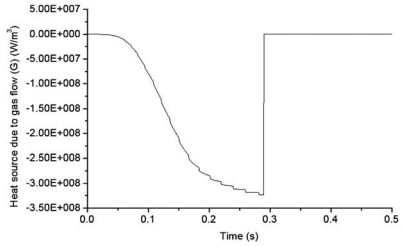

(b) Heat source $G(0, t)$ due to pyrolysis gas flow

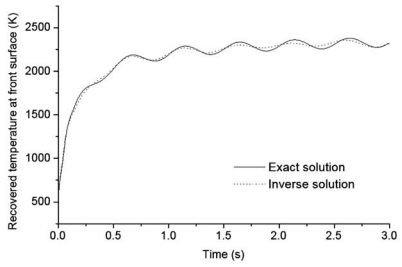

(c) Recovered front-surface temperature

Fig. 2 Heat sources and recovered temperatures for the case where the interior temperature sensor is located at $x_1=L/3$ and the frequency of the periodic laser heating is $f=2$ Hz

sensor as a function of the periodic laser flux frequency are presented in Fig. 3. The vertical coordinate variable is the relative position of the temperature sensor. For example, a value of 0.2 means that the position of the temperature sensors is at $x=0.2L$. As can be seen, when the frequency of the periodic laser heating flux is increased, the interior temperature sensor needs to be moved toward the laser heating surface.

Figure 4 shows the results for the composite material whose thermal properties (thermal conductivity and specific heat) con-

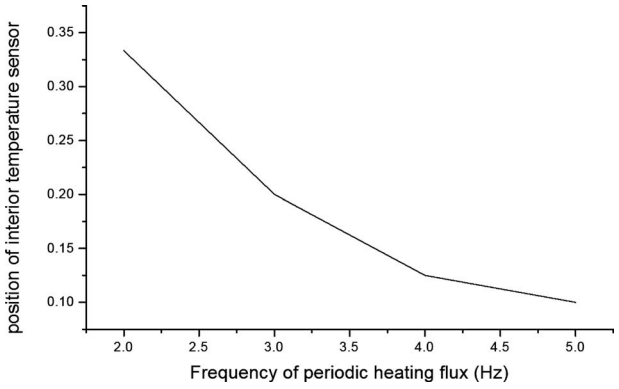

Fig. 3 Positions of interior temperature sensor as a function of periodic heating frequency

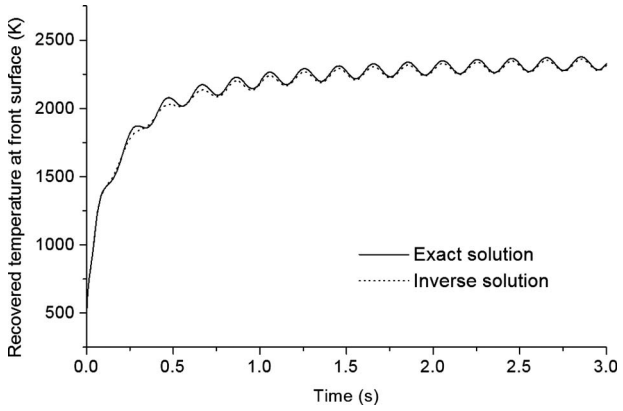

Fig. 4 Recovered temperatures for composite material whose thermal properties include 5% random errors (frequency f = 5 Hz, single interior temperature sensor is used at $x_1 = L/10$)

tains 5% random perturbation. The frequency of the periodic laser heating flux is 5 Hz. A single interior temperature sensor located at $x_1 = L/10$ is used. It is seen that the inverse algorithm and the numerical model formulated in this study have very good performance in handling this type of problems where uncertainty-containing thermal properties are involved.

4 Conclusions

A conjugate gradient model is formulated to recover the periodic heating condition at the front-surface of a composite material using the back-surface temperature and heat flux measurements as well as interior temperature readings. The pyrolysis chemical reaction and outgassing flow effects are incorporated in the model. It is found that for the low-thermal-conductivity composite materials, it is necessary to measure the temperatures at an interior location as additional information to recover the front-surface periodic heating condition. It is also shown that the frequency of the periodic laser heating flux plays a dominant role in the determination of the interior sensor position. The robustness of the proposed algorithm is also demonstrated by its capability in handling the case of thermophysical properties with uncertainties.

Acknowledgment

This work is funded by the Test and Evaluation/Science & Technology (T&E/S&T) Program through the U.S. Army Program Executive Office for Simulation, Training, and Instrumentation's Contract No. W900KK-08-C-0002. Valuable discussions with Dr. James L. Griggs are gratefully appreciated.

References

[1] Beck, J. V., Blackwell, B., and St-Clair, C. R., 1985, *Inverse Heat Conduction: Ill Posed Problems*, Wiley, New York.
[2] Özisik, M. N., and Orlande, H. R. B., 2000, *Inverse Heat Transfer: Fundamentals and Applications*, Taylor & Francis, New York.
[3] Yang, C. Y., and Chen, C. K., 1996, "The Boundary Estimation in Two-Dimensional Inverse Heat Conduction Problems," J. Phys. D, **29**, pp. 333–339.
[4] Emery, A. F., Nenarokomov, A. V., and Fadale, T. D., 2000, "Uncertainties in Parameter Estimation: The Optimal Experimental Design," Int. J. Heat Mass Transfer, **43**, pp. 3331–3339.
[5] Frankel, J. I., Osborne, G. E., and Taira, K., 2006, "Stabilization of Ill-Posed Problems Through Thermal Rate Sensors," J. Thermophys. Heat Transfer, **20**, pp. 238–246.
[6] Loulou, T., and Scott, E. P., 2006, "An Inverse Heat Conduction Problem With Heat Flux Measurements," Int. J. Numer. Methods Eng., **67**, pp. 1587–1616.
[7] Zhou, J., Zhang, Y., Chen, J. K., and Feng, Z. C., 2009, "Inverse Heat Conduction in a Finite Slab With Measured Back Heat Flux," *Proceedings of the 47th AIAA Aerospace Sciences Meeting*, Orlando, FL, Jan. 5–9.
[8] Aviles-Ramos, C., Haji-Sheikh, A., and Beck, J. V., 1998, "Exact Solution of Heat Conduction in Composite Materials and Application to Inverse Problems," ASME J. Heat Transfer, **120**, pp. 592–599.
[9] Zhou, J., Zhang, Y., Chen, J. K., and Smith, D. E., 2008, "A Non-Equilibrium Thermal Model for Rapid Heating and Pyrolysis of Organic Composites," ASME J. Heat Transfer, **130**, pp. 064501.
[10] Chen, J. K., Perea, A., and Allahdadi, F. A., 1995, "A Study of Laser/Composite Material Interactions," Compos. Sci. Technol., **54**, pp. 35–44.
[11] Kaviany, M., 1995, *Principles of Heat Transfer in Porous Media*, 2nd ed., Springer-Verlag, New York.
[12] Childs, P. R. N., 2002, "Advances in Temperature Measurement," Adv. Heat Transfer, **36**, pp. 111–181.
[13] Incropera, F. P., Dewitt, D. P., Bergman, T. L., and Lavine, A. S., 2007, *Fundamentals of Heat and Mass Transfer*, 6th ed., Wiley, New York.

Investigation of Heat Transfer Enhancement Through Permeable Fins

A.-R. A. Khaled[1]
Department of Thermal Engineering and Desalination Technology,
King Abdulaziz University,
P.O. Box 80204,
Jeddah 21589, Saudi Arabia
e-mail: akhaled@kau.edu.sa

Heat transfer through rectangular permeable fins is modeled and analyzed theoretically in this work. The free stream fluid flow is considered to be normal to the upper surface of the permeable fin. The flow across the permeable fin is permitted in this work. The continuity, momentum, and energy equations are solved for the fluid flow using a similarity transformation and an iterative tridiagonal finite difference method. As such, a correlation for the Nusselt number is generated as functions of the Prandtl number (Pr) and dimensionless suction velocity (f_o) for $0.7<Pr\leq 10$ and $0<f_o\leq 5$, respectively. The energy equation for the permeable fin is generated and solved analytically using the developed correlation. It was found that permeable fins may have superiority in transferring heat over ordinary solid fins, especially at large f_o values and moderate holes-to-fin surface area ratios. In addition, the critical holes-to-fin surface area ratios, below which the permeable fins transfer more heat than solid fins, is found to increase as Pr and f_o increase. Finally, this work paves a way for a new passive method for enhancing heat transfer.
[DOI: 10.1115/1.4000056]

Keywords: conduction, heat transfer, enhancement, permeable fins, convection

1 Introduction

Fins are quite often found in the industry, especially in the heat exchanger industry as in finned tubes of double-pipe, shell-and-tube, and compact heat exchangers [1–6]. As an example, fins are used in air cooled finned tube heat exchangers like car radiators and heat rejection devices. Also, they are used in refrigeration systems, and in condensing central heating exchangers. Moreover, fins are also utilized in the cooling of large heat flux electronic devices, and in the cooling of gas turbine blades [7].

According to design aspects, fins can have simple designs such as rectangular, triangular, parabolic, annular, and pin rod fins [1–3]. On the other hand, fin design can be complicated such as spiral fins [8,9]. In addition, fins can have a simple network as in finned tubes heat exchangers [6]. In contrast, they can be arranged in a complex network, as can be seen in the works of Alebrahim and Bejan [10], Almogbel and Bejan [11], and Khaled [12]. Moreover, fins can be further classified, based on the fact whether they interact thermally with a single fluid reservoir or with two different fluid reservoirs. Example of works, based on the last classification, are those of Khaled [13,14]. In addition, fins can be attached to the surface, as in the works in Refs. [1–9], or they may have roots in the heated/cooled walls [15]. Finally, fins can be solid [1–9], porous [16], or permeable [14]. Of special interest to this work is the permeable fins, which received less attention in the literature.

In this work, rectangular permeable fins have been theoretically investigated. The flow is assumed to be normal to the upper fin surface area. As such, normal flow across the fin is induced. Appropriate forms of momentum and energy equations have been developed for the flow above the fin surface area and across its thickness. The major controlling dimensionless parameters affecting the heat transfer through the fin are determined. A well defined performance indicator [16] was selected. As such, extensive parametric study is performed in order to thermally characterize the permeable fins, and to explore their superiority in conducting heat as compared with solid rectangular fins.

2 Problem Formulation

2.1 Convection Heat Transfer Coefficient for a Permeable Plate. Consider a plate fin having a thickness t and a width $2H$. The plate is permeable and it is subjected to a fluid flow normal to its width with a far stream normal velocity of V, as shown in Fig. 1. The conservation of mass necessitates that the axial velocity gradient near the plate surface be equal to the following:

$$\frac{du_\infty}{dx}=\left(\frac{V-\varepsilon V_o(x)}{l}\right) \tag{1}$$

where x is along the width direction of the plate, and it starts at its center. $V_o(x)$ is the suction speed at the plate, and ε is the ratio of holes area to the total surface area. l is the characteristic normal distance between the far stream and the plate. $V_o(x)$ can be related to the pressure across the permeable plate through the following relation:

$$V_o(x)=\frac{d}{12\mu}\left(\frac{d}{t}\right)(P_\infty(x)-P_a) \tag{2}$$

where P_a and d are the atmospheric pressure and the diameter of the holes on the plate, respectively.

Applying the Bernoulli equation between the far stream and the stream near the plate excluding the viscous boundary layer will result in the following relation:

$$\frac{(P_\infty(x)-P_a)}{\rho}=\frac{V^2}{2}-\frac{u_\infty^2}{2}-\frac{\varepsilon^2V_o^2}{2}\cong\frac{V^2}{2}-\frac{u_\infty^2}{2} \tag{3}$$

The term $\varepsilon^2V_o^2/2$ is negligible, relative to $V^2/2$, especially for viscous fluids or when d and (d/t) are very small. As such, it is eliminated. Substituting Eq. (3) in Eq. (2), then in Eq. (1), results in the following differential equation:

$$\frac{du_\infty}{u_\infty^2+a^2}=cdx \tag{4}$$

where a and c are defined as follows:

$$c=\frac{\varepsilon}{24}\left(\frac{\rho}{\mu}\right)\left(\frac{d}{l}\right)\left(\frac{d}{t}\right) \tag{5}$$

$$a=\sqrt{\frac{V}{lc}}\sqrt{1-\frac{\varepsilon}{24}\mathrm{Re}_d\left(\frac{d}{t}\right)} \tag{6}$$

where

$$\mathrm{Re}_d=\frac{\rho Vd}{\mu}$$

The solution of Eq. (4) is as follows:

$$u_\infty(x)=a\tan(acx) \tag{7}$$

For small values of c, as when viscous fluids or when (d/t) is very small, Eq. (4) can be reduced to the following:

[1]Corresponding author.

Contributed by the Heat Transfer Division of ASME for publication in the JOURNAL OF HEAT TRANSFER. Manuscript received April 10, 2009; final manuscript received July 30, 2009; published online December 29, 2009.

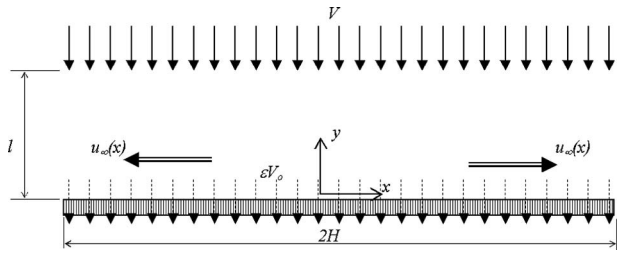

Fig. 1 Schematic diagram for the present permeable plate with flow configuration

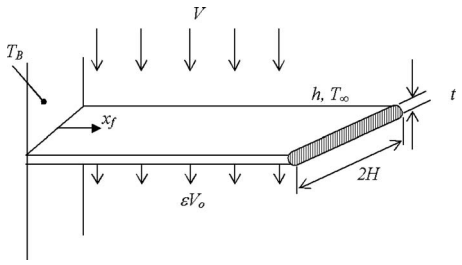

Fig. 2 Schematic diagram for the permeable fin

$$u_\infty(x) = a^2 cx = u_{\infty o}\left(\frac{x}{H}\right) \tag{8}$$

where

$$u_{\infty o} = \frac{VH}{l}\left(1 - \frac{\varepsilon}{24}\left(\frac{d}{t}\right)\mathrm{Re}_d\right) \tag{9}$$

Therefore, the suction velocity at the plate and the pressure gradient above the plate can be calculated, and they are equal to

$$V_o = \frac{1}{24}\left(\frac{d}{t}\right)\mathrm{Re}_d\, V \tag{10}$$

$$\frac{dP_\infty}{dx} = -\rho\frac{u_{\infty o}^2}{H^2}x \tag{11}$$

The dimensionless continuity, momentum, and energy equations in the boundary layer above the permeable plate's surface are

$$\frac{\partial \bar{u}}{\partial \bar{x}} + \frac{\partial \bar{v}}{\partial \bar{y}} = 0 \tag{12}$$

$$\bar{u}\frac{\partial \bar{u}}{\partial \bar{x}} + \bar{v}\frac{\partial \bar{u}}{\partial \bar{y}} = -\frac{d\bar{p}_\infty}{d\bar{x}} + \frac{1}{\mathrm{Re}_H}\frac{\partial^2 \bar{u}}{\partial \bar{y}^2} \tag{13}$$

$$\bar{u}\frac{\partial \theta}{\partial \bar{x}} + \bar{v}\frac{\partial \theta}{\partial \bar{y}} = \frac{1}{\mathrm{Re}_H\,\mathrm{Pr}}\frac{\partial^2 \theta}{\partial \bar{y}^2} \tag{14}$$

where $\bar{u}=u/u_{\infty o}$, $\bar{v}=v/u_{\infty o}$, $\bar{x}=x/H$, $\bar{y}=y/H$, $\theta(\eta)=(T-T_\infty)/(T_w - T_\infty)$, $\bar{P}_\infty=P_\infty/(\rho u_{\infty o}^2/H)$, and $\mathrm{Re}_H=\rho u_{\infty o}H/\mu$.

Equations (13) and (14) can be transformed to similarity equations when the following variables are implemented:

$$\eta = \frac{\bar{y}}{\sqrt{\mathrm{Re}_H}} \tag{15a}$$

$$f'(\eta) = \frac{\overline{u(x,y)}}{\bar{x}} \tag{15b}$$

$$f(\eta) = -\sqrt{\mathrm{Re}_H}\,\overline{v(x,y)} \tag{15c}$$

The resulting similarity equations are

$$f''' + ff'' - f'^2 = -1.0 \tag{16}$$

$$\frac{1}{\mathrm{Pr}}\theta'' + f\theta' = 0 \tag{17}$$

and the similarity boundary conditions are

$$f'(0) = 0 \tag{18a}$$

$$f(0) = \varepsilon f_o \tag{18b}$$

$$f'(\eta \to \infty) = 1.0 \tag{18c}$$

$$\theta(0) = 1.0 \tag{18d}$$

$$\theta(\eta \to \infty) = 0 \tag{18e}$$

where $f_o=(V_o/u_{\infty o})\sqrt{\mathrm{Re}_H}$. The local Nusselt number is calculated from

$$Nu = \frac{hH}{k} = \frac{H}{k}\left(\frac{-k\,\partial T/\partial y|_{y=0}}{[T_w - T_\infty]}\right) = -\theta'(0)\sqrt{\mathrm{Re}_H} \tag{19}$$

2.2 Permeable Fins. Consider a permeable fin with uniform a cross section $A_C(A_C=2Ht)$ and a perimeter $P(P=2H)$, having a thermal conductivity k_f and a very long length. The fin encounters uniform flow (with density ρ, and specific heat c_p) across its thickness with an average suction speed at the upper surface of εV_o. The upper surface of the fin is subjected to convection with a free stream temperature of T_∞, and a convection coefficient h (calculated from correlation (28)), as shown in Fig. 2. The direction of V_o is from the upper surface to the lower surface of the fin.

Assuming that the temperature of the fin T_f does not vary along the cross section of the fin, the differential energy equation is equal to

$$k_f(1-\varepsilon)A_C\frac{d^2T_f}{dx_f^2} - \{hP(1-\varepsilon) + \rho c_P \varepsilon V_o\}(T_f - T_\infty) = 0 \tag{20}$$

where the rate of heat conducted through the fin at any section is

$$q_x = -\left(k_f(1-\varepsilon)A_C\frac{dT_f}{dx_f} + k\varepsilon A_C\frac{dT}{dx_f}\right) \cong -k_f(1-\varepsilon)A_C\frac{dT_f}{dx} \tag{21}$$

and the differential rate of heat convected by the fluid over and through the permeable fin from a section of length dx_f is calculated from the following:

$$dq_{\mathrm{conv}} = \{hP(1-\varepsilon) + \rho c_p V_o \varepsilon\}dx_f(T_f - T_\infty) \tag{22}$$

The boundary conditions for Eq. (20) are

$$T_f(x_f = 0) = T_B \tag{23a}$$

$$\left.\frac{dT_f}{dx_f}\right|_{x_f \to \infty} = 0 \tag{23b}$$

The solution of Eq. (20) subject to boundary conditions (23) is

$$\theta(x_f) = \frac{T_f(x_f) - T_\infty}{T_B - T_\infty} = e^{-\sqrt{h_{\mathrm{eff}}P/k_f A_C}x_f} \tag{24}$$

where h_{eff} is the total convection heat transfer coefficient. It is equal to

$$h_{\mathrm{eff}} = h + \rho c_P\left(\frac{\varepsilon}{1-\varepsilon}\right)V_o = \frac{k\sqrt{\mathrm{Re}_H}}{H}\left[-\theta'(0) + \left(\frac{\varepsilon}{1-\varepsilon}\right)\mathrm{Pr}\, f_o\right] \tag{25}$$

Define the fin indicator γ as follows:

Table 1 Comparison between $-\theta'(0)$ obtained using the present method and that reported in Ref. [18] when $f_o=0$

Pr	$-\theta'(0)$ (Present method)	$-\theta'(0)$ (Ref. [18])	Difference (%)
0.7	0.4959	0.496	0.02
0.8	0.5227	0.523	0.057
1	0.5705	0.570	0.088
5	1.0434	1.043	0.038
10	1.3388	1.344	0.39

$$\gamma = \frac{q_f}{(q_f)_{\varepsilon=0}} = \frac{-k_f(1-\varepsilon)A_C dT_f/dx_f|_{x_f=0}}{\sqrt{k_f A_C h_{\varepsilon=0}}P(T_B - T_\infty)} \tag{26}$$

As such, γ is equal to

$$\gamma = (1-\varepsilon)\sqrt{\frac{u_{\infty o}}{u_{\infty}|_{\varepsilon=0}}}\sqrt{\frac{h_{\text{eff}}}{h_{\varepsilon=0}}} \cong (1 - \varepsilon)\sqrt{\left[\frac{\theta'(0)}{\theta'(0)|_{\varepsilon=0}} - \left(\frac{\varepsilon}{1-\varepsilon}\right)\frac{\text{Pr}\, f_o}{\theta'(0)|_{\varepsilon=0}}\right]} \tag{27}$$

3 Numerical Methods, Validation, and a Useful Correlation

Equations (16) and (17) were descritized using three points center differencing. The resulting tridiagonal system of algebraic equations was then solved using the well established Thomas algorithm [17]. Iterations were implemented in the solution of Eq. (16) because the second and third terms of this equation are nonlinear. The values of 0.01 and 10^{-7} were selected for $\Delta\eta$ and the convergence criteria for the maximum difference for f' between the two consecutive iterations. The results of solving Eqs. (16) and (17) are used to calculate the Nusselt number for different Pr and f_o values. Table 1 shows a comparison between the Nusselt number values obtained by the present numerical method, and reported values obtained from Ref. [18], when $f_o=0$. The percentage difference is less than 0.5%. This led to a great confidence in the obtained results.

3.1 Useful Correlation. Nusselt numbers obtained from the present method is correlated with the different values of Pr and f_o values through the following correlation:

$$\text{Nu} = \frac{hH}{k} = \frac{b_1\,\text{Pr}^{b_2}(\text{Pr}^{b_3} + b_4(\varepsilon f_o)^{b_5})^{b_6}}{(1 + b_7\,\text{Pr}^{b_8})}\sqrt{\text{Re}_H} \tag{28}$$

where

$$b_1 = 1.0605 \tag{29a}$$

$$b_2 = 1.1424 \tag{29b}$$

$$b_3 = -1.6070 \tag{29c}$$

$$b_4 = 4.7261 \tag{29d}$$

$$b_5 = 2.3293 \tag{29e}$$

$$b_6 = 0.3782 \tag{29f}$$

$$b_7 = 0.6104 \tag{29g}$$

$$b_8 = 0.4466 \tag{29h}$$

$$R^2 = 0.99967 \tag{29i}$$

R^2 is the correlation coefficient ($R^2 \leq 1$). Correlation (28) is valid for the following ranges of Pr and f_o:

$$0.7 < \text{Pr} \leq 10; \tag{30a}$$

$$0 < f_o \leq 5.0 \tag{30b}$$

4 Discussions of the Results

Figure 3 illustrates the effects of the suction dimensionless velocity f_o and the holes-to-fin surface area ratio ε on the fin performance factor γ. This figure shows that γ can be greater than 1, especially at large f_o values for a given ε, indicating the superiority of permeable fins over solid rectangular fins. This superiority increases as Pr increases, as seen from Fig. 4. Moreover, Fig. 3 shows that the critical holes-to-fin surface area ratio, below which permeable fins transfers more heat than solid fins, increases as

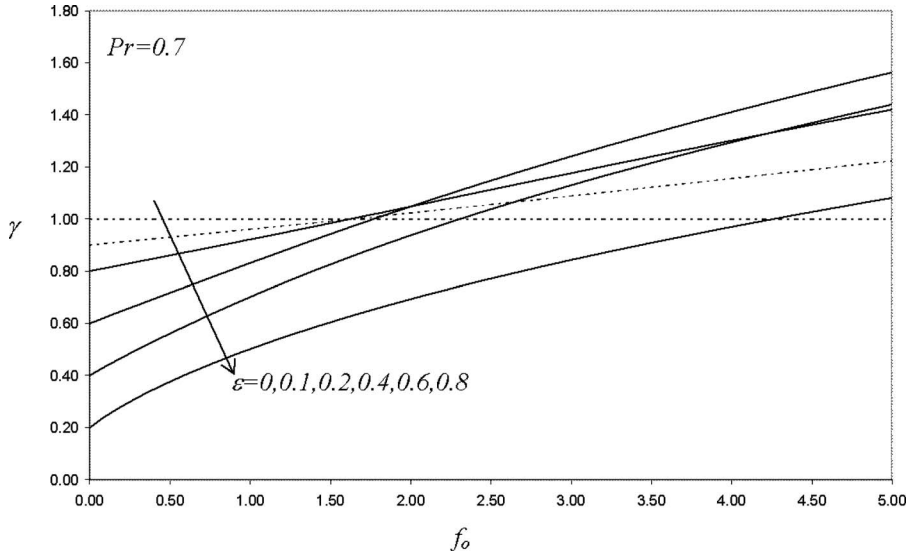

Fig. 3 Effects of the dimensionless suction velocity f_o and the holes-to-fin surface area ratio ε on the fin performance indicator γ

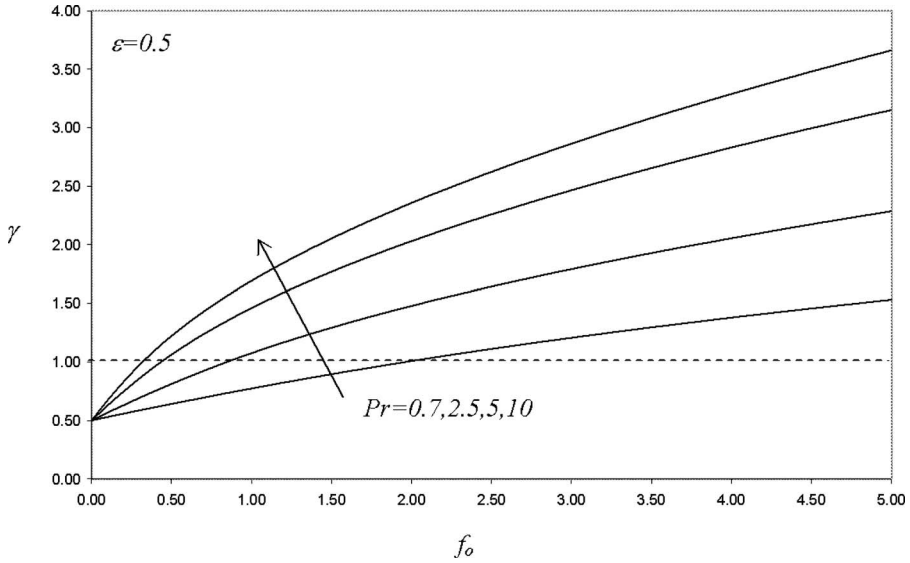

Fig. 4 Effects of the dimensionless suction velocity f_o and Prandtl number Pr on the fin performance indicator γ

suction velocities increase. However, the increase in the heat transfer is significant at moderate holes-to-fin surface area ratio (maximum at $\varepsilon=0.4$)

Figure 5 shows the effect of the holes-to-fin area ratio ε on the fin performance indicator γ at different dimensionless suction velocities f_o. As ε increases, the axial conduction through the fin decreases, while transverse convection increases. As such, it is expected to have an optimum value of γ at a specific ε, as shown in Fig. 5. Moreover, the critical ε that maximizes γ is found to increase as f_o increases. Figures 4 and 5 show clearly that the specific ε values, below which $\gamma>1$, increases as both f_o and Pr increase.

5 Conclusions

Heat transfer through rectangular permeable fins was modeled theoretically in this work. The fins were assumed to be subjected to normal fluid flow over their upper surface. The flow across the permeable fin was considered. The continuity, momentum, and energy equations were solved for the fluid flow using a similarity transformation and an iterative tridiagonal finite difference method. Therefore, the Nusselt number is obtained and correlated as functions of the Prandtl number Pr and dimensionless suction velocity f_o for the following ranges: $0.7<\mathrm{Pr}\leq 10$ and $0<f_o\leq 5$. The energy equation for the permeable fin was generated and solved analytically. The following findings were reported.

- Permeable fins transfers more heat than ordinary solid fins at higher f_o values.
- Maximum heat transfer enhancements in permeable fins can be obtained at moderate holes-to-fin surface area ratio ($0.3<\varepsilon<0.7$).
- The critical holes-to-fin surface area ratio, below which permeable fins transfers more heat than ordinary solid fins, increases as Pr and f_o increase.

Finally, this work reports an additional passive method for heat transfer enhancements.

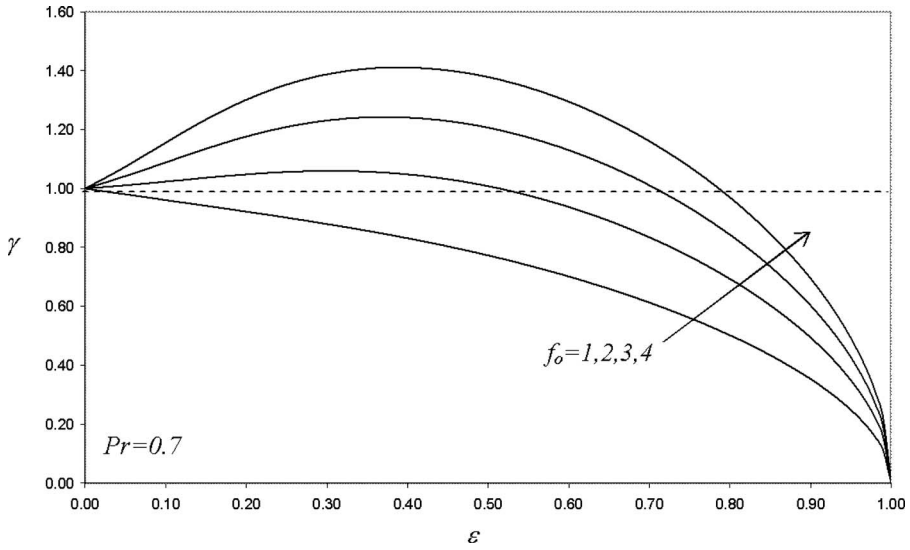

Fig. 5 Effects of holes-to-fin area ratio ε and dimensionless suction velocity f_o on the fin performance indicator γ

Nomenclature

A_C = fin cross-sectional area
a = the first flow configuration constant
c = the second flow configuration constant
d = holes diameter
f_o = dimensionless suction velocity parameter
f' = dimensionless transformed axial velocity above the fin surface
H = half width of the fin
h = convection heat transfer coefficient
h_{eff} = total convection heat transfer coefficient
k = fluid thermal conductivity
k_f = fin thermal conductivity
l = characteristic normal distance
P = perimeter of the fin cross section
P_∞ = free stream pressure
P_a = atmospheric pressure
q_f = fin heat transfer rate
Re_H = external flow Reynolds number
Re_d = Reynolds number for the flow through the fin
T = temperature field
T_f = fin temperature
T_B = base temperature
T_∞ = free stream temperature
t = fin thickness
$u_{\infty o}$ = reference axial velocity
V = free stream velocity
V_o = suction velocity across the fin
x = coordinate axis along the fin width
$\overline{x}$ = dimensionless x-coordinate
x_f = fin axial coordinate
y = transverse coordinate axis
$\overline{y}$ = dimensionless y-coordinate

Greek Symbols

ε = ratio of holes area to the fin surface area
η = similarity transformation variable
θ = dimensionless temperature
γ = fin performance factor

References

[1] Kays, W. M., 1955, "Pin-Fin Heat-Exchanger Surfaces," ASME J. Heat Transfer, **77**, pp. 471–483.
[2] Kern, D. O., and Kraus, A. D., 1972, *Extended Surface Heat Transfer*, McGraw-Hill, New York.
[3] Kraus, A. D., 1988, "Sixty-Five Years of Extended Surface Technology (1922–1987)," Appl. Mech. Rev., **41**, pp. 321–364.
[4] Schenider, P. J., 1955, *Conduction Heat Transfer*, Addison-Wesley, Reading, MA.
[5] Kraus, A. D., Aziz, A., and Welty, J. R., 2001, *Extended Surface Heat Transfer*, Wiley, New York.
[6] Kakaş, S., and, Liu, H., 2001, *Heat Exchangers: Selection, Rating, and Thermal Design*, CRC, Boca Raton, FL.
[7] Sahiti, N., Lemouedda, A., Stojkovie, D., Durst, F., and Franz, E., 2006, "Performance Comparison of Pin Fin In-Duct Flow Arrays With Various Cross-Sections," Appl. Therm. Eng., **26**, pp. 1176–1192.
[8] Nuntaphan, A., Kiatsiriroat, T., and Wang, C. C., 2005, "Air Side Performance at Low Reynolds Number of Cross-Flow Heat Exchanger Using Crimped Spiral Fins," Int. Commun. Heat Mass Transfer, **32**, pp. 151–165.
[9] Manglik, R. M., and Bergles, A. E., 2002, "Swirl Flow Heat Transfer and Pressure Drop With Twisted-Tape Inserts," Adv. Heat Transfer, **36**, pp. 183–266.
[10] Alebrahim, A., and Bejan, A., 1999, "Constructal Trees of Circular Fins for Conductive and Convective Heat Transfer," Int. J. Heat Mass Transfer, **42**, pp. 3585–3597.
[11] Almogbel, M., and Bejan, A., 2000, "Cylindrical Trees of Pin Fin," Int. J. Heat Mass Transfer, **43**, pp. 4285–4297.
[12] Khaled, A.-R. A., 2007, "Heat Transfer Enhancement in Hairy Fin Systems," Appl. Therm. Eng., **27**, pp. 250–257.
[13] Khaled, A.-R. A., 2006, "'Maximizing Heat Transfer Through Joint Fin Systems," Trans. ASME, Ser. C: J. Heat Transfer, **128**, pp. 203–206.
[14] Khaled, A.-R. A., 2009, "Analysis of Heat Transfer Through Bi-Convection Fins," Int. J. Therm. Sci., **48**, pp. 122–132.
[15] Khaled, A.-R. A., 2008, "Heat Transfer Analysis Through Solar and Rooted Fins," Trans. ASME, Ser. C: J. Heat Transfer, **130**, p. 074503.
[16] Kiwan, S., and Al-Nimr, M. A., 2001, "Using Porous Fin for Heat Transfer Enhancement," ASME J. Heat Transfer, **123**, pp. 790–795.
[17] Blottner, F. G., 1970, "Finite-Difference Methods of Solution of the Boundary-Layer Equations," AIAA J., **8**, pp. 193–205.
[18] Oosthuizen, P. H., and Naylor, D., 1999, *Introduction to Convective Heat Transfer Analysis*, McGraw-Hill, New York, p. 113–114.

Heat Transfer Characterization of Two Isothermal Circular Cylinders in Proximity

Taeheon Han

Kyung-Soo Yang[1]
e-mail: ksyang@inha.ac.kr

Kyongjun Lee

Department of Mechanical Engineering,
Inha University,
Incheon 402-751, Republic of Korea

Heat transfer on two nearby isothermal circular cylinders of equal diameter immersed in a uniform crossflow at Re=120 and Pr=0.7 was numerically studied. We consider all possible arrangements of the two cylinders in terms of the distance between the two cylinders and the inclination angle with respect to the direction of the main flow. It turns out that significant changes in the characteristics of heat transfer are noticed depending on how they are positioned, resulting in quantitative changes in heat transfer coefficients of both cylinders. Collecting all of the numerical results obtained, we propose a contour diagram for averaged Nusselt number for each of the two cylinders. The geometrical symmetry implied in the flow configuration allows one to use those diagrams to estimate heat transfer rates on two isothermal circular cylinders of equal diameter arbitrarily positioned in physical space with respect to the main flow direction.
[DOI: 10.1115/1.4000058]

Keywords: convective heat transfer, immersed boundary method, flow pattern, vortex shedding, wake interaction

1 Introduction

The forced convective heat transfer around a group of cylinders immersed in crossflow is often found in many practical engineering applications. For instance, heat transfer between coolant flow and heat exchanger tubes, or heat transfer on fuel rods in a nuclear reactor, to name a few. In designing such devices, it is essential to understand effects of interference among adjacent wakes on heat transfer characteristics as well as flow fields to achieve high efficiency in their performance. In particular, forced convective heat transfer on two nearby isothermal circular cylinders of equal diameter immersed in crossflow would be the simplest model of all heat transfer models with wake interaction.

Many researchers have been involved in studying forced convective heat transfer in the flow configuration involving one or multiple circular cylinders. Juncu [1] carried out a numerical investigation on the convective heat transfer in laminar flow past two circular cylinders placed in tandem, and Buyruk [2] also numerically studied convective heat transfer in the presence of multiple circular cylinders in a staggered arrangement as well as in tandem in the laminar flow range. Yamamoto and Hattori [3] considered laminar heat transfer in side-by-side arrangements and reported their numerical results. Zhou and Yiu [4] experimentally studied turbulent heat transfer when the two cylinders are aligned in the direction of the main flow. Li et al. [5] and Wang and Georgiadis [6] carried out numerical investigations on laminar heat transfer with in-line arrays of cylinders in the laminar flow range.

In spite of the numerous studies carried out so far, the case where the two cylinders are placed in a staggered position has been rarely studied, especially in the laminar flow regime. In this investigation, heat transfer characteristics of the flow past two nearby isothermal circular cylinders of equal diameter at Re=120 and Pr=0.7 are numerically studied as a basic model. Flow-induced forces at Re=100 in the same flow configuration was numerically studied and published elsewhere [7]. We focus on the effects of the cylinder arrangement on the heat transfer characteristics. The possibility of radiative heat transfer is excluded based on the assumption that the temperature difference between the cylinders and the freestream is moderate. We consider all possible arrangements of the two circular cylinders in terms of the distance between them and the inclination angle of the line connecting their centers with respect to the main flow direction. Collecting all of the results obtained, we propose an averaged Nusselt number diagram ("map") for each cylinder to provide an overall picture on the heat transfer characteristics.

2 Formulation and Numerical Methodology

The current investigation requires a parametric study where numerous numerical simulations must be performed with various values of the streamwise center distance (L) and the vertical center distance (H) (see Fig. 1(a)). This kind of parametric study demands a considerable amount of computing resources; the computing efforts can be significantly reduced by employing an immersed boundary method, which facilitates implementing the solid surfaces of the arbitrarily positioned cylinders on a Cartesian grid system [8].

The governing equations for two-dimensional incompressible flow, modified for the immersed boundary method, are as follows:

$$\frac{\partial u_j}{\partial x_j} - q = 0 \tag{1}$$

$$\frac{\partial u_i}{\partial t} + \frac{\partial u_i u_j}{\partial x_j} = -\frac{\partial p}{\partial x_i} + \frac{1}{\mathrm{Re}}\frac{\partial^2 u_i}{\partial x_j \partial x_j} + f_i, \quad i = 1,2 \tag{2}$$

$$\frac{\partial \Theta}{\partial t} + \frac{\partial u_j \Theta}{\partial x_j} = \frac{1}{\mathrm{Re}\ \mathrm{Pr}}\frac{\partial^2 \Theta}{\partial x_j \partial x_j} + h_E \tag{3}$$

where u_i (or u, v), p, q, and Θ represent the velocity components in the x_i (or x, y) direction, pressure, mass source/sink, and temperature, respectively; f_i and h_E denote momentum forcing and heat source/sink, respectively. All of the physical variables except p and Θ are nondimensionalized by the uniform freestream velocity (U) and the cylinder diameter (D). Pressure is nondimensionalized by far-field pressure (P_∞) and the dynamic pressure. Fluid temperature (T) is nondimensionalized as $\Theta=(T-T_\infty)/(T_s-T_\infty)$, where T_s and T_∞ represent cylinder surface temperature and far-field temperature, respectively. Reynolds number (Re) and Prandtl number (Pr) are defined as UD/ν and ν/α, respectively, where ν and α are kinematic viscosity and thermal diffusivity, respectively. The governing equations were discretized using a finite-volume method in a nonuniform staggered Cartesian grid system. A second-order central differencing was employed for spatial discretization of derivatives. A hybrid scheme was used for time advancement; nonlinear terms were explicitly advanced by a third-order Runge–Kutta scheme, and the other terms were implicitly advanced by the Crank–Nicolson method. A fractional step method was employed to decouple the continuity and momentum equations. The Poisson equation resulting from the second stage of the fractional step method was solved by a multigrid

[1]Corresponding author.

Contributed by the Heat Transfer Division of ASME for publication in the JOURNAL OF HEAT TRANSFER. Manuscript received May 5, 2009; final manuscript received July 23, 2009; published online December 29, 2009. Review conducted by Yogesh Jaluria.

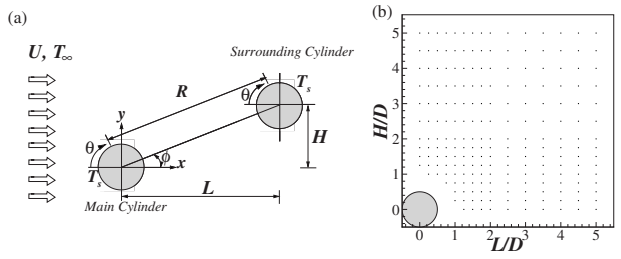

Fig. 1 Physical configuration: (*a*) staggered position of two circular cylinders and (*b*) locations of the center of the surrounding circular cylinder, indicated by dots

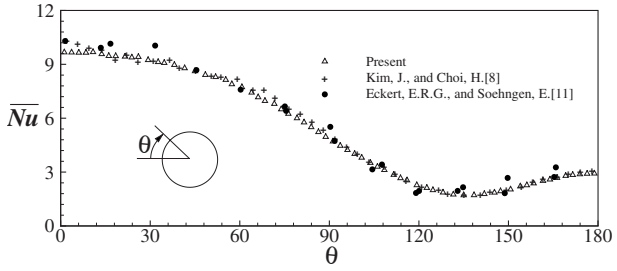

Fig. 3 Distribution of $\overline{Nu}$ along the cylinder surface at Re=120 and Pr=0.7

method. For a detailed description of the numerical method used in the current investigation, see Yang and Ferziger [9].

3 Boundary Conditions and Numerical Parameters

The main cylinder (MC) is fixed at the origin of the coordinate system, and the surrounding cylinder (SC) is placed at various locations relative to the MC, which are represented by the dots in Fig. 1(*b*).

Actual computations have been carried out only for the cases where the SC is located in the first quadrant (Fig. 1(*b*)). The total number of cases computed is 208. In the case where the center distance (R, Fig. 1(*a*)) is minimum, $L/D=0.25$, $H/D=1.0$, and the inclination angle (ϕ, Fig. 1(*a*)) is 75.96 deg. The entire computational domain was defined as $-35D \le x \le 35D$ and $-50D \le y \le 50D$. For each cylinder, 48×48 uniform grid cells in the x and y directions, respectively, were allocated, and uniform grid cells of the same cell size as in the cylinder region were employed between the cylinders. In the other region of the domain, nonuniform grid cells were used. The numerical resolution was determined by a grid-refinement study to ensure grid-independency. In the case of $L/D=1.5$ and $H/D=0.5$ (Fig. 2), for instance, the total number of grid cells were 552×312, while 720×528 grid cells were allocated in the most demanding case ($L/D=5.0$ and $H/D=5.0$).

The no-slip condition ($u=0$ and $v=0$) and isothermal condition ($\Theta=1$) were imposed on the cylinder surfaces; a Dirichlet boundary condition ($u=U$, $v=0$, and $\Theta=0$) was used on the inlet boundary of the computational domain, while a convective boundary condition [10] was employed for u_i and Θ at the outlet. A slip boundary condition ($\partial u/\partial y=0$ and $v=0$) and the adiabatic condition ($\partial\Theta/\partial y=0$) were imposed on the other boundaries.

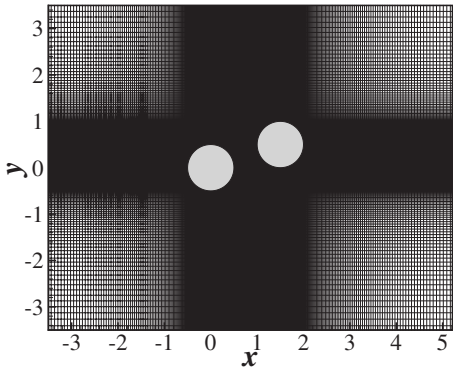

Fig. 2 Computational mesh for the case of $L/D=1.5$ and $H/D=0.5$

4 Verification of the Code

For verifying our numerical methodology and resolution, flow past single circular cylinder at Re=100 was computed and our results were compared with other authors' results (see Table 1 of Ref. [7]). Next, the mean Nusselt number ($\overline{Nu}$) defined as the time mean of hD/k (here, h and k represent heat transfer coefficient and heat conductivity of the fluid, respectively) was computed for the flow past single circular cylinder at Re=120 and Pr=0.7, and was presented as a function of the surface angle (θ) in Fig. 3, together with other authors' experimental [11] and numerical [8] results, revealing good agreement with them. The two test results mentioned above verify that the numerical scheme and resolution used in the present simulation are adequate and reliable in computing temperature field as well as flow field.

5 Results and Discussion

The results presented in this section correspond to Re=120 and Pr=0.7 with $T_s > T_\infty$. Since the Nusselt number can be regarded as the nondimensionalized temperature gradient ($\partial\Theta/\partial n|_s$, where n denotes the coordinate normal to the cylinder surface) evaluated on the cylinder surface, a large $\overline{Nu}$ implies a high heat transfer rate at that specific location.

Various flow patterns are observed depending on the arrangements of the two cylinders, affecting heat transfer characteristics accordingly. To obtain an overall picture on how heat transfer from a heated circular cylinder is affected by its neighbor of equal temperature, we collected all of the results computed and proposed a contour diagram of the Nusselt number averaged in time and on the cylinder surface ($\overline{Nu_s}$) for each cylinder on a L-H plane. In this way, one can easily identify influences of a neighboring cylinder on the heat transfer characteristics of the single cylinder case. For convenience, $\overline{Nu_s}$ is normalized by the value corresponding to the single cylinder case ($\overline{Nu_s}=5.36$) in the contour diagrams.

Although the actual computations have been carried out only for the first quadrant (Fig. 1(*b*)), the results can be easily extended to the other quadrants by using the symmetries implied in the flow configuration.

In Fig. 4(*a*), contours of normalized $\overline{Nu_s}$ are presented for the MC. Recall that the MC is fixed at the origin. The maximum value of $\overline{Nu_s}$ (5.56) is noticed at $L/D=-1.0$ and $H/D=\pm 2.5$, while the minimum value (1.78) is identified at $L/D=-1.25$ and $H/D=0.0$. It is seen that the heat transfer from the MC is significantly reduced when the MC is positioned in the near-wake region of the SC.

Figure 4(*b*) shows contours of normalized $\overline{Nu_s}$ for the SC. Again, the MC is located at the origin. In fact, Fig. 4(*b*) is the reflection of Fig. 4(*a*) with respect to the H axis, and is included here for convenience. The maximum value (5.56) at $L/D=1.0$ and $H/D=\pm 2.5$, and with the minimum value (1.78) at $L/D=1.25$ and $H/D=0.0$. The heat transfer from the SC is greatly reduced in

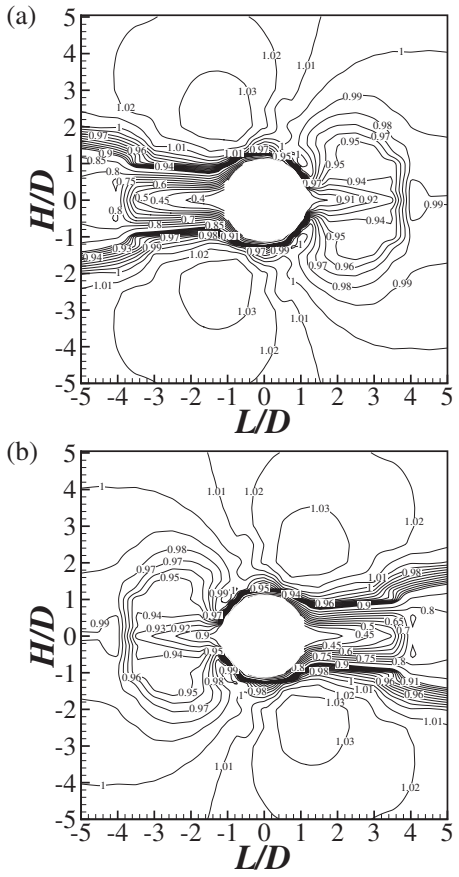

Fig. 4 Contours of normalized $\overline{Nu_s}$ for two staggered circular cylinders at Re=120, Pr=0.7, normalized with the single cylinder value ($\overline{Nu_s}$=5.36): (*a*) main cylinder and (*b*) surrounding cylinder. Increment: 0.05 from 0.4 to 0.9; 0.01 from 0.9 to 1.05.

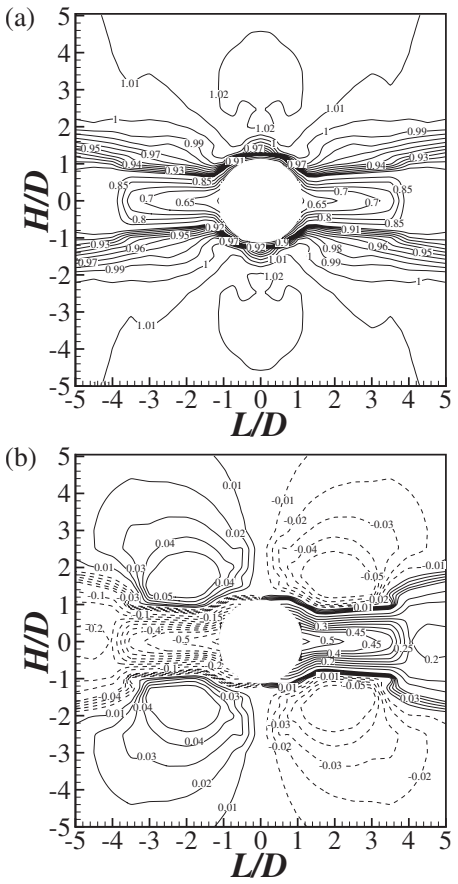

Fig. 5 (*a*) Contours of average of normalized $\overline{Nu_s}$ of the main and the surrounding cylinders and (*b*) contours of difference in normalized $\overline{Nu_s}$ between the main cylinder and the surrounding cylinder; Re=120 and Pr=0.7. Increment: (*a*) 0.05 from 0.4 to 0.9; 0.01 from 0.9 to 1.05; and (*b*) 0.05 from −0.6 to −0.05 and from 0.05 to 0.6; 0.01 from −0.05 to 0.05.

tandem arrangements, and is very sensitive to H in an approximate range of $1.0<L/D<4.0$ and $-1.0<H/D<1.0$.

To identify which arrangements effectively enhance the overall heat transfer from both cylinders, we present the averaged $\overline{Nu_s}$ of the two cylinders, normalized with the single cylinder value, in Fig. 5(*a*). The averaged value of $\overline{Nu_s}$ for the two cylinders reaches the maximum (5.52) at $L/D=0.0$ and $H/D=\pm 3.0$, and the minimum (3.25) at $L/D=\pm 1.0$ and $H/D=\pm 0.25$. Since $\overline{Nu_s}=5.36$ in the case of the single cylinder immersed in the freestream at Re =120 and Pr=0.7, the contour lines corresponding to $\overline{Nu_s}=5.36$ (normalized $\overline{Nu_s}=1.0$) serve as the "boundaries" of heat transfer effectiveness. Any SC arrangement outside these boundaries enhances the overall heat transfer from the two cylinders due to the "blockage effect." For example, when the two cylinders are placed side-by-side, the blockage effect is significant, producing $\overline{Nu_s}$ values of the two cylinders higher than that of the corresponding single cylinder case, if $|H|/D\geq 1.75$.

When the SC is located inside the boundaries, the overall heat transfer diminishes because heated fluid in the wake of the upstream cylinder is "fed" to the downstream cylinder. In addition, the suppression of vortex shedding also contributes to the reduction in heat transfer capacity. For example, when the two cylinders are placed in tandem, the vortex shedding of the upstream cylinder is completely suppressed if $|L|/D<3.75$, resulting in the reduced heat transfer capacities of both cylinders. For $|L|/D\geq 4.0$, the vortex shedding of the upstream cylinder resumes, leading to active heat transfer from both cylinders.

Figure 5(*b*) illustrates the difference in normalized $\overline{Nu_s}$ between the MC and the SC, indicating the relative effectiveness in heat transfer. The solid line implies that $\overline{Nu_s}$ of the MC is higher than that of the SC, and dashed lines do the opposite. In a typical case where $\overline{Nu_s}$ of the SC is higher than that of the MC ($L/D=2.0$ and $H/D=2.0$), the vortex shedding of the MC is weakened by the presence of the SC, causing a reduced heat transfer from the base-point region. On the contrary, the vortex shedding of the SC is active, causing an enhanced heat transfer from its base-point region. On the other portion of each cylinder surface, the heat transfer capacity is quite similar. Thus, $\overline{Nu_s}$ of the SC is higher than that of the MC in this particular case (Fig. 5(*b*)).

6 Conclusions

A parametric study has been carried out to investigate the effects of wake interactions on the heat transfer characteristics of two neighboring circular cylinders of equal diameter and temperature, immersed in the freestream of lower temperature at Re =120 and Pr=0.7.

Collecting all of the results actually computed and utilizing the symmetries implied in the flow configuration, we propose the contour diagrams of $\overline{Nu_s}$ for the MC and the SC, respectively, in order to provide an overall picture on the heat transfer characteristics of each cylinder under an interaction with a neighboring one. Contour diagrams for the average and the difference of $\overline{Nu_s}$ between the MC and the SC are also presented to identify which arrangements are effective for the overall heat transfer and to indicate the relative effectiveness in heat transfer, respectively.

Acknowledgment

This work was financially supported by the Underwater Vehicle Research Center in Korea.

References

[1] Juncu, G., 2007, "A Numerical Study of Momentum and Forced Convection Heat Transfer Around Two Tandem Circular Cylinders at Low Reynolds Numbers. Part II: Forced Convection Heat Transfer," Int. J. Heat Mass Transfer, **50**, pp. 3799–3808.

[2] Buyruk, E., 2002, "Numerical Study of Heat Transfer Characteristics on Tandem Cylinders, Inline and Staggered Tube Banks in Cross-Flow of Air," Int. Commun. Heat Mass Transfer, **29**(3), pp. 355–366.

[3] Yamamoto, H., and Hattori, N., 1996, "Flow and Heat Transfer Around a Single Row of Circular Cylinders," Heat Transfer-Jpn. Res., **25**(3), pp. 192–200.

[4] Zhou, Y., and Yiu, M. W., 2006, "Flow Structure, Momentum and Heat Transport in a Two-Tandem-Cylinder Wake," J. Fluid Mech., **548**, pp. 17–48.

[5] Li, T., Deen, N. G., and Kuipers, J. A. M., 2005, "Numerical Investigation of Hydrodynamics and Mass Transfer for In-Line Fiber Arrays in Laminar Cross-Flow at Low Reynolds Numbers," Chem. Eng. Sci., **60**(7), pp. 1837–1847.

[6] Wang, M., and Georgiadis, J. G., 1996, "Conjugate Forced Convection in Crossflow Over a Cylinder Array With Volumetric Heating," Int. J. Heat Mass Transfer, **39**(7), pp. 1351–1361.

[7] Lee, K., Yang, K. S., and Yoon, D. H., 2009, "Flow-Induced Forces on Two Circular Cylinders in Proximity," Comput. Fluids, **38**(1), pp. 111–120.

[8] Kim, J., and Choi, H., 2004, "An Immersed-Boundary Finite-Volume Method for Simulation of Heat Transfer in Complex Geometries," KSME Int. J., **18**(6), pp. 1026–1035.

[9] Yang, K. S., and Ferziger, J. H., 1993, "Large-Eddy Simulation of Turbulent Obstacle Flow Using a Dynamic Subgrid-Scale Model," AIAA J., **31**(8), pp. 1406–1413.

[10] Kim, D. H., Yang, K. S., and Senda, M., 2004, "Large Eddy Simulation of Turbulent Flow Past a Square Cylinder Confined in a Channel," Comput. Fluids, **33**(1), pp. 81–96.

[11] Eckert, E. R. G., and Soehngen, E., 1952, "Distribution of Heat Transfer Coefficients Around Circular Cylinders in Crossflow at Reynolds Numbers From 20 to 500," ASME Trans. J. Heat Transfer, **74**, pp. 343–347.